SEISMICITY IN VOLCANIC AREAS

EDITED BY: Derek Keir, Luca De Siena, Cecile Doubre, Jessica Helen Johnson, Francesco Maccaferri and Luigi Passarelli

PUBLISHED IN: Frontiers in Earth Science

frontiers Research Topics

Frontiers eBook Copyright Statement

The copyright in the text of individual articles in this eBook is the property of their respective authors or their respective institutions or funders. The copyright in graphics and images within each article may be subject to copyright of other parties. In both cases this is subject to a license granted to Frontiers.

The compilation of articles constituting this eBook is the property of Frontiers.

Each article within this eBook, and the eBook itself, are published under the most recent version of the Creative Commons CC-BY licence. The version current at the date of publication of this eBook is CC-BY 4.0. If the CC-BY licence is updated, the licence granted by Frontiers is automatically updated to the new version.

When exercising any right under the CC-BY licence, Frontiers must be attributed as the original publisher of the article or eBook, as applicable.

Authors have the responsibility of ensuring that any graphics or other materials which are the property of others may be included in the CC-BY licence, but this should be checked before relying on the CC-BY licence to reproduce those materials. Any copyright notices relating to those materials must be complied with.

Copyright and source acknowledgement notices may not be removed and must be displayed in any copy, derivative work or partial copy which includes the elements in question.

All copyright, and all rights therein, are protected by national and international copyright laws. The above represents a summary only. For further information please read Frontiers' Conditions for Website Use and Copyright Statement, and the applicable CC-BY licence.

ISSN 1664-8714
ISBN 978-2-88974-330-8
DOI 10.3389/978-2-88974-330-8

About Frontiers

Frontiers is more than just an open-access publisher of scholarly articles: it is a pioneering approach to the world of academia, radically improving the way scholarly research is managed. The grand vision of Frontiers is a world where all people have an equal opportunity to seek, share and generate knowledge. Frontiers provides immediate and permanent online open access to all its publications, but this alone is not enough to realize our grand goals.

Frontiers Journal Series

The Frontiers Journal Series is a multi-tier and interdisciplinary set of open-access, online journals, promising a paradigm shift from the current review, selection and dissemination processes in academic publishing. All Frontiers journals are driven by researchers for researchers; therefore, they constitute a service to the scholarly community. At the same time, the Frontiers Journal Series operates on a revolutionary invention, the tiered publishing system, initially addressing specific communities of scholars, and gradually climbing up to broader public understanding, thus serving the interests of the lay society, too.

Dedication to Quality

Each Frontiers article is a landmark of the highest quality, thanks to genuinely collaborative interactions between authors and review editors, who include some of the world's best academicians. Research must be certified by peers before entering a stream of knowledge that may eventually reach the public - and shape society; therefore, Frontiers only applies the most rigorous and unbiased reviews.
Frontiers revolutionizes research publishing by freely delivering the most outstanding research, evaluated with no bias from both the academic and social point of view. By applying the most advanced information technologies, Frontiers is catapulting scholarly publishing into a new generation.

What are Frontiers Research Topics?

Frontiers Research Topics are very popular trademarks of the Frontiers Journals Series: they are collections of at least ten articles, all centered on a particular subject. With their unique mix of varied contributions from Original Research to Review Articles, Frontiers Research Topics unify the most influential researchers, the latest key findings and historical advances in a hot research area! Find out more on how to host your own Frontiers Research Topic or contribute to one as an author by contacting the Frontiers Editorial Office: frontiersin.org/about/contact

SEISMICITY IN VOLCANIC AREAS

Topic Editors:
Derek Keir, University of Southampton, United Kingdom
Luca De Siena, Johannes Gutenberg University Mainz, Germany
Cecile Doubre, Université de Strasbourg, France
Jessica Helen Johnson, University of East Anglia, United Kingdom
Francesco Maccaferri, Vesuvius Observatory, National Institute of Geophysics and Volcanology (INGV), Italy
Luigi Passarelli, Istituto Nazionale di Geofisica e Vulcanologia, Italy

Citation: Keir, D., De Siena, L., Doubre, C., Johnson, J. H., Maccaferri, F., Passarelli, L., eds. (2022). Seismicity in Volcanic Areas. Lausanne: Frontiers Media SA. doi: 10.3389/978-2-88974-330-8

Table of Contents

05 ***Editorial: Seismicity in Volcanic Areas***
Derek Keir, Luca De Siena, Cécile Doubre, Jessica H. Johnson, Francesco Maccaferri and Luigi Passarelli

08 ***Balance Between Deformation and Seismic Energy Release: The Dec 2018 'Double-Dike' Intrusion at Mt. Etna***
Alessandro Bonaccorso and Elisabetta Giampiccolo

15 ***The Coupled Magmatic and Hydrothermal Systems of the Restless Aluto Caldera, Ethiopia***
M. Wilks, N. Rawlinson, J.-M. Kendall, A. Nowacki, J. Biggs, A. Ayele and J. Wookey

29 ***Mt. Etna Feeding System and Sliding Flank: A New 3D Image From Earthquakes Distribution in a Customisable GIS***
R. Guardo, L. De Siena and C. Dreidemie

41 ***Characterization of Acoustic Infrasound Signals at Volcán de Fuego, Guatemala: A Baseline for Volcano Monitoring***
A. Diaz-Moreno, A. Roca, A. Lamur, B. H. Munkli, T. Ilanko, T. D. Pering, A. Pineda and S. De Angelis

57 ***RETREAT: A REal-Time TREmor Analysis Tool for Seismic Arrays, With Applications for Volcano Monitoring***
Patrick J. Smith and Christopher J. Bean

70 ***Seismo-Acoustic Characterization of Mount Cleveland Volcano Explosions***
Alexandra M. Iezzi, David Fee, Matthew M. Haney and John J. Lyons

89 ***Earthquake Analysis Suggests Dyke Intrusion in 2019 Near Tarawera Volcano, New Zealand***
Thomas W. Benson, Finnigan Illsley-Kemp, Hannah C. Elms, Ian J. Hamling, Martha K. Savage, Colin J. N. Wilson, Eleanor R. H. Mestel and Simon J. Barker

100 ***Practical Volcano-Independent Recognition of Seismic Events:* VULCAN.ears *Project***
Guillermo Cortés, Roberto Carniel, Philippe Lesage, M. Ángeles Mendoza and Ivo Della Lucia

111 ***The 2002–2005 Changbaishan Volcanic Unrest Triggered by the 2002* M 7.2 *Wangqing Deep Focus Earthquake***
Guoming Liu, Chenyu Li, Zhigang Peng, Yinan Liu, Yu Zhang, Dongyang Liu, Maoliang Zhang and Bo Pan

123 ***Dike Inflation Process Beneath Sakurajima Volcano, Japan, During the Earthquake Swarm of August 15, 2015***
Midori Koike and Haruhisa Nakamichi

141 ***The Impact of Complex Volcanic Plumbing on the Nature of Seismicity in the Developing Magmatic Natron Rift, Tanzania***
Miriam Christina Reiss, James D. Muirhead, Amani S. Laizer, Frederik Link, Emmanuel O. Kazimoto, Cynthia J. Ebinger and Georg Rümpker

162 ***Source Mechanism of Seismic Explosion Signals at Santiaguito Volcano, Guatemala: New Insights From Seismic Analysis and Numerical Modeling***
Alicia Rohnacher, Andreas Rietbrock, Ellen Gottschämmer, William Carter, Yan Lavallée, Silvio De Angelis, Jackie E. Kendrick and Gustavo Chigna

179 ***Seismicity of the Northern Volcanic Zone of Iceland***
Páll Einarsson and Bryndís Brandsdóttir

196 ***Thermo-Rheological Properties of the Ethiopian Lithosphere and Evidence for Transient Fluid Induced Lower Crustal Seismicity Beneath the Ethiopian Rift***
Ameha A. Muluneh, Derek Keir and Giacomo Corti

207 ***Imaging the Subsurface Structure of Mount Agung in Bali (Indonesia) Using Volcano-Tectonic (VT) Earthquake Tomography***
Ardianto Ardianto, Andri Dian Nugraha, Haunan Afif, Devy Kamil Syahbana, David P. Sahara, Zulfakriza Zulfakriza, Sri Widiyantoro, Awali Priyono, Shindy Rosalia, Asep Saepuloh, Kasbani Kasbani, Faiz Muttaqy, Puput P. Rahsetyo, Imam C. Priambodo and Martanto Martanto

220 ***Repeating Earthquakes During Multiple Phases of Unrest and Eruption at Mount Agung, Bali, Indonesia, 2017***
John J. Wellik, Stephanie G. Prejean and Devy K. Syahbana

231 ***Use of Local Seismic Network in Analysis of Volcano-Tectonic (VT) Events Preceding the 2017 Agung Volcano Eruption (Bali, Indonesia)***
David P. Sahara, Puput P. Rahsetyo, Andri Dian Nugraha, Devy Kamil Syahbana, Sri Widiyantoro, Zulfakriza Zulfakriza, Ardianto Ardianto, Aria W. Baskara, Shindy Rosalia, Martanto Martanto and Haunan Afif

246 ***Campi Flegrei, Vesuvius and Ischia Seismicity in the Context of the Neapolitan Volcanic Area***
Flora Giudicepietro, Patrizia Ricciolino, Francesca Bianco, Stefano Caliro, Elena Cubellis, Luca D'Auria, Walter De Cesare, Prospero De Martino, Antonietta M. Esposito, Danilo Galluzzo, Giovanni Macedonio, Domenico Lo Bascio, Massimo Orazi, Lucia Pappalardo, Rosario Peluso, Giovanni Scarpato, Anna Tramelli and Giovanni Chiodini

267 ***Revealing 60 years of Earthquake Swarms in the Southern Red Sea, Afar and the Gulf of Aden***
Joël Ruch, Derek Keir, Luigi Passarelli, Domenico Di Giacomo, Ghebrebrhan Ogubazghi and Sigurjón Jónsson

frontiers in Earth Science

EDITORIAL
published: 24 December 2021
doi: 10.3389/feart.2021.829460

Editorial: Seismicity in Volcanic Areas

Derek Keir[1,2], Luca De Siena[3], Cécile Doubre[4], Jessica H. Johnson[5], Francesco Maccaferri[6] and Luigi Passarelli[7]*

[1]School of Ocean and Earth Science, University of Southampton, Southampton, United Kingdom, [2]Dipartimento di Scienze della Terra, University of Florence, Florence, Italy, [3]Institute of Geosciences, Johannes Gutenberg University Mainz, Mainz, Germany, [4]Institut Terre et Environnement de Strasbourg, ITES, CNRS, ENGEES, Université de Strasbourg, Strasbourg, France, [5]School of Environmental Sciences, University of East Anglia, Norwich, United Kingdom, [6]Vesuvius Observatory, National Institute of Geophysics and Volcanology, Naples, Italy, [7]National Institute of Geophysics and Volcanology, Bologna, Italy

Keywords: earthquake, volcano, tectonic, magma "mush", dyke, eruption, seismicity analysis

Editorial on the Research Topic

Seismicity in Volcanic Areas

Seismic activity (e.g., earthquakes, tremors) beneath volcanic areas is primarily caused by the dynamic interaction of molten rock and hydrothermal fluids with the solid host rock, by fracturing and fragmentation of the magma itself, and by tectonic processes interacting with the volcano. In addition, near-surface phenomena such as explosions and rockfalls at a volcanic edifice also produce seismic events. At volcano observatories globally, the real-time monitoring of the spatial and temporal patterns of seismic events is an essential geophysical tool to quantify the state of unrest, and forecast eruptions successfully. Seismic waveforms, earthquake catalogues and earthquake ray-path properties commonly supplement this tool to model the complex processes responsible for the earthquakes quantitatively, and to image subsurface magmatic and tectonic structures. Independent constraints provided by other disciplines such as geodesy and structural geology also significantly help scientists to understand the volcanic processes. Recent advances in earthquake recording technology, computing power and algorithms in artificial intelligence, allow processing and interpretation of large and complex multi-parametric datasets and scenarios.

"*Our Seismicity in Volcanic Areas*" research topic attracted 19 original research articles using seismic datasets to understand the processes acting in volcanic areas and their evolution in space and time. Such studies are critical for building a picture of how, when and where molten rock and volatile phases move and are stored in the crust, and how fluids interact with stressed and fractured rock. The result is an enhanced understanding of magmatic systems and more robust forecasts of future volcanic activity.

For this Editorial we divided the contributions to the research topic in five categories, which are articles that use: 1) Infrasound and seismic waveform data to constrain explosion related seismic sources; 2) Analysis and modelling of the space-time evolution of specific seismic swarms to understand the subsurface processes and triggering mechanisms causing them; 3) Spatially-large and/or temporarily-long earthquake catalogues to better understand subsurface magmatic processes and plumbing systems; 4) Earthquake tomography to image 3D variability of rock properties and interpret subsurface magmatic structures; 5) Automation of real-time analyses for large seismic datasets. A number of the studies in all of these themes also incorporate multi-disciplinary constraints to aid the interpretation of seismic results.

Seismology and infrasound are among the most popular techniques for monitoring volcanoes since they offer an excellent temporal resolution of subsurface and near-surface earthquakes and eruptive activity. However, a key element of volcano monitoring is understanding what magmatic and volcanic processes are responsible for seismic and acoustic signals observed. Diaz-Moreno et al. present the first comprehensive observational baseline characterization of acoustic signals at Volcán de Fuego in Guatemala. They find that acoustic signals are dominantly short-duration acoustic

OPEN ACCESS

Edited and reviewed by:
Valerio Acocella,
Roma Tre University, Italy

***Correspondence:**
Derek Keir
d.keir@soton.ac.uk

Specialty section:
This article was submitted to Volcanology, a section of the journal Frontiers in Earth Science

Received: 05 December 2021
Accepted: 07 December 2021
Published: 24 December 2021

Citation:
Keir D, De Siena L, Doubre C, Johnson JH, Maccaferri F and Passarelli L (2021) Editorial: Seismicity in Volcanic Areas. Front. Earth Sci. 9:829460. doi: 10.3389/feart.2021.829460

transients linked to discrete ash-rich and gas-rich explosions, and other indirect volcanic processes such as lahars. They also find more sustained seismo-acoustic tremors and chugging emissions likely sourced from pressurized magma and gas and explosions. Iezzi et al. and Rohnacher et al. use both seismic and infrasound data to quantitatively model source characteristics of seismo-acoustic signals associated with explosions at Mount Cleveland in the United States, and Santiaguito volcano in Guatemala, respectively. Iezzi et al. identify time lags in the arrival time of the acoustic and seismic signals associated with explosions. Using a combination of waveform cross-correlation and analysis of particle motion dip angles, they show that a varying explosion source depth between 1.5 and 2 km within the conduit likely plays a dominant role in the observed variations in time lag. Rohnacher et al. constrain source mechanisms and depths of seismic signals leading up to explosions using array and particle motion analyses. Results suggest the seismic signals are caused by the opening of tensile fractures at a few hundred meters depth followed by rapid gas ascent leading to the explosion.

Earthquake swarms in volcanic areas carry a wealth of information on their causative processes. Spatial and temporal evolution of earthquake hypocentres and their source characteristics can be diagnostic on whether earthquake swarms are caused by magmatic intrusion or due to aseismic processes (i.e., pore-pressure diffusion and aseismic slip) facilitated by crustal fluid redistribution. However, independent observations such as deformation and geophysical data, modelling processes along with consideration of tectonic setting are essential to single out the triggering mechanisms of seismicity in volcanic areas. Seven contributions of this research topic clearly represent good practice of using multiple complementary datasets to eventually understand the nature of seismic activity. For example, fast migration velocity of accurately located earthquake hypocentres and normal faulting earthquakes inferred by Benson et al. indicate that the 2019 earthquake swarm underneath Tarawera volcano, New Zealand, is the seismic signature of a dike intrusion at the brittle-ductile transition. During the 2015 earthquake swarm at Sakurajima volcano, Japan, Midori and Nakamichi interpret the spatial distribution of precisely located earthquakes and the temporal changes in their source mechanism as caused by local stress changes imparted by a fast inflating dike intrusion. Bonaccorso and Giampiccolo successfully apply an equation that links the seismic energy associated to dike-induced earthquakes to the geodetically inferred dimension of the 2018 complex dike intrusion at Mt. Etna, Italy. Future fine tuning of this equation could eventually allow the magnitude of radiated seismic energy to be used as a proxy for the size of dike intrusions in early warning applications.

The analysis of earthquake catalogues combined with thermo-rheological modelling constrained by various geophysical observations at the Main Ethiopian Rift performed by Muluneh et al. indicate lower-crust earthquake swarms sourced from redistribution of crustal fluids. The authors focus on differences in lower crustal seismicity directly beneath, and outboard the rift valley, and estimate lower crust permeability values. They inferred that pore-pressure diffusion processes are the driving mechanism for the observed swarm-like seismicity. Sahara et al. revise the locations of almost 3,000 VT seismic events that occurred during nearly 6 weeks prior the November 21, 2017 Agung volcano eruption (Bali, Indonesia). The authors reconstruct the complex dynamics of magma rising through the plumbing system, and conclude that the intrusion was temporarily arrested by a lithological discontinuity at around 6 km depth. For the same eruption, Wellik et al. focus on seismic rate variations and repeating earthquake families showing that the evolution of earthquake families reveal the progression toward eruption even though the overall earthquake rates and seismic energy release declined. Liu et al. use template matching techniques on micro-seismic events recorded by a local station near Changbaishan volcano on the China and North Korea border. Their analysis suggests that during the 2002–2005 unrest—which was triggered by a large regional earthquake - a swarm of VT events was caused by deep magma degassing that promoted a small magmatic injection to a shallower reservoir at about 5 km depth.

Long time series of seismological measurements have led to highly accurate depictions of the evolution of seismic activity affecting volcanic areas. These have helped to elucidate the processes that take place at depth, and in particular the transfer of fluids towards the surface. A challenge with this type of analysis is to properly visualize the hypocentral data in space and time, and with respect to other datasets. Guardo et al. propose a method based on a Machine-Cube algorithm to identify seismic and aseismic volumes below the Etna edifice. Using previous tomographic images and modelled deformation sources deduced from surface measurements, they refine the 3D image of the magma storage and explain the deep instability below the eastern flank by both the magmatic and gravitational origins. The re-evaluation of large seismic catalogues acquired over a long time period allows a wide overview on the evolution of the volcanoes themselves and on their main seismogenic structures required for risk assessment. For the Campanian volcanoes in Southern Italy, Giudicepietro et al. point out the role of hydrothermal activity in the recent increase of seismicity in this highly populated region.

In rifting context, the co-existence of tectonic-regional and magmatic-local stress fields remains the main challenge to understanding the origin of both the background seismicity and the occurrence of swarms. In the Natron rift of the continental rift of East Africa, a dense temporary network has allowed a large seismic catalogue of hypocentres and focal mechanisms to be established. Reiss et al. separate tectonic and volcano-induced stresses to demonstrate the role of volcanic activity on the transfer of deformation from border faults to the centre of the magmatic rifts. In a more evolved rift setting, the 60-year-long compilation of catalogues in the northernmost East African rift by Ruch et al. revealed unprecedented details of the seismic swarms episodically affecting the same areas, and which have mainly been induced by transient magma supply at depth. Finally in oceanic context, Einarsson and Brandsdottir present a catalogue of 50 years of

monitoring in Northern Iceland, offering an extremely precise picture of the dyking sequence in the Krafla and adjacent segments. The time-space evolution of the seismicity, together with surface deformation data and geophysical investigations, are crucial for depicting the processes involved in the creation of oceanic crust.

Localizing earthquakes requires the assessment of the velocity structure of the volcano. A resolved 3D velocity model can dramatically improve the accuracy of seismic locations, while the comparison between locations and velocity anomalies helps clarify the magmatic, hydrothermal or tectonic origin of seismicity. Wilks et al. present the first velocity and velocity-ratio model of Aluto volcano (Ethiopia), obtained using travel-time tomography based on grid-based eikonal solvers and probabilistic location algorithms. The study shows sufficient resolution to distinguish shallow hydrothermal and deeper magmatic systems and detect their connection. Ardianto et al. use a similar combination of travel-time tomography and probabilistic location to resolve velocity and velocity ratios at Mt. Agung volcano (Indonesia), using data recorded around its 2017 eruption. The study highlights an aseismic zone of low velocity and high velocity ratios, from which magma could have migrated sub-vertically to feed the eruption. Seismicity also clusters in a region of moderate-to-high ratios, interpreted as a sub-vertical dyke complex interacting with the local fault network.

The recognition of earthquake and tremor characteristics and the ability to track their migrations in space and time are becoming standard practice; however, when automatized and applied in real-time, these techniques acquire unprecedented value for volcano monitoring institutions and eruption forecasting. Cortés et al. propose an automatic Volcano-Seismic Recognition system trained using data collected at global volcanoes, to overcome the lack of unified criteria for earthquake characterization. The four example applications show the recognition potential of the tool, especially for volcano observatories lacking a working recognition system. Smith and Bean develop a REal-Time TREmor Analysis Tool (RETREAT) comprising advanced array-analysis techniques for the real-time detection and characterization of tremors. Their two example applications demonstrate the flexibility of the web-based interface at the scales of the European Arctic and Bárðarbunga (Iceland) dike intrusion.

AUTHOR CONTRIBUTIONS

DK, LS, CD, JJ, FM, and LP edited the Research Topic "*Seismicity in Volcanic Areas*." All the authors listed have made a substantial direct and intellectual contribution to the work and approved it for publication.

FUNDING

The Research Topic Editorial activities of DK were supported in part by the Ministero dell'Universitàe della Ricerca (MiUR) through PRIN grant 2017P9AT72. The Research Topic Editorial activities of LS were supported by the Terrestrial Magmatic Systems Research Platform, a high-potential research initiative of the universities of Mainz, Frankfurt and Heidelberg partially funded by the state of Rheinland-Pfalz. LP acknowledges funds of NEWTON-g project grant agreement no. 801221.

ACKNOWLEDGMENTS

We thank the authors for their contributions, and the reviewers and editorial staff for their efforts to pull together this article collection. We also thank the Editorial Office of Frontiers in Earth Science for the kind invitation to edit this Research Topic and editor in chief VA for his support.

Conflict of Interest: The authors declare that the research was conducted in the absence of any commercial or financial relationships that could be construed as a potential conflict of interest.

Publisher's Note: All claims expressed in this article are solely those of the authors and do not necessarily represent those of their affiliated organizations, or those of the publisher, the editors and the reviewers. Any product that may be evaluated in this article, or claim that may be made by its manufacturer, is not guaranteed or endorsed by the publisher.

Copyright © 2021 Keir, De Siena, Doubre, Johnson, Maccaferri and Passarelli. This is an open-access article distributed under the terms of the Creative Commons Attribution License (CC BY). The use, distribution or reproduction in other forums is permitted, provided the original author(s) and the copyright owner(s) are credited and that the original publication in this journal is cited, in accordance with accepted academic practice. No use, distribution or reproduction is permitted which does not comply with these terms.

frontiers in Earth Science

BRIEF RESEARCH REPORT
published: 09 October 2020
doi: 10.3389/feart.2020.583815

Balance Between Deformation and Seismic Energy Release: The Dec 2018 'Double-Dike' Intrusion at Mt. Etna

Alessandro Bonaccorso and Elisabetta Giampiccolo*

Istituto Nazionale di Geofisica e Vulcanologia - Osservatorio Etneo, Catania, Italy

Dikes are the primary mechanisms to transport magma and feed eruptions. Investigations of the surface deformation and seismicity caused by a dike can potentially provide useful information to forecast the expected propagation and associated hazard. On December 24, 2018, a dike intrusion reached the summit of Mt. Etna, feeding an effusive fissure. The intrusion was accompanied by a seismic swarm, with hypocenters beneath the summit craters and eruptive fissure, and by ground deformation. The seismicity continued the following day, with the hypocenters deepening to 3 km b.s.l. due to the propagation of a deeper and thicker dike. This situation generated the fear of feeding a more dangerous eruption in the medium-low flank. Recently it was found an equation that relates the average thickness and dimension of the dike with the expected released mechanical energy and, therefore, to the seismic moment. By using this updated application, it is shown that the observed seismicity could not be accounted for by the first dike. Instead, the cumulative effect of both dikes indicates a total moment from available energy expected that balances the moment recorded by the seismicity. The proposed approach proved very useful in the specific case of Etna volcano eruptions, resulting an effective tool to monitor the state of the intrusion of the magma and, therefore, to predict if a dike has enough energy to continue propagating or to stop.

Keywords: Etna volcano, dike intrusion, eruption monitoring, volcano seismicity, volcano deformation, energy balance

OPEN ACCESS

Edited by:
Cecile Doubre,
Université de Strasbourg, France

Reviewed by:
Eisuke Fujita,
National Research Institute for Earth Science and Disaster Resilience (NIED), Japan
Finnigan Illsley-Kemp,
Victoria University of Wellington, New Zealand

****Correspondence:***
Alessandro Bonaccorso
alessandro.bonaccorso@ingv.it

Specialty section:
This article was submitted to Volcanology, a section of the journal Frontiers in Earth Science

Received: *15 July 2020*
Accepted: *22 September 2020*
Published: *09 October 2020*

Citation:
Bonaccorso A and Giampiccolo E (2020) Balance Between Deformation and Seismic Energy Release: The Dec 2018 'Double-Dike' Intrusion at Mt. Etna. Front. Earth Sci. 8:583815. doi: 10.3389/feart.2020.583815

INTRODUCTION

Dike propagation is a main process for magma transport and eruptions. Several studies have investigated this mechanism involving different approaches such as solid mechanics, field mapping and analogue lab experiments. Review presentations on dike investigations are reported in Pollard (1987), Lister and Kerr (1991), Rubin (1995), and Rivalta et al. (2015). A critical and intriguing aspect is dike arrest. In fact, in most cases propagating dikes can stop before reaching the free surface (e.g., Gudmundsson et al., 1999; Gudmundsson, 2003). Dike stopping may occur for different reasons: driving pressure decreasing (e.g., Rivalta, 2010; Taisne et al., 2011), magma solidification (e.g., Lister and Kerr, 1991), structural barrier (e.g., Geshi et al., 2010; Gudmundsson, 2011) and stress perturbation (Maccaferri et al., 2015; Xu et al., 2016). Despite the complexity of the issue, the goal of having a tool to track the propagation state of the dike is fundamental at frequently erupting volcanoes whose flanks are densely populated, such as at Mt. Etna. Bonaccorso et al. (2017)

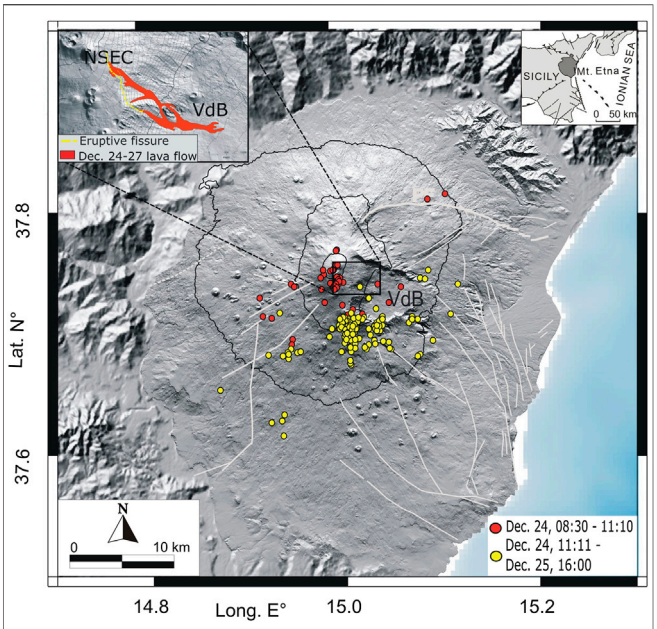

Figure 1 | 3D location of the seismicity occurring at Mt. Etna between 08: 30, December 24 and 16:00, December 25 (modified after Alparone et al., 2020). In the inset top left, the lava flow during the December 24–27eruption (Calvari et al., 2020) is shown together with the eruptive fissure that opened on December 24.

investigated the relationship between measured dike-induced deformation and the seismicity released during its propagation. The authors devised a simple equation related to the dike's average thickness that can be used as a proxy of the expected mechanical energy to be released during its propagation. They also obtained an empirical law that quantifies the expected seismic energy released before arrest. The authors found a general law from data of different volcanoes around the world where dikes were modeled and seismicity recorded (Afar region, Japanese volcanoes, Etna volcano). However, if robust data for single volcanoes areas are available, then the goodness of the equation improves and it is better to use the representative equation of the specific investigated volcano.

So far, the equation fitted the recent dikes feeding the flank eruptions of the last 2 decades very well (2001, 2002-two dikes, 2008), suggesting it is a valid tool to determine the total seismic moment to be released by an intrusion, and thus potentially able to follow the energy status during the dike propagation and the timing of its possible arrest.

On December 24, 2018, in the early morning, a fast dike crossed Mt. Etna volcano and reached the surface at 11:10. It produced an eruptive fissure in the summit area and began emitting a lava flow in the high eastern flank (Calvari et al., 2020). From 8:30 to 11:10, the dike intrusion was accompanied by a seismic swarm located beneath the shallow (0–2 km a.s.l.) central portion of the volcano (Alparone et al., 2020; Giampiccolo et al., 2020) (**Figure 1**). One interesting aspect was that the seismic swarm continued even during the following 24 h, decreasing in the afternoon-evening of December 25th. This seismicity was localized in a more decentralized portion toward the SE of the volcano. This behavior raised great concern about the possibility that another intrusion with greater lateral extension was acting inside the volcanic building. This dike could have been a significant hazard if it reached the surface, resulting in more eruptive activity. In fact, the more an intrusion extends laterally, the greater the risk that the eruptive fissure and lava flows may approach small towns and villages. Similarly to the 2002 eruption, the intrusive process triggered an acceleration of the eastward sliding of the unstable eastern sector of the volcano (Bonforte et al., 2019). Following the eruptive period, this marked sliding was also accommodated by fault slip that on 26 December culminated with the M_L 4.8 earthquake along the Fiandaca fault in the low Eastern flank (Alparone et al., 2020; Giampiccolo et al., 2020).

However, the effusive activity of the eruption lasted only a few days and emitted a modest lava volume of ca. ~3 × 10^6 m^3. Therefore, the critical aspect regarding the second major intrusion that did not feed any eruption, and whether this behavior could have been better tracked, remained unclear.

Recently, Aloisi et al. (2020) jointly analyzed and modeled different types of continuous deformation data (strainmeters, tiltmeters and high-rate GPS) to constrain a detailed and complete model and the time evolution for the December 24–25, 2018 eruptive intrusion. The result improves the previous interpretative models that were not based on continuous deformation measurements. The authors showed that the data are robustly modeled by a first shallow dike departing under central crater area from sea level, and by a second deeper and larger dike that stopped below sea level without crossing the final portion of the volcano.

In this study, in "Estimation of Dike Energy from Inferred Dike Shape" section we present the approach from Bonaccorso et al. (2017) by using the observables of the energy released during diking, namely seismicity and deformation, and clarifying their mutual relationship. In "The Multiple Intrusions of the Etna Dec 2018 Eruption" section, we present the complex December 24–25, 2018 intrusion by reporting the 3D high-precision locations of the earthquakes and recent advanced modeling of the ground deformation during these two days. In "Updated Relationship Between Energy Expected from Dike Shape vs. Measured Seismic Energy" section, we update with the 2018 case the equation relating the energy expected from a dike with a determined geometry and the seismic energy released, and verify how this equation can provide useful information on the propagation of intrusions also in the recent case of the December 2018 eruption. Finally, we discuss the potential danger of the 2018 eruption and, even in this complex case characterized by a double intrusion, show that the proposed approach and updated equation prove a useful tool to obtain information on the state of the dike's propagation.

ESTIMATION OF DIKE ENERGY FROM INFERRED DIKE SHAPE

Following the linear elastic theory, in which the thickness t to length l ratio of a dike is related to the driving pressure P_d able to

open the dike walls (i.e., Pollard, 1987; Rubin, 1995), Bonaccorso et al. (2017) obtained an equation for the available mechanical elastic strain energy U_E as a function of the dike thickness t:

$$U_E = \pi/8 \times \mu/(1-\nu) \times t^2 \quad (1)$$

where μ is the medium rigidity and ν is the Poisson coefficient.

Equation 1 was used both on a world mean scale (Etna, Japan volcanoes and Afar eruptions) and on a single volcano (Etna) to obtain the relation linking the energy of the dikes modeled from the deformation measurements and the seismic energy release during the dike propagation. On Etna volcano, the modeled dike shapes and the seismic recordings are very robust for the recent eruptions thanks to an integrated monitoring system of ground deformation (static and continuous GPS measurements and continuous borehole tilt) and the dense seismic network around the volcano.

Bonaccorso et al. (2017) correlated the mechanical energy U_E to the seismic moment released by the induced earthquakes. In particular, the authors obtained a linear relation between $\log_{10} M_o$ and $\log_{10} U_T$, where M_o is the cumulative recorded seismic moment and U_T the total 3D available mechanical elastic strain energy, obtained multiplying the U_E of **Eq. 1** by the length of the dike in the direction perpendicular to the propagation (i.e., the estimated width).

The purpose of this result is to obtain a tool for tracking the energy released by the intrusion to evaluate its propagation. The logical chain of the proposed process essentially followed four steps:

1) The dike model parameters are obtained from the deformation measurements. This is possible since the size and shape of the dike can be modeled from the deformations recorded by the permanent monitoring system, in principle also from the first initial phases of the dike propagation.
2) From the dike model we can estimate the energy to be released, since from **Eq. 1** this can be calculated from the dimension of the dike, mainly in terms of its thickness.
3) Defining the relationship between energy associated with the dike and energy released by earthquakes. From the numerous recent eruptions already studied and modeled, this energy estimated from the model obtained can, in turn, be related to the seismic energy released by the earthquakes induced by the propagation of the eruptive intrusion. A relation of type $\log_{10}(M_o) = a \log_{10}(U_T) + b$ is used, where a and b are the coefficients to fix by the fit of M_o and U_T data.
4) Tracking the evolution of the process. Finally, we can estimate the expected energy, namely the one that the eruptive fissure (dike) should release during its propagation. We can also monitor the discharge of energy over time, and observe when it is approaching the expected value to be released. . This allows us to evaluate the state of the intrusion of the magma, and if this would continue to propagate (its cumulated energy is below the expected energy level) or if it is about to stop (the expected energy level is reached).

As a real case application, Bonaccorso et al. (2017) considered the December 27, Etna 2002 dike propagation modeled by the continuous borehole tiltmeters data that allowed inferring a near constant thickness of 3.35 m (Aloisi et al., 2006). The dike propagated in the NE flank, reaching a distance of ~5 km from the summit craters area. Once again, there was concern that this eruptive fissure could propagate in the lower flank and discharge magma. Following the proposed approach, Bonaccorso et al. (2017) estimated the available elastic strain energy U_T and then calculated the expected seismic moment M_o to be released and verified that the recorded cumulated M_o approached the expected M_o limit.

THE MULTIPLE INTRUSIONS OF THE ETNA DEC 2018 ERUPTION

The December 24, 2018 flank eruption at Mt. Etna began in the early morning with intense degassing from the summit craters. It was accompanied by both a seismic sequence, starting at 08:30, and a fast increase in the volcanic tremor amplitude (Alparone et al., 2020). At 11:10, an eruptive fissure, about 2 km long and SE-trending, opened between 3,000 and 2,400 m a.s.l. at the southern base of the New Southeast Crater (NSEC, inset in **Figure 1**) producing lava fountain and lava flows that spread eastward over the upper western flank of the Valle del Bove depression (VdB). The lava fountain lasted just half an hour, whereas the lava flow output from the main eruptive fissure remained copious on December 25, decreasing significantly on December 26, in conjunction with a drastic decrease in the volcanic tremor amplitude (Alparone et al., 2020 and references therein). Lava emission stopped definitively on December 27. The total length of the lava flow field was 0.88 km^2 (Calvari et al., 2020), and the emitted volume was 1.4 ± 0.5 Mm^3 of summit outflows and 0.85 ± 0.3 Mm^3 of lateral flows, as calculated from spectroradiometers of the satellites MODIS and Sentinel-2 (Laiolo et al., 2019).

To study the process of the December 2018 intrusive episode, we used precise 3D hypocenters of the earthquakes recorded from the beginning of the dike intrusion (08:30, December 24 until 16:00, December 25 (Alparone et al., 2020; Giampiccolo et al., 2020). These locations, compared to 1D ones (GADS, 2020; **Supplementary Table S1**), show a sharpening of clustered seismicity features with a significant reduction in uncertainties (about 40% RMS reduction and average location errors less than 0.2 km in both the horizontal and vertical directions) and, therefore, provide a clearer picture of how seismicity evolved within the edifice.

The earthquake locations during the first 30 h (December 24–25; **Figures 1 and 2**). from 8:30 to 11:10 indicated an initial cluster of events with epicenters aligned in a N-S direction, located between −1 km b.s.l. and 2 km a.s.l., beneath the summit craters and along the eruptive vent (red circles in **Figures 1 and 2**). Then, the seismicity moved southeastwards and, starting from 16:30, it migrated toward the western wall of VdB with a deepening of the hypocenters up to −3 km b.s.l. (yellow circles in **Figures 1 and 2**). The seismicity occurring

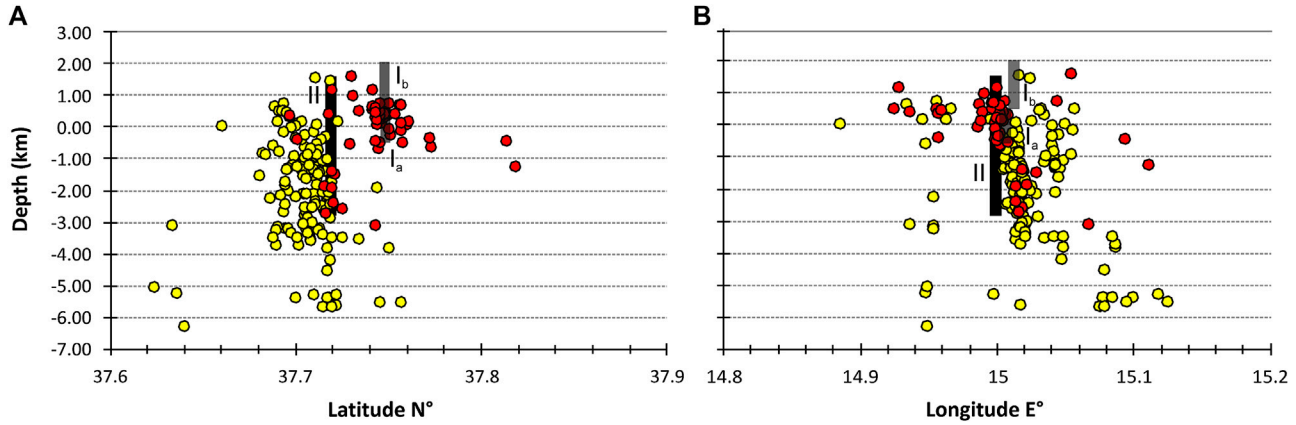

Figure 2 | Depth vs. latitude **(A)** and longitude **(B)** distribution of the earthquakes occurring from 08:30 to 11:10 on December 24 (red circles) and from 11:11 to 16:00 on December 25 (yellow circles). The positions of the two dikes inferred by Aloisi et al. (2020) are also shown. The first dike, composed by two parts (I_a–I_b), is indicated in dark gray, the second dike (II) is indicated in black. For dike parameters see **Supplementary Table S2**.

from 20:00 on December 24 until the afternoon (16:00) of December 25 affected a wider and deeper volume with respect to the main earthquake clusters (Alparone et al., 2020; yellow circles in **Figures 1 and 2**). The prevailing normal faulting mechanism of the earthquakes located beneath the summit craters and along the eruptive fractures matches well with the direction of extensional stress regime and is consistent with a magma push which favored the magma ascent through the shallow crust (Alparone et al., 2020).

During the initial phase of the eruption, the INGV provided a first estimation of the dike model in order to quickly assist the Italian Civil Protection Authorities in monitoring the on-going phenomenon. By using the real time GPS solutions exclusively, a shallow near-vertical dike was inferred, located between the sea level and the summit eruptive fissure, with a horizontal length of 2 km, vertical width of 1 km and an opening of 3 m (Aloisi et al., 2020). This modeling was then refined including more reliable displacement estimations, but it did not change much from the initial estimation. It provided a good indication of the intrusion acting during the early morning of December 24 until the eruption start at 11:10, but does not fit with the continuation of the seismicity for the whole day of December 25. So, after the start of the eruption the scenario was not as one would expect, in the sense that usually at volcanoes, once the eruption begins and the propagation of the feeder dike ends, the seismic activity diminishes and the deformation changes end. Instead, during the December 2018 intrusion, the seismicity continued after the eruption onset and, besides the summit area, also affected the southwestern flanks of the volcanic edifice (Alparone et al., 2020). Moreover, it promoted a strong acceleration of the eastern flank movements toward the SE direction (Bonforte et al., 2019; Alparone et al., 2020). These aspects clearly indicated that the intrusive process was more complex than the shallow intrusion modeled from 8:30 to 11:10.

A turning point for a more complete understanding of the intrusive process was recently provided by Aloisi et al. (2020).

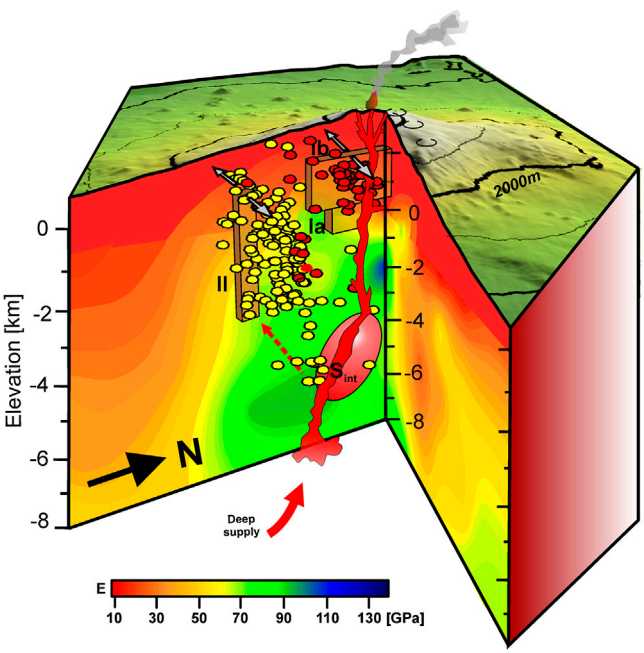

Figure 3 | 3D sketch map showing the two dikes inferred by Aloisi et al. (2020) and the 3D high-precision locations (Alparone et al., 2020; Giampiccolo et al., 2020) of the earthquakes which accompanied the eruptive episode during the first 30 h. The first shallower eruptive dike increased its width during the propagation and is made up of the two parts Ia and Ib (see **Supplementary Table S2**). It reached the surface and generated the eruption. The second deeper non-eruptive dike II halted before reaching the free surface. See text for the detailed parameters and modeling description. The positions of the modeled dikes are well matched by the two main clusters of the seismicity. The S_{int} is the zone of the intermediate storage modeled by the recorded deformation during the inflation/deflation periods that precede/accompany the main eruptions at Etna (i.e., Bonforte et al., 2008 and references therein). The seismic tomography from Aloisi et al. (2002) is also reported along the cross-sections by representing the deduced Young's modulus E.

The authors integrated all the continuous deformation data (GPS, borehole strainmeters and tiltmeters), inferring a more detailed and robust model. The multi-parametric approach revealed the complexity of the real volcanic processes, involving two separate dikes rather than just one. The first dike is the shallower one departing in the last 3 km below the summit craters area (dike I_a), gradually increasing its horizontal dimension (dike I_b). It began propagating on December 24 at 8:20, reached the ground surface at 11:10 and fed the short-lived lateral eruption. After the start of the eruption and until the afternoon of December 25, a second dike penetrated the high southern eastern flank but did not reach the surface (dike II). This dike was very thick (~5 m opening) and deeper, departing from about 3 km b.s.l. and stopping inside the volcano edifice at 1.5 km a.s.l. The parameters of the dikes modeled by Aloisi et al. (2020) are reported in **Supplementary Table S2**. The modeled dike positions are shown in **Figure 2** together with the hypocentral location of the earthquakes. The 3D sketch map of the seismicity and the dike positions are shown in **Figure 3**, where the match between the earthquake locations and the dike positions inferred by geodetic models is evident.

UPDATED RELATIONSHIP BETWEEN ENERGY EXPECTED FROM DIKE SHAPE VS MEASURED SEISMIC ENERGY

In quantifying the released energy during dike propagation, the seismic moment of the earthquakes accompanying and tracking the migratory path of the intruding magma can be considered not only the seismic energy which is radiated seismically but also a measure of the total energy released during the intrusion process (Bonaccorso et al., 2017). We derived the seismic moment of the earthquakes recorded during the intrusive episode of December 24 from the local magnitude M_L, according to **Eq. 2**, obtained for Mt. Etna earthquakes by Giampiccolo et al. (2007):

$$\log_{10}(M_o) = (17.60 \pm 0.37) \pm (1.12 \pm 0.10)\, M_L \qquad (2)$$

From the onset of the dike intrusion until the opening of the eruptive fissure (08:30–11:10), about 60 earthquakes with $1.1 \leq M_L \leq 4.0$ were extracted from the INGV-OE Catalog (GADS, 2020; **Supplementary Table S1**). The total seismic moment released is about 10^{15} J. A second phase spans from the beginning of the eruption to 16:00 on December 25 and includes about 135 earthquakes with magnitude $1.4 \leq M_L \leq 4.3$. The cumulative energy released until the afternoon of December 25 reaches the value of 1.16×10^{16} J.

Supplementary Table S3 shows an updated scheme, also containing the dikes of the 2018 eruption, which summarizes the parameters of the eruptive dikes modeled from ground deformation and the associated recorded total seismic moment M_o released during their propagations. From the values reported in **Supplementary Table S3**, we estimated the updated relationship between the energy expected from dike shape/dimensions modeled from ground deformation measurements and the seismic energy measured from the cumulative seismic moment of the earthquakes recorded during the dike propagation. We obtained:

$$\log_{10}(M_o) = 1.21 \cdot \log_{10}(U_T) - 0.86 \qquad (3)$$

confirming the same previous coefficients found in Bonaccorso et al. (2017) and maintaining a very good correlation coefficient R^2 equal to 0.97 (**Figure 4A**).

After U_T is estimated from the dike parameters, **Eq. 3** allows determining the seismic moment expected by the release of the dike's available energy that can be compared with the recorded seismic moment, hence providing a tool to evaluate when the energy is balancing. In the case of the December 2018 eruption, the method highlights that the first eruptive dike, promptly modeled on the morning of December 24, did not release enough energy to

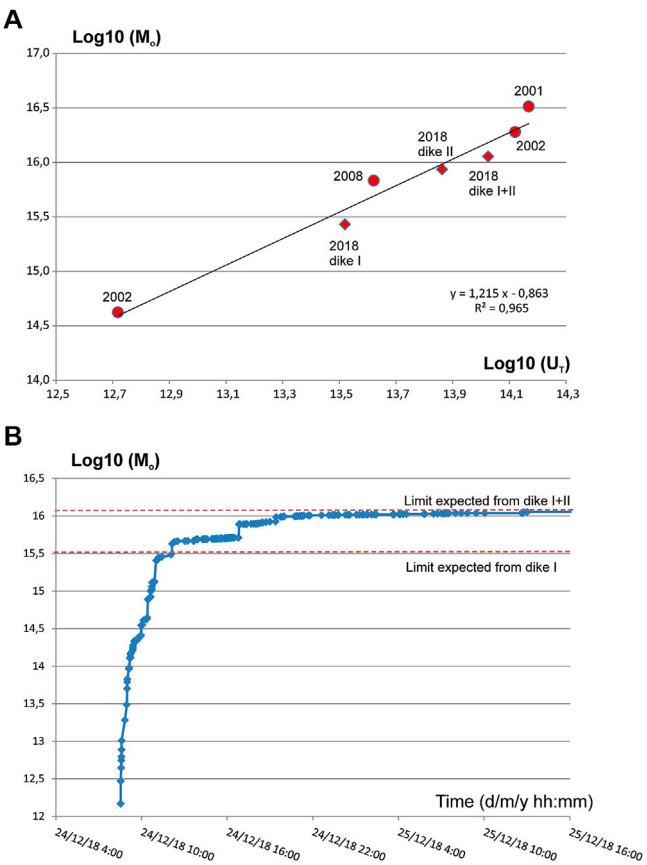

Figure 4 | (A) Total seismic moment M_o (J) calculated from the seismicity recorded during the dike propagation vs. total 3-D available mechanical elastic strain energy UT (J) estimated from **Eq. 4** for the modeled dikes of Etna's eruptions (see **Supplementary Table S3**). The rhombuses are for the dike I, dike II and dikes (I + II), respectively, of 24–25 December 2018, while the circles are for the dikes of the 2001, 2002 (two dikes) and 2008 eruptions (see **Supplementary Table S2**). **(B)** Application example of the 24–25 December 2018 double dike intrusion of Etna. log10(M_o) vs. time. From the initial phases of the dike, after its opening is inferred, the available energy can be estimated from **Eq. 2** and the expected total seismic moment to be released (dashed line) from **Eq. 3**. This M_o value is the limit to be reached by the cumulative recorded seismic moment to obtain the energy equilibrium and the dike stopping.

balance the recorded seismic moment that continued to accumulate in the following hours (**Figure 4B**). Therefore, the proposed approach clearly suggests that another seismic source was active after the eruption started. From continuous deformation data, Aloisi et al. (2020) inferred a second deeper and thicker dike, located slightly further south than the first, that did not reach the free surface. If we consider the total moment from available energy expected by the cumulative effect of both dikes, then the expected M_o and the recorded one are well balanced (**Figure 4B**).

DISCUSSION AND CONCLUSION

The eruption of Christmas 2018 was a peculiar event for two main aspects: i) in spite of a powerful intrusion, the ensuing effusive activity lasted only about 3 days, stopping on the morning of December 27; ii) it was accompanied by a seismic swarm that did not stop after the start of the eruption (morning of 24 December) but continued until the afternoon of the following day.

The first dike, the eruptive one crossing the surface portion of the volcanic building and reaching the surface to feed the eruption, produced a clear deformation pattern on a scale of the entire volcano, more marked in the summit area and with a strong amplitude decay toward the external flanks, this due to the shallow position of this dike. The continuation of seismicity was associated with the propagation of a second deeper dike, which was unable to reach the surface but stopped 1.5 km below the crater area. This second dike instead caused a wide deformation detected more clearly in the southern flank portion above its projection. This dike stopped below the ground surface and did not cross the final portion of the volcano pile where the main deformation was produced. It was characterized by relatively small width (about 600 m) compared to the shallow dike (about 2,700 m) (see **Figure 3**; **Supplementary Table S1**). If the deeper dike had been >1.5–2 km wider, it would have caused marked deformation on the scale of the entire volcano edifice (Aloisi et al., 2020). The detail of the recorded and the expected deformation patterns is clearly shown in Figure 9 by Aloisi et al. (2020). After the start of the eruption, the main concern was the possible propagation of a more external and dangerous dike. In fact, because of its location shifted southward from the crater area, this second dike, if further propagating, could have been hazardous by generating a low flank eruption. In general, the longer the propagation, the more dangerous it is since the dike could approach towns and infrastructures, densely located on the volcano's lower flanks. The risk map of lava flows shows that the highest risk is found in the south-eastern flank due to the combination of high hazard and population density (Del Negro et al., 2019). Related to this sector of the volcano, a famous example was the 1,669 eruption: an eruptive fissure propagated 16 km in the southern flank, fed an eruptive vent in the low flank and went on to destroy several villages and partially the main town of Catania (Branca et al., 2013). Today, an eruption similar to the 1,669 event would cause damage amounting to about seven billion Euros (Del Negro et al., 2016).

Fortunately, the scenario of a flank eruption in the lower flank did not take place probably because the first intrusion and the resulting eruption released most of the energy, as testified by the decreasing seismicity rate (Alparone et al., 2020) and by its distribution throughout the whole volcanic edifice and along well-known fault zones (Alparone et al., 2020). However, during the 24th and 25th of December it would have been very important and strategic to have valid tools to evaluate the propagation status.

In this work, we have updated the equation obtained by Bonaccorso et al. (2017) and subsequently verified its applicability to the 2018 eruption. The approach is based on the monitoring of the expected energy calculated starting from the main parameters of the dike (thickness and width) and the seismic energy released by the earthquakes accompanying the dike intrusion. With this approach, a key aspect is that the expected energy is calculated from the main parameters of the dike, i.e., thickness and width which, in principle, can be modeled in the early stages of dike propagation when its effect on the surface begins to be revealed by the deformation monitoring systems. The seismic energy can be calculated in near real-time from the seismic moment M_o obtained from the seismic recordings. Since the comparison of the seismic moment expected by the release of the available energy with the moment calculated in real-time provides a forecast of when the energy is balancing and, hence, when the dike is expected to stop, the proposed approach is very helpful to estimate the dike propagation hazard during the early phase of an eruptive intrusion.

Clearly, the more robust the data for a single volcano, the better the quality of the relationship. As shown in the application case reported in Bonaccorso et al. (2017) for the recent eruptions of Etna volcano, the modeled dike shapes and the seismic recordings are particularly robust. This is thanks both to the integrated monitoring system of ground deformation (static and continuous GPS measurements and continuous borehole tilt) and the dense seismic network around the volcano (Bonaccorso et al., 2017). Our analysis supports the robustness of the empirical law proposed by Bonaccorso et al. (2017) and its validity also for the 2018 Mt. Etna eruption. So, for purposes of supporting an understanding of the state of intrusion propagation, it is fundamental to develop real-time modeling of ground deformation data. Such an approach can be used to have integrated information during intrusive processes that at Etna and other active volcanoes are frequent and require maximum attention and the best possible interpretation during their evolution.

DATA AVAILABILITY STATEMENT

The data are available in **Supplementary Materials**. The localizations and magnitudes of the recorded earthquakes are reported in **Table S1**, the parameters of the modeled dikes from previous published studies are reported in **Tables S2 and S3**.

AUTHOR CONTRIBUTIONS

AB conceived this work and traced its scheme. EG prepared and revised seismic data. Both the authors contributed in writing the manuscript and shared the discussion of the results.

ACKNOWLEDGMENTS

We kindly acknowledge the INGV-OE seismic network staff who ensure the regular working of seismic stations and the "Gruppo Analisi Dati Sismici" for providing earthquake data. AB is particularly indebted to the technical staff of the Ground Deformation Group of INGV-OE for the regular operation of the tilt and GPS monitoring networks, which enabled the previous studies over the last 3 decades. We thank S. Conway for revising the English language of the manuscript.

SUPPLEMENTARY MATERIAL

The Supplementary Material for this article can be found online at: https://www.frontiersin.org/articles/10.3389/feart.2020.583815/full#supplementary-material

REFERENCES

Aloisi, M., Bonaccorso, A., Cannavò, F., Currenti, G., and Gambino, S. (2020). The 24 december 2018 eruptive intrusion at Etna volcano as revealed by multidisciplinary continuous deformation networks (CGPS, Borehole Strainmeters and Tiltmeters). *J. Geophys. Res. Solid Earth* 125, e2019JB019117. doi:10.1029/2019JB019117.

Aloisi, M., Bonaccorso, A., and Gambino, S. (2006). Imaging composite dike propagation (Etna, 2002 case). *J. Geophys. Res.* 111, 219–223. doi:10.1029/2005JB003908.

Aloisi, M., Cocina, O., Neri, G., and Orecchio, B. E. (2002). Seismic tomography of the crust underneath the Etna volcano, Sicily. *Phys. Earth Planet. Inter.* 134, 139–155. doi:10.1016/S0031-9201(02)00153-X

Privitera, S., Barberi, G., Giampiccolo, E., Maiolino, V., Mostaccio, A., Musumeci, C., et al. (2020). *Seismological constraints on the 2018 Mt. Etna (Italy) flank eruption and implications for the flank dynamics of the volcano*. New Mexico: Terra Nova, 1–11. doi:10.1111/ter.12463.

Bonaccorso, A., Aoki, Y., and Rivalta, E. (2017). Dike propagation energy balance from deformation modeling and seismic release. *Geophys. Res. Lett.* 44, 5486–5494. doi:10.1002/2017GL074008.

Bonforte, A., Bonaccorso, A., Guglielmino, F., Palano, M., and Puglisi, G. (2008). Feeding system and magma storage beneath Mt. Etna as revealed by recent inflation/deflation cycles. *J. Geophys. Res.* 113, B05406. doi:10.1029/2007JB005334.

Bonforte, A., Guglielmino, F., and Puglisi, G. (2019). Large dyke intrusion and small eruption: the December 24, 2018 Mt. Etna eruption imaged by Sentinel-1 data. *Terra. Nova* 31, 405–412. doi:10.1111/ter.12403.

Branca, S., De Beni, E., and Proietti, C. (2013). The large and destructive 1669 AD eruption at Etna volcano: reconstruction of the lava flow field evolution and effusion rate trend. *Bull. Volcanol.* 75, 694. doi:10.1007/s00445-013-0694-5.

Calvari, S., Bilotta, G., Bonaccorso, A., Caltabiano, T., Cappello, A., Corradino, C., et al. (2020). The VEI 2 Christmas 2018 Etna eruption: a small but intense eruptive event or the starting phase of a larger one? *Remote Sens.* 12 (6), 905 doi:10.3390/rs1206905.

Del Negro, C., Cappello, A., Bilotta, G., Ganci, G., and Herault, A. (2016). "Risk from lava flow inundations in densely populated areas: the case of Etna volcano, Abstract V12A-08," in 2016 Fall Meeting, AGU, San Francisco, CA, 12–16 December.

Del Negro, C., Cappello, A., Bilotta, G., Ganci, G., Hérault, A., and Zago, V. (2019). Living at the edge of an active volcano: risk from lava flows on Mt. Etna. *Geol. Soc. Am. Bull.* 132, 1615. doi:10.1130/B35290.1

GADS - Gruppo Analisi Dati Sismici (2020). *Catalogo dei terremoti della Sicilia Orientale—Calabria Meridionale (1999–2020)*. Catania, Italy: INGV. . Available at: http://sismoweb.ct.ingv.it/maps/eq_maps/sicily/catalogue.php

Geshi, N., Kusumoto, S., and Gudmundsson, A. (2010). Geometric difference between non-feeder and feeder dikes. *Geology* 38 (3), 195–198. doi:10.1130/G30350.1.

Giampiccolo, E., Cocina, O., De Gori, P., and Chiarabba, C. (2020). Dyke intrusion and stress-induced collapse of volcano flanks: the example of the 2018 event at Mt. Etna (Sicily, Italy). *Sci. Rep.* 10, 6373. doi:10.1038/s41598-020-63371-3.

Giampiccolo, E., D'Amico, S., Patane, D., and Gresta, S. 2007). Attenuation and source parameters of shallow microearthquakes at Mt. Etna volcano, Italy. *Bull. Seismol. Soc. Am.* 97, 184–197. doi:10.1785/0120050252.

Gudmundsson, A. (2011). Deflection of dykes into sills at discontinuities and magma-chamber formation. *Tectonophysics* 500, 50–64. doi:10.1016/j.tecto.2009.10.015.

Gudmundsson, A., Marinoni, L. B., and Martí, J. (1999). Injection and arrest of dykes: implications for volcanic hazards. *J. Volcanol. Geotherm.* 88 (1–2), 1–13. doi:10.1016/S0377-0273(98)00107-3.

Gudmundsson, A. (2003). Surface stresses associated with arrested dykes in rift zones. *Bull. Volcanol. Res.* 65, 606–619. doi:10.1016/S0377-0273[98]00107-3

Laiolo, M., Ripepe, M., Cigolini, C., Coppola, D., Della Schiava, M., Genco, R., et al. (2019). Space- and ground-based geophysical data tracking of magma migration in shallow feeding system of mount Etna volcano. *Rem. Sens.* 11 (10), 1182. doi:10.3390/rs11101182.

Lister, J. R., and Kerr, R. C. (1991). Fluid-mechanical models of crack propagation and their application to magma transport in dykes. *J. Geophys. Res.* 96, 10049110–077. doi:10.1029/91jb00600

Maccaferri, F., Rivalta, F., Passarelli, L., and Aoki, Y. (2015). On the mechanisms governing dike arrest: insight from the 2000 Miyakejima dike injection, Earth Planet. *Sci. Lett.* 434 (64–7), 42016. doi:10.1016/j.epsl.2015.11.024.

Pollard, D. D. (1987). "Elementary fracture mechanics applied to the structural interpretation of dykes," in *Mafic Dyke swarms*, Editors H. C. Halls and W. H. Fahrig, Geological Association of Canada special paper, Vol. 34, pp. 112–128.

Rivalta, E. (2010). Evidence that coupling to magma chambers controls the volume history and velocity of laterally propagating intrusions. *J. Geophys. Res.* 115, B07203. doi:10.1029/2009jb006922

Rivalta, E., Taisne, B., Bunger, A. P., and Katz, R. F. (2015). A review of mechanical models of dike propagation: schools of thought, results and future directions. *Tectonophysics* 638, 1–42. doi:10.1016/j.tecto.2014.10.003

Rubin, A. M. (1995). Propagation of magma-filled cracks, *Annu. Rev. Earth Planet. Sci.* 23, 287–336. doi:10.1146/annurev.ea.23.050195.001443

Taisne, B., Tait, S., and Jaupart, C. (2011). Conditions for the arrest of a vertical propagating dyke. *Bull. Volcanol.* 73, 191–204. doi:10.1007/s00445-010-0440-1.

Xu, W., Jónsson, S., Corbi, F., and Rivalta, E. (2016). Graben formation and dike arrest during the 2009 Harrat Lunayyir dike intrusion in Saudi Arabia: insights from InSAR, stress calculations and analog experiments. *J. Geophys. Res. Solid Earth* 121, 2837–2851. doi:10.1002/2015JB012505.

Conflict of Interest: The authors declare that the research was conducted in the absence of any commercial or financial relationships that could be construed as a potential conflict of interest.

Copyright © 2020 Bonaccorso and Giampiccolo. This is an open-access article distributed under the terms of the Creative Commons Attribution License (CC BY). The use, distribution or reproduction in other forums is permitted, provided the original author(s) and the copyright owner(s) are credited and that the original citation in this journal is cited, in accordance with accepted academic practice. No use, distribution or reproduction is permitted which does not comply with these terms.

frontiers in Earth Science

ORIGINAL RESEARCH
published: 14 October 2020
doi: 10.3389/feart.2020.579699

The Coupled Magmatic and Hydrothermal Systems of the Restless Aluto Caldera, Ethiopia

M. Wilks[1], N. Rawlinson[2], J.-M. Kendall[3]*, A. Nowacki[4], J. Biggs[1], A. Ayele[5] and J. Wookey[1]*

[1]School of Earth Sciences, University of Bristol, Bristol, United Kingdom, [2]Department of Earth Sciences—Bullard Labs, University of Cambridge, Cambridge, United Kingdom, [3]Department of Earth Sciences, University of Oxford, Oxford, United Kingdom, [4]School of Earth and Environment, University of Leeds, Leeds, United Kingdom, [5]Institute of Geophysics Space Science & Astronomy, Addis Ababa University, Addis Ababa, Ethiopia

Seismicity can be used to better understand interactions between magma bodies, hydrothermal systems and their host rocks—key factors influencing volcanic unrest. Here, we use earthquake data to image, for the first time, the seismic velocity structure beneath Aluto, a deforming volcano in the Main Ethiopian Rift. Traveltime tomography is used to jointly relocate seismicity and image 3D P- and S-wave velocity structures and the ratio between them (V_P/V_S). At depths of 4–9 km, the seismicity maps the top of a large low velocity zone with high V_P/V_S, which we interpret as a more ductile and melt-bearing region. A shallow (<3 km) hydrothermal system exhibits low seismic velocities and very low V_P/V_S (~1.40), consistent with the presence of gases exsolved from a deeper melt-rich mush body. The Artu Jawe fault and fracture system provides the migration pathway that connects the deeper mush body with the shallow hydrothermal system. Together, these observations demonstrate that the interaction between magmatic and hydrothermal systems, driven by the exchange of fluids, is responsible for the restless behavior of Aluto.

Keywords: tomography, volcano seismicity, magmatic systems, hydrothermal, systems, seismic imaging, restless volcano

OPEN ACCESS

Edited by:
Luca De Siena,
Johannes Gutenberg University
Mainz, Germany

Reviewed by:
Miriam Christina Reiss,
Goethe University Frankfurt, Germany
Andrey Jakovlev,
Institute of Petroleum Geology and Geophysics (RAS), Russia

****Correspondence:***
N. Rawlinson
nr441@cam.ac.uk,
J.-M. Kendall
mike.kendall@earth.ox.ac.uk

Specialty section:
This article was submitted to Volcanology, a section of the journal Frontiers in Earth Science

Received: *03 July 2020*
Accepted: *02 September 2020*
Published: *14 October 2020*

Citation:
Wilks M, Rawlinson N, Kendall J-M, Nowacki A, Biggs J, Ayele A and Wookey J (2020) The Coupled Magmatic and Hydrothermal Systems of the Restless Aluto Caldera, Ethiopia. Front. Earth Sci. 8:579699. doi: 10.3389/feart.2020.579699

INTRODUCTION

Interactions between magmatic and hydrothermal systems beneath volcanoes are poorly understood, but play a crucial role in eruptions, especially those that are phreatomagmatic (Pritchard et al., 2019; Troise et al., 2019). This interaction is also important for successful geothermal energy production in high-enthalpy volcanic systems (Reinsch et al., 2017). Seismic methods offer insights into the nature of these thermo-magmatic systems (e.g., Greenfield et al., 2016; Hooft et al., 2019; Wespestad et al., 2019). Seismicity indicates fluid movements through faults and conduits (e.g., Prejean et al., 2002; Hudson et al., 2017; Greenfield et al., 2019a), but can also be used to image their subsurface structure. For example, seismic velocities and their ratio (V_P/V_S), can be used to image fault structures and regions of partial melt and over-pressured gases (e.g., Johnson and Polland, 2013; Muksin et al., 2013). Such observations have implications for understanding volcanic unrest, assessing volcanic hazard and optimizing geothermal exploration.

The dynamic nature of the volcanoes of the Main Ethiopian Rift (MER) has only recently been realized (Biggs et al., 2011). The population exposure index for these volcanos is high (PEI five or greater), as nearly 10 million people live in the region (Brown et al., 2015). Over the past decade, a

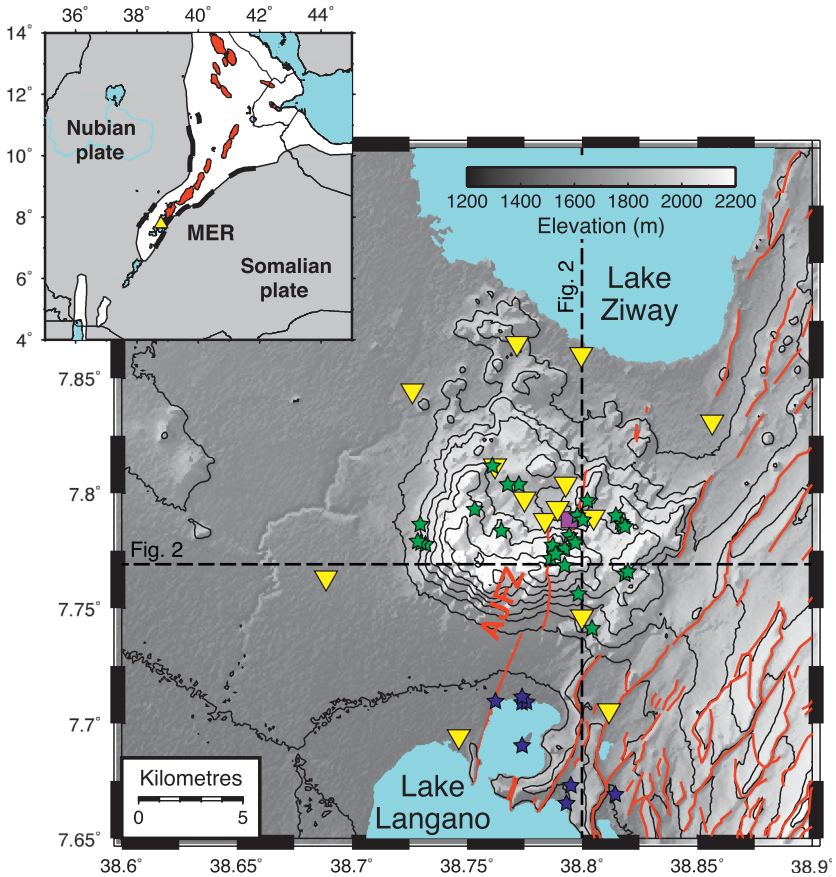

FIGURE 1 | The ARGOS seismic network (yellow triangles), faults (red lines) (Agostini et al., 2011; Hutchison et al., 2015) and the Artu Jawe Fault Zone. Green and blue stars are fumaroles and hot springs, respectively (Braddock et al., 2017; Hochstein et al., 2017). Black dashed lines indicate the location of the north-south and east-west profiles shown in **Figure 2**. Inset: Aluto and the study region (yellow triangle) within the Main Ethiopian Rift with rift regions (white), border faults (thick black lines) and magmatic segments (red) marked.

number of studies have sought to better understand the dynamics and eruptive histories of these volcanoes. Experiments have revealed a rich complexity of seismicity beneath Corbetti (Lloyd, et al., 2018a; Lavayssière et al., 2019), Bora–Tulu Moye (Greenfield et al., 2019a; Greenfield et al., 2019b) and Aluto (Wilks et al., 2017). Satellite imaging suggests frequently recurring and shallow magmatic activity (Biggs et al., 2011; Hutchison et al., 2016b; Lloyd et al., 2018a), and a role for pre-existing structures in the development of volcanism (Lloyd et al., 2018b). Magnetotellurics (Samrock et al., 2015; Lloyd et al., 2018a; Hübert et al., 2018) and gravity (Gottsmann et al., 2020) offer further insights into melt storage and migration beneath these volcanoes. However, the location of magmatic and hydrothermal reservoirs is still somewhat elusive. Here we focus on Aluto volcano, which lies just south of the town of Ziway, between Lake Ziway and Lake Langano (**Figure 1**).

Aluto is a silicic volcanic center that is thought to have begun erupting at about 0.5 Ma in association with the development of the regional Wonji Fault Belt (Hutchison et al., 2016a; Agostini et al., 2011), and whose most recent volcanic deposits are dated to 0.4 ka (Hutchison et al., 2016a). Regional earthquake catalogs (Keir et al., 2006) suggest that earthquakes up to magnitude three occur along the relatively low-seismicity Aluto–Gedemsa magmatic segment, but are likely associated with the border faults to the east of our study region (**Figure 1**) rather than volcanic activity itself. The volcano has however displayed episodic surface deformation (Biggs et al., 2011; Hutchison et al., 2016b). Two pulses of rapid uplift were observed in 2003 and 2008 (15 cm in 10 months and 10 cm in 6 months), but since then the volcano has been slowly subsiding at rates <3 mm/yr (Biggs et al., 2011; Birhanu et al., 2019).

A series of recent experiments have provided further insights into the active nature of Aluto. Seismicity (Wilks et al., 2017) and observations of fracture-induced seismic anisotropy (Nowacki et al., 2018) reveal a complex fault system and fracture network that extends well below an active hydrothermal system. The pattern of seismicity is seasonal, with the peak of seismicity occurring 2–3 months after the heavy rainy season coincident with lake loading and subsidence (Birhanu et al., 2019). Surface and satellite mapping and CO_2 flux surveys have shown that magmatic and hydrothermal upwelling follows recent faults and fracture networks generated by Quaternary to Recent rifting,

namely the Wonji Fault Belt and the associated Artu Jawe Fault Zone (AJFZ) (ELC Electroconsult, 1986; Hutchison et al., 2015; Hutchison et al., 2016a; Braddock et al., 2017). The high temperature gradient and active hydrothermal system has made Aluto a viable and productive geothermal resource; Ethiopia's first, and at present only, geothermal power plant was built within the caldera in 1999 (Hochstein et al., 2017).

In this study, we image the seismic structure beneath Aluto using local earthquake tomography, providing new insight into the magmatic and hydrothermal processes that drive volcanic unrest. Earthquake locations reveal the dynamic nature of the volcano, whilst seismic velocities can be used to map fluids. Fluid-rich rocks exhibit reduced shear moduli, but their bulk moduli are sensitive to the gas content of the fluid. Gases are compressible, whilst liquids are less so. Therefore, tomographic images of V_P/V_S ratios can be used to further highlight fluid-rich regions, but also provide information about the nature of the fluid. Broad, high V_P/V_S regions have been identified beneath volcanic arcs (Syracuse et al., 2008), while small pockets of V_P/V_S >1.8 at depths less than 5 km have been interpreted as individual melt reservoirs beneath volcanoes (Koulakov et al., 2009; Jaxybulatov et al., 2011). Smaller elevated V_P/V_S anomalies (1.7–1.8), have been interpreted as fluid-rich sediments (Hansen, 2004; Muksin et al., 2013) and shallow steam condensates (Chiarabba and Moretti, 2006). In contrast, shallow, low V_P/V_S ratios (~1.6) have been observed within geothermal areas such as Mammoth Mountain and the Geysers, California (Julian et al., 1998; Dawson et al., 2016). Theoretical considerations (Mavko and Mukerji, 1995), experimental results (Dvorkin et al., 1999) and insights from the hydrocarbon industry (e.g., Harris et al., 1996; Yu et al., 2015) show that V_P/V_S ratios are sensitive to pore-fluid compressibility through its effect on V_P, and suggest that low V_P/V_S regions represent gas-rich reservoirs. Thus, 3-D images of V_P/V_S are extremely useful in mapping melt (in mush or magma), fluids and gases within geothermal and volcanic environments.

MATERIALS AND METHODS

We use local earthquakes from the Aluto Research and Geophysical ObservationS (ARGOS) event catalog (Wilks et al., 2017) that were recorded at 14 sites between January 2012 and January 2014 (**Figure 1**), during which time the volcano was slowly subsiding. Event detection was performed manually for P- and S-wave arrivals, with the arrival picks given weightings that reflect the clarity of their onsets (Wilks et al., 2017).

Initially, hypocentral locations and origin times were determined using NONLINLOC (Lomax et al., 2000), a nonlinear probabilistic global search algorithm, as outlined in Wilks et al. (2017). Since seismic tomography is heavily reliant on travel time accuracy, we restrict the number of events we use from this catalog based on NONLINLOC location statistics, pick weightings and a minimum detection threshold of six stations per event; this leaves 161 events and 1,672 arrivals (1,038 P- and 634 S-waves). A 1-D starting velocity model was initially developed by combining well-log data in the uppermost 2–3 km (Gianelli and Teklemariam, 1993; Gizaw, 1993) with a regional tomographic model derived from earthquakes in the Main Ethiopian Rift and Ethiopian Plateau (Daly et al., 2008). This 1-D model is further refined via joint hypocenter and velocity inversion using FMTOMO (Rawlinson and Urvoy, 2006)—see **Supplementary Section 2.0**, for further details. This refinement reveals that in general the velocity structure beneath Aluto is much slower (up to 20% for P-waves and up to 11% for S-waves; see **Supplementary Figure 2.1**) than the velocity model for the wider region (i.e., that of Daly et al., 2008).

For the seismic tomography, we use a modified version of the FMTOMO code of Rawlinson and Urvoy (2006), which was originally developed to permit the joint inversion of multiple data types (teleseismic, local earthquake, active source) for several classes of unknowns, including layer velocity, interface geometry and hypocenter location. A grid based eikonal solver known as the Fast Marching Method (Rawlinson and Sambridge, 2003) is used to solve the forward problem of traveltime prediction, and a subspace inversion method (Kennett et al., 1988) is used to adjust the unknowns at each step of the iterative non-linear solution process. Pilia et al. (2013) modified FMTOMO to permit recovery of V_P, V_S and V_P/V_S and fully non-linear location of hypocenters (via a grid search). We use this modified version of FMTOMO, but further develop it to produce robust estimates of hypocenter uncertainty based on computing the 95% confidence region around each event. The additional computational effort required to retrieve this information is minimal, because the objective function is already computed at every point during the grid search.

Assessing the Data and Model Fit and Optimization of the Inversion Parameters

For the 3-D seismic tomography we perform six iterations, each of which involves: 1) solution of the forward problem through the current model; 2) inversion for velocity parameters using a 20-D (the number of orthogonal search directions in model space) subspace inversion scheme; 3) hypocenter relocation, based on both P- and S- wave arrival times, using a fully non-linear grid search in the presence of the updated velocity model (Pilia et al., 2013). The inversion for P- and S-wave velocities is done together, along with hypocenter location, since both P-wave and S-wave arrival times are used to constrain velocity and location. The inversion for V_P/V_S is done separately, since it is a linear inversion performed along the ray paths from the S-wave model.

Structure is defined on a cubic B-spline grid that spans 0.8° horizontally and 44 km in depth, with an approximately uniform node spacing in all three dimensions of ~2.2 km (42,527 nodes in total). Within our inversion grid, nodes which are relatively undersampled by the data will take values close to the initial reference model, and appear to have ~0% deviation. These tend to lie at the edges of the model where few events or receivers are present. This attraction to the reference values is due to two features of our inversion approach: 1) regularization, which penalizes changes to model parameters not required by the data, and 2) the subspace inversion scheme, which only modifies parameters that have an effect on the data fit. For a

more complete description of FMTOMO and its modifications for local earthquake tomography, refer to de Kool et al. (2006), Rawlinson and Urvoy (2006), and Pilia et al. (2013).

We consider the trade-off between the complexity of the final model (which is a function of the model roughness and model variance) and the accuracy of the data fitting by performing numerous inversions with a range of damping and smoothing parameters (e.g., Eberhart-Phillips, 1986). This is performed using the following trade-off curves: data fit (variance of the residuals) vs. model roughness, while varying the smoothing parameter; data fit vs. model variance, while varying the damping parameter. The details of how we choose the damping and smoothing parameters are included the **Supplementary Material**. The final variance reduction for each model is: 56% for the V_P model; 49% for the V_S model; and 34% for the V_P/V_S model.

Earthquake Relocation Uncertainty

The non-linear inverse problem that we solve is to find the location of each earthquake such that the differences between the observed and predicted arrival times (through a 3-D velocity model) are minimized. This is formalized by specifying an objective function $S(m)$, where m is a vector that defines the latitude, longitude and depth of the earthquake, such that

$$S(m) = (d_{obs} - d_m(m))^T C_0^{-1} (d_{obs} - d_m(m)), \quad (1)$$

where d_{obs} is a set of N observed arrival times (from a given hypocenter) with the mean subtracted, C_0^{-1} is a data covariance or weighting matrix which accounts for data picking uncertainty, and d_m (m) is a set of predicted traveltimes with the mean subtracted. By removing the mean, we can eliminate the origin time as an unknown in the inversion, since source location can be constrained by the relative on-set times of a phase at a set of stations.

We locate the minimum of $S(m)$ using a grid-search, which is a fully non-linear technique capable of locating the global minimum of $S(m)$ and providing valuable information on location uncertainty [see Lomax et al. (2000) for a comprehensive review of nonlinear earthquake location methods]. The method works by computing $S(m)$ at a regular grid of points in latitude, longitude and depth. This regular sampling of the objective function in 3-D space means that the point of minimum misfit, which coincides with our preferred earthquake location, can be readily identified. A nested grid search is used to locate the hypocenters. In the first step, a coarse step size of 1 km is used, but once the optimum location is found, the search is repeated in the neighborhood of this point using a step size of 100 m.

One advantage of heavily sampling the objective function across a dense 3-D grid is that hypocenter uncertainty information can be obtained with little additional computational effort. Here, we adopt the approach described by Sambridge and Kennett (1986) for defining the 95% confidence region around the solution $\hat{m}$ obtained from the grid search. This is achieved by identifying the region of parameter space which satisfies

$$T(m, \hat{m}) = \frac{S(m) - S(\hat{m})}{S(\hat{m})} \leq \frac{\chi_3^2(0.95)}{(N-3)}, \quad (2)$$

where N is the number of data picks and $\chi_3^2(0.95) = 7.815$ is the Chi-square statistic for a p-value of 0.05 and three degrees of freedom. This approach is valid since the objective function **1**, with $[C_0^{-1}]_{ij} = \delta_{ij}\sigma_{ij}$ (where $\delta_{ij} = 1$ when $i = j$ and $\delta_{ij} = 0$ otherwise), can be written as

$$S(m) = \sum_{i=1}^{N} \frac{\left[d_{obs}^i - d_m^i(m)\right]^2}{\sigma_i^2}, \quad (3)$$

which has a chi-square distribution with N–M degrees of freedom, where $M = 3$ is the number of model parameters. **Equation 3** accounts for the effect of errors in the velocity model (which are usually unclear) by rescaling S so that $S(\hat{m}) = N - 3$, which is simply the expectation value of a chi-square distribution with N−3 degrees of freedom. This is obtained by multiplication with the factor $(N - 3)/S(\hat{m})$. Both the objective function **1** and method for computing confidence intervals assume that the data errors are Gaussian, which will influence the final hypocenter locations and uncertainty estimates.

In our application of this approach, we use the boundary of the 95% confidence region as a proxy for location uncertainty and summarize our results in terms of uncertainty in depth, latitude and longitude, as shown in **Figure 2**. As expected, uncertainty in depth tends to be larger in comparison to uncertainty in latitude and longitude, although for most events it is well below 5 km. A number of events cluster near the upper boundary of the model, and of these a noticeable proportion have depth uncertainties that are larger than average. This occurs because shallow events that are not well constrained in depth cannot be relocated above the model, and hence are forced to reside immediately below the surface. The upper surface of the model is set to be 2.5 km above sea level, which means that all receivers and sources lie within the model volume. While it would be possible to exclude these events from the inversion, they are no less valid than deeper events, which have a similar location uncertainty. Overall, these results suggest that the distribution of seismicity that we interpret in terms of volcanic processes is robust, including the observation that the zone of earthquake activity tends to deepen as we move away from the volcanic center.

Checkerboard Resolution Tests

Since geophysical inverse problems are almost invariably underdetermined and hence solutions are nonunique, it is useful to evaluate the robustness of model solutions derived by seismic tomography. Inherent uncertainties in the data and varying raypath coverage mean that it is important to assess which features of a model are required by the data and which are not, so that a model's robustness can be quantified. Therefore, using the optimized regularization parameters described previously, we evaluate solution robustness using the so-called "checkerboard test" (Glahn and Granet, 1993; Rawlinson and Sambridge, 2003). In this test, the source-receiver configurations of the observational dataset are used to compute a synthetic travel

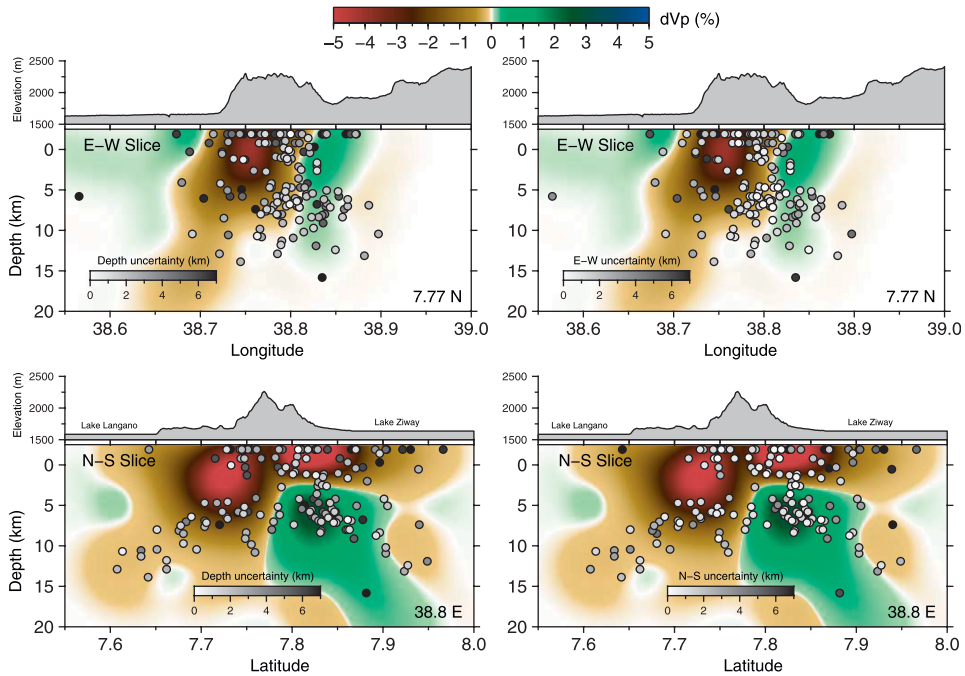

FIGURE 2 | Relocated earthquake uncertainties. East–west **(upper)** and north–south **(lower)** slices through the P-wave solution model with all earthquakes superimposed. Earthquakes are shaded using a grey-scale that indicates uncertainty in depth **(left)** and uncertainty in longitude/latitude **(right)**. The top profiles are along a latitude of 7.77 N and the bottom profiles are along a longitude of 38.8 E.

time dataset. This is calculated through an artificial "checkerboard" structure, which is overlain on the original input model. Gaussian noise with a standard deviation of 20 ms is also added to the synthetic datasets to simulate the assumed picking errors in the "real" data.

The checkerboard comprises a 3-D region of alternating high and low velocity anomalies, where the perturbations are set to be ±0.5 km/s for V_P (±6.6–16.2%) and ±0.2 km/s (±4.8–9.6%) for V_S. The V_P/V_S input checkerboard is obtained by dividing the V_P checkerboard by the V_S checkerboard. The tomography is then run with the 1-D reference model as the starting model (whilst also relocating hypocenters) in an attempt to recover the checkerboard pattern. Regions of the solution model that sufficiently recover the checkerboard pattern are considered to be "well-resolved."

A known weakness of checkerboard tests is that it is possible for small-scale structures to be well retrieved in comparison to larger scale structures (Léveque et al., 1993); consequently, we generate checkerboards with differing scale lengths of ~8.8, ~4.4, and ~2.2 km. By adopting this approach, we are well positioned to interpret both larger and smaller scale structure in regions of good recovery. We also include a spike test to determine the resolution of discrete velocity anomalies. The input spike is comprised of a low V_P, high V_S and low V_P/V_S anomaly centered at approximately 7.78N, 28.8E and ~1 km depth.

The input checkerboard model for V_P/V_S is shown in **Figure 3** and the recovered model is shown in **Figure 4**. Details of the synthetic recovery tests for V_P and V_S velocity structure, and the spike test, are presented in **Supplementary Section 4** (**Supplementary Figures 4.1–4.5**). The results of the synthetic testing using a checkerboard structure for the 161 events is presented in horizontal and vertical slices. For the coarse checkerboard (**Figure 4A**), it is evident that V_P/V_S anomalies are well resolved within the seismic network and down to at least 10 km depth. Outside of the array and below 10 km depth, however, smearing distorts the recovery and highlights that these regions of the model are much less well resolved. The same features are evident in the intermediate checkerboards (**Figure 4B**), where the lack of events and poor raypath coverage restrict resolution outside of the network and deeper than 8 km. At a finer scale [**Figure 4C**], the checkerboard is even less well defined with restricted recovery below sea level and toward the periphery of the array. Cumulatively this suggests we cannot recover structure on length scales finer than 3 km. With respect to the spike test, as expected, the recovered spike exhibits a decrease in amplitude and a larger footprint compared to the input spike (**Supplementary Material 4.5**); in the E–W direction this is minimal, but is more noticeable in the N–S direction, which is consistent with the raypath coverage. Nevertheless, this test clearly shows that the anomalies recovered at this location in the final model are likely correct.

The observed lack of resolution at depth is caused by the predominance of events occurring between the surface and 10 km depth, with the region beneath relatively aseismic in comparison. Lateral smearing is particularly evident in the north-south depth slices due to the high concentrations of events to the north and south of the caldera and the increased density of ray paths orientated in that direction. The poor recovery of the

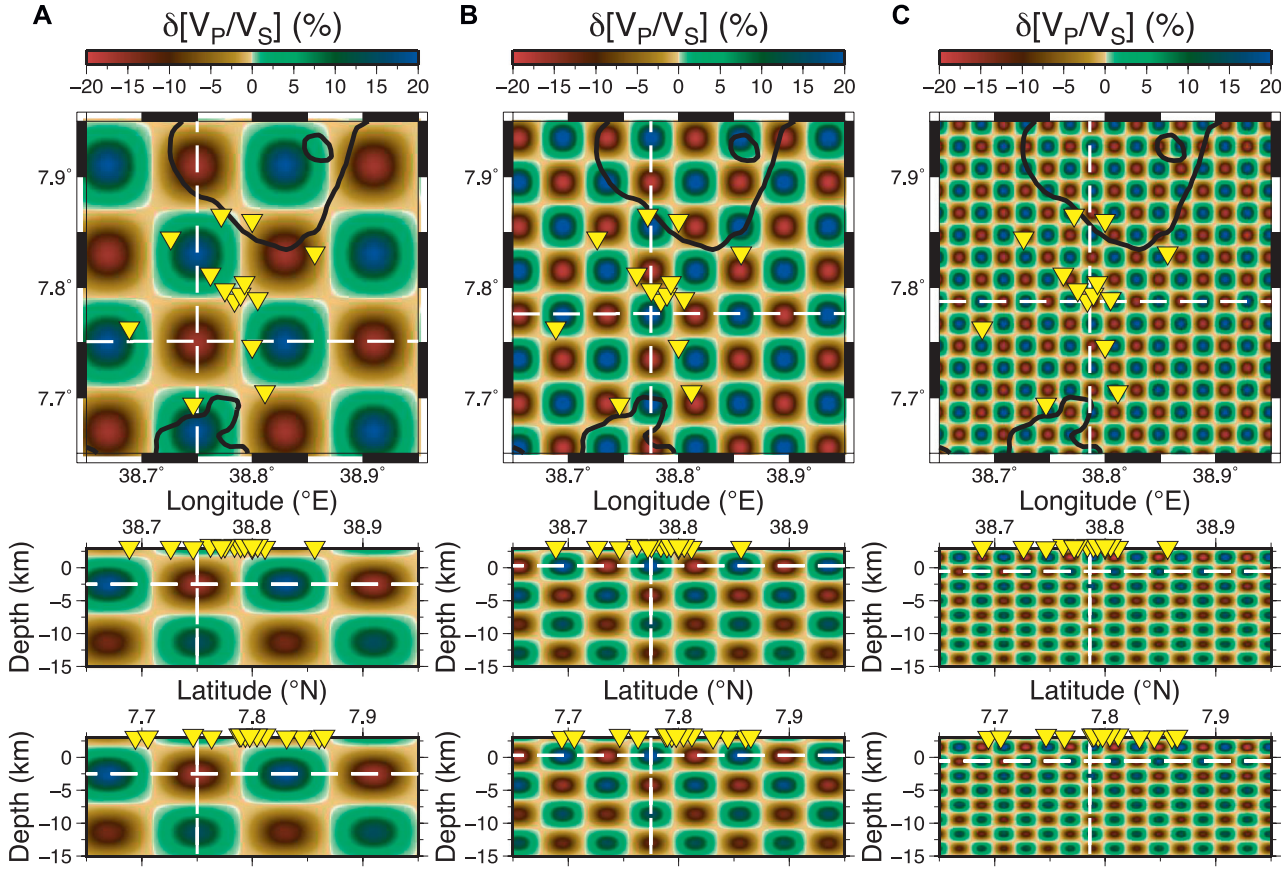

FIGURE 3 | Input V_P/V_S checkerboard models for resolution testing. Slices are taken through the maximum perturbations of **(A)** coarse (~8.8 km), **(B)** intermediate (~4.4 km) and **(C)** fine checkerboards (~2.2 km), to constrain the resolving power at differing scale lengths.

checkerboard at the edges of the east-west cross-sections is caused by the relative lack of events to the east and west of the network (i.e., toward the border faults). At all scale lengths, the amplitudes of the perturbations are underestimated in comparison to the input checkerboards. This occurs due to the damping and smoothing regularization parameters implemented in the inversion, which favor a conservative solution (in terms of amplitude and wavelength of structure) unless required by the data.

RESULTS

Over a 2-year period between 2012 and 2014, Wilks et al. (2017) located 1,361 earthquakes within 15 km of the center of the caldera. As discussed, in an effort to use only the best located events for imaging and to stabilize the inversions, we use a subset of these data comprised of 161 events and 1,672 source-receiver raypaths. Nevertheless, the resulting patterns in seismicity are similar between the original 1,361 events and the final relocated 161 events. **Figure 5** shows how the relocated events change with respect to the original locations and **Figure 2** shows the uncertainties in the new event locations. In agreement with Wilks et al. (2017), most events are located above sea level, beneath the volcano edifice. Beneath this lies a gap in seismicity until a depth of roughly 5 km. **Figures 2 and 5** show how this seismicity deepens to the north and south, capping what Wilks et al. (2017) interpret as a ductile deeper region. There is a weak bimodal distribution, with more events lying beneath the north and south rim of the volcano. Furthermore, the events cluster along the north-south trend of the AJFZ, which was a particularly clear feature in the original seismicity catalog.

Figure 6 shows the V_P/V_S model obtained from the inversion; the V_P and V_S models are presented in the **Supplementary Material**, but **Figure 2** shows two cross-sections through the V_P model. Poorly constrained regions of the model are masked according to the sum of the absolute values of the Fréchet derivatives, which is a similar approach to the so-called Derivative Weight Sum method (e.g., Biryol et al., 2013). Reduced seismic velocities are more prominent in the P-wave model and in the shallow regions. Low V_P/V_S ratios of 1.45–1.65 (a Poisson's ratio of $\nu = 0.05$–0.21) and a negative V_P anomaly (up to −5%) extend across the entire range of the volcano that lies above sea level (**Figures 2** and **6**). The checkerboard tests (**Figures 3** and **4**; **Supplementary Section 3**) show that this is a

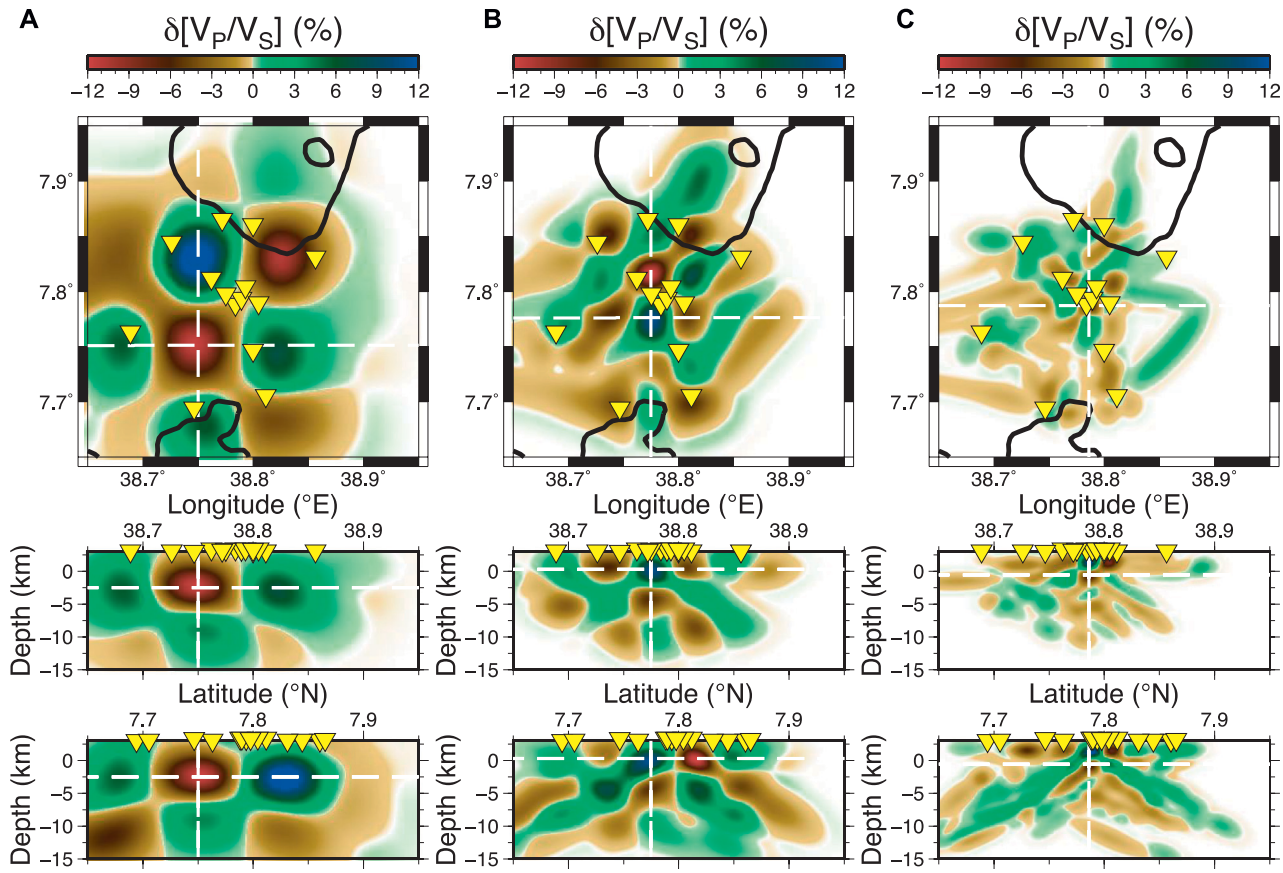

FIGURE 4 | Checkerboard recovery results for V_P/V_S of differing checkerboard scale lengths **(A–C)**. Compare with input checkerboard structure shown in **Figure 3**. See **Supplementary Figures 4.1–4.5** for equivalent V_P and V_S checkerboard test results.

robust and well resolved feature. Deeper than this, average to elevated V_P/V_S ratio are observed. It is particularly high (>2.0) in the well resolved region beneath the central stations of the caldera between 5 and 8 km deep (**Figure 6**). Furthermore, we observe an additional high V_P/V_S region to the south of the caldera at ~3 km depth (**Figure 6**). We note that this region is located toward the periphery of the receiver array, but our synthetic resolution tests suggest that it is reasonably well resolved. Due to a lack of deep seismicity, resolution in these models decreases rapidly below ~10 km.

In summary, a shallow region above sea level and beneath the volcano is characterized by abundant seismicity that follows the trend of faults and fractures in the region. It exhibits low seismic velocities and a low V_P/V_S ratio. Beneath this lies a region of decreased seismicity with evidence for a narrow high- V_P/V_S region beneath the volcano. There is also evidence for a high V_P/V_S region to the south of the volcano. Deeper seismicity marks a brittle region that envelops a more ductile region, deepening to south and north of the caldera. There is some evidence for high V_P/V_S in this region, but resolution is lacking. In the next section we interpret the shallow region in terms of an active hydrothermal system and the deeper region as magmatic in nature.

DISCUSSION AND INTERPRETATION

A conceptual interpretation of the results is shown in **Figure 7**. Here we discuss characteristics of the hydrothermal system and the deeper magmatic system and how they interact.

Hydrothermal System

We interpret the region of low V_P/V_S ratios that lies above sea level in terms of an over-pressurized gas-rich volume (e.g., Dvorkin et al., 1999; Lees and Wu, 2000) occupying highly fractured and hydrothermally altered volcanic products. Low Poisson's ratios are likely amplified by the presence of aligned cracks, fractures and faults, as Poisson's ratios below 0.1 are uncommon in unfractured isotropic materials (Walsh, 1965). Such structural heterogeneities have been shown to decrease Poisson's ratio and V_P/V_S in low stress environments. We suggest that structures such as ring faults and the AJFZ contribute to the low ratios that we observe (Hutchison et al., 2015). These are linked to fumarolic activity around the volcanic edifice and at the surface (see **Figures 1**; Braddock et al., 2017). This inference is also supported by shear-wave splitting observations, which imply that the volcanic center above sea level is highly fractured due to at least two dominant fracture sets (Nowacki et al., 2018). The sharp transition from low

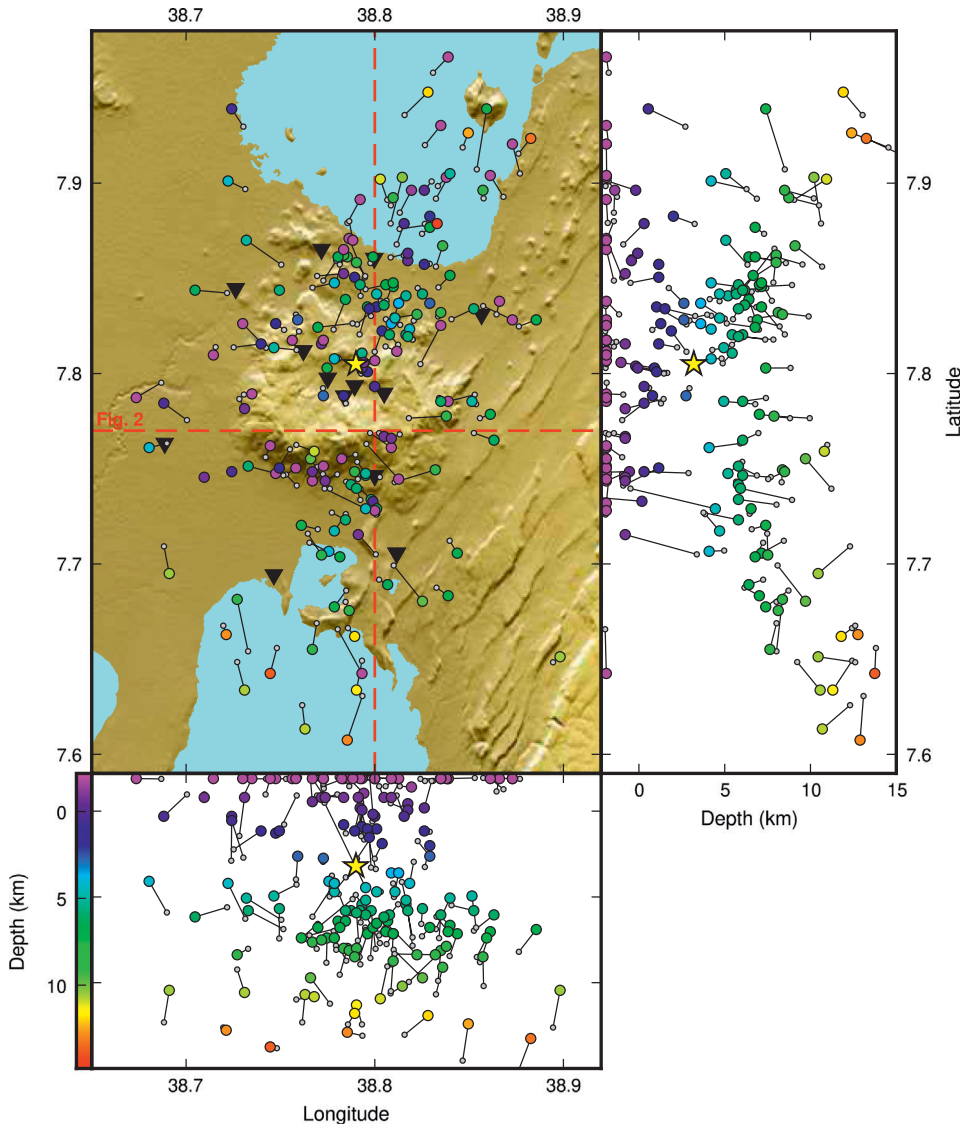

FIGURE 5 | Map of original and relocated hypocenters found by joint inversion for velocity structure and earthquake location. Small white circles show the starting location from Wilks et al. (2017), whilst larger circles show the final relocations. Lines connect the original and relocated hypocenters. Color shows the depth of the relocations. The yellow star shows the inferred subsidence source found by Hutchison et al. (2016b). Red dashed lines indicate the location of the north-south and east-west profiles shown in **Figure 2**.

to higher V_P/V_S at around sea level may also be influenced by the change in lithology from the silicic volcanic rhyolites of Aluto's recent effusive volcanism and lacustrine sediments to the underlying unit of Bofa Basalt, as observed in well log data (Teklemariam, 1996; Teklemariam et al., 1996). The magnetotelluric (MT) study of Samrock et al. (2015) shows a high conductivity (1–2 Ω m) layer above sea level, which they interpret as a hydrothermally altered clay cap.

Experiments show that the compressibility of supercritical fluids bears a greater resemblance to steam than liquid and can also produce low V_P/V_S anomalies in the subsurface (Burnham et al., 1969). At Aluto, deep well data (to 2,500 m below the surface) have shown that temperatures reach a maximum of 360°C at pressures greater than 22 MPa (Gizaw, 1993), conditions at or above the threshold required for water to become supercritical (e.g., Chouet et al., 2008; Zollo et al., 2008). Under the assumption that this maximum temperature is exceeded, we suggest that supercritical fluids might also contribute to the low V_P/V_S anomaly.

Magmatic System

High V_P/V_S ratios in volcanic regions are commonly associated with the presence of partial melt in the crust (e.g., Hammond and Kendall, 2016). Fluids have a shear modulus of zero, which reduces V_S in partially molten rocks. In the absence of gas there is little change in fluid compressibility and therefore

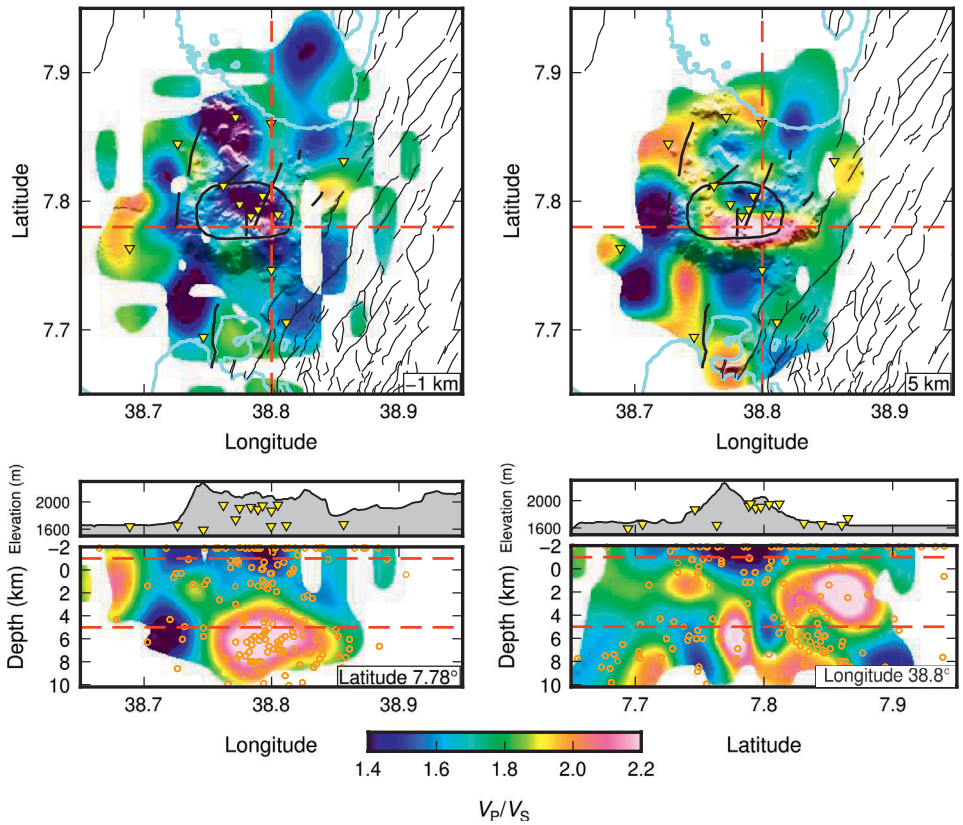

FIGURE 6 | Depth slices (at 1 km above sea level and 5 km below sea level) and east–west and north–south cross-sections through the tomographic solution model of the V_P/V_S structure (shown as an absolute value). The model is only plotted in regions where there is resolution based on Fréchet derivatives (see **Supplementary Material**). Yellow triangles indicate station locations, black lines on the depth slices indicate mapped fault locations and small open circles on the cross-sections indicate event locations. Topography is shown above the cross-sections and indicated by hillside shading on the depth slices. See **Supplementary Material** for the V_P and V_S models.

little change in V_P. Hence, the high V_P/V_S regions beneath sea level in our inversion results suggests a region of partial melt at depth beneath the hydrothermal system. A crystalline mush zone has also been suggested by Gleesen et al. (2017), who through phase equilibria modeling proposed a magma storage depth of 5.6 ± 1 km below the surface. However, it is difficult to convert V_P/V_S ratios to melt volume fraction, as seismic velocities are as sensitive to the shape of melt inclusions as they are to volume fraction (Hammond and Kendall, 2016).

Due to the underlying physics and differences in array geometries, there are often differences between seismic and magnetotelluric images of melt reservoirs (e.g., Whaler and Hautot, 2016; Pritchard et al., 2018). Seismic velocities are sensitive to volume fraction of melt and the shape of the melt inclusions (wetting angle) whereas MT is most sensitive to the connectivity, composition and amount of melt. Previous MT studies show the Aluto upper crust that lies beneath sea level to be relatively resistive (>100 Ω m) and hence melt-poor (Samrock et al., 2015; Hübert, et al., 2018), whereas we see localized regions of high (>2.0) V_P/V_S values suggesting the presence of partial melt. A suggested explanation for some discrepancy between MT and seismic results is that the melt exists in isolated pockets which are not sufficiently connected for the rock to be conductive. Alternatively, low temperature peralkaline melts with a low wt% H_2O are relatively resistive and consistent with the observed values (Guo et al., 2016; Hübert, et al., 2018). Such low water content could be achieved following repeated cycles of melting and recrystallisation within a long-lived crystal mush zone. However, the more recent study of Samrock et al. (2020), which reprocessed the same data using the method of Grayver et al. (2019), but accounts for topography and galvanic distortion, shows evidence of moderately conductive (10–20 Ω m) regions in an otherwise resistive crust below sea level. These values can be explained with higher temperature and melt fractions.

The hypocentral relocations improve the delineation of the convex lower boundary of seismicity, which corresponds to the brittle-ductile transition. This boundary is roughly 5 km beneath the edifice, but deepens to 15 km to the north and south (**Figure 7G**). Our error analysis of the relocations suggest, with most events having <3 km uncertainties both laterally and in depth, that the pattern of seismicity is robust. While a contribution to hypocenter depth uncertainty may also come from the velocity-depth trade-off, the simple convex shape of seismicity spans the entire model in the N–S direction, which would require a very

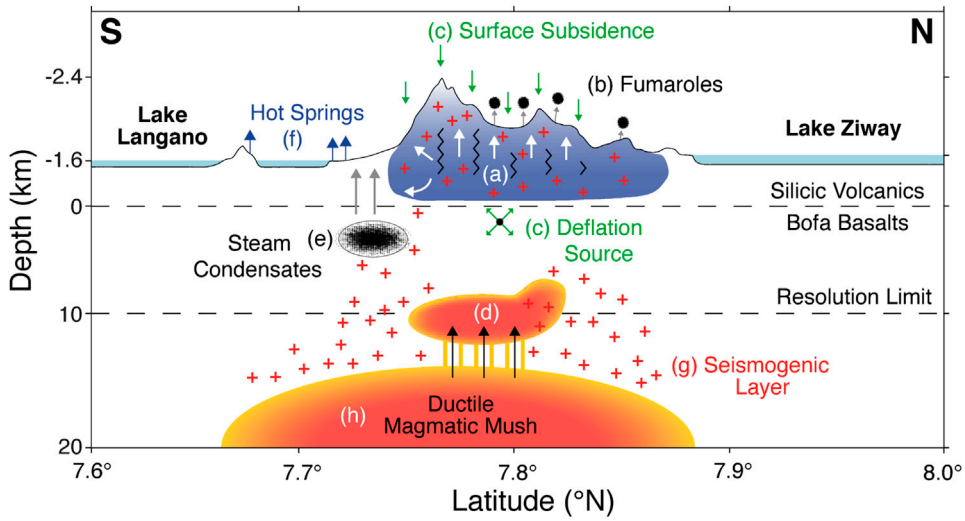

FIGURE 7 | Schematic diagram of the interpreted subsurface structure and processes at Aluto, based on the new results and constraints from previously published studies. The key features are: **(A)** high seismicity within a low V_P/V_S region of over-pressurized gas at/close to a supercritical state, associated with **(B)** fumarolic activity and causing **(C)** outflow driven surface deflation; **(D)** a high V_P/V_S region with a significant melt component that has ascended from below; **(E)** shallow high V_P/V_S regions of steam condensates that release volatiles to the surface via **(F)** hot springs; **(G)** a deeper seismogenic region, convex with latitude; **(H)** a ductile reservoir of magmatic mush.

broad, coherent and high amplitude velocity anomaly to explain the convexity (noting that at 10 km depth, a 1 km increase in hypocenter depth would require a ~10% increase in the overlying velocity, assuming a background velocity of 5 km/s). As such, we propose that the general increase in depth of the seismicity zone away from the volcanic center is meaningful. Deepening of seismicity away from volcanic centers has also been observed at Corbetti (Lavayssière, et al., 2019) and at Fentale and Dofen, which are volcanoes in the northern MER (Keir et al., 2006), where earthquakes occurred between 8 and 10 km depth beneath each volcano but as deep as 16 km elsewhere in the magmatic segment. Similarly, Hudson et al. (2017) see a similar pattern directly beneath Bárðarbunga caldera in Iceland.

A lack of seismicity more than 10 km below the center of the volcano implies a hot, ductile crust, which in turn may suggest a melt-rich mush storage region, consistent with petrological observations (Hutchison, et al., 2016a). There is also some suggestion of a conductive body at these depths beneath Aluto (Samrock et al., 2020). We also see some evidence for high V_P/V_S ratios in this region, but note that the resolution of our V_P/V_S inversions is poor below 10 km depth. However, these results together with the convex pattern of deep seismicity observed at Aluto suggests that the seismicity delineates the upper boundary of a region of higher heat flux (spanning ~20 km laterally), which has a more ductile rheology and little seismicity (**Figure 7H**). This is also consistent with the models of the upper crustal plumbing systems at other rift calderas such as Corbetti (Gottsmann et al., 2020).

Coupled Magmatic and Hydrothermal Systems and Uplift

Aluto is a rapidly deforming volcano which shows episodic ground deformation (Biggs, et al., 2011; Hutchison et al., 2016b). Hutchison et al. (2016b) proposed that the uplift was caused by injection of new material into the magmatic system, and subsidence was associated with the magmatic degassing and depressurization of the hydrothermal system. Based on MT results that show a clay cap ~500 m thick and ~2–3 km wide, Samrock et al. (2015) also propose that swelling clays and freshwater incursion may be agents for uplift and subsidence at Aluto. Our model, however, suggests the presence of velocity anomalies of significantly larger dimensions and hence supports the hypothesis that the driver of deformation is deeper in origin. Proximal seismicity and high V_P/V_S ratios delineate a narrow region that connects a deeper magmatic body to the hydrothermal system. Support for this comes from carbon isotope sampling, which shows that Aluto's magmatic and hydrothermal systems are physically connected, where deep (>2 km), hot (>250°C) geothermal fluids receive ongoing input of magmatic volatiles from beneath (Hutchison et al., 2016b). We therefore propose that it is episodic pulses of magma injection at depth that drives this volatile release, which then causes the uplift-subsidence events observed at the surface in this coupled system. Similar mechanisms have been proposed at other volcanoes (e.g., Bárðarbunga, Iceland—Hudson et al., 2017; Corbetti, Ethiopia—Lloyd et al., 2018b).

Reservoir seismicity occurs with deformation, which can be associated with inflation (e.g., Stork et al., 2015) or deflation (e.g., Segall, 1989; van Thienen-Visser and Breunese, 2015), both of which can be at play in a coupled magmatic and hydrothermal system. A sudden release of volatiles from the deeper magmatic system can lead to over-pressured gases within the hydrothermal system (Battaglia et al., 2006), which in turn leads to inflation. The subsequent outflow of volatiles and hydrothermal fluids from the geothermal system generates subsidence at the surface (De Natale

et al., 2001), which at Aluto was observed for the majority of the seismic experiment (Wilks et al., 2017). The sources responsible for significant (>4.3 cm) subsidence prior to 2012 have been located in the uppermost 2–3 km (Biggs et al., 2011; Hutchison et al., 2016b), which correlates with the base of our low V_P/V_S region (**Figure 6**). We note that there may also be subsidence effects associated with cooling.

Campi Flegrei, another young, geothermally-active caldera in a state of unrest, exhibits similar gaseous controls in a shallow seismogenic zone (Di Vito et al., 1999; Chiarabba and Moretti, 2006; Battaglia et al., 2008; Chiodini et al., 2012; De Siena et al., 2017). The values of the low V_P/V_S anomaly are similar in magnitude to those observed at Aluto (~1.45), with an accompanying low V_P anomaly, estimated to be the primary source location of subsidence. At Campi Flegrei, it has been suggested that supercritical fluids beneath a more rigid clay cap are responsible for uplift (Vanorio and Kanitpanyacharoen, 2015). We suggest that shallow hydrothermal processes at Aluto are comparable to Campi Flegrei in terms of the structure and the processes that drive seismicity and deformation. However, the low V_P/V_S anomaly at Aluto seems to be within or above the clay cap (Samrock et al., 2015). We attribute high-pressure gas phases and the subsequent outflow from the geothermal reservoir as the primary cause of subsidence in the absence of any eruptive behavior. As these are the first seismic images of the volcanoes of the MER, it is not clear how unique Aluto is with respect to other volcanoes in the MER.

The high V_P/V_S (**Figure 6**) region to the south of the caldera at 3 km depth may represent steam condensates (**Figure 7E**) that manifest at shallower depths, away from the main volcanic edifice where temperatures are reduced (Aster and Meyer, 1988; Simiyu, 1999). Samrock et al. (2020) observe a highly conductive anomaly at the same depth but more to the east of the volcano. Condensates may form brines that then migrate toward the surface due to increasing pore pressure along fracture networks associated with the AJFZ (Hutchison et al., 2016b). These may feed or heat the hot springs seen at the surface near Lake Langano (**Figures 1** and **7F**) (Kebede et al., 1985; Hutchison et al., 2015; Braddock et al., 2017; Hochstein et al., 2017). This is also compatible with the elevation-driven, southerly groundwater flow direction from Lake Ziway to Lake Langano (Bernacsek et al., 1992).

Aluto, one of numerous calderas in the MER, is a surface expression of magma-assisted continental rifting. As rifting progresses, strain is localised in magmatic segments rather than the border faults. However, how magma at depth (e.g., as tomographically imaged, for example, by Bastow et al., 2005 and Gallacher et al., 2016) feeds the axial magmatic segments of the MER is still to be determined.

CONCLUSIONS

Our study has produced the first seismic images of Aluto, a geothermally active volcano in the Main Ethiopian Rift, which was only recently discovered to be in a state of unrest. These images, coupled with the relocated earthquake hypocenters, provide constraints on the plumbing system beneath the volcano, which has provided new insight into its possible pre-eruptive behavior. Major findings include: 1) a volatile-rich ductile "magmatic mush" region below 10 km depth, which is capped by a convex layer of seismicity; 2) a region of elevated V_P/V_S at intermediate depths (5–8 km), also defined by an absence of seismicity, which likely represents the storage of partially molten material from below; 3) the presence of shallow and localized high V_P/V_S zones away from the volcano, which may represent concentrations of steam condensates that release volatiles to the surface; and 4) a shallow volume of rock (above sea level) containing over-pressurized gas at or close to supercritical conditions (defined by abundant seismicity, low V_P and low V_P/V_S). Together, these findings demonstrate that unrest at Aluto is driven by the coupling between magma ascent and hydrothermal response, which produce the inflationary and deflationary episodes that have been recently observed. This model is likely applicable to other hydrothermally active volcanoes in a state of unrest.

DATA AVAILABILITY STATEMENT

The seismic dataset analyzed for this study is open access and available on IRIS (Network Code XM). See Wilks et al. (2017) for more information on the ARGOS seismic project. Files containing the final V_P, V_S and V_P/V_S solution models and the relocated hypocenters are available at https://doi.org/10.6084/m9.figshare.5892775.v4.

AUTHOR CONTRIBUTIONS

MW processed the data, performed the analysis and wrote the first draft of the paper, as part of his PhD, which was supervised by JK and JW. JK and JB formulated the project. NR developed the inversion code and provided guidance on its use and implementation, and interpretations. MW, JK, AA, AN, and JB acquired the field data. All authors contributed to the interpretation of the results and the writing of the paper. MW, NR, and AN prepared the Figures.

FUNDING

The Bristol University Microseismic ProjectS (BUMPS) provided funding for the seismic experiment and the equipment was loaned from SEIS-UK, a NERC Service and Facility (GEF loan 962). MW was funded by an EPSRC studentship. AN was funded by BUMPS, a Leverhulme Early Career Fellowship, and a NERC standard grant (NE/R001154/1, REMIS: Reliable Earthquake Magnitudes for Induced Seismicity). JW and AN received funding from the European Research Council under the European Union's Seventh Framework Program (FP7/2007–2013)—ERC Grant agreement 240473, CoMITAC. JB was funded by NERC COMET. JB and JMK were funded by the Natural Environment Research Council (NERC) RiftVolc

Large Grant (NE/L013932/1, Rift volcanism: past, present, and future).

ACKNOWLEDGMENTS

We thank Tom Hudson for useful discussions and helpful comments on the manuscript. Comments from two reviewers, the guest editor, LD, and the chief editor, Valerio Acocella, helped improve the presentation; we thank them for their time and efforts.

SUPPLEMENTARY MATERIAL

The Supplementary Material for this article can be found online at: https://www.frontiersin.org/articles/10.3389/feart.2020.579699/full#supplementary-material

REFERENCES

Agostini, A., Bonini, M., Corti, G., Sani, F., and Mazzarini, F. (2011). Fault architecture in the Main Ethiopian Rift and comparison with experimental models: implications for rift evolution and Nubia-Somalia kinematics. *Earth Planet. Sci. Lett.* 301, 479–492. doi:10.1016/j.epsl.2010.11.024

Aster, R. C., and Meyer, R. P. (1988). Three-dimensional velocity structure and hypocenter distribution in the Campi Flegrei caldera, Italy. *Tectonophysics* 149, 195–218. doi:10.1016/0040-1951(88)90173-4

Bastow, I. D., Stuart, G. W., Kendall, J.-M., and Ebinger, C. J. (2005). Upper-mantle seismic structure in a region of incipient continental breakup: northern Ethiopian rift. *Geophys. J. Int.* 162 479–493. doi:10.1111/j.1365-246X.2005.02666.x

Battaglia, J., Zollo, A., Virieux, J., and Dello Iacono, D. (2008). Merging active and passive data sets in traveltime tomography: the case study of Campi Flegrei caldera (Southern Italy). *Geophys. Prospect.* 56, 555–573. doi:10.1111/j.1365-2478.2007.00687.x

Battaglia, M., Troise, C., Obrizzo, F., Pingue, F., and De Natale, G. (2006). Evidence for fluid migration as the source of deformation at Campi Flegrei caldera (Italy). *Geophys. Res. Lett.* 33, a. doi:10.1029/2005GL024904

Bernacsek, G. M., Hughes, J. S., and Hughes, R. H. (1992). *A directory of African Wetlands*, Cambridge: IUCN, UNEP and WCMC, 820.

Biggs, J., Bastow, I. D., Keir, D., and Lewi, E. (2011). Pulses of deformation reveal frequently recurring shallow magmatic activity beneath the Main Ethiopian Rift. *Geochem. Geophys. Geosyst.* 12, 1–11. doi:10.1029/2011GC003662

Birhanu, Y., Wilks, M., Biggs, J., Kendall, J. M., Ayele, A., and Lewi, E. (2019). Seasonal patterns of seismicity and deformation at the Alutu geothermal reservoir, Ethiopia, induced by hydrological loading. *J. Volcanol. Geother. Res.* 356, 175–182. doi:10.1016/j.jvolgeores.2018.03.008

Biryol, C. B., Leahy, G. M., Zandt, G., and Beck, S. L. (2013). Imaging the shallow crust with local and regional earthquake tomography. *J. Geophys. Res. Solid Earth.* 118, 2289–2306. doi:10.1002/jgrb.50115

Braddock, M., Biggs, J., Watson, I. M., Hutchison, W., Pyle, D. M., and Mather, T. A. (2017). Satellite observations of fumarole activity at Aluto volcano, Ethiopia: implications for geothermal monitoring and volcanic hazard. *J. Volcanol. Geothermal Res.* 341, 70–83. doi:10.1016/j.jvolgeores.2017.05.006

Brown, S. K., Sparks, R. S. J., Mee, K., Vye-Brown, C., Ilyinskaya, E., Jenkins, S. F., et al. (2015). "Country and regional profiles of volcanic hazard and risk," in *Global volcanic hazards and risk*, Editors S. C. Loughlin, R. S. J. Sparks, S. K. Brown, S. F. Jenkins, and C. Vye-Brown. Cambridge: Cambridge University Press.

Burnham, C. W., Holloway, J. R., and Davis, N. F. (1969). Thermodynamic properties of water to 1,000° C and 10,000 bars. *Geo. Soc. Am. Spec. Paper.* 132, 1–96. doi:10.1130/SPE132-p1

Chiarabba, C., and Moretti, M. (2006). An insight into the unrest phenomena at the Campi Flegrei caldera from V_p and V_p/V_s tomography. *Terra. Nova.* 18, 373–379. doi:10.1111/j.1365-3121.2006.00701.x

Chiodini, G., Caliro, S., De Martino, P., Avino, R., and Gherardi, F. (2012). Early signals of new volcanic unrest at Campi Flegrei caldera? Insights from geochemical data and physical simulations. *Geology* 40, 943–946. doi:10.1130/g33251.1

Chouet, B., Dawson, P., and Martini, M. (2008). Shallow-conduit dynamics at Stromboli Volcano, Italy, imaged from waveform inversions. *Geo. Soc. Lond.* 307, 57–84. doi:10.1144/SP307.5

Daly, E., Keir, D., Ebinger, C. J., Stuart, G. W., Bastow, I. D., and Ayele, A. (2008). Crustal tomographic imaging of a transitional continental rift: the Ethiopian rift. *Geophys. J. Int.* 172, 1033–1048. doi:10.1111/j.1365-246X.2007.03682.x

Dawson, P., Chouet, B. A., and Pitt, A. (2016). Tomographic image of a seismically active volcano: Mammoth Mountain, California. *J. Geophys. Res. Solid Earth.* 121, 114–133. doi:10.1002/2015JB012537

de Kool, M., Rawlinson, N., and Sambridge, M. (2006). A practical grid-based method for tracking multiple refraction and reflection phases in three-dimensional heterogeneous media. *Geophys. J. Int.* 167, 253–270. doi:10.1111/j.1365-246X.2006.03078.x

De Natale, G., Troise, C., and Pingue, F. (2001). A mechanical fluid-dynamical model for ground movements at Campi Flegrei caldera. *J. Geodyn.* 32, 487–517. doi:10.1016/S0264-3707(01)00045-X

De Siena, L., Chiodini, G., Vilardo, G., Del Pezzo, E., Castellano, S. C., Colombelli, S., et al. (2017). Source and dynamics of a volcanic caldera unrest: Campi Flegrei, 1983–84. *Sci. Rep.* 7, 8099. doi:10.1038/s41598-017-08192-7

Di Vito, M. A., Isaia, R., Orsi, G., Southon, J., de Vita, S., D'Antonio, M., et al. (1999). Volcanism and deformation since 12,000 years at the Campi Flegrei caldera (Italy). *J. Volcanol. Geothermal Res.* 91, 221–246. doi:10.1016/S0377-0273(99)00037-2

Dvorkin, J., Mavko, G., and Nur, A. (1999). Overpressure detection from compressional- and shear-wave data. *Geophys. Res. Lett.* 26, 3417–3420. doi:10.1029/1999gl008382

Eberhart-Phillips, D. (1986). Three-dimensional velocity structure in northern California coast ranges from inversion of local earthquake arrival times. *Bull. Seis. Soc. Am.* 76(4), 1025–1052.

E. L. C. Electroconsult (1986). "Exploitation of Langano-Aluto geothermal resources feasibility report," in *Geothermal exploration project, Ethiopian lake district rift.* Milano, Italy: Tech. Rep., Ministry of Mines and Energy. 1-iii/8-7.

Gallacher, R. J., Keir, D., Harmon, N., Stuart, G., Leroy, S., Hammond, J. O. S., et al. (2016). The initiation of segmented buoyancy-driven melting during continental breakup. *Nat. Commun.* 7, 13110. doi:10.1038/ncomms13110

Gianelli, G., and Teklemariam, M. (1993). Water-rock interaction processes in the Aluto-Langano geothermal field (Ethiopia). *J. Volcanol. Geothermal Res.* 56, 429–445. doi:10.1016/0377-0273(93)90007-E

Gizaw, B. (1993). Aluto-Langano geothermal field, Ethiopian Rift Valley: physical characteristics and the effects of gas on well performance. *Geothermics* 22, 101–116. doi:10.1016/0375-6505(93)90050-W

Glahn, A., and Granet, M. (1993). Southern Rhine Graben: small-wavelength tomographic study and implications for the dynamic evolution of the Graben. *Geophys. J. Int.* 113, 399–418. doi:10.1111/j.1365-246x.1993.tb00896.x

Gleeson, M. L. M., Stock, M. J., Pyle, D. M., Mather, T. A., Hutchison, W., Yirgu, G., et al. (2017). Constraining magma storage conditions at a restless volcano in the Main Ethiopian Rift using phase equilibria models. *J. Volcanol. Geothermal Res.* 337, 44–61. doi:10.1016/j.jvolgeores.2017.02.026

Gottsmann, J., Biggs, J., Lloyd, R., Biranhu, Y., and Lewi, E. (2020). Ductility and compressibility accommodate high magma flux beneath a silicic continental rift caldera: insights from Corbetti caldera (Ethiopia). *Geochem. Geophys. Geosyst.* 21, e2020GC008952. doi:10.1029/2020GC008952

Grayver, A. V., van Driel, M., and Kuvshinov, A. V. (2019). Three-dimensional magnetotelluric modelling in spherical Earth. *Geophys. J. Int.* 217 (1), 532–557. doi:10.1093/gji/ggz030

Greenfield, T., Keir, D., Kendall, J.-M., and Ayele, A. (2019b). Low-frequency earthquakes beneath Tullu Moye volcano, Ethiopia, reveal fluid pulses from shallow magma chamber. *Earth Planet. Sci. Lett.* 526, 115782. doi:10.1016/j.epsl.2019.115782

Greenfield, T., Keir, D., Kendall, J. M., and Ayele, A. (2019a). Seismicity of the Bora-Tullu Moye Volcanic Field, 2016–2017. *Geochem. Geophys. Geosyst.* 20, 548–570. doi:10.1029/2018gc007648

Greenfield, T., White, R. S., and Roecker, S. (2016). The magmatic plumbing system of the Askja central volcano, Iceland, as imaged by seismic tomography. *J. Geophys. Res. Solid Earth.* 121, 7211–7229. doi:10.1002/2016JB013163

Guo, X., Zhang, L., Behrens, H., and Ni, H. (2016). Probing the status of felsic magma reservoirs: Constraints from the P–T-H_2O dependences of electrical conductivity of rhyolitic melt. *Earth Planet. Sci. Lett.* 433, 54–62. doi:10.1016/j.epsl.2015.10.036

Hübert, J., Whaler, K., and Fisseha, S. (2018). The electrical structure of the Central Main Ethiopian Rift as imaged by magnetotellurics: implications for magma storage and pathways. *J. Geophys. Res. Solid Earth.* 123, 6019–6032. doi:10.1029/2017jb015160

Hammond, J. O. S., and Kendall, J. M. (2016). "Constraints on melt distribution from seismology: a case study in Ethiopia," in *Magmatic rifting and active volcanism*. Editors T. J. Wright, A. Ayele, D. J. Ferguson, T. Kidane, and C. Vye-Brown (London: Special Publications), 420. doi:10.1144/SP420.14

Hansen, S. (2004). Seismic velocity and Attenuation structure of the east rift zone and south Flank of Kilauea volcano, Hawaii. *Bull. Seismol. Soc. Am.* 94, 1430–1440. doi:10.1785/012003154

Harris, J. M., Langan, R. T., Fasnacht, T., Melton, D., Smith, B., Sinton, J., et al. (1996). *Experimental verification of seismic monitoring of CO_2 injection in carbonate reservoirs*. SEG Technical Program Expanded Abstracts, 1870–1872. doi:10.1190/1.1826505

Hochstein, M. P., Oluma, B., and Hole, H. (2017). Early exploration of the Aluto geothermal field, Ethiopia (history of discovery well LA-3). *Geothermics* 66, 73–84. doi:10.1016/j.geothermics.2016.11.010

Hooft, E. E. E., Heath, B. A., Toomey, D. R., Paulatto, M., Papazachos, C. B., Papazachos, C. B., Nomikou, P., et al.. (2019). Seismic imaging of Santorini: subsurface constraints on caldera collapse and present-day magma recharge. *Earth Planet. Sci. Lett.* 514, 48–61. doi:10.1016/j.epsl.2019.02.033

Hudson, T. S., White, R. S., Greenfield, T., Ágústsdóttir, T., Brisbourne, A., and Green, R. G. (2017). Deep crustal melt plumbing of Bárðarbunga volcano, Iceland, *Geophys. Res. Lett.* 44, 8785–8794. doi:10.1002/2017GL074749.

Hutchison, W., Biggs, J., Mather, T. A., Pyle, D. M., Lewi, E., Yirgu, G., et al. (2016b). Causes of unrest at silicic calderas in the East African Rift: new constraints from InSAR and soil-gas chemistry at Aluto volcano, Ethiopia. *Geochem. Geophys. Geosyst.* 17, 3008–3030. doi:10.1002/2016GC006395

Hutchison, W., Mather, T. A., Pyle, D. M., Biggs, J., and Yirgu, G. (2015). Structural controls on fluid pathways in an active rift system: a case study of the Aluto volcanic complex. *Geosphere* 11, 542–562. doi:10.1130/GES01119.1

Hutchison, W., Pyle, D. M., Mather, T. A., Yirgu, G., Biggs, J., Cohen, B. E., et al. (2016a). The eruptive history and magmatic evolution of Aluto volcano: new insights into silicic peralkaline volcanism in the Ethiopian rift. *J. Volcanol. Geothermal Res.* 328, 9–33. doi:10.1016/j.jvolgeores.2016.09.010

Jaxybulatov, K., Koulakov, I., Seht, M. I.-V., Klinge, K., Reichert, C., Dahren, B., et al. (2011). Evidence for high fluid/melt content beneath Krakatau volcano (Indonesia) from local earthquake tomography. *J. Volcanol. Geothermal Res.* 206, 96–105. doi:10.1016/j.jvolgeores.2011.06.009

Johnson, J. H., and Poland, M. P. (2013). Seismic detection of increased degassing before Kīlauea's 2008 summit explosion. *Nat. Commun.* 4, 1668. doi:10.1038/ncomms2703

Julian, B. R., Pitt, A. M., and Foulger, G. R. (1998). Seismic image of a CO_2 reservoir beneath a seismically active volcano. *Geophys. J. Int.* 133, F7–F10. doi:10.1046/j.1365-246X.1998.1331540.x

Kebede, S., Mamo, T., and Abebe, T. (1985). Explanation to the geological map of Aluto-Langano geothermal area. *Geothermal exploration project Report No. 26.* Ethiopia: Ministry of Mines and energy, Ethiopian Institute of Geological Surveys, 60.

Keir, D., Ebinger, C. J., Stuart, G. W., Daly, E., and Ayele, A. (2006). Strain accommodation by magmatism and faulting as rifting proceeds to breakup: seismicity of the northern Ethiopian rift. *J. Geophys. Res.* 111 a. doi:10.1029/2005JB003748

Kennett, B. L. N., Sambridge, M. S., and Williamson, P. R. (1988). Subspace methods for large inverse problems with multiple parameter classes. *Geophys. J. Int.* 94, 237–247. doi:10.1111/j.1365-246X.1988.tb05898.x

Koulakov, I., Yudistira, T., Luehr, B.-G., and Wandono (2009). P,Svelocity and VP/VSratio beneath the Toba caldera complex (Northern Sumatra) from local earthquake tomography. *Geophys. J. Int.* 177, 1121–1139. doi:10.1111/j.1365-246X.2009.04114.x

Léveque, J.-J., Rivera, L., and Wittlinger, G. (1993). On the use of the checkerboard test to assess the resolution of tomographic inversions. *Geophys. J. Int.* 115, 313–318. doi:10.1111/j.1365-246X.1993.tb05605.x

Lavayssière, A., Greenfield, T., Keir, D., Ayele, A., and Kendall, J.-M. (2019). Local seismicity near the actively deforming Corbetti volcano in the Main Ethiopian Rift. *J. Volcanol. Geothermal Res.* 381, 227–237. doi:10.1016/j.jvolgeores.2019.06.008

Lees, J. M., and Wu, H. (2000). Poisson's ratio and porosity at Coso geothermal area, California. *J. Volcanol. Geothermal Res.* 95, 157–173. doi:10.1016/S0377-0273(99)00126-2

Lloyd, R., Biggs, J., Birhanu, Y., Wilks, M., Gottsmann, J., Kendall, J.-M., et al. (2018a). Sustained uplift at a continental rift caldera. *J. Geophys. Res. Solid Earth.* 123 (6), 5209–5226. doi:10.1029/2018JB015711.

Lloyd, R., Biggs, J., Wilks, M., Nowacki, A., Kendall, J.-M., Ayele, A., et al. (2018b). Evidence for cross rift structural controls on deformation and seismicity at a continental rift caldera. *Earth Planet. Sci. Lett.* 487, 190–200. doi:10.1016/j.epsl.2018.01.037

Lomax, A., Virieux, J., Volant, P., and Berge-Thierry, C. (2000). "Probabilistic earthquake location in 3D and layered models—introduction of a Metropolis-Gibbs method and comparison with linear locations," in *Advances in seismic event location*. Editors C. H. Thurber and N. Rabinowitz (Amsterdam: Kluwer), 101–134.

Mavko, G., and Mukerji, T. (1995). Seismic pore space compressibility and Gassmann's relation. *Geophysics* 60, 1743–1749. doi:10.1190/1.1443907

Muksin, U., Bauer, K., and Haberland, C. (2013). Seismic Vp and V_p/V_s structure of the geothermal area around Tarutung (North Sumatra, Indonesia) derived from local earthquake tomography. *J. Volcanol. Geothermal Res.* 260, 27–42. doi:10.1016/j.jvolgeores.2013.04.012

Nowacki, A., Wilks, M., Kendall, J.-M., Biggs, J., and Ayele, A. (2018). Characterising hydrothermal fluid pathways beneath Aluto volcano, Main Ethiopian Rift, using shear wave splitting. *J. Volcanol. Geothermal Res.* 356, 331–341. doi:10.1016/j.jvolgeores.2018.03.023

Pilia, S., Rawlinson, N., Direen, N. G., Cummins, P. R., and Balfour, N. (2013). Structural controls on localized intraplate deformation and seismicity in Southern Australia: insights from local earthquake tomography of the Flinders Ranges. *J. Geophys. Res. Solid Earth.* 118, 2176–2190. doi:10.1002/jgrb.50168

Prejean, S., Ellsworth, W., Zoback, M., and Waldhauser, F. (2002). Fault structure and kinematics of the Long Valley Caldera region, California, revealed by high-accuracy earthquake hypocenters and focal mechanism stress inversions. *J. Geophys. Res.* 107 (B12), 9. doi:10.1029/2001JB001168.

Pritchard, M. E., de Silva, S. L., Michelfelder, G., Zandt, G., McNutt, S. R., Gottsmann, J., et al. (2018). Synthesis: PLUTONS: investigating the relationship between pluton growth and volcanism in the Central Andes. *Geosphere* 14(3), 954–982. doi:10.1130/GES01578.1

Pritchard, M. E., Mather, T. A., McNutt, S. R., Delgado, F. J., and Reath, K. (2019). Thoughts on the criteria to determine the origin of volcanic unrest as magmatic or non-magmatic. *Phil. Trans. R. Soc. A.* 377 (2139), 20180008. doi:10.1098/rsta.2018.0008

Rawlinson, N., and Sambridge, M. (2003). "Seismic traveltime tomography of the crust and lithosphere," in *Advances in geophysics*, Editor R. Dmowska (New York, NY: Elsevier), Vol. 46, 81–198. doi:10.1016/S0065-2687(03)46002-0

Rawlinson, N., and Urvoy, M. (2006). Simultaneous inversion of active and passive source datasets for 3-D seismic structure with application to Tasmania. *Geophys. Res. Lett.* 33, L24213. doi:10.1029/2006GL028105

Reinsch, T., Dobson, P., Asanuma, H., Huenges, E., Poletto, F., and Sanjuan, B. (2017). Utilizing supercritical geothermal systems: a review of past ventures and ongoing research activities. *Geotherm. Energy.* 5, 16. doi:10.1186/s40517-017-0075-y

Sambridge, M. S., and Kennett, B. L. N. (1986). A novel method of hypocentre location. *Geophys. J. Int.* 87 (2), 679–697. doi:10.1111/j.1365-246X.1986.tb06644.x

Samrock, F., Grayver, A. V., Cherkose, B., Kuvshinov, A., and Saar, M. O. (2020). "Aluto-Langano geothermal field, Ethiopia: complete image of underlying magmatic-hydrothermal system revealed by revised interpretation of magnetotelluric data," in World geothermal Congress (WGC 2021).

Samrock, F., Kuvshinov, A., Bakker, J., Jackson, A., and Fisseha, S. (2015). 3-D analysis and interpretation of magnetotelluric data from the Aluto-Langano geothermal field, Ethiopia. *Geophys. J. Int.* 202, 1923–1948. doi:10.1093/gji/ggv270

Segall, P. (1989). Earthquakes triggered by fluid extraction, *Geol* 17, 942–946. doi:10.1130/0091-7613(1989)017<0942:etbfe>2.3.co;2

Simiyu, S. (1999). "Seismic velocity analysis in the Olkaria geothermal field," in Twenty-fourth workshop on geothermal reservoir Engineering, Stanford University, Menlo Park, CA, 7.

Stork, A. L., Verdon, J. P., and Kendall, J.-M. (2015). The microseismic response at the in Salah carbon capture and storage (CCS) site. *Int. J. Greenhouse Gas Control.* 32, 159–171. doi:10.1016/j.ijggc.2014.11.014

Syracuse, E. M., Abers, G. A., Fischer, K., MacKenzie, L., Rychert, C., Protti, M., et al. (2008). Seismic tomography and earthquake locations in the Nicaraguan and Costa Rican upper mantle. *Geochem. Geophys. Geosyst.* 9, a. doi:10.1029/2008GC001963

Teklemariam, M., Battaglia, S., Gianelli, G., and Ruggieri, G. (1996). Hydrothermal alteration in the Aluto-Langano geothermal field, Ethiopia. *Geothermics*, 25, 679–702. doi:10.1016/S0375-6505(96)00019-3

Teklemariam, M. (1996). Water-rock interaction processes in the Aluto-Langano geothermal field, Ethiopia. Ph.D. Thesis, University of Pisa, 245 p.

Troise, C., De Natale, G., Schiavone, R., Somma, R., and Moretti, R. (2019). The Campi Flegrei caldera unrest: discriminating magma intrusions from hydrothermal effects and implications for possible evolution. *Earth-Sci. Rev.* 188, 108–122. doi:10.1016/j.earscirev.2018.11.007

van Thienen-Visser, K., and Breunese, J. N. (2015). Induced seismicity of the Groningen gas field: history and recent developments. *Lead. Edge.* 34, 664–671. doi:10.1190/tle34060664.1

Vanorio, T., and Kanitpanyacharoen, W. (2015). Rock physics of fibrous rocks akin to Roman concrete explains uplifts at Campi Flegrei Caldera. *Science* 349, 617–621. doi:10.1126/science.aab1292

Walsh, J. B. (1965). The effect of cracks in rocks on Poisson's ratio. *J. Geophys. Res.* 70, 5249–5257. doi:10.1029/jz070i020p05249

Wespestad, C. E., Thurber, C. H., Andersen, N. L., Singer, B. S., Cardona, C., Zeng, X., et al. (2019). Magma reservoir below Laguna del Maule Volcanic Field, Chile, imaged with surface-wave tomography. *J. Geophys. Res. Solid Earth.* 124 (3), 2858–2872. doi:10.1029/2018jb016485

Whaler, K., and Hautot, S. (2006). "The electrical resistivity structure of the crust beneath the northern Main Ethiopian Rift," in *Structure and evolution of the rift systems within the Afar volcanic Province, Northeast Africa*. Editors G. Yirgu, C. J. Ebinger, and P. K. H. Maguire (London, Special Publications), 295–305. doi:10.1144/GSL.SP.2006.259.01.22

Wilks, M., Kendall, J.-M., Nowacki, A., Biggs, J., Wookey, J., Birhanu, Y., et al. (2017). Seismicity associated with magmatism, faulting and hydrothermal circulation at Aluto Volcano, Main Ethiopian Rift. *J. Volcanol. Geothermal Res.* 340, 52–67. doi:10.1016/j.jvolgeores.2017.04.003

Yu, J., Byun, J., and Seol, S. J. (2015). VP/VS monitoring of CO_2 sequestration using virtual horizontal crosswell tomography. *Geosci. J.* 19, 441–448. doi:10.1007/s12303-014-0053-3

Zollo, A., Maercklin, N., Vassallo, M., Dello Iacono, D., Virieux, J., and Gasparini, P. (2008). Seismic reflections reveal a massive melt layer feeding Campi Flegrei caldera. *Geophys. Res. Lett.* 35, a–n. doi:10.1029/2008GL034242

Conflict of Interest: The authors declare that the research was conducted in the absence of any commercial or financial relationships that could be construed as a potential conflict of interest.

The handling editor declared a past co-authorship with one of the authors NR.

Copyright © 2020 Wilks, Rawlinson, Kendall, Nowacki, Biggs, Ayele and Wookey. This is an open-access article distributed under the terms of the Creative Commons Attribution License (CC BY). The use, distribution or reproduction in other forums is permitted, provided the original author(s) and the copyright owner(s) are credited and that the original publication in this journal is cited, in accordance with accepted academic practice. No use, distribution or reproduction is permitted which does not comply with these terms.

frontiers in Earth Science

ORIGINAL RESEARCH
published: 28 October 2020
doi: 10.3389/feart.2020.589925

Mt. Etna Feeding System and Sliding Flank: A New 3D Image From Earthquakes Distribution in a Customisable GIS

R. Guardo[1], *L. De Siena*[2]* *and C. Dreidemie*[3]

[1]*Instituto de Investigaciòn en Paleobiologìa y Geologìa, UNRN, CONICET, IIPG, General Roca, Argentina,* [2]*Institute of Geosciences, Johannes Gutenberg University, Mainz, Germany,* [3]*LVCC Laboratorio de Investigaciòn y Desarrollo en Tecnologìas de Visualizaciòn, Computaciòn Gràfica y Còdigo Creativo, Universidad Nacional de Rìo Negro, San Carlos de Bariloche, Argentina*

High-resolution seismic imaging enables the reconstruction of ascending paths of magma and fluids, shallow molten accumulation and flank collapse areas, all crucial information for developing an efficient eruption forecasting strategy. Here, the Marching Cubes algorithm (MC - generally applied to medical visualization and three-dimensional (3D) modeling) is applied to 16 years of earthquake location data at Mt. Etna (Italy). The algorithm defines three-dimensional seismic clusters that take into account seismic location uncertainties and are embedded in a novel volcano-oriented Geographyc Information Systems (VolGIS) offering an interpretational environment comprising tomographic images and alternative geophysical models. The results show that a volume of very-low-seismicity is embedded in a high-velocity body, and acts as a zone of transition between transient magmatic events (west) and eastern deep seismicity related to the sliding eastern flank. The eastern cluster represents the 3D seismic signature of a deep (2–8 km below sea level) instability, affecting the portion of the eastern flank nearest to the feeding systems. This instability is likely caused by a combination of gravitational spreading and magmatic intrusions.

Keywords: feeding system, sliding flank, seismic imaging, Marching Cubes, GIS-based system

OPEN ACCESS

Edited by:
Yosuke Aoki,
The University of Tokyo, Japan

Reviewed by:
Alessandro Tibaldi,
University of Milano-Bicocca, Italy
Mimmo Palano,
Istituto Nazionale di Geofisica e Vulcanologia, Italy

***Correspondence:**
L. De Siena
ldesiena@uni-mainz.de

Specialty section:
This article was submitted to Volcanology, a section of the journal Frontiers in Earth Science

Received: *31 July 2020*
Accepted: *24 September 2020*
Published: *28 October 2020*

Citation:
Guardo R, De Siena L and Dreidemie C (2020) Mt. Etna Feeding System and Sliding Flank: A New 3D Image From Earthquakes Distribution in a Customisable GIS. Front. Earth Sci. 8:589925. doi: 10.3389/feart.2020.589925

1 INTRODUCTION

Imaging a volcano with seismic waves is challenging but rewarding. A reliable image of the structural features of a volcano allows to reconstruct the regions where molten materials rise across the lithosphere (Jaxybulatov et al., 2014; Huang et al., 2015). These images can be linked with field observations, giving us a clear picture of ongoing volcano dynamics (Patanè et al., 2003). They can also discriminate zones of fluid and magma accumulation (Koulakov, 2013) as well as interfaces that release stress at depth (De Siena et al., 2017), providing better constraints for seismic and volcanic hazard assessment. Regardless, the resolution of these maps is of the order of kilometres. Seismic locations, and particularly their "clustering," generally recorded across short periods of unrest, are often used to interpret tomographic anomalies, and from these the larger-scale dynamics leading to volcanism (e.g., Giampiccolo et al., 2020). It is thus necessary: 1) to develop more quantitative methods to define seismic clustering at a volcano; 2) to apply these methods to seismic locations recorded across years or decades, most likely to represent stationary or recurrent processes at a volcano.

Such an ideal dataset of seismic locations is available at Mt. Etna volcano. Mt. Etna is one of the most hazardous and monitored volcanoes in the world due to both its persistent eruptive activity and its proximity to highly-urbanized areas. The volcano is monitored by permanent and mobile networks and produces dense seismicity related to eruptive events and volcanic unrests (Alparone et al., 2015; Gruppo Analisi Dati Sismici, 2017). This seismicity has been used for decades to image shape, dimension and location of the volcano feeding systems with seismic tomography. The resolution of the resulting models, reaching a maximum depth of 20 km, has steadily increased (Sharp et al., 1980; Hirn et al., 1991; Cardaci et al., 1993; De Luca et al., 1997; Villaseñor et al., 1998). From the beginning of this century, researchers have interpreted the models jointly with remote sensing and field data, providing reliable interpretations of the shallow volcano dynamics (De Gori et al., 1999; Chiarabba et al., 2000; Laigle et al., 2000; Patanè et al., 2002; Patanè et al., 2003; Chiarabba et al., 2004; Patanè et al., 2006; Alparone et al., 2012; Díaz-Moreno et al., 2018; Giampiccolo et al., 2020). These studies have progressively recognized and improved the reconstruction of a high-velocity body (HVB) below both the central cone and the eastern sides of the volcano (De Gori et al., 1999; Alparone et al., 2012; Giampiccolo et al., 2020), generally interpreted as a solidified intrusive body (Aloisi et al., 2002; Patanè et al., 2006; Alparone et al., 2012).

Unfortunately, seismic tomography models are affected by uneven resolution and instabilities caused by insufficient ray coverage (Rawlinson and Spakman, 2016). This makes it difficult, if not impossible, to model structures smaller than 1–2 km in an ever-changing volcanic environment (Koulakov, 2013). Due to the intrinsic limitations of the datasets used and the uncertainties related to ray-tracing algorithms in volcanic edifices, the highest resolution achieved by tomography on both the HVB and the nearby feeding systems is 1 km (De Gori et al., 1999; Alparone et al., 2012; Giampiccolo et al., 2020). The thickness of dikes is of the order of a few meters (Gudmundsson, 1983; Tibaldi, 2015), resolving them with travel time tomography is likely impossible. Also, there are strong uncertainties when detecting magma accumulation with tomography as demonstrated at Krafla volcano, where extensive geophysical imaging was available since the 90s (e.g., Julian et al., 1993). Based on these models, no large magma accumulation region was expected between depths of 3 and 7 km under the central caldera, at least until a deep geothermal well didn't drill into rhyolitic magma at these depths in 2009. Even novel tomographic imaging performed after drilling is unable to reconstruct magma at these depths at resolutions higher than 2 km^3 (Schuler et al., 2015).

Despite the dense seismicity and coverage offered by several seismic arrays, all recent tomographic works at Etna focus on specific time intervals related to volcanic eruptions (e.g., Patanè et al., 2002; Giampiccolo et al., 2020). In this way, the tomographic maps can be interpreted using geological and geophysical data produced by visible eruptive events. Regardless, such a dense seismicity should provide benchmark imaging models, necessary to understand the evolution of volcano dynamics across decades, including the relevant gravitational spreading observed across the wider eastern flank (Borgia et al., 1992; Urlaub et al., 2018). The shallow eastern flank is known to develop primarily aseismic creep (Rasà et al., 1996; Mattia et al., 2015; Bruno et al., 2017) and the wider flank is considered mostly aseismic. However, recent studies show that the deeper flank nearest to the feeding systems is associated with intense seismicity during unrest (Giampiccolo et al., 2020). At the edge of Mt. Etna's unstable sector intrusions encourage sliding during unrest (Alparone et al., 2020). Understanding if and how widely this seismicity has clustered across years and decades can thus help clarify the nature of sliding and its debated origin (Tibaldi and Groppelli, 2002; Acocella et al., 2003; Urlaub et al., 2018). In particular, it can test numerical models proposing the existence of two sliding interfaces separating two domains: 1) a shallower flank, subject to gravitational instability and 2) a deeper flank, where compression is also caused by magmatic intrusions (Tibaldi and Groppelli, 2002; Apuani et al., 2013).

Forward methods that can properly account for data uncertainties can improve the resolution on, and interpretation of, seismic models. The "Marching Cubes" (MC - also known as "3D Contouring" o "Surface Reconstruction") is an algorithm for surface reconstruction that generates the 3D contour of a volume in space (Lorensen and Cline, 1987). It operates over a scalar field defined on a given volume. The algorithm approximates the data, which have to be related to physical quantities, to an isosurface, i.e., the surface of constant values in the scalar field. For example, the isosurface generated at the constant value greater than zero represents the enveloping surface around the volume where the scalar field is not null. The MC algorithm is used in medical imaging for 3D surface reconstructions of organs, tissues and anatomic parts and applied to datasets obtained by magnetic resonance tomography (Cline et al., 1987) as well as in pharmacology, chemistry, and meteorology (Newman and Yi, 2006). It is a fundamental tool in the framework of computational graphics and 3D modeling and has become an important technique for visual communication in the 3D animation and gaming industries. A review of the steady advances made by this approach can be found in Masala et al. (2013).

In seismology, the MC algorithm has been used for quick visualization of three-dimensional meshes and voxels. Typical examples are those proposed by Subramanian and Fussell (1990), who used it to make voxels for volume rendering in a ray tracing algorithm, and Ma and Rokne (2004), who developed a mesh propagation algorithm useful for the generation of seismic horizon surfaces. As of today, the MC algorithm has never been applied directly to seismic data and metadata, like earthquake locations, for the purpose of interpretation. With their uncertainties (hundreds of meters), the earthquake locations available from INGV across 16 years (Alparone et al., 2015; Gruppo Analisi Dati Sismici, 2017) can be used as the scalar field in the MC algorithm, at a resolution unavailable to tomography. The resulting isosurfaces will envelope volumes of seismic clustering and contour aseismic zones, whose discussion is always part of tomographic interpretations. The application of the MC algorithm to locations recorded across

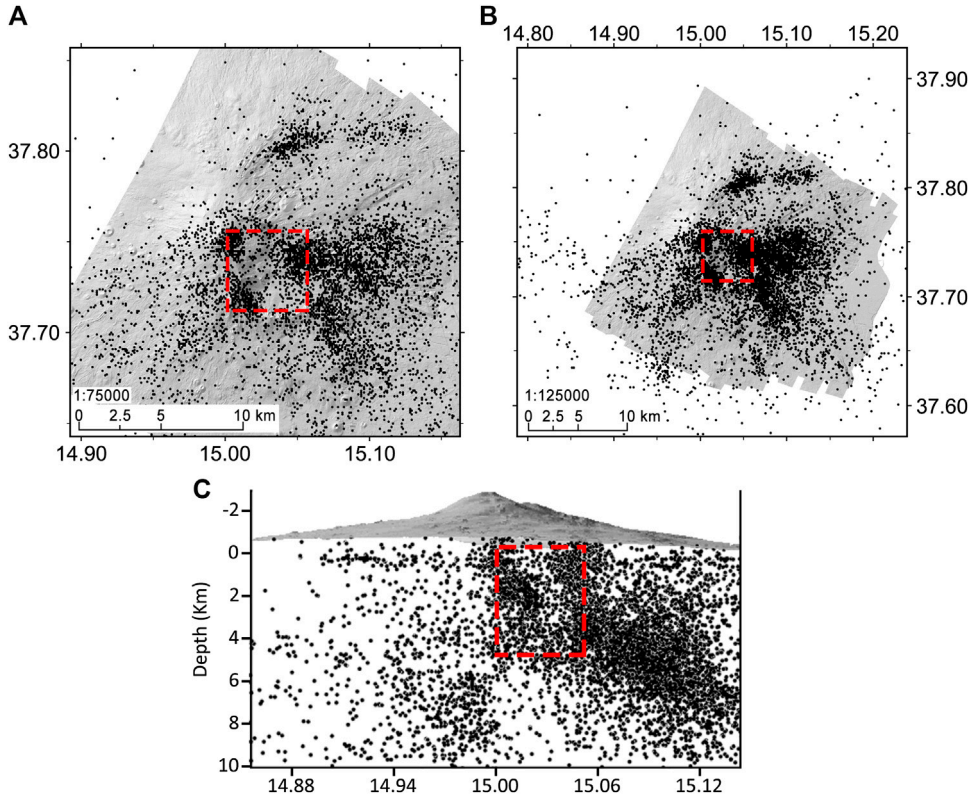

FIGURE 1 | Earthquakes distribution at 1:75,000 **(A)** and 1:125,000 **(B)**. **(C)** Earthquakes distribution from a W-E view. The red dashed rectangles outline the area of low-to-zero seismicity.

decades offers a unique method to define background (tectonic or gravitational) or repeated (likely magmatic) processes acting inside the volcano quantitatively.

To support interpretation of volcanic processes, any algorithm designed to interpret volcano dynamics must be implemented in an interactive visualization environment able to localize geological, geographical and geophysical data and models. Such an environment (VolGIS) has been developed to enable users to: 1) control visualization parameters in real-time; 2) locate the MC isosurfaces geographically, with precision sufficient to compare them with geophysical and geological data; 3) perform queries such as measure size and extension of the imaged structures (Guardo and De Siena, 2017). The integration of VolGIS and the MC algorithm is aimed at refining interpretations of volcano seismicity considering both imaged structures and dynamics modeled from geophysical signals. Once applied to seismic locations spanning years, it provides a tool to mitigate several limitations in our ability to interpret volcano dynamics, including: 1) the possibility of accounting for uncertainties in seismic locations when interpreting them with geophysical models; 2) a quantitative definition of "seismic clustering" and aseismicity in a geolocalized environment developed explicitly for the interpretation of seismic tomographic maps; 3) a seismic model of the volcano unrelated to specific volcanic unrest and representative of decadal-scale volcano dynamics.

2 DATA AND METHODS

In the present application, the MC algorithm uses as data the earthquakes nucleated between the years 2000 and 2016 at Mt. Etna, in the framework of the VolGIS. The first ten years of data are described and analyzed by Alparone et al. (2015). We added six years of location data (from 2010 to 2016), which were provided by the Gruppo Analisi Dati Sismici (2017). These earthquakes are located in an area that spans between 14.707 and 15.295°E and from 37.509 to 37.900°N, in a depth range from −3 to 10 km b.s.l. We selected the "Date," "Latitude," "Longitude," "Depth," "Magnitude," "RMS," "ERH" and "ERZ" from the event location file. The last two fields, ERH and ERZ, indicate the horizontal and vertical uncertainties in localization (in kilometres), respectively.

2.1 Geographical Information System Setup

After setting the data-frame coordinate system, both a DEM of Etna (Bisson et al., 2016) and all the seismic events were loaded to the GIS-Workspace. Without any selection dependent on location uncertainties, both the top view (at different scales, i.e., 1:75,000, 1:125,000) (**Figures 1A,B**) and W-E cross-section view (**Figure 1C**) of the earthquake spatial distribution highlight a volume of low-to-zero seismicity for the selected period. The methods proposed allow to assess if this anomaly is an effect of graphic visualization or a feature related to the volcano dynamics.

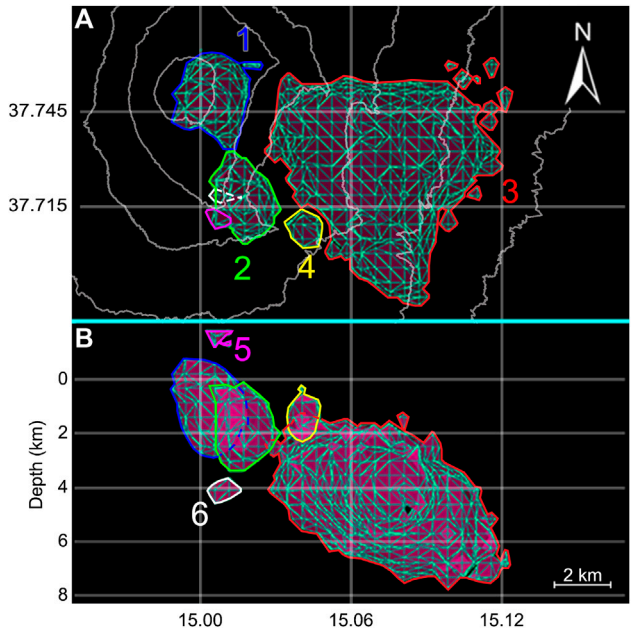

FIGURE 2 | Isosurfaces obtained in the second analysis. **(A)** Top view. **(B)** W-E cross section. The clusters C1 to C6 are outlined in blue, green, red, yellow, magenta and white, respectively.

VolGIS incorporates the Marching Cubes algorithm (MC) and analyses the earthquake distribution in order to create a quantitative 3D model of the high-seismicity volumes. Geo-localized tomographic maps and models of deformation are then included in the GIS for interpretation.

2.2 Marching Cubes

The MC samples a point cloud set by taking eight vertices simultaneously from a provided spatial grid, marking a cube. For each cube, the algorithm computes $2^8 = 256$ possible polygons configurations values that, due to symmetries, are reduced to 15 possible polygons configurations (**Supplementary Figure 1A**). The MC then queries a list of pre-calculated geometries to pick the combination of polygons that best represents the isosurface passing through the cube, given a predefined grid spacing and density isovalue set by VolGIS. Once the user inputs these parameters, the software applies the algorithm and generates the isosurface according to the spherical spreading law:

$$W(i) = \sum_j \frac{1}{d(i,j)^2} \tag{1}$$

Our point cloud-set is the dataset of earthquake locations. After defining a grid, the contribution of each earthquake location (j) in the cloud to the vertices (i) of the grid is thus computed using the inverse square of the distance dependency ($d(i,j)^2$) between each location and the vertex. The result is a scalar field defined over the grid vertices by adding up all the inverse distances j. From **Eq. 1** we obtain a value $W(i)$ for each vertex of the cube (**Supplementary Figure 1B**); the value decreases when the number of locations near to a vertex increases.

For a given dataset, the isovalue establishes what percentage of earthquake locations near to each vertex is required for the vertex to be inside the surface. The i-th vertex is included if $W(i)$ has a value less than or equal to the isovalue, otherwise it falls outside of the surface (**Supplementary Figure 1C**). Another way to achieve the same effect is to uniformly increase or decrease all the vertices values (Lopes and Brodlie, 2003).

3 RESULTS

The MC algorithm solves a forward problem. It is thus necessary to test different datasets in order to assess the robustness of the imaged structures. The MC was applied to three different datasets (**Figure 2**; **Supplementary Figure 2, 3**), created according to three different horizontal and vertical uncertainties (ERH and ERZ). These applications test the robustness of the reconstructed structures, providing a control on visualization based on modeled uncertainties. We also test the stability of structure locations and shapes applying a bootstrap test.

3.1 Dataset 1: 6,907 Earthquakes

The first dataset comprises 6,907 earthquakes with a root-mean-squared (RMS) average value of 0.135. We took into consideration that the average ERH and ERZ are equal to 548 and 712 m, respectively. By dividing the entire area (51,779,297 m for each side) by the ERZ (712 m), we obtained the maximum amount of cells that can be included in the analysis (72.7). The software rounded down (72) to respect the ERH-ERZ constrain. Then the area was separated into 72 cells, obtaining a value equal to 719,15 m per each cell-side.

The MC algorithm produced three isosurfaces, or clusters, that envelope the high seismicity volumes and constrain a volume of low (almost absent) seismicity (**Supplementary Figure 2A**):

- The first two clusters, located beneath the summit craters (C1) and south to it (C2), have a vertical extent of 2.79 km (from 0.24 km above sea level to 2.56 km below it) and 3.6 km (from 0.56 to 4.16 km b.s.l.), respectively.
- The third cluster (C3) is located under the eastern sector of the volcano. It has an approximated thickness of 5 km, dipping eastward from its shallow point at 1.4–7.39 km b.s.l. (**Supplementary Figure 3B**).
- The algorithm allows the imaging of a fourth cluster, located between the second and third one. However, its dimension is smaller than the earthquake vertical uncertainty, so it is not interpreted in this first analysis.

3.2 Dataset 2: 2,824 Earthquakes

Here, we set the grid spacing to 505.45 m, since the used events have both ERH and ERZ equal or less than 500 m. In this case the total earthquakes and the average RMS are equal to 2,824 and 0.149, respectively. The results show the same three clusters obtained using the first dataset, together with three smaller ones of measurable dimensions (**Figure 2A**). The clusters

obtained with this dataset have a smaller extension compared to those obtained using Dataset 1, but the variations are within the dataset uncertainty. Both shape and position of the clusters remain the same. This result is due to the lower uncertainties in source location.

- The cluster C1 has a vertical extent of 3.28 km (from 550 m a.s.l. to 2.73 km b.s.l.). The second cluster (C2) extends for 3.05 km, spanning from 0.12 to 3.17 km b.s.l.
- Cluster C3 keeps both the same dimensions and position of the previous analysis.
- Located between C2 and C3, cluster C4 is now measurable, with a focal point at about 1.19 km b.s.l. and a vertical extent of 1.67 km.
- Two additional clusters are located above (C5) and below (C6) the second one (C2). They have both an average vertical extent of about 1 km and they range from 1.89 to 0.71 km a.s.l. and from 3.52 to 4.52 km b.s.l., respectively (**Figure 2B**).

3.3 Dataset 3: 1,937 Earthquakes

In the third and last analysis we selected earthquakes with both ERH and ERZ equal to or less than 400 m, for a total of 1,937 events. The RMS average value is again 0.149 and the grid spacing is set to 402.73 m. The clusters imaged at this resolution are five in total (**Supplementary Figure 3A**) - with C6 (defined in the previous analysis - **Figure 2**) having dimensions smaller than the uncertainties. In this case, one of the clusters (C1) has a vertical extent higher than in the previous cases (3.72 km compared to 3.28 km for Dataset 2). This variation is higher than the uncertainty and changes the cluster shape. The other four clusters keep their average thickness and position, but their shape changes due to the limited number of earthquakes taken into account (**Supplementary Figure 3B**).

3.4 Robustness of the Isosurfaces Relative to the Amount of Data

Dataset 2 (ERH and ERZ ≤ 500 m) shows the highest numbers of clusters and will be used for both the bootstrap test, which is independent of the underlying spatial distribution of the data, and further discussions. The isosurfaces are defined robust in the sense that they are visually continuous as the data change in value (Lopes and Brodlie, 2003). We subtracted 10% (2,542 earthquakes), 20% (2,259) and 40% (1,694) from Dataset 2 randomly and the procedure was then repeated 10 times for each percentage value. The MC algorithm reconstructs isosurfaces almost identical to those generated using the original dataset (**Supplementary Figure 4,5**), confirming that Dataset 2 provides a robust spatial distribution of isosurfaces with reductions up to 40%.

4 DISCUSSIONS

The MC algorithm applied to the seismicity of Mt. Etna reveals three-dimensional high-resolution seismically-dense structures, which visually and spatially constrain a volume with low seismicity (VLS). A comparison of the retrieved structures with studies related to the 2000–2016 activity of the volcano (Bonaccorso et al., 2002; Bonforte et al., 2008; Currenti et al., 2008; Alparone et al., 2012; Bonforte et al., 2013; Carbone et al., 2014; Bruno et al., 2017): 1) shows that the VLS is enclosed in the high-velocity body (HVB) depicted by previous tomographic models; 2) allows to characterize the VLS as a portion of the feeding system; and 3) images the persistent seismicity associated to the sliding of the combination of gravitational and magmatic forces affecting the deeper eastern flank, closest to the feeding system.

4.1 Spatial Relation with Seismic and Deformation Models

The comparison between both the tomographic maps and geodetic models with the seismic clusters allows to define a preliminary seismic zonation map of the volcano without separating the seismicity in different time periods. It is hence possible to characterize the clusters as produced by either gravitational or magmatic processes, such as dikes' intrusion.

The HVB is generally interpreted as a single solidified intrusive body (Hirn et al., 1991; Villaseñor et al., 1998; De Gori et al., 1999; Laigle et al., 2000; Aloisi et al., 2002; Patanè et al., 2002; Patanè et al., 2003; Patanè et al., 2006; Díaz-Moreno et al., 2018; Giampiccolo et al., 2020). Imaged as a high-velocity volume (Alparone et al., 2012), the most obvious explanation is that this represents the buried, cooled signature of older magmatic activities. Regardless, the location of the MC clusters relative to the HVB reveals that:

- between 1 and 2 km b.s.l., C2 and C4 are included in the HVB (Alparone et al., 2012) (Vp > 6 km/s - from cyan to purple), while C3 only contours its eastern edge (**Supplementary Figure 6A,B**).
- cluster C1, located between 37.737° and 37.765° latitude North and from 14.995° to 15.015° longitude East, is also inside the HVB between 2 and 3 km b.s.l. (**Supplementary Figure 6B,C**).
- At 3 km b.s.l. the HVB comprises the VLS as well as all the clusters except for C3 (**Supplementary Figure 6C**).

The HVB thus consistently comprises all clusters and the VLS except for C3 (red contour). The VLS is thus a smaller-scale feature inside the high-velocity pattern that separates the main western clusters C1 and C2 from C3, under the eastern part of the volcano. The obvious questions are if the clusters are caused by different dynamics (magmatic, tectonic and gravitational) and if the VLS is part of the feeding systems of the volcano.

We also compare clusters C1 and C2 with the location of the dike and crack models obtained from geodetic and GPS analyses performed between 2000 and 2016 (**Figure 3**).

- The locations and main orientations of clusters C1 and C2 match the crack projection modeled by Bonaccorso et al. (2002) relative to the lateral eruption of July 2001 (**Figure 3A**). The source of ground deformation modeled

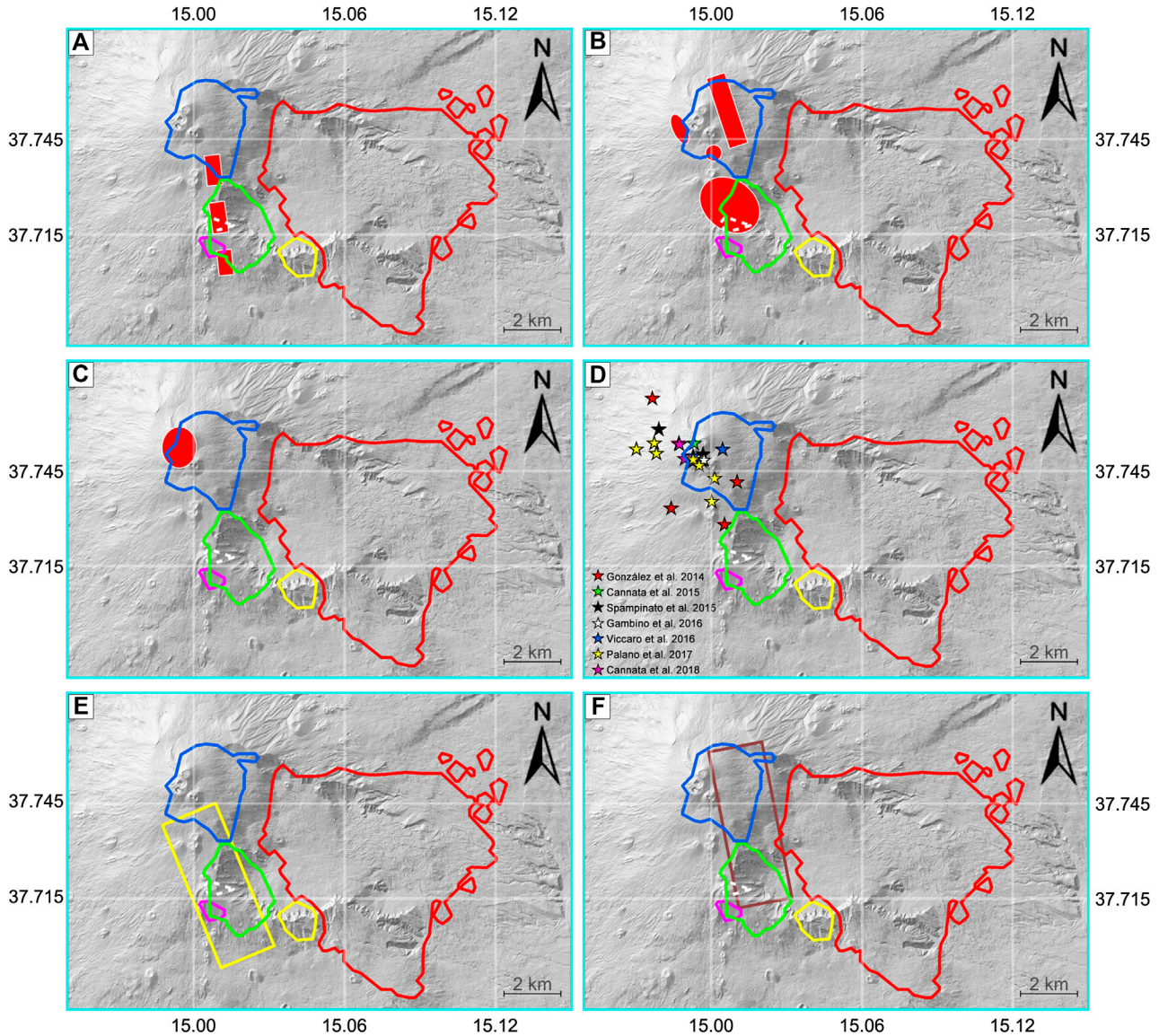

FIGURE 3 | Comparison between the clusters and previous deformation models. **(A)** The crack projection (red rectangles) modeled by Bonaccorso et al. (2002). **(B)** The average ground deformation sources by Bonforte et al. (2008) (red ellipses); dike models from the second and third inversion (red rectangle and circle, respectively) obtained by Bonforte et al. (2013). **(C)** The source of deformation model by Bruno et al. (2017). **(D)** The deformation sources modeled by González and Palano (2014): (red stars), (Cannata et al., 2015) (green stars), (Spampinato et al., 2015) (black stars), (Gambino et al., 2016) (white stars), (Viccaro et al., 2016) (blue stars), (Palano et al., 2017) (yellow stars) and (Cannata et al., 2018) (magenta stars). **(E)** The fracture-weakness-zone (FWZ) (yellow rectangle) modeled by Carbone et al. (2014). **(E)** The surface dike projection (brown rectangle) modeled by Pezzo et al. (2020).

in this study lies 1.5 km SW and at the same depth of the VLS.

- The deflation source related to the July 2004–July 2005 period (Bonforte et al., 2008) is modeled just 1 km west of the VLS, matching the location of cluster C2. The source linked to an inflation stage (July 2005–June 2006) is instead vertically located on the western side of C1. These are averaged sources because they are related to inhomogeneous deformative stages of the volcanic edifice. The inversion of both GPS and satellite data provided two dike models related to the May 6–13 and May–July 2008 eruptions, respectively (Bonforte et al., 2013). Both models are located less than 1 km west of the VLS - the first below cluster C1, the second on top of it (**Figure 3B**).
- The model proposed by Bruno et al. (2017), relative to the May 2015-September 2016 period, is located in the first cluster, in a range that spans between 2 and 6 km b.s.l., about 2 km west of the VLS (**Figure 3C**).
- The deformation sources modeled using continuous GPS data (Cannata et al., 2018) are related to several eruptive events. They highlight a more complex ground deformation patterns then those obtained by measurements performed

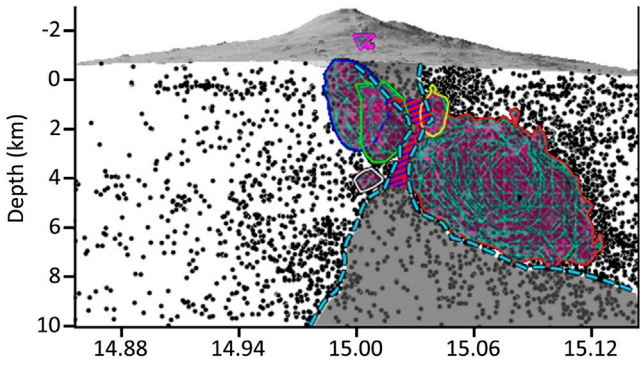

FIGURE 4 | W-E cross-section highlighting (in gray) the area with low-seismicity above and below the VLS (in dashed blue-red).

during a specific eruptive event (e.g., compare the deformation sources from (Bonforte et al., 2008) (**Figure 3B**) and (Palano et al., 2017) (**Figure 3D**), for the period July 2004–July 2005). However all these ground deformations are primarily located inside or around cluster C1 (**Figure 3D**).

- Clusters C1 and C2 are adjacent to the fracture-weakness-zone (FWZ) modeled by Carbone et al. (2014). This zone, located just 1.6 km SW from the VLS, is interpreted as a deeper pressure source filled with highly-pressurized gases (**Figure 3E**).
- The surface dike projection modeled by Pezzo et al. (2020) comprises most of C1, C2 and most of the VLS (**Figure 3F**).
- The spatial relation between these models and the clusters west of the VLS (C1 and C2) shows that the corresponding seismicity is produced by transient magmatic activity, marking the well known "South-rift" (Acocella and Neri, 2003; Pezzo et al., 2020). The weak zone modeled by Pezzo et al. (2020), considered as the superficial evidence of a deeper dike intrusion, is the only deformation anomaly crossing the VLS consistently.

4.2 The Volume with Low Seismicity as Portion of the Feeding System

The VLS is in an extensional regime between the eastern and western flanks of the volcano (Barberi et al., 2000; Alparone et al., 2011; Carbone et al., 2014; Murray et al., 2018). A comparison between the VLS and different Coulomb stress distribution models (Currenti et al., 2008) (**Supplementary Figure 7**) shows that the VLS falls inside a wide volume, extending to a depth of 6–7 km b.s.l., characterized by positive Coulomb stress changes (values equal and higher than 0.8 MPa). Here failure on a fault is favored (Cocco and Rice, 2002). If the VLS falls in a fragile HVB, why doesn't it show seismicity?

In active volcanoes earthquake-free zones are typically interpreted as the result of magma storage (Decker, 1984; Scandone and Malone, 1985; Parfitt and Wilson, 2008). At Mt. Etna such a seismic gap was previously recognized and considered as a magma supply in the shallow HVB (Chiarabba et al., 2000). If the origin of the HVB are cooled magmatic rocks they can thus pass from a brittle fracture behavior to a plastic deformation one after dikes' intrusion (Parisio et al., 2019). Such a dike intrusion has been modeled for the 2018 eruption (Aloisi et al., 2020; Pezzo et al., 2020) inside the VLS. Rocks near these dikes intrusions can deform in a ductile manner (aseismically) while the cooler rocks far from the dike will fail in brittle mode (Parisio et al., 2019). This justifies the drastic seismicity decrease

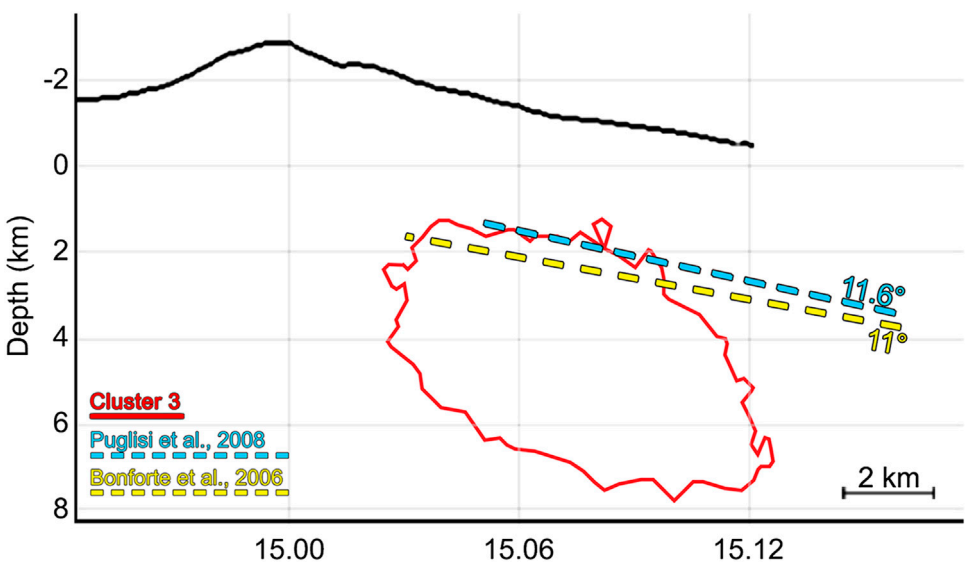

FIGURE 5 | A W-E cross-section view of Cluster C3 (red outline). The previously modeled detachment planes are represented in yellow (Bonforte and Puglisi, 2006) and light blue (Puglisi et al., 2008).

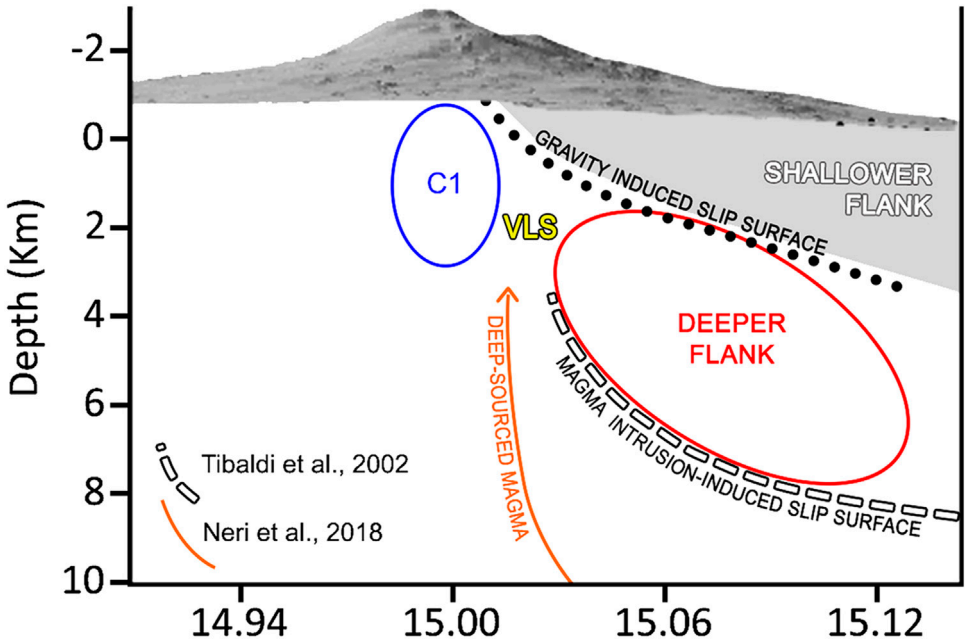

FIGURE 6 | A W-E conceptual model explaining seismicity and sliding of the eastern flank of Mt. Etna.

in the VLS, making it aseismic even if in a fragile environment [1.3% of the total earthquakes nucleated between 2000 and 2016, i.e., 89 earthquakes over 6,907 (**Supplementary Figure 8**)]. The VLS maintains its size and location, between depths of 1.9 and 3.6 km b.s.l. (minimum), across the considered time period (2000–2016). These results support the interpretation of the VLS as a portion of the feeding system of the volcano (Scandone and Malone, 1985; Murru et al., 1999; Puglisi et al., 2001).

4.3 Cluster East of theVolume with Low Seismicity: Seismicity Underlying Flank Instability

Cluster C3, located east of the VLS is oriented W-E and has a thickness of 5 km and a length of about 7.4 km (**Figure 5**). The top surface of C3 matches the element known in literature as "décollement" or detaching plane (Puglisi et al., 2001; Tibaldi and Groppelli, 2002; Bonforte and Puglisi, 2003; Lundgren et al., 2003, Lundgren et al., 2004; Walter et al., 2005; Bonforte and Puglisi, 2006; Puglisi et al., 2008; Aloisi et al., 2011; Palano, 2016). This plane is located at about 3 km depth, dipping from 1.4 km b.s.l. to almost 4 km b.s.l., from top to bottom, respectively. It is in overall agreement with previous models (Acocella and Neri, 2003; Bonforte and Puglisi, 2003; Bonforte and Puglisi, 2006; Puglisi et al., 2008; Azzaro et al., 2013) (**Figure 5**) despite being obtained with seismic locations distribution instead of deformation data. It is thus possible to consider the top of the 3D surface of this cluster as the boundary zone between rocks with different mechanical properties (Chiarabba et al., 2000; Laigle et al., 2000; Alparone et al., 2011; Palano, 2016), on which the superficial mass of the volcano flank slides due to gravitational instability (Puglisi et al., 2001; Tibaldi and Groppelli, 2002; Bonforte and Puglisi, 2003; Lundgren et al., 2003, Lundgren et al., 2004; Walter et al., 2005; Apuani et al., 2013) (**Figure 6**). On the other hand the bottom surface of cluster C3 dips from 4 to 7.39 km b.s.l. This surface fits with a magma intrusion-induced slip surface hypothesized by previous studies (Borgia et al., 1992, Borgia et al., 2000; Tibaldi and Groppelli, 2002; Acocella et al., 2003; Lundgren et al., 2004; Neri et al., 2004; Walter et al., 2005; Apuani et al., 2013).

There is a general agreement that the wider eastern flank, especially the portion in the coastal area, is sliding primarily due to gravitational forces (Urlaub et al., 2018). However it is unlikely that a 5 km-thick seismic structure (C3) is produced by gravitational collapse only. If our interpretation of the VLS is correct, a portion of the western seismicity inside C3, with volume equivalent to C1 and C2, could be equally caused by dikes' intrusions. It is thus possible to explain the seismicity across the eastern flank using a simple conceptual model of two flanks: a shallower and a deeper one (Tibaldi and Groppelli, 2002) (**Figure 6**). The shallower one, above the cluster C3, is mostly affected by gravitational collapse and is sliding along the C3 top surface. The deeper flank is constrained by cluster C3 and slides along its bottom surface. The corresponding seismicity is due to a combination of gravitational and magmatic forces, most likely from an intermediate storage zone like that modeled by Aloisi et al. (2020) between 4 and 7 km under the central cone. The VLS represents the shallowest evidence of magmatic intrusions (Neri et al., 2018; Aloisi et al., 2020) contributing to the sliding of the deeper eastern flank.

In our interpretation C3 thus represents the first 3D seismic image of the deeper portion of the eastern flank, in contact with the feeding systems and sliding due to both magmatic and gravitational forces. The seismicity inside the cluster has already been associated with magmatic or hydrothermal

activity during the 2018 unrest (Giampiccolo et al., 2020): we prove that this seismicity is a consistent feature before this event, likely related to gravitational sliding (at the top of the cluster) and repeated magmatic intrusions. The existence of a ductile VLS where dikes can intrude thus better agrees with a reciprocal feedback between: 1) gravitational collapse encouraging the uprizing of magma and 2) dikes' intrusions favoring sliding in the deeper part of this portion of the eastern flank (Tibaldi and Groppelli, 2002; Acocella et al., 2003; Bonforte and Puglisi, 2003; Aloisi et al., 2011; Apuani et al., 2013; Bruno et al., 2017).

Previous authors have underlined that "eruptions do not trigger catastrophic flank collapses" analyzing displacement of aseismic shallow faults related to the flank kinematics (Urlaub et al., 2018). Our results show that deep magmatic activity produces persistent (at least decadal-long) seismic signatures that strongly differ from those at surface. Deeper magmatic activity or flank eruption (Alparone et al., 2020) are thus a likely trigger of shallower sliding and, consequently, catastrophic collapse of the shallower portion of the flank. For a complete understanding of how catastrophic this pattern would be, it is necessary to consider the relation between local tectonic and eruptive events (Bonforte et al., 2019; De Novellis et al., 2019; Aloisi et al., 2020; Pezzo et al., 2020), i.e., conducting a time dependent analysis.

5 CONCLUSIONS

The earthquakes nucleated between 2000 and 2016 at Mt. Etna have been used as data in the Marching Cube algorithm, a 3D modeling and visualization analysis. The MC has been framed in an experimental GIS (VolGIS), which allows the users to obtain a three-dimensional seismic image in a few seconds and with a high quality graphics output. The system offers unique support in the imaging of relatively small-sized volumes within tomographic and deformation models resolved over kilometres. The framework allows to establish benchmark seismic zonation-mapping at volcanoes including uncertainties from seismic locations. It is specifically designed for volcanoes that have been mapped with seismic tomography and where extensive seismic networks and high-rate seismicity are available. These are today standards at many volcanoes worldwide, like Kilauea, La Réunion and those of the Canary Island, all characterized by high-rate seismicity and flank instability.

The results at Etna constrain a volume of low (almost-absent) seismicity, persistent across a 16 years period. We interpret this volume as a portion of the feeding system of the volcano embedded in a high velocity body. In this interpretation, the VLS represents the zone of transition between seismicity caused only by transient dike-related activity (west of the VLS) and seismicity caused by mixed magmatic and gravitational components. The model provides the first 3D seismic evidence of the different dynamics affecting the deeper and shallower portion of flank closest to the feeding systems, with important implications on the estimation of the volumes affected by sliding and the forces causing it. Only time-dependent analyses will provide exact spatial correlations of the VLS with source deformation models, insight into the temporal instability of the eastern flank and whether the VLS is a stationary feature or can be reconstructed only after a major eruption of the volcano.

DATA AVAILABILITY STATEMENT

The used software (VolGIS) provides graphic outputs that coincide with those shown in the article and in the **Supplementary Material**. The earthquake location data can be requested to the INGV-Osservatorio Etneo (Gruppo Analisi Dati Sismici, 2017).

AUTHOR CONTRIBUTIONS

RG designed the software and directed its development, built the 3D models, generated the maps and wrote the first draft text. LS guided the overarching research direction and advised on the geophysics and volcanology. CD coordinated the technical work on the software. All authors contributed to revising the text.

FUNDING

RG acknowledges the financial support of the Consejo Nacional de Investigaciones Científicas y Técnicas (CONICET) Argentina. CD acknowledges the financial support of the project "Pi UNRN 40B-634" entitled "Desarrollo, Integración e Implementación de Herramienta de Visualización y Análisis 3D y 4D (convocatoria trianual 2017)."

ACKNOWLEDGMENTS

This work was made possible by the outstanding efforts of the staff at the INGV-Osservatorio Etneo. We are particularly grateful to A. Ursino, S. Alparone, and G. Currenti, who provided us the seismic dataset and helped us to correctly interpret the variations of Coulomb stress at Etna. We thank Jurgen Neuberg for suggesting the comparison with the Coulomb stress and Guido Ventura for the insightful discussions on the volcanological significance of our results. We also thank the computer scientists of the LVCC for the support in the software development and A. Colubri for suggesting the application of the Marching Cube algorithm.

SUPPLEMENTARY MATERIAL

The Supplementary Material for this article can be found online at: https://www.frontiersin.org/articles/10.3389/feart.2020.589925/full#supplementary-material

REFERENCES

Acocella, V., Behncke, B., Neri, M., and D'Amico, S. (2003). Link between major flank slip and 2002–2003 eruption at Mt. Etna (Italy). *Geophys. Res. Lett.* 30, 2286. doi:10.1029/2003gl018642.

Acocella, V., and Neri, M. (2003). What makes flank eruptions? The 2001 Etna eruption and its possible triggering mechanisms. *Bull. Volcanol.* 65, 517–529. doi:10.1007/s00445-003-0280-3.

Aloisi, M., Bonaccorso, A., Cannavò, F., Currenti, G., and Gambino, S. (2020). The 24 December 2018 eruptive intrusion at etna volcano as revealed by multidisciplinary continuous deformaion networks (CGPS, borehole strainmeters and tiltmeters). *J. Geophys. Res. Solid Earth* 125, e2019JB019117. doi:10.1029/2019jb019117.

Aloisi, M., Cocina, O., Neri, G., Orecchio, B., and Privitera, E. (2002). Seismic tomography of the crust underneath the etna volcano, Sicily. *Phys. Earth Planet. Inter.* 134, 139–155. doi:10.1016/s0031-9201(02)00153-x.

Aloisi, M., Mattia, M., Monaco, C., and Pulvirenti, F. (2011). Magma, faults, and gravitational loading at Mount Etna: the 2002–2003 eruptive period. *J. Geophys. Res. Solid Earth* 116, B05203. doi:10.1029/2010jb007909.

Alparone, S., Barberi, G., Bonforte, A., Maiolino, V., and Ursino, A. (2011). Evidence of multiple strain fields beneath the eastern flank of Mt. Etna volcano (Sicily, Italy) deduced from seismic and geodetic data during 2003-2004. *Bull. Volcanol.* 73, 869–885. doi:10.1007/s00445-011-0456-1.

Alparone, S., Barberi, G., Cocina, O., Giampiccolo, E., Musumeci, C., and Patanè, D. (2012). Intrusive mechanism of the 2008-2009 Mt. Etna eruption: constraints by tomographic images and stress tensor analysis. *J. Volcanol. Geoth. Res.* 229-230, 50–63. doi:10.1016/j.jvolgeores.2012.04.001.

Alparone, S., Barberi, G., Giampiccolo, E., Maiolino, V., Mostaccio, A., Musumeci, C., et al. (2020). Seismological constraints on the 2018 Mt. Etna (Italy) flank eruption and implications for the flank dynamics of the volcano. *Terra Nova* 32, 334–344. doi:10.1111/ter.12463

Alparone, S., Maiolino, V., Mostaccio, A., Scaltrito, A., Ursino, A., Barberi, G., et al. (2015). Instrumental seismic catalogue of Mt. Etna earthquakes (Sicily, Italy): ten years (2000-2010) of instrumental recordings. *Ann. Geophys.* 58, 0435. 10.4401/ag-6591

Apuani, T., Corazzato, C., Merri, A., and Tibaldi, A. (2013). Understanding Etna flank instability through numerical models. *J. Volcanol. Geoth. Res.* 251, 112–126. doi:10.1016/j.jvolgeores.2012.06.015.

Azzaro, R., Bonforte, A., Branca, S., and Guglielmino, F. (2013). Geometry and kinematics of the fault systems controlling the unstable flank of Etna volcano (Sicily). *J. Volcanol. Geoth. Res.* 251, 5–15. doi:10.1016/j.jvolgeores.2012.10.001.

Barberi, G., Cocina, O., Neri, G., Privitera, E., and Spampinato, S. (2000). Volcanological inferences from seismic-strain tensor computations at Mt. Etna Volcano, Sicily. *Bull. Volcanol.* 62, 318–330. doi:10.1007/s004450000101.

Bisson, M., Spinetti, C., Neri, M., and Bonforte, A. (2016). Mt. Etna volcano high-resolution topography: airborne LiDAR modelling validated by GPS data. *Int. J. Digital Earth* 9, 710–732. doi:10.1080/17538947.2015.1119208.

Bonaccorso, A., Aloisi, M., and Mattia, M. (2002). Dike emplacement forerunning the Etna July 2001 eruption modeled through continuous tilt and GPS data. *Geophys. Res. Lett.* 29, 1624. doi:10.1029/2001gl014397.

Bonforte, A., Bonaccorso, A., Guglielmino, F., Palano, M., and Puglisi, G. (2008). Feeding system and magma storage beneath Mt. Etna as revealed by recent inflation/deflation cycles. *J. Geophys. Res. Solid Earth* 113, B05406. doi:10.1029/2007jb005334.

Bonforte, A., Guglielmino, F., and Puglisi, G. (2013). Interaction between magma intrusion and flank dynamics at Mt. Etna in 2008, imaged by integrated dense GPS and DInSAR data. *G-cubed* 14, 2818–2835. doi:10.1002/ggge.20190.

Bonforte, A., Guglielmino, F., and Puglisi, G. (2019). Large dyke intrusion and small eruption: the December 24, 2018 Mt. Etna eruption imaged by Sentinel-1 data. *Terra Nova* 31, 405–412doi:10.1111/ter.12403.

Bonforte, A., and Puglisi, G. (2003). Magma uprising and flank dynamics on Mount Etna volcano, studied using GPS data (1994–1995). *J. Geophys. Res. Solid Earth* 108, 2153. doi:10.1029/2002jb001845.

Bonforte, A., and Puglisi, G. (2006). Dynamics of the eastern flank of Mt. Etna volcano (Italy) investigated by a dense GPS network. *J. Volcanol. Geoth. Res.* 153, 357–369. doi:10.1016/j.jvolgeores.2005.12.005.

Borgia, A., Delaney, P. T., and Denlinger, R. P. (2000). Spreading volcanoes. *Annu. Rev. Earth Planet Sci.* 28, 539–570. doi:10.1146/annurev.earth.28.1.539.

Borgia, A., Ferrari, L., and Pasquarè, G. (1992). Importance of gravitational spreading in the tectonic and volcanic evolution of Mount Etna. *Nature* 357, 231–235. doi:10.1038/357231a0.

Bruno, V., Mattia, M., Montgomery-Brown, E., Rossi, M., and Scandura, D. (2017). Inflation leading to a slow slip event and volcanic unrest at Mount Etna in 2016: insights from CGPS data. *Geophys. Res. Lett.* 44, 141–149. doi:10.1002/2017gl075744.

Cannata, A., Spedalieri, G., Behncke, B., Cannavó, F., Di Grazia, G., Gambino, S., et al. (2015). Pressurization and depressurization phases inside the plumbing system of Mount Etna volcano: evidence from a multiparametric approach. *J. Geophys. Res. Solid Earth* 120 (9), 5965–5982.

Cannata, A., Di Grazia, G., Giuffrida, M., Gresta, S., Palano, M., Sciotto, M., et al. (2018). Space-time evolution of magma storage and transfer at Mt. Etna volcano (Italy): the 2015–2016 reawakening of Voragine crater. *Geochem. Geophys. Geosyst.* 19, 471–495. doi:10.1002/2017gc007296.

Carbone, D., Gibert, D., Marteau, J., Diament, M., Zuccarello, L., and Galichet, E. (2014). An experiment of muon radiography at Mt Etna (Italy). *Geophys. J. Int.* 196, 633–643. doi:10.1093/gji/ggt403.

Cardaci, C., Coviello, M., Lombardo, G., Patané, G., and Scarpa, R. (1993). Seismic tomography of Etna volcano. *J. Volcanol. Geoth. Res.* 56, 357–368. doi:10.1016/0377-0273(93)90002-9.

Chiarabba, C., Amato, A., Boschi, E., and Barberi, F. (2000). Recent seismicity and tomographic modeling of the Mount Etna plumbing system. *J. Geophys. Res.* 105, 10923–10938. doi:10.1029/1999jb900427.

Chiarabba, C., De Gori, P., and Patane, D. (2004). *The Mt. Etna plumbing system: the contribution of seismic tomography*. Mt. Etna: Volcano Laboratory.

Cline, H. E., Dumoulin, C. L., Hart, H. R., Jr., Lorensen, W. E., and Ludke, S. (1987). 3D reconstruction of the brain from magnetic resonance images using a connectivity algorithm. *Magn. Reson. Imag.* 5, 345–352. doi:10.1016/0730-725x(87)90124-x.

Cocco, M., and Rice, J. R. (2002). Pore pressure and poroelasticity effects in Coulomb stress analysis of earthquake interactions. *J. Geophys. Res. Solid Earth* 107, ESE–2. doi:10.1029/2000jb000138.

Currenti, G., Del Negro, C., Ganci, G., and Williams, C. A. (2008). Static stress changes induced by the magmatic intrusions during the 2002-2003 Etna eruption. *J. Geophys. Res.: Solid Earth* 113, B10206. doi:10.1029/2007jb005301.

Díaz-Moreno, A., Barberi, G., Cocina, O., Koulakov, I., Scarfì, L., Zuccarello, L., et al. (2018). New insights on Mt. Etna's crust and relationship with the regional tectonic framework from joint active and passive P-wave seismic tomography. *Surv. Geophys.* 39, 57–97. doi:10.1007/s10712-017-9425-3.

De Gori, P., Chiarabba, C., and Patanè, D. (2005). Qp structure of mount etna: constraints for the physics of the plumbing system. *J. Geophys. Res.* 110, B05303. doi:10.1029/2003JB002875.

De Luca, G., Filippi, L., Patanè, G., Scarpa, R., and Vinciguerra, S. (1997). Three-dimensional velocity structure and seismicity of Mt. Etna volcano, Italy. *J. Volcanol. Geotherm. Res.* 79, 123–138. doi:10.1016/s0377-0273(97)00026-7.

De Novellis, V., Atzori, S., De Luca, C., Manzo, M., Valerio, E., Bonano, M., et al. (2019). DInSAR analysis and analytical modeling of mount etna displacements: the december 2018 volcano-tectonic crisis. *Geophys. Res. Lett.* 46, 5817–5827. doi:10.1029/2019gl082467.

De Siena, L., Chiodini, G., Vilardo, G., Del Pezzo, E., Castellano, M., Colombelli, S., et al. (2017). Source and dynamics of a volcanic caldera unrest: Campi Flegrei, 1983–84. *Sci. Rep.* 7, 8099. doi:10.1038/s41598-017-08192-7.

Decker, R. W. (1984). Dynamics of Hawaiian volcanoes: an overview. US Geological Survey Professional Paper 2, 997.

Giampiccolo, E., Cocina, O., De Gori, P., and Chiarabba, C. (2020). Dyke intrusion and stress-induced collapse of volcano flanks: the example of the 2018 event at mt. etna (sicily, Italy). *Sci. Rep.* 10, 6373. doi:10.1038/s41598-020-63371-3.

Gambino, S., Cannata, A., Cannavó, F., La Spina, A., Palano, M., Sciotto, M., et al. (2016). The unusual 28 December 2014 dike-fed paroxysm at Mount Etna: timing and mechanism from a multidisciplinary perspective. *J. Geophys. Res. Solid Earth* 121(3), 2037–2053.

González, P. J., and Palano, M. (2014). Mt. Etna 2001 eruption: new insights into the magmatic feeding system and the mechanical response of the

western flank from a detailed geodetic dataset. *J. Volcanol. Geotherm. Res.* 274, 108–121.

Gruppo Analisi Dati Sismici, G. (2017). *Catalogo dei terremoti della Sicilia Orientale-Calabria Meridionale (1999–2017)*. Catania, Italy: INGV. Available at: http://sismoweb.ct.ingv.it/maps/eq_maps/sicily/index.php (Accessed December 12, 2017).

Guardo, R., and De Siena, L. (2017). Integrating ambient noise with GIS for a new perspective on volcano imaging and monitoring: the case study of Mt. Etna. *J. Volcanol. Geoth. Res.* 347, 397–407. doi:10.1016/j.jvolgeores.2017.10.007.

Gudmundsson, A. (1983). Form and dimensions of dykes in eastern Iceland. *Tectonophysics* 95, 295–307. doi:10.1016/0040-1951(83)90074-4.

Hirn, A., Nercessian, A., Sapin, M., Ferrucci, F., and Wittlinger, G. (1991). Seismic heterogeneity of Mt Etna: structure and activity. *Geophys. J. Int.* 105, 139–153. doi:10.1111/j.1365-246x.1991.tb03450.x.

Huang, H.-H., Lin, F.-C., Schmandt, B., Farrell, J., Smith, R. B., and Tsai, V. C. (2015). The Yellowstone magmatic system from the mantle plume to the upper crust. *Science* 348, 773–776. doi:10.1126/science.aaa5648.

Jaxybulatov, K., Shapiro, N. M., Koulakov, I., Mordret, A., Landès, M., and Sens-Schönfelder, C. (2014). A large magmatic sill complex beneath the Toba caldera. *Science* 346, 617–619. doi:10.1126/science.1258582.

Julian, B., Prisk, A., Foulger, G., and Evans, J. (1993). "Three dimensional images of geothermal systems: local earthquake P-wave velocity tomography at the Hengill and Krafla geothermal areas, Iceland, and the Geysers, California," in Proceedings of the 1993 annual meeting on utilities and geothermal: an emerging partnership, Burlingame, CA, Vol. 17, 113–121.

Koulakov, I. (2013). Studying deep sources of volcanism using multiscale seismic tomography. *J. Volcanol. Geotherm. Res.* 257, 205–226. doi:10.1016/j.jvolgeores.2013.03.012

Laigle, M., Hirn, A., Sapin, M., Lépine, J.-C., Diaz, J., Gallart, J., et al. (2000). Mount Etna dense array local earthquakePandStomography and implications for volcanic plumbing. *J. Geophys. Res.* 105, 21633–21646. doi:10.1029/2000jb900190.

Lopes, A., and Brodlie, K. (2003). Improving the robustness and accuracy of the marching cubes algorithm for isosurfacing. *IEEE Trans. Visual. Comput. Graph.* 9, 16–29. doi:10.1109/tvcg.2003.1175094.

Lorensen, W. E., and Cline, H. E. (1987). Marching cubes: a high resolution 3D surface construction algorithm. *SIGGRAPH Comput. Graph.* 21, 163–169. doi:10.1145/37402.37422.

Lundgren, P., Berardino, P., Coltelli, M., Fornaro, G., Lanari, R., Puglisi, G., et al. (2003). Coupled magma chamber inflation and sector collapse slip observed with synthetic aperture radar interferometry on Mt. Etna volcano. *J. Geophys. Res.: Solid Earth* 108, 2247. doi:10.1029/2001jb000657.

Lundgren, P., Casu, F., Manzo, M., Pepe, A., Berardino, P., Sansosti, E., et al. (2004). Gravity and magma induced spreading of Mount Etna volcano revealed by satellite radar interferometry. *Geophys. Res. Lett.* 31, L04602. doi:10.1029/2003gl018736.

Ma, C., and Rokne, J. (2004). "3D seismic volume visualization," in *Integrated image and graphics technologies* (Boston, MA Springer), 241–262.

Masala, G. L., Golosio, B., and Oliva, P. (2013). An improved marching cube algorithm for 3D data segmentation. *Comput. Phys. Commun.* 184, 777–782. doi:10.1016/j.cpc.2012.09.030.

Mattia, M., Bruno, V., Caltabiano, T., Cannata, A., Cannavò, F., D'Alessandro, W., et al. (2015). A comprehensive interpretative model of slow slip events on Mt. Etna's eastern flank. *Geochem. Geophys. Geosyst.* 16, 635–658. doi:10.1002/2014gc005585.

Murray, J. B., de Vries, B. v. W., Pitty, A., Sargent, P., and Wooller, L. (2018). Gravitational sliding of the Mt. Etna massif along a sloping basement. *Bull. Volcanol.* 80, 40. doi:10.1007/s00445-018-1209-1.

Murru, M., Montuori, C., Wyss, M., and Privitera, E. (1999). The locations of magma chambers at Mt. Etna, Italy, mapped by b-values. *Geophys. Res. Lett.* 26, 2553–2556. doi:10.1029/1999gl900568.

Neri, M., Acocella, V., and Behncke, B. (2004). The role of the Pernicana fault system in the spreading of Mt. Etna (Italy) during the 2002–2003 eruption. *Bull. Volcanol.* 66, 417–430. doi:10.1007/s00445-003-0322-x.

Neri, M., Rivalta, E., Maccaferri, F., Acocella, V., and Cirrincione, R. (2018). Etnean and Hyblean volcanism shifted away from the Malta Escarpment by crustal stresses. *Earth Planet Sci. Lett.* 486, 15–22. doi:10.1016/j.epsl.2018.01.006.

Newman, T. S., and Yi, H. (2006). A survey of the marching cubes algorithm. *Comput. Graph.* 30, 854–879. doi:10.1016/j.cag.2006.07.021.

Palano, M. (2016). Episodic slow slip events and seaward flank motion at Mt. Etna volcano (Italy). *J. Volcanol. Geotherm. Res.* 324, 8–14. doi:10.1016/j.jvolgeores.2016.05.010.

Palano, M., Viccaro, M., Zuccarello, F., and Gresta, S. (2017). Magma transport and storage at Mt. Etna (Italy): a review of geodetic and petrological data for the 2002–03, 2004 and 2006 eruptions. *J. Volcanol. Geotherm. Res.* 347, 149–164. doi:10.1016/j.jvolgeores.2017.09.009.

Parfitt, L., and Wilson, L. (2008). *Fundamentals of physical volcanology*. Oxford, United Kingdom: Blackwell Publishing.

Parisio, F., Vinciguerra, S., Kolditz, O., and Nagel, T. (2019). The brittle-ductile transition in active volcanoes. *Sci. Rep.* 9, 143. doi:10.1038/s41598-018-36505-x.

Patanè, D., Barberi, G., Cocina, O., De Gori, P., and Chiarabba, C. (2006). Time-resolved seismic tomography detects magma intrusions at Mount Etna. *Science* 313, 821–823. doi:10.1126/science.1127724.

Patanè, D., Chiarabba, C., Cocina, O., Gori, P. D., Moretti, M., and Boschi, E. (2002). Solid Earth-135. Tomographic images and 3D earthquake locations of the seismic swarm preceding the 2001 Mt. Etna eruption: evidence for a dyke intrusion. *Geophys. Res. Lett.* 29. doi:10.1029/2001gl014391.

Patanè, D., De Gori, P., Chiarabba, C., and Bonaccorso, A. (2003). Magma ascent and the pressurization of Mount Etna's volcanic system. *Science* 299, 2061–2063. doi:10.1126/science.1080653.

Pezzo, G., Palano, M., Tolomei, C., De Gori, P., Calcaterra, S., Gambino, P., et al. (2020). Flank sliding: a valve and a sentinel for paroxysmal eruptions and magma ascent at Mount Etna, Italy. *Geology 48*. doi:10.1130/g47656.1.

Puglisi, G., Bonforte, A., Ferretti, A., Guglielmino, F., Palano, M., and Prati, C. (2008). Dynamics of Mount Etna before, during, and after the July–August 2001 eruption inferred from GPS and differential synthetic aperture radar interferometry data. *J. Geophys. Res. Solid Earth* 113, B06405. doi:10.1029/2006jb004811.

Puglisi, G., Bonforte, A., and Maugeri, S. R. (2001). Ground deformation patterns on Mount Etna, 1992 to 1994, inferred from GPS data. *Bull. Volcanol.* 62, 371–384. doi:10.1007/s004450000112.

Rasà, R., Azzaro, R., and Leonardi, O. (1996). Aseismic creep on faults and flank instability at Mount Etna volcano, Sicily. *Geol. Soc. London Special Public.* 110, 179–192. doi:10.1144/gsl.sp.1996.110.01.14.

Rawlinson, N., and Spakman, W. (2016). On the use of sensitivity tests in seismic tomography. *Geophys. J. Int.* 205, 1221–1243. doi:10.1093/gji/ggw084.

Scandone, R., and Malone, S. D. (1985). Magma supply, magma discharge and readjustment of the feeding system of Mount St. Helens during 1980. *J. Volcanol. Geoth. Res.* 23, 239–262. doi:10.1016/0377-0273(85)90036-8.

Schuler, J., Greenfield, T., White, R. S., Roecker, S. W., Brandsdóttir, B., Stock, J. M., et al. (2015). Seismic imaging of the shallow crust beneath the Krafla central volcano, NE Iceland. *J. Geophys. Res. Solid Earth* 120, 7156–7173. doi:10.1002/2015jb012350.

Sharp, A. D. L., Davis, P. M., and Gray, F. (1980). A low velocity zone beneath Mount Etna and magma storage. *Nature* 287, 587–591. doi:10.1038/287587a0.

Spampinato, L., Sciotto, M., Cannata, A., Cannavó, F., La Spina, A., Palano, M., et al. (2015). Multiparametric study of the February–April 2013 paroxysmal phase of Mt. Etna New South-East crater. *Geochem. Geophys. Geosyst.* 16 (6), 1932–1949.

Subramanian, K. R., and Fussell, D. S. (1990). "Applying space subdivision techniques to volume rendering," in Proceedings of the 1st conference on Visualization'90, San Francisco, CA, October 23–26, 1990 (IEEE Computer Society Press), 150–159.

Tibaldi, A. (2015). Structure of volcano plumbing systems: a review of multi-parametric effects. *J. Volcanol. Geoth. Res.* 298, 85–135. doi:10.1016/j.jvolgeores.2015.03.023.

Tibaldi, A., and Groppelli, G. (2002). Volcano-tectonic activity along structures of the unstable NE flank of Mt. Etna (Italy) and their possible origin. *J. Volcanol. Geoth. Res.* 115, 277–302. doi:10.1016/s0377-0273(01)00305-5.

Urlaub, M., Petersen, F., Gross, F., Bonforte, A., Puglisi, G., Guglielmino, F., et al. (2018). Gravitational collapse of Mount Etna's southeastern flank. *Sci. Adv.* 4, eaat9700. doi:10.1126/sciadv.aat9700.

Viccaro, M., Zuccarello, F., Cannata, A., Palano, M., and Gresta, S. (2016). How a complex basaltic volcanic system works: constraints from integrating seismic, geodetic, and petrological data at Mount Etna volcano during the July–August 2014 eruption. *J. Geophys. Res. Solid Earth* 121 (8), 5659–5678.

Villaseñor, A., Benz, H. M., Filippi, L., De Luca, G., Scarpa, R., Patanè, G., et al. (1998). Three-dimensional P-wave velocity structure of Mt. Etna, Italy. *Geophys. Res. Lett.* 25, 1975–1978. doi:10.1029/98gl01240.

Walter, T. R., Acocella, V., Neri, M., and Amelung, F. (2005). Feedback processes between magmatic events and flank movement at Mount Etna (Italy) during the 2002–2003 eruption. *J. Geophys. Res. Solid Earth* 110, B10205. doi:10.1029/2005jb003688.

Conflict of Interest: The authors declare that the research was conducted in the absence of any commercial or financial relationships that could be construed as a potential conflict of interest.

Copyright © 2020 Guardo, De Siena and Dreidemie. This is an open-access article distributed under the terms of the Creative Commons Attribution License (CC BY). The use, distribution or reproduction in other forums is permitted, provided the original author(s) and the copyright owner(s) are credited and that the original publication in this journal is cited, in accordance with accepted academic practice. No use, distribution or reproduction is permitted which does not comply with these terms.

frontiers in Earth Science

ORIGINAL RESEARCH
published: 29 October 2020
doi: 10.3389/feart.2020.549774

Characterization of Acoustic Infrasound Signals at Volcán de Fuego, Guatemala: A Baseline for Volcano Monitoring

A. Diaz-Moreno[1], A. Roca[2], A. Lamur[3], B. H. Munkli[3], T. Ilanko[4], T. D. Pering[4], A. Pineda[5] and S. De Angelis[3]*

[1]School of Geography, Politics and Sociology, Newcastle University, Newcastle Upon Tyne, NW, United Kingdom, [2]Instituto Nacional de Sismología, Vulcanología, Meteorología e Hidrología, INSIVUMEH, Guatemala City, Guatemala, [3]School of Environmental Sciences, University of Liverpool, Liverpool, United Kingdom, [4]Department of Geography, University of Sheffield, Sheffield, United Kingdom, [5]Pineda Consulting and Services, Finca Xejuyu, Chimaltenango, Guatemala

OPEN ACCESS

Edited by:
Valerio Acocella, Roma Tre University, Italy

Reviewed by:
Luca De Siena, Johannes Gutenberg University Mainz, Germany
Derek Keir, University of Southampton, United Kingdom

***Correspondence:**
A. Diaz-Moreno
aledmoreno@hotmail.com

Specialty section:
This article was submitted to Volcanology, a section of the journal Frontiers in Earth Science

Received: *07 April 2020*
Accepted: *22 September 2020*
Published: *29 October 2020*

Citation:
Diaz-Moreno A, Roca A, Lamur A, Munkli BH, Ilanko T, Pering TD, Pineda A and De Angelis S (2020) Characterization of Acoustic Infrasound Signals at Volcán de Fuego, Guatemala: A Baseline for Volcano Monitoring. Front. Earth Sci. 8:549774. doi: 10.3389/feart.2020.549774

Monitoring volcanic unrest and understanding seismic and acoustic signals associated with eruptive activity is key to mitigate its impacts on population and infrastructure. On June 3, 2018, Volcán de Fuego, Guatemala, produced a violent eruption with very little warning. The paroxysmal phase of this event generated pyroclastic density currents (PDC) that impacted nearby settlements resulting in 169 fatalities, 256 missing, and nearly 13,000 permanently displaced from their homes. Since then, Volcán de Fuego has been instrumented with an extensive network of seismic and infrasound sensors. Infrasound is a new monitoring tool in Guatemala. A key step toward its effective use in volcano monitoring at Volcán de Fuego is establishing a baseline for the interpretation of the recorded signals. Here, we present the first comprehensive characterization of acoustic signals at Volcán de Fuego for the whole range of surface activity observed at the volcano. We use data collected during temporary deployments in 2018 and from the permanent infrasound network. Infrasound at Fuego is dominated by the occurrence of short-duration acoustic transients linked to both ash-rich and gas-rich explosions, at times associated with the generation of shock waves. The rich acoustic record at Fuego includes broadband and harmonic tremor, and episodes of chugging. We explore the occurrence of these signals in relation to visual observations of surface activity, and we investigate their source mechanisms within the shallow conduit system. This study provides a reference for the interpretation of acoustic signals at Volcán de Fuego and a baseline for real-time monitoring of its eruptive activity using infrasound data. Our results suggest that changes in the style of activity and morphology of the summit crater are reflected in the acoustic signature of eruption; as such our study provides a reference for the interpretation of acoustic signals at Volcán de Fuego and a baseline for real-time monitoring of its eruptive activity using infrasound.

Keywords: acoustic infrasound, Volcán de Fuego, monitoring, Strombolian activity, paroxysmal activity

1. INTRODUCTION

Effective monitoring strategies are a key aspect of hazard mitigation near volcanoes (Tilling, 2008). Real-time, multi-parameter, monitoring of volcanoes is key to reduce the impact of eruptions on communities and infrastructure (McNutt et al., 2015; Pallister and McNutt, 2015; Ripepe and Marchetti, 2019). At present, less than half of the world's active volcanoes with Holocene eruptions in historical times, that is in the past 10,000 years, are instrumentally monitored (McNutt et al., 2015). At many volcanoes, resources devoted to developing monitoring programs have traditionally been scarce, leading to severe impacts of eruptions on population and infrastructure. A recent example is Volcán de Fuego, Guatemala, where an eruption with associated pyroclastic flows occurred on June 3, 2018 causing 169 confirmed casualties, 256 missing, severe damage to population centers and infrastructure, and associated economic losses (Global Volcanism Program, 2018c). Interest in understanding the eruptive behavior of Volcán de Fuego, sparkled after a sub-plinian event in 1974 (Rose et al., 1978; Chesner and Rose, 1984; Yuan et al., 1984; Berlo et al., 2012). Early monitoring efforts consisted of visual and field observations; short-term multi-parameter deployments including gas, seismic and infrasound measurements became increasingly common through the past decade (e.g., Lyons et al., 2010; Lyons and Waite, 2011; Nadeau et al., 2011; Brill et al., 2018; Naismith et al., 2019). Before the eruption on June 3, 2018, the permanent network operated by Instituto Nacional de Sismología, Vulcanología, Meteorología e Hidrología (INSIVUMEH) consisted of a single seismic station located 7.5 km from the active vent streaming data in real-time to INSIVUMEH headquarters. However, data dropouts were frequent and until 2018 continuous seismic data were not archived. Since June 2018, the monitoring capabilities at Volcán de Fuego have been greatly enhanced; at the time of this writing, the monitoring network operated by INSIVUMEH consists of three 6-channel seismo-acoustic arrays (each including one 3-component broadband seismometer and three infrasound microphones), three 3-component broadband seismic stations, and one 6-channel infrasound array deployed at distances of 3–15 km from the vent, transmitting data in real-time to the INSIVUMEH headquarters in Guatemala City.

Among the different techniques used in volcano observatories, seismology and infrasound continue to offer unmatched temporal resolution for near real-time volcano monitoring (Brill et al., 2018; Marchetti et al., 2019). In recent times, acoustic infrasound has emerged as an increasingly popular tool for volcano remote sensing. The term infrasound identifies atmospheric acoustic waves with frequencies typically <20 Hz, below the audible range of humans. Volcanoes are prolific radiators of infrasound, generated by eruptive processes that cause rapid acceleration of the atmospheric mass (Garcés et al., 2013); these low-frequency acoustic waves can be detected at distances of up to several thousands of kilometers from their source lending themselves to volcano monitoring at different scales, from local to global (Matoza et al., 2018). The use of infrasound for regional and local volcano monitoring, with applications in volcano early warning, has become increasingly popular (Kamo et al., 1994; Garcés et al., 2008; Fee et al., 2010b; De Angelis et al., 2012; De Angelis et al., 2019; Ripepe et al., 2018). Different configurations for deployment of infrasound microphones generate different products and therefore, sensors are generally installed according to specific scopes (Matoza et al., 2019b). Local distributed networks of individual microphones are ideal for locating and characterizing eruptive activity offering potential to assess open conduit volcanic emissions in real- or near real-time (Cannata et al., 2009a; Johnson and Ripepe, 2011; Fee and Matoza, 2013; De Angelis et al., 2019; Iezzi et al., 2019). On the other hand, arrays, that is clusters of three or more tightly spaced sensors, are commonly used to detect and locate low-amplitude signals (i.e., tremor, lahars, Johnson and Palma, 2015). Arrays can also detect and identify volcanic infrasound transients at global and regional distances contributing to monitoring of non-accessible remote volcanoes (Walker et al., 2010; Lyons et al., 2020). Co-location of seismic and acoustic sensors can provide additional insights into the dynamics of volcanic activity where a more extensive monitoring network is not available (Nishida and Ichihara, 2016; Matoza et al., 2019a).

Volcán de Fuego has hosted several seismo-acoustic experiments since 2005. These campaigns have shed light into the dynamics of the volcanic system, from the occurrence of cycles of activity to the source mechanisms of individual explosions. Observations during 2005–2007 including seismo-acoustic deployments led to the first comprehensive study of eruption dynamics at Volcán de Fuego (Lyons et al., 2010), a milestone for future experiments. Two temporary seismo-acoustic deployments in January 2008 and 2009 gathered valuable data that further contributed to our knowledge on the occurrence of very-long period seismicity (Lyons and Waite, 2011; Waite et al., 2013), SO2 imaging (Nadeau et al., 2011), tilt changes and ultra-long-period events (Lyons et al., 2012), and seismo-acoustic tremor (Lyons et al., 2013) and allowed modeling of the processes that control eruption dynamics at Fuego. Recent experiments, conducted in January 2012, included seismo-acoustic deployments, collection of thermal infrared imagery, and gas and tilt measurements; some of the data collected in 2012 were recently used to define a baseline for seismic monitoring at the volcano (Brill et al., 2018). We conducted temporary deployments during 18–23 May 2018 and 26 November–3 December 2018 to gather infrasound data from activity at Volcán de Fuego. A new geophysical permanent monitoring network was installed at the volcano in the aftermath of the June 2018 eruption, including six new seismic stations and four infrasound arrays (**Figure 1**).

The scope of this manuscript is to present an overview of the range of infrasound signals associated with recent eruptive activity using data from the above mentioned temporary deployments, and link them to surface activity observed at the volcano. We envision that this work will serve as an initial baseline to inform infrasound monitoring of Volcán de Fuego.

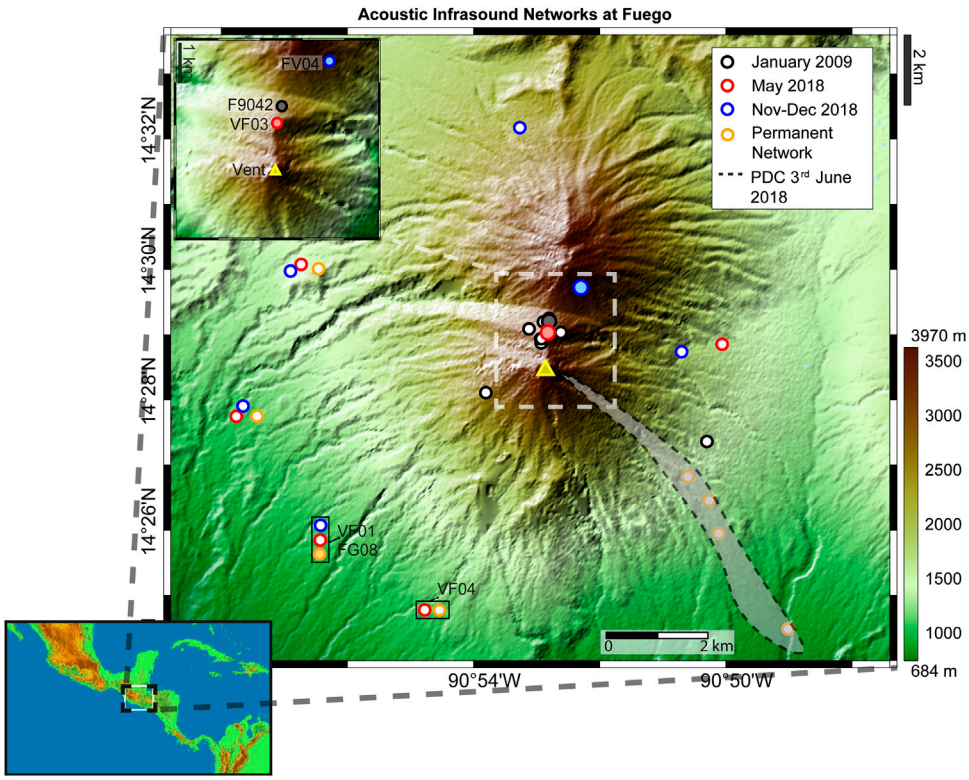

FIGURE 1 | Locations of sites for temporary and permanent acoustic monitoring networks at Volcán de Fuego. Red (May 2018) and blue circles (November–December 2018) are temporary deployments used in this study; orange circles indicate the permanent seismo-acoustic network. Color-filled circles identify stations from which data are plotted in the figures in this manuscript. The dashed white square outlines the area shown in the inset map. The grey-filled area illustrates, qualitatively, the footprint of the 3 June Pyroclastic Density Current (PDC).

2. VOLCÁN DE FUEGO

Volcán de Fuego is one of the most active volcanoes in central and south America (Wolf-Escobar, 2013). It is a basaltic strato-volcano standing nearly 3,800 m above sea level in the Central America Volcanic Arc (14.47°N, 90.88°W), and marks the southernmost active part of the four-vent Fuego-Acatenango volcanic complex (Guatemala), which has been migrating southwards since 230 ka (Chesner and Rose, 1984). While the main growth period of this complex is dated 84 ka (Vallance and Iverson, 2015), volcanic activity at the current vent may have begun 13 ka (Martin and Rose, 1981). Bulk rock data collected at Meseta and Volcán de Fuego showed fractionation of plagioclase, olivine, clinopyroxene, and magnetite consistent with a high-aluminium basaltic composition (51% SiO2; Chesner and Rose, 1984). Moreover, melt inclusions in erupted olivine indicate that Fuego's magmas, like many other arc basalts and basaltic andesites, contain dissolved H_2Oconcentrations between 2.1 and 6.1 wt% (Sisson and Layne, 1993; Roggensack, 2001). This high volatile content is thought to influence eruptive behavior during open-vent periods. Reports of activity since 1954 include at least 60 eruptions characterized by Volcanic Explosivity Index (VEI) 2 with associated pyroclastic flows, and interspersed with frequent Strombolian activity (Rose et al., 1978; Berlo et al., 2012; Naismith et al., 2019). During the last century, three sub-Plinian events have occurred: i) a VEI 4 eruption in January 1932 that generated a >5 km a.s.l. plume and modified the vent's morphology leaving ash deposits across Guatemala (Deger, 1932; Naismith et al., 2019); ii) a VEI 4 eruption in October 1974, which included four major stages producing lava flows, ash fall, pyroclastic flows and lahars, forced the mobilization of population, and caused important damage on the agriculture (Rose et al., 1978); and iii) the recent eruption on June 3, 2018 (Global Volcanism Program, 2018c).

2.1. Long-Term Evolution of Eruptive Activity

Activity at Volcán de Fuego since 1974 can be summarized as long quiescence until 1999, followed by the reactivation of eruptive processes that remained nearly continuous until present. Persistent activity at Fuego is characterized by extended periods of lava effusion, frequent but moderate explosions, and episodes of paroxysmal activity. Paroxysms at Volcán de Fuego are defined as eruptive phases that start with the onset of energetic explosive activity rapidly increasing in rates and intensity leading to large sustained emission of pyroclastic material, which persists for 24–48 h (e.g., Lyons et al., 2010). Indeed, the rate of occurrence of paroxysms has greatly increased since late 2014 (**Figure 2**).

The 1974 eruption of Fuego had an estimated VEI = 4, generated sustained ash columns reaching a height of over

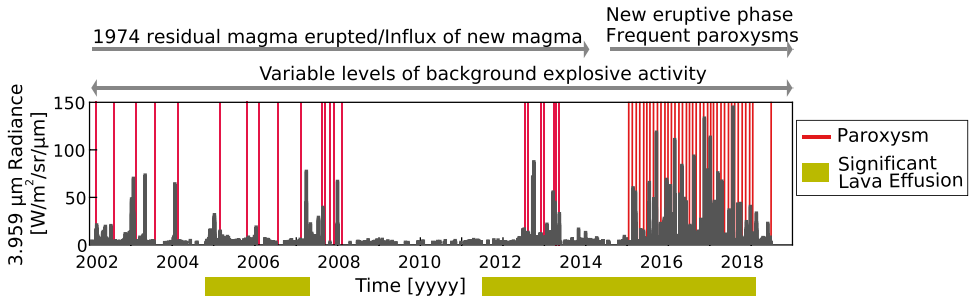

FIGURE 2 | Histogram of thermal radiance detected by the moderate resolution imaging spectroradiometer (MODIS) sensors (mounted onboard the Earth Observing System (EOS) Terra and Aqua platforms, and available at http://modis.higp.hawaii.edu) combined with periods of significant lava effusion and paroxysms reported by Instituto Nacional de Sismología, Vulcanología, Meteorología e Hidrología (INSIVUMEH) and the Smithsonian Global Volcanism Program. Note a significant increase in the rate of occurrence of paroxysms and lava effusion since 2015.

7 km above the vent, and produced Pyroclastic Density Currents (PDC) with a run-out of 8 km. The eruption, composed of four major events, lasted 14 days and led to substantial damage in villages up to 40 km from the summit mainly caused by PDCs and ashfall (Roggensack, 2001; Naismith et al., 2019). Many studies link this event to the ascent of magma from a lens-shaped vertical body located at about 8 km depth connected to a larger, deeper, storage region, with some suggesting the presence of an even deeper reservoir near the crust-mantle boundary (Rose et al., 1978; Martin and Rose, 1981; Chesner and Rose, 1984; Roggensack, 2001). Nearly 2 decades of quiescence followed the 1974 eruption.

In 1999 a new period of unrest began, characterized by periods of lava effusion accompanied by Strombolian explosions and episodic paroxysmal activity. **Figure 2** illustrates this behavior from thermal radiance data since 2002 plotted alongside reported paroxysms and periods of significant lava effusion. Note that moderate resolution imaging spectroradiometer (MODIS) pixel resolution varies from 250 m to 1 km, and thus, the thermal radiance data showed in **Figure 2** do not allow separating activity at the summit from that occurring on the upper flanks of the volcanic edifice. Lack of data resolution (flank activity vs. summit activity) does not influence interpretation of the activity over this 20-years scale. Current resolution does not allow us to establish which thermal anomalies are caused by active lava flows or which by significant explosions. Qualitatively, both lava flows and large explosions increase contemporaneously. However additional data will be needed to accurately answer this question (i.e., better satellite resolution images, visual data from field). During 1999–2003, erupted products were similar in composition to 1974 although more differentiated, that is showing more evolved melt inclusions. This activity was interpreted as linked to remaining magma from 1974 stored at shallow depths and being pushed out by the ascent of a new batch of magma from depth. Berlo et al. (2012) suggested that paroxysmal activity would continue in the years to come, fueled by renewed supply of fresh magma. Intermittent activity reported throughout the period 2000–2014 confirmed a new phase of volcanic activity, dominated by relatively frequent explosive eruptions and effusive activity (Lyons et al., 2010; Naismith et al., 2019).

Starting in early 2015 activity was characterized by more regular cycles of lava effusion (5–10 days) accompanied by frequent Strombolian explosions, preceding (1–2 days) episodes of more vigorous and sustained explosive activity, followed by a decrease in activity (Naismith et al., 2019). Since 2015 paroxysms at Volcán de Fuego have occurred more frequently until the event on June 3, 2018 (**Figure 1**). During this eruptive episode intense degassing and sustained ash plumes rising up to 3 km above the vent were followed by PDCs. The pyroclastic flows, with a run-out of more than 11 km along the Las Lajas valley, destroyed part of La Reunion Resort, the Las Lajas bridge on the National Route (RN) 14, and buried the village of San Miguel Los Lotes. Official figures report at least 169 casualties, 256 people missing, and nearly 13,000 people evacuated (Global Volcanism Program, 2018c; Ferrés, 2019; Naismith et al., 2019; Pardini et al., 2019). Furthermore, the ash and pyroclastic deposits during the rainy season fueled several lahars in the following months (Global Volcanism Program, 2018c).

3. DATA AND RECENT ACTIVITY

Here, we take advantage of data collected during two campaigns that were conducted in 18–23 May and 26 November - December 3, 2018 (**Figure 1**).

3.1. May 2018 Deployment

Activity reports from INSIVUMEH describe activity during the period 16–22 May 2018 as characterized by frequent explosions (5–8 per hour), some of which injected ash at elevations of up to 1 km above the vent. The explosive activity caused rumbling sounds and produced shock waves (pressure perturbations that move faster than the speed of sound in the atmosphere) locally referred to as cañonazos. The loud noise produced by shock waves was frequently heard as far as 30 km from the volcano (Global Volcanism Program, 2018a). In May 2018 we deployed a temporary network (18–23 May 2018) of six infrasound sensors

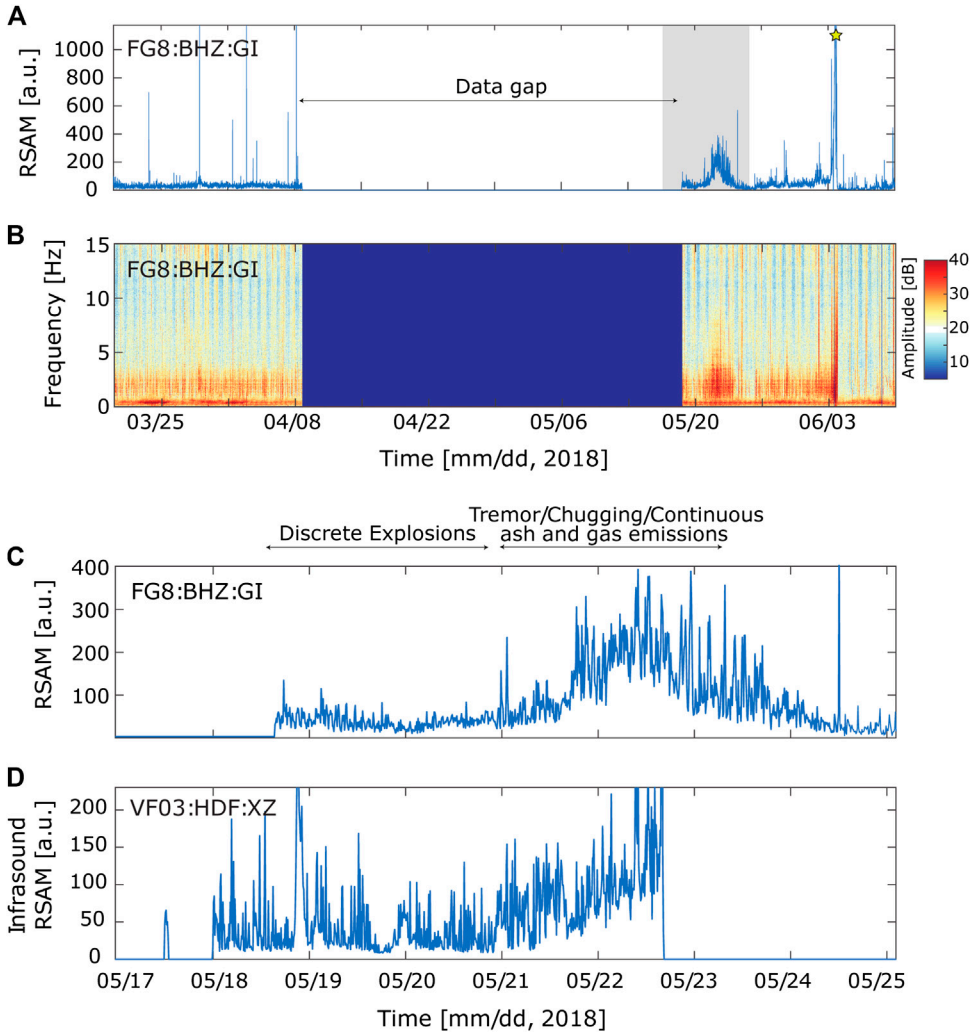

FIGURE 3 | A) RSAM (Real-time Seismic Amplitude Measurement) and **(B)** spectrogram from seismic permanent station FG8 (7.5 km from vent) during the period March–June 2018. Gray area highlights the period when a temporary acoustic network was deployed. The yellow star marks the June 3, 2018 paroxysm. **(C)** RSAM of the 17–25 May period at FG08 station and **(D)** RSAM of the infrasound temporary station VF03 for the same period. Clear changes in the recorded signals are visible in both the RSAM and spectrogram (**Figure 1B**) on the 21 May.

(Chaparral M60-UHP), located between 1 and 9 km from the active vent. The sensors have a sensitivity of 9 mV/Pa, flat response between 0.03 and 245 Hz, and a full-scale range of 2,000 Pa. Data were sampled at 100 Hz with 24-bit resolution using DiGOS DATA-CUBE digitizers. During the deployment eruptive activity shifted from discrete and energetic gas-rich explosions to Strombolian-type explosions, then to sustained ash and gas emissions accompanied by quasi-continuous acoustic tremor on 21–23 May. This change is visible as an increase in amplitude in both RSAM (Real-time seismic amplitude measurement) and spectrogram from the only broadband seismic station available at the time, and one of the temporary infrasound sensors illustrated in **Figure 3**. Data gathered from this campaign show a wide range of infrasound waveforms, some of which resemble previously reported signals at Volcán de Fuego (Lyons et al., 2010; Lyons, 2011) including gas- and ash-rich explosions, shock waves, harmonic, and broadband tremor. We also recorded periods of strong chugging, described in the literature (e.g., Johnson and Lees, 2000; Lees and Ruiz, 2008) as a particular instance of quasi-periodic harmonic tremor. Chugging was observed at Volcán de Fuego for the first time by Lyons et al. (2010). During this period INSIVUMEH reported the presence of two active vents within the summit area at Fuego (G. Chigna, personal communication July 2018). This configuration is typical at Fuego when the crater is filled by lava and the two vents are frequently observed to produce distinct types of explosions, one gas-rich and another ash-rich (**Figure 4**).

3.2. November-December 2018 Deployment

During November-December 2018 — soon after the most recent paroxysm in mid-November 2018 — INSIVUMEH reported

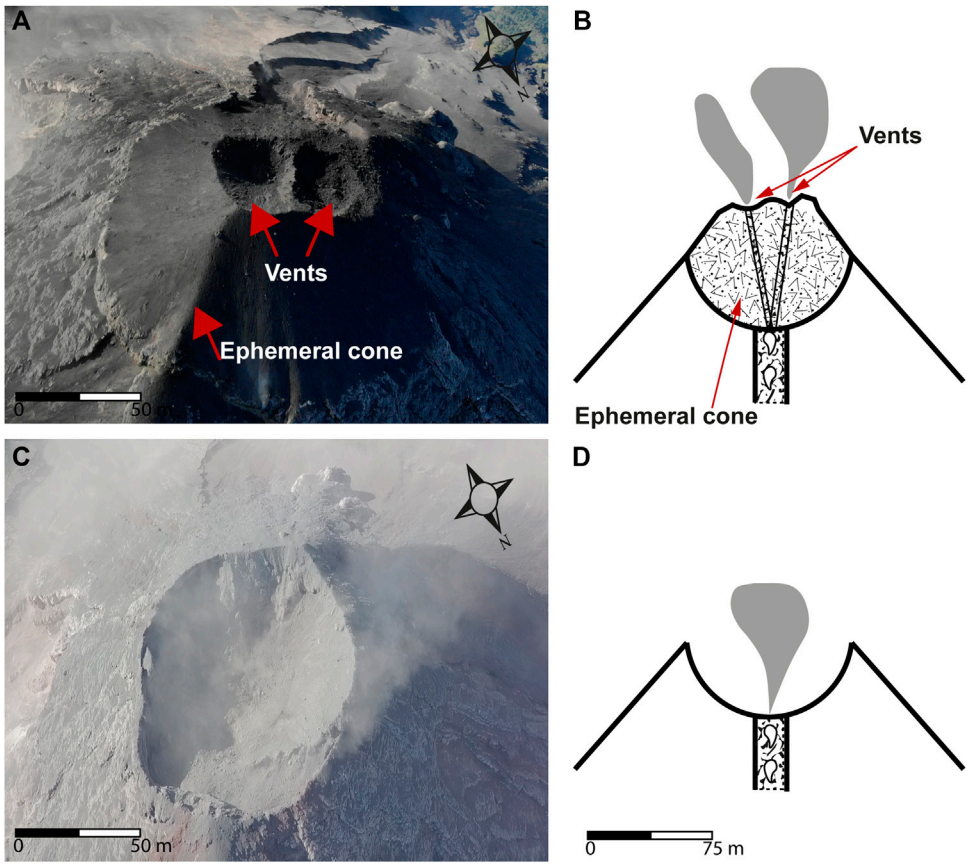

FIGURE 4 | (A) Aerial view from Volcan de Fuego's crater taken using Unmanned Aerial Vehicles (UAV). Photo taken by University of Liverpool on the January 29, 2020. Note the presence of an ephemeral cone that fills the crater and two active vents. This setting is similar to June 2018 as confirmed by M. Watson, personal communication in July 2018; **(B)** cartoon illustrating the ephemeral cone setting; **(C)** photo taken by University of Liverpool on the November 28, 2018. No ephemeral cone is visible and only one vent is active; **(D)** cartoon illustrating the empty cone setting.

moderate to strong explosions (10–15 per hour), some of them accompanied by audible noise heard at 20–25 km from the vent, and ash plumes rising up to 1.3 km above the summit during 21–27 November (Global Volcanism Program, 2018b). In the period between 26 November and December 3, 2018 we deployed a temporary network, consisting of six acoustic infrasound sensors (5 Chaparral M60-UHP and one IST-2018 differential microphone). The IST-2018 sensor has a sensitivity of 19.8 mV/Pa, corner frequency of 7 mHz, and full-scale range of +/−230 Pa (Grangeon and Lesage, 2019). Data were sampled at 100 Hz with 24-bit resolution using DiGOS DATA-CUBE digitizer. The activity recorded consisted of discrete explosions with variable intensity and gas and ash content, interspersed with periods of persistent degassing lasting up to 2 h (**Supplementary Material SM1**). Unmanned Aerial Vehicle (UAV) footage recorded during this deployment shows an empty crater with only one clearly visible active vent (**Figure 4**).

3.3. Permanent Network

A permanent seismo-acoustic network was installed at Volcán de Fuego after the June 2018 eruption. The network consists of three 6-channel seismo-acoustic arrays (one 3-component broadband seismometer and three infrasound microphones), three 3-channel broadband seismic stations, and one 6-channel infrasound array deployed at distances between 3 and 15 km from the vent. All stations were installed between July 30, 2018 and April 2, 2019. Data are telemetered in real-time to the INSIVUMEH headquarters in Guatemala City. The most notable activity recorded since the first deployment in July 2018 was one paroxysm on 17–18 November 2018 — leading to the evacuation of 3,925 people from nearby villages — and vigorous lava effusion during March-April 2019.

4. INFRASOUND SIGNALS AT VOLCÁN DE FUEGO

Locally recorded (<10 km from source) volcanic infrasound at Volcán de Fuego ranges from impulsive transients to tremor-like sustained waveforms, with a number of other intermediate types (McNutt et al., 2015). The impulsive transients, characterized by short duration (5–15 s) and sharp onsets (**Figures 4A–C**), are commonly generated by short-duration explosive sources. These signals feature a rapid compression followed by a rarefaction

phase with a nearly symmetrical shape (e.g., 5 d, g, and **Supplementary Material SM2**), which is indicative of a flow rate source time function symmetrically distributed in time around a peak value (Brogi et al., 2018; De Angelis et al., 2019). In other instances waveforms are non-symmetrical, exhibiting rapid compression onsets followed by rarefaction phases with reduced amplitudes (e.g., 5 a); waveform asymmetry may represent either a non-symmetrical flow rate source function, or reflect a shock-type source mechanism similar to blast waves produced by chemical explosions (Marchetti et al., 2013; Brogi et al., 2018). Typically, blast waves can be separated from other explosion mechanisms due to their characteristic appearance and much larger peak amplitudes, of the order of several hundreds of Pa at few hundred meters from the source. Diversity in the characteristics of infrasound signals reflects variety in their source mechanisms, and may provide additional clues on whether explosions are gas- or tephra-rich (Matoza et al., 2014). Observational evidence from our campaigns and continuous visual monitoring of activity at Volcán de Fuego by INSIVUMEH suggests that waveforms featuring impulsive onsets followed by several additional pulses, or by a prolonged coda (e.g., 5 g), are frequently associated to the generation of tephra-rich plumes. Generally, longer duration signals reflect sustained source caused either by multiple short pulses or longer duration pulses. Waveform and frequency content depend also on the ash content in the plume, turbulence in the plume and other factors still to be studied. At the other end of the spectrum of infrasound signals we find non-impulsive, low-amplitude, and long-duration waveforms known as acoustic tremor. These events — considered one of the best precursors of an eruption (Fee and Garcés, 2007) — are typical at many other volcanoes and result from processes within the magmatic fluid (Fee et al., 2010a). Acoustic tremor can last from minutes to days and is frequently recorded along with its seismic counterpart. It is classified into different categories according to its spectral characteristics, including broadband, and harmonic tremor (Lyons et al., 2013). In this section, we describe the near-field acoustic fingerprint of volcanic activity at Volcán de Fuego during 2018 and draw a comparison with previous observations (Lyons, 2011), which shows similar events (**Supplementary Material SM3**).

4.1. Strombolian Explosive Activity

Strombolian activity generally occurs in silica-poor, low-viscosity magmas (e.g., Parfitt and Wilson, 1995; Taddeucci et al., 2015), similar to the composition at Volcán de Fuego (Chesner and Rose, 1984; Berlo et al., 2012). It commonly manifests as discrete bursts associated with the rise of gas slugs through the magmatic column, producing variable amounts of tephra and pyroclasts (Taddeucci et al., 2015). The overpressures during such explosions at Volcán de Fuego suggest a more complex mechanism than a simple slug burst through consistently low viscosity magma. In fact, previous works by Lyons (2011) and Nadeau et al. (2011) describe the presence of a viscous magma plug at the top of the magma column, able to retain overpressure prior to brittle failure, which is responsible for explosive activity. This model acknowledges the role of a crystal mush or plug at the top of the column proposed by other authors (Suckale et al., 2016; Barth et al., 2019; Girona et al., 2019), highlighting its importance in defining explosion dynamics. At Volcán de Fuego, these discrete explosions together with longer duration signals associated to non-explosive activity (**Supplementary Material SM2 d**), represent the dominant background through the past decade. Explosive activity generally accompanies periods of active lava effusion and precedes the nearly-periodic occurrence of violent paroxysms.

Acoustic records of explosive activity at Volcán de Fuego exhibit differences in amplitude, frequency content, and coda duration. According to these observations infrasound waveforms can be grouped into three main categories: i) Gas-rich explosions; ii) Tephra-rich explosions and iii) Long duration events. **Figure 5** shows infrasound waveforms, spectra, and spectrograms of all three types of events. Note that despite the common impulsive symmetric onset for both gas- and tephra-rich explosions, these types of events clearly differ in coda length, signal amplitude, and spectral content; gas-rich events generally deliver acoustic energy at higher frequencies, and feature more energetic signals and shorter duration coda.

Gas-Rich Explosions

Gas-rich explosions are short-duration (order of 2–3 s) acoustic transients with variable peak amplitudes (**Figure 5B** and **Supplementary Material SM2 b**; Johnson, 2003; Fee and Matoza, 2013). Examples of these type of events have been reported at multiple volcanoes worldwide including Stromboli (Ripepe and Marchetti, 2002), Etna (Cannata et al., 2009b; Marchetti et al., 2009), and Yasur (Marchetti et al., 2013). Visual observations, conducted in the field by the authors during the November 2018 campaign, confirmed that gas-rich explosions produced light gray plumes formed from a single initial pulse rising between 500–1,500 m above the vent. Some gas-rich bursts are driven by sufficient overpressure to generate shock waves; the associated waveforms are characterized by a sharp compressive onset followed by a longer-lasting smaller-amplitude rarefaction, well-described by the Friedlander equation (Marchetti et al., 2013). Shock waves at Volcán de Fuego are dominated by energy peaking in the 0.8–2 Hz band (**Figures 5A,B** and **Supplementary Material SM2 a**).

Figure 6A shows a record section plot for an explosion recorded across the 2018 temporary infrasound network with a peak overpressure of 370 Pa at 1 km from the source, on 19 May at 04:19:05 (UTC Time). The Mach number for this explosion was estimated to be 1.3, using procedures described by Marchetti et al. (2013). A propagation speed of 442 m/s is consistent with the infrasound onset at the closest station to the vent — VF03, 1 km from source — and reflects non-linear propagation of a shock-wave. The propagation speed between the vent and VF03 was estimated using the explosion onset time calculated from data recorded at all other stations in the network. Infrasound propagates at 330 m/s across the network beyond VF03 reflecting the transition between the supersonic and sonic regimes at greater distances from the vent (**figure 6A**). The event registered at 5.2 km from the vent (station VF04) also displays the characteristic N-shape, which is expected for shock waves that have propagated far from their source (Marchetti et al., 2013).

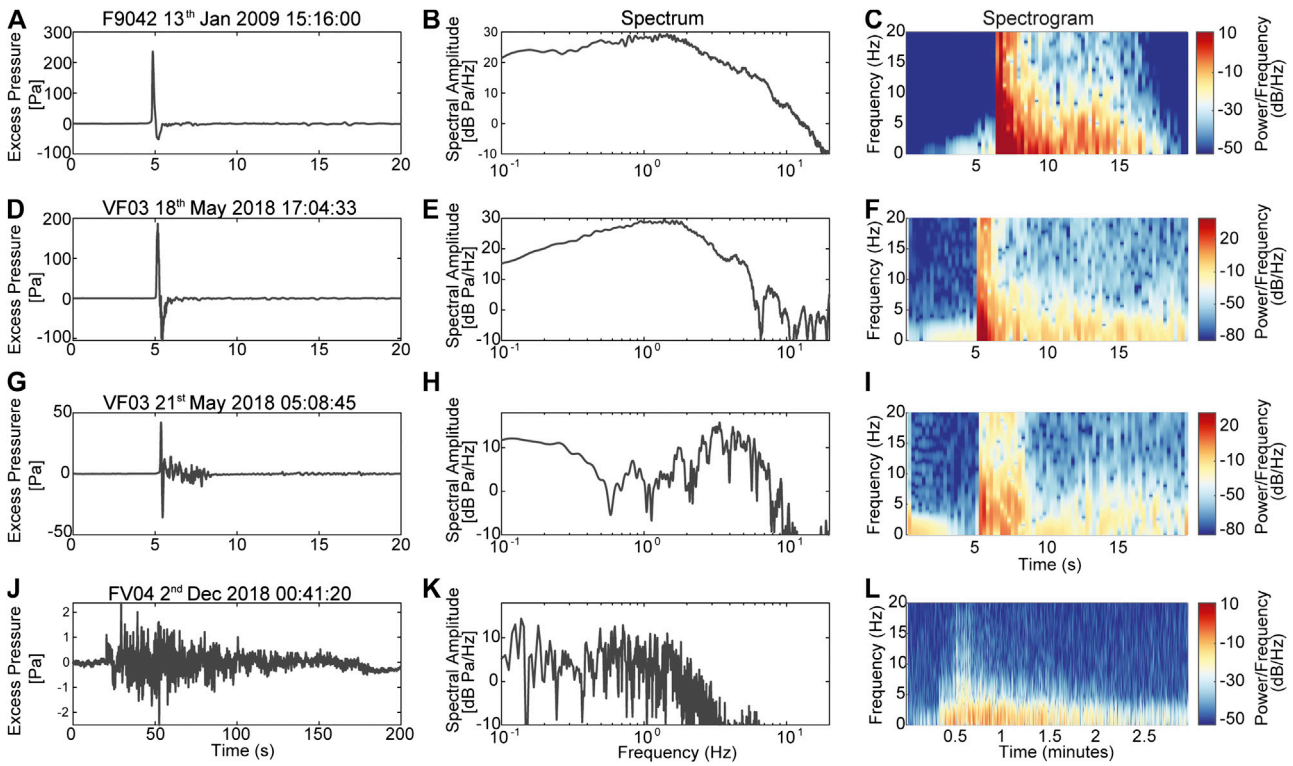

FIGURE 5 | Acoustic waveforms, spectra, and spectrograms of shock-wave **(A,B,C)**, gas-rich **(D,E,F)**, tephra-rich explosions **(G,H,I)**, and longer duration explosions **(J,K,L)**. Note differences in amplitude, duration, and spectral content between events.

Tephra-Rich Explosions

Tephra-rich explosions are recorded as symmetric transients with a longer (order of 10–15 s) and more complex coda (**Figure 5G**, and **Supplementary Material SM2 c**). Examples of these explosions have also been reported at Sakurajima, Japan (Matoza et al., 2014), Karymsky, Russia (Johnson and Malone, 2007; Lopez et al., 2013), and Tungurahua, Ecuador (Fee et al., 2010b), among other volcanoes. Tephra-rich explosions were dominant during November–December 2018, generally associated with lower recorded pressures. Field observations report dark plumes reaching 500–1,500 m above the vent.

Longer Duration Explosions

We also recorded explosive activity characterized by longer duration transients (order of 1–4 min) here referred to as longer duration explosions. These events are common at Volcán de Fuego, particularly during inter-paroxysm periods and effusive phases (**Figure 5J** and **Supplementary Material SM2 d**). Visual observations during these events describe turbulent plumes reaching 500–1,000 m above the vent and varying from light to dark gray depending on ash content (Field observations, **Supplementary Material SM 4**). The corresponding infrasound signature is characterized by low-amplitude emergent onsets followed by a long-lasting (1–4 min) low-frequency complex coda. Visual imagery (**Supplementary Material SM4**) of these events confirms the presence of multiple pulses at the vent, some more gas-rich (light gray plume) and some more tephra-rich (dark-grey plume) being responsible for the long low-frequency coda in the infrasound record. On the other hand, turbulence of the plume might also play a role in shaping these complex signals (**Figures 5J,K,L**, and **Supplementary Material SM2 d**).

4.2. Harmonic and non-Harmonic Acoustic Tremor

Seismic tremor (ST) is a sustained-amplitude signal frequently observed at active volcanoes, commonly associated with magma ascent, surface degassing, lava fountains, and other eruption activity (McNutt, 1994; Chouet and Matoza, 2013). Recently, owing to development of volcano infrasound, observations of its acoustic counterpart have become commonplace; seismo-acoustic tremor (SAT) refers to the case in which the volcano radiates energy into both the ground and the atmosphere (Lees et al., 2004; Lesage et al., 2006; Lyons et al., 2013; Matoza et al., 2014). As for ST, SAT presents sub-types where the spectrum is dominated by multiple uncorrelated frequency peaks (broadband, SAT-BT) or by regularly spaced peaks (harmonic, SAT-HT), with consequent implications for its source mechanisms. Recently, Girona et al. (2019) modeled different types of tremor based on a conduit topped with a permeable cap setting and different gas flow regimes. BT was associated with random gas supply, while HT with periodic gas supply both with relatively thin caps (≤100 m).

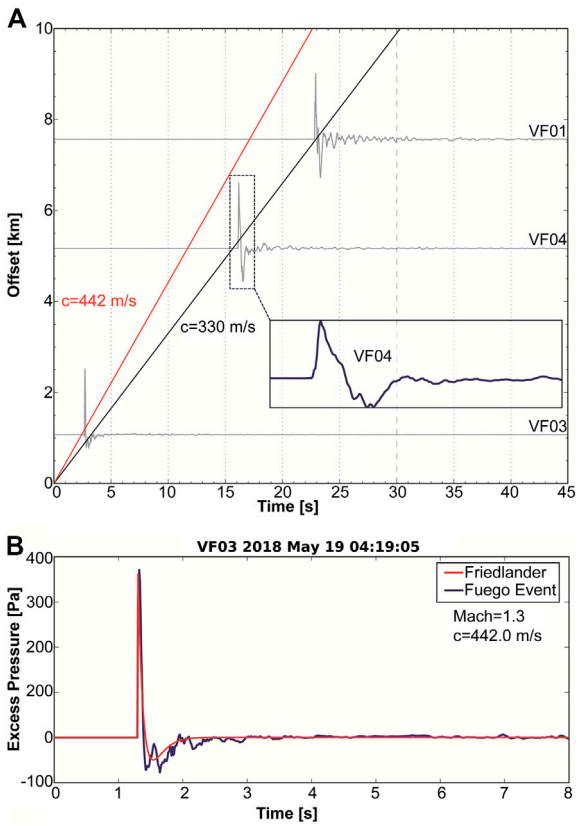

FIGURE 6 | Shock wave record at Volcán de Fuego: **(A)** record section plot showing a shock wave recorded at three stations across the network. A typical sound speed of 330 m/s (black line) does not fit the arrival time of the wave at the closest station, VF03. For a source located at the summit of Volcán de Fuego, the arrival time at VF03 is consistent with a sound speed of 442 m/s (red line). Also, note how the waveform recorded at station VF04 (5 km from the vent) displays the characteristic symmetric N-wave shape typical of blast waves at larger distance from the source; **(B)** comparison between theoretical Friedlander wave (red) and the shock wave signal recorded at station VF03 (black).

At Volcán de Fuego we recorded SAT, previously described by Lyons et al. (2013), with both broadband and harmonic signatures in May 2018. SAT was particularly intense starting on May 21, 2018, accompanying visible changes in eruptive activity, that shifted from discrete Strombolian explosions to sustained ash and gas emissions (**Figures 7,10**). In addition, we recorded characteristic form of quasi-periodic harmonic tremor referred to as "chugging". Chugging is a tremor-like signal that appears as a sequence of repeating explosions in rapid succession (**Figures 7C,8**). SAT-BT at Volcán de Fuego delivers energy between 0.5–8 Hz similar to the events described by Brill et al. (2018) (**Figure 7A**). Tremor episodes last between 1 and 60 min and were recorded during both campaigns in May and November 2018, although particularly intense during the second half of May (starting on the 21st). According to McNutt et al. (2015), SAT-BT can typically be associated with more vigorous and continuous ash and gas emissions. SAT-HT appears with non-stationary fundamental frequency between 1.5 and 2 Hz and three to six clear overtones (**Figure 7B**). SAT-HT episodes present similar duration as the SAT-BT and were more energetic during the last days of May. Both types of events (SAT-BT and SAT-HT) were clearly recorded at the closest station (VF03, 1 km from the vent) and still visible at the furthest stations (VF01, 7 km from the vent).

Chugging

Chugging waveforms resemble an amplitude modulated convolution between a simple base wavelet and a sequence of spikes, which would produce a quasi-harmonic spectrum (Lees and Ruiz, 2008). Examples of such signals have been reported in the past from Karymsky (Russia, Lopez et al., 2013)), Sangay (Ecuador, Johnson and Lees, 2000), Arenal (Costa Rica, Garcés and McNutt, 1997), Semeru (Indonesia, Schlindwein et al., 1995), Sabancaya (Peru, Ilanko et al., 2019) and Mt Etna (Italy, De Angelis et al., 2020), where chugging waveforms were associated with both pulsating degassing and vigorous repetitive Strombolian activity. In the literature, chugging associated with degassing explosions has been interpreted as resulting from the presence of a viscous plug at the vent acting as a valve over a pressurized system of volatiles and magma. The opening and closing of such a valve allows release of gas as a series of regular impulsive events (Lees and Bolton, 1998). At Volcán de Fuego, we recorded intense periods of acoustic chugging between 21 and May 23, 2018, associated with both strong pulsating degassing and frequent Strombolian explosions ejecting incandescent rock at heights of about 150–200 m above the vent (Visual observations by A. Lamur, May 2018). Episodes of chugging at Fuego last between 10 min and 1 h. In May 2018, we recorded peak infrasound amplitudes of about 3 Pa at 1 km from the vent (**Figures 7C,8** and **Supplementary Material SM2 g**). The appearance of this signal in May 2018 marked a clear transition in activity evolving from discrete Strombolian explosions to more sustained emissions and semi-continuous lava fountaining.

4.3. Lahars

Lahars (mud flows) are gravity-driven mixture of rock, debris, and water from a volcano (Vallance and Iverson, 2015). They are a frequent and major threat for population and infrastructure on the slopes of Volcán de Fuego. Lahars are triggered when rain interacts with pyroclastic deposits on the flanks of volcanoes (Thouret and Lavigne, 2000). These conditions are found at many volcanoes around the world and examples of the occurrence and, at times, catastrophic impacts of lahars are numerous: Nevado del Ruiz, Colombia (Lowe et al., 1986), Villarica, Chile (Johnson and Palma, 2015), Merapi, Indonesia (Lavigne et al., 2000b), Mayon, Philipines (Rodolfo and Arguden, 1991), among others.

At Volcán de Fuego, a regular rainy season combined with the significant volume of eruptive deposits on the flanks of the volcano, produce frequent lahars that can travel tens of kilometers down the steep-sided valleys (barrancas) affecting fluvial systems and disrupting communication and access to nearby villages (Naismith et al., 2019). The seismic and infrasonic signatures of lahars are characterized by complex waveforms lasting between tens of minutes up to several hours (Zobin, 2012; Buurman et al., 2013). The acoustic signal, at Fuego, is made up of large-amplitude, short-duration, pulses with energy

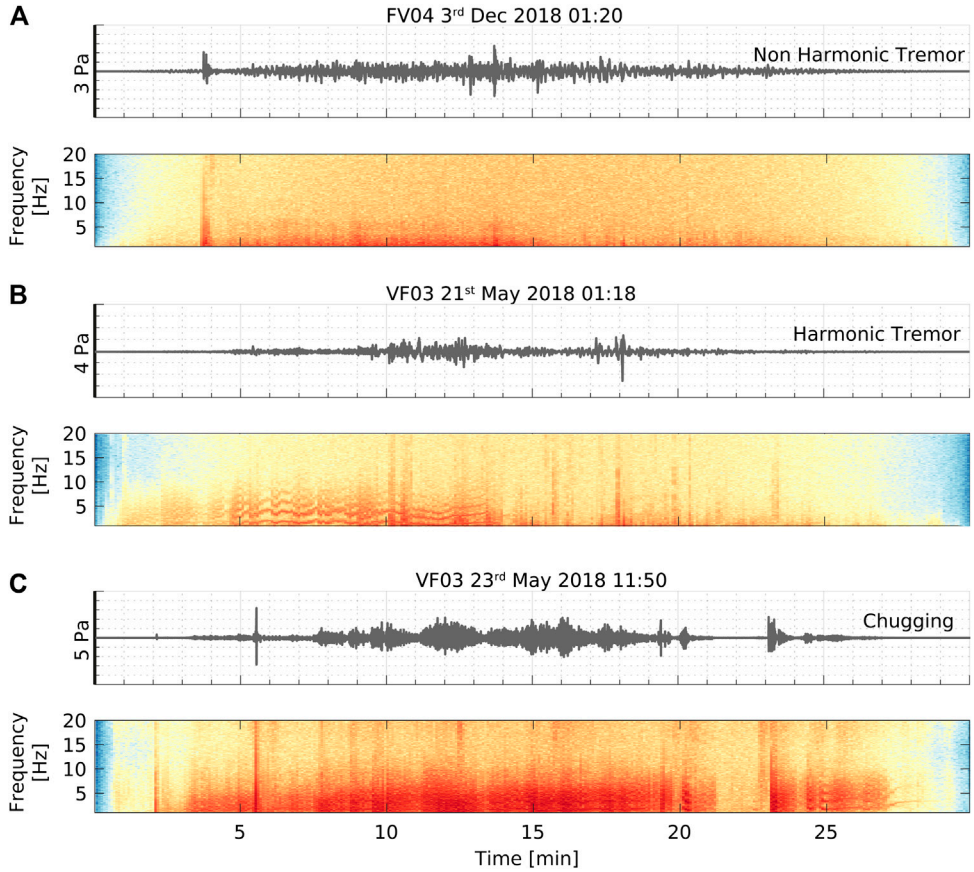

FIGURE 7 | Waveforms and spectrograms for **(A)** non-harmonic tremor. **(B)** Harmonic tremor, with fundamental frequency at 1.4 Hz and four to six overtones; and **(C)** chugging. Note the presence of discrete explosions in all three waveforms marked by impulsive signals high amplitude and high frequency.

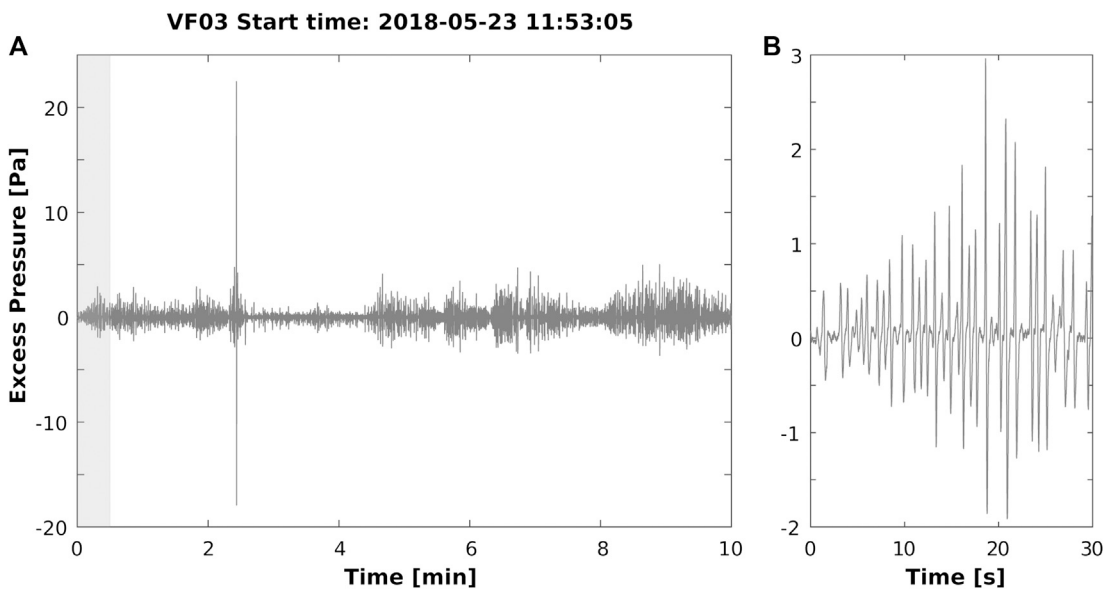

FIGURE 8 | (A) 10 min of chugging recorded on the May 23, 2018 at VF03 (1 km from the vent). Note the occurrence of an explosion at 2.5 min marked by a high amplitude peak. **(B)** 30 s detail of chugging (gray shaded area). Signal is high-pass filtered above 0.1 Hz.

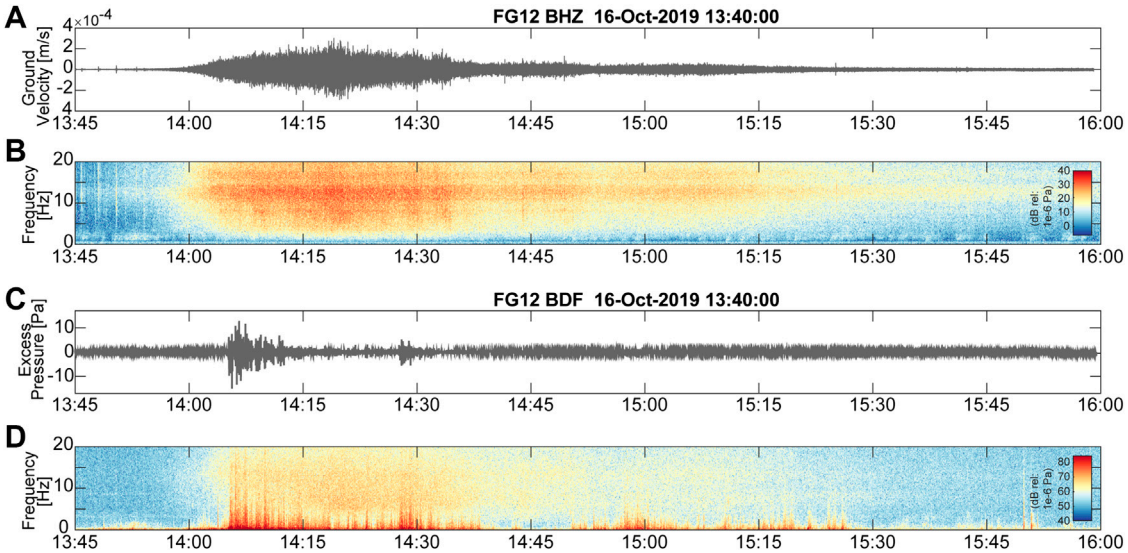

FIGURE 9 | Lahar recorded the October 16, 2019 at the seismo-acoustic site FG12. **(A)** Ground velocity and **(B)** its spectrogram; **(C)** infrasound trace and **(D)** its spectrogram.

dominantly in the 1–15 Hz frequency band. The seismic signal has a characteristic spindle-like appearance and delivers energy in the 5–20 Hz band (**Figures 9A,B**). The high-frequency pulses observed in lahar infrasound might be caused by lightnings and thunders evidencing the passage of thunderstorms. Other potential explanation for the high-frequency pulses is the impact of larger-size boulders on the channel bed as they are transported along by the bulk of the slurry of pyroclastic materials, debris and water (broadband part of the signal). At Volcán de Fuego, the recent deployment of the permanent seismo-acoustic network allows reliable detection of these events during the rainy season (**Figures 9A,B**).

Timely detection of lahar onset is key to mitigating their hazard. The most common monitoring strategies range from human-observers (Tungurahua, Ecuador), to webcams (Sakurajima, Japan), and seismic monitoring (Merapi, Indonesia, Lavigne et al., 2000a; Hadley and LaHusen, 1995). At Volcán de Fuego, lahars represent a major threat for local communities and infrastructure, damaging farmlands and causing severe traffic disruptions, potentially isolating communities. Recently, many efforts have focused on monitoring and tracking their occurrence using seismo-acoustic arrays, which has proven a powerful tool for detecting, characterizing, and tracking sustained lahar activity.

5. DISCUSSION

5.1. Infrasound Signals and Monitoring

In this study we have presented the most common infrasound signals recorded at Volcán de Fuego. Discrete events range from pure gas-rich to tephra-rich explosions, with several intermediate types. Infrasound amplitudes range from several hundreds of Pa (measured at about 1 km from the vent) for gas-rich explosions that generate shock waves, to tens of Pa for tephra-rich events (**Figure 5**). These types of signals typically coexist during periods between paroxysms. We also detect previously reported longer duration explosion with duration up to few minutes and smaller amplitudes **Figure 5**. We recorded a notable shift in eruptive activity from discrete and energetic gas-rich explosions to Strombolian-type explosions, then to sustained ash and gas emissions accompanied by quasi-continuous acoustic tremor on 21–23 May (**Figure 10**). This change in activity is translated to infrasound data as a marked increase in the overall amplitude and energy of the signal as illustrated by RSAM (Real-time seismic amplitude measurement) and spectrogram methods (**Figures 3,10**). A manually produced catalog with daily explosion counts and SAT-BT, SAT-HT, and chugging events and durations is provided for both experiments (**Supplementary Tables S1, S2**). We have observed two distinct vent configurations during the periods when these signals are recorded: a crater filled with lava forming an ephemeral cone with two or more active vents (**Figures 4A,B**), and an empty summit crater with explosions originating from a single vent (**Figures 4C,D**). It is clear, from observations reported in previous studies, that the presence of an ephemeral cone within the summit crater at Volcán de Fuego is mostly cyclical (Naismith et al., 2019). Conduit bifurcation during periods when an ephemeral cone is present has been associated with multiple vents within the crater area: a central vent predominantly characterized by Strombolian explosive activity, and a secondary one (or more) typically located on the flank of the ephemeral cone, associated with near-continuous degassing (Nadeau et al., 2011). Waite et al. (2013) observed and characterized different VLP events associated with sources linked to activity from both central and flank vents, remarking their importance in the explosions signature. Conduit

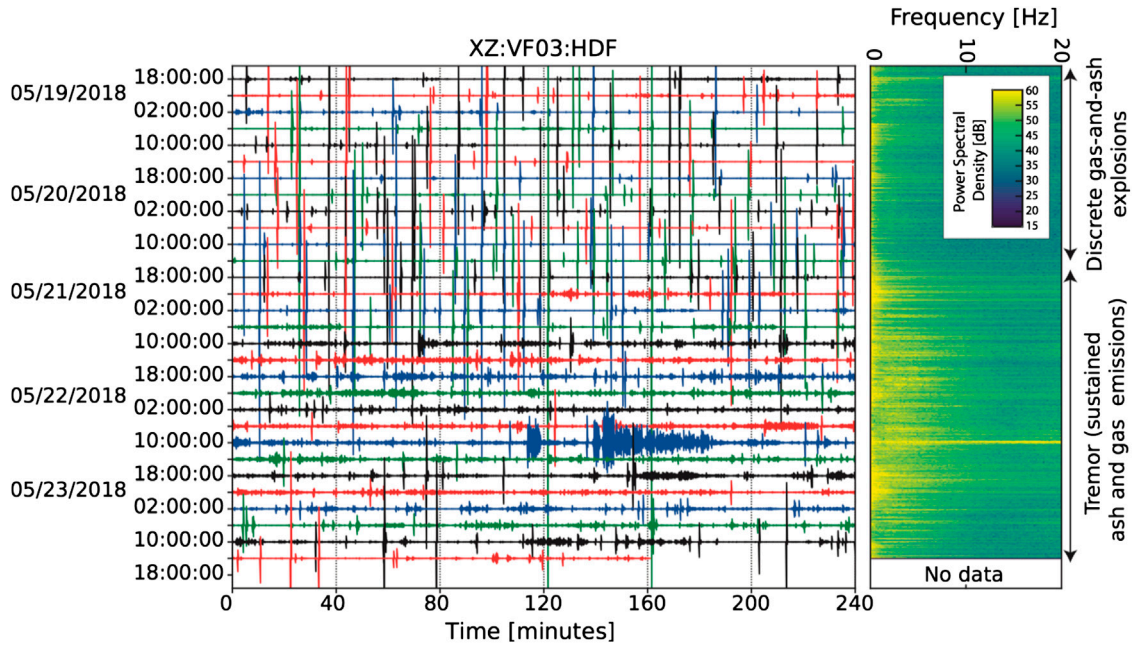

FIGURE 10 | Helicorder plot and spectrogram of station VF03 (1 km from vent) during the temporary deployment of 18–23 May 2018. Note the change in activity starting on 21 May.

bifurcation is particularly clear when an ephemeral cone is present within the summit crater (**Figures 4A,B**). In contrast, during periods when the crater is empty, a secondary vent is either not visible or less active (**Figures 4C,D**). From visual observations, we favor the presence of multiple vents as shallow features related to the presence of ephemeral unstable cones, where new sets of shallow fractures can be easily formed (Nadeau et al., 2011). The ephemeral cone might also play an important role in controlling the gas/ash ratio in the plumes; absence of the cone appears to favor gas-rich explosions with some ballistics, while its presence seems to be linked to larger quantities of ash in the plume (Patrick et al., 2007, **Figure 8**).

Unlike past observations, during our study period characterized by the presence two or more active vents, ash-, and gas-rich explosions occurred from all vents rather than preferentially at a given location (**Figure 4**). We suggest a model of conduit topped with a permeable plug and explosions linked to slug burst (Spina et al., 2019) underneath or within this viscous plug. Within the framework of this model explosion occurrence and intensity are controlled by the permeability of the upper conduit and ephemeral cone, and gas overpressure within the shallow conduit (Suckale et al., 2016; Barth et al., 2019). The characteristics of acoustic waveforms are controlled by the interaction of variable gas flow rates with the permeable plug. A numerical model recently presented by Girona et al. (2019) accounts for the presence of a viscous plug in the upper portions of the conduit and can accommodate all acoustics signals described in this manuscript. Similar models for explosion mechanisms have recently been proposed at Stromboli (Suckale et al., 2016; Barth et al., 2019) and further tested with analogue and numerical modeling (Oppenheimer et al., 2019), and possibly through direct gas measurements (Pering et al., 2020).

5.2. Paroxysmal Activity

Paroxysms at Volcán de Fuego, similarly to other volcanoes, are eruptive episodes of rapid increase in the strength and occurrence of activity. During paroxysms, within the span of few hours, explosions rapidly increase in intensity and rates of occurrence, transitioning to semi-continuous explosive activity and eventually to sustained emission of pyroclastic materials from the vent. Several models have been proposed to explain the mechanisms involved in Volcán de Fuego's paroxysmal activity. Lyons et al. (2010), following two years of continuous observations at Volcán de Fuego (2005–2007), suggested two alternative models for explaining paroxysms: i) the collapsing foam model, originally proposed by Jaupart and Vergniolle (1988), where the accumulation and release of gas from an unstable foam layer are responsible for both effusive and explosive activity; and ii) rise-speed dependent model, introduced by Parfitt and Wilson (1995), where paroxysms are caused by higher rise-speeds of magma that prevent bubble coalescence and speed up fragmentation. In this latter model, lower rise-speeds would favor bubble coalescence into slugs, responsible for Strombolian activity. Both models can accommodate the observed cycles of lava effusion and mild strombolian explosions followed by paroxysmal eruptions and a final phase of discrete degassing explosions with no effusion. Building upon those models, rheological stiffening of basaltic and andesitic magmas in the upper portion of the conduit leads to a

plugged vent, below which gas accumulates before its periodic released (Johnson and Lees, 2000; Lyons and Waite, 2011). Moreover, the role of a permeable plug in generating common volcanic signals has been extensively investigated (Suckale et al., 2016; Barth et al., 2019; Girona et al., 2019).

A recent conceptual model for the trigger mechanism of paroxysms at Volcán de Fuego is introduced by Naismith et al. (2019), who supports the gravity-driven shedding of material from an ephemeral summit cone. According to these authors, an ephemeral cone is built up by fountaining ejected material and when the crater overspills, lava effusion begins. If the lava flow rate exceeds a certain threshold, the ephemeral cone might be destroyed, causing a depressurization of the system and thus trigger paroxysmal activity. Naismith et al. (2019) base their model on the presence of an ephemeral cone, which has been described in many eruptions at Volcán de Fuego (e.g., February 2017, October 2018) and acknowledge that it cannot explain episodes with no ephemeral cone (e.g., January 2016).

5.3. Long-Term Monitoring

Unfortunately, detailed long-term analyses of eruptive activity at Volcán de Fuego is limited by present data availability. Additional data would be required, for instance, to identify recurring patterns in the lead-up to paroxysms. Only one comparatively minor paroxysm has occurred since extensive and permanent geophysical monitoring of Volcán de Fuego was established in the summer of 2018. Geophysical data pre-2018 are limited to the temporary deployments mentioned in this manuscript. Available data from past deployments demonstrate consistent geophysical signatures for explosions at Volcan de Fuego over the past 10 years pointing to a rather stable and cyclic open-vent system. This evidence leaves us confident that, in the future, escalating activity leading to paroxysms could be detected by the newly established geophysical network. Data analyses from seismic and infrasound arrays have potential to underpin the development of alarm systems for Fuego, similar to present practice at other volcanoes such as Mt. Etna, Italy, (Ripepe et al., 2018; De Angelis et al., 2020), Alaskan volcanoes, USA, (Coombs et al., 2018; Power et al., 2020), and Soufrière Hills Volcano, Montserrat Island, (Thompson et al., 2020).

6. CONCLUSIVE REMARKS

We have presented and discussed the most common types of infrasound signals recorded at Volcán de Fuego during 2018-present. These range from discrete activity (including shock waves, gas-rich, and tephra-rich explosions) to more sustained emissions (seismo-acoustic broadband and harmonic tremor and chugging, and indirect volcanic processes as lahars).

We have reviewed previous acoustic studies at Volcán de Fuego. We have linked state-of-the-art numerical modeling available in literature to our gathered acoustic data. Data shown in this paper agree with recent models invoking the presence of a permeable plug on top of the magma column as a main feature controlling the infrasound signature of Volcán de Fuego.

We envision this work will serve as a baseline to interpret infrasound data recorded at Volcán de Fuego. Although infrasound is a valuable technique for volcano monitoring with robust workflows, we emphasize that effective volcano monitoring to support decision making and risk mitigation during eruptive crizes must include input from other disciplines such as seismology, gas geochemistry, and thermal remote sensing.

DATA AVAILABILITY STATEMENT

The datasets presented in this study can be found in online repositories. The names of the repository/repositories and accession number(s) can be found below: http://ds.iris.edu/mda/3E/?starttime=2018-01-01T00:00:00&endtime=2018-12-31T23:59:59.

AUTHOR CONTRIBUTIONS

All authors participated in the field experiments and contributed to the discussion of the manuscript. SA produced **Figures 2, 3**; AD produced all other figures with input from all co-authors; AD wrote the manuscript with input from all co-authors.

FUNDING

AD and SA are funded by NERC grant number NE/P00105X/1. TI is Commonwealth Rutherford Fellow, supported by the United Kingdom government.

ACKNOWLEDGMENTS

Thanks to INSIVUMEH (in particular Robin, Gustavo, Raul, and the INSIVUMEH technical team). Special thanks to AP for his support during fieldwork.

SUPPLEMENTARY MATERIAL

The Supplementary Material for this article can be found online at: https://www.frontiersin.org/articles/10.3389/feart.2020.549774/full#supplementary-material

REFERENCES

Barth, A., Edmonds, M., and Woods, A. (2019). Valve-like dynamics of gas flow through a packed crystal mush and cyclic strombolian explosions. *Sci. Rep.* 9, 821. doi:10.1038/s41598-018-37013-8

Berlo, K., Stix, J., Roggensack, K., and Ghaleb, B. (2012). A tale of two magmas, Fuego, Guatemala. *Bull. Volcanol.* 74, 377–390. doi:10.1007/s00445-011-0530-8

Brill, K. A., Waite, G. P., and Chigna, G. (2018). Foundations for forecasting: defining baseline seismicity at Fuego volcano, Guatemala. *Front. Earth Sci.* 6, 87. doi:10.3389/feart.2018.00087

Brogi, F., Ripepe, M., and Bonadonna, C. (2018). Lattice Boltzmann modeling to explain volcano acoustic source. *Sci. Rep.* 8, 9537. doi:10.1038/s41598-018-27387-0

Buurman, H., West, M. E., and Thompson, G. (2013). The seismicity of the 2009 Redoubt eruption. *J. Volcanol. Geotherm. Res.* 259, 16–30. doi:10.1016/J.JVOLGEORES.2012.04.024

Cannata, A., Hellweg, M., Di Grazia, G., Ford, S., Alparone, S., Gresta, S., et al. (2009a). Long period and very long period events at Mt. Etna volcano: characteristics, variability and causality, and implications for their sources. *J. Volcanol. Geotherm. Res.* 187, 227–249. doi:10.1016/j.jvolgeores.2009.09.007

Cannata, A., Montalto, P., Privitera, E., and Russo, G. (2009b). Characterization and location of infrasonic sources in active volcanoes: Mount Etna, September-November 2007. *J. Geophys. Res.: Solid Earth* 114, 1–15. doi:10.1029/2008JB006007

Chesner, C. A., and Rose, W. I. (1984). Geochemistry and evolution of the Fuego Volcanic complex, Guatemala. *J. Volcanol. Geotherm. Res.* 21, 25–44, doi:10.1016/0377-0273(84)90014-3

Chouet, B. A., and Matoza, R. S. (2013). A multi-decadal view of seismic methods for detecting precursors of magma movement and eruption. *J. Volcanol. Geotherm. Res.* 252, 108–175. doi:10.1016/j.jvolgeores.2012.11.013

Coombs, M. L., Wech, A. G., Haney, M. M., Lyons, J. J., Schneider, D. J., Schwaiger, H. F., et al. (2018). Short-term forecasting and detection of explosions during the 2016–2017 eruption of Bogoslof Volcano, Alaska. *Front. Earth Sci.* 6, 122. doi:10.3389/feart.2018.00122

De Angelis, S., Diaz-Moreno, A., and Zuccarello, L. (2019). Recent developments and applications of acoustic infrasound to monitor volcanic emissions. *Remote Sens.* 11, 1302. doi:10.3390/rs11111302

De Angelis, S., Fee, D., Haney, M., and Schneider, D. (2012). Detecting hidden volcanic explosions from Mt. Cleveland Volcano, Alaska with infrasound and ground-coupled airwaves. *Geophys. Res. Lett.* 39, L21312. doi:10.1029/2012GL053635

De Angelis, S., Haney, M., Lyons, J., Wech, A., Fee, D., Diaz-Moreno, A., et al. (2020). A simple framework to track the evolution of volcanic activity with infrasound arrays: examples from Mt. Etna, Italy. *Frontiers in Volcanology* (under rev). 8, 169. Available at: https://www.frontiersin.org/article/10.3389/feart.2020.00169. doi:10.3389/feart.2020.00169. ISSN: 2296-6463.

Deger, E. (1932). Der Ausbruch des Vulkans Fuego in Guatemala am 21 Januar 1932 und die chemische Zusammensetzung seiner Auswurfsmaterialien. *Chemie Der Erde* 7, 291–297.

Fee, D., and Garcés, M. (2007). Infrasonic tremor in the diffraction zone. *Geophys. Res. Lett.* 34, 1–5. doi:10.1029/2007GL030616

Fee, D., and Matoza, R. (2013). An overview of volcano infrasound: From Hawaiian to Plinian, local to global. *J. Volcanol. Geotherm. Res.* 249, 123–139. doi:10.1016/j.jvolgeores.2012.09.002

Fee, D., Garcés, M., Patrick, M., Chouet, B., Dawson, P., and Swanson, D. (2010a). Infrasonic harmonic tremor and degassing bursts from Halema'uma'u Crater, Kilauea Volcano, Hawaii. *J. Geophys. Res.: Solid Earth* 115, 1–15. doi:10.1029/2010JB007642

Fee, D., Steffke, A., and Garces, M. (2010b). Characterization of the 2008 Kasatochi and Okmok eruptions using remote infrasound arrays. *J. Geophys. Res.* 115, D00L10. doi:10.1029/2009JD013621

Ferrés, D. (2019). *Informe Técnico: Volcán de Fuego*. Mexico: Universidad Nacional Autónoma de México, 1–170.

Garcés, M. A., and McNutt, S. R. (1997). Theory of the airborne sound field generated in a resonant magma conduit. *J. Volcanol. Geotherm. Res.* 78, 155–178. doi:10.1016/S0377-0273(97)00018-8

Garcés, M., Fee, D., and Matoza, R. (2013). "Volcano Acoustics," in *Modeling volcanic processes: the physics and mathematics of volcanism*. Cambridge: Cambridge University Press.

Garcés, M., Fee, D., Steffke, A., McCormack, D., Servranckx, R., Bass, H., et al. (2008). Capturing the acoustic fingerprint of stratospheric ash injection. *Eos, Trans. AGU* 89, 377–378. doi:10.1029/2008EO400001

Girona, T., Caudron, C., and Huber, C. (2019). Origin of shallow volcanic tremor: the dynamics of gas pockets trapped beneath thin permeable media. *J. Geophys. Res.: Solid Earth* 124, 4831–4861. doi:10.1029/2019JB017482

Global Volcanism Program (2018a). Report on Fuego (Guatemala), 16 May-22 May 2018. Editor S. K. Sennert, Weekly Volcanic Activity Report, Smithsonian Institution and US Geological Survey

Global Volcanism Program (2018b). Report on Fuego (Guatemala), 21 November–27 November 2018. Editor S K Sennert, Weekly Volcanic Activity Report, Smithsonian Institution and US Geological Survey.

Global Volcanism Program (2018c). Report on Fuego (Guatemala), 30 May-5 June 2018. Editor S K Sennert, Weekly Volcanic Activity Report, Smithsonian Institution and US Geological Survey.

Grangeon, J., and Lesage, P. (2019). A robust, low-cost and well-calibrated infrasound sensor for volcano monitoring. *J. Volcanol. Geotherm. Res.* 387, 106668. doi:10.1016/J.JVOLGEORES.2019.106668

Hadley, K., and LaHusen, R. (1995). Technical manual for the experimental acoustic flow monitor (US Geological Survey).

Iezzi, A. M., Fee, D., Kim, K., Jolly, A., and Matoza, R. S. (2019). 3-D acoustic multipole waveform inversion at Yasur volcano, Vanuatu. *J. Geophys. Res.: Solid Earth* 124, 8679–8703. doi:10.1029/2018JB017073

Ilanko, T., Pering, T., Wilkes, T., Apaza Choquehuayta, F., Kern, C., Díaz Moreno, A., et al. (2019). Degassing at Sabancaya volcano measured by UV cameras and the NOVAC network. *Volcanica* 2, 239–252. doi:10.30909/vol.02.02.239252

Jaupart, C., and Vergniolle, S. (1988). Laboratory models of Hawaiian and Strombolian eruptions. *Nature* 331, 58–60. doi:10.1038/331058a0

Johnson, J. B. (2003). Generation and propagation of infrasonic airwaves from volcanic explosions. *J. Volcanol. Geotherm. Res.* 121, 1–14. doi:10.1016/S0377-0273(02)00408-0

Johnson, J. B., and Palma, J. L. (2015). Lahar infrasound associated with Volcán Villarrica's 3 March 2015 eruption. *Geophys. Res. Lett.* 42, 6324–6331. doi:10.1002/2015GL065024

Johnson, J. B., and Ripepe, M. (2011). Volcano infrasound: a review. *J. Volcanol. Geotherm. Res.* 206, 61–69. doi:10.1016/j.jvolgeores.2011.06.006

Johnson, J., and Lees, J. (2000). Plugs and chugs□seismic and acoustic observations of degassing explosions at Karymsky, Russia and Sangay, Ecuador. *J. Volcanol. Geotherm. Res.* 101, 67–82. doi:10.1016/S0377-0273(00)00164-5

Johnson, J., and Malone, S. (2007). Ground-coupled acoustic airwaves from Mount St. Helens provide constraints on the May 18, 1980 eruption. *Earth Planet. Sci. Lett.* 1-2, 16–31. doi:10.1016/j.epsl.2007.03.001

Kamo, K., Ishihara, K., and Tahira, M. (1994). "Infrasonic and seismic detection of explosive eruptions at Sakurajima volcano, Japan, and the PEGASAS-VE early-warning system. in Proceedings of the First International Symposium on Volcanic Ash and Aviation Safety. Editor T. C. Casadevall, Seattle, Washington, July 1991. (Washington: United States Government Printing Office) (U.S. Geol. Surv. Bull.), Vol. 2047, 357–365

Lavigne, F., Thouret, J., Voight, B., Young, K., LaHusen, R., Marso, J., et al. (2000a). Instrumental lahar monitoring at Merapi Volcano, Central Java, Indonesia. *J. Volcanol. Geotherm. Res.* 100, 457–478. doi:10.1016%2FS0377-0273(00)00151-7

Lavigne, F., Thouret, J., Voight, B., Suwa, H., and Sumaryono, A. (2000b). Lahars at Merapi volcano, Central Java: an overview. *J. Volcanol. Geotherm. Res.* 100, 423–456. doi:10.1016%2FS0377-0273(00)00150-5

Lees, J., and Bolton, E. (1998). Pressure cookers as volcano analogues. *EOS, Trans. Am. Geophys. Union* 79, 45.

Lees, J. M., Gordeev, E. I., and Ripepe, M. (2004). Explosions and periodic tremor at Karymsky volcano, Kamchatka, Russia. *Geophys. J. Int.* 158, 1151–1167. doi:10.1111/j.1365-246X.2004.02239.x

Lees, J. M., and Ruiz, M. (2008). Non-linear explosion tremor at Sangay, Volcano, Ecuador. *J. Volcanol. Geotherm. Res.* 176, 170–178. doi:10.1016/j.jvolgeores.2007.08.012

Lesage, P., Mora, M. M., Alvarado, G. E., Pacheco, J., and Métaxian, J. P. (2006). Complex behavior and source model of the tremor at Arenal volcano, Costa Rica. *J. Volcanol. Geotherm. Res.* 157, 49–59. doi:10.1016/j.jvolgeores.2006.03.047

Lopez, T., Fee, D., Prata, F., and Dehn, J. (2013). Characterization and interpretation of volcanic activity at Karymsky Volcano, Kamchatka, Russia, using observations of infrasound, volcanic emissions, and thermal imagery. *Geochem., Geophys., Geosys.* 14, 5106–5127. doi:10.1002/2013GC004817

Lowe, D. R., Williams, S. N., Leigh, H., Connort, C. B., Gemmell, J. B., and Stoiber, R. E. (1986). Lahars initiated by the 13 November 1985 eruption of Nevado del Ruiz, Colombia. *Nature* 324, 51–53. doi:10.1038/324051a0

Lyons, J. J. (2011). *Dynamics and kinematics of eruptive activity at Fuego volcano , Guatemala 2005 – 2009*. Michigan: Michigan Technological University.

Lyons, J. J., Ichihara, M., Kurokawa, A., and Lees, J. M. (2013). Switching between seismic and seismo-acoustic harmonic tremor simulated in the laboratory:

Insights into the role of open degassing channels and magma viscosity. *J. Geophys. Res.: Solid Earth* 118, 277–289. doi:10.1002/jgrb.50067

Lyons, J. J., Iezzi, A. M., Fee, D., Schwaiger, H. F., Wech, A. G., and Haney, M. M. (2020). Infrasound generated by the 2016–2017 shallow submarine eruption of Bogoslof volcano, Alaska. *Bull. Volcanol.* 82, 19. doi:10.1007/s00445-019-1355-0

Lyons, J. J., and Waite, G. P. (2011). Dynamics of explosive volcanism at Fuego volcano imaged with very long period seismicity. *J. Geophys. Res.* 116, B09303. doi:10.1029/2011JB008521

Lyons, J. J., Waite, G. P., Rose, W. I., and Chigna, G. (2010). Patterns in open vent, strombolian behavior at Fuego volcano, Guatemala, 2005-2007. *Bull. Volcanol.* 72, 1–15. doi:10.1007/s00445-009-0305-7

Lyons, J. J., Waite, G. P., Ichihara, M., and Lees, J. M. (2012). Tilt prior to explosions and the effect of topography on ultra-long-period seismic records at Fuego volcano, Guatemala. *Geophys. Res. Lett.* 39. doi:10.1029/2012GL051184

Marchetti, E., Ripepe, M., Campus, P., Le Pichon, A., Brachet, N., Blanc, E., et al. (2019). "Infrasound monitoring of volcanic eruptions and contribution of ARISE to the Volcanic Ash Advisory Centers," in *Infrasound monitoring for atmospheric studies*. New York, NY: Springer International Publishing, 1141–1162.

Marchetti, E., Ripepe, M., Delle Donne, D., Genco, R., Finizola, A., and Garaebiti, E. (2013). Blast waves from violent explosive activity at Yasur Volcano, Vanuatu. *Geophys. Res. Lett.* 40, 5838–5843. doi:10.1002/2013GL057900

Marchetti, E., Ripepe, M., Ulivieri, G., Caffo, S., and Privitera, E. (2009). Infrasonic evidences for branched conduit dynamics at Mt. Etna volcano, Italy. *Geophys. Res. Lett.* 36, L19308. doi:10.1029/2009GL040070

Martin, D. P., and Rose, W. I. (1981). Behavioral patterns of Fuego volcano, Guatemala. *J. Volcanol. Geotherm. Res.* 10, 67–81. doi:10.1016/0377-0273(81)90055-X

Matoza, R., Arciniega-Ceballos, A., Sanderson, R., Mendo-Perez, G., Rosado-Fuentes, A., and Chouet, B. (2019a). High-broadband seismoacoustic signature of Vulcanian explosions at Popocatépetl volcano, Mexico. *Geophys. Res. Lett.* 46, 148–157. doi:10.1029/2018GL080802

Matoza, R., Fee, D., Green, D., and Mialle, P. (2019b). "Volcano Infrasound and the International Monitoring System," in *Infrasound monitoring for atmospheric studies*. New York, NY: Springer International Publishing, 1023–1077.

Matoza, R. S., Fee, D., Green, D. N., Le Pichon, A., Vergoz, J., Haney, M. M., et al. (2018). Local, regional, and remote seismo-acoustic observations of the April 2015 VEI 4 eruption of Calbuco Volcano, Chile. *J. Geophys. Res.: Solid Earth* 123, 3814–3827. doi:10.1002/2017JB015182

Matoza, R. S., Fee, D., and Lopez, T. M. (2014). Acoustic characterization of explosion complexity at Sakurajima, Karymsky, and Tungurahua Volcanoes. *Seismol Res. Lett.* 85, 1187–1199. doi:10.1785/0220140110

McNutt, S. R., Thompson, G., Johnson, J., Angelis, S. D., and Fee, D. (2015). "Chapter 63 - seismic and infrasonic monitoring," in *The encyclopedia of volcanoes*. 2nd Edn. Editor H. Sigurdsson (Amsterdam: Academic Press), 1071–1099.

McNutt, S. (1994). Volcanic tremor from around the world: 1992 update. *Acta Vulcanol.* 5, 197–200.

Nadeau, P. A., Palma, J. L., and Waite, G. P. (2011). Linking volcanic tremor, degassing, and eruption dynamics via SO2 imaging. *Geophys. Res. Lett.* 38. doi:10.1029/2010GL045820

Naismith, A. K., Matthew Watson, I., Escobar-Wolf, R., Chigna, G., Thomas, H., Coppola, D., et al. (2019). Eruption frequency patterns through time for the current (1999–2018) activity cycle at Volcán de Fuego derived from remote sensing data: Evidence for an accelerating cycle of explosive paroxysms and potential implications of eruptive activity. *J. Volcanol. Geotherm. Res.* 371, 206–219. doi:10.1016/J.JVOLGEORES.2019.01.001

Nishida, K., and Ichihara, M. (2016). Real-time infrasonic monitoring of the eruption at a remote island volcano using seismoacoustic cross correlation. *Geophys. J. Int.* 204, 748–752. doi:10.1093/gji/ggv478

Oppenheimer, J., Capponi, A., Cashman, K. V., Lane, S. J., Rust, A. C., and James, M. R. (2019). Analogue experiments on the rise of large bubbles through a solids-rich suspension : A " weak plug " model for Strombolian eruptions. *Earth Planet. Sci. Lett.* 1, 115931. doi:10.1016/j.epsl.2019.115931

Pallister, J., and McNutt, S. R. (2015). Synthesis of volcano monitoring. *The Encyclopedia of Volcanoes*, 1151–1171. doi:10.1016/B978-0-12-385938-9.00066-3

Pardini, F., Queißer, M., Naismith, A., Watson, I., Clarisse, L., and Burton, M. (2019). Initial constraints on triggering mechanisms of the eruption of Fuego volcano (Guatemala) from 3 June 2018 using IASI satellite data. *J. Volcanol. Geoth. Res.* 376, 54–61. doi:10.1016/J.JVOLGEORES.2019.03.014

Parfitt, E. A., and Wilson, L. (1995). Explosive volcanic eruptions-IX. The transition between Hawaiian-style lava fountaining and Strombolian explosive activity. *Geophys. J. Int.* 121, 226–232. doi:10.1111/j.1365-246X.1995.tb03523.x

Patrick, M. R., Harris, A. J., Ripepe, M., Dehn, J., Rothery, D. A., and Calvari, S. (2007). Strombolian explosive styles and source conditions: Insights from thermal (FLIR) video. *Bull. Volcanol.* 69, 769–784. doi:10.1007/s00445-006-0107-0

Pering, T., Liu, E., Wood, K., Wilkes, T., Aiuppa, A., Tamburello, G., et al. (2020). Combined ground and aerial measurements resolve vent-specific gas fluxes from a multi-vent volcanic system. *Nat. Commun.* 11, 3038. doi:10.1038%2Fs41467-020-16862-w

Power, J. A., Haney, M. M., Botnick, S. M., Dixon, J. P., Fee, D., Kaufman, A. M., et al. (2020). Goals and development of the Alaska volcano observatory seismic network and application to forecasting and detecting volcanic eruptions. *Seismol Res. Lett.* 91, 647–659. doi:10.1785/0220190216

Ripepe, M., and Marchetti, E. (2002). Array tracking of infrasonic sources at Stromboli volcano. *Geophys. Res. Lett.* 29, 33-1–33-4. doi:10.1029/2002GL015452

Ripepe, M., Marchetti, E., Delle Donne, D., Genco, R., Innocenti, L., Lacanna, G., et al. (2018). Infrasonic early warning system for explosive eruptions. *J. Geophys. Res.: Solid Earth* 123, 9570–9585. doi:10.1029/2018JB015561

Ripepe, M., and Marchetti, E. (2019). "Infrasound monitoring of volcano-related hazards for civil protection," in *Infrasound monitoring for atmospheric studies*. New York, NY: Springer International Publishing, 1107–1140

Rodolfo, K., and Arguden, A. (1991). "Rain-lahar generation and sediment delivery systems at Mayon Volcano, Philippines," in *Sedimentation in volcanic settings*. Tulsa, Oklahoma: SEPM Special Publication, Vol. 45.

Roggensack, K. (2001). Unraveling the 1974 eruption of Fuego volcano (Guatemala) with small crystals and their young melt inclusions. *Geology* 29, 911. doi:10.1130/0091-7613(2001)029□0911:UTEOFV□2.0.CO;2

Rose, W. I., Anderson, A. T., Woodruff, L. G., and Bonis, S. B. (1978). The october 1974 basaltic tephra from Fuego volcano: Description and history of the magma body. *J. Volcanol. Geoth. Res.* 4, 3–53. doi:10.1016/0377-0273(78)90027-6

Schlindwein, V., Wassermann, J., and Scherbaum, F. (1995). Spectral analysis of harmonic tremor signals at Mt. Semeru Volcano, Indonesia. *Geophys. Res. Lett.* 22, 1685–1688. doi:10.1029/95GL01433

Sisson, T., and Layne, G. (1993). H2O in basalt and basaltic andesite glass inclusions from four subduction-related volcanoes. *EarthPlanet. Sci. Lett.* 117 (3–4), 619–635. doi:10.1016/0012-821X(93)90107-K

Spina, L., Cannata, A., Morgavi, D., and Perugini, D. (2019). Degassing behaviour at basaltic volcanoes: new insights from experimental investigations of different conduit geometry and magma viscosity. *Earth-Sci. Rev.* 192, 317–336. doi:10.1016/j.earscirev.2019.03.010

Suckale, J., Keller, T., Cashman, K. V., and Persson, P. O. (2016). Flow-to-fracture transition in a volcanic mush plug may govern normal eruptions at Stromboli. *Geophys. Res. Lett.* 43, 12071–12081. doi:10.1002/2016GL071501

Taddeucci, J., Edmonds, M., Houghton, B., James, M. R., and Vergniolle, S. (2015). "Hawaiian and Strombolian Eruptions," in *The encyclopedia of volcanoes*. New York, NY: Elsevier, 485–503

Thompson, G., Power, J. A., Braunmiller, J., Lockhart, A. B., Lynch, L., Mccausland, W., et al. (2020). Capturing, preserving, and digitizing legacy seismic data from the montserrat volcano observatory analog seismic network. *Seismol Res. Lett.* 91, 2127–2140. doi:10.1785/0220200012

Thouret, J., and Lavigne, F. (2000). "Lahars: occurrence, deposits and behaviour of volcano-hydrologic flows," in *Volcaniclastic rocks from magma to sediments*. Amsterdam, The Netherlands: Gordon and Breach Science Publishers, 151–174

Tilling, R. I. (2008). The critical role of volcano monitoring in risk reduction. *Adv. Geosci.* 14, 3–11. doi:10.5194%2Fadgeo-14-3-2008

Vallance, J. W., and Iverson, R. M. (2015). "Lahars and Their Deposits," in *The Encyclopedia of Volcanoes*. 2nd Edn. New York, NY: Elsevier

Waite, G. P., Nadeau, P. A., and Lyons, J. J. (2013). Variability in eruption style and associated very long period events at Fuego volcano, Guatemala. *J. Geophys. Res.: Solid Earth* 118, 1526–1533. doi:10.1002/jgrb.50075

Walker, K. T., Hedlin, M. A. H., de Groot-Hedlin, C., Vergoz, J., Le Pichon, A., and Drob, D. P. (2010). Source location of the 19 February 2008 Oregon bolide using seismic networks and infrasound arrays. *J. Geophys. Res.* 115, B12329. doi:10.1029/2010JB007863

Wolf-Escobar, R. (2013). *Volcanic processes and human exposure as elements to build a risk model for Volcan de Fuego, Guatemala*. Michigan: Michigan Technological University.

Yuan, A. T. E., Mcnutt, S. R., and Harlow, D. H. (1984). Seismicity and eruptive activity at Fuego Volcano, Guatemala: February 1975–January 1977. *J. Volcanol. Geotherm. Res.* 21, 277–296. doi:10.1016/0377-0273(84)90026-X

Zobin, V. M. (2012). "Acoustic Waves Generated by Volcanic Eruptions," *in Introduction to Volcanic Seismology*, 381–406. Elsevier, London, UK.

Conflict of Interest: The authors declare that the research was conducted in the absence of any commercial or financial relationships that could be construed as a potential conflict of interest.

Copyright © 2020 Díaz Moreno, Roca, Lamur, Munkli, Ilanko, Pering, Pineda and De Angelis. This is an open-access article distributed under the terms of the Creative Commons Attribution License (CC BY). The use, distribution or reproduction in other forums is permitted, provided the original author(s) and the copyright owner(s) are credited and that the original publication in this journal is cited, in accordance with accepted academic practice. No use, distribution or reproduction is permitted which does not comply with these terms.

frontiers in Earth Science

TECHNOLOGY AND CODE
published: 11 November 2020
doi: 10.3389/feart.2020.586955

RETREAT: A REal-Time TREmor Analysis Tool for Seismic Arrays, With Applications for Volcano Monitoring

Patrick J. Smith and Christopher J. Bean*

Geophysics Section, School of Cosmic Physics, Dublin Institute for Advanced Studies, Dublin, Ireland

Volcanic tremor is a sustained seismic signal associated with volcanic unrest and is often linked to movement of magmatic fluids in the subsurface. However, signals with similar spectral content can be generated by other surface processes. Hence, one of the best ways of distinguishing between different possible mechanisms is by tracking the location of its source, which is also important for mitigating volcanic risk. Due to its emergent nature, tremor cannot be located using travel-time based methods, therefore alternatives such as amplitude-based techniques or array analysis must be used. Dense, small-aperture arrays are particularly suited for analyzing volcanic tremor, yet costs associated with installation and maintenance have meant few long-term or permanent seismic arrays in use for routine monitoring. Given the potential for wider usage of arrays, this work presents a python-based software tool that uses array data and array processing techniques to analyze and locate volcanic tremor signals. RETREAT utilizes existing routines from the open-source ObsPy framework to carry out analysis of seismic array data in real-time and performs f-k (frequency-wavenumber) analysis, or Least-Squares beamforming, to calculate the backazimuth and slowness in overlapping time windows, which can help track the location of volcanic tremor sources. A graphical, or web-based, interface is used to configure a set of input parameters, before fetching chunks of waveform data and performing the array analysis. On each update the tool returns several plots, including timeseries of the backazimuth and slowness, a polar representation of the power and a map of the array with dominant backazimuth overlaid. The tool has been tested using real-time seismic data from the small-aperture SPITS array in Spitsbergen, as well as on data from an array deployed during the 2014 eruption of Bárðarbunga volcano, Iceland. Configuration files and waveform data for these examples are supplied with the distribution. RETREAT can also be used for infrasound and has been tested on infrasonic array data recorded at Mt. Etna, Italy. RETREAT is intended for use in real-time monitoring settings and it is hoped that it will facilitate greater use of arrays in tracking volcanic tremor sources in real-time, thereby enhancing monitoring capabilities.

Keywords: volcano seismology, software, volcanic tremor, seismic arrays, real-time monitoring, infrasound arrays

OPEN ACCESS

Edited by:
Luigi Passarelli,
King Abdullah University of Science and Technology, Saudi Arabia

Reviewed by:
Eisuke Fujita,
National Research Institute for Earth Science and Disaster Resilience (NIED), Japan
Matthew Haney,
Alaska Volcano Observatory (AVO), United States

****Correspondence:***
Patrick J. Smith
psmith@cp.dias.ie

Specialty section:
This article was submitted to Volcanology, a section of the journal Frontiers in Earth Science

Received: *24 July 2020*
Accepted: *16 October 2020*
Published: *11 November 2020*

Citation:
Smith PJ and Bean CJ (2020) RETREAT: A REal-Time TREmor Analysis Tool for Seismic Arrays, With Applications for Volcano Monitoring. Front. Earth Sci. 8:586955. doi: 10.3389/feart.2020.586955

INTRODUCTION

Volcanoes exhibit a very broad range of seismic source types (see e.g., Wassermann (2012)). Monitoring seismicity remains at the core of most volcano observatories (Sparks et al., 2012), and in a crisis, one of the key challenges for monitoring agencies is identifying the source type and tracking its location. This can be difficult to achieve with a sparse seismic network or when seismic signals have an emergent onset or lack of clear phase arrivals and in particular for continuous signals such as volcanic tremor.

Widely observed at many volcanoes (McNutt, 2011), volcanic tremor is a sustained seismic signal associated with eruptions and is often linked to movement of magmatic fluids in the subsurface (Julian, 1994; Hellweg, 2000; Jellinek and Bercovici, 2011). However, it can occur pre-, syn- and post-eruption and signals with similar spectral content can be generated by several other processes such as subglacial flooding (Eibl et al., 2020), lahars (Kumagai et al., 2009) other surficial mass flows (Allstadt et al., 2018) or even tectonic sources such as deeper slow slip earthquakes in subduction zones (Beroza and Ide, 2011). Hence one of the best ways of distinguishing between the processes underlying tremor generation is by determining and tracking its spatial location. As tremor cannot be located using classical travel-time methods, because of its emergent and sustained nature and lack of clear body-wave phases, its source must be determined using alternatives such as amplitude-based techniques (Battaglia et al., 2005; Taisne et al., 2011; Morioka et al., 2017) or, as in this tool, seismic array analysis.

A seismic *array* is a cluster of stations lying outside the seismic source area which can be used to point to the source location by measuring the back azimuth of the arriving signal (Rost and Thomas, 2002). An array can therefore be used to estimate lateral and vertical migration of tremor sources (Almendros et al., 1997; Di Lieto et al., 2007; Eibl et al., 2017a; Eibl et al., 2017b). Seismic arrays are frequently used for research, but not often as an operational tool for volcano monitoring in real-time, although arrays of infrasound sensors have been used for real-time alarms, e.g., at the Alaska Volcano Observatory (Coombs et al., 2018). Hence, this software aims to provide a convenient tool to facilitate processing and interpretation of both seismic, and potentially infrasonic, array data in real-time, to allow such data to be used more routinely for volcano monitoring.

This software has been developed within the framework of the EUROVOLC project, which aims to promote an integrated and harmonized European volcanological community (Vogfjörd et al., 2019). One of the major themes of the project focuses on understanding sub-surface processes, since early identification of magma moving toward the surface is very important for the mitigation of risk from volcanic hazards. Joint research activities within the project aim to develop volcano pre-eruptive detection schemes, in particular through the use of tremor as a real-time unrest indicator.

Given this context, we present RETREAT–a **RE**al-time **TRE**mor **A**nalysis **T**ool–that uses seismic array data and array processing techniques to help detect, quantify and locate volcanic tremor signals.

TABLE 1 | List of external python modules and packages required by RETREAT software and their purposes.

Package/Module	Purpose
Scipy	Mathematical functions and support for arrays and matrices
Numpy	
ObsPy	Handling and processing of seismological data
Matplotlib	Plotting routines, image and mapping libraries
Pillow	
Cartopy	
PySimpleGUI	Creation of graphical user interface (GUI) or web-interface
PySimpleGUIWeb	
Psutil	Retrieval of information on running processes

DESCRIPTION OF THE REAL-TIME TREMOR ANALYSIS TOOL SOFTWARE

Philosophy of Approach

In developing this software several choices had to be made–such as the programming language and type of user-interface–keeping in mind that its intended use is in real-time monitoring settings. The overall aim was to produce a tool that was as open and flexible as practicable, hence the choice to use the popular open source and platform independent python programming language, so as to keep the software as generic and as widely compatible as possible. Using python allowed us to build upon the popular ObsPy framework (The ObsPy Development Team, 2020b), which is widely used within the seismological community. This approach has the advantage of drawing on a large library of existing processing routines, with no reinvention of the wheel required (Megies et al., 2011). The disadvantage is that some flexibility is perhaps sacrificed by making it more difficult to design and implement custom processing routines, but the goal was to produce a tool that was easy to use and could be quickly and easily installed with as little additional packages required as possible. This and other limitations of the current implementation are further explored in *Limitations of the Current Implementation*. Since it is intended as a real-time tool, rapid processing of the array data becomes important, and computationally intensive tasks have been minimized where possible, with process-based parallelism exploited through python's multiprocessing capabilities.

The choice of python as the development language also makes the tool theoretically platform independent, again offering flexibility, and the software has been successfully tested in both Linux and Microsoft Windows environments.

Requirements

RETREAT requires python3 to be installed, and a list of required python modules is contained in the *requirements.txt* file supplied with the distribution. These are also summarized in **Table 1**.

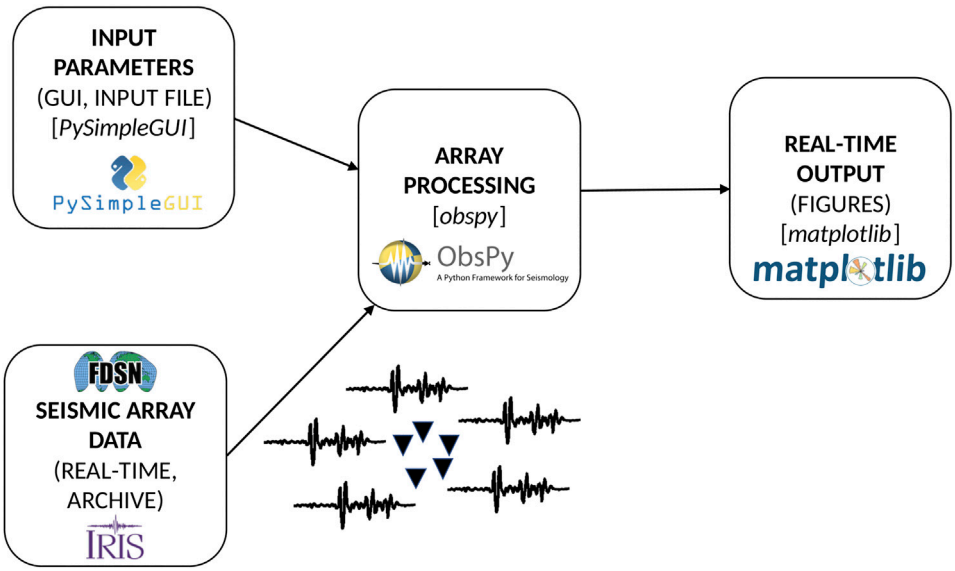

FIGURE 1 | Schematic overview of the RETREAT software package. Input parameters and configuration are collected from the GUI or web interface that was built using the PySimpleGUI module. Next, these settings allow seismic array data (real-time data from external sources, e.g. IRIS or any other server, or existing archive data) to be processed and analyzed using the standard array processing routines in ObsPy. Output figures displaying the results of the array analysis are then produced using the matplotlib python module and are continuously updated as new data is processed.

The key modules utilized by the tool are those that create the GUI or web interface and those that perform the data handling and array analysis.

PySimpleGUI

The user interface for the RETREAT code was built using the PySimpleGUI python package, (PySimpleGUI.org, 2020), that allows creation of simple but powerful GUIs as well as web interfaces that can run within a web browser window. More information on PySimpleGUI is available from https://pysimplegui.readthedocs.io/en/latest/.

ObsPy

Pre-processing and analysis of the seismic array data in RETREAT is performed by ObsPy (The ObsPy Development Team, 2020) an open-source framework for processing seismological data using python. The framework provides parsers for reading common seismic data and metadata formats, clients to access data centers and servers (for the real-time analysis) and seismological signal processing routines which allow processing and array analysis of the seismic data (Beyreuther et al., 2010).

Plotting of the output figures is handled by the matplotlib (Hunter, 2007) python plotting library, with array maps produced using Cartopy (Elson et al., 2020).

Schematic Overview

A schematic overview of the software workflow is shown **Figure 1**. A GUI or web-based interface, built using the PySimpleGUI python module, provides the first strand of input: a set of highly configurable input parameters. These include options for choosing and configuring the data source, pre-processing, timing and update options as well as the parameters for the seismic array analysis, which must be carefully selected and tuned for the specific array. The GUI also starts and controls the analysis. The other strand of input into the software is the seismic waveform data, which can be retrieved from either a real-time source or an existing data archive. These two input strands feed into the main data processing section, which utilizes ObsPy to perform the pre-processing and array analysis. The output from the software is a set of figures, produced using the matplotlib plotting libraries, that display the updated results of the array analysis.

Data Processing and Array Analysis

The array processing performed by this software uses the standard array analysis routines that are supplied with ObsPy to retrieve estimates of the back azimuth and slowness values from a series of overlapping sub-windows.

Array processing methods utilize beamforming techniques, which enhance the signal-to-noize ratio (SNR) by stacking coherent parts of the input signals in order to suppress noise in the data (Rost and Thomas, 2002). A widely used array method to estimate the slowness of seismic waves arriving at an array is frequency wavenumber (f-k) analysis (Capon and Bolt, 1973; Harjes and Henger, 1973) which uses multi-dimensional Fourier Transforms to transform the wave-field to the frequency-wavenumber domain. The slowness vector is then estimated by using the absolute power as a measure of coherency, with the analysis performed in the frequency domain for a number of different slowness values in a pre-defined grid (Schweitzer et al., 2012). This particular beamforming method was chosen for this

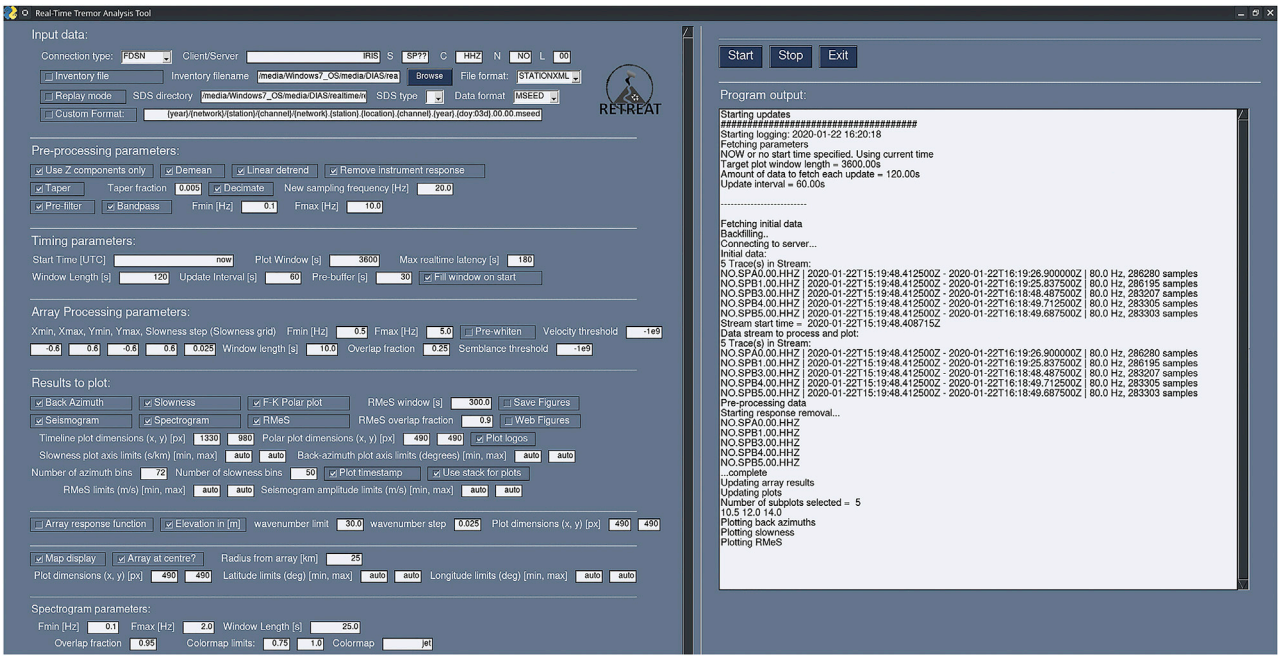

FIGURE 2 | Example screenshot of the GUI interface for the RETREAT tool, showing the program controls, configurable input parameters and program output window.

initial version of the software for convenience, as it is a commonly used, well-tested and readily available method built into ObsPy. This was a deliberate design choice as the primary aim was to produce a working tool that can easily be applied to real-time data.

The analysis procedure performed by RETREAT largely follows the ObsPy tutorial on "Beamforming - FK Analysis" (The ObsPy Development Team, 2020a), and the software carries out the f-k analysis based on the parameters supplied from the GUI interface. These parameters, which must be carefully selected for a particular array, include: the array geometry (calculated from station location metadata), the frequency range of interest in the signal and the grid of slowness values on which to evaluate the beam power.

Additionally, there is also an option to use Least-Squares beamforming, using cross-correlation to calculate delay times, as an alternative to f-k analysis (e.g., for infrasound data). Low velocity (and therefore high slowness) values for infrasonic data mean a large slowness grid is required which can affect the computation time. The implementation in this code follows exactly the method described by De Angelis et al. (2020) and allows for significantly faster computation as well as explicit uncertainty estimates for the back azimuth and velocity (slowness). More details and an example comparing this method to f-k analysis for an infrasound dataset are discussed in *Application to Infrasound Data*.

Prior to the array analysis the waveform data may be pre-processed to facilitate the computation. This includes options to remove the instrument response, demean or detrend the data and to filter to the input signals to the frequency range of interest. Since minimizing the processing time becomes important for real-time analysis, there is also an option to decimate the data to a lower sampling rate while still retaining relevant frequencies.

Input Parameters

The GUI interface allows input parameters to be defined which configure and control the software. These parameters include options for choosing and configuring the data source, pre-processing, timing and update options and the parameters for the array analysis. The parameters are divided into several sections, as shown in the screenshot of the GUI interface in **Figure 2**.

All parameters that can be set using the GUI or web interface can also be defined in advance of runtime. This is controlled by a text file containing a simple python dictionary comprised of pairs of parameters and their default values, which can be edited to change the values as desired. The repository contains two example files containing default values that can be used to run the two examples described in *Example Configuration and Datasets Included With the Distribution*.

More detailed information for each input parameter is provided in the documentation supplied with the software distribution.

Input Data

These parameters define the source and properties of the input seismic data. The software operates in two modes, depending on whether the data source is real-time or archive data.

In real-time mode, the user can choose their data source from either an FDSN client or a SeedLink server. Other sources

supported by ObsPy are possible, but have not yet been implemented. Data are fetched at regular intervals controlled by parameters in the timing section. The other mode is a "replay" mode for archive data, that must be supplied in a (customizable) Seiscomp Directory Structure (SDS). All seismic data formats supported by ObsPy can be used, and in both modes station metadata containing the station coordinates must be supplied in order to perform the array analysis.

Pre-Processing

This set of parameters define any pre-processing applied to the data before the array analysis is carried out. This includes options to demean, detrend, taper and filter the input data, as well as to decimate the signals to a lower sampling rate to reduce the computation time.

Timing

This set of parameters define the amount of data to be processed, by defining the length of the window and how often it is updated (in real-time mode). Updates of new data are managed by the python code, with the update interval specified by the user as an input parameter. If the processing for each update step takes longer than this update interval to complete, the software will warn the user that real-time processing may lag. For non-real-time archive data in "replay" mode, this parameter is ignored and the next chunk of data is processed immediately.

Latency and buffering options can also be set, as well as the start time for analysis if running in replay mode.

Array Processing Parameters

This section sets parameters for the array processing, using either the standard array analysis routines in ObsPy or a Least-squares beamforming method. These include the frequency range of interest and the slowness grid over which to perform the f-k analysis, with the choice of these values depending on the specific array. To provide a timeseries output, the beamforming for both methods is performed by using shorter time windows, with a defined amount of overlap, and sliding these windows across the entire input signal.

Results and Plots

The parameters in this section allow the output figures to be selected from the choices outlined in *Array Processing Parameters*, as well as various settings for these plots such as the axis limits and plot dimensions. The results can also be displayed in a web browser instead of a GUI window, and images can be stored with unique filenames based on their timestamp.

Output

These settings control where the output produced by the software is stored on the system, including the figures, log file and array processing results. The GUI interface also includes an output pane to the right of the input parameters (**Figure 2**) that displays diagnostic and (any) error messages in the log file in real-time.

Output and Array Processing Results

Once configured and launched, the tool fetches chunks of waveform data (in real time or from files) and updates its output accordingly. On each update the tool returns a choice of plots, as shown in the schematic in **Figure 3**. The results of the array processing are presented as timeseries of the back azimuth and slowness values determined in each sub-window of the input data, with the temporal resolution dependent on the window length of each sub-window and desired amount of overlap. A timeseries of the relative power (f-k) or mean correlation (Least-Squares beamforming) can also be plotted, which may be a useful threshold parameter for event detection or alarm triggering. Alongside these array analysis results, the seismic waveform, its envelope (root-median-square is used to remove transients) and a spectrogram can optionally be plotted on a common timebase. Additionally, a separate plot displays the relative power (or correlation for Least-Squares) returned by the array processing in polar form, as a histogram of the back azimuth and slowness values, which can also be normalized. A third optional panel can display either the array response function, or, a map of the array locale overlain by a line representing the back azimuth derived from the maximum relative power in the histogram. Maps are produced by the Cartopy package using topographic data from the OpenTopoMap project, with tiles automatically downloaded for the geographic area of the array at the chosen zoom level. Output figures for the example datasets supplied with the distribution are shown in *Example Configuration and Datasets Included With the Distribution*.

EXAMPLE CONFIGURATION AND DATASETS INCLUDED WITH THE DISTRIBUTION

Configuration files and data to run processing of two examples, of both real-time and archive data, are included with the software distribution. Due to financial and technical constraints seismic arrays are not often used routinely for volcano monitoring, and therefore real-time data from such arrays are not available from many volcanoes. Hence, we opted to use freely available real-time data from the small aperture SPITS array as a development and demonstrator dataset for our real time application. Archived data from a deployment in Iceland, carried out during the 2014–2015 Bárðarbunga eruption as part of the FUTUREVOLC project, were used to develop and test the application of this tool on archived data (Bean and Vogfjörd, 2020).

Real-Time Mode Using Data From SPITS Array

As we currently do not have any real time seismic array data from a volcano available within the EUROVOLC project or its partners, the tool has been tested using both the FDSN and SeedLink clients of ObsPy to fetch data from the IRIS datacenter, using example real-time data from the small-aperture SPITS seismic array (Gibbons et al., 2011) in Spitsbergen, Svalbard, as shown in **Figure 4**. This small-aperture array comprising nine

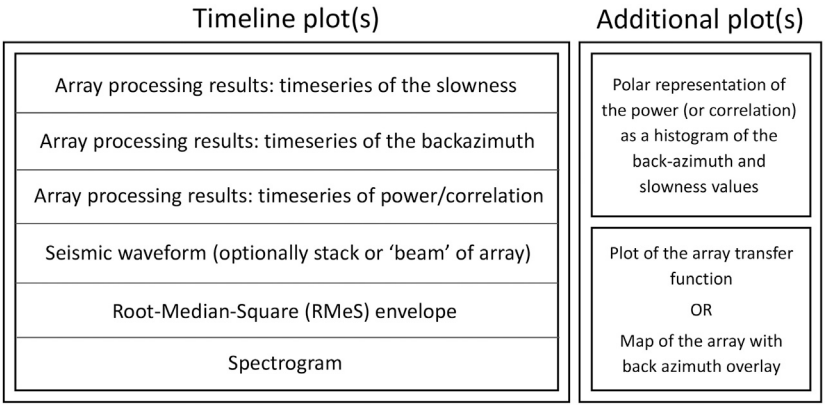

FIGURE 3 | Schematic diagram showing the possible output figures that can be produced by RETREAT. The left-hand pane features timeseries of several parameters (slowness, back azimuth, power/correlation, waveform, envelope, spectrogram) plotted on a common timebase. The right-hand plots show a polar representation of the back azimuth and slowness values as well an optional plot of either the Array Response Function or a map of the array.

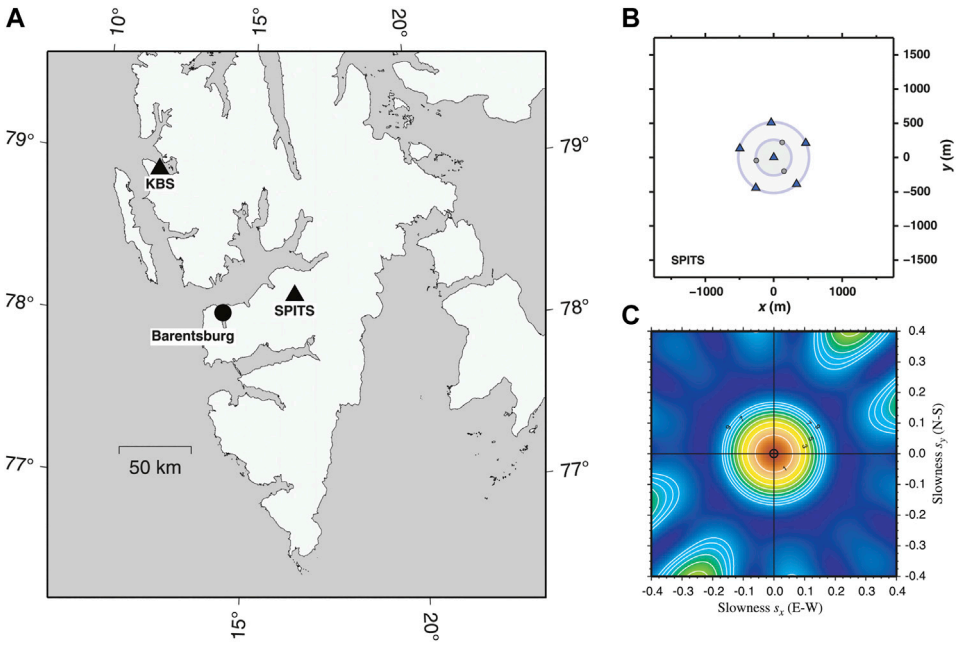

FIGURE 4 | (A) Map showing the location of the small-aperture SPITS array (black triangle) on Spitsbergen; **(B)** station locations showing the nine-station array design with approximate 1 km aperture, with three-component stations shown by triangles and single component stations by circles; and **(C)** the associated array response as a function of the horizontal slowness evaluated at 4 Hz. Map and figures taken from Gibbons (2006) and Gibbons et al. (2011).

stations is part of the larger NORSAR array, but with an aperture of around 1 km is more typical of the size and characteristics of seismic arrays deployed in volcanic environments.

To run the real-time example, the end-user can choose the appropriate default values file (NO array) before starting the software. This should begin analysis of real-time data, with results similar to those shown in the screenshot of an example output window in **Figure 5**.

As mentioned previously, for real-time or near real-time use, the processing and computation time for any data analysis becomes critically important, as data must be able to be processed rapidly enough to match the acquisition. While care has been taken to minimize computationally intensive tasks, including making use of python's multiprocessing capabilities, the code has not been formally optimized. The approach taken with this tool is to acquire data in chunks (of a size and at a frequency defined by the user) and then update the array results with each new acquisition of data. The processing time for each update will vary depending on many factors, including: the window length or amount of data analyzed, the download

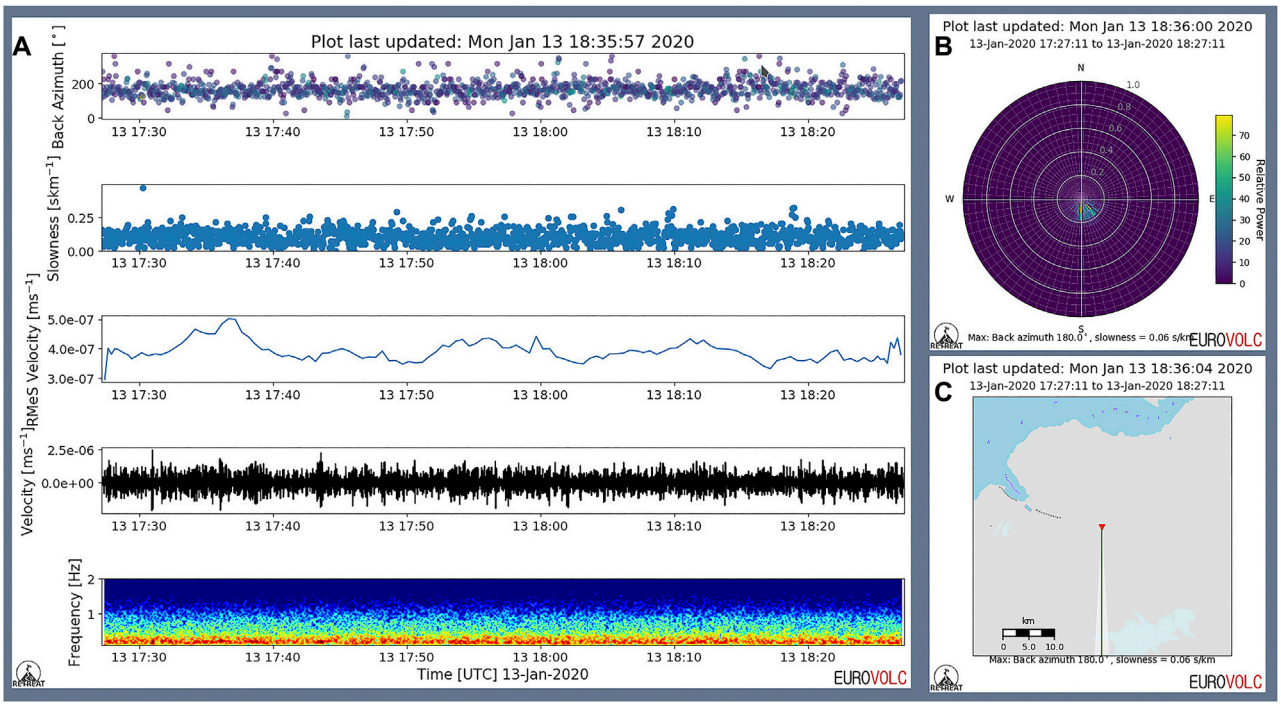

FIGURE 5 | Example of the output figures produced by the RETREAT software tool, showing **(A)** timeseries of the slowness and backazimuth calculated from the f-k analysis, alongside the seismic waveform, envelope and spectrogram and **(B)** a polar representation of the array processing results. Also shown is **(C)** a map of the area surrounding the SPITS array, with the resulting back azimuth overlaid. The azimuth error is illustrative only, determined from the resolution of the histogram. Implementation of uncertainty estimation for the back azimuth values is discussed further in *Discussion*.

speed of the data over the network or internet, the number of stations and channels in the array, the sampling rate, whether the data are decimated, other pre-processing steps and finally the hardware capabilities of the machine on which the software is run. Therefore, some experimentation will be required to determine the limitations for any particular dataset and configuration. For this example, using data from the SPITS array, five stations with a sampling rate of 80 Hz are used, with the data decimated to 20 Hz before the array analysis. The tool is configured to analyze 1 h of data, updating every minute. The processing time for each update for this configuration is approximately 18 s on a modern desktop machine (12x Intel Xeon W-2135, 64 GB RAM) and around 30 s on a laptop with similar specifications (4x Intel Core i7-6600U, 32 GB RAM). This is therefore adequate for an update interval of 60 s in this example.

Archive Mode Using Data from the 2014–2015 Eruption of Bárðarbunga.

An example dataset and configuration that uses archive seismic array data has also been included with the distribution, to demonstrate analysis of non-real-time datasets. This second example uses array data from the 2014–2015 eruption of Bárðarbunga volcano in Iceland (Sigmundsson et al., 2015), collected as part of the FUTUREVOLC project. Several hours of data from the UR array between 00:00 and 08:00 UTC on September 03, 2014 are included with the distribution, corresponding to part of the time period analyzed in Eibl et al. (2017b). The map in **Figure 6** shows the geometry and location of the seven station UR array in Iceland, relative to the erupted lava

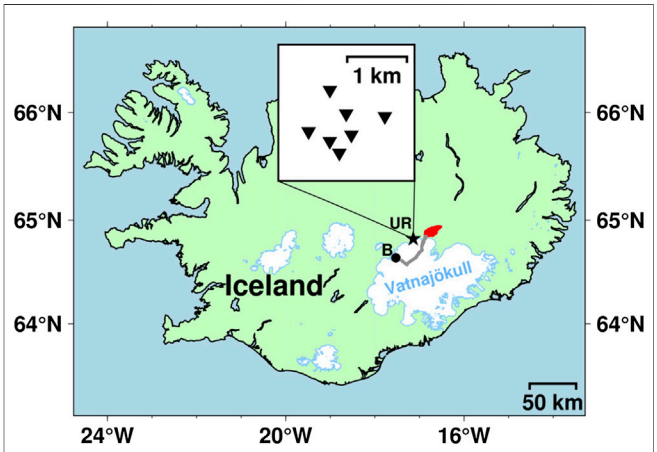

FIGURE 6 | Map showing location and geometry of the seven station UR seismic array deployed as part of FUTUREVOLC to collect data during the 2014–2015 eruption at Bárðarbunga volcano in Iceland. The location of the erupted lava flow field in Holuhraun is indicated in red, Bárðarbunga volcano by the black letter B and the approximate propagation path of the dyke intrusion below the glacier by the gray line.

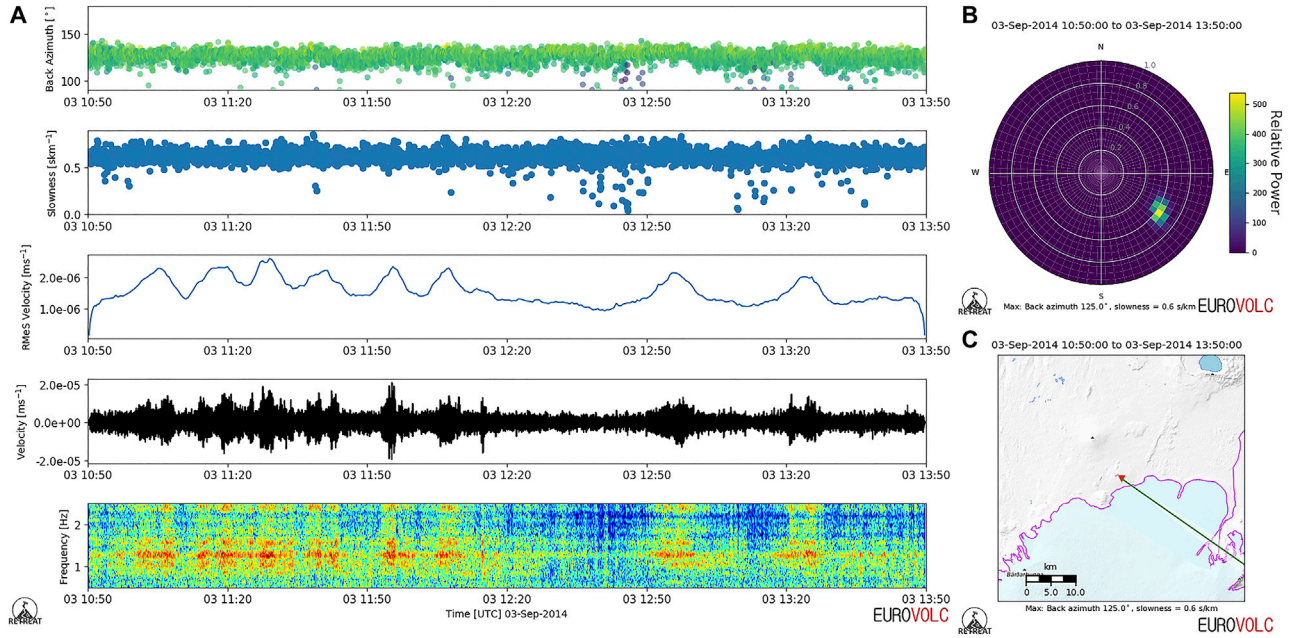

FIGURE 7 | Output figures produced by the RETREAT software for the archive data example. **(A)** Time series of slowness and backazimuth calculated from f-k analysis, alongside the seismic waveform, envelope and spectrogram and **(B)** a polar representation of the array processing results. Also shown is **(C)** a map of the area surrounding the UR array, with the resulting back azimuth overlaid, closely matching the results found by Eibl et al. (2017b).

flow field in Holuhraun and Bárðarbunga volcano. Example results of the analysis of these data using RETREAT are shown in **Figure 7**.

The configuration for this example closely follows the parameters used by Eibl et al. (2017b), with the data from the seven station array filtered between 0.8 and 2.6 Hz after being downsampled to 20 Hz. The time period analyzed represents pre-eruptive tremor prior to a suspected sub-glacial eruption, based on observed cauldron formation approximately, 12 km from the UR array. The tremor signal is centered around 1.3 Hz, with harmonic overtones at 0.25 Hz spacing, and the upper end of measured slowness values of 0.6–0.75 skm^{-1} from the array analysis support a strong surface wave component. Array analysis and location of the tremor signal, along with mapping of the slowness changes to depth changes by modeling the tremor as a comb function, is interpreted by Eibl et al. (2017b) as the tremor representing microseismicity resulting from brittle failure in the weak uppermost crust, marking the onset of shallow dyke formation.

DISCUSSION

The particular suitability of seismic arrays for the analysis of volcanic tremor has been long noted (Chouet, 1996), yet seismic arrays and array processing are not routinely or widely used operationally in volcano monitoring, with local monitoring networks often being distributed and wide aperture to maximize spatial coverage (Allstadt et al., 2018). As Wassermann (2012) notes, most of the barriers to greater operational use of denser, smaller aperture arrays are technical in nature, and include the comparatively higher costs of installation and maintenance, as well the need for expertize, requiring significant economic and human resources. This has meant array installations on volcanoes have often been short-term campaign deployments, with few long-term or permanent seismic arrays in use for routine monitoring purposes. However, with increasing instrumentation and monitoring of volcanic systems there is potential and scope for more routine use. The software developed and presented in this manuscript is intended to ease and facilitate greater use of seismic arrays for such operational purposes, but we reiterate here that arrays should be seen as complementary to, and not a replacement for, existing seismic networks.

Limitations of the Current Implementation

The current implementation of the software is intended specifically for: 1) seismic array data, for 2) arrays away from the target tremor source, i.e., the source is outside of the array or network and 3) real-time applications. RETREAT is not intended as a comprehensive solution for tremor analysis, and its limitations are to some extent controlled by the availability and quality of the input data. Specific constraints, such as the optimum frequency range and slowness resolution, will depend on the geometry and number of stations in the end-user's specific array and how these compare to the characteristics of the recorded signals.

Dealing with error estimates of the slowness and azimuth values retrieved from f-k analysis is not straightforward (La Rocca et al., 2008) as the uncertainties depend on multiple factors;

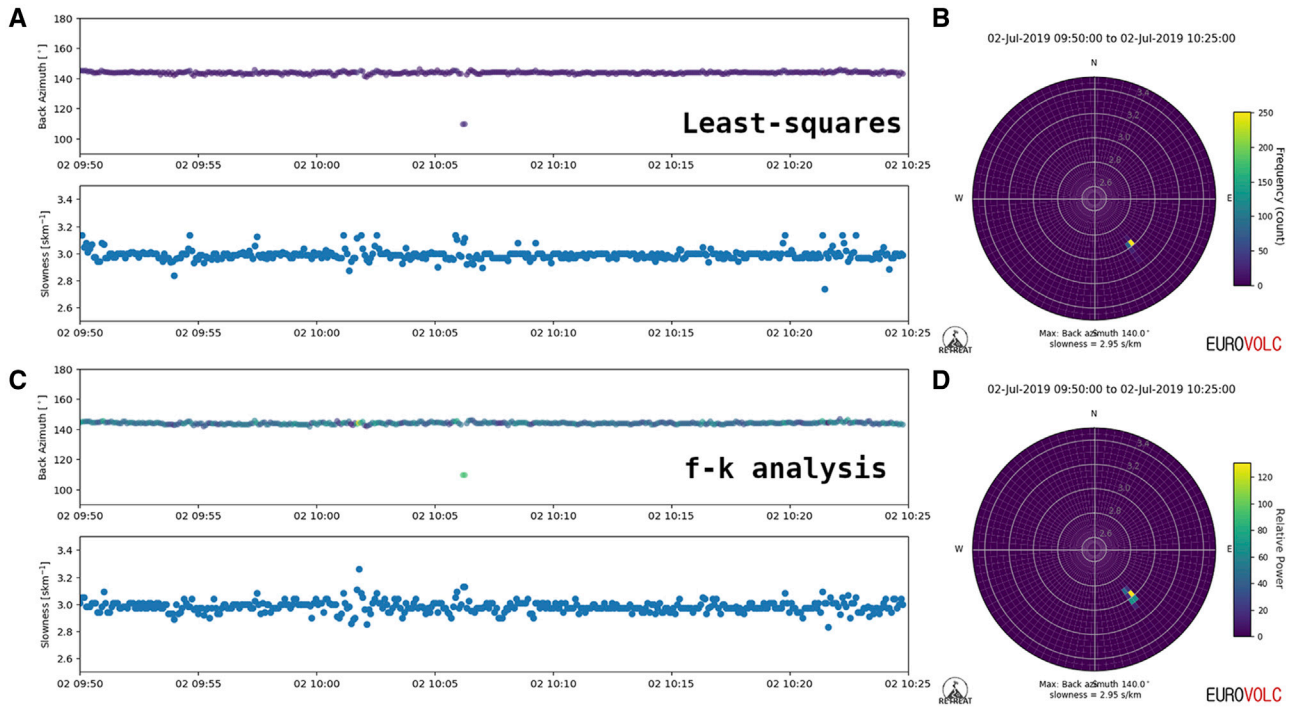

FIGURE 8 | Comparison of RETREAT applied to infrasonic array data using two different beamforming methods. **(A)** Timeseries of backazimuth and slowness values derived using Least-Squares inversion and **(B)** corresponding histogram of slowness and backazimuth values in polar form. Note that this is weighted by the MCCM (mean cross-correlation maxima) rather than the relative power as in the f-k case. **(C)** Timeseries of backazimuth and slowness values derived using f-k analysis and **(D)** the corresponding histogram of slowness and backazimuth values in polar form, weighted by the relative power.

including aspects of the array characteristics (geometry, number of stations) and data quality (coherence, noise, site effects). One method of estimation is to use the size or width of the peak around the maximum power in the f-k plot (Schweitzer et al., 2012), but this method cannot easily be extended across a timeseries of shorter windows into a single uncertainty value. How errors should be calculated and displayed within RETREAT is an unresolved problem, and a fuller treatment of uncertainties may increase the computation time and compromise the ability to process data fast enough to achieve real-time results. However, improved error estimation is an important feature that is in development and it is intended to implement this feature in future versions of the software. One alternative could be to use a Least-Squares beamforming method, such as that described in the next section.

Application to Infrasound Data

The use of infrasound to monitor volcanic activity has become increasingly common, and infrasound sensors are often deployed alongside existing seismic and deformation networks as part of a multi-disciplinary monitoring approach (e.g., Fee and Matoza, 2013; McNutt et al., 2015). In a similar manner to seismology, as well as more widely distributed networks, tight clusters of stations or small aperture arrays of infrasound sensors have been used extensively (e.g., Ripepe and Marchetti, 2002; Yamakawa et al., 2018; De Angelis et al., 2020) to monitor and track the location of sub-aerial volcanic phenomena, such as explosions, gas and ash emission, dome or sector collapses, pyroclastic density currents and lahars. Analysis of data from infrasonic arrays has also been used to implement automated early warning systems for explosive eruptions (Ripepe et al., 2018).

Although designed specifically for seismic array data (with a particular focus on volcanic tremor), RETREAT can also be applied to data from an array of infrasound sensors, using f-k analysis in the same way as for seismic data to retrieve the azimuth and slowness of infrasonic acoustic waves arriving at the array (**Figure 8**). However, due to the lower velocity of acoustic waves compared to seismic waves (and therefore higher slowness–up to 3 skm^{-1} and beyond), a larger slowness grid is required for the analysis. Therefore, a larger grid, while keeping a small enough slowness step to maintain adequate resolution, is far less computationally efficient and results in significantly longer processing times.

With this in mind, RETREAT also contains a python implementation of a time-domain Least-Squares inversion method that uses cross-correlation to compute time delays between station pairs to carry out the beamforming and derive an estimate of the apparent horizontal velocity. This method (Olson and Szuberla, 2005; Haney et al., 2018) is also applied on a series of overlapping sub-windows to produce timeseries of the

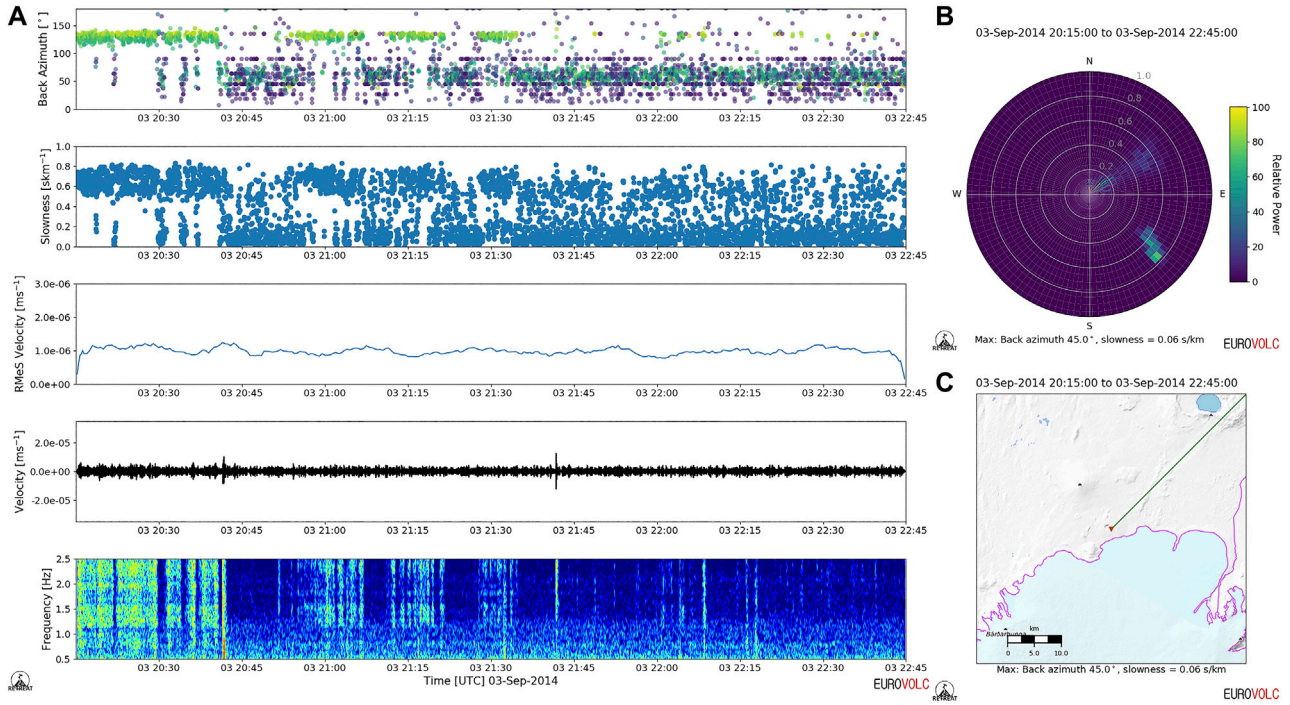

FIGURE 9 | Output figures produced by the RETREAT software that illustrate its capacity to analyze time periods containing multiple tremor sources. **(A)** Time series of slowness and backazimuth calculated from f-k analysis, alongside the seismic waveform, envelope and spectrogram showing a switch from one dominant source to another during this time period. **(B)** A polar representation of the array processing results, with the histogram highlighting the two tremor sources to the north-east and south-east of the array. Also shown is **(C)** a map of the area surrounding the UR array, with the azimuth of the more dominant source, associated with lava flows at the surface, overlaid.

back azimuth and slowness, and has the advantage of being faster to compute, while developments by De Angelis et al. (2020) also allow for direct estimates of the uncertainties of these measurements. It also returns a timeseries of the mean cross-correlation maxima (MCCM), which by choosing a certain threshold can be a useful parameter for event detection, or even alarm triggering.

In order to illustrate the capability of RETREAT to analyze infrasonic array data in addition to seismic data, **Figure 8** shows a comparison between the two beamforming methods. The data analyzed are from a 2019 deployment of two 6-sensor infrasound arrays at Mt. Etna in Italy, and are exactly the same as those analyzed and presented in Figure 4 of De Angelis et al. (2020), containing 35 min of data from July 2, 2019 at the ENEA array, approximately 1 km to the NW of the summit. The dominant activity is from deep intra-crater explosions at the more southerly Bocca Nuova crater (~145°), occurring consistently across the timeseries, with a brief interruption from a larger ash-rich explosion at the North East Crater (~110°) at around 10:06 UTC. Data are pre-processed by filtering between 0.7 and 15 Hz, and a 10 s window with 50% overlap is used. The results of the analysis in **Figure 8** show that both methods are capable of reproducing the results of De Angelis et al. (2020) and resolving the change in location of activity at around 10:06 UTC; however the Least-Squares method is much faster, which is a key advantage for real-time applications. This method also produces more tightly clustered values, particularly in slowness, and with a step of 0.05 skm^{-1} in the slowness grid limiting the resolution, the f-k analysis takes around two orders of magnitude longer to complete than the Least-Squares inversion.

Tremor Location Methods and Features for Future Versions

As discussed earlier, the choice to use f-k analysis as the basis for determining the tremor source in this software was a deliberate one, as it is a widely used and well tested technique, and as a standard component of ObsPy it is easily and readily available.

Another advantage of using f-k analysis is that multiple simultaneous sources can theoretically be resolved, appearing as multiple peaks at different points in the slowness grid. An example of analysis using RETREAT where there are multiple simultaneous sources is shown in **Figure 9**, where 2.5 h of data from September 03, 2014 during the Bárðarbunga eruption, using the same UR array as previously, are shown. In this example, the tremor source attributed to the shallow sub-glacial dyke to the south-east of the array is still visible, but a second source to the north-east, corresponding to lava flows and fountaining at the surface, also appears from around 20:45 UTC and becomes the dominant source from 21:30 onwards (see Eibl et al. (2017a) for more details of multiple simultaneous tremor sources during this eruption).

However, this analysis is not strictly utilizing a unique capacity of the f-k technique, as identification of the two sources arises from visualization of the data in the timeseries and histogram, where single values for the slowness and azimuth returned for each sub-window, derived from choosing a single peak (corresponding to the maximum power) in the slowness grid, are not averaged out, but appear as distinct separate sources. A modified version of the f-k analysis routine could therefore be developed to search for and choose multiple peaks in power from the slowness grid, and while this moves away from using the standard version supplied with ObsPy, it could prove a useful addition in complex areas with multiple potential sources of tremor. But whether this offers a sufficient advantage over the current capabilities, as shown in **Figure 9**, would need to be tested. One obvious disadvantage of using the f-k method is that by searching over a grid it is not optimally efficient, particularly for infrasonic data, and may struggle to produce results in real-time for large datasets.

In addition to the f-k analysis, the software could be extended with further or alternative methods for beamforming and tremor location. As described above, a Least-Squares inversion beamforming method has already been implemented, with particular applications for infrasound array data in mind. The advantages of this method are that it gives faster results (important for real-time analysis) and also direct error and uncertainty estimates, but at the cost of assuming a single plane-wave (and hence single source) in the time window analyzed. It is intended mainly for infrasonic data as further testing and benchmarking would be required to fully compare the performance of the two methods for a variety of seismic datasets.

Besides the two beamforming methods already implemented in this software, other approaches for locating and analyzing tremor signals that could be developed and integrated into RETREAT are:

- Three-component beamforming (e.g., Löer et al., 2018), which can help to identify the types of waves arriving at the array by providing information on the polarization of the wavefield. This, alongside the location from more traditional beamforming approaches, could help place further constraints on the characteristics of the tremor source.
- Improvements on the least-squares inversion method by using more robust estimators (e.g., Bishop et al. (2020)) that can handle outliers, such as timing or polarity errors.
- Amplitude Source Location (ASL) or other amplitude based methods (e.g., Battaglia et al., 2005; Taisne et al., 2011; Morioka et al., 2017) that use amplitudes at different stations or radiated seismic intensity ratios to determine the source location.
- Back-projection methods (e.g., Haney, 2014; Li et al., 2017) which use time-reversal to refocus energy at the location of the source.

The latter two techniques in particular could well be useful complements and would provide powerful additional constraints on the tremor location and dynamics when used in conjunction with array-based beamforming methods. However, such methods generally require a more distributed seismic network, with the source inside the network, and are hence moving beyond the scope of this initial version of the RETREAT tool that is specifically focused on arrays and real-time array data.

CONCLUSION

Due to the inherent nature of the signals and often sparse monitoring networks, accurate tracking of volcanic tremor sources is a challenging task. Seismic arrays, however, are a powerful additional tool that can provide unique insights into the source dynamics of volcanic tremor at active volcanoes.

In this manuscript we have introduced RETREAT, a python-based software tool that utilizes existing routines from the open-source ObsPy framework to carry out analysis of seismic array data in real-time by performing either f-k analysis, or optionally Least-Squares beamforming, to determine the back azimuth that points toward the source. Although RETREAT has been designed for deployment as part of volcano monitoring systems and provides the ability to track tremor sources in real-time, it also has the capability to analyze existing datasets for testing, comparison and research purposes.

These abilities have been demonstrated using real-time data from the small aperture SPITS seismic array in Spitsbergen, Svalbard, as well as on archive data from an array deployed during the 2014–2015 eruption of Bárðarbunga volcano in Iceland.

While primarily intended as a tool for utilizing seismic array data to locate and track volcanic tremor, RETREAT also has the capability to analyze infrasonic array data to track acoustic sources, and has been successfully tested on and applied to data from two infrasound arrays deployed close to the summit of Mt. Etna, Italy, in 2019.

We suggest that the implementation of real-time software applications such as RETREAT is crucial to fully exploit the power of seismic arrays as a volcano monitoring tool and to improve our ability to detect, monitor and understand unrest at active volcanoes.

DATA AVAILABILITY STATEMENT

RETREAT is available from a GitLab repository at https://git.dias.ie/paddy/retreat (Smith, 2020), and is compatible with Windows, Linux, and Apple operating systems. The repository includes configuration files for the specified examples in this paper, along with the accompanying waveform data for the archive example. See also Bean and Vogfjörd (2020) for more details on this dataset.

The software is freely available and is licensed under the open-source European Union Public Licence (EUPL), v1.2. More information is available in the LICENCE.txt file supplied with the distribution.

AUTHOR CONTRIBUTIONS

PS developed the RETREAT software package. Both authors contributed to the preparation of the manuscript.

FUNDING

The research leading to the development of the RETREAT software tool was carried out as part of the EUROVOLC project (https://eurovolc.eu) and received funding from the

European Union's Horizon 2020 research and innovation program under grant agreement No. 731070.

ACKNOWLEDGMENTS

The authors wish to thank colleagues at DIAS for internal testing and review of the software and its documentation, as well as the two reviewers for their time in providing critical reading and suggestions which helped to improve both this manuscript and the software. The data used in the archive example were collected as part of the FUTUREVOLC project, which received funding from the European Union's Seventh Program for research, technological development and demonstration under grant agreement No. 308377.

REFERENCES

Allstadt, K. E., Matoza, R. S., Lockhart, A. B., Moran, S. C., Caplan-Auerbach, J., Haney, M. M., et al. (2018). Seismic and acoustic signatures of surficial mass movements at volcanoes. *J. Volcanol. Geotherm. Res.* 364, 76–106. doi:10.1016/j.jvolgeores.2018.09.007

Almendros, J., Ibáñez, J. M., Alguacil, G., Del Pezzo, E., and Ortiz, R. (1997). Array tracking of the volcanic tremor source at Deception Island, Antarctica. *Geophys. Res. Lett.* 24 (23), 3069–3072. doi:10.1029/97GL03096

Battaglia, J., Aki, K., and Ferrazzini, V. (2005). Location of tremor sources and estimation of lava output using tremor source amplitude on the Piton de la Fournaise volcano: 1. location of tremor sources. *J. Volcanol. Geoth. Res.* 147 (3), 268–290. doi:10.1016/j.jvolgeores.2005.04.005

Bean, C. J., and Vogfjörd, K. S. (2020). Seismic array data for monitoring and tracking tremor sources during subglacial floods and volcanic eruptions at Vatnajökull (Vatna Glacier), Iceland. *GFZ Data Services.*. doi:10.14470/0Y7568667884

Beroza, G. C., and Ide, S. (2011). Slow earthquakes and nonvolcanic tremor. *Annu. Rev. Earth Planet Sci.* 39 (1), 271–296. doi:10.1146/annurev-earth-040809-152531

Beyreuther, M., Barsch, R., Krischer, L., Megies, T., Behr, Y., and Wassermann, J. (2010). ObsPy: a Python toolbox for seismology. *Seismol Res. Lett.* 81 (3), 530–533. doi:10.1785/gssrl.81.3.530

Bishop, J. W., Fee, D., and Szuberla, C. A. L. (2020). Improved infrasound array processing with robust estimators. *Geophys. J. Int.* 221 (3), 2058–2074. doi:10.1093/gji/ggaa110

Capon, J., and Bolt, B. A. (1973). "Signal processing and frequency-wavenumber spectrum analysis for a large aperture seismic array," in *Methods in computational physics* (Amsterdam, Netherlands: Elsevier), 13, 1–59.

Chouet, B. A. (1996). "New methods and future trends in seismological volcano monitoring," in *Monitoring and mitigation of volcano hazards*. Editors R. Scarpa and R.I. Tilling (Berlin, Heidelberg: Springer Berlin Heidelberg), 23–97.

Coombs, M. L., Wech, A. G., Haney, M. M., Lyons, J. J., Schneider, D. J., Schwaiger, H. F., et al. (2018). Short-term forecasting and detection of explosions during the 2016–2017 eruption of bogoslof volcano, Alaska. *Front. Earth Sci.* 6, 122. doi:10.3389/feart.2018.00122

De Angelis, S., Haney, M. M., Lyons, J. J., Wech, A., Fee, D., Diaz-Moreno, A., et al. (2020). Uncertainty in detection of volcanic activity using infrasound arrays: examples from Mt. Etna, Italy. *Front. Earth Sci.* 8, 169. doi:10.3389/feart.2020.00169

Di Lieto, B., Saccorotti, G., Zuccarello, L., Rocca, M. L., and Scarpa, R. (2007). Continuous tracking of volcanic tremor at Mount Etna, Italy. *Geophys. J. Int.* 169 (2), 699–705. doi:10.1111/j.1365-246X.2007.03316.x

Eibl, E. P. S., Bean, C. J., Einarsson, B., Pàlsson, F., and Vogfjörd, K. S. (2020). Seismic ground vibrations give advanced early-warning of subglacial floods. *Nat. Commun.* 11 (1), 2504. doi:10.1038/s41467-020-15744-5Pubmed |

Eibl, E. P. S., Bean, C. J., Jónsdóttir, I., Höskuldsson, A., Thordarson, T., Coppola, D., et al. (2017a). Multiple coincident eruptive seismic tremor sources during the 2014-2015 eruption at Holuhraun, Iceland. *J. Geophys. Res. Solid Earth.* 122 (4), 2972–2987. doi:10.1002/2016jb013892

Eibl, E. P. S., Bean, C. J., Vogfjörd, K. S., Ying, Y., Lokmer, I., Möllhoff, M., et al. (2017b). Tremor-rich shallow dyke formation followed by silent magma flow at Bárðarbunga in Iceland. *Nat. Geosci.* 10 (4), 299–304. doi:10.1038/ngeo2906

Elson, P., de Andrade, E. S., Hattersley, R., Campbell, E., May, R., Dawson, A., et al. (2020). SciTools/cartopy. *Cartopy*. doi:10.5281/zenodo.3783894

Fee, D., and Matoza, R. S. (2013). An overview of volcano infrasound: from Hawaiian to Plinian, local to global. *J. Volcanol. Geotherm. Res.* 249, 123–139. doi:10.1016/j.jvolgeores.2012.09.002

Gibbons, S. J. (2006). On the identification and documentation of timing errors: an example at the KBS station, spitsbergen. *Seismol Res. Lett.* 77 (5), 559–571. doi:10.1785/gssrl.77.5.559

Gibbons, S. J., Schweitzer, J., Ringdal, F., Kvaerna, T., Mykkeltveit, S., and Paulsen, B. (2011). Improvements to seismic monitoring of the European Arctic using three-component array processing at SPITS. *Bull. Seismol. Soc. Am.* 101 (6), 2737–2754. doi:10.1785/0120110109

Haney, M. M. (2014). Backprojection of volcanic tremor. *Geophys. Res. Lett.* 41 (6), 1923–1928. doi:10.1002/2013GL058836

Haney, M. M., Van Eaton, A. R., Lyons, J. J., Kramer, R. L., Fee, D., and Iezzi, A. M. (2018). Volcanic thunder from explosive eruptions at bogoslof volcano, Alaska. *Geophys. Res. Lett.* 45 (8), 3429–3435. doi:10.1002/2017GL076911

Harjes, H. P., and Henger, M. (1973). Array-seismologie. *Z. Geophys.* 39, 865–905.

Hellweg, M. (2000). Physical models for the source of Lascar's harmonic tremor. *J. Volcanol. Geotherm. Res.* 101 (1), 183–198. doi:10.1016/s0377-0273(00)00163-3

Hunter, J. D. (2007). Matplotlib: a 2D graphics environment. *Comput. Sci. Eng.* 9 (3), 90–95. doi:10.1109/mcse.2007.55

Jellinek, A. M., and Bercovici, D. (2011). Seismic tremors and magma wagging during explosive volcanism. *Nature* 470 (7335), 522–525. doi:10.1038/nature09828Pubmed |

Julian, B. R. (1994). Volcanic tremor: nonlinear excitation by fluid flow. *J. Geophys. Res.* 99 (B6), 11859–11877. doi:10.1029/93JB03129

Kumagai, H., Palacios, P., Maeda, T., Castillo, D. B., and Nakano, M. (2009). Seismic tracking of lahars using tremor signals. *J. Volcanol. Geotherm. Res.* 183 (1), 112–121. doi:10.1016/j.jvolgeores.2009.03.010

La Rocca, M., Galluzzo, D., Malone, S., McCausland, W., Saccorotti, G., and Del Pezzo, E. (2008). Testing small-aperture array analysis on well-located earthquakes, and application to the location of deep tremor. *Bull. Seismol. Soc. Am.* 98 (2), 620–635. doi:10.1785/0120060185

Li, K. L., Sadeghisorkhani, H., Sgattoni, G., Gudmundsson, O., and Roberts, R. (2017). Locating tremor using stacked products of correlations. *Geophys. Res. Lett.* 44 (7), 3156–3164. doi:10.1002/2016GL072272

Löer, K., Riahi, N., and Saenger, E. H. (2018). Three-component ambient noise beamforming in the Parkfield area. *Geophys. J. Int.* 213 (3), 1478–1491. doi:10.1093/gji/ggy058

McNutt, S. R., Thompson, G., Johnson, J., Angelis, S. D., and Fee, D. (2015). "Chapter 63—seismic and infrasonic monitoring," in *The encyclopedia of volcanoes*. 2nd Edn, Editor H. Sigurdsson (Amsterdam, Netherlands: Academic Press), 1071–1099.

McNutt, S. R. (2011). Volcanic tremor wags on. *Nature* 470 (7335), 471–472. doi:10.1038/470471aPubmed |

Megies, T., Beyreuther, M., Barsch, R., Krischer, L., and Wassermann, J. (2011). ObsPy—what can it do for data centers and observatories? *Ann. Geophys.* 54 (1), 47–58. doi:10.4401/ag-4838

Morioka, H., Kumagai, H., and Maeda, T. (2017). Theoretical basis of the amplitude source location method for volcano-seismic signals. *J. Geophys. Res. Solid Earth.* 122 (8), 6538–6551. doi:10.1002/2017JB013997

Olson, J. V., and Szuberla, C. A. L. (2005). Distribution of wave packet sizes in microbarom wave trains observed in Alaska. *J. Acoust. Soc. Am.* 117 (3), 1032–1037. doi:10.1121/1.1854651

PySimpleGUI.org (2020). PySimpleGUI, GitHub. Available at: https://github.com/PySimpleGUI/PySimpleGUI (Accessed June, 2020).

Ripepe, M., and Marchetti, E. (2002). Array tracking of infrasonic sources at Stromboli volcano. *Geophys. Res. Lett.* 29 (22), 33–34. doi:10.1029/2002GL015452

Ripepe, M., Marchetti, E., Delle Donne, D., Genco, R., Innocenti, L., Lacanna, G., et al. (2018). Infrasonic early warning system for explosive eruptions. *J. Geophys. Res. Solid Earth*. 123 (11), 9570–9585. doi:10.1029/2018JB015561

Rost, S., and Thomas, C. (2002). Array seismology: methods and applications. *Rev. Geophys.* 40 (3), 2-1–2-27. doi:10.1029/2000rg000100

Schweitzer, J., Fyen, J., Mykkeltveit, S., Gibbons, S. J., Pirli, M., Kühn, D., et al. (2012). "Seismic arrays," in *New manual of seismological observatory practice 2 (NMSOP-2)*. Editor P. Bormann (Potsdam, Brandenburg: Deutsches GeoForschungsZentrum GFZ), 1–80.

Sigmundsson, F., Hooper, A., Hreinsdóttir, S., Vogfjörd, K. S., Ófeigsson, B. G., Heimisson, E. R., et al. (2015). Segmented lateral dyke growth in a rifting event at Bárðarbunga volcanic system, Iceland. *Nature* 517 (7533), 191–195. doi:10.1038/nature14111Pubmed |

Smith, P. (2020). Retreat—a REal-time TREmor analysis tool. *Zenodo*. Available at: http://dx.doi.org/10.5281/zenodo.3820867

Sparks, R. S. J., Biggs, J., and Neuberg, J. W. (2012). Monitoring volcanoes. *Science* 335, 1310–1311. doi:10.1126/science.1219485

Taisne, B., Brenguier, F., Shapiro, N. M., and Ferrazzini, V. (2011). Imaging the dynamics of magma propagation using radiated seismic intensity. *Geophys. Res. Lett.* 38 (4). doi:10.1029/2010GL046068

The ObsPy Development Team (2020a). Beamforming—FK Analysis [Online]. Available at: https://docs.obspy.org/tutorial/code_snippets/beamforming_fk_analysis.html (Accessed June 01, 2020).

The ObsPy Development Team (2020b). ObsPy 1.2.1. *Zenodo* Available at: https://doi.org/10.5281/zenodo.3674645 (Accessed March 11, 2020).

Vogfjörd, K. S., Puglisi, G., and Sigmundsson, F. (2019). Eurovolc—a European network of observatories and research infrastructures for volcanology. *Geophys. Res. Abstr.* 21, 11920.

Wassermann, J. (2012). "Volcano seismology," in *New manual of seismological observatory practice 2 (NMSOP-2)*. Editor. P. Bormann (Potsdam, Brandenburg: Deutsches GeoForschungsZentrum GFZ), 1–77.

Yamakawa, K., Ichihara, M., Ishii, K., Aoyama, H., Nishimura, T., and Ripepe, M. (2018). Azimuth estimations from a small aperture infrasonic array: test observations at stromboli volcano, Italy. *Geophys. Res. Lett.* 45 (17), 8931–8938. doi:10.1029/2018GL078851

Conflict of Interest: The authors declare that the research was conducted in the absence of any commercial or financial relationships that could be construed as a potential conflict of interest.

Copyright © 2020 Smith and Bean. This is an open-access article distributed under the terms of the Creative Commons Attribution License (CC BY). The use, distribution or reproduction in other forums is permitted, provided the original author(s) and the copyright owner(s) are credited and that the original publication in this journal is cited, in accordance with accepted academic practice. No use, distribution or reproduction is permitted which does not comply with these terms.

frontiers in Earth Science

ORIGINAL RESEARCH
published: 24 November 2020
doi: 10.3389/feart.2020.573368

Seismo-Acoustic Characterization of Mount Cleveland Volcano Explosions

Alexandra M. Iezzi[1]†, David Fee[1], Matthew M. Haney[2] and John J. Lyons[2]*

[1]*Geophysical Institute, Alaska Volcano Observatory, University of Alaska Fairbanks, Fairbanks, AK, United States,* [2]*U.S. Geological Survey, Alaska Volcano Observatory, Anchorage, AK, United States*

Volcanic explosions can produce large, ash-rich plumes that pose great hazard to aviation, yet may often have few precursory geophysical signals. Mount Cleveland is one of the most active volcanoes in the Aleutian Arc, Alaska (United States) with at least 65 explosions between December 2011 and June 2020. We characterize the seismo-acoustic signals from explosions at Mount Cleveland over a period of 4 years starting in 2014 when the permanent local instrumentation was installed. While the seismic explosion signals are similar, the acoustic signals vary between explosions. Some explosion acoustic waveforms exhibit a single main compressional phase while other waveforms have multiple compressions. The time lag between seismic and acoustic arrivals varies considerably (up to 2.20 s) at a single station ~3 km from the vent, suggesting a change in propagation path for the signals between explosions. We apply a variety of methods to explore the potential contributions to this variable time lag from atmospheric conditions, nonlinear propagation, and source depth within the conduit. This variable time lag has been observed elsewhere, but explanations are often unresolved. Our results indicate that while changes in atmospheric conditions can explain some of the variation in acoustic arrival time relative to the seismic signal arrivals, substantial residual time lag variations often still exist. Additionally, nonlinear propagation modeling results do not yield a change in the onset time of the acoustic arrival with source amplitudes comparable to (and larger) than Cleveland explosions. We find that a spectrum of seismic cross-correlation values between events and particle motion dip angles suggests that a varying explosion source depth within the conduit likely plays a dominant role in the observed variations in time lag. Explosion source depths appear to range from very shallow depths down to ~1.5–2 km. Understanding the seismo-acoustic time lag and the subsequent indication of a variable explosion source depth may help inform explosion source modeling for Mount Cleveland, which remains poorly understood. We show that even with a single co-located seismic and acoustic sensor that does not always remain on scale, it is possible to provide meaningful interpretations of the explosion source depth which may help monitoring agencies understand the volcanic system.

Keywords: volcano, infrasound, seismology, seismo-acoustic, source depth, explosion

OPEN ACCESS

Edited by:
Jessica Helen Johnson, University of East Anglia, United Kingdom

Reviewed by:
Silvio De Angelis, University of Liverpool, United Kingdom
Stephen R. McNutt, University of South Florida, United States

***Correspondence:**
Alexandra M. Iezzi
amiezzi@ucsb.edu

†Present address:
Alexandra M. Iezzi
Department of Earth Science and Earth Research Institute, University of California, Santa Barbara, California, United States

Specialty section:
This article was submitted to Volcanology, a section of the journal Frontiers in Earth Science

Received: *16 June 2020*
Accepted: *02 October 2020*
Published: *24 November 2020*

Citation:
Iezzi AM, Fee D, Haney MM and Lyons JJ (2020) Seismo-Acoustic Characterization of Mount Cleveland Volcano Explosions. Front. Earth Sci. 8:573368. doi: 10.3389/feart.2020.573368

1. INTRODUCTION

Coupled seismic and acoustic analyses can be used to help understand shallow to subaerial explosion sources, including buried chemical explosions (e.g., Arrowsmith et al., 2010; Jones et al., 2015; Blom et al., 2020) and volcanic eruptions (e.g., Johnson and Aster, 2005; Petersen and McNutt, 2007; Wech et al., 2018). While some volcanoes are heavily instrumented and monitored, many eruptions occur in remote regions where minimal local monitoring equipment exists. Therefore, the ability to characterize a volcanic system with limited equipment (e.g., a single seismo-acoustic pair of sensors, McKee et al., 2018) is valuable to the volcano monitoring community.

Vulcanian eruptions tend to be violent in nature due to the formation of a dome or plug at the top of the conduit allowing for a buildup of pressure beneath (Clarke et al., 2015). The explosive destruction of this plug and subsequent fragmentation of magma in the conduit results in ash-rich volcanic plumes that are hazardous to aviation and pyroclastic fallout that can impact local communities or observers. Infrasound recordings of Vulcanian eruptions are typically characterized by short duration, high-amplitude signals with the potential for jetting or sustained tremor to occur for several minutes after the initial blast (Fee and Matoza, 2013). Sakurajima volcano, Japan is often viewed as a classic example of a Vulcanian system and its seismic and infrasonic explosion signals have been well studied over many years (e.g., Tameguri et al., 2002; Yokoo et al., 2009; Fee et al., 2014; Kim et al., 2015; Fee et al., 2017). Tameguri et al. (2002) describe the "bottom-up" explosion source model of Sakurajima as beginning with an isotropic expansion at a few kilometers depth, whose pressure waves propagate up the conduit, inducing an expansion of the lava cap or plug (viewed as a small increase in pressure on the infrasound sensor) followed by the main acoustic explosion signal. In contrast, a "top-down" model is sometimes considered, where the explosion initiates near the surface due to the pressurized build-up and failure of the plug or lava dome. This model also causes a very long period earthquake (VLP) at depth (Lyons and Waite, 2011).

Mount Cleveland, Alaska, is one of the most active volcanoes in the Aleutian Arc, with recent activity characterized by nearly continuous degassing and elevated surface temperatures, punctuated by short-lived ash-rich explosions that destroy small domes (De Angelis et al., 2012; Dixon et al., 2017; Werner et al., 2017) (www.avo.alaska.edu). The explosion signals at Mount Cleveland appear to be Vulcanian in nature (De Angelis et al., 2012), yet due to its remote setting, the volcanic system is not well-understood. Prompt and accurate characterization of explosions is essential due to the ash hazard to aviation. Satellite observations of ash plume heights resulting from these explosions can be limited because of meteorological clouds as well as latency issues, so geophysical instrumentation is often used for explosion characterization. The first local seismo-acoustic instrumentation included two stations installed at Mount Cleveland in the summer of 2014, so permanent local monitoring data are limited. Temporary, non-telemetered deployments help better understand the volcanic system, such as the installation of six broadband sensors from 2015 to 2016 (Werner et al., 2020; Haney et al., 2019; Power et al., in review). Remote infrasound recordings supplement the local instrumentation for monitoring large explosions (e.g., De Angelis et al., 2012; Iezzi et al., 2019b). While the Alaska Volcano Observatory (AVO) reports observations of Mount Cleveland at the time of each explosion, detailed characterization of the seismo-acoustic signals from Cleveland has not been performed. Here we use local seismo-acoustic instrumentation to better understand and characterize the Mount Cleveland explosions and volcanic system by taking a holistic look at trends in a variety of analysis techniques from numerous explosions. By analyzing Mount Cleveland explosions, we not only will enhance our knowledge of that particular volcano, but our investigations may illuminate similarities to analogous volcanoes worldwide.

A notable feature of the seismo-acoustic observations from Mount Cleveland explosions over the 4-year time period between 2014 and 2018 is that the difference between the acoustic arrival time in relation to the seismic arrival at station CLES (**Figure 1**, referred to as the "seismo-acoustic time lag") is found to vary by up to 2.20 s. If the path and propagation conditions between the explosion source and the receiver are the same, the relative timing between the seismic and acoustic arrivals are expected also to be the same. However, a variable time delay between seismic and acoustic arrivals is observed at many volcanoes similar to Cleveland, implying that the path effects between the explosion source and the receiver may also change. The relative timing between the seismic and acoustic arrivals at co-located seismo-acoustic sensors has been used to help constrain the explosion source location within the conduit of Strombolian and Vulcanian systems, although full explanations are still elusive. Yamada et al. (2016) found that the arrival time differences between seismic and acoustic waveforms vary between 0.5 and 2.1 s at a distance of 5.1 km from the vent of Lokon-Empung volcano, Indonesia. They propose that the cause of the discrepancies does not appear solely to be the atmosphere based on a simple calculation of sound speed given realistic temperature and wind conditions (T = 293 K, winds ±5 m/s), and therefore may be due to source depth changes within the conduit. Ruiz et al. (2006) noted varying time lags of ~9.3–12.6 s (3.516 km from vent) at Tungurahua volcano, Ecuador, which they contend supports a model where explosions occur at different depths within the shallow portion of the conduit (<200 m depth). Ruiz et al. (2006) presented a model consisting of a spatially fixed point source with a variable velocity of the pressure wave in the conduit, but deemed it less likely than the spatially varying source depth. Sahetapy-Engel et al. (2008) used the thermo-acoustic delay times to calculate explosion source depths between 100 and 600 m below the vent at Santiaguito volcano, Guatemala. More recently, Wallace et al. (2020) observed single station seismo-acoustic time lags between

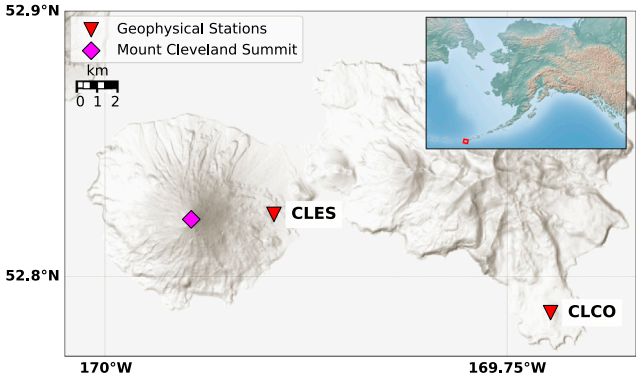

FIGURE 1 | Map of Mount Cleveland and the surrounding area. The summit is denoted by a pink diamond, while the two geophysical stations CLES (3.5 km from summit) and CLCO (15.6 km from summit) are denoted by inverted red triangles. Inset map shows location of Mount Cleveland (red square) in relation to the state of Alaska.

~6 and 17 s (2.1 km from the vent) at Santiaguito over a four-year study, and concluded that the larger time differences suggests a potentially deeper fragmentation source, which is consistent with their petrologic analyses. However, Wallace et al. (2020) do not explore the variability further to calculate corresponding depths of the seismo-acoustic time lag and assumed fragmentation depth. While these studies explore a few of the factors that may affect the seismo-acoustic time delay, none combine the three effects we assume most plausible.

In this manuscript, we perform the first local seismic and acoustic analyses and characterization of explosions at Mount Cleveland between 2014 and 2018. We identify three main factors that may affect the seismo-acoustic time lag, and explore their relative contributions: atmospheric conditions, nonlinear propagation, and source depth within the conduit. We apply a variety of methods on acoustic, seismic, and coupled seismo-acoustic observations aimed at extracting as much information as possible about Mount Cleveland using a single co-located seismo-acoustic station. We then combine the methods to interpret their meaning for the volcanic system and how it may be evolving through time.

2. MOUNT CLEVELAND

Mount Cleveland is a stratovolcano located in the central Aleutians on Chuginadak Island that is roughly 8.5 km in diameter near its base and 1.73 km in elevation above sea level (Miller et al., 1998). As of June 2020, Cleveland has exploded at least 65 times since December 25, 2011, making it one of the most frequently active volcanoes in Alaska and the United States. Recent activity is characterized by nearly continuous degassing and elevated surface temperatures, as well as short-lived ash-rich explosions that destroy small domes (Dixon et al., 2017; Werner et al., 2017) (www.avo.alaska.edu). The closest inhabited community is the village of Nikolski, located 75 km to the east of the volcano on Umnak Island. Due to its remote location, the main hazards from Mount Cleveland explosions are to aviation and scientists visiting the island, with at least ten explosions since 2014 resulting in detectable ash plumes to an altitude surpassing 15,000 ft (4.572 km) (www.avo.alaska.edu). Explosions occur with little to no known precursory activity suggesting explosion sources to be shallow and/or aseismic.

Previous studies on Mount Cleveland include those using satellite observations (Simpson et al., 2002; Dean et al., 2004; Gu et al., 2005; Worden et al., 2014; Wang et al., 2015; Werner et al., 2017), sparse summit gas flights (Werner et al., 2017; Werner et al., 2020), temporary seismic deployments (Janiszewski et al., 2020; Power et al., in review; Haney et al., 2019), and long range infrasound recordings (De Angelis et al., 2012; Iezzi et al., 2019b). Janiszewski et al. (2020) used receiver functions to find a low seismic velocity zone below Cleveland with a minimum vertical extent of 10–17.5 km below sea level that is <5 km in diameter. This suggests a vertically extensive magma storage region with a lack of sharp horizontal boundaries at the top and bottom of this region (Janiszewski et al., 2020). Janiszewski et al. (2020) note that their results are consistent with a well-developed open volcanic conduit system, which may help explain the general lack of precursory seismicity at Cleveland. A recent study by Werner et al. (2020) used a combination of volcanic gas emission rates and melt inclusion compositions from 2016 and found evidence that magma may be residing and degassing in a vertically extensive conduit region ranging in depth between 0.5 and 3.0 km below the summit. Power et al. (in review) focused on characterizing the general seismicity at Mount Cleveland and located hypocenters of volcano-tectonic earthquakes using a temporary seismic deployment in 2015–2016. Haney et al. (2019) performed moment tensor inversions on the three explosions that occurred during the same 2015–2016 deployment, finding a volumetric source in the VLP band (0.25–0.5 Hz) located 400–640 m above sea level (depths of ~1.090–1.330 km beneath the summit). Werner et al. (2017) utilized gas emissions, thermal output, and lava extrusion rates to inform their interpretations on the Cleveland volcanic system. They suggest that the lack of precursory geophysical signals are due to small magma volumes, slow ascent rates, and low magma viscosity. Werner et al. (2017) also note that the persistently high thermal output of Mount Cleveland, even in inter-eruptive periods, is indicative of hot magma high in the conduit and suggest that convection causes the continued presence of shallow magma in the upper conduit. Previous studies such as De Angelis et al. (2012) and Iezzi et al. (2019b) have analyzed infrasound signals from Cleveland explosions. However, these previous studies were based on long-range signals where source observations are complicated by propagation in the atmosphere.

2.1. Monitoring Data

Prior to the installation of the local instruments at Mount Clevelend, the closest seismic station was ~75 km away (Nikolski) and infrasound monitoring was predominantly done using the Dillingham infrasound array (992 km away, De Angelis et al., 2012; Iezzi et al., 2019b) as well as ground-coupled

airwaves (GCAs) on nearby seismic networks (De Angelis et al., 2012; Fee et al., 2016). Cleveland is also monitored by AVO using satellite imagery, both in the visible and infrared bands, but the region is regularly cloudy which often obscures smaller explosion plumes below the cloud deck. Temporary seismic deployments, such as a year-long deployment from 2015 to 2016 (Janiszewski et al., 2020; Haney et al., 2019; Power et al., in review), have also been used to gain information about Mount Cleveland, though they were not telemetered in real time.

The first permanent telemetered local instrumentation was installed in the summer of 2014, allowing for more detailed studies of the volcano than previously possible. This instrumentation currently consists of two stations, each with multiple geophysical instruments. Station CLES (52.8235°N, 169.8951°W) is located 3.5 km east of the summit (**Figure 1**) and consists of a Trillium Compact (120 s period) broadband seismometer sampled at 50 Hz as well as an infrasound sensor. Beginning in August 2014, the infrasound sensor was a USGS VDP-5 sampled at 50 Hz which was replaced in July 2016 by a Chaparral 60UHP sensor sampled at 100 Hz. Station CLCO, located on Concord Point 15.6 km east–southeast of the summit, has a broadband and short period seismometer, web camera, and a 5-element infrasound array (**Figure 1**). In this study we focus on explosion signals recorded by the closest station (CLES) with co-located seismic and infrasound sensors. We do not use station CLCO for most of the analyses due to the increased influence of path effects over the longer distance, lower signal-to-noise ratio, and the station being roughly in line with station CLES and the summit, thereby not increasing azimuthal coverage around the explosion source. Additionally, part of the purpose of this study is to determine how much information about the explosion mechanism can be extracted from a single co-located seismic and infrasound sensor pair, which can sometimes be the only local instrumentation at remote volcanoes.

3. EXPLOSION CHARACTERIZATION

AVO began consistently counting Mount Cleveland explosions on December 25, 2011 with monitoring capabilities consisting of remote infrasound arrays, GCAs detected by regional seismic networks, and satellite imagery (De Angelis et al., 2012). From 2011 onward, most of the activity at Cleveland consisted of cycles of dome building and subsequent dome destruction via explosive eruptions. This study focuses on 22 explosions between November 2014 and May 2018 which corresponds to Explosions 37 through 59 in the current AVO catalog. The explosion numbers considered here are limited by the installation of the first permanent local instrumentation in the summer of 2014 and a long term data outage that began in September 2018 (ending in August 2019). Detailed information on the explosions used in this study are found in **Table 1**. The seismic and infrasound traces at station CLES (**Figure 1**) for these explosions are shown in **Figures 2A,B**, respectively. Explosions are, in general, short-duration Vulcanian blasts, sometimes with infrasonic tremor occurring for several minutes after the initial explosion signal. The characteristics of the seismic signal produced by explosions consists of a low amplitude compressional first motion on the vertical component (**Figure 2A**) and positive first motion on the radial component (outward). The peak velocity for the first 9 s of the explosion signal on the vertical component ranges between 109 and 376 μm/s at a distance of 3.5 km from the vent (**Table 1**). For most explosions, the higher frequency GCA shows up on the seismometer after >9.5 s from the initial arrival, also showing the same variable seismo-acoustic time lag observed by the infrasound sensor. Unlike the similar nature of the seismic signals, the characteristics of the infrasound signal vary substantially between explosions. Peak pressures of the explosion infrasound waveforms at 3.5 km distance range between 21 and 260+ Pa (**Table 1**) and were generally short-duration. Note that 260 Pa represents the maximum pressure range of the infrasound sensor for much of the time period, thus numerous signals are saturated (clipped) and are higher than 260 Pa at a range of 3.5 km. Some explosions exhibit a single main compressional phase (e.g., Explosions 44, **Figure 2B** and **Supplementary Figure S1A**), while other explosions have multiple compressions in a row (e.g., Explosion 42, **Figure 2B** and **Supplementary Figure S1B**). A few explosions have a preceding low amplitude infrasound phase <0.5 s prior to the main explosion onset (e.g., Explosion 40, **Figure 2B** and **Supplementary Figure S1C**).

The state of dome emplacement in Vulcanian systems affects the pressurization in the shallow conduit system (Clarke et al., 2015) and thus influences the explosion process. The repose time (number of days since previous explosion), as calculated from explosion dates provided by AVO (www.avo.alaska.edu), varied between 2 and 257 days over the 4-year study period but generally decreased with time (**Figure 3A**). During some intervals, for example between Explosions 45–49 and 56–59, the repose time remained relatively consistent at less than 54 and 22 days, respectively. AVO reported that at least ten of the 22 explosions resulted in eruption plumes visible in satellite imagery greater than 15,000 ft (4.572 km) in altitude (www.avo.alaska.edu), reinforcing the need and importance of characterizing Mount Cleveland explosions. When possible, AVO records observations of the lava dome in Cleveland's crater using satellite imagery. There appears to be no clear relationship between whether there is no visible dome at the bottom of the crater, dome growth, or a static dome (i.e., dome that has stopped growing) and an explosion occurring (**Figure 3B**). For the 14 explosions for which we have reliable satellite observations before and after the explosion, 8 explosions destroyed an existing dome, 2 explosions left at least part of the dome intact, and 4 explosions occurred with no confirmed dome prior to the explosion. Dome observations, including whether there was no dome, a growing dome, or a static dome prior to explosion, as well as the dome area (and therefore height estimate) used in the propagation calculations,

TABLE 1 | Mount Cleveland seismo-acoustic time lag investigation results.

Explosion number	Date	Seismic onset (UTC)	Time lag (s)	Peak pressure (Pa)	Peak velocity (μm/s)	Repose time (days)	Travel time residual (s)	$VASR_{rel}$	X-corr with Exp 45	Dip angle (°)
37	6 Nov 2014	07:42:49.70	11.95	30	162	154	1.81	3.9	0.48	34.5
38	21 Jul 2015	16:17:41.55	9.75	74	200	257	−0.26	14.1	0.59	25.5
39	7 Aug 2015	06:02:57.90	10.00	61	109	17	−0.35	40.3	0.71	–
40	16 Apr 2016	18:58:05.50	10.20	>260	273	243	−0.28	–	0.95	35.1
41	6 May 2016	02:43:33.60	10.85	>260	354	30	0.88	–	0.73	43.3
42	10 May 2016	15:31:38.90	11.95	140	257	4	1.77	35.4	0.58	43.9
43	24 Oct 2016	21:10:24.55	10.15	>260	161	167	−0.12	–	0.86	21.8
44	24 Mar 2017	16:15:23.90	10.80	260	245	151	−0.32	70.0	0.90	34.0
45	17 May 2017	03:17:38.80	10.00	250	186	54	−0.09	180.6	1.0	32.6
46	4 Jul 2017	11:18:48.15	10.00	>260	243	48	−0.26	–	0.91	36.3
47	22 Aug 2017	18:43:44.10	10.00	260	165	49	−0.02	258.7	0.87	34.3
48	26 Sep 2017	01:47:06.35	9.90	200	145	35	−0.09	260.9	0.94	35.9
49	28 Oct 2017	18:45:01.55	10.15	110	187	32	−0.39	20.1	0.68	–
50	30 Oct 2017	11:19:57.85	9.90	35	288	2	0.03	7.8	0.33	–
51	14 Nov 2017	12:15:24.75	11.40	22	146	15	1.21	3.6	0.60	48.3
52	16 Nov 2017	22:44:06.45	11.10	21	298	2	0.94	3.7	0.59	–
53	13 Dec 2017	13:20:40.90	10.20	>260	372	27	0.06	–	0.81	36.0
54	18 Dec 2017	03:17:46.80	10.65	56	131	5	0.61	45.0	0.80	32.1
55	2 Mar 2018	14:57:01.00	10.85	235	235	74	0.95	73.8	0.90	31.5
56	15 Mar 2018	06:18:55.20	11.30	78	201	13	0.62	7.1	0.87	28.0
57	4 Apr 2018	11:55:21.80	10.30	170	284	20	−0.02	39.4	0.88	29.5
58	13 Apr 2018	15:59:18.50	9.85	24	300	9	−0.66	0.8	0.79	26.8
59	5 May 2018	05:48:45.30	11.00	89	376	22	0.86	10.4	0.80	29.7

Explosion number in AVO catalog, date of explosion, arrival time of seismic onset (UTC), seismo-acoustic time lag (s), unfiltered peak infrasound pressure at CLES (Pa), unfiltered peak velocity (vertical) at CLES (μm/s), repose time since previous explosion (days), travel time residual between observed acoustic travel time and the travel time predicted by atmospheric effective sound speed (s), relative VASR ($VASR_{rel}$), cross-correlation value in relation to example Explosion 45, and dip angle from horizontal (°).

are subject to the availability of clear satellite imagery. Explosions 37–59 (November 2014 to May 2018) are also plotted in **Figure 3B**, showing the varying repose time over the course of the study period.

We note two important caveats for CLES data analysis. The first is that amplitude- and frequency-based analysis can only be used for some of the explosions due to clipping of the CLES infrasound sensor for larger explosions (5 explosions, see **Figure 2B**). Additionally, a GCA appears on CLES seismic data for most explosions (see **Figure 2A**), so some analyses are limited to the first ~9 s of the explosion signal recorded by the seismometer. Station CLCO is farther away from the source than station CLES, so propagation effects to CLCO would likely be more substantial and harder to accurately determine than to CLES. Therefore, arrival time-based analysis of Cleveland acoustic signals at station CLES provides the most complete and reliable assessment, more so than amplitude- or frequency-based calculations at either station.

4. SEISMO-ACOUSTIC TIME LAG INVESTIGATION

The observed variable seismo-acoustic time lag (tt_{obs}) is defined as the time difference between the infrasound travel time (tt_{infra}) and the seismic travel time (tt_{seis})

$$tt_{\mathrm{obs}} = tt_{\mathrm{infra}} - tt_{\mathrm{seis}} \tag{1}$$

The acoustic arrival time in relation to the seismic arrival of the explosion signal at station CLES is found to vary up to 2.20 s for the 22 explosions investigated, as shown by **Figure 2B** where traces are aligned to the seismic arrival. The seismic and acoustic arrival times are picked on unfiltered vertical seismic and infrasound data, respectively, first using a short term average long term average algorithm (STA/LTA, STA length = 0.01 s, LTA length = 0.3 s) before values are manually refined. These seismo-acoustic time lags vary with explosion number (**Figure 4A**) and span a range of 9.75–11.95 s at a distance of 3.5 km from the vent. The distribution of seismo-acoustic time lags for the 22 explosions investigated is skewed towards shorter time lags, with a mean time lag of 10.53 s and median of 10.20 s (**Figure 4B**).

A schematic of the seismo-acoustic propagation paths is shown by **Figure 5**. The seismic wave travels directly from the explosion source (**Figure 5**, Location 1) to station CLES (**Figure 5**, Location 4). This distance is dependent on the explosion source depth. However, because the seismic velocity is an order of magnitude greater than the acoustic velocity (~2,500 m/s compared to ~340 m/s) and the source-receiver distance is small (~3.5 km), the exact distance does not have a major effect on the seismic travel time (tt_{seis}). We also assume that the seismic velocity is constant and does not change between explosions or along the path. The calculation of tt_{seis} is shown by the following equation.

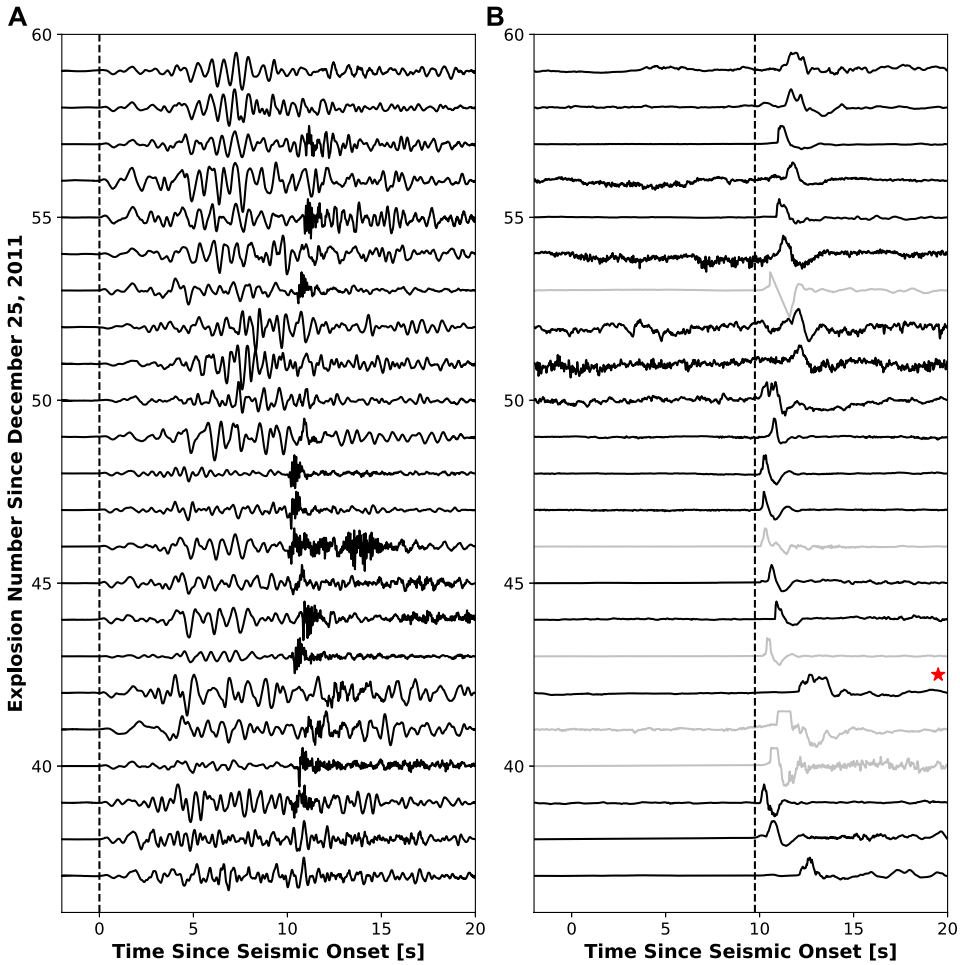

FIGURE 2 | Normalized, unfiltered **(A)** seismic and **(B)** infrasound waveforms at station CLES for explosions used in this study (Explosions 37–59). Waveforms are aligned where time zero corresponds to the onset of the explosion signal on the seismometer. The infrasound waveforms that clipped are shown in gray in **(B)** and the date of the infrasound sensor change in July 2016 is shown by a red star. The higher frequency ground-coupled airwave can be seen for most explosions arriving after ~9.75 s in **(A)**. Vertical line in **(B)** represents the earliest acoustic arrival of 9.75 s.

$$tt_{\text{seis}} = \frac{d_{\text{seis}}}{v_{\text{seis}}} \tag{2}$$

Using values of v_{seis} = 2,500 m/s and d_{seis} = 3,800 m (assuming an explosion source near the summit), the seismic travel-time between the explosion and receiver (tt_{seis}) is 1.52s. The wave recorded by the infrasound sensor has a more complex propagation path. It propagates from the explosion source in the conduit (**Figure 5**, Location 1) to the bottom of the crater and vent location (**Figure 5**, Location 2) at acoustic velocity within the conduit (v_{conduit}) over a distance equivalent to the source depth (d_{source}). Then, the wave propagates from the bottom of the crater (**Figure 5**, Location 2) to the top of the crater (**Figure 5**, Location 3) then to station CLES (**Figure 5**, Location 4) at the effective sound speed (c_{eff}) ("Atmospheric Effects" section).

The travel time of the pressure wave that is recorded by the infrasound sensor (tt_{infra}), and therefore variable observed acoustic time lag (tt_{obs}), is most likely affected by the following factors: the atmosphere (tt_{atm}, "Atmospheric Effects" section), potential nonlinear propagation ($tt_{\text{nonlinear}}$, "Nonlinear Propagation" section), and distance from the crater floor to the source in the conduit (d_{source}) coupled with potentially varying conduit material velocities (tt_{conduit}, "Source Depth Within the Conduit" section). We summarize the various contributions on the arrival time recorded by the infrasound sensor (tt_{infra}) as follows, and discuss them in subsequent sections:

$$tt_{\text{infra}} = tt_{\text{atm}} - \Delta tt_{\text{nonlinear}} + tt_{\text{conduit}} \tag{3}$$

4.1. Atmospheric Effects

Variations in wind and temperature affect the propagation velocity of infrasound. These effects have been the source of multiple recent studies of volcanic explosions in Alaska (e.g., De Angelis et al., 2012; Iezzi et al., 2019b; Schwaiger et al., 2019;

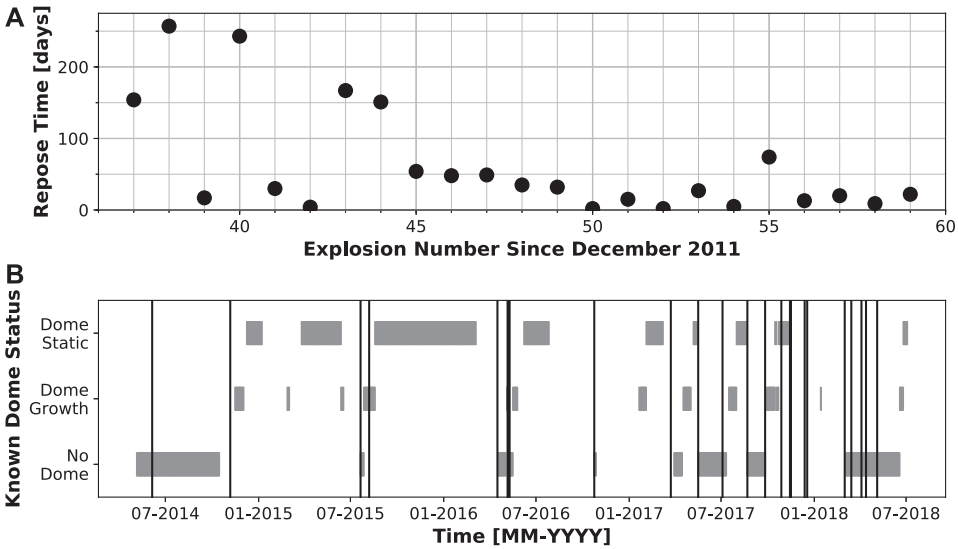

FIGURE 3 | Dome emplacement and explosion relationship from mid-2014 to mid-2018. **(A)** Repose time (in days) prior to each explosion as a function of explosion number. **(B)** Dome status confirmed by satellite imagery. Categories consist of (i) "no dome": when there was no visible dome within the crater, (ii) "dome growth": when a dome was actively growing in size, and (iii) "dome static": when there was a dome that had ceased growing. Vertical lines denote explosions, which vary in repose time over the course of the study period.

Schwaiger et al., 2020). Infrasound propagates in the atmosphere at the speed of sound, defined as

$$c = \sqrt{\gamma R T} \tag{4}$$

where γ is the specific heat ratio, R is the universal gas constant, and T is the temperature (Pierce, 1981). In a realistic moving atmosphere, this adiabatic sound speed (**Eq. 4**) is modified by the vector component of the horizontal wind velocity in a particular direction ($\vec{u} \cdot \vec{v}$) and is termed the effective sound speed (c_{eff}), defined as (Salomons, 2001; Fee and Matoza, 2013)

$$c_{\text{eff}} = c + \vec{u} \cdot \vec{v} \tag{5}$$

For Cleveland explosions registered at station CLES, the shortest observed time lag is 9.75 s (requiring a c_{eff} of 0.392 km/s over a range of 3.826 km) while the longest time lag is 11.95 s (requiring a c_{eff} of 0.320 km/s over a range of 3.826 km). This spread in effective sound speeds is unlikely, even considering the range of extreme wind and temperatures at Cleveland, as it would require winds of approximately 70 m/s sustained along the entire travel path. This would create very high noise levels at the site. We apply two different methods for inferring the contribution of the atmosphere on acoustic arrival time at CLES (i.e., estimating a unique c_{eff} for each explosion).

The first method to better understand the possibility of the atmosphere causing the variable observed seismo-acoustic time lags uses an atmospheric reconstruction model, AVO-G2S (Schwaiger et al., 2019), as no local weather stations or *in-situ* atmospheric data are available. The atmospheric conditions at Mount Cleveland are reconstructed at the closest 6-h interval for each explosion. Within AVO-G2S we use the National Centers for Environmental Prediction (NCEP) Reanalysis data (Kistler et al., 2001) for the lower atmosphere with resolution of 2.5° spatially and 6 h temporally. Once the atmosphere is reconstructed, a 1D stratified atmospheric profile at the location of Mount Cleveland (52.822°N, 169.945°W) is extracted from the reconstruction. The scalar value for effective sound speed (c_{eff}) above the vent (z = 1.8 km asl) in the direction of CLES (86.6° from N) is used to calculate the predicted acoustic travel time from the summit to CLES based on atmospheric conditions at the time of each explosion:

$$tt_{\text{atm}} = \frac{d}{c_{\text{eff}}} \tag{6}$$

where d = 3.826 km (the hypotenuse distance from the summit to station CLES) plus the hypotenuse distance from the top of the dome to the crater rim (**Figure 5**, Locations 2–3). This distance is calculated by converting the dome area observed in satellite imagery by AVO to a dome height above the crater floor, using the ArcticDEM digital elevation model (Porter et al., 2018) for crater shape. We note that the presence or absence of a dome only changed the infrasonic path length by ~40 m at most (depending on the size of the dome), which at a reasonable acoustic speed corresponds to 0.12 s.

The second method leverages the use of the explosion signal arrival time at one of the elements from the infrasound array (CLCO, element 1) that is at a similar azimuth from the vent as station CLES. The azimuths from the Cleveland summit to stations CLES and CLCO are 86.6° and 109.5°, respectively, so the azimuthal difference between the two stations is 22.9°. The infrasound arrival time of the

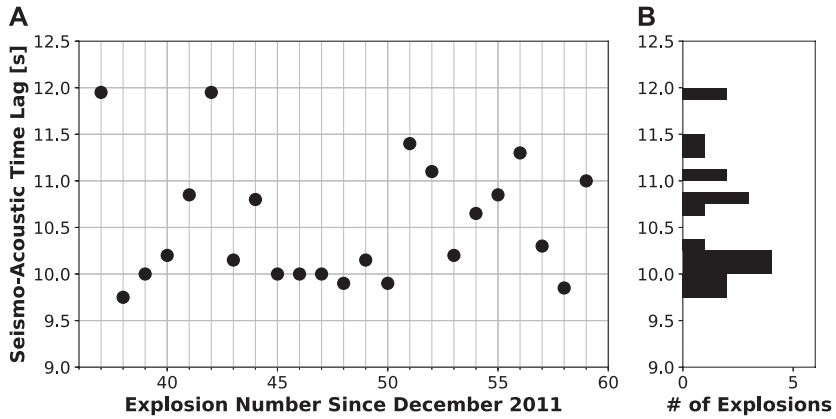

FIGURE 4 | Seismo-acoustic time lag for Mount Cleveland explosions **(A)** as a function of explosion number, and **(B)** as a histogram of the time lag distribution. Histogram bins are 0.125 s in width.

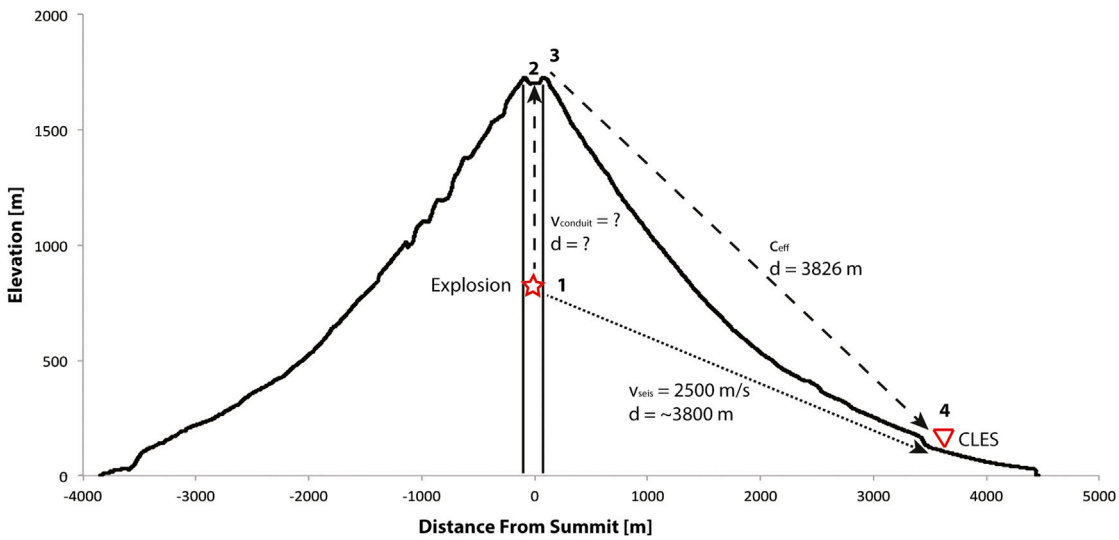

FIGURE 5 | Breakdown of propagation segments for the seismic and infrasound paths. Location 1 is the explosion, Location 2 is the bottom of the crater (dome surface), Location 3 is the summit, and Location 4 is station CLES. The signal recorded by the infrasound sensor (dashed line) propagates from Location 1 through Locations 2, 3, and 4, while the initial signal recorded by the seismometer (dotted line) travels directly from Location 1 to Location 4. Elevation profile from the Polar Geospatial Center ArcticDEM (Porter et al., 2018). Vertical exaggeration is ~2.5.

explosion at station CLCO is picked and the two acoustic arrival times are subtracted. Using the distance between the stations (12.33 km) and the difference in arrival times, the effective sound speed based on station arrival times is calculated using **Eq. 6**.

Our results indicate that AVO-G2S-derived c_{eff} values are systematically lower than c_{eff} values found using the acoustic arrival time difference between CLES and CLCO by 0–25 m/s (**Figure 6A**). The observed travel time is calculated as the time lag between the seismic and infrasound arrivals at CLES, plus seismic travel time from the conduit to CLES (tt_{seis}, **Eq. 2**). Both the observed and predicted (tt_{atm}) travel times as a function of explosion number are shown in **Figure 6B**. It is clearly seen that the relatively large variation in observed acoustic travel times is not well predicted by either the atmospheric conditions of global reanalysis files (model-based) or calculations between CLES and CLCO arrivals (data-based). For the rest of our analyses, we choose the second method for effective sound speed (c_{eff}) calculation. If the seismo-acoustic time lags were solely due to changes in the atmosphere, we would expect a very strong correlation with the effective sound speed. However, there is only a weak negative relationship between the two values (**Figure 6C**). From these analyses, we conclude that while changing atmospheric conditions may partially contribute to the variable seismo-acoustic time lag observed at Cleveland, there is a lack of evidence that it is the main cause for the observed variations.

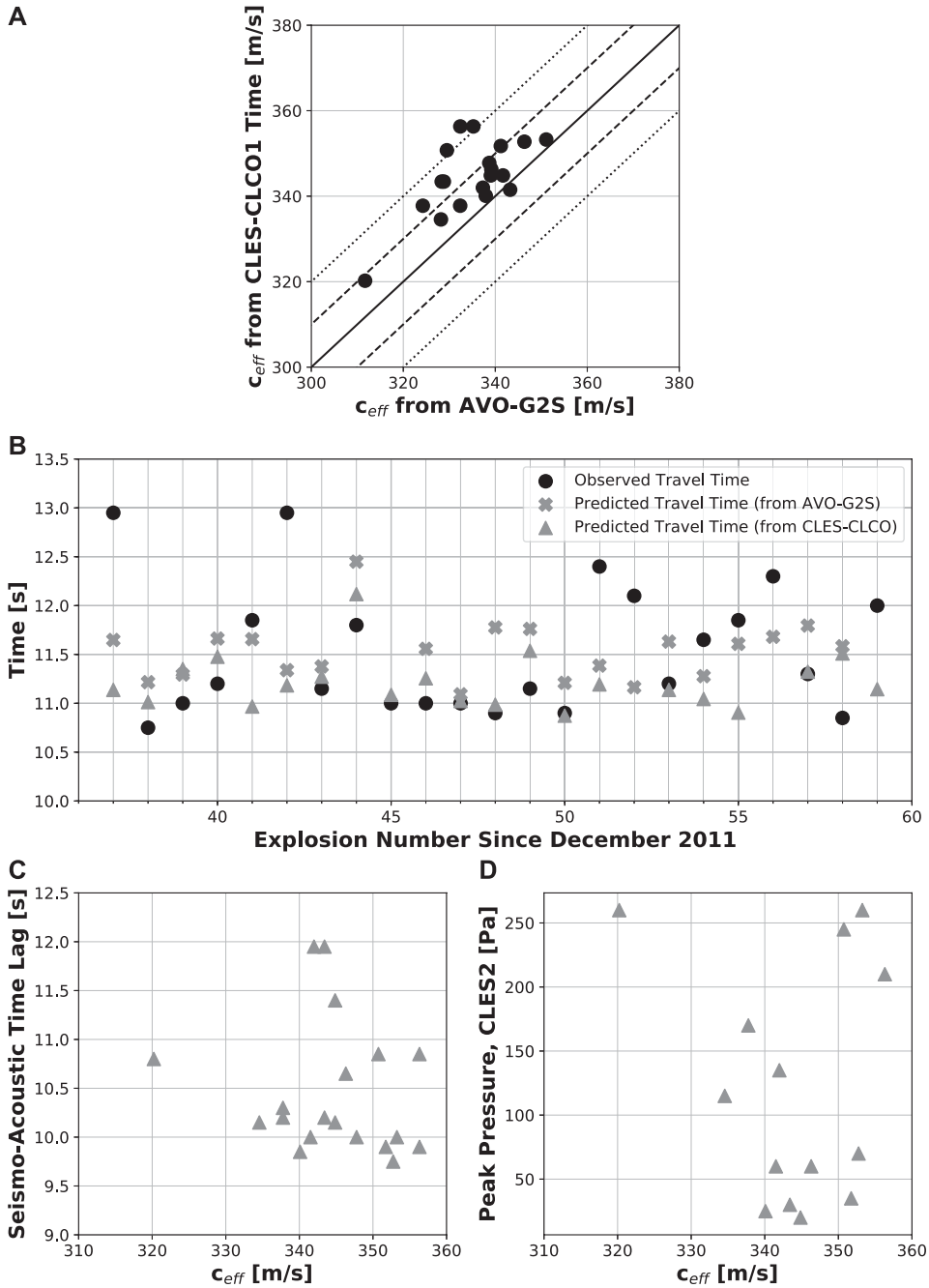

FIGURE 6 | Predicted acoustic travel time based on atmospheric effects. **(A)** Derived c_{eff} from the two methods, 1) using AVO-G2S and 2) the acoustic arrival time difference between stations CLES and CLCO1. The solid line is 1:1 (values are exactly the same), with dotted lines being successively offset by 10 m/s. **(B)** Observed (tt_{obs}, black dots) acoustic travel time, predicted (tt_{atm}) acoustic travel time from the summit to station CLES using AVO-G2S (gray crosses), and predicted (tt_{atm}) acoustic travel time from the acoustic arrival time difference between stations CLES and CLCO1 (gray triangles). **(C)** Seismo-acoustic time lag vs effective sound speed (c_{eff}) using the CLES/CLCO arrival times for each explosion, showing a weak negative relationship. **(D)** Peak pressure at station CLES vs effective sound speed (c_{eff}) for each explosion that did not clip the infrasound sensor. No correlation indicates that the larger amplitude explosions did not happen to occur during times of higher effective sound speeds.

4.2. Nonlinear Propagation

A second factor that may contribute to a change in acoustic propagation time is nonlinear propagation, which is often neglected in local infrasound studies but mentioned as a potential source of error and uncertainty (e.g., Fee et al., 2017; Iezzi et al., 2019a). However, the potential impact of nonlinear propagation on the arrival time ($tt_{\text{nonlinear}}$) should be quantified, as nonlinear waves with supersonic sound speeds have been

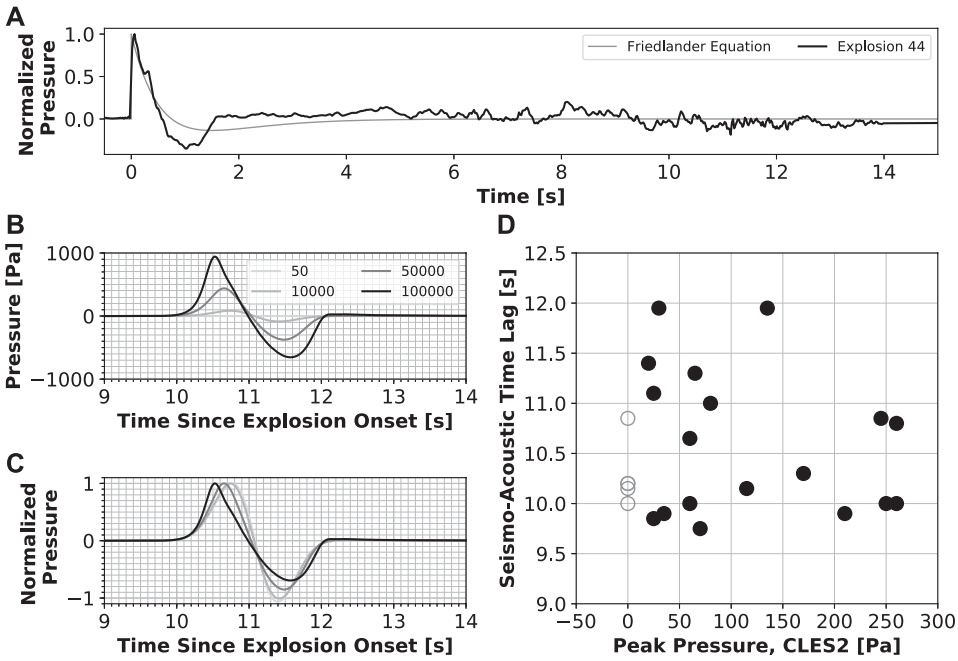

FIGURE 7 | Potential contributions to the seismo-acoustic time lag from nonlinear propagation. **(A)** Friedlander Equation for a blast wave (gray) with normalized Explosion 44 waveform (black). **(B)** FDTDWave simulation results over a flat plane for source pressures between 50 Pa and 100 kPa at a range of 3.8 km from the source. **(C)** Normalized FDTDWave simulation results from the previous subplot. **(D)** Seismo-acoustic time lag vs peak pressure at CLES for explosions that did not clip the infrasound sensor. Open circles represent the time lag for explosions that clipped the infrasound sensor, plotted at a peak pressure of zero.

observed for volcanic explosions (e.g., Yokoo and Ishihara, 2007; Marchetti et al., 2013).

For very high amplitude acoustic sources such as some Vulcanian explosions, the sound waves produced may travel faster than the speed of sound (i.e., supersonic) and propagate nonlinearly. In nonlinear propagation, the waveform distorts as it travels, where the compressional phase travels faster than the rarefaction, potentially steepening into a shock wave (Atchley, 2005; Reichman et al., 2016; Maher et al., 2020). This shock wave is often described by the Friedlander equation (Friedlander, 1946), which defines the pressure of a shock wave ($p(t)$) as

$$p(t) = P_s e^{-\frac{t}{t^*}}\left(1 - \frac{t}{t^*}\right) \tag{7}$$

where P_s is the source overpressure and t^* is the relaxation time (time when the rarefaction begins after the compression returns the ambient pressure). This equation for a theoretical blast wave using $t^* = 0.75$ (value chosen to resemble data from Cleveland explosions) is shown as **Figure 7A**, along with the waveform for Explosion 44 from Cleveland. A recent study by Maher et al. (2020) performed a detailed analysis of local infrasound data from Sakurajima volcano and the potential impact of spectral energy transfer to higher frequencies due to nonlinear propagation. They find that the effects of nonlinear propagation have a second-order impact on source quantification, whereas the effects of wind and topography may be more influential on the recorded waveform. de Groot-Hedlin (2016) find that nonlinearity has a greater effect on the frequency of the waveform as compared to the amplitude as infrasound propagates away from the source. To our knowledge, there has not been a thorough study on the impact on arrival time due to nonlinear propagation for volcanic explosions.

We note that peak pressures at CLES do not appear to strongly correlate with seismo-acoustic time lags (**Figure 7D**), indicating that nonlinear propagation (if present) has minimal effect on the seismio-acoustic time lag for Cleveland explosions. This is consistent with the findings of Maher et al. (2020), where nonlinear propagation was found to be a secondary effect on the observed waveform. However, it does appear that the highest peak pressures and those that clipped the infrasound sensor (**Figure 7D**, open circles) had lower seismo-acoustic time lags. Additionally, we investigate the connection between higher amplitude explosions and the atmospheric conditions. The lack of correlation between the peak pressure at station CLES (for events that did not clip the sensor) and the effective sound speed (**Figure 6D**), indicates that the larger amplitude explosions did not occur during times of higher effective sound speeds.

We use a 2D finite-difference time-domain (FDTD) code, FDTDWave (de Groot-Hedlin, 2016), to model the potential impact of nonlinear propagation on the acoustic arrival time. Our simulations involve propagating a source with a maximum frequency of 2.0 Hz over a flat plane to a range of 20 km with synthetic receivers spaced every 100 m. We set the transition from nonlinear to linear propagation at 1% ambient pressure (de Groot-Hedlin, 2016), though we note that testing was performed varying this parameter between 0.5 and 5% with no change in our results. We input source pressures ranging from 50 Pa to 100 kPa and note that

current modeling capabilities using this code are limited to a linear, Gaussian input source.

Nonlinear propagation modeling results for a synthetic receiver at 3.8 km from the source (slant distance from the Cleveland summit to station CLES) show the expected distortion due to increasingly nonlinear propagation (**Figures 7B,C**). As the source pressure increases, the compression travels faster while the rarefaction travels relatively slower, similar to results in Maher et al. (2020). Therefore, the arrival time of the peak compression decreases with higher source pressure (**Figure 7C**). However, even using extreme values of source peak overpressures (**Figure 7C**, approximately 1,000 Pa at the range of CLES), we are not able to form a full shock front or detect a noticeable change in arrival time of the initial explosion signal recorded by the infrasound sensor. Therefore, we do not find a quantifiable impact on tt_{infra} from nonlinear propagation effects.

4.3. Source Depth Within the Conduit

The effects of the atmosphere and nonlinear propagation can be reasonably approximated using available data and modeling. Therefore, in previous sections we constrained these values first and assume all residual time discrepancies are due to a variable explosion source depth (d_{source}) within the conduit and/or conduit velocity (v_{conduit}). Explosion source depth and conduit conditions are less well-understood than other aforementioned factors affecting the seismo-acoustic time lag.

The travel time of a pressure wave in the conduit from the explosion depth to the bottom of the crater can be estimated by:

$$tt_{\mathrm{conduit}} = \frac{d_{\mathrm{source}}}{v_{\mathrm{conduit}}} \tag{8}$$

Due to the poorly understood conditions within the conduit and limited seismo-acoustic data, we investigate the potential variable explosion source depth using three techniques: volcano acoustic seismic ratio (VASR), seismic cross-correlation between explosions, and seismic particle motion analysis. We also tried methods of investigating the arrival time of various seismic frequency components and CLES/CLCO seismic amplitude ratio. We include those analyses in the **Supplemental Material**, as they were not found to be as useful as the three methods in this section (see **Supplementary Figures S2 and S3** along with associated text). We are not able to estimate the actual source depth due to the limited data.

4.3.1. Volcano Acoustic Seismic Ratio

Volcanic explosion energy couples into both the atmosphere as acoustic energy and ground as seismic energy. We follow the methods of Johnson and Aster (2005) to calculate the relative partitioning of the energy that is recorded as acoustic and seismic waves, termed Volcano Acoustic Seismic Ratio (VASR). Lower VASR may suggest a deeper explosion source within the conduit; however, caution should be exercised in this interpretation as there are many other factors that can affect the energy partitioning. Note, this can only be used for explosions that did not clip the infrasound sensor.

The acoustic energy (E_{acoustic}) radiated can be calculated by integrating over a hemispherical surface, assuming a monopole source and homogeneous atmosphere (e.g., Firstov and Kravchenko, 1996; Johnson, 2003; Vergniolle et al., 2004; Johnson and Aster, 2005)

$$E_{\mathrm{acoustic}} = \frac{2\pi r^2}{\rho_{\mathrm{atmos}} c_{\mathrm{atmos}}} \int \Delta P(t)^2 \mathrm{d}t \tag{9}$$

where ρ_{atmos} is the air density, c_{atmos} is the speed of sound, and ΔP is the excess pressure. Similarly, the seismic energy (E_{seismic}) for an isotropic source located at the top of a homogeneous halfspace can be calculated using (Boatwright, 1980; Johnson and Aster, 2005)

$$E_{\mathrm{seismic}} = 2\pi r^2 \rho_{\mathrm{earth}} v_{\mathrm{seis}} \frac{1}{A} \int S^2 U(t)^2 \mathrm{d}t \tag{10}$$

where r is the distance between source and receiver, S is the seismic site response, A is the attenuation, ρ_{earth} is the volcano density, and U^2 is the squared particle velocity.

We follow suggestions of Johnson and Aster (2005) and use a bandpass filter between 0.5 and 12 Hz for both acoustic and seismic traces, ρ_{atmos} = 1.2 kg/m^3, c_{atmos} = 340 m/s, ρ_{earth} = 2,000 kg/m^3, and v_{seis} = 2,500 m/s. Note since we do not have good estimates of the seismic attenuation or site response, the values we calculate are only relative to other Cleveland explosions (termed "relative VASR", VASR$_{\mathrm{rel}}$) since we set S and A equal to one (i.e., the seismic portion is not true "energy") and should therefore not be compared with values from other studies. A similar method was used in Fee et al. (2020). Energies are calculated over the first 9 s of the explosion signal onset (infrasound calculation is delayed by the seismo-acoustic time lag) since GCAs appear for most explosions on the seismic data after this time.

VASR$_{\mathrm{rel}}$ is variable for the explosions investigated here (**Figure 8A**), with Explosions 45, 47–48 having the highest VASR$_{\mathrm{rel}}$ and the rest of the explosions being lower. While there is no trend observed between low values of VASR$_{\mathrm{rel}}$ and the seismo-acoustic time lag (**Figure 8B**), the three explosions with the highest VASR$_{\mathrm{rel}}$ values (Explosions 45, 47–48) have low seismo-acoustic time lags and none of the explosions with higher seismo-acoustic time lags exhibited high values of VASR$_{\mathrm{rel}}$.

4.3.2. Seismic Cross-Correlation

Correlation between seismic waveforms can be used to help determine precise seismic source locations and identify similar source properties from the recorded waveforms. The premise is that seismicity that occurs in the same location may have very similar waveforms due to the seismicity experiencing the same propagation effects over the same path between the source and receiver (Waldhauser and Ellsworth, 2000; Green and Neuberg, 2006; Varley et al., 2010). Using each explosion as a template, we cross-correlate the vertical trace with the rest of the explosions. The seismic data are trimmed to a 10.5 s window surrounding

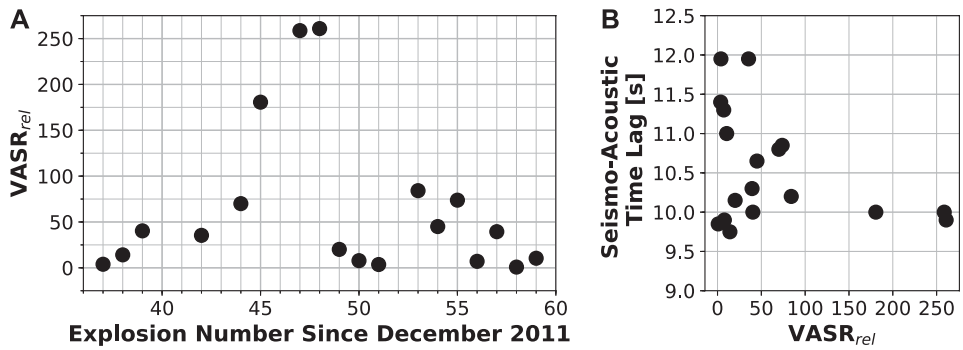

FIGURE 8 | Relative VASR (VASR$_{rel}$) for explosions that did not clip the infrasound sensor **(A)** as a function of explosion number and **(B)** compared to the seismo-acoustic time lag.

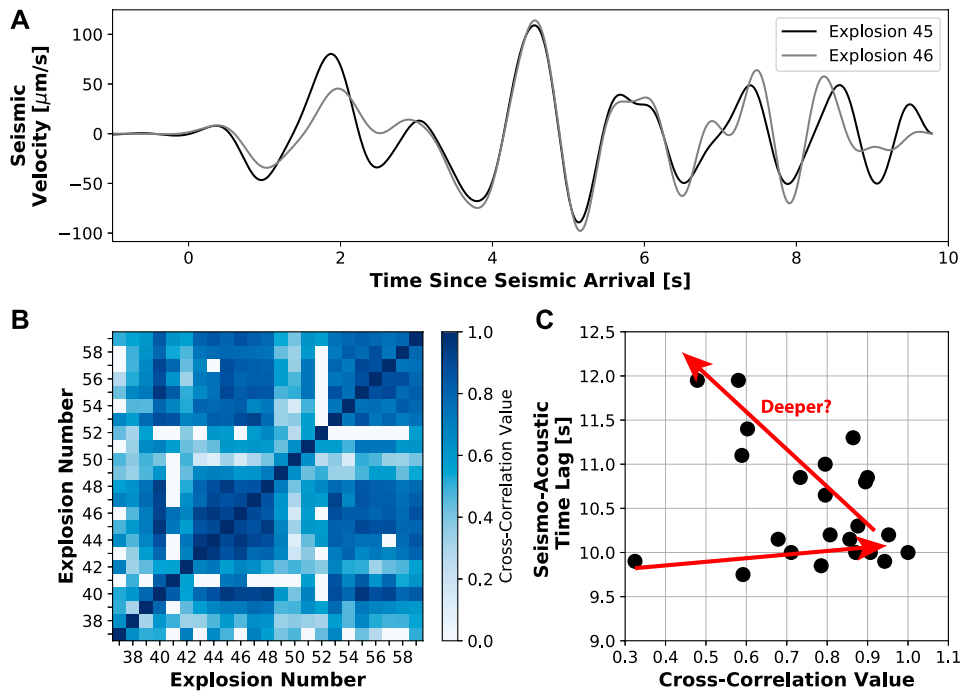

FIGURE 9 | Seismic cross-correlation analysis in the 0.1–1.0 Hz frequency band. **(A)** Waveforms for Explosions 45 and 46 with a cross-correlation value of 0.91. **(B)** Seismic cross-correlation values for all explosions. **(C)** Seismo-acoustic time lag vs cross-correlation value for example Explosion 45 compared to other explosions. As the time lag increases, the cross-correlation value increases to a maximum and then decreases again (red arrows).

each explosion, starting 1.5 s prior to the explosion onset and ending 9 s after to avoid the GCAs. The data are bandpass filtered between 0.1 and 1.0 Hz.

The correlation of the seismic waveforms between explosions is variable. An example of the similarity between the highly correlated Explosions 45 and 46 (correlation value of 0.91) in this frequency band is shown by **Figure 9A**. Cross-correlation results for all explosions are shown in **Figure 9B**, where the diagonal line represents each event correlated with itself (cross-correlation value of 1). There is a section of higher correlation values in the center of **Figure 9B** (Explosions 43–48), which not only occur sequentially in time, but also have a fairly stable time lag around 10.0 s (**Figure 4A**). We discuss this further in the "General Characterization of Explosions" section. Explosions 53–59 also have high correlation values (**Figure 9B**), but in contrast to the previous cluster, the corresponding seismo-acoustic time lags are not similar (**Figure 4A**). Explosion 45 appears to have higher correlation values with the other explosions (**Figure 9B**) as well as a time lag close to the median (**Figure 4A**). The cross-correlation values between Explosion 45 and all other explosions are compared with the seismo-acoustic time lag of each explosion (**Figure 9C**). The relationship has a "V" shape, where the cross-correlation

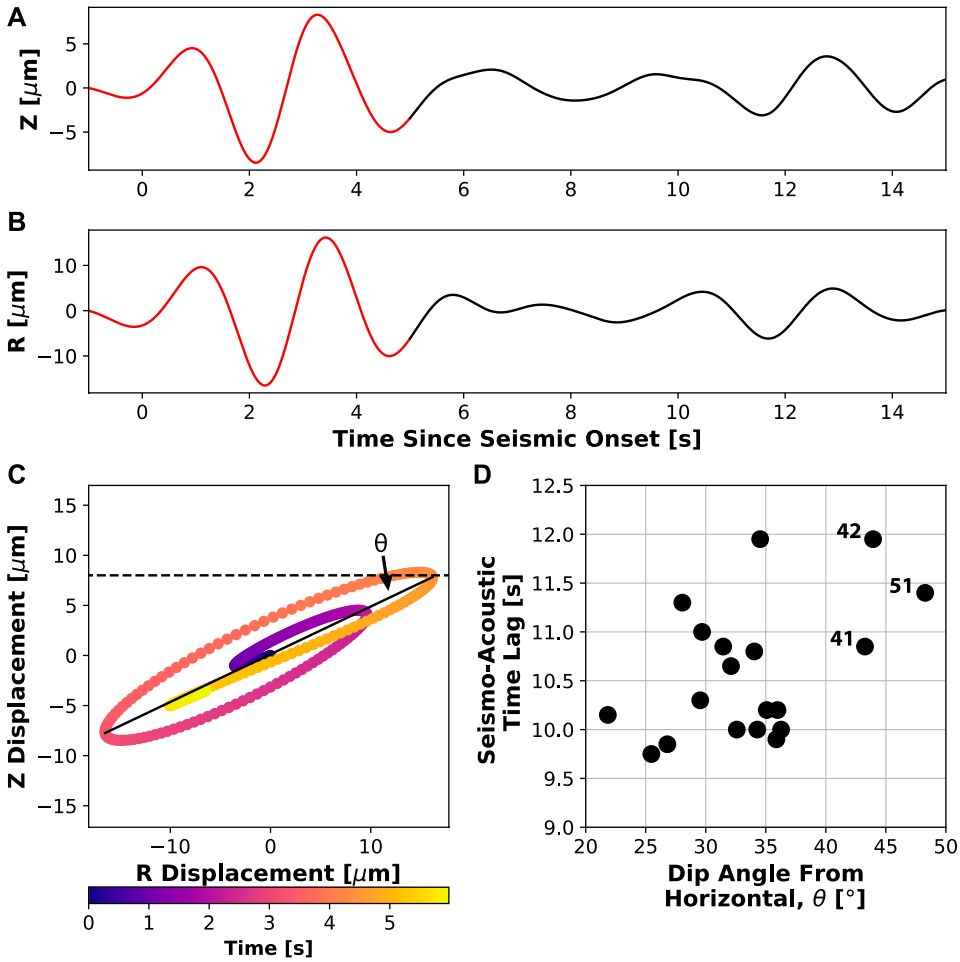

FIGURE 10 | Particle motion analysis for example Explosion 38 in the 0.25–0.5 Hz frequency band. **(A)** Vertical seismic displacement. **(B)** Radial seismic displacement. **(C)** Particle motion for the first 6 s of the explosion (red section in panels **(A)** and **(B)**), colored as a function of time. The solid black line is the least-squares fit, allowing for the computation of dip angle from horizontal (θ) **(D)** Time lag vs. dip angle from horizontal (θ), generally showing a trend where larger time lags tend to have larger dip angles (R-squared value of 0.22).

value increases slightly/remains constant from the lowest time lag, reaches a maximum correlation value at the time lag associated with Explosion 45 (time lag = 10.00 s, cross-correlation value = 1), then the cross-correlation value decreases again as the time lag continues to increase. This indicates that explosion waveforms become more similar as they approach the time lag of Explosion 45. This pattern occurs, to some extent, for most of the explosions with time lags around 10 s. Therefore, explosions with similar seismic waveforms, as measured by the cross-correlation value between them, may occur at similar depths within the conduit, assuming that the seismo-acoustic time lag is related to the source depth.

4.3.3. Seismic Particle Motion

Analysing the particle motion of the three-component seismic data may help understand the explosion source depth within the conduit (e.g., Rowe et al., 1998), or at least the source depth relative to other explosions at Mount Cleveland. Here we examine the particle motion and dip angle for each explosion to get an estimate of the depth. Seismic data at station CLES are integrated from velocity to displacement. Then they are bandpass filtered between 0.25–0.5 Hz and rotated from North (N) and East (E) components to Radial (R) and Transverse (T) components with respect to the vent location (**Figures 10A,B**). Particle motion analysis is performed for the first 6 s of the seismic explosion signals, which generally shows stable particle motion.

The dip angle (θ) is defined as the angle below the horizontal of the least squares fit to the first 6 s of the R and Z components of the displacement (**Figure 10C**). Dip angles range from 21.8–48.3° and are distributed fairly uniformly across this range. Explosions with larger dip angles from horizontal tend to correspond to larger seismo-acoustic time lags (**Figure 10D**). Four explosions are excluded from this analysis (Explosions 39, 49, 50, and 52) for not having rectilinear motion in the first 6 s of the explosion, and therefore no clear dip angle. We caution that near-surface effects (e.g., Neuberg and Pointer, 2000) may affect the absolute dip angle so a direct conversion to depth is not taken here. However,

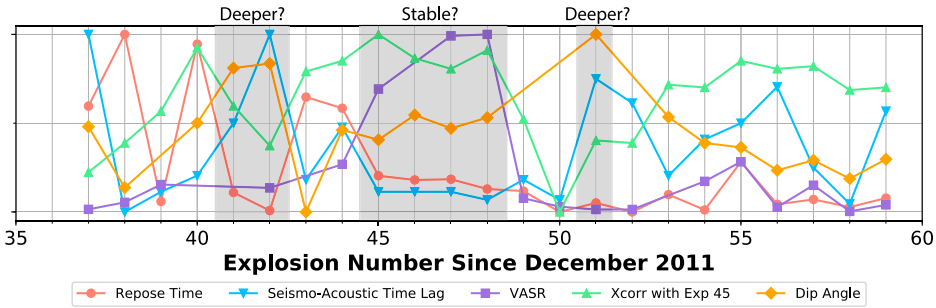

FIGURE 11 | Summary figure of trends as a function of explosion number. The five parameters plotted have each been normalized between 0 and 1 and consist of repose time (days), seismo-acoustic time lag (s), $VASR_{rel}$, cross-correlation value with Explosion 45, and dip angle from horizontal (θ) (°). The period of apparent stability in the volcanic system (Explosions 45–48) and explosions that are believed to be initiated deeper within the conduit (Explosions 41, 42, and 51) are highlighted with gray shading.

these near surface effects are assumed to be constant over time and minimal in this low frequency band, therefore the relative changes in dip angle between explosions indicate a changing source depth. The three events with dip angles >40° are Explosions 41, 42, and 51, all of which have large differences (>1 s) between the observed and predicted arrival time based on atmospheric conditions (**Figure 6B**). This suggests relatively deeper sources for explosions with larger time lags than those with shorter time lags. Thus, the pressure wave travels a longer distance prior to reaching CLES, therefore having a larger time delay compared with the seismic arrival.

5. DISCUSSION

5.1. General Characterization of Explosions

The activity of Mount Cleveland has fluctuated through time and it remains one of Alaska's most historically active volcanoes. The time period analyzed in this study (2014–2018) contains the transient dome building and destruction styles that Cleveland has been known to produce. In 2001, Cleveland exhibited higher eruptive activity with large volcanic plumes (Dean, 2002; Simpson et al., 2002; Dean et al., 2004; Gu et al., 2005). After this time, the volcano was relatively quiet until December 2011, when activity was again heightened and AVO began recording their current explosion catalog. While most of the activity from 2011 to the time of writing was Vulcanian in nature, two explosions in 2013 book-ended a continuous eruption lasting 44 h that was recorded by the infrasound array and as GCAs by the seismic network at Okmok volcano (Power et al., 2020). Additionally, we note that the repose time prior to the most recent explosion at the time of writing (June 2, 2020), was 510 days, the longest repose time in 9 years so it appears the volcano may have entered a new eruptive phase. Explosion dynamics may still be similar though.

Repose time prior to explosions within the study period varied between 2 and 257 days and appeared to occur irrespective of whether a lava dome extruded and was visible on the crater floor (**Figure 3B**). This is surprising, as we expected the existence and size of a dome to have an impact on the amount of pressure that can be built up in the shallow conduit system prior to the explosion. Therefore, we assume that the observation of "no dome" visible on the crater floor in satellite imagery still means that some form of hardened plug occurs at the top of the conduit that causes pressure to build within the conduit and create the next Vulcanian explosion. We note that permanent gas instrumentation may help better understand this relationship between the dome and subsequent build up of pressure, due to the nearly continuous degassing from fractures within the dome surface.

Unlike the similar nature of the seismic explosion signals, the characteristics of the infrasound signal varied substantially between explosions. Peak pressures at 3.5 km distance from the summit ranged between 20 and 260+ Pa for short-duration Vulcanian explosions, sometimes with acoustic tremor occurring for several minutes after the initial blast. The waveforms of some explosions were similar to a typical blast wave (e.g., Explosion 44, **Figure 7A**) where the onset is very sharp, and potentially propagated faster than the expected speed of sound. Some explosions have a preceding low amplitude infrasound phase <0.5 s prior to the main explosion onset that may be attributed to a minor increase in pressure due to the swelling or "uncorking" of the lava plug within the crater (e.g., Explosion 40, **Figure 2B**). This has been seen at other similar volcanoes such as Lokon-Empung (Yamada et al., 2016), Sakurajima (Yokoo et al., 2009), and Suwanosejima (Yokoo and Iguchi, 2010). Some explosions exhibit a single main compressional phase (e.g., Explosion 44, **Figure 2B** and **Supplementary Figure S1A**) while other explosions have multiple compressions in a row, which may correspond to a "slow" or complex destruction of the dome (e.g., Explosion 42, **Figure 2B** and **Supplementary Figure S1B**). These explosions with multiple compressions have been seen at Sakurajima volcano (e.g., Fee et al., 2014) as well. These observations suggest the surficial component of the explosions, including dome destruction, is complex and variable at Mount Cleveland. We note that some of these features may be obscured in the signals that clipped the infrasound sensor. AVO installed an

infrasound sensor in July 2018 with a higher dynamic range that should not clip at station CLES for future explosions of Mount Cleveland.

A notable period of activity is the cluster of Explosions 45–48 (May 2017 to September 2017, see **Figure 11**). These events had repose intervals between 35 and 54 days (**Figure 3A**), similar seismo-acoustic time lags of ~10.00 s (**Figure 4A**), similar seismic cross-correlation values (**Figure 9B**), and dip angles tightly clustered between 32.5° and 36.3° (**Figure 10D**). Given the plethora of similarities, we conclude that Cleveland was in a relatively stable and regular state of activity during this time period.

5.2. Implications for Source Depth Within the Conduit

Our results indicate that the explosion depth varied notably between different events and is likely responsible for the variable seismo-acoustic time lag. While an absolute calculation of explosion depth for all 22 explosions in this study does not appear feasible due to our limited data, some trends exist that allow for inferences on relative explosion source depths. Results from the seismo-acoustic time lag investigation are summarized in **Table 1** and **Figure 11**, where **Figure 11** shows the repose time, seismo-acoustic time lag, $VASR_{rel}$, cross-correlation with Explosion 45, and dip angle from horizontal, each normalized between 0 and 1. It is also clear, from analyses of the atmospheric effect on travel time using two independent methods, that the atmosphere is not the sole cause of the observed variable seismo-acoustic time lags (**Figure 6B**). Additionally, nonlinear propagation modeling did not yield a change in the onset time of the acoustic arrival at 3.8 km range and source amplitudes comparable (and larger) to those of Cleveland explosions, just a change in the arrival time of the peak pressure. Therefore, we conclude that something else must play a critical role in the variable seismo-acoustic time lags observed, which we argue is a change in explosion source depth within the conduit.

Explosions with shorter seismo-acoustic time lags (<~10.2 s) may have shallower source depths within the conduit. This is evidenced by small residuals between observed and predicted travel times based on atmospheric effects (<0.5 s) (**Figure 6B**), higher $VASR_{rel}$ in some cases (Explosions 45, 47, and 48, **Figure 8A**), higher seismic-cross correlation values in general (**Figure 9B**) and in relation to Explosion 45 (**Figure 9C**), and lower-to-average dip angles based on seismic particle motion (**Figure 10D**). These results are also summarized in **Table 1** and **Figure 11**. The low residuals between observed and predicted travel times based on atmospheric effects mean that the atmospheric predictions for the entire acoustic propagation path (Locations 1 through 4, **Figure 5**) are well predicted by the path length within the atmosphere (Locations 2 through 4, **Figure 5**). Therefore, the distance between Locations 1 and 2 in **Figure 5** (i.e., explosion source depth) may be small. Explosions 45, 47, and 48 have high $VASR_{rel}$ values, which indicates that a higher fraction of the explosion energy coupled into the atmosphere as compared with other explosions, also suggesting a shallow source or change in coupling from the conduit to the conduit wall. The seismic signatures of these events have high correlation, suggesting they may occur in a similar location and thus have the same propagation path to the seismic sensor. Finally, the dip angles of the seismic particle motion analysis for these events are smaller than explosions with larger time lags (e.g., Explosions 41, 42, and 51, dip angles >40°), suggesting a shallower source. While the dip angles seem to point to a source lower than station CLES for all explosions (e.g., **Figure 10C**), the travel time residuals are low (i.e., the observed time lag seems to be explained well by the predicted acoustic travel time based on the effective sound speed) and may therefore have a short path within the conduit. This is likely related to the surface displacement for P-waves incident at a sloped free surface (e.g., Ben-Menahem and Singh, 2012, their Figure 3), which causes the observed motion to be upward and outward even though the explosion source may be shallower than station CLES. The combination of these observations suggests these events with shorter seismo-acoustic time lags have a shallower source than other explosions at Mount Cleveland.

Explosions with larger seismo-acoustic time lags are likely associated with deeper explosions. This is evidenced by the higher travel time residuals between observed values and those predicted using the effective sound speed (**Figure 6B**), low cross-correlation values with respect to Explosion 45 (**Figure 9C**), and larger dip angles from particle motion analysis (>40°, **Figure 10D**) (**Table 1**, **Figure 11**). The three events with dip angles greater than 40° are Explosions 41, 42, and 51, all of which have large differences between the observed and predicted arrival time based on atmospheric conditions (>0.88 s, **Figure 6B**). We use these three likely deeper explosions to perform calculations on maximum source depths for explosions at Mount Cleveland where the residual travel times (after accounting for atmospheric effects) are 0.88, 1.77, and 1.21 s, respectively. Tameguri et al. (2002) find a reasonable conduit propagation velocity for Sakurajima to be in the range of 1,400–1,900 m/s and Yamada et al. (2016) estimate the velocity of the pressure wave to be > 1,000 m/s at Lokon-Empung. If we use a lower conduit velocity of $v_{conduit}$ = 1,000 m/s, explosion depths would be 880, 1770, and 1,210 m, respectively. If we choose a higher conduit velocity of $v_{conduit}$ = 1,500 m/s, explosion depths would be 1,320, 2,655, and 1,815 m, respectively. Haney et al. (2019) finds volumetric source locations using moment tensor inversions in the VLP band from 0.25 to 0.5 Hz for the first 2 s of the waveform of 400–640 m above sea level (depths of ~1,090–1,330 m beneath the summit), which appear to be in the range of our results and favor the lower $v_{conduit}$. We note that moment tensor inversions for explosions from the analogous Tungurahua volcano, Ecuador, point to a source region 1.5 km below the summit (Kim et al., 2014), comparable to estimates for deeper explosions at Mount Cleveland. Additionally, the range of potential source depths we calculate is consistent

with the proposed vertically extensive region of magma degassing between 0.5 and 3.0 km beneath the summit at Mount Cleveland in 2016 (Werner et al., 2020).

While changing the depth of the seismic explosion source would affect the time the pressure wave propagates up the conduit, the conduit propagation velocity may also vary due to changing composition and density of the conduit material between explosions. This has been hypothesized in previous studies of analogous volcanoes, including Tungarahua (Ruiz et al., 2006) and Santiaguito (Sahetapy-Engel et al., 2008). While this may occur to some extent at Mount Cleveland, we believe that a changing source depth potentially occurs for Mount Cleveland due to the positive relationship between increasing seismo-acoustic time lag with increasing dip angle from seismic particle motion analysis (**Figure 10D**), which suggests a changing source location.

Explosion 37 has a similarly large residual between the observed and predicted arrival time based on atmospheric conditions (1.81 s) but lacks the large dip angle observed for other explosions with large residuals (Explosions 41, 42, and 51, explained above). Upon closer inspection of the infrasound waveform, a small compression is noted ~1.8 s prior to the main onset. This feature is likely not noise, as it shows up at the infrasound array CLCO as well. Therefore, we conclude that the small compression may be an arrival from movement of the dome surface, and that the dome did not completely rupture until ~1.8 s later, causing a larger delay in the main acoustic onset.

5.3. Other Potential Impacts on Seismo-Acoustic Time Lag

Uncertainties can be introduced when picking the seismic and infrasound onset times. The seismic onsets are low-amplitude compressions which are consistent with studies of similar volcanoes such as Sakurajima (Tameguri et al., 2002), Tungurahua (Ruiz et al., 2006), and Lokon-Empung (Yamada et al., 2016). We chose to pick seismic arrivals on unfiltered waveforms to obtain the first sign of signal onset, as filtering in certain bands may obscure the subtle onset. The infrasound arrival is generally signified by a rapid increase in pressure. However, some explosions have a slow compressional onset (<0.5 s) prior to the rapid onset, which may introduce a small (few tenths of a second) error (e.g., Explosion 40, **Supplementary Figure S1C**). Both of these potential onset time errors do not change the fact that large variations (up to 2.20 s) in seismo-acoustic time lag exist between explosions at Mount Cleveland.

Two methods were used to determine the impact of the atmosphere on the propagation velocity of the infrasound signal, both of which have pros and cons. The first method used an atmospheric reconstruction model, AVO-G2S (Schwaiger et al., 2019). Using models such as this to obtain atmospheric information is known to not fully capture the exact atmospheric conditions at the time and location of the event (e.g., Iezzi et al., 2019b; Schwaiger et al., 2020). For example, these models have been found to be inadequate for the local atmospheric and boundary layer properties for propagation distances similar to that explored in this study (e.g., Kim et al., 2018). Therefore, atmospheric conditions may not capture smaller-scale changes such as variations within the 6 h increments, transient wind gusts, or flow around topography (i.e., a volcanic edifice). These inaccuracies and simplifications (both spatially and temporally) can be due to using coarse resolution input windfiles (NCEP reanalysis files, 2.5° and 6 h, respectively), as well as smoothing and interpolation during the reconstruction process in order to obtain a 1D atmospheric profile above the volcano. This may explain why the AVO-G2S derived effective sound speed values were systematically lower than those from our second method by 0–25 m/s (**Figure 6A**). The second method used to obtain effective sound speeds took advantage of the infrasound array CLCO, located 12.33 km further and 22.9° south of the CLES-summit azimuth. While 22.9° is a relatively low azimuthal deviation, if winds were strong the effective sound speed comparison would have error. However, we use this value because it is likely a more accurate representation of the atmospheric conditions at the time of each explosion.

To further investigate the potential effect of wind noise that may remain unresolved by both methods for determining the impact of the atmosphere on the propagation velocity, we look at the low frequency (0.02–0.3 Hz) component of infrasound for each explosion, as the spectral amplitude in this frequency band can sometimes be used as a proxy for wind noise (e.g., Fee and Garces, 2007). We include the infrasound power spectral density (PSD) for the 60 min prior to each explosion in **Supplemental Figure S4**, and note that the magnitude of the noise levels in this frequency band varies between explosions and does not show a clear correlation with time lag. However, it is not possible to fully interpret wind-related travel time effects on the time lag analysis because the noise conditions captured by the PSD do not account for directionality of the wind. For future studies that may be interested in obtaining explosion source depth from the seismo-acoustic time lag, we suggest adding an *in-situ* measurement of wind speed and direction using an anemometer along with the co-located seismic and infrasound sensors in order to more thoroughly capture the influence of the atmosphere.

The nonlinear FDTD modeling results in this study did not produce a measurable difference in the onset time of the explosion signal, nor the formation of a shock front. We note that our interpretations are limited by current modeling capabilities only using a linear source. Some of the waveforms at CLES show similarities to shock waves, which we believe would impact the acoustic arrival time observed at CLES due to the shock front overtaking the gradual onset observed for many of the Cleveland explosions. We surmise that future simulations performed that include a nonlinear source may produce a more realistic acoustic travel time. While the simulations performed here did not reproduce nonlinear impacts to the explosion arrival times, we believe there still may be a small contribution due to the highest peak pressures and those that clipped (**Figure 7D**, open circles) having lower seismo-acoustic time lags. This could be a coincidence, but should be explored further. Building upon a study on Bromo volcano, Indonesia, by Gottschämmer and

Surono (2000), Kim et al. (2014) corrected their infrasound onset times for explosions at Tungurahua volcano, Ecuador, using a constant shock velocity of 560 m/s within 2 km of the source, then 340 m/s beyond 2 km. However, we do not feel confident enough to include this type of sound speed assumption in our study with data from only a single station. Due to the uncertainties from a variety of features of potential nonlinear propagation, we chose to not include the potential contribution to our calculations on explosion source depth.

Observing nonlinear propagation near the source is difficult because infrasound sensors are generally placed far enough away from the source in order to decrease hazard to the field team and equipment. Therefore, interpretations often integrate multidisciplinary observations of pressure waves in order to better understand near source pressure dynamics. The propagation of pressure waves or "flashing arcs" has been observed and studied using image luminance techniques (e.g., Genco et al., 2014) and thermal imagery (e.g., Marchetti et al., 2013) then connected to the acoustic propagation velocity of volcanic explosions. Genco et al. (2014) find that explosions at Stromboli volcano propagate at the expected speed of sound, not faster. Marchetti et al. (2013) find that acoustic waves from explosions at Yasur volcano propagate supersonically, along with the observation of blast wave shapes in the infrasound traces. Recall that in nonlinear propagation every point on the waveform travels with a different speed (compression faster than rarefaction), which begs the question of exactly which part of the acoustic waveform this supersonic propagation speed corresponds to, the initial onset (which we are exploring in this study) or the peak compression (which has been shown to arrive faster in both this study and in others)? This remains unclear and should be investigated more thoroughly in the future.

6. CONCLUSION

Multi-year studies of volcanic activity provide observations of trends. Deviations from those trends prove useful for volcano monitoring that may not be apparent for studies using temporary deployment data that may only catch a few explosions (e.g., Lamb et al., 2019; Wallace et al., 2020). Here we examined the activity at Mount Cleveland from 2014 to 2018 and put it in context of recent work focused on shorter-term, dense observations. We find that Mount Cleveland generally followed a pattern of dome building and subsequent Vulcanian explosions, but parameters including repose time, explosion amplitude, and explosion characteristics varied substantially over the 4 years. In general, seismo-acoustic data from these explosions consisted of typical Vulcanian eruption signals. The seismic arrival for all explosions is a low-amplitude, compressional onset with a GCA often visible on the trace. The acoustic signal generally consists of a high-amplitude compressional onset, followed by a long duration coda. Some acoustic signals resemble high-amplitude, sharp-onset shock waves, while others have a complicated onset indicating a slower, multi-stage destruction of the lava dome. Notably, a variable seismo-acoustic time lag of up to 2.20 s is observed by co-located seismo-acoustic sensors at a station 3.5 km from the summit. Similarly variable seismo-acoustic time lags have been observed at analogous volcanoes such as Santiaguito and Tungurahua, though their precise cause is not well understood. We attribute the variable seismo-acoustic time lags to be due to a combination of varying atmospheric conditions (e.g., winds and temperature), nonlinear propagation, conduit velocity variations, and varying source depth within the conduit. Atmospheric effects were examined using two independent measurements, neither of which could entirely explain the variation observed. Nonlinear propagation impacts were determined to be minimal in relation to the onset time of the infrasound arrival, though they were difficult to quantify and model completely. We find that results from seismic cross-correlation and particle motion analysis suggest that a varying explosion source depth within the conduit may play a role in the observed variations in seismo-acoustic time lag. These results suggest explosion source depths ranging from near the surface down to ~1.5–2 km beneath the summit. This range in explosion depths is consistent with the evidence of magma potentially residing and degassing in a vertically extensive conduit region ranging in depth between 0.5 and 3.0 km below the summit found by Werner et al. (2020). We stress that no one method provides a complete depiction of the observed variance for all explosions, but a combination of methods is required to help understand the observations. Additionally, we note that combining observations of repose time, seismo-acoustic time lag, seismic cross-correlation values, and seismic particle motion dip angles illuminated periods of stable volcanic activity for Mount Cleveland. This may be useful for the future monitoring of the volcano, such as inferring the potential repose time before another explosion occurs if the system appears to be in a stable period (e.g., Explosions 45–48).

This study was performed primarily using a single co-located seismic and acoustic station. We suggest that similar analyses may be performed at other volcanoes worldwide that have sparse monitoring networks. Even with a single co-located seismic and acoustic sensor that clips sometimes, we show that it is possible to provide meaningful interpretations on the explosion source depth which may help understand the volcanic system during times of unrest. In future years, we anticipate more geophysical and geochemical instrumentation to be installed at Mount Cleveland, which will increase our understanding of the volcanic system, build upon the results of this study, and increase the ability of AVO to monitor and forecast future eruptions of the volcano. Additionally, while this study focuses on volcanic explosions, the goal of finding depth from coupled seismic and acoustic observations is not unique to volcanic studies and can be applied to other disciplines such as the study of buried chemical explosions.

DATA AVAILABILITY STATEMENT

Seismic and infrasound data used in this study are available from the Incorporated Research Institutions for Seismology Data Management Center (https://ds.iris.edu/ds/nodes/dmc/) under network code AV.

AUTHOR CONTRIBUTIONS

AI led the analysis and writing of the manuscript under the supervision of DF. All authors provided critical feedback and helped shape the research, analysis, and structure of the manuscript.

FUNDING

The authors acknowledge support from the Alaska Volcano Observatory through the U.S. Geological Survey Volcano Hazards Program.

ACKNOWLEDGMENTS

The authors thank Sean Maher and Catherine de Groot-Hedlin for helpful discussion on nonlinear propagation and the use of the FDTDWave code. We are also grateful to Pavel Izbekov, Carl Tape, and Michael West for discussions on the analyses as well as David Green for discussion on the use of seismic cross-correlation. We would also like to thank Taryn Lopez, Cheryl Searcy, Cheryl Cameron, and Rick Wessels for their help with gathering dome observations and discussions on Mount Cleveland. Helpful reviews were done by Silvio De Angelis, Stephen McNutt, and Rebecca Kramer. Observations of volcanic activity were made by AVO and are detailed on its website (avo.alaska.edu/volcanoes/volcact.php?volcname=Cleveland). Any use of trade, firm, or product names is for descriptive purposes only and does not imply endorsement by the U.S. Government.

SUPPLEMENTARY MATERIAL

The Supplementary Material for this article can be found online at: https://www.frontiersin.org/articles/10.3389/feart.2020.573368/full#supplementary-material

REFERENCES

Arrowsmith, S. J., Johnson, J. B., Drob, D. P., and Hedlin, M. A. H. (2010) The seismoacoustic wavefield: a new paradigm in studying geophysical phenomena. *Rev. Geophys.* 48, RG4003. doi:10.1029/2010RG000335

Atchley, A. A. (2005). Not your ordinary sound experience: a nonlinear-acoustics primer. *Acoust. Today.* 1, 19–24. doi:10.1121/1.2961122

Ben-Menahem, A., and Singh, S. J. (2012). *Seismic waves and sources.* Berlin: Springer Science & Business Media.

Blom, P., Iezzi, A., and Euler, G. (2020). Seismoacoustic analysis of underground explosions using the Rayleigh integral. *Geophys. J. Int.* 223, 1069–1085. doi:10.1093/gji/ggaa363

Boatwright, J. (1980). A spectral theory for circular seismic sources; simple estimates of source dimension, dynamic stress drop, and radiated seismic energy. *Bull. Seismol. Soc. Am.* 70, 1–27. doi:10.1785/0120000932

Clarke, A. B., Esposti Ongaro, T., and Belousov, A. (2015). Vulcanian eruptions. *Encycl. Volcanoes.* 10, 505–518. doi:10.1016/b978-0-12-385938-9.00028-6

De Angelis, S., Fee, D., Haney, M., and Schneider, D. (2012). Detecting hidden volcanic explosions from Mt. Cleveland Volcano, Alaska with infrasound and ground-coupled airwaves. *Geophys. Res. Lett.* 39. 19–24. doi:10.1029/2012GL053635

de Groot-Hedlin, C. D. (2016). Long-range propagation of nonlinear infrasound waves through an absorbing atmosphere. *J. Acoust. Soc. Am.* 139, 1565–1577. doi:10.1121/1.4944759

Dean, K. G., Dehn, J., Papp, K. R., Smith, S., Izbekov, P., Peterson, R., et al. (2004). Integrated satellite observations of the 2001 eruption of Mt. Cleveland, Alaska. *J. Volcanol. Geoth. Res.* 135, 51–73. doi:10.1016/j.jvolgeores.2003.12.013

Dean, K. G. (2002). Satellite imagery proves essential for monitoring erupting aleutian volcano. *Eos* 83, 19–21. doi:10.1029/2002eo000168

Dixon, J., Cameron, C., Iezzi, A., and Wallace, K. (2017). Report 2017-5104. 2015 Volcanic activity in Alaska-Summary of events and response of the Alaska Volcano Observatory. U.S. Geological Survey Scientific Investigations. doi:10.3133/sir20175104

Fee, D., and Garces, M. (2007). Infrasonic tremor in the diffraction zone. *Geophys. Res. Lett.* 34, 24–42. doi:10.1029/2007GL030616

Fee, D., Haney, M., Matoza, R., Szuberla, C., Lyons, J., and Waythomas, C. (2016). Seismic envelope-based detection and location of ground-coupled airwaves from volcanoes in Alaska. *Bull. Seismol. Soc. Am.* 106, 72–85. doi:10.1785/0120150244

Fee, D., Izbekov, P., Kim, K., Yokoo, A., Lopez, T., Prata, F., et al. (2017). Eruption mass estimation using infrasound waveform inversion and ash and gas measurements: evaluation at Sakurajima Volcano, Japan. *Earth Planet Sci. Lett.* 480, 42–52. doi:10.1016/j.epsl.2017.09.043

Fee, D., Lyons, J., Haney, M., Wech, A., Waythomas, C., Diefenbach, A. K., et al. (2020). Seismo-acoustic evidence for vent drying during shallow submarine eruptions at Bogoslof volcano, Alaska. *Bull. Volcanol.* 82, 1–14. doi:10.1007/s00445-019-1326-5

Fee, D., and Matoza, R. S. (2013). An overview of volcano infrasound: from hawaiian to plinian, local to global. *J. Volcanol. Geoth. Res.* 249, 123–139. doi:10.1016/j.jvolgeores.2012.09.002

Fee, D., Yokoo, A., and Johnson, J. B. (2014). Introduction to an open community infrasound dataset from the actively erupting Sakurajima Volcano, Japan. *Seismol Res. Lett.* 85, 1151–1162. doi:10.1785/0220140051

Firstov, P., and Kravchenko, N. (1996). Estimation of the amount of explosive gas released in volcanic eruptions using air waves. *Volcanol. Seismol.* 17, 547–560

Friedlander, F. (1946). The diffraction of sound pulses. I. Diffraction by a semi-infinite plate. *Proc. Roy. Soc. Lond.* 186, 322–344. doi:10.1098/rspa.1946.0046

Genco, R., Ripepe, M., Marchetti, E., Bonadonna, C., and Biass, S. (2014). Acoustic wavefield and Mach wave radiation of flashing arcs in strombolian explosion measured by image luminance. *Geophys. Res. Lett.* 41, 7135–7142. doi:10.1002/2014GL061597

Gottschämmer, E., and Surono, I. (2000). Locating tremor and shock sources recorded at Bromo Volcano. *J. Volcanol. Geoth. Res.* 101, 199–209. doi:10.1016/S0377-0273(00)00171-2

Green, D. N., and Neuberg, J. (2006). Waveform classification of volcanic low-frequency earthquake swarms and its implication at Soufrière Hills Volcano, Montserrat. *J. Volcanol. Geoth. Res.* 153, 51–63. doi:10.1016/j.jvolgeores.2005.08.003

Gu, Y., Rose, W. I., Schneider, D. J., Bluth, G. J. S., and Watson, I. M. (2005). Advantageous GOES IR results for ash mapping at high latitudes: cleveland Eruptions 2001. *Geophys. Res. Lett.* 32, 1–5. doi:10.1029/2004GL021651

Haney, M., Lyons, J., Power, J., and Roman, D. (2019). "Moment tensors of small vulcanian explosions at Mount Cleveland, Alaska," in AGU Fall Meeting, San Fransisco, CA, 2019, V41A-05.

Iezzi, A. M., Fee, D., Kim, K., Jolly, A. D., and Matoza, R. S. (2019a). Three-dimensional acoustic multipole waveform inversion at Yasur volcano, Vanuatu. *J. Geophys. Res.: Solid Earth.* 124, 8679–8703. doi:10.1029/2018JB017073

Iezzi, A. M., Schwaiger, H. F., Fee, D., and Haney, M. M. (2019b). Application of an updated atmospheric model to explore volcano infrasound propagation and detection in Alaska. *J. Volcanol. Geoth. Res.* 371, 192–205. doi:10.1016/j.jvolgeores.2018.03.009

Janiszewski, H. A., Wagner, L. S., and Roman, D. C. (2020). Aseismic mid-crustal magma reservoir at Cleveland Volcano imaged through novel receiver function analyses. *Sci. Rep.* 10, 1–9. doi:10.1038/s41598-020-58589-0

Johnson, J. B., and Aster, R. C. (2005). Relative partitioning of acoustic and seismic energy during Strombolian eruptions. *J. Volcanol. Geoth. Res.* 148, 334–354. doi:10.1016/j.jvolgeores.2005.05.002

Johnson, J. B. (2003). Generation and propagation of infrasonic airwaves from volcanic explosions. *J. Volcanol. Geoth. Res.* 121, 1–14. doi:10.1016/S0377-0273(02)00408-0

Jones, K. R., Whitaker, R. W., and Arrowsmith, S. J. (2015). Modelling infrasound signal generation from two underground explosions at the Source Physics Experiment using the Rayleigh integral. *Geophys. J. Int.* 200, 779–790. doi:10.1093/gji/ggu433

Kim, K., Fee, D., Yokoo, A., and Lees, J. M. (2015). Acoustic source inversion to estimate volume flux from volcanic explosions. *Geophys. Res. Lett.* 42, 5243–5249. doi:10.1002/2015GL064466

Kim, K., Lees, J. M., and Ruiz, M. C. (2014). Source mechanism of Vulcanian eruption at Tungurahua Volcano, Ecuador, derived fromseismic moment tensor inversions. *J. Geophys. Res.: Solid Earth.* 119, 1145–1164. doi:10.1002/2013JB010590

Kim, K., Rodgers, A., and Seastrand, D. (2018). Local infrasound variability related to in situ atmospheric observation. *Geophys. Res. Lett.* 45, 2954–2962. doi:10.1002/2018GL077124

Kistler, R., Kalnay, E., Collins, W., Saha, S., White, G., Woollen, J., et al. (2001). The NCEP-NCAR 50-year reanalysis: Monthly means CD-ROM and documentation. *Bull. Am. Meteorol. Soc.* 82, 247–267. doi:10.1175/1520-0477(2001)082<0247:TNNYRM>2.3.CO;2

Lamb, O. D., Lamur, A., Díaz-Moreno, A., De Angelis, S., Hornby, A. J., von Aulock, F. W., et al. (2019). Disruption of long-term effusive-explosive activity at Santiaguito, Guatemala. *Front. Earth Sci.* 6, 1–14. doi:10.3389/feart.2018.00253

Lyons, J. J., and Waite, G. P. (2011). Dynamics of explosive volcanism at Fuego volcano imaged with very long period seismicity. *J. Geophys. Res. Solid Earth.* 116, 1–18. doi:10.1029/2011JB008521

Maher, S. P., Matoza, R. S., Groot-Hedlin, C. D., Gee, K. L., Fee, D., and Yokoo, A. (2020). Investigating spectral distortion of local volcano infrasound by nonlinear propagation at Sakurajima volcano, Japan. *J. Geophys. Res. Solid Earth.* 125, 19–27. doi:10.1029/2019JB018284

Marchetti, E., Ripepe, M., Delle Donne, D., Genco, R., Finizola, A., and Garaebiti, E. (2013). Blast waves from violent explosive activity at Yasur Volcano, Vanuatu. *Geophys. Res. Lett.* 40, 5838–5843. doi:10.1002/2013GL057900

McKee, K., Fee, D., Haney, M., Matoza, R. S., and Lyons, J. (2018). Infrasound signal detection and back azimuth estimation using ground-coupled airwaves on a seismo-acoustic sensor pair. *J. Geophys. Res. Solid Earth.* 123, 6826–6844. doi:10.1029/2017JB015132

Miller, T., McGimsey, R., Richter, D., Riehle, J., Nye, C., Yount, M., et al. (1998). Catalog of historically active volcanoes in Alaska. U.S. Geological Survey Open-File Report. 98–582

Neuberg, J., and Pointer, T. (2000). Effects of volcano topography on seismic broad-band waveforms. *Geophys. J. Int.* 143, 239–248. doi:10.1046/j.1365-246X.2000.00251.x

Petersen, T., and McNutt, S. R. (2007). Seismo-acoustic signals associated with degassing explosions recorded at Shishaldin Volcano, Alaska, 2003-2004. *Bull. Volcanol.* 69, 527–536. doi:10.1007/s00445-006-0088-z

Pierce, A. (1981). *Acoustics: an introduction to its physical principles and applications*. New York, NY: McGraw-Hill.

Porter, C., Morin, P., Howat, I., Noh, M.-J., Bates, B., Peterman, K., et al. (2018). *Arctic*. [Dataset]. doi:10.7910/DVN/OHHUKH

Power, J. A., Haney, M. M., Botnick, S. M., Dixon, J. P., Fee, D., Kaufman, A. M., et al. (2020). Goals and development of the Alaska Volcano Observatory seismic network and application to forecasting and detecting volcanic eruptions. *Seismol Res. Lett.* 91, 647–659. doi:10.1785/0220190216

Power, J., Roman, D., Lyons, J., Haney, M., Werner, C., Rasmussen, D., et al., A seismic investigation of Mount Cleveland volcano and pre-historic volcanic vents on Chuginadak Island, Alaska and implications for forecasting eruptions at open-vent volcanoes. *J. Volcanol. Geoth. Res.*, in review.

Reichman, B. O., Gee, K. L., Neilsen, T. B., and Miller, K. G. (2016). Quantitative analysis of a frequency-domain nonlinearity indicator. *J. Acoust. Soc. Am.* 139, 2505–2513. doi:10.1121/1.4945787

Rowe, C. A., Aster, R. C., Kyle, P. R., Schlue, J. W., and Dibble, R. R. (1998). Broadband recording of Strombolian explosions and associated very-long-period seismic signals on Mount Erebus volcano, Ross Island, Antarctica. *Geophys. Res. Lett.* 25, 2297–2300. doi:10.1029/98GL01622

Ruiz, M. C., Lees, J. M., Johnson, J. B., Hall, M., Box, C., and Hill, C. (2006). Source constraints of Tungurahua volcano explosion events. *Bull. Volcanol.* 68, 480–490. doi:10.1007/s00445-005-0023-8

Sahetapy-Engel, S. T., Harris, A. J., and Marchetti, E. (2008). Thermal, seismic and infrasound observations of persistent explosive activity and conduit dynamics at Santiaguito lava dome, Guatemala. *J. Volcanol. Geoth. Res.* 173, 1–14. doi:10.1016/j.jvolgeores.2007.11.026

Salomons, E. (2001). *Computational atmospheric acoustics*. Dordrecht, The Netherlands: Kluwer Academic Publishers.

Schwaiger, H. F., Lyons, J. J., Iezzi, A. M., Fee, D., and Haney, M. M. (2020). Evolving infrasound detections from Bogoslof volcano, Alaska: insights from atmospheric propagation modeling. *Bull. Volcanol.* 82, 27. doi:10.1007/s00445-020-1360-3

Schwaiger, H., Iezzi, A., and Fee, D. (2019). AVO-G2S: a modified, open-source Ground-to-Space atmospheric specification for infrasound modeling. *Comput. Geosci.* 125, 90–97. doi:10.1016/j.cageo.2018.12.013

Simpson, J., Hufford, G., Pieri, D., Servranckx, R., Berg, J., and Bauer, C. (2002). The february 2001 eruption of Mount Cleveland, Alaska: case study of an aviation hazard. *Am. Meteorol. Soc.* 17, 691–704. doi:10.1175/1520-0434(2002)017

Tameguri, T., Iguchi, M., and Ishihara, K. (2002). Mechanism of explosive eruptions from moment tensor analyses of explosion earthquakes at Sakurajima volcano, Japan. *Bull. Volcanol. Soc. Jpn.* 47, 197–215. doi:10.1186/bf03352363

Varley, N., Arámbula-Mendoza, R., Reyes-Dávila, G., Sanderson, R., and Stevenson, J. (2010). Generation of vulcanian activity and long-period seismicity at volcán de colima, Mexico. *J. Volcanol. Geoth. Res.* 198, 45–56. doi:10.1016/j.jvolgeores.2010.08.009

Vergniolle, S., Boichu, M., and Caplan-Auerbach, J. (2004). Acoustic measurements of the 1999 basaltic eruption of Shishaldin volcano, Alaska 1. Origin of Strombolian activity. *J. Volcanol. Geoth. Res.* 137, 109–134. doi:10.1016/j.jvolgeores.2004.05.003

Waldhauser, F., and Ellsworth, W. L. (2000). A double-difference earthquake location algorithm: method and application to the Northern Hayward fault, California. *Bull. Seismol. Soc. Am.* 90, 1353–1368. doi:10.1785/0120000006

Wallace, P. A., Lamb, O. D., Angelis, S. D., Kendrick, J. E., Hornby, J., Díaz-moreno, A., et al. (2020). Integrated constraints on explosive eruption intensification at Santiaguito dome complex , Guatemala. *Earth Planet Sci. Lett.* 536, 116139. doi:10.1016/j.epsl.2020.116139

Wang, T., Poland, M. P., and Lu, Z. (2015). Dome growth at Mount Cleveland, Aleutian Arc, quantified by time series TerraSAR-X imagery. *Geophys. Res. Lett.* 42, 10614–10621. doi:10.1002/2015GL066784

Wech, A., Tepp, G., Lyons, J., and Haney, M. (2018). Using earthquakes, T waves, and infrasound to investigate the eruption of bogoslof volcano, Alaska. *Geophys. Res. Lett.* 45, 6918–6925. doi:10.1029/2018GL078457

Werner, C., Kern, C., Coppola, D., Lyons, J. J., Kelly, P. J., Wallace, K. L., et al. (2017). Magmatic degassing, lava dome extrusion, and explosions from Mount Cleveland volcano, Alaska, 2011–2015: insight into the continuous nature of volcanic activity over multi-year timescales. *J. Volcanol. Geoth. Res.* 337, 98–110. doi:10.1016/j.jvolgeores.2017.03.001

Werner, C., Rasmussen, D. J., Plank, T., Kelly, P. J., Kern, C., Lopez, T., et al. (2020). Linking subsurface to surface using gas emission and melt inclusion data at Mount Cleveland volcano, Alaska. *G-cubed* 21, 141–167. doi:10.1029/2019GC008882

Worden, A., Dehn, J., and Webley, P. (2014). Frequency based satellite monitoring of small scale explosive activity at remote North Pacific volcanoes. *J. Volcanol. Geoth. Res.* 286, 1–14. doi:10.1016/j.jvolgeores.2014.08.019

Yamada, T., Aoyama, H., Nishimura, T., Yakiwara, H., Nakamichi, H., Oikawa, J., et al. (2016). Initial phases of explosion earthquakes accompanying Vulcanian eruptions at Lokon-Empung volcano , Indonesia. *J. Volcanol. Geoth. Res.* 327, 310–321. doi:10.1016/j.jvolgeores.2016.08.011

Yokoo, A., and Iguchi, M. (2010). Using infrasound waves from eruption video to explain ground deformation preceding the eruption of Suwanosejima volcano, Japan. *J. Volcanol. Geoth. Res.* 196, 287–294. doi:10.1016/j.jvolgeores.2010.08.008

Yokoo, A., and Ishihara, K. (2007). Analysis of pressure waves observed in Sakurajima eruption movies. *Earth Planets Space.* 59, 177–181. doi:10.1186/BF03352691

Yokoo, A., Tameguri, T., and Iguchi, M. (2009). Swelling of a lava plug associated with a Vulcanian eruption at Sakurajima Volcano, Japan, as revealed by infrasound record: case study of the eruption on January 2, 2007. *Bull. Volcanol.* 71, 619–630. doi:10.1007/s00445-008-0247-5

Conflict of Interest: The authors declare that the research was conducted in the absence of any commercial or financial relationships that could be construed as a potential conflict of interest.

The reviewer (SDA) declared a past co-authorship with the authors to the handling editor.

Copyright © 2020 Iezzi, Fee, Haney and Lyons. This is an open-access article distributed under the terms of the Creative Commons Attribution License (CC BY). The use, distribution or reproduction in other forums is permitted, provided the original author(s) and the copyright owner(s) are credited and that the original publication in this journal is cited, in accordance with accepted academic practice. No use, distribution or reproduction is permitted which does not comply with these terms.

frontiers in Earth Science

ORIGINAL RESEARCH
published: 14 January 2021
doi: 10.3389/feart.2020.606992

Earthquake Analysis Suggests Dyke Intrusion in 2019 Near Tarawera Volcano, New Zealand

Thomas W. Benson[1], Finnigan Illsley-Kemp[1], Hannah C. Elms[1], Ian J. Hamling[2], Martha K. Savage[1], Colin J. N. Wilson[1], Eleanor R. H. Mestel[1] and Simon J. Barker[1]*

[1]School of Geography, Environment and Earth Sciences, Victoria University of Wellington, Wellington, New Zealand, [2]GNS Science, Avalon, New Zealand

Tarawera volcano (New Zealand) is volumetrically dominated by rhyolitic lavas and pyroclastic deposits, but the most recent event in AD 1886 was a basaltic Plinian fissure eruption. In March 2019 a swarm of at least 64 earthquakes occurred to the NE of Tarawera volcano, as recorded by the New Zealand Geohazard Monitoring Network (GeoNet). We use seismological analysis to show that this swarm was most likely caused by a dyke that intruded into the brittle crust between depths of 8–10 km and propagated toward Tarawera volcano for 2 km at a rate of 0.3–0.6 m s^{-1}. We infer that this was a dyke of basaltic composition that was stress-guided toward Tarawera volcano by the topographic load of the volcanic edifice. Dyke intrusions of this nature are most likely a common occurrence but a similar process may have occurred during the 1886 eruption with a dyke sourced from some lateral distance away from the volcano. The 2019 intrusion was not detected by InSAR geodesy and we use synthetic models to show that geodetic monitoring could only detect a ≥6 m wide dyke at these depths. Improvements to geodetic monitoring, combined with detailed seismological analysis, could better detect future magmatic intrusions in the region and serve to help assess ongoing changes in the magmatic system and the associated possibilities of a volcanic event.

Keywords: dyke intrusion, volcano seismicity, seismology, volcanology, InSAR, Okataina Volcanic Center, Tarawera volcano

OPEN ACCESS

Edited by:
Francesco Maccaferri, Vesuvius Observatory, National Institute of Geophysics and Volcanology (INGV), Italy

Reviewed by:
Yohei Yukutake, Hot Spring Geology Research Institute, Japan
Francesca Di Luccio, Istituto Nazionale di Geofisica e Vulcanologia (INGV), Italy

****Correspondence:***
Finnigan Illsley-Kemp
finnigan.illsleykemp@vuw.ac.nz

Specialty section:
This article was submitted to Solid Earth Geophysics, a section of the journal Frontiers in Earth Science

Received: *16 September 2020*
Accepted: *11 November 2020*
Published: *14 January 2021*

Citation:
Benson TW, Illsley-Kemp F, Elms HC, Hamling IJ, Savage MK, Wilson CJ N, Mestel ERH and Barker SJ (2021) Earthquake Analysis Suggests Dyke Intrusion in 2019 Near Tarawera Volcano, New Zealand. Front. Earth Sci. 8:606992. doi: 10.3389/feart.2020.606992

1. INTRODUCTION

Forecasting volcanic eruptions is inherently challenging due to the wide range of unrest signals (e.g., ground deformation, elevated seismicity, gas emissions) that can occur at variable rates and over variable timescales prior to eruption (e.g., Sparks et al., 2012). Many of these unrest signals can also occur without leading to eruption, highlighting the complex nature of the subsurface plumbing systems and the numerous processes that occur beneath dormant volcanoes (Moran et al., 2011). Monitoring subsurface processes is important for developing an understanding of how different volcanoes operate and for assessing any deviation from the normal background state (e.g., Cashman and Sparks, 2013; Acocella, 2014).

Many of the challenges with assessing volcanic unrest are exemplified with caldera volcanoes, which are among the most complex and dangerous types of volcano (Acocella et al., 2015). Caldera volcanoes often cover a wide geographical area (up to several ten of kilometers wide) with large, geometrically complex and heterogeneous magmatic systems that are capable of producing explosive eruptions, sometimes of great size. However, understanding of the current state of these systems is

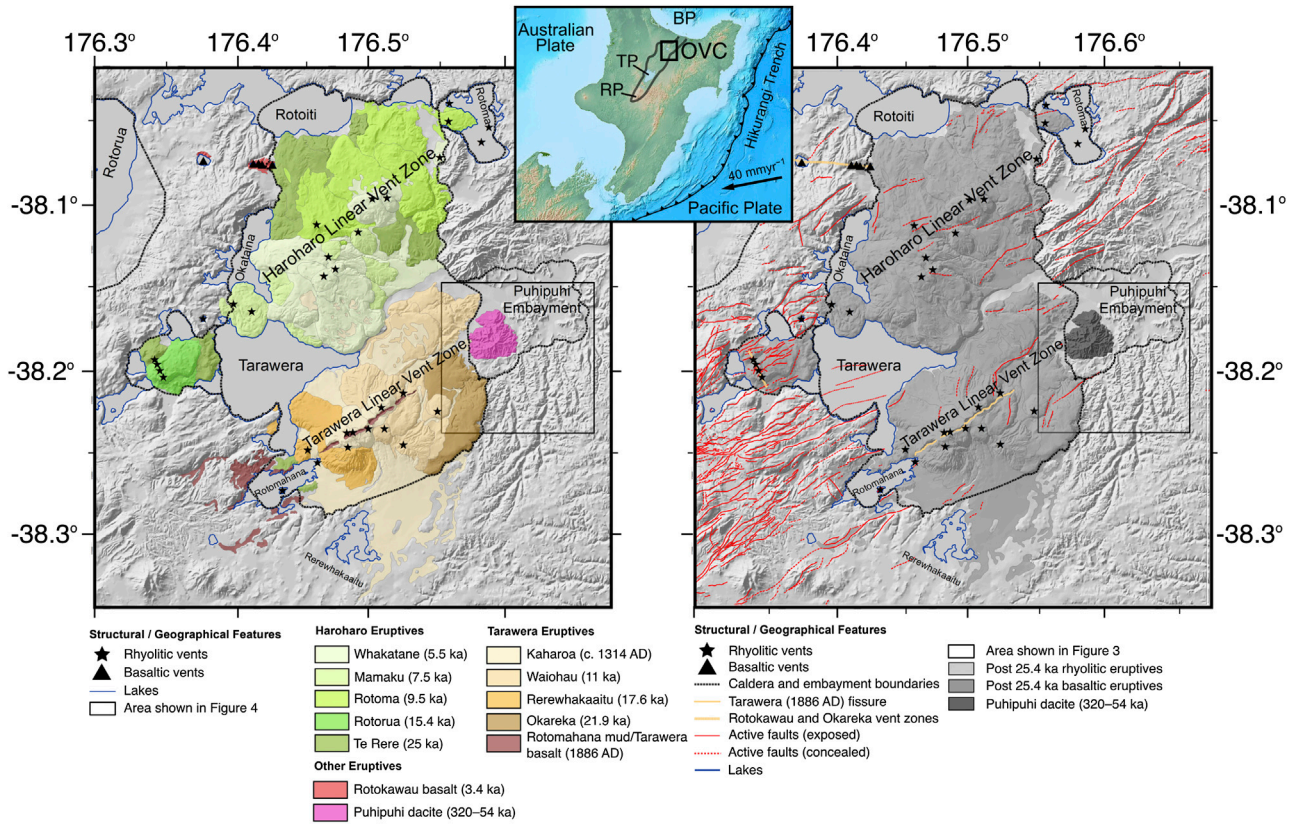

FIGURE 1 | Left: Young (≤25 ka) eruptive units of the Okataina Volcanic Center. **Right:** Structural features of the Okataina Volcanic Center, including the location of the 1886 AD Tarawera eruptive fissure. Inset shows the location of the TVZ (black outline) and the OVC (black box) in the North Island, New Zealand. BP: Bay of Plenty, TP: Taupō, RP: Ruapehu.

often made complex by the presence of active, shallower hydrothermal systems and fault structures (e.g., Sandri et al., 2017; Mantiloni et al., 2020). Disentangling the signals of magmatic unrest (e.g., variations in the pressure of the system due to magma recharge or ascent) vs. non-magmatic unrest (e.g., changes in the hydrothermal system or tectonic earthquakes) can be difficult, with the potential for many different mechanisms that can produce similar unrest symptoms (Acocella et al., 2015).

Here we document and interpret a series of earthquakes that occurred over a 3 day period near Tarawera volcano (New Zealand) in March 2019. Tarawera is the site of a large basaltic fissure eruption in AD 1886, but is positioned within a larger caldera structure that has a history of producing high-silica (rhyolitic) magmas (**Figure 1**). As such, it is important to constrain the origin of these earthquakes and to consider how they relate to the modern magmatic system and ongoing activity in the broader region around the caldera.

2. GEOLOGICAL BACKGROUND

The Taupō Volcanic Zone (TVZ) in the central North Island of New Zealand (**Figure 1**) has been volcanically active since approximately 2 Ma, and from 1.85 Ma eruptions have been dominated by high-silica (rhyolitic) magmas (Eastwood et al., 2013; Chambefort et al., 2014). The TVZ can be subdivided into three segments along its length. The southern and northern segments are characterized by andesite volcanism building composite cones, whereas the central TVZ is dominated by voluminous rhyolite volcanism associated with caldera volcanoes and unusually high surface heat-flow (Bibby et al., 1995; Wilson et al., 1995). Over the last 50–60 kyr this rhyolitic volcanism has mainly been focused at Taupō and Okataina volcanoes, at the southern and northern limits of the central TVZ respectively. The TVZ also hosts the Taupō continental rift with present-day rates of extension increasing from ≤5 mm/yr at Ruapehu in the south, to 13–19 mm/yr at the Bay of Plenty coastline and increasing farther offshore (Wallace et al., 2004; Lamarche et al., 2006). The orientation of present-day extension within the Taupō rift varies from rift-orthogonal in the south to oblique in the north (Rowland and Sibson, 2001; Acocella et al., 2003; Townend et al., 2012; Seebeck et al., 2014; Illsley-Kemp et al., 2019). Several studies have suggested that extension within the Taupō rift is partially accommodated by magmatic intrusions (Rowland et al., 2010), however this may not be ubiquitous throughout the rift (Villamor et al., 2011).

The Okataina Volcanic Center (OVC) is built on a system of nested calderas formed by multiple large-volume rhyolite

eruptions over at least the last ~340 kyr (Nairn, 2002; Cole et al., 2010, 2014) (**Figure 1**). Over the past ~25 kyr volcanism has been focused at the Haroharo and Tarawera volcanic complexes, in the northern and southern parts of the OVC, respectively (Nairn, 2002). Both complexes are volumetrically dominated by rhyolitic eruptive products, including voluminous lavas forming the respective edifices, erupted from vents aligned along two linear vent zones. A notable feature is that rhyolitic eruptions from the Tarawera complex have often been associated with basaltic intrusion and eruption. The most recent rhyolite eruption (the AD 1314 ± 10 Kaharoa eruption from the Tarawera complex: Hogg et al., 2003) was primed and triggered by the intrusion of primitive basalt (containing primitive olivines: Barker et al., 2020) that was mixed into the rhyolite magma reservoir (Leonard et al., 2002; Nairn et al., 2004). There is also evidence that many of the previous rhyolite eruptions from the Tarawera complex had basaltic input/interaction (Nairn, 1992; Darragh et al., 2006; Shane et al., 2007; Shane et al., 2008). The composition of basaltic magmas erupted from the OVC show little variation between eruptions but they are distinct in their composition compared to basalts erupted outside the caldera to the south (Barker et al., 2020).

The influence of basaltic magmatism at the OVC was most dramatically illustrated in the AD 1886 Tarawera basaltic Plinian eruption, sourced from a ~17 km long fissure (Nairn, 1979; Walker et al., 1984; Sable et al., 2006) (**Figure 1**). However, the 1886 eruptive products show no physical evidence for any interaction with a melt-dominant rhyolite magma reservoir, only shallow xenolithic incorporation (Cole, 1970; Cole et al., 2014; Carey et al., 2007; Carey and Houghton, 2010), although some crustal contamination is indicated from trace element and isotopic data (Gamble et al., 1993; Waight et al., 2017). The inference, therefore, is that the feeder dyke rose from the base of the quartzofeldspathic crust and ascended rapidly while avoiding any interaction with evolved melt-rich magmatic reservoirs. The location of this primitive source, and the pathway of the eruptive dyke are largely unknown. Nairn and Cole (1981) document the 1886 eruptive fissures and find that the surface dykes are arrayed in a left-stepping en-echelon pattern within a larger fissure structure. The dykes have a common orientation of ~70°, while the eruptive fissure strikes at ~60°. This led Nairn and Cole (1981) to suggest that orientation of the dyke intrusions reflect the modern day orientation of maximum horizontal compression (SH_{max}), whereas the eruptive fissure reflects the orientation of an older fault structure. Vents during the eruption began at two locations at the Tarawera summit and spread both NE (for a short distance) and SW (for ~11 km) along the fissure line during the course of the eruption (Sable et al., 2006).

In addition to the ample evidence that dyke intrusions, specifically of basaltic composition, play an important role in OVC eruptions, they are also thought to play a key role in the accommodation of extension in the Taupō rift (Rowland et al., 2010; Villamor et al., 2011). However, while dyke-accommodated rifting has been directly observed in other continental rifts (Kendall et al., 2005; Ebinger et al., 2013) and realistically has to have occurred during the 1886 eruption, it has not yet been detected in the TVZ in the modern instrumental era. Analysis of GPS data from the OVC area found that strain in the region surrounding the Tarawera fissure should promote the intrusion of dykes (Holden et al., 2015). Other geodetic studies, however, found that the OVC and TVZ are more accurately described as contractional areas at present (Hamling et al., 2015; Dimitrova et al., 2016; Haines and Wallace, 2020).

Knowledge of the modern-day location or state of the magmatic system(s) at OVC is limited. Electrical resistivity imaging shows evidence for a broadly distributed low-resistivity structure across the OVC between 10 and 20 km depth (Heise et al., 2010) and a region of partial melt to the SW of the OVC at depths ≥8 km (Heise et al., 2016). In contrast, seismic anisotropy suggests the presence of a large upper-crustal magma body (Illsley-Kemp et al., 2019). Earthquake activity in the OVC is highly swarm-like, and in the instrumental era (post-1985) has been largely limited to the Haroharo complex and to the southwest of Tarawera beneath Lake Rotomahana, outside the OVC caldera (Hurst et al., 2008; Bannister et al., 2016) (**Figure 1**). The Lake Rotomahana earthquake activity is thought to be caused by geothermal fluid migration along sub-surface faults between 4 and 7 km depth (Bannister et al., 2016). Eruptive histories and phenocryst mineralogies for the ≤25 ka products of the OVC suggest that Haroharo and Tarawera have different upper crustal magmatic systems, albeit at comparable depths (Cole et al., 2014). Petrological studies based on volatile concentrations in quartz-hosted melt inclusions have suggested storage pressures for the erupted rhyolitic magmas in the range of 130–160 MPa (5–7 km) for most examples (Johnson et al., 2011) with greater depths (to ~12 km) proposed for some (Shane et al., 2007). Also, the presence of cummingtonite as a phenocryst phase in many of the young Okataina rhyolites indicates similar maximum pressures and depths (Nicholls et al., 1992). An improved understanding of the modern system would assist with the monitoring of the volcanoes, particularly as studies by Sherburn and Nairn (2004) and Holden et al. (2017) suggest that it may be possible for significant subsurface magmatic activity to occur in the OVC without detection by the geodetic monitoring currently in place. Building a better understanding of modern magmatic activity is also important for constraining tipping points that could result in magmatic activity/unrest at the OVC cascading toward major unrest and/or eruption (Acocella et al., 2015; Wilson, 2017). In this regard, it is significant that on March 12, 2019, the New Zealand Geohazard Monitoring Network (GeoNet) recorded a cluster of 64 earthquakes to the northeast of Tarawera volcano. In this paper we investigate this seismic cluster and its cause in more detail.

3. DATA AND METHODS

For this study, we downloaded continuous seismic data from March 12, 2019 to March 15, 2019 (inclusive) from seven short-period GeoNet seismometers (**Figure 2**). We manually detected earthquakes within the continuous data and picked all visible P

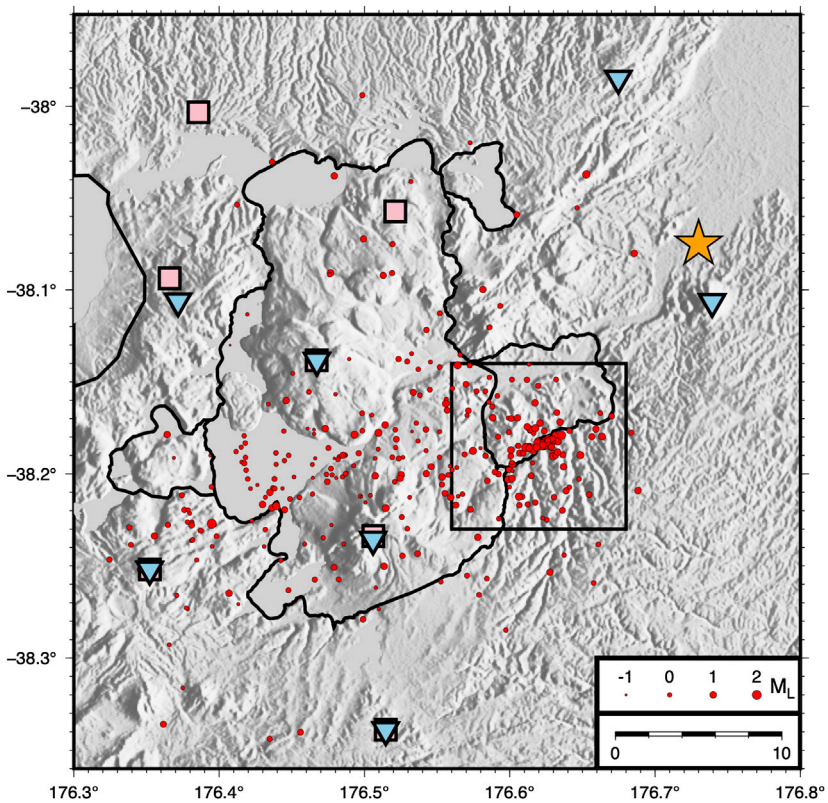

FIGURE 2 | Map of 348 earthquakes (red circles, scaled by magnitude) that occurred in the Okataina region between the 12th–15th March 2019. The blue inverted triangles denote the seven short-period GeoNet seismometers used to detect and locate the earthquakes. Pink squares denote the location of the GeoNet GNSS network. The black box shows the location of **Figure 3**. The orange star marks the location of Kawerau geothermal field, where the velocity model used in this study was derived (Clarke et al., 2009, Figure S1).

and S phase-arrivals resulting in a total of 348 earthquakes. These earthquakes were initially located with NonLinLoc (Lomax et al., 2000), using a velocity model derived from the nearby Kawerau geothermal field (Clarke et al., 2009) (**Supplementary Figure S1**). We then used waveform correlation to generate differential pick times with the Obspy package (Beyreuther et al., 2010). We used a 2 s window around each pick, beginning 0.5 s before the pick, allowing the pick to adjust by up to 0.3 s, and each event pair had a maximum hypocentral separation of 8 km. These differential pick times were then used to relocate the entire catalog using the double-difference relocation program GrowClust (Trugman and Shearer, 2017), requiring a minimum correlation of 0.5. This resulted in 94 relocated earthquakes in total (**Figure 2**). We calculate local-magnitudes by measuring the peak displacement on a simulated Wood-Anderson seismometer on each seismometer, for each earthquake. We then use the local-magnitude scale developed for New Zealand (Ristau et al., 2016). This results in magnitudes over the range −1.12 to 2.54 M_L, and for earthquakes also detected by GeoNet our magnitudes are comparable. We then compute moment tensors using P-wave polarities picked on the wider North Island GeoNet network and the Bayesian moment tensor source inversion software MTfit (Pugh and White, 2018).

4. RESULTS

The main concentration of earthquakes (131 events total, 71 relocated) occurred in the Puhipuhi embayment to the northeast of Tarawera (**Figure 3**) and ranged from −0.47 to 2.54 M_L in magnitude. The mean horizontal and vertical errors from the initial location are ±0.8 and ±0.68 km respectively, and the relative horizontal and vertical errors after relocation are ±0.036 and ±0.005 km, respectively. The relocated earthquakes form a clear lineation with a strike of ~70°. When viewed in cross-section the earthquakes appear to have occurred along a ~3 km long, vertical plane between 8 and 10.5 km depth (**Figure 3**). The earthquakes migrated from NE to SW at an apparent rate of 0.3–0.6 m s^{-1}, and their range of depths increased at the same time (**Figure 4**). These spatial patterns are also produced when using locations generated using GrowClust's internal bootstrapping approach (Efron and Tibshirani, 1991; Efron and Tibshirani, 1994; Trugman and Shearer, 2017), demonstrating that they are not an artifact of data or station distribution (**Supplementary Figures S1, S2**). We are able to calculate four reliable moment tensor solutions for earthquakes in this swarm (**Figure 5**). These all produce double-couple, normal fault solutions with nodal plane strikes very similar to the strike of the earthquake cluster lineation. The

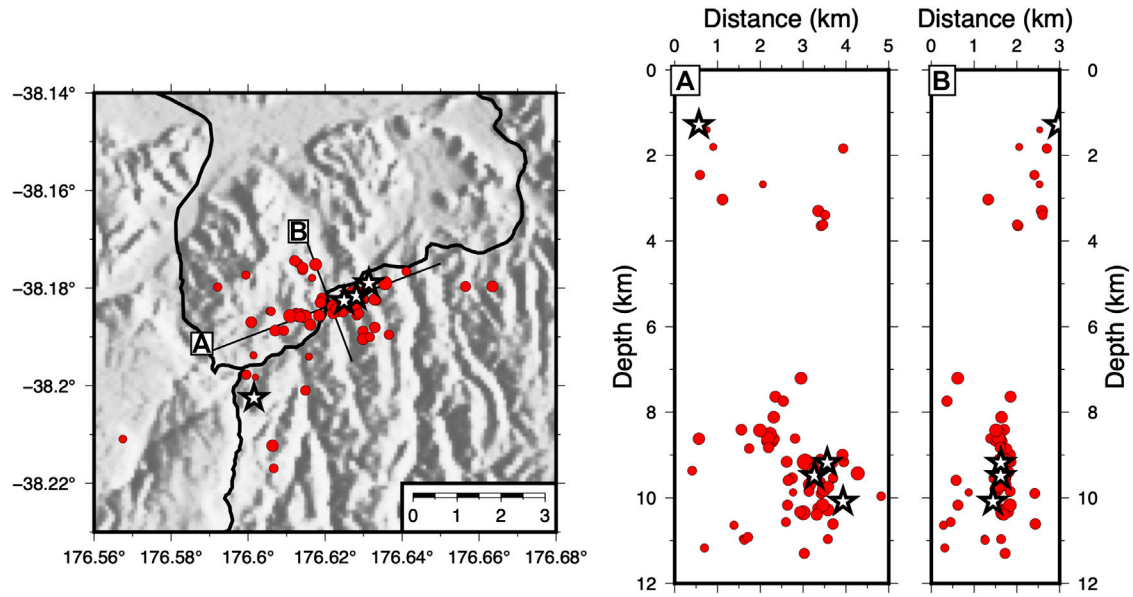

FIGURE 3 | Relocated earthquakes (red circles, scaled by magnitude) show a clear lineation striking at ~70°. Along **(A)** and across **(B)** strike cross-sections show that these earthquakes are occurring on a vertical plane. White stars show the locations of earthquakes with calculated moment tensors, shown in **Figure 5**.

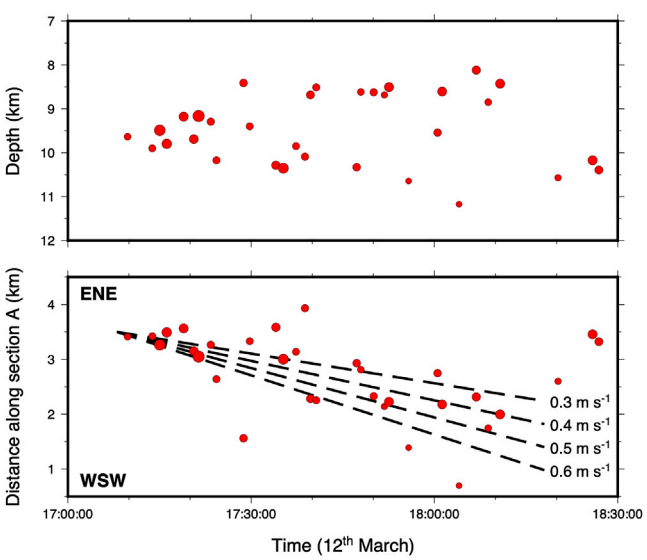

FIGURE 4 | Top: The variations of earthquake depth vs time (UTC) for the 12th March cluster in **Figure 3**. This shows that the earthquakes increase in their depth extent through time. **Bottom:** Earthquake distance along section A (**Figure 3**) vs. time. This shows a clear propagation of the seismicity WSW along-strike at a rate of 0.3–0.6 m s^{-1}.

three solved moment-tensors which occur within the dyke-cluster (2019p191131, 2019p191139, 2019p191176) can be solved with a non-double-couple component but as a double-couple solution can adequately explain the data, we select this as the least complicated solution (**Supplementary Figures S4–S7**).

5. DISCUSSION

5.1. Origin of the 2019 Earthquake Swarm

The March 2019 earthquake cluster has several notable characteristics. First, it delineates a vertical structure between ~8 and 10.5 km depth (**Figure 3**), which is close to the base of the generally observed seismogenic depth in the TVZ (Bryan et al., 1999). Second, the vertical structure has a strike of ~70° (**Figure 3**), near identical to the observed surficial orientation of dyke intrusions during the 1886 Tarawera eruption (Nairn and Cole, 1981). Third, the earthquakes migrated laterally, from ENE to WSW, at a rate of 0.3–0.6 m s^{-1} and their depth distribution range expanded during this lateral migration (**Figure 4**). There are three possible causes for earthquake swarms in the TVZ; slip on a fault-plane, diffusion of geothermal fluids, or intrusion of a magmatic body. Given that the earthquake cluster occurs below the brittle-ductile transition in the TVZ (Bryan et al., 1999) and occurs along a vertical plane, inconsistent with extensional faulting, we suggest it is unlikely that the cluster was caused by slip along a fault-plane. Lateral propagation of seismicity along vertically inclined faults has been observed at oceanic transform faults and interpreted as aseismic creep along a fault-plane (Roland and McGuire, 2009). While these observations are similar to those presented here, the tectonic setting in the TVZ is quite different and we feel it is therefore unlikely that our observations are explained by strike-slip creep. Smith et al. (2007) proposed that subsidence at Taupō caldera (New Zealand) in 1983 was caused by the dewatering of a magma body at depth, and at Yellowstone caldera (USA) this process has been shown to cause propagating seismicity on a vertical plane, similar to our observations (Waite and Smith, 2002). However, the diffusion velocity of hydrothermal fluids resulting from dewatering is

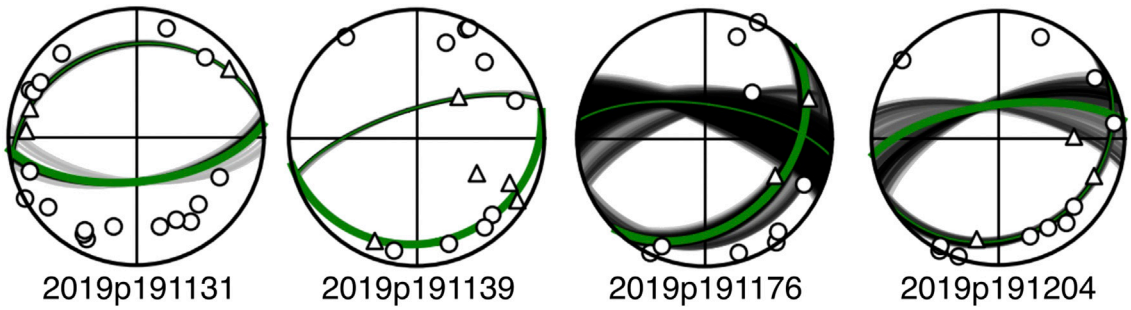

FIGURE 5 | Moment tensors for four earthquakes associated with the dyke intrusion, earthquake ID numbers are below each. Locations are indicated by white stars in **Figure 3**. Events 2019p191131, 2019p191139, and 2019p191176 occur within the deep dyke-associated cluster, while event 2019p191204 occurs in the shallow cluster at a depth of 1.3 km. Moment tensors are calculated using MTfit (Pugh and White, 2018) and show the full range of possible nodal planes, with the highest probability solution shown in green. Further details of the moment tensor solutions is shown in **Supplementary Figures S4–S7**. Circles and triangles represent positive and negative polarity picks respectively.

estimated, and observed, to be several orders of magnitude slower than the intrusion rate we observe, and thus our data is not satisfactorily explained by the diffusion of geothermal fluids from a dewatering magma body. In addition, upwelling geothermal fluids have been observed to cause seismicity in nearby Rotomahana (Bannister et al. 2016; **Figure 1**). However, the seismicity at Rotomahana shows no lateral migration, occurs between 4 and 6.5 km depth, and occurs in repetitive "bursts" over at least the past 25 years (Bannister et al., 2016). These characteristics suggest that the March 2019 earthquake cluster is unlikely to be caused by a similar upwelling of geothermal fluids.

We therefore suggest that the 2019 earthquake swarm was most likely caused by a dyke, intruding to depths as shallow as ~8–10.5 km, that migrated toward Tarawera volcano in a WSW direction. The migrating earthquakes are inferred to have been caused by country rock opening at the tip of the propagating dyke (Belachew et al., 2011; Sigmundsson et al., 2015), and this is evidenced by the normal fault moment tensors (**Figure 5**). These moment tensors may also be explained by a component of non-double-couple deformation (**Supplementary Figures S4–S7**), which would also support a dyke model. We can thus use the migration rate of earthquakes as a proxy for the intrusion rate of the dyke (i.e. 0.3–0.6 m s^{-1}). Our calculated intrusion rate of 0.3–0.6 m s^{-1} is very similar to those recorded for basaltic dyke intrusions in the Afar rift (Belachew et al., 2011; Barnie et al., 2015), Red Sea (Eyles et al., 2018), El Hierro (Martí et al., 2013), and Iceland (Einarsson and Brandsdóttir, 1980). However, it is significantly faster than intrusion rates calculated from a rhyolite dyke intrusion in the Main Ethiopian Rift (3×10^{-3} m s^{-1}; Temtime et al., 2020). We therefore propose that the dyke intrusion was most likely basaltic in composition.

5.2. Volume Estimate

Dyke intrusions represent movement of magma that can often be detected by volcanic monitoring through measuring surface deformation. However, the ability to detect intrusions depends on many factors including the volume and location of the intrusion. Based on the energy balance caused by an intrusion and the seismic moment release, Bonaccorso et al. (2017) derived an empirical relationship relating seismic moment to dyke thickness. Using this relationship, and the total seismic moment release of 1.77×10^{13} N m, the thickness of the 2019 dyke near Tarawera would be ~0.15 cm. Alternatively, global observations of dyke intrusions suggest length to thickness ratios of 1,500 (Gudmundsson, 1987, 2011) giving a thickness of ~2 m. Therefore, based on the dyke's length and associated seismic moment release, we could expect an intrusion with a volume of $1.1–15 \times 10^6$ m^3. Ground deformation as a result of discrete dyking events has been well documented in a number of volcanic and rift environments (Hamling et al., 2009; Sigmundsson et al., 2015; Hamling et al., 2019). To investigate whether the inferred dyke was detected geodetically, we use ascending and descending synthetic aperture radar (SAR) data acquired by the Sentinel-1 satellite to generate two co-intrusion interferograms (**Figure 6**). Neither of the interferograms show an obvious signal consistent with an intrusion, and there is no detectable signal in the GNSS network (**Figure 2**). However, given the depth of the dyke intrusion, it is possible that ground deformation was too small to be detected.

To investigate how much volume could be hidden before deformation would be detected by the InSAR data, we generated a suite of synthetic intrusions. We fixed the geometry of the dyke based on the earthquake observations and examined the effect of the dyke thickness on the detectable signal. For each thickness value, we generated a synthetic interferogram by adding the modeled deformation to the ascending and descending interferograms respectively. We then evaluated the signal to noise ratio using the deformation from the modeled intrusion as the reference signal. For both the ascending and descending datasets, the signal to noise ratio only becomes positive once the thickness of the dyke exceeds ~5–6 m (**Figure 6**). This suggests that for a similar sized intrusion, at these depths, we would be unlikely to detect it with current geodetic monitoring unless its volume exceeds ~$37–45 \times 10^6$ m^3.

Our estimated intrusion volume of $1.1–15 \times 10^6$ m^3, based on dyke length and seismic moment release, should be considered as a minimum estimate, as the maximum depth of the

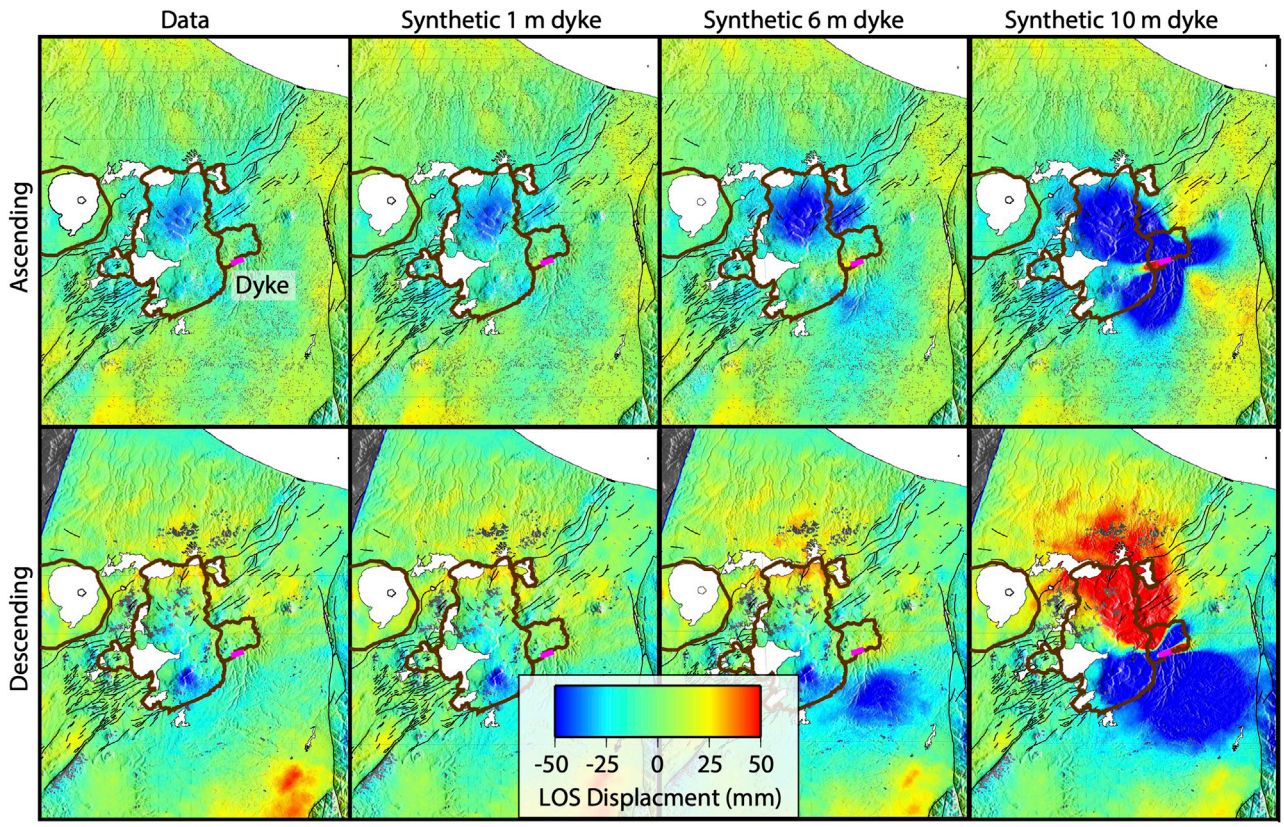

FIGURE 6 | Line of site displacement for ascending **(top)** and descending **(bottom)** SAR data acquired by Sentinel-1. The data **(left)** shows no observable ground deformation from the dyke intrusion. We then use synthetic dykes, centered on the 2019 dyke location but with varying thickness, to show that only a dyke intrusion with thickness ≥6 m would be detectable.

earthquake sequence may not provide a lower limit on the intrusion. Evidence from elsewhere in the TVZ (e.g., Bryan et al., 1999), suggests the depths of the earthquake sequence may only reflect the maximum depth to which brittle failure occurred. It is therefore likely that the source reservoir for the 2019 dyke intrusion lies at depths ≥10 km in the vicinity of the Puhipuhi embayment. Further geophysical imaging in this region may be able to determine the location and depth of this magma reservoir.

5.3. Structural and Magmatic Implications

Our results lend contemporary evidence to the suggestion of Villamor et al. (2011) that extension within the OVC is accommodated by dyke intrusions. We also observe shallow (1-4 km depth) earthquakes directly above the dyke during intrusion (**Figure 3**), this is most likely caused by dyke-induced mechanical faulting accommodating extension in the brittle shallow crust (e.g., Belachew et al., 2011). Dyke intrusions can also yield good indications of the orientation of the crustal stress field (Wadge et al., 2016). The orientation (~70°) of this dyke intrusion suggests that this is also the orientation of the maximum horizontal compression (SH_{max}). This orientation differs slightly to observations from the rest of the TVZ which suggest an SH_{max} orientation of 40°–60° (Townend et al., 2012; Illsley-Kemp et al., 2019). It has been previously suggested that the direction of extension in the Taupō rift becomes more oblique in the Okataina region (Seebeck et al., 2014), possibly influenced by the presence of a large magma reservoir (Ellis et al., 2014). Our results support these previous observations and may suggest a higher degree of rift-obliquity within the Okataina region than that proposed by Seebeck et al. (2014). However, multiple studies have also shown that dyke orientations and trajectories can be influenced by local changes to crustal stresses. Topographic loads (e.g., volcanic edifices) have been shown to modify the local stress field and cause dykes to propagate toward them (Maccaferri et al., 2011; Rivalta et al., 2015), whereas topographic depressions (e.g., calderas) promote circumferential dyke intrusions (Gaete et al., 2019). The 2019 dyke intrusion propagated toward the Tarawera volcanic edifice, perpendicular to the major OVC caldera boundary, but sub-parallel to the Puhipuhi embayment margin (Nairn, 2002, **Figure 3**). For comparison, the 3.4 ka Rotokawau basalt in the northwestern region of the OVC (**Figure 1**) erupted along a fissure that is perpendicular to both the OVC caldera and Haroharo volcanic complex, and oblique to the rift orientation (Nairn, 2002). Shortly following the Kaharoa eruption there were multiple hydrothermal eruptions SW of Tarawera. Nairn et al. (2005) propose that these were caused by the intrusion of a SW–NE oriented basaltic dyke. Similarly, the 1886 eruptive fissure extended along-axis to the SW beyond the OVC

caldera margin and into Lake Rotomahana, showing no evidence that its extent or trajectory were influenced by the OVC caldera boundary (Nairn, 1979; Nairn, 2002). This suggests that within the OVC, the load of the volcanic edifices (rather than the collapse caldera margin) are exerting a first order control on crustal stress and dyke trajectories, promoting dyke propagation toward the base of these volcanic edifices (Maccaferri et al., 2011; Rivalta et al., 2015). These are important considerations for volcanic hazard assessment and for interpreting future signals of unrest in the OVC.

Given that dyke intrusions are shown to propagate toward the volcanic edifices from outside the OVC caldera, we speculate that the basalts which have been shown to influence Tarawera eruptions are not necessarily sourced from directly beneath the volcano. A lateral migration of basaltic magma toward Tarawera may also help explain the lack of evidence for interaction with the silicic magma reservoir in the 1886 eruption (Carey et al., 2007; Carey and Houghton, 2010). In such a case, the 1886 dyke may have completely bypassed the silicic system that is presumably still present at depth (but not yet detected by geophysics) beneath Tarawera from the Kaharoa eruption in AD 1314. Alternatively, the 1886 dyke may have intersected the silicic system beneath Tarawera, but the silicic system had since cooled beyond the solidus and is now moribund. Further geophysical assessment of the magmatic plumbing system beneath the OVC is required to address these unknowns.

It is likely that the 2019 dyke intrusion may have had similarities to the early dyke intrusions that fed the 1886 Tarawera eruption. But what were the controlling factors that caused the 2019 dyke to arrest, whereas the 1886 dyke intrusion led to a deadly and violent eruption? There are numerous potential causes for the arrest of the 2019 dyke, including magma solidification within the dyke (Fialko and Rubin, 1999), pressure decrease at the source magma reservoir (Rivalta, 2010), or stress and/or structural barriers. It is also important to consider that although the earthquake activity ceased, the 2019 dyke may have continued to propagate aseismically due to the crust becoming more ductile in the region closer to the caldera boundary. If a dyke intrusion were to reach the Tarawera Volcanic complex, we suggest that the load of the Tarawera edifice would cause it to shallow (Rivalta et al., 2015) and it could then take advantage of pre-existing crustal weaknesses to propagate to the surface and erupt. This may have been the case in 1886, and if a dyke intrusion were to propagate toward, and reach, Tarawera volcano in the modern day then a similar basaltic eruption may occur. However, it's important to note that geological evidence suggests that a high flux of primitive melt is required to sustain the rhyolite volcanism observed in the TVZ (Barker et al., 2020). This means that dyke intrusions are likely to be common and thus the vast majority do not lead to an eruption. Developing a better understanding of the tipping points that cause dyke intrusions to erupt on rare occasions is an important research goal.

5.4. Implications for Monitoring and Future Activity

Our analysis of a series of earthquakes that occurred in 2019 suggests a recent dyke intrusion that propagated toward Tarawera volcano, the site of New Zealand's largest and most destructive historical eruption (Walker et al., 1984). The OVC is monitored by GeoNet, primarily through seismometers and GNSS sensors though they are fairly sparse in the Puhipuhi embayment (**Figure 2**). In an active magmatic system, dyke intrusion can occur as a common process without necessarily resulting in an eruption (Acocella, 2014). However, detecting these events is critical for evaluating volcanic hazards and for monitoring ongoing surface changes. If a future dyke intrusion was identified early in its propagation, and the dyke dimensions were constrained by geodetic techniques, then the expected total mechanical energy release could be calculated using derived relationships (Bonaccorso et al., 2017; Bonaccorso and Giampiccolo, 2020). This, alongside detailed seismic analysis of the dyke-induced earthquakes, would allow for the forecast of the time and location of dyke arrest, and the associated likelihood of significant unrest and/or eruption (e.g., Aspinall et al., 2006; Constantinescu et al., 2016). We have shown that the requisite seismological analysis is possible with the current GeoNet seismic monitoring system albeit with detailed analysis long after the earthquake swarm. This process could be significantly improved using real-time detection and location of earthquakes (e.g., Chamberlain et al., 2020). However the geodetic monitoring network, particularly GNSS station density, would need to be improved in order to detect and constrain a similar future dyke intrusion. We have also shown that dyke intrusions sourced from outside the OVC caldera can propagate toward Tarawera, and we speculate that similar "external" dyke intrusions may have influenced past eruptive activity. Therefore, monitoring of Tarawera volcano should not focus solely on the region directly beneath the volcanic edifice but consider the broader surrounding area.

6. CONCLUSION

On the 12th March 2019, a swarm of 131 earthquakes occurred to the NE of Tarawera volcano, within the OVC. We use high-precision earthquake locations to demonstrate that the swarm was most likely caused by the WSW intrusion of a ~2 km long dyke, with seismicity occurring between 8 and 11 km depth. By tracking the migration of seismicity we estimate that the dyke propagated at a rate of 0.3–0.6 m s^{-1}, a very similar propagation speed to that observed for basaltic dyke intrusions in global extensional tectonic settings. The intrusion rate, coupled with the depth of the dyke intrusion, indicate that this was most likely a basaltic dyke intrusion. Based on the dyke length and seismic moment release we estimate a total (minimum) intrusion volume of $1.1–15\times10^6$ m^3, and use a suite of synthetic models to show that the associated ground deformation could not have been detected by co-intrusion interferograms. The 2019 dyke intrusion propagated toward the Tarawera volcanic complex from outside the OVC, suggesting that this topographic load has a first-order control over the local crustal stress. Improvements to geodetic monitoring in the OVC could help to better identify future dyke intrusions and allow for the early assessment of the volcanic hazard they may or may not pose.

DATA AVAILABILITY STATEMENT

All seismic data used in this study are freely available from GeoNet (https://www.geonet.org.nz/). The earthquake catalogue is provided in QuakeML format in the Supplementary Material and as an online dataset: 10.5281/zenodo.4035171.

AUTHOR CONTRIBUTIONS

TB performed seismological analysis. FI-K supervised TB and led writing of the article. HE produced **Figure 1** and helped write the article. IH performed geodetic analysis and helped write the article. MS supervised TB and helped write the article. CW helped write the article. EM supervised TB and helped write the article. SB helped write the article.

FUNDING

TB was funded by a Victoria University of Wellington Summer Scholarship and the ECLIPSE program, which is funded by the New Zealand Ministry of Business, Innovation and Employment. FI-K, EM are fully funded, and SB, CW, IH, and MS are part supported by the ECLIPSE program. HE is part supported by the ECLIPSE program and a Victoria University of Wellington doctoral scholarship.

ACKNOWLEDGMENTS

This project analyzed and plotted the seismic data using EQcorrscan (Chamberlain et al., 2018), Obspy (Beyreuther et al., 2010), GMT (Wessel et al., 2019), and Pyrocko (Heimann et al., 2017). We thank Nico Fournier for constructive feedback on the manuscript. We also thank the constructive reviews of Yohei Yukutake and Francesca Di Luccio.

SUPPLEMENTARY MATERIAL

The Supplementary Material for this article can be found online at: https://www.frontiersin.org/articles/10.3389/feart.2020.606992/full#supplementary-material.

REFERENCES

Acocella, V., Di Lorenzo, R., Newhall, C., and Scandone, R. (2015). An overview of recent (1988–2014) caldera unrest: knowledge and perspectives. *Rev. Geophys.* 53, 896–955. doi:10.1002/2015rg000492

Acocella, V. (2014). Great challenges in volcanology: how does the volcano factory work? *Front. Earth Sci.* 2, 4. doi:10.3389/feart.2014.00004

Acocella, V., Spinks, K., Cole, J. W., and Nicol, A. (2003). Oblique back arc rifting of Taupo Volcanic zone, New Zealand. *Tectonics* 22, 1045. doi:10.1029/2002tc001447

Aspinall, W. P., Carniel, R., Jaquet, O., Woo, G., and Hincks, T. (2006). Using hidden multi-state Markov models with multi-parameter volcanic data to provide empirical evidence for alert level decision-support. *J. Volcanol. Geoth. Res.* 153, 112–124. doi:10.1016/j.jvolgeores.2005.08.010

Bannister, S., Sherburn, S., and Bourguignon, S. (2016). Earthquake swarm activity highlights crustal faulting associated with the Waimangu–Rotomahana–Mt Tarawera geothermal field, Taupo Volcanic Zone. *J. Volcanol. Geoth. Res.* 314, 49–56. doi:10.1016/j.jvolgeores.2015.07.024

Barker, S. J., Rowe, M. C., Wilson, C. J. N., Gamble, J. A., Rooyakkers, S. M., Wysoczanski, R. J., et al. (2020). What lies beneath? Reconstructing the primitive magmas fueling voluminous silicic volcanism using olivine-hosted melt inclusions. *Geology* 48, 504–508. doi:10.1130/g47422.1

Barnie, T. D., Keir, D., Hamling, I., Hofmann, B., Belachew, M., Carn, S., et al. (2015). A multidisciplinary study of the final episode of the Manda Hararo dyke sequence, Ethiopia, and implications for trends in volcanism during the rifting cycle. *Geol. Soc. Lond. Spec. Pub.* 420, 149–163. doi:10.1144/sp420.6

Belachew, M., Ebinger, C., Coté, D., Keir, D., Rowland, J., Hammond, J., et al. (2011). Comparison of dike intrusions in an incipient seafloor-spreading segment in Afar, Ethiopia: seismicity perspectives. *J. Geophys. Res.* 116, B06405. doi:10.1029/2010jb007908

Beyreuther, M., Barsch, R., Krischer, L., Megies, T., Behr, Y., and Wassermann, J. (2010). ObsPy: a Python toolbox for seismology. *Seismol Res. Lett.* 81, 530–533. doi:10.1785/gssrl.81.3.530

Bibby, H. M., Caldwell, T. G., Davey, F. J., and Webb, T. H. (1995). Geophysical evidence on the structure of the Taupo Volcanic Zone and its hydrothermal circulation. *J. Volcanol. Geoth. Res.* 68, 29–58. doi:10.1016/0377-0273(95)00007-h

Bonaccorso, A., Aoki, Y., and Rivalta, E. (2017). Dike propagation energy balance from deformation modeling and seismic release. *Geophys. Res. Lett.* 44, 5486–5494. doi:10.1002/2017gl074008

Bonaccorso, A., and Giampiccolo, E. (2020). Balance between deformation and seismic energy release: the Dec 2018 'double-dike' intrusion at Mt. Etna. *Front. Earth Sci.* 8, 463. doi:10.3389/feart.2020.583815

Bryan, C. J., Sherburn, S., Bibby, H. M., Bannister, S. C., and Hurst, A. W. (1999). Shallow seismicity of the central Taupo Volcanic Zone, New Zealand: its distribution and nature. *N. Z. J. Geol. Geophys.* 42, 533–542. doi:10.1080/00288306.1999.9514859

Carey, R. J., Houghton, B. F., Sable, J. E., and Wilson, C. J. N. (2007). Contrasting grain size and componentry in complex proximal deposits of the 1886 Tarawera basaltic Plinian eruption. *Bull. Volcanol.* 69, 903–926. doi:10.1007/s00445-007-0117-6

Carey, R. J., and Houghton, B. F. (2010). "Inheritance": an influence on the particle size of pyroclastic deposits. *Geology* 38, 347–350. doi:10.1130/g30573.1

Cashman, K. V., and Sparks, R. S. J. (2013). How volcanoes work: a 25 year perspective. *GSA Bulletin* 125, 664–690. doi:10.1130/b30720.1

Chambefort, I., Lewis, B., Wilson, C. J. N., Rae, A. J., Coutts, C., Bignall, G., et al. (2014). Stratigraphy and structure of the Ngatamariki geothermal system from new zircon U–Pb geochronology: implications for Taupo Volcanic Zone evolution. *J. Volcanol. Geoth. Res.* 274, 51–70. doi:10.1016/j.jvolgeores.2014.01.015

Chamberlain, C. J., Hopp, C. J., Boese, C. M., Warren-Smith, E., Chambers, D., Chu, S. X., et al. (2018). EQcorrscan: repeating and near-repeating earthquake detection and analysis in python. *Seismol Res. Lett.* 89, 173–181. doi:10.1785/0220170151

Chamberlain, C. J., Townend, J., and Gerstenberger, M. C. (2020). RT-EQcorrscan: near-real-time matched–filtering for rapid development of dense earthquake catalogs. *Seismol Res. Lett.* 1–11, 23. doi:10.1785/0220200171

Clarke, D., Townend, J., Savage, M. K., and Bannister, S. (2009). Seismicity in the Rotorua and Kawerau geothermal systems, Taupo Volcanic Zone, New Zealand, based on improved velocity models and cross-correlation measurements. *J. Volcanol. Geoth. Res.* 180, 50–66. doi:10.1016/j.jvolgeores.2008.11.004

Cole, J. W., Deering, C. D., Burt, R. M., Sewell, S., Shane, P. A. R., and Matthews, N. E. (2014). Okataina Volcanic Centre, Taupo Volcanic Zone, New Zealand: a review of volcanism and synchronous pluton development in an active, dominantly silicic caldera system. *Earth Sci. Rev.* 128, 1–17. doi:10.1016/j.earscirev.2013.10.008

Cole, J. W. (1970). Petrology of the basic rocks of the Tarawera volcanic complex. *N. Z. J. Geol. Geophys.* 13, 925–936. doi:10.1080/00288306.1970.10418210

Cole, J. W., Spinks, K. D., Deering, C. D., Nairn, I. A., and Leonard, G. S. (2010). Volcanic and structural evolution of the Okataina Volcanic Centre: dominantly silicic volcanism associated with the Taupo Rift, New Zealand. *J. Volcanol. Geoth. Res.* 190, 123–135. doi:10.1016/j.jvolgeores.2009.08.011

Constantinescu, R., Robertson, R., Lindsay, J. M., Tonini, R., Sandri, L., Rouwet, D., et al. (2016). Application of the probabilistic model BET_UNREST during a volcanic unrest simulation exercise in Dominica, Lesser Antilles. *G-cubed* 17, 4438–4456. doi:10.1002/2016gc006485

Darragh, M., Cole, J. W., Nairn, I. A., and Shane, P. A. R. (2006). Pyroclastic stratigraphy and eruption dynamics of the 21.9 ka Okareka and 17.6 ka Rerewhakaaitu eruption episodes from Tarawera volcano, Okataina Volcanic Centre, New Zealand. *N. Z. J. Geol. Geophys.* 49, 309–328. doi:10.1080/00288306.2006.9515170

Dimitrova, L. L., Wallace, L. M., Haines, A. J., and Williams, C. A. (2016). High-resolution view of active tectonic deformation along the Hikurangi subduction margin and the Taupo Volcanic Zone, New Zealand. *N. Z. J. Geol. Geophys.* 59, 43–57. doi:10.1080/00288306.2015.1127823

Eastwood, A. A., Gravley, D. M., Wilson, C. J. N., Chambefort, I., Oze, C., Cole, J. W., et al. (2013). "U-Pb dating of subsurface pyroclastic deposits (Tahorakuri Formation) at Ngatamariki and Rotokawa geothermal fields," in Proceedings of the 35th New Zealand geothermal workshop, Rotorua, New Zealand.

Ebinger, C. J., van Wijk, J., and Keir, D. (2013). The time scales of continental rifting: implications for global processes. *Geol. Soc. Am. Spec. Pap.* 500, 371–396. doi:10.1130/2013.2500(11)

Efron, B., and Tibshirani, R. (1991). Statistical data analysis in the computer age. *Science* 253, 390–395. doi:10.1126/science.253.5018.390

Efron, B., and Tibshirani, R. J. (1994). *An introduction to the bootstrap*. Boca Raton, Florida: CRC Press.

Einarsson, P., and Brandsdóttir, B. (1980). Seismological evidence for lateral magma intrusion during the July 1978 deflation of the Krafla volcano in NE-Iceland. *J. Geophys.* 47, 160–165. doi:10.2172/890964

Ellis, S. M., Heise, W., Kissling, W., Villamor, P., and Schreurs, G. (2014). The effect of crustal melt on rift dynamics: case study of the Taupo Volcanic Zone. *N. Z. J. Geol. Geophys.* 57, 453–458. doi:10.1080/00288306.2014.972961

Eyles, J. H., Illsley-Kemp, F., Keir, D., Ruch, J., and Jónsson, S. (2018). Seismicity associated with the formation of a new island in the Southern Red Sea. *Front. Earth Sci.* 6, 141. doi:10.3389/feart.2018.00141

Fialko, Y. A., and Rubin, A. M. (1999). Thermal and mechanical aspects of magma emplacement in giant dike swarms. *J. Geophys. Res.* 104, 23033–23049. doi:10.1029/1999jb900213

Gaete, A., Kavanagh, J. L., Rivalta, E., Hazim, S. H., Walter, T. R., and Dennis, D. J. (2019). The impact of unloading stresses on post-caldera magma intrusions. *Earth Planet Sci. Lett.* 508, 109–121. doi:10.1016/j.epsl.2018.12.016

Gamble, J. A., Smith, I. E. M., McCulloch, M. T., Graham, I. J., and Kokelaar, B. P. (1993). The geochemistry and petrogenesis of basalts from the Taupo Volcanic Zone and Kermadec island arc, SW Pacific. *J. Volcanol. Geoth. Res.* 54, 265–290. doi:10.1016/0377-0273(93)90067-2

Gudmundsson, A. (1987). Formation and mechanics of magma reservoirs in Iceland. *Geophys. J. Int.* 91, 27–41. doi:10.1111/j.1365-246x.1987.tb05211.x

Gudmundsson, A. (2011). Deflection of dykes into sills at discontinuities and magma-chamber formation. *Tectonophysics* 500, 50–64. doi:10.1016/j.tecto.2009.10.015

Haines, A. J., and Wallace, L. M. (2020). New Zealand-wide geodetic strain rates using a physics-based approach. *Geophys. Res. Lett.* 47, e2019GL084606. doi:10.1029/2019gl084606

Hamling, I. J., Ayele, A., Bennati, L., Calais, E., Ebinger, C., Keir, D., et al. (2009). Geodetic observations of the ongoing Dabbahu rifting episode: new dyke intrusions in 2006 and 2007. *Geophys. J. Int.* 178, 989–1003. doi:10.1111/j.1365-246x.2009.04163.x

Hamling, I. J., Cevuard, S., and Garaebiti, E. (2019). Large-scale drainage of a complex magmatic system: observations from the 2018 eruption of Ambrym volcano Vanuatu. *Geophys. Res. Lett.* 46, 4609–4617. doi:10.1029/2019gl082606

Hamling, I. J., Hreinsdottir, S., and Fournier, N. (2015). The ups and downs of the TVZ: geodetic observations of deformation around the Taupo Volcanic Zone, New Zealand. *J. Geophys. Res.: Sol. Earth* 120, 4667–4679. doi:10.1002/2015jb012125

Heimann, S., Kriegerowski, M., Isken, M., Cesca, S., Daout, S., Grigoli, F., et al. (2017). *Pyrocko-an open-source seismology toolbox and library*. London: GFZ Data Services.

Heise, W., Caldwell, T. G., Bertrand, E. A., Hill, G. J., Bennie, S. L., and Palmer, N. G. (2016). Imaging the deep source of the Rotorua and Waimangu geothermal fields, Taupo Volcanic Zone, New Zealand. *J. Volcanol. Geoth. Res.* 314, 39–48. doi:10.1016/j.jvolgeores.2015.10.017

Heise, W., Caldwell, T. G., Bibby, H. M., and Bennie, S. L. (2010). Three-dimensional electrical resistivity image of magma beneath an active continental rift, Taupo Volcanic Zone, New Zealand. *Geophys. Res. Lett.* 37, L10301. doi:10.1029/2010gl043110

Hogg, A. G., Higham, T. F. G., Lowe, D. J., Palmer, J. G., Reimer, P. J., and Newnham, R. M. (2003). A wiggle-match date for Polynesian settlement of New Zealand. *Antiquity* 77, 116–125. doi:10.1017/s0003598x00061408

Holden, L., Cas, R., Fournier, N., and Ailleres, L. (2017). Modelling ground deformation patterns associated with volcanic processes at the Okataina Volcanic Centre. *J. Volcanol. Geoth. Res.* 344, 65–78. doi:10.1016/j.jvolgeores.2017.04.014

Holden, L., Wallace, L. M., Beavan, J., Fournier, N., Cas, R., Ailleres, L., et al. (2015). Contemporary ground deformation in the Taupo rift and Okataina Volcanic Centre from 1998 to 2011, measured using GPS. *Geophys. J. Int.* 202, 2082–2105. doi:10.1093/gji/ggv243

Hurst, T., Bannister, S., Robinson, R., and Scott, B. (2008). Characteristics of three recent earthquake sequences in the Taupo Volcanic Zone, New Zealand. *Tectonophysics* 452, 17–28. doi:10.1016/j.tecto.2008.01.017

Illsley-Kemp, F., Savage, M. K., Wilson, C. J. N., and Bannister, S. (2019). Mapping stress and structure from subducting slab to magmatic rift: crustal seismic anisotropy of the North Island, New Zealand. *G-cubed* 20, 5038–5056. doi:10.26686/wgtn.12309776.v1

Johnson, E. R., Kamenetsky, V. S., McPhie, J., and Wallace, P. J. (2011). Degassing of the HO-rich rhyolites of the Okataina Volcanic Center, Taupo Volcanic Zone, New Zealand. *Geology* 39, 311–314. doi:10.1130/g31543.1

Kendall, J. M., Stuart, G. W., Ebinger, C. J., Bastow, I. D., and Keir, D. (2005). Magma-assisted rifting in Ethiopia. *Nature* 433, 146–148. doi:10.1038/nature03161

Lamarche, G., Barnes, P. M., and Bull, J. M. (2006). Faulting and extension rate over the last 20,000 years in the offshore Whakatane Graben, New Zealand continental shelf. *Tectonics* 25, TC4005. doi:10.1029/2005tc001886

Leonard, G. S., Cole, J. W., Nairn, I. A., and Self, S. (2002). Basalt triggering of the c. AD 1305 Kaharoa rhyolite eruption, Tarawera Volcanic Complex, New Zealand. *J. Volcanol. Geoth. Res.* 115, 461–486. doi:10.1016/s0377-0273(01)00326-2

Lomax, A., Virieux, J., Volant, P., and Berge-Thierry, C. (2000). Probabilistic earthquake location in 3D and layered models. *Mod. Approaches Geophys.* 18, 101–134. doi:10.1007/978-94-015-9536-0_5

Maccaferri, F., Bonafede, M., and Rivalta, E. (2011). A quantitative study of the mechanisms governing dike propagation, dike arrest and sill formation. *J. Volcanol. Geoth. Res.* 208, 39–50. doi:10.1016/j.jvolgeores.2011.09.001

Mantiloni, L., Nespoli, M., Belardinelli, M. E., and Bonafede, M. (2020). Deformation and stress in hydrothermal regions: the case of a disk-shaped inclusion in a half-space. *J. Volcanol. Geoth. Res.* 403, 107011. doi:10.1016/j.jvolgeores.2020.107011

Martí, J., Pinel, V., López, C., Geyer, A., Abella, R., Tárraga, M., et al. (2013). Causes and mechanisms of the 2011–2012 El Hierro (Canary Islands) submarine eruption. *J. Geophys. Res.: Sol. Earth* 118, 823–839. doi:10.1002/jgrb.50087

Moran, S. C., Newhall, C., and Roman, D. C. (2011). Failed magmatic eruptions: late-stage cessation of magma ascent. *Bull. Volcanol.* 73, 115–122. doi:10.1007/s00445-010-0444-x

Nairn, I. A. (2002). *Geology of the Okataina Volcanic Center, scale 1:50,000, 25*. New Zealand: Institute of Geological and Nuclear Sciences Geological Map, Lower Hutt.

Nairn, I. A., and Cole, J. W. (1981). Basalt dikes in the 1886 Tarawera rift. *N. Z. J. Geol. Geophys.* 24, 585–592. doi:10.1080/00288306.1981.10421534

Nairn, I. A., Hedenquist, J. W., Villamor, P., Berryman, K. R., and Shane, P. A. (2005). The AD1315 Tarawera and Waiotapu eruptions, New Zealand: contemporaneous rhyolite and hydrothermal eruptions driven by an arrested basalt dike system?. *Bull. Volcanol.* 67, 186–193. doi:10.1007/s00445-004-0373-7

Nairn, I. A. (1979). Rotomahana—Waimangu eruption, 1886: base surge and basalt magma. *N. Z. J. Geol. Geophys.* 22, 363–378. doi:10.1080/00288306.1979.10424105

Nairn, I. A., Shane, P. R., Cole, J. W., Leonard, G. J., Self, S., and Pearson, N. (2004). Rhyolite magma processes of the AD 1315 Kaharoa eruption episode, Tarawera volcano, New Zealand. *J. Volcanol. Geoth. Res.* 131, 265–294. doi:10.1016/s0377-0273(03)00381-0

Nairn, I. A. (1992). The Te Rere and Okareka eruptive episodes—Okataina Volcanic Centre, Taupo Volcanic Zone, New Zealand. *N. Z. J. Geol. Geophys.* 35, 93–108. doi:10.1080/00288306.1992.9514503

Nicholls, I. A., Oba, T., and Conrad, W. K. (1992). The nature of primary rhyolitic magmas involved in crustal evolution: evidence from an experimental study of cummingtonite-bearing rhyolites, Taupo Volcanic Zone, New Zealand. *Geochem. Cosmochim. Acta* 56, 955–962. doi:10.1016/0016-7037(92)90039-l

Pugh, D. J., and White, R. S. (2018). MTfit: a Bayesian approach to seismic moment tensor inversion. *Seismol Res. Lett.* 89, 1507–1513. doi:10.1785/0220170273

Ristau, J., Harte, D., and Salichon, J. (2016). A revised local magnitude (M_L) scale for New Zealand earthquakes. *Bull. Seismol. Soc. Am.* 106, 398–407. doi:10.1785/0120150293

Rivalta, E. (2010). Evidence that coupling to magma chambers controls the volume history and velocity of laterally propagating intrusions. *J. Geophys. Res.* 115, B07203. doi:10.1029/2009jb006922

Rivalta, E., Taisne, B., Bunger, A. P., and Katz, R. F. (2015). A review of mechanical models of dike propagation: schools of thought, results and future directions. *Tectonophysics* 638, 1–42. doi:10.1016/j.tecto.2014.10.003

Roland, E., and McGuire, J. J. (2009). Earthquake swarms on transform faults. *Geophys. J. Int.* 178, 1677–1690. doi:10.1111/j.1365-246x.2009.04214.x

Rowland, J. V., and Sibson, R. H. (2001). Extensional fault kinematics within the Taupo Volcanic Zone, New Zealand: soft-linked segmentation of a continental rift system. *N. Z. J. Geol. Geophys.* 44, 271–283. doi:10.1080/00288306.2001.9514938

Rowland, J. V., Wilson, C. J. N., and Gravley, D. M. (2010). Spatial and temporal variations in magma-assisted rifting, Taupo Volcanic Zone, New Zealand. *J. Volcanol. Geoth. Res.* 190, 89–108. doi:10.1016/j.jvolgeores.2009.05.004

Sable, J. E., Houghton, B. F., Wilson, C. J. N., and Carey, R. J. (2006). Complex proximal sedimentation from Plinian plumes: the example of Tarawera 1886. *Bull. Volcanol.* 69, 89–103. doi:10.1007/s00445-006-0057-6

Sandri, L., Acocella, V., and Newhall, C. (2017). Searching for patterns in caldera unrest. *G-cubed* 18, 2748–2768. doi:10.1002/2017gc006870

Seebeck, H., Nicol, A., Villamor, P., Ristau, J., and Pettinga, J. (2014). Structure and kinematics of the Taupo rift, New Zealand. *Tectonics* 33, 1178–1199. doi:10.1002/2014tc003569

Shane, P., Martin, S. B., Smith, V. C., Beggs, K. F., Darragh, M. B., Cole, J. W., et al. (2007). Multiple rhyolite magmas and basalt injection in the 17.7 ka Rerewhakaaitu eruption episode from Tarawera volcanic complex, New Zealand. *J. Volcanol. Geoth. Res.* 164, 1–26. doi:10.1016/j.jvolgeores.2007.04.003

Shane, P., Nairn, I. A., Smith, V. C., Darragh, M., Beggs, K., and Cole, J. W. (2008). Silicic recharge of multiple rhyolite magmas by basaltic intrusion during the 22.6 ka Okareka Eruption Episode, New Zealand. *Lithos* 103, 527–549. doi:10.1016/j.lithos.2007.11.002

Sherburn, S., and Nairn, I. A. (2004). Modelling geophysical precursors to the prehistoric c. AD1305 Kaharoa rhyolite eruption of Tarawera volcano, New Zealand. *Nat. Hazards* 32, 37–58. doi:10.1023/b:nhaz.0000026791.16566.96

Sigmundsson, F., Hooper, A., Hreinsdóttir, S., Vogfjörd, K. S., Ófeigsson, B. G., Heimisson, E. R., et al. (2015). Segmented lateral dyke growth in a rifting event at Bárðarbunga volcanic system, Iceland. *Nature* 517, 191–195. doi:10.1038/nature14111

Smith, E. G. C., Williams, T. D., and Darby, D. J. (2007). Principal component analysis and modeling of the subsidence of the shoreline of Lake Taupo, New Zealand,1983–1999: evidence for dewatering of a magmatic intrusion?. *J. Geophys. Res.* 112, B08406. doi:10.1029/2006jb004652

Sparks, R. S., Biggs, J., and Neuberg, J. W. (2012). Monitoring volcanoes. *Science* 335, 1310–1311. doi:10.1126/science.1219485

Temtime, T., Biggs, J., Lewi, E., and Ayele, A. (2020). Evidence for active rhyolitic dike intrusion in the Northern Main Ethiopian Rift from the 2015 Fentale seismic swarm. *G-cubed* 21, e2019GC008550. doi:10.1029/2019gc008550

Townend, J., Sherburn, S., Arnold, R., Boese, C., and Woods, L. (2012). Three-dimensional variations in present-day tectonic stress along the Australia–Pacific plate boundary in New Zealand. *Earth Planet Sci. Lett.* 353–354, 47–59. doi:10.1016/j.epsl.2012.08.003

Trugman, D. T., and Shearer, P. M. (2017). GrowClust: a hierarchical clustering algorithm for relative earthquake relocation, with application to the Spanish Springs and Sheldon, Nevada, earthquake sequences. *Seismol Res. Lett.* 88, 379–391. doi:10.1785/0220160188

Villamor, P., Berryman, K. R., Nairn, I. A., Wilson, K., Litchfield, N., and Ries, W. (2011). Associations between volcanic eruptions from Okataina volcanic center and surface rupture of nearby active faults, Taupo rift, New Zealand: insights into the nature of volcano-tectonic interactions. *Bull. Geol. Soc. Am.* 123, 1383–1405. doi:10.1130/b30184.1

Wadge, G., Biggs, J., Lloyd, R., and Kendall, J.-M. (2016). Historical volcanism and the state of stress in the East African Rift system. *Front. Earth Sci.* 4, 86. doi:10.3389/feart.2016.00086

Waight, T. E., Troll, V. R., Gamble, J. A., Price, R. C., and Chadwick, J. P. (2017). Hf isotope evidence for variable slab input and crustal addition in basalts and andesites of the Taupo Volcanic Zone, New Zealand. *Lithos* 284, 222–236. doi:10.1016/j.lithos.2017.04.009

Waite, G. P., and Smith, R. B. (2002). Seismic evidence for fluid migration accompanying subsidence of the Yellowstone caldera. *J. Geophys. Res.: Sol. Earth* 107, 2177. doi:10.1029/2001JB000586

Walker, G. P., Self, S., and Wilson, L. (1984). Tarawera 1886, New Zealand—a basaltic plinian fissure eruption. *J. Volcanol. Geoth. Res.* 21, 61–78. doi:10.1016/0377-0273(84)90016-7

Wallace, L. M., Beavan, J., McCaffrey, R., and Darby, D. (2004). Subduction zone coupling and tectonic block rotations in the North Island, New Zealand. *J. Geophys. Res.: Sol. Earth* 109, B12406. doi:10.1029/2004jb003241

Wessel, P., Luis, J. F., Uieda, L., Scharroo, R., Wobbe, F., Smith, W. H. F., et al. (2019). The generic mapping tools version 6. *G-cubed* 20, 5556–5564. doi:10.5194/egusphere-egu2020-2245

Wilson, C. J. N., Houghton, B. F., McWilliams, M. O., Lanphere, M. A., Weaver, S. D., and Briggs, R. M. (1995). Volcanic and structural evolution of Taupo Volcanic Zone, New Zealand: a review. *J. Volcanol. Geoth. Res.* 68, 1–28. doi:10.1016/0377-0273(95)00006-g

Wilson, C. J. N. (2017). Volcanoes: characteristics, tipping points, and those pesky unknown unknowns. *Elements* 13, 41–46. doi:10.2113/gselements.13.1.41

Conflict of Interest: The authors declare that the research was conducted in the absence of any commercial or financial relationships that could be construed as a potential conflict of interest.

Copyright © 2021 Benson, Illsley-Kemp, Elms, Hamling, Savage, Wilson, Mestel and Barker. This is an open-access article distributed under the terms of the Creative Commons Attribution License (CC BY). The use, distribution or reproduction in other forums is permitted, provided the original author(s) and the copyright owner(s) are credited and that the original publication in this journal is cited, in accordance with accepted academic practice. No use, distribution or reproduction is permitted which does not comply with these terms.

frontiers in Earth Science

BRIEF RESEARCH REPORT
published: 28 January 2021
doi: 10.3389/feart.2020.616676

Practical Volcano-Independent Recognition of Seismic Events: *VULCAN.ears* Project

Guillermo Cortés[1], Roberto Carniel[1], Philippe Lesage[2], M. Ángeles Mendoza[3] and Ivo Della Lucia[1]*

[1]*Dipartimento Politecnico di Ingegneria e Architettura (DPIA), Università degli Studi di Udine, Udine, Italy,* [2]*Université Grenoble Alpes, Université Savoie Mont Blanc, CNRS, IRD, IFSTTAR, ISTerre, Grenoble, France,* [3]*Departamento de Física Teórica y del Cosmos, Universidad de Granada, Granada, Spain*

Recognizing the mechanisms underlying seismic activity and tracking temporal and spatial patterns of earthquakes represent primary inputs to monitor active volcanoes and forecast eruptions. To quantify this seismicity, catalogs are established to summarize the history of the observed types and number of volcano-seismic events. In volcano observatories the detection and posterior classification or labeling of the events is manually performed by technicians, often suffering a lack of unified criteria and eventually resulting in poorly reliable labeled databases. State-of-the-art automatic Volcano-Seismic Recognition (VSR) systems allow real-time monitoring and consistent catalogs. VSR systems are generally designed to monitor one station of one volcano, decreasing their efficiency when used to recognize events from another station, in a different eruptive scenario or at different volcanoes. We propose a Volcano-Independent VSR (VI.VSR) solution for creating an exportable VSR system, whose aim is to generate labeled catalogs for observatories which do not have the resources for deploying their own systems. VI.VSR trains universal recognition models with data of several volcanoes to obtain portable and robust characteristics. We have designed the *VULCAN.ears* ecosystem to facilitate the VI.VSR application in observatories, including the *pyVERSO* tool to perform VSR tasks in an intuitive way, its graphical interface, *geoStudio*, and *liveVSR* for real-time monitoring. Case studies are presented at Deception, Colima, Popocatépetl and Arenal volcanoes testing VI.VSR models in challenging scenarios, obtaining encouraging recognition results in the 70–80% accuracy range. VI.VSR technology represents a major breakthrough to monitor volcanoes with minimal effort, providing reliable seismic catalogs to characterise real-time changes.

Keywords: volcano monitoring, eruption forecasting, machine learning, data mining, VULCAN.ears, volcano-seismic recognition, volcano-independent VSR, seismic recognition

OPEN ACCESS

Edited by:
Luca De Siena,
Johannes Gutenberg University Mainz, Germany

Reviewed by:
Andrea Cannata,
University of Catania, Italy
Alicia Jean Hotovec-Ellis,
United States Geological Survey, United States

****Correspondence:***
Guillermo Cortés
guillermo.cortes@uniud.it

Specialty section:
This article was submitted to Volcanology, a section of the journal Frontiers in Earth Science

Received: *12 October 2020*
Accepted: *15 December 2020*
Published: *28 January 2021*

Citation:
Cortés G, Carniel R, Lesage P, Mendoza MÁ and Della Lucia I (2021) Practical Volcano-Independent Recognition of Seismic Events: VULCAN.ears *Project. Front. Earth Sci. 8:616676. doi: 10.3389/feart.2020.616676*

1 INTRODUCTION

Volcanoes have a big impact on the global economy, society and more relevant, in human casualties. It is estimated that about 800 million people live inside the risk area of the 1,500 active volcanoes in the world (Brown et al., 2017). To address this issue, continuous volcano monitoring is performed by volcano observatories feeding eruption forecasting and early warning systems. These systems need to provide a fast response in case of crisis to evaluate the hazards related to an imminent eruption,

playing a crucial role in the decision-making of an eventual evacuation. Current monitoring is mainly performed in two stages: 1) *detection* of Volcano-Seismic (VS) events in continuous data streams received from monitoring stations (Sparks et al., 2012) and 2) *classification* of events according to their spectral and temporal features. These tasks allow to track the seismic activity of some specific event classes considered as 1) *eruption precursors*, such as volcanic tremors and long-period events (Chouet, 1996) or volcano-tectonic earthquakes (White and McCausland, 2016) and, 2) *imminent-risk* classes as collapses, lahars and pyroclastic flows. While the detection of events can be accomplished by automatic systems (Álvarez et al., 2013; García et al., 2020), the classification is generally manually done by experts, encompassing an inherent high level of subjectivity and lack of reliability. Manual classification cannot be achieved fast enough during a major unrest and/or an eruptive episode because of the strong increase of seismic activity before an eruption (Orozco-Alzate et al., 2012). Hence, in order to efficiently detect and classify volcano-seismic events, there is a need of automatic Volcano-Seismic Recognition (VSR) systems (Malfante et al., 2018), able to operate in nearly real-time (McNutt et al., 2015; Boué et al., 2016). However, the deployment of VSR systems in observatories suffers from three major drawbacks:

(1) Designing costs: *supervised VSR* systems need to be trained using previously labeled catalogs of events gathered in a database (DB) to characterize the volcano-seismic classes. This so-called *training stage* requires considerable human resources and time (Langer et al., 2019), not always affordable for modest observatories. *Unsupervised VSR (U.VSR)* does not need this training step, but achieves a lower recognition accuracy being relegated mainly to data mining purposes.
(2) Lack of robustness: observed seismicity patterns and event types, thus, the seismic features and volcano-seismic catalogs on which supervised VSR is based, vary according to the current state of the volcano (Carniel, 2014), to the environmental noise (Lecocq et al., 2020) and to the type and location of the stations. This variability can decrease the efficiency of the VSR systems designed to model a fixed configuration of networks, classes and patterns.
(3) Poor usability and integrability: installing a VSR system in a monitoring platform requires expert staff. Complex VSR software implies the training of technicians, making the interoperability with standardized protocols and services difficult.

At present, only few volcano observatories have operational VSR systems running in real-time (Cortés et al., 2009b; Maggi et al., 2017). This work presents a *Volcano-Independent Seismic Recognition* (VI.VSR) approach as the solution to the above VSR issues. VI.VSR (Cortés et al., 2017; 2019a) represents a promising trade-off between classic VSR and U.VSR paradigms: it can recognize events from a local volcano without any previous information about it, achieving an acceptable efficiency without implementing the whole system from scratch. It relies on prebuilt, universal VSR models describing universal databases of labeled events recorded on several volcanoes. Hence, our proposal provides a *volcano-portable*, *operational* and *robust VSR platform*, developed under the EU-funded *VULCAN.ears* project, which includes tools to build local VSR models or alternatively, to use prebuilt VI.VSR universal ones. *VULCAN.ears* deployed VI.VSR systems in several observatories, partnering with 18 international institutions to create the *VSR-ALUE* collaboration group. As a result, data from 21 volcanoes have been gathered and currently *VSR-ALUE* continues the support and development of the volcano-independent approach and application to real-case scenarios.

2 VOLCANO-INDEPENDENT SEISMIC RECOGNITION (VI.VSR)

VSR field has intensively grown in the last two decades boosted by the evolution of Machine Learning (Bergen et al., 2019) and by the need of modern observatories of having reliable and robust VSR systems (Langer et al., 2019). A myriad of classifiers have been tested, being Artificial Neuronal Networks (Falsaperla et al., 1996; Langer et al., 2003) and Support Vector Machines (Masotti et al., 2006; Curilem et al., 2014) the most popular ones in early 2000s, followed by advanced Probabilistic Graphical Models (Ohrnberger, 2001; Benítez et al., 2007; Trujillo-Castrillón et al., 2018) popularized in 2007 and Deep Learning approaches since 2017 (Titos et al., 2018, 2019a; Bueno et al., 2019a). Starting with the simple task of classifying events already detected in the data flow in the so-called *isolated VSR*, three major breakthroughs have been deployed in the VSR area (Malfante et al., 2018):

(1) **Continuous VSR** is able to detect and classify volcano-seismic events appearing in a continuous data stream. It can be subdivided in:

    a. *One-step VSR* implements detection and classification in the same stage. Actually, only few recognizers can achieve this, mostly structured graphical models as Hidden Markov Models (HMMs). (Benítez et al., 2007; Beyreuther et al., 2008; Ibáñez et al., 2009).
    b. Two-step VSR requires an extra processing stage to isolate the events. Bayesian Networks (Riggelsen et al., 2007) and Recurrent Networks (Titos et al., 2019b) handle continuous input data but need additional algorithms to delimit events. Most isolated VSR systems can be converted into continuous adding some detection technique such as classic signal triggers or advanced phase picking methods (Álvarez et al., 2013; Bueno et al., 2019b; García et al., 2020), which segment a continuous data stream into a sequence of time-delimited events.
(2) Robust VSR gathers information from different stations monitoring the same volcano, even in different epochs (Cortés et al., 2019a). This yields robust systems than can recognize events in any station of the network, in noisy

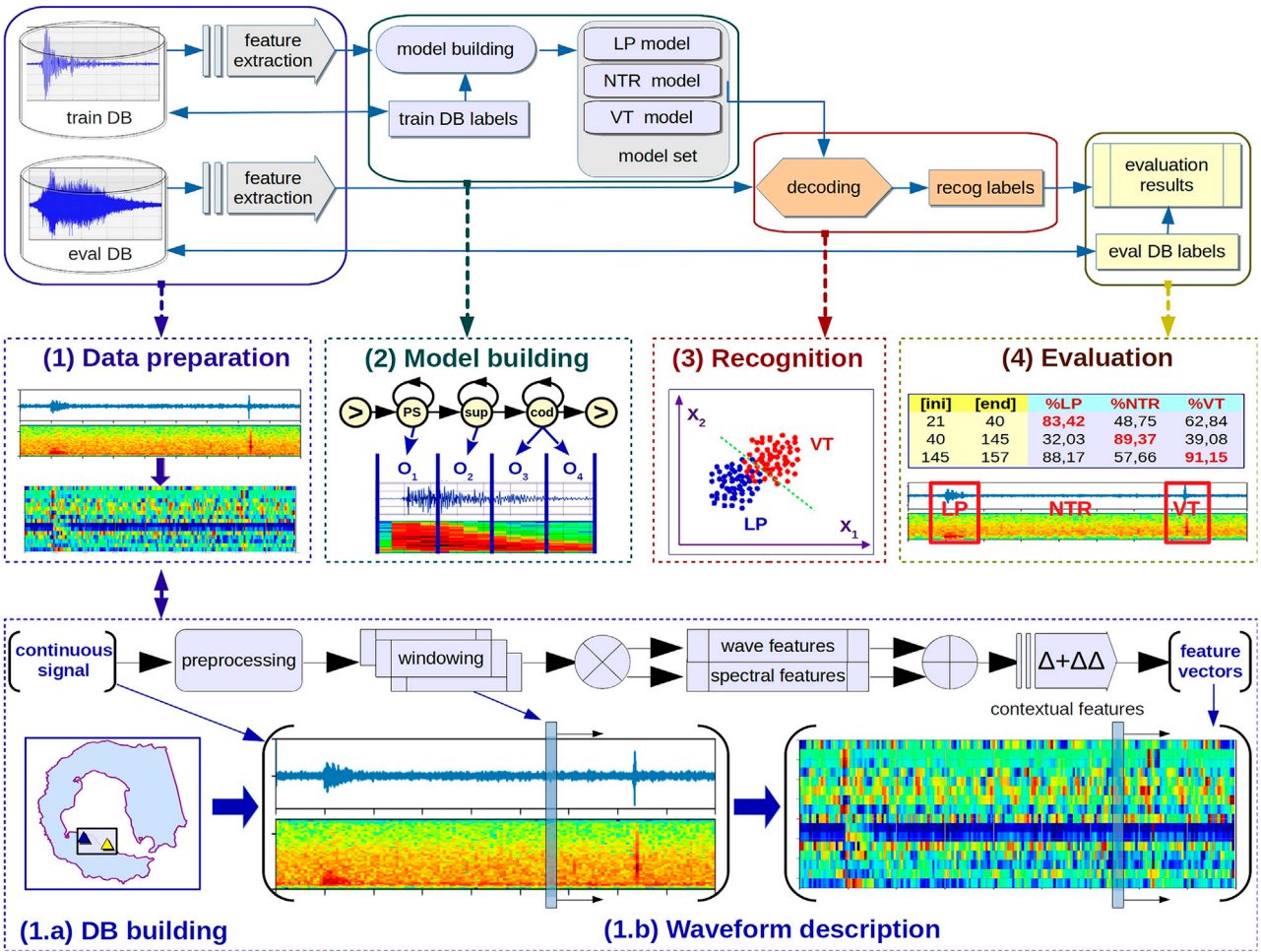

FIGURE 1 | Development stages of an automatic, supervised Volcano-Seismic Recognition (VSR) system. **(1) Data preparation** encompasses the data recording at monitoring stations and the data description **(1. a)** DB building: events in the data files are manually labeled and grouped in *train DB* and *eval DB* databases **(1. b)** Waveform description: a *continuous signal* containing a sequence of events is described as a sequence of *feature vectors*. **(2)** Model building: events in the *train DB* labeled as the same class are characterized by the same model, which is added to the VSR *model set*. **(3)** Recognition: *eval DB* events will be automatically detected and classified, outputting the *recog labels*. **(4)** Evaluation of the system is measured comparing those *recog labels* with the manual *eval DB labels*.

conditions and with different types of seismic activity without a noticeable decrease in its efficiency (Maggi et al., 2017; Journeau et al., 2020).

(3) Unsupervised VSR (U.VSR) unlike the two approaches above, does not require labeled data neither modeling, saving resources. Self Organized Maps (Köhler et al., 2010; Carniel et al., 2013a, b) are the standard to cluster volcano-seismic patterns even though recent deep learning technologies (Cannavo' et al., 2020) are obtaining interesting insights related with precursors.

These VSR types have their own application scopes and are not directly comparable. Most classifiers overpass the 90% of recognition accuracy when processing isolated VSR (Cortés, 2015). However, real-time, *online VSR* applied on continuous data ranges a 80–90% of accuracy. U.VSR schemes hardly surpass 70%. Nevertheless, due to the cost required to design supervised systems and their drop of effectiveness when the feature patterns of the events highly vary reflecting changes in the eruptive cycle, the current trend (Khan et al., 2019; Langer et al., 2019) is to use simpler U.VSR. Despite their low classification scores, U.VSR properly responds to the inherent variability of the seismic activity (Peltier et al., 2018). Conceived as a logical evolution of the robust VSR (Cortés et al., 2009a), the **hybrid VI.VSR** technology aims to be the future state-of-the-art joining supervised VSR scores within U.VSR goals to reach promising recognition results in the 70–80% band (Cortés et al., 2019a). In the following **Sections 2.1** and **2.2** we present our VSR baseline system and its improvements towards the *volcano-independent* VSR platform.

2.1 Automatic Volcano-Seismic Recognition (VSR)

A classic supervised VSR operation is divided in two stages shown in **Figure 1**: 1) the *training* step, including the data preparation,

description and classes characterization and, 2) the system *evaluation*, encompassing the automatic recognition of volcano-seismic events and measuring the performance. The system design is structured in:

(1) Data preparation consisting of:

   a. DB building: expert technicians manually detect and classify seismic events to prepare a labeled catalog which is split into the train DB and eval DB databases to train and evaluate the system, respectively. Their related train DB labels and eval DB labels detail the duration and type of the events appearing in each database.
   b. Waveform description consists of extracting relevant information from the data to be learnt by the system. To perform real-time VSR the continuous waveform is parametrized as a sequence of signal segments, each one described by a feature vector, resulting in a sequence $O = \{o_t\} = \{o_1, o_2, \ldots, o_t\}$ of observable vectors. An adequate scheme description of the data increases the robustness, exportability and recognition scores (Álvarez et al., 2012; Soto et al., 2018). Hybrid features describing waveform, geophysical and spectral information combined with their contextual, time derivatives components, provide an optimal scheme according to Cortés et al. (2016) and Maggi et al. (2017).

(2) Model building or learning phase to characterize the feature space projected by the $\{o_t\}$ feature vectors. Discriminative classifiers as neuronal networks and most deep learning structures delimit the space in clusters assigning each one to a volcano-seismic class of the train DB. Generative classifiers as graphical models independently model each class c estimating its joint probability $P(c, \{o_t\})$ to quantify the relationship between a vector and a class.

(3) Recognition of the events existing in each data file of the eval DB. Given a waveform file described as a sequence $\{o_v\}$ of V feature vectors, the recognition algorithm will uncover its corresponding sequence $\{c_r\}$ of R detected and classified events, mapping $\{o_v\} \rightarrow \{c_r\}$. The type and temporal limits of the recognized R events are outputted in the automatically generated recog labels catalog. In isolated VSR $R = 1$, thus, only substitution errors when an event is wrongly cataloged can be committed. Normally, in continuous VSR $R > 1$, hence, events not previously tagged by experts in the eval DB labels can be mistakenly detected (inserted) by the system which also can not detect (delete) other events actually registered.

(4) Evaluation measuring the similarity between the recog labels outputted by the system and the eval DB labels manually tagged. Precision, recall and F-score measures are common in machine learning literature but more natural comparisons are done counting the event insertion (I), deletion (D) and substitution (S) errors defined by the accuracy (%Acc) score:

$$\%\mathrm{Acc} = \mathrm{mean}_l\{\%\mathrm{Acc}(c_l)\} = \mathrm{mean}_l\left\{100\left[1 - \frac{E(c_l)}{N(c_l)}\right]\right\}, \quad (1)$$

with $N(c_l)$ the number of class c_l events in the *eval DB*, $E(c_l)$ the recognition errors and l an integer ranging from one to L, being L the number of evaluation classes. In continuous VSR $E = D + S + I$ while in isolated VSR $D = I = 0$, which explains its higher scores. The average $\overline{R}$ number of events in the evaluation data files has a large impact when comparing isolated vs. continuous tasks, as the accuracy exponentially decreases by the $\overline{R}$ factor.

2.2 Proposed Volcano-independent Seismic Recognition (VI.VSR) Framework

2.2.1 VI.VSR Underlying Technology

Given the similarities between speech and seismic events (Ohrnberger, 2001), former VI.VSR was inspired by the classic speech recognition area which successfully accomplishes speaker-independent tasks gathering multi-speaker databases modeled with HMMs (Rabiner and Schafer, 2007). HMMs characterize structured patterns, as volcano-seismic events, modeling not only the pattern waveforms, but also the relationship among patterns given by the temporal distribution of the HMM states. Each state represents a pattern observed in the $\{o_t\}$ sequence of feature vectors, such as *P*, S and superficial phase arrivals (**Figure 1**). HMMs are suitable for one-step continuous VSR in real-time, outperforming classic seismic detection algorithms even in noisy scenarios (Beyreuther and Wassermann, 2008). For boosting the system robustness and portability, VI.VSR has pushed beyond the state-of-the-art these innovative concepts:

- Universal databases: gathering data from different types of volcanoes increases the number and variety of patterns found in events of the same seismic class, improving the completeness and robustness of the given class model (Cortés et al., 2009a).
- Standardization of the seismic waveform based on unsupervised, data-driven decomposition and posterior selective reconstruction of a signal. Standardized events are less noisy and, hence, easier to recognize (Cortés et al., 2019b).
- Efficient data description: the extended Discriminative Feature Selection algorithm extracts the most relevant information of a seismogram when selecting the most efficient components of a feature vector to describe it (Álvarez et al., 2012; Cortés et al., 2016). In each iterative step, the worst feature according to a loss function is removed from the original vector, keeping only the most valuable components. This encompasses a better description of the seismic classes, simplifying their models and enhancing the system portability.
- Dedicated parallel VSR channels for each class: they are complete VSR systems specialized and customized in the detection and classification of just one type of seismic events (Cortés et al., 2014). A system unifying the output of these independent, class-focused, recognition channels surpasses the classic serial architecture depicted in **Figure 1** whereas all the classes share the same system configuration (Cortés et al., 2016).

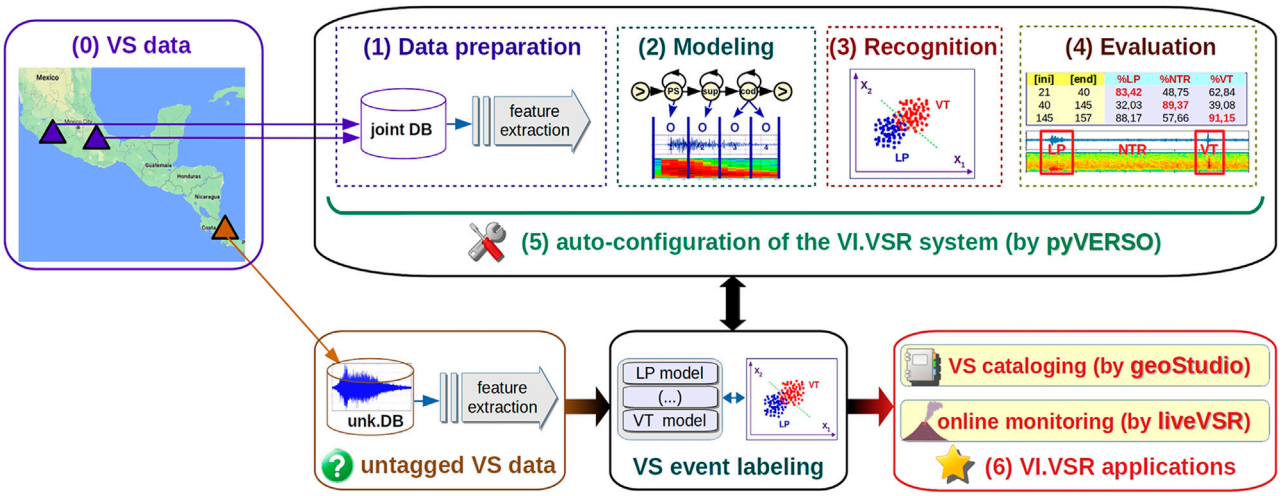

FIGURE 2 | *VULCAN.ears*—Volcano-Independent Seismic Recognition (VI.VSR) platform and the role of its supporting tools. Manually labeled volcano-seismic **(0)** VS data recorded at several volcanoes compose the *joint DB* feeding the VI.VSR system. Usual **(1)**, **(2)**, **(3)** and **(4)** stages for building the VI.VSR model set are guided by **(5)** *pyVERSO* in order to optimize the recognition results. **(6)** VI.VSR applications: events in untagged VS data from a volcano can be detected and classified in an online monitoring loop by the *liveVSR* script, or analyzed offline by *geoStudio* providing automatically labeled VS catalogs.

Figure 2 depicts the structure of the developed VI.VSR platform and its utilization steps. Basically, it encloses the usual (1)-(4) VSR stages detailed in **Section 2.1** to deploy an improved VSR system but fed with labeled events from several volcanoes composing the universal *joint DB*. An extra 5) *auto-configuration* stage optimizes the system to maximize its efficiency by performing iterative train-evaluation tests to select the best data description scheme and modeling setups. The (1)–(5) stages are guided by suitable *pyVERSO* scripts accomplished to obtain robust VI.VSR models. The automatic recognition of events embedded in the seismic records of the *untagged VS data* can be carried out in two different manners:

- Offline cataloging via geoStudio: data stored in files are loaded into a graphical interface and their events are recognized by VSR models selected from a prebuilt set. Then, the tagged data can be plotted for inspection and the resulting catalog is stored for further analysis.
- Online monitoring via *liveVSR* to perform a continuous, real-time monitoring of an active volcano. The *liveVSR* script is able to connect to any available FDSN data server plotting the recognized events and generating volcano-seismic catalogs. Several instances of *liveVSR* can be run concurrently receiving data from several stations or volcanoes.

The resulting labeled catalogs are the input to posterior 6) *VI.VSR applications*.

2.2.2 Building VI.VSR Models With *pyVERSO*

pyVERSO is a collection of Python scripts designed to perform VSR tasks from the command line. It has libraries to prepare and describe data, including many time-domain, cepstral and hybrid parametrization schemes and advanced feature selection routines. It is highly configurable and easy to use. Taking as input a labeled database and a configuration file it can implement serial or parallel architectures based on HMMs, Gaussian Mixture Models and Conditional Random Fields. *pyVERSO* main aim is to build own, local VSR systems of an active volcano. Once the system is optimized, its models can be exported to be used on online monitoring via *liveVSR* or offline analysis by *geoStudio*. *pyVERSO* is highly integrated within the Python scientific ecosystem and, currently, relies on the *HMM Toolkit* (Young et al., 2006) when using HMMs.

2.2.3 Graphical VI.VSR With *geoStudio*

geoStudio is the graphical frontend of *pyVERSO* developed to simplify seismic analysis (Carmona et al., 2014) and recognition tasks (**Figure 3**). It provides the following complementary functionalities:

- Loading and saving of data supporting several seismological formats. Also it can handle *NumPy* arrays and *HMM Toolkit* encoded files (**Figure 3A 2**).
- Data filtering (**Figure 3A 3**) and advanced seismogram visualization of any custom description scheme defined by *pyVERSO* (**Figure 3A 4**).
- 2D seismic source location by slowness maps via zero-lag cross-correlation (Almendros et al., 1999).

A Volcano-Independent VSR test in *geoStudio* can be easily carried out as follows (**Figure 3B**):

(1) *Load data files* (**Figure 3B 1**). Several formats are directly supported, including those readable by *ObsPy*.
(2) *Select VSR models* suitable to your data among a built-in set of models trained with 10 databases from 10 different volcanoes respectively, six joint databases mixing two

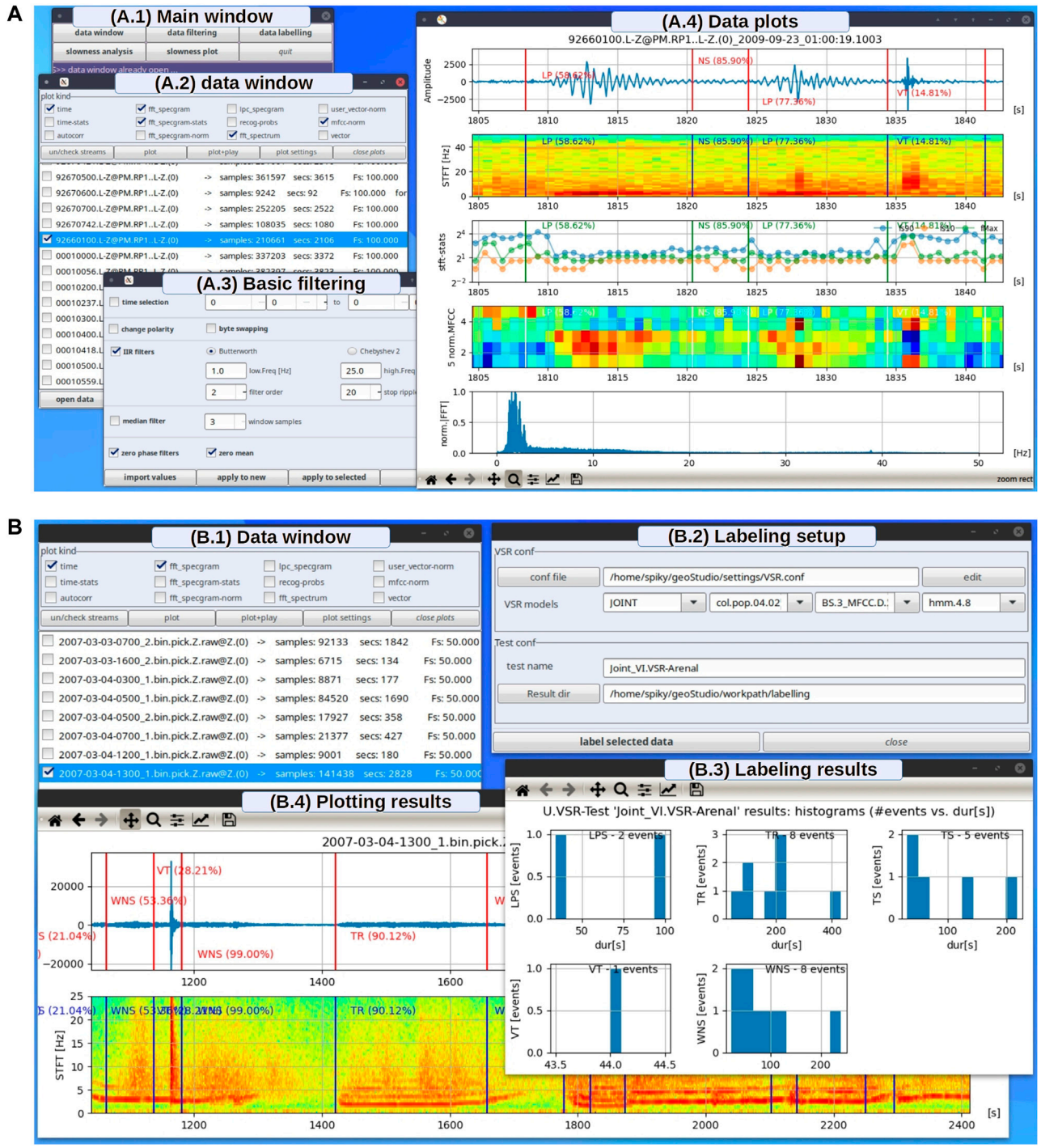

FIGURE 3 | *geoStudio* graphical interface of the *VULCAN.ears* - Volcano-Independent VSR ecosystem **(A)** Plotting a file in different representation spaces **(A.1)** Main window groups the main tasks, from where the **(A.2)** data window is opened to load files **(A.3)** Basic filtering can be performed on the selected items prior to draw the **(A.4)** data plots **(B)** Offline VI.VSR: automatically labeling an Arenal file selected in the **(B.1)** data window by models built from Colima and Popocatépetl data chosen in the **(B.2)** labeling setup. The **(B.3)** labeling results window summarizes the event distribution of the generated seismic catalog. The already labeled file can be visualized **(B.4)** plotting results.

volcanoes and two universal volcano-independent solutions with data of several volcanoes (**Figure 3B 2**). Custom models created by *pyVERSO* can also be selected.

(3) *Launch the labeling task* and *examine the results* plotting the event distribution of the generated catalog (**Figure 3B 3**) and the files automatically labeled (**Figure 3B 4**).

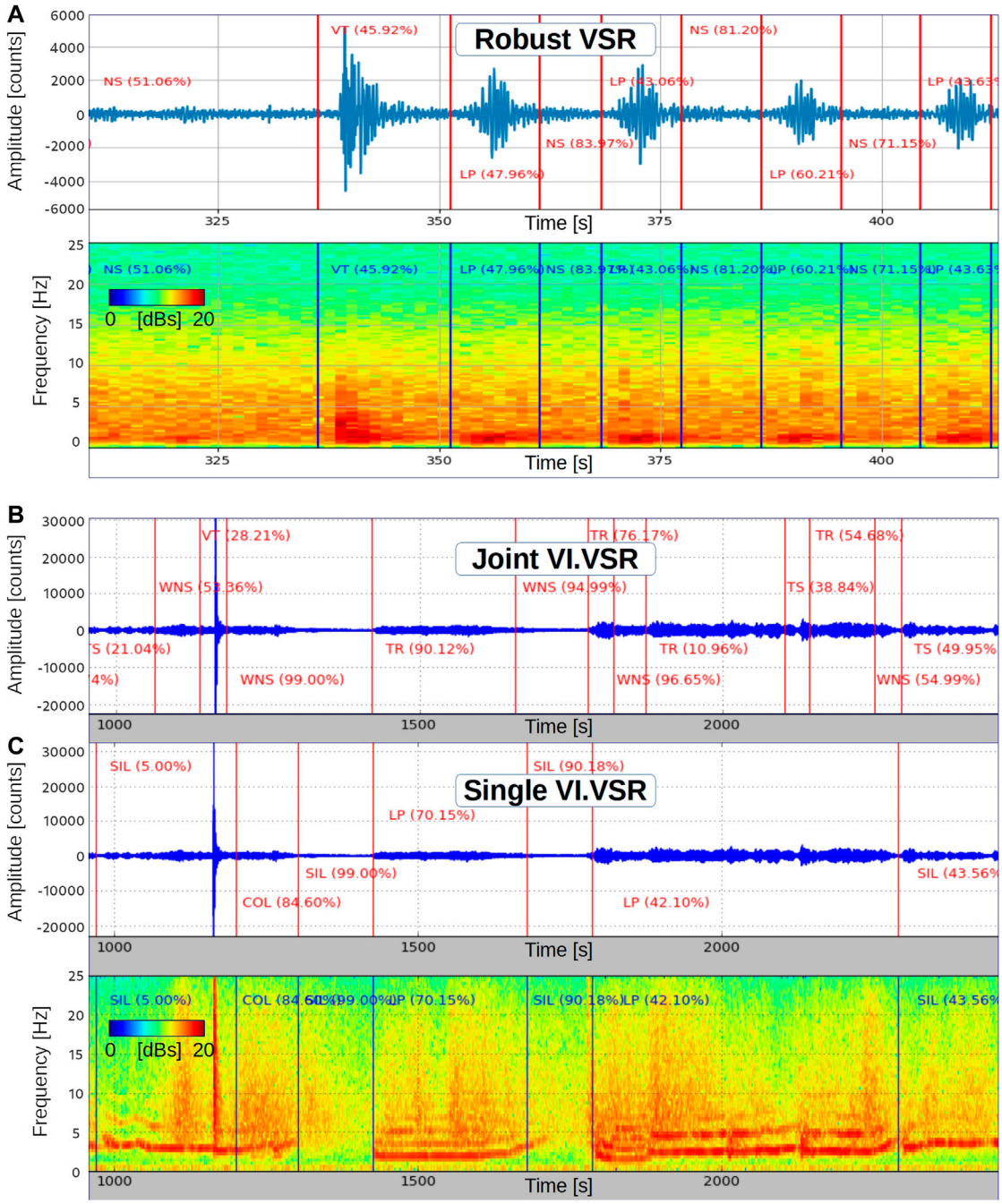

FIGURE 4 | VSR cataloging with *geoStudio* and *pyVERSO*. NS, SIL and WNS labels represent noisy signals. A score measuring the % of the recognition reliability for each event is shown **(A)** Robust VSR: models built from data recorded in 1995 and 1998 by different stations at Deception Island Volcano automatically detect and classify events recorded in 2009 by a broad-band station located in another place of Deception **(B)** Joint VI.VSR models characterizing a joint database of Colima and Popocatépetl Mexican volcanoes are used to recognize events of Arenal volcano in Costa Rica, improving the results of just recognizing with Colima models plotted in **(C)** Single VI.VSR panel; harmonic (TR) and spasmodic (TS) tremors are correctly labeled instead of long-period (LP) or collapses (COL) ones. Joint models also detect overlapped volcano-tectonic earthquakes (VT).

3 CASE STUDIES AND RESULTS

This section presents some baseline results obtained with *pyVERSO* and *geoStudio* as application of the VI.VSR innovations detailed in **Section 2.2.1**. We start with robust VSR examples evolving to volcano-independent cases, evaluated in typical monitoring scenarios as a volcanic island with noisy recordings or highly active stratovolcanoes with recent eruptive episodes. Demo videos

of geoStudio running these case studies are supplied as **Supplementary Material**.

3.1 Robust VSR at Deception Island

Deception Island Volcano has been a relevant VSR laboratory to evaluate new algorithms since 2006 (Benítez et al., 2007, 2009; Cortés et al., 2014; Titos et al., 2019b). Robust VSR experiments have been deployed involving noisy scenarios and data from different stations installed at different locations and years as short-period clean recordings in 1995, short-period noisy signals acquired in 1998 close to a hydrothermal area and broad-band noisy data from a station in 2009 (Carmona et al., 2014):

- A Multi-station VSR system was trained with 4,011 events from the 1995 and 1998 stations. It was able to automatically catalog long period (LP) events, volcano-tectonic (VT) and hybrid earthquakes, noisy (NS) and tremor segments in the continuous recordings of the whole 2009 years. The test only took 20 h of a modest 2.5 GHz, 2-threads computer (Cortés et al., 2017). **Figure 4A** shows how LP swarms are correctly recognized even in noisy conditions.
- Parallel vs. serial (classic) architecture in continuous VSR: pyVERSO auto-configuration improved the precision from 52% up to 72% of a classic VSR system by using dedicated parallel recognition channels. 40 LPs, 113 VTs and 292 noise-tremor events of the 1998 station were automatically labeled by models trained with 58 LPs, 41 VTs and 189 noise-tremor signals manually cataloged in 1995 (Cortés et al., 2019a).
- Waveform standardization increased from 66–76% the precision in continuous VSR recognizing 204 LPs, 467 noise-tremors and 36 VTs in the noisy 2009 recordings (Cortés et al., 2019b). The models were built describing 58 LPs, 189 noise-tremors and 41 VTs gathered in 1995.

3.2 Volcano-independent VSR at Colima, Popocatépetl and Arenal Volcanoes

The proposed volcano-independent recognition approach has been tested in some of the most active American volcanoes thanks to the collaboration of the *VULCAN.ears* partners. Signals of the andesitic Colima, Popocatépetl and Arenal stratovolcanoes monitored in 2002, 2004, and 2007, respectively, were labeled to evaluate our system (Cortés et al., 2009b).

37 hours of continuous data recorded by a short-period station at Popocatépetl were analyzed by models trained with 17 h of labeled events acquired at Colima by broad-band and short-period sensors. 282 LPs, 184 VTs, 50 regional tectonic earthquakes (REG), 164 noisy segments, 75 harmonic (TR) and 59 spasmodic (TS) tremors were detected and classified with an efficiency of 59%, raised up to 65% after auto-configuring the most convenient waveform description and standardization schemes. 52 h of Mexican Colima and Popocatépetl events were combined to deploy a volcano-independent system for classifying Arenal events detected by a broad-band sensor in Costa Rica. It was able to discriminate 46 TSs, 46 TRs, 53 pulsant tremors, 46 explosions, 26 REGs, 50 VTs and 285 noises, increasing the precision from 50% to 71% after auto-selecting the best hybrid features to describe the seismograms (Cortés et al., 2019b). Precisely, **Figure 4** presents an example of the accuracy improvements when the training database is enlarged with events of a new volcano: *Joint VI.VSR* models (**Figure 4B**) trained with Colima and Popocatépetl databases perform better recognizing Arenal events than *Single VI.VSR* models (**Figure 4C**) built only with Colima.

4 DISCUSSION AND CONCLUSION

4.1 Discussion

Several alternatives can be found to facilitate the integration and use of VSR systems at volcano observatories but most of them are designed for a determined volcano or focused on pattern discovery (Carniel et al., 2006; Langer et al., 2009; Messina and Langer, 2011). Some graphical programs are useful to characterize events guiding the manual labelling of data (Lesage, 2009). Bueno et al. (2020) designed an interesting interface based on two-step VSR recognition able to cluster events in basic categories. *VULCAN.ears* framework offers a complete volcano-independent VSR solution to monitor volcanoes providing built-in models for *geoStudio* and *liveVSR* alongside the *pyVERSO* ecosystem to build customized VSR systems focused on low-level integration. The proposed approach is an *ongoing project* and the current universal models are only trained with events from three volcanoes. A universal database gathering events of, at least, 10 volcanoes is in preparation in strict cooperation with our partners including catalogs from Copahue, Etna, Flegrei, Merapi, Piton de la Fournaise, San Miguel, Soufrière of Guadeloupe, Stromboli, Turrialba, Ubinas and others publicly available as Llaima and Cotopaxi. *geoStudio* only wraps few functionalities of its *pyVERSO* backend, having a huge potential to be accomplished.

The innovative techniques specified in **Section 2.2.1** and designed to achieve the volcano-independent milestone are functional and their baseline results encouraging, scoring an efficiency in the 70–80% interval in challenging scenarios as continuous recognition under noisy conditions in different stations and epochs, achieving a 76%, or volcano-independent classification and recognition reaching 71 and 65%, respectively. These are promising outcomes, specially, recognizing more than five classes in continuous records from different volcanoes. In addition, experts rarely agree on an 80% when labeling the same data and classic evaluation metrics of most VSR literature do not properly account insertion and deletion errors, providing overrated values compared to the defined in **Equation (1)**. The building of different types of universal recognition models is an attractive option to raise the efficiency, i.e., models of open vent volcanoes vs. closed vent ones, or specific universal models for island volcanoes with oceanic noises. There are still open issues to solve, as the strong influence that the quality of the manual labeling and the data description scheme have on the VSR

scores. In any case, having a robust volcano-independent solution allows to recognize events which have not previously appeared in the volcano recordings. This provides a valuable input to early warning systems monitoring dormant volcanoes and to properly characterize the current volcano state in its eruptive cycle.

4.2 Concluding Remarks and Future Work

This work presents the *Volcano-Independent Seismic Recognition* as a solution to classic issues when implementing automatic *Volcano-Seismic Recognition* systems in volcano observatories. Current monitoring centers usually have limited resources to develop their own systems. They still detect and classify manually, which restrains their response in case of volcanic unrest. The authors have deployed a platform to develop portable recognition systems providing several tools to easily integrate and use the framework in observatories and to build applications for cataloging volcano-seismic events: *pyVERSO* to design recognition systems adapted to a given volcano, *geoStudio* to graphically detect and classify events in offline interactive operations, and *liveVSR* to continuously recognize in real-time events from remote or local data servers. Even though these programs are still in development, their application examples and baseline results point out the proposed approach as an exciting breakthrough in the volcano monitoring area.

Next efforts will be directed to increase the number of prebuilt volcano-independent models for enhancing the system robustness and to extend *geoStudio* capabilities with an interface to manually label data and with a guided-process to deploy customized recognition systems.

DATA AVAILABILITY STATEMENT

Following the recommendations of the European Commission regarding Open Science in EU-funded programmes, several material related with VULCAN.ears project are available, free of charge, in the Zenodo repository, including conference talks and posters, datasets and software. Specifically, the software preview versions and manuals of geoStudio, liveVSR and pyVERSO documented with demo videos of geoStudio running the case studies presented in **Section 3**. VULCAN.ears main webpage can be found at ResearchGate.

AUTHOR CONTRIBUTIONS

GC designed and implemented most of the VI.VSR framework, wrote the manuscript, and produced the figures. RC and PL were the scientific mentors of the *VULCAN.ears* project, providing support and insights regarding the machine learning area and VI.VSR applications in eruption forecasting, respectively. RC and PL actively boosted the VI.VSR dissemination and support over several volcano observatories. MM developed part of the platform technology and statistical modeling. ID worked on data labeling, model building, software testing and experimentation. All authors contributed to the manuscript review.

FUNDING

This project has received funding from the European Union's Horizon 2020 research and innovation programme under the Marie Skłodowska-Curie Grant Agreement No. (749249) (*VULCAN.ears*).

ACKNOWLEDGMENTS

We would like to thank every contribution to the universal databases and everybody involved in the labeling process. A special acknowledge goes to all the partners in the *VSR-ALUE* group, and the many institutions developing the VI.VSR platform, including the Instituto Andaluz de Geofísica and the Department de Teoría de la Señal, Telemática y Comunicaciones, both of the University of Granada, Spain, whereas the former VI.VSR technology was developed. We also thank the reviewers, the guest associate editor Luca de Siena and the chief editor Valerio Acocella for their valuable comments, which significantly improved the manuscript.

SUPPLEMENTARY MATERIAL

The Supplementary Material for this article can be found online at: https://www.frontiersin.org/articles/10.3389/feart.2020.616676/full#supplementary-material.

REFERENCES

Almendros, J., Ibáñez, J. M., Alguacil, G., and Del Pezzo, E. (1999). Array analysis using circular-wave-front geometry: an application to locate the nearby seismo-volcanic source. *Geophys. J. Int.* 136, 159–170. doi:10.1046/j.1365-246X.1999.00699.x

Álvarez, I., García, L., Cortés, G., Benítez, C., and De la Torre, Á. (2012). Discriminative feature selection for automatic classification of volcano-seismic signals. *Geosci. Rem. Sens. Lett. IEEE* 9, 151–155. doi:10.1109/LGRS.2011.2162815

Álvarez, I., Garcia, L., Mota, S., Cortés, G., Benitez, C., and De la Torre, A. (2013). An automatic P-phase picking algorithm based on adaptive multiband processing. *Geosci. Rem. Sens. Lett. IEEE* 10, 1488–1492. doi:10.1109/LGRS.2013.2260720

Benítez, C., Ibáñez, J., García, L., Cortés, G., and Álvarez, I. (2009). "Analysis of volcanic seismicity at Deception Island, Stromboli volcano and Mt. Etna using an automatic CHMM-based recognition method," in *Volume project: VOLcanoes, understanding subsurface mass MoveMEnt, eds. C. B. A. Bean and E. C. P. 6th framework (school of geological sciences, university college dublin:* C. J. Bean, A. K. Braiden, I. Lokmer, F. Martini, and G. S. O'Brien, 140–149.

Benítez, C., Ramírez, J., Segura, J. C., Ibáñez, J., Almendros, J., García-Yeguas, A., et al. (2007). Continuous HMM-based seismic-event classification at deception island, Antarctica, *IEEE Transactions on Geoscience and remote sensing*. NY, United States: IEEE, 45, 138–146. doi:10.1109/TGRS.2006.882264

Bergen, K. J., Johnson, P. A., de Hoop, M. V., and Beroza, G. C. (2019). Machine learning for data-driven discovery in solid earth geoscience. *Science* 363, eaau0323. doi:10.1126/science.aau0323

Beyreuther, M., Carniel, R., and Wassermann, J. (2008). Continuous hidden Markov models: application to automatic earthquake detection and classification at las cañadas caldera. *Tenerife. J. Volcanol. Geoth. Res.* 176, 513–518. doi:10.1016/j.jvolgeores.2008.04.021

Beyreuther, M., and Wassermann, J. (2008). Continuous earthquake detection and classification using discrete Hidden Markov Models. *Geophys. J. Int.* 175, 1055–1066. doi:10.1111/j.1365-246X.2008.03921.x

Boué, A., Lesage, P., Cortés, G., Valette, B., Reyes-Dávila, G., Arámbula-Mendoza, R., et al. (2016). Performance of the "material Failure Forecast Method" in real-time situations: a Bayesian approach applied on effusive and explosive eruptions. *J. Volcanol. Geoth. Res.* 327, 622–633. doi:10.1016/j.jvolgeores.2016.10.002

Brown, S. K., Jenkins, S. F., Sparks, R. S. J., Odbert, H., and Auker, M. R. (2017). Volcanic fatalities database: analysis of volcanic threat with distance and victim classification. *J. of Appl. Volcan.* 6, 1–20. doi:10.1186/s13617-017-0067-4

Bueno, A., Benítez, C., De Angelis, S., Díaz Moreno, A., and Ibáñez, J. M. (2019a). volcano-seismic transfer learning and uncertainty quantification with bayesian neural networks. *IEEE Trans. Geosci. Rem. Sens.*, 1–11. doi:10.1109/TGRS.2019.2941494

Bueno, A., Zuccarello, L., Díaz-Moreno, A., Woollam, J., Titos, M., Benitez, C., et al. (2020). Picoss: Python interface for the classification of seismic signals. *Comput. Geosci.* 142, 104531. doi:10.1016/j.cageo.2020.104531

Bueno, Á., Díaz-Moreno, A., De Angelis, S., Benítez, C., and Ibáñez, J. M. (2019b). Recursive entropy method of segmentation for seismic signals. *Seismol Res. Lett.* 90, 1670–1677. doi:10.1785/0220180317

Cannavo', F., Cannata, A., Palazzo, S., Spampinato, C., Faraci, D., Castagnolo, G., et al. (2020). Unsupervised deep learning on seismic data to detect volcanic unrest, *EGU general assembly conference abstracts*. Vienna, Austria: 22nd EGU General Assembly, 18631. doi:10.5194/egusphere-egu2020-18631

Carmona, E., Almendros, J., Martín, R., Cortés, G., Alguacil, G., Moreno, J., et al. (2014). Advances in seismic monitoring at deception island Volcano (Antarctica) since the international polar year. *Ann. Geophys.* 57. doi:10.4401/ag-6378

Carniel, R., Barbui, L., and Jolly, A. (2013a). Detecting dynamical regimes by self-organizing map (som) analysis: an example from the march 2006 phreatic eruption at raoul island, New Zealand kermadec arc. *Boll. Geofis. Teor. Appl.* 54, 39–52. doi:10.4430/bgta0077

Carniel, R. (2014). Characterization of volcanic regimes and identification of significant transitions using geophysical data: a review. *Bull. Volcanol* 76, 848. doi:10.1007/s00445-014-0848-0

Carniel, R., Di Cecca, M., and Jaquet, O. (2006). A user-friendly, dynamic web environment for remote data browsing and analysis of multiparametric geophysical data within the MULTIMO project. *J. Volcanol. Geoth. Res.* 153, 80–96. doi:10.1016/j.jvolgeores.2005.08.005

Carniel, R., Jolly, A. D., and Barbui, L. (2013b). Analysis of phreatic events at Ruapehu volcano, New Zealand using a new SOM approach. *J. Volcanol. Geoth. Res.* 254, 69–79. doi:10.1016/j.jvolgeores.2012.12.026

Chouet, B. A. (1996). Long-period volcano seismicity: its source and use in eruption forecasting. *Nature* 380, 309–316. doi:10.1038/380309a0

Cortés, G., Arambula, R., Gutiérrez, L., Benítez, C., Ibáñez, J., Lesage, P., et al. (2009a). Evaluating robustness of a HMM-based classification system of volcano-seismic events at Colima and Popocatépetl volcanoes, *IEEE International, IGARSS 2009 Geoscience and remote sensing symposium, 2009*. (NY, United States: IEEE), 2, 1012–1015. doi:10.1109/Igarss.2009.5418275

Cortés, G., Arámbula, R., Álvarez, I., Benítez, C., Ibáñez, J., Lesage, P., et al. (2009b). "Analysis of Colima, Popocatépetl and arenal volcanic seismicity using an automatic continuous hidden Markov models-based recognition system," in *VOLUME project: VOLcanoes, understanding subsurface mass MoveMEnt. 6th framework (Dublin: School of Geological Sciences, University College Dublin)*: eds. C.J. Bean, A.K. Braiden, I. Lokmer, C. B. A. E. C. P. Bean, F. Martini, and G. S. O'Brien, 150–160.

Cortés, G., García, L., Álvarez, I., Benítez, C., de la Torre, Á., and Ibáñez, J. (2014). Parallel System Architecture (PSA): an efficient approach for automatic recognition of volcano-seismic events. *J. Volcanol. Geoth. Res.* 271, 1–10. doi:10.1016/j.jvolgeores.2013.07.004

Cortés, G. (2015). Reconocimiento de señales sismo-volcánicas mediante canales específicos basados en modelos ocultos de Markov. PhD. thesis. Granada (Spain): Universidad de Granada.

Cortés, G., Benítez, M. C., García, L., Álvarez, I., and Ibáñez, J. M. (2016). A comparative study of dimensionality reduction algorithms applied to volcano-seismic signals. *IEEE J. Sel. Top. Appl.* 9, 253–263. doi:10.1109/JSTARS.2015.2479300

Cortés, G., Lesage, P., Carniel, R., Benítez, C., Almendros, J., and Arámbula-Mendoza, R. (2017). Unsupervised volcano-seismic event recognition as a tool for real-time monitoring and eruption forecasting: the VULCAN.ears project. Portland, OR: Scientific assembly, IAVCEI, 224.

Cortés, G., Carniel, R., Lesage, P., Ángeles Mendoza, M., and Della Lucia, I. (2019a). Volcano-Independent Seismic Recognition: detecting and classifying events of a given volcano using data from others, EGU general assembly conference abstracts. Vienna, Austria, April, 2019, 11386. doi:10.1002/essoar.10500900.1

Cortés, G., Carniel, R., Mendoza, M., and Lesage, P. (2019b). Standardization of noisy volcanoseismic waveforms as a key step toward station- independent, robust automatic recognition. *Seismol Res. Lett.* 90, 581–590. doi:10.1785/0220180334

Curilem, M., Vergara, J., San Martin, C., Fuentealba, G., Cardona, C., Huenupan, F., et al. (2014). Pattern recognition applied to seismic signals of the Llaima volcano (Chile): an analysis of the events' features. *J. Volcanol. Geoth. Res.* 282, 134–147. doi:10.1016/j.jvolgeores.2014.06.004

Falsaperla, S., Graziani, S., Nunnari, G., and Spampinato, S. (1996). Automatic classification of volcanic earthquakes by using multi-layered neural networks. *Nat. Hazards* 13, 205–228. doi:10.1007/BF00215816

García, L., Alguacil, G., Titos, M., Cocina, O., De la Torre, Á., and Benítez, C. (2020). Automatic S-phase picking for volcano-tectonic earthquakes using spectral dissimilarity analysis. *Geosci. Rem. Sens. Lett. IEEE* 17, 874–878. doi:10.1109/LGRS.2019.2934220

Ibáñez, J., Benítez, C., Gutiérrez, L., Cortés, G., García-Yeguas, A., and Alguacil, G. (2009). The classification of seismo-volcanic signals using Hidden Markov Models as applied to the Stromboli and Etna volcanoes. *J. Volcanol. Geoth. Res.* 187, 218–226. doi:10.1016/j.jvolgeores.2009.09.002

Journeau, C., Shapiro, N. M., Seydoux, L., Soubestre, J., Ferrazzini, V., and Peltier, A. (2020). Detection, classification, and location of seismovolcanic signals with multi-component seismic data, example from the Piton de la Fournaise volcano (La Réunion, France). *J. Geophys. Res.: Solid Earth* 125, e2019JB019333. doi:10.1029/2019JB019333

Khan, M. S., Curilem, M., Huenupan, F., Khan, M. F., and Becerra Yoma, N. (2019). A signal processing perspective of monitoring active volcanoes [applications corner]. *IEEE Signal Process. Mag.* 36, 125–163. doi:10.1109/MSP.2019.2930427

Köhler, A., Ohrnberger, M., and Scherbaum, F. (2010). Unsupervised pattern recognition in continuous seismic wavefield records using Self-Organizing Maps. *Geophys. J. Int.* 182, 1619–1630. doi:10.1111/j.1365-246X.2010.04709.x

Langer, H., Falsaperla, S., and Hammer, C. (2019). *Advantages and pitfalls of pattern recognition: selected cases in geophysics*. 1st Edn. Amsterdam, Netherlands: ISSN Elsevier Science. doi:10.1016/c2016-0-00254-1

Langer, H., Falsaperla, S., Masotti, M., Campanini, R., Spampinato, S., and Messina, A. (2009). Synopsis of supervised and unsupervised pattern classification techniques applied to volcanic tremor data at Mt Etna. *Italy. Geophys. J. Int.* 178, 1132–1144. doi:10.1111/j.1365-246X.2009.04179.x

Langer, H., Falsaperla, S., and Thompson, G. (2003). Application of artificial neural networks for the classification of the seismic transients at Soufrière hills volcano, Montserrat. *Geophys. Res. Lett.* 30, 2090. doi:10.1029/2003GL018082

Lecocq, T., Hicks, S. P., Van Noten, K., van Wijk, K., Koelemeijer, P., De Plaen, R. S. M., et al. (2020). Global quieting of high-frequency seismic noise due to covid-19 pandemic lockdown measures. *Science* 369 (6509), 1338–1343. doi:10.1126/science.abd2438

Lesage, P. (2009). Interactive Matlab software for the analysis of seismic volcanic signals. *Comput. Geosci.* 35, 2137–2144. doi:10.1016/j.cageo.2009.01.010

Maggi, A., Ferrazzini, V., Hibert, C., Beauducel, F., Boissier, P., and Amemoutou, A. (2017). Implementation of a multistation approach for automated event classification at Piton de la Fournaise volcano. *Seismol Res. Lett.* 88, 878–891. doi:10.1785/0220160189

Malfante, M., Dalla Mura, M., Métaxian, J.-P., Mars, J. I., Macedo, O., and Inza, A. (2018). Machine learning for volcano-seismic signals: challenges and perspectives. *IEEE Signal Process. Mag.* 35, 20–30. doi:10.1109/MSP.2017.2779166

Masotti, M., Falsaperla, S., Langer, H., Spampinato, S., and Campanini, R. (2006). Application of support vector machine to the classification of volcanic tremor at Etna. *Italy. Geophys. Res. Lett.* 33, L20304. doi:10.1029/2006GL027441

McNutt, S. R., Thompson, G., Johnson, J., Angelis, S. D., and Fee, D. (2015). "Chapter 63—seismic and infrasonic monitoring," in *The encyclopedia of volcanoes*. Editor H. Sigurdsson 2nd edn (Amsterdam, Netherlands: Academic Press), 1071–1099. doi:10.1016/B978-0-12-385938-9.00063-8

Messina, A., and Langer, H. (2011). Pattern recognition of volcanic tremor data on Mt. Etna (Italy) with KKAnalysis—A software program for unsupervised classification. *Comput. Geosci.* 37, 953–961. doi:10.1016/j.cageo.2011.03.015

Ohrnberger, M. (2001). *Continuous automatic classification of seismic signals of volcanic origin at Mt. Merapi, Java, Indonesia*. PhD. thesis. Potsdam, Germany: Universität Potsdam

Orozco-Alzate, M., Acosta-Muñoz, C., and Londoño-Bonilla, J. M. (2012). "The automated identification of volcanic earthquakes: concepts, applications and challenges," in *Earthquake research and analysis*. Editors S. D'Amico and Rijeka (Rijeka, Croatia: IntechOpen), Chap. 19. 345–370. doi:10.5772/27508

Peltier, A., Villeneuve, N., Ferrazzini, V., Testud, S., Hassen Ali, T., Boissier, P., et al. (2018). Changes in the long-term geophysical eruptive precursors at Piton de la Fournaise: implications for the response management. *Front. Earth Sci.* 6, 104. doi:10.3389/feart.2018.00104

Rabiner, L. R., and Schafer, R. W. (2007). Introduction to digital speech processing. *Found. Trends Signal Process* 1, 1–194. doi:10.1561/2000000001

Riggelsen, C., Ohrnberger, M., and Scherbaum, F. (2007). Dynamic bayesian networks for real-time classification of seismic signals, *Knowledge discovery in databases: PKDD 2007*. Berlin, Germany: Springer, 4702, 565–572. doi:10.1007/2F978-3-540-74976-9_59

Soto, R., Huenupan, F., Meza, P., Curilem, M., and Franco, L. (2018). Spectro-temporal features applied to the automatic classification of volcanic seismic events. *J. Volcanol. Geoth. Res.* 358, 194–206. doi:10.1016/j.jvolgeores.2018.04.025

Sparks, R. S., Biggs, J., and Neuberg, J. W. (2012). Geophysics. Monitoring volcanoes. *Science* 335, 1310–1311. doi:10.1126/science.1219485

Titos, M., Bueno, A., García, L., Benítez, C., and Segura, J. C. (2019a). Classification of isolated volcano-seismic events based on inductive transfer learning. *IEEE Geoscience and Remote Sensing Letters*, NY, United States: IEEE, 17, 869-873. doi:10.1109/LGRS.2019.2931063

Titos, M., Bueno, A., García, L., and Benítez, C. (2018). A deep neural networks approach to automatic recognition systems for volcano-seismic events. *IEEE J. Sel. Top. Appl.* 11, 1533–1544. doi:10.1109/JSTARS.2018.2803198

Titos, M., Bueno, A., García, L., Benítez, M. C., and Ibáñez, J. (2019b). Detection and classification of continuous volcano-seismic signals with recurrent neural networks. *IEEE Trans. Geosci. Rem. Sens.* 57, 1936–1948. doi:10.1109/TGRS.2018.2870202

Trujillo-Castrillón, N., Valdés-González, C. M., Arámbula-Mendoza, R., and Santacoloma-Salguero, C. C. (2018). Initial processing of volcanic seismic signals using Hidden Markov Models: nevado del Huila, Colombia. *J. Volcanol. Geoth. Res.* 364, 107-120. doi:10.1016/j.jvolgeores.2018.09.008

White, R., and McCausland, W. (2016). Volcano-tectonic earthquakes: a new tool for estimating intrusive volumes and forecasting eruptions. *J. Volcanol. Geoth. Res.* 309, 139–155. doi:10.1016/j.jvolgeores.2015.10.020

Young, S. J., Evermann, G., Gales, M. J. F., Hain, T., Kershaw, D., Moore, G., et al. (2006). *The HTK book*. Cambridge, United Kingdom: Cambridge University Engineering Department). version 3.4.

Conflict of Interest: The authors declare that the research was conducted in the absence of any commercial or financial relationships that could be construed as a potential conflict of interest.

Copyright © 2021 Cortés, Carniel, Lesage, Mendoza and Della Lucia. This is an open-access article distributed under the terms of the Creative Commons Attribution License (CC BY). The use, distribution or reproduction in other forums is permitted, provided the original author(s) and the copyright owner(s) are credited and that the original publication in this journal is cited, in accordance with accepted academic practice. No use, distribution or reproduction is permitted which does not comply with these terms.

frontiers in Earth Science

ORIGINAL RESEARCH
published: 09 February 2021
doi: 10.3389/feart.2020.599329

The 2002–2005 Changbaishan Volcanic Unrest Triggered by the 2002 *M* 7.2 Wangqing Deep Focus Earthquake

Guoming Liu[1,2,3,4], Chenyu Li[5], Zhigang Peng[5], Yinan Liu[4], Yu Zhang[4], Dongyang Liu[6], Maoliang Zhang[7] and Bo Pan[1]*

[1]Jilin Changbaishan Volcano National Observation and Research Station, Institute of Geology, China Earthquake Administration, Beijing, China, [2]Institute of Volcanology, China Earthquake Administration, Changchun, China, [3]Changbai Mountain Volcano, The Academician Workstation of Jilin Province, Antu, China, [4]Jilin Earthquake Agency, Changchun, China, [5]School of Earth and Atmospheric Sciences, Georgia Institute of Technology, Atlanta, CO, United States, [6]School of Earth Sciences and Resources, China University of Geosciences, Beijing, China, [7]Institute of Surface-Earth System Science, School of Earth System Science, Tianjin University, Tianjin, China

OPEN ACCESS

Edited by:
Derek Keir,
University of Southampton,
United Kingdom

Reviewed by:
Finnigan Illsley-Kemp,
Victoria University of Wellington,
New Zealand
James Oliver Scott Hammond,
Birkbeck, University of London,
United Kingdom
Diana Roman,
Carnegie Institution for Science (CIS),
United States

***Correspondence:**
Chenyu Li
lchenyu1992@gmail.com

Specialty section:
This article was submitted to
Volcanology,
a section of the journal
Frontiers in Earth Science

Received: 27 August 2020
Accepted: 08 December 2020
Published: 09 February 2021

Citation:
Liu G, Li C, Peng Z, Liu Y, Zhang Y, Liu D, Zhang M and Pan B (2021) The 2002–2005 Changbaishan Volcanic Unrest Triggered by the 2002 M 7.2 Wangqing Deep Focus Earthquake. Front. Earth Sci. 8:599329. doi: 10.3389/feart.2020.599329

One of the most active intraplate volcanoes in East Asia, Changbaishan volcano experienced unrest from July 2002 to July 2005. On 2002/06/28, the *M* 7.2 Wangqing deep-focus earthquake occurred ~290 km northeast of Changbaishan volcano. While some studies have suggested a possible triggering relationship, the physical mechanism of such distant interaction is still not well understood. Using a template matching technique, which cross-correlates waveform of known events with continuous data, we perform systematic detection of microseismic events recorded by station CBS near Changbaishan volcano from July 1999 to July 2007. The detected earthquakes can be further categorized into three different types: volcano-tectonic (VT) events, long-period (LP) events and harmonic-spectra (HS) events. We detect 3763 VT events between July 2002 and July 2007. The intense VT earthquake swarm during the period from July 2002 to July 2005, along with recurring LPs and HSs and other geodetic/geochemical evidence, suggest magma movement during unrest. Compared with the hand-picked catalogue, the catalogue obtained by template matching technique reveals a delayed-triggering relationship between Wangqing deep-focus earthquake and unrest. The small magnitudes of the VT events and the limited numbers of LP and HS events suggest that the Wangqing mainshock likely triggered bubble excitation in the mid-crust magma system, resulting in overpressure and a small magma injection into the shallow magma chamber at a depth of ~5 km, leading to the 3-years unrest.

Keywords: Changbaishan volcano, volcanic tremor, deep-focus earthquake, matching template, long-period earthquake

INTRODUCTION

It is well known that large earthquakes are capable of triggering small to moderate-size earthquakes at long distances, especially in geothermal or volcanic regions (Hill and Prejean, 2015). A few studies have also documented significant increase of volcanic eruptions within a few days of large distant earthquakes (Linde and Sacks, 1998; Manga and Brodsky, 2006; Walter and Amelung, 2007; Sawi and

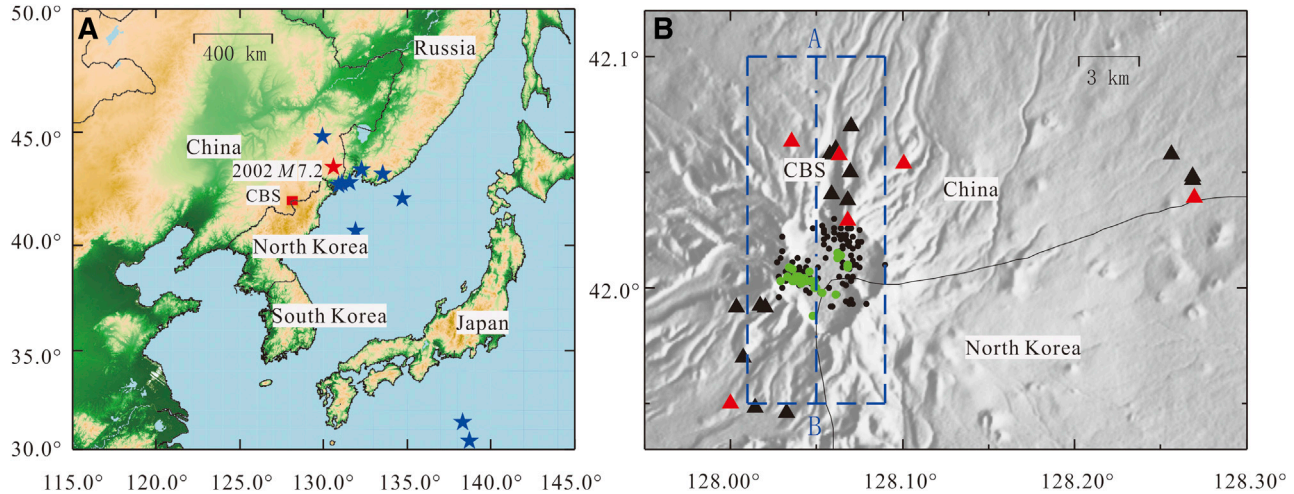

FIGURE 1 | (A) Map showing the location of Changbaishan volcano in East Asia. The red star marks the location of the 2002 *M* 7.2 Wangqing earthquake. Blue stars mark other deep-focus earthquakes in this region. The blue triangles indicate the JEA catalogue stations, and the red box marks the location of the enlarged plot in **(B)**. **(B)** Distribution of seismic stations and different types of seismic events during the volcanic unrest period. The red triangles mark stations used to build the CHVO catalogue, the black triangles indicate stations for the Wu catalogue, the black dots indicate VT events, and the green dots indicate HS events.

Manga, 2018). At distance of more than a few hundred kilometers, static stress changes become negligible (King et al., 1994; King and Deves, 2015). Hence, mechanisms such as magma overpressure due to permanent volumetric expansions, or unclamping of dikes are not relevant (Walter and Amelung, 2007). Possible shaking related mechanisms due to dynamic seismic waves include gas bubble nucleation and growth in magma (Crews and Cooper, 2014), changes in permeability (Manga et al., 2018), or sloshing of a bubbly magma reservoir (Namiki et al., 2016). However, the physical mechanism involved in such remote interaction is still in debate. In addition, most remote earthquake-triggered eruptions occur along major plate boundaries and are associated with shallow subduction-zone earthquakes (e.g., Hill et al., 2002; Lara et al., 2004; Walter and Amelung, 2006, 2007; Sawi and Manga, 2018; Farías and Basualto, 2020). It is not clear whether deep-focus earthquakes are capable of triggering unrest and eruptions.

Most of the microseismicity around active volcanoes belongs to VT-type, which is likely caused by shear slip on a fault near a volcano, and produces clear P and S waves with sharp onset. In addition, there are some other types of seismic events associated with volcanoes. For example, long-period (LP) events exhibit emergent P waves, but no clear S waves, with dominant frequencies of 0.5–5 Hz (Chouet, 1996; McNutt, 2002). A harmonic-spectra (HS) event is another special type of fluid-related seismic event. Whose spectral signature is strikingly harmonic (Hough et al., 2000; Milluzzo et al., 2010). Both LP and HS events are associated with either magma or magma-derived fluid-controlled sources (Chouet, 1996; Hough et al., 2000; McNutt, 2002).

Changbaishan volcano (also known as Paektu/Baekdu in Korea) is one of the most active intraplate volcanoes in East Asia (Liu et al., 1998; Zhang et al., 2018) (**Figure 1A**). Its summit caldera is called Tianchi (Chinese for "Heaven Lake"), which situates at the border between China and North Korea. Continuous seismic monitoring of Changbaishan volcano has been in operation since the establishment of Changbaishan Volcano Observatory (CHVO) in July 1999. Volcanic unrest during the period from July 2002 to July 2005 has been reported by previous studies, which was accompanied by earthquake swarms, surface inflation, uplift of the cone, and geochemical anomalies in the gas emissions (Wu et al., 2005; Liu et al., 2011a; Liu et al., 2011b; Xu et al., 2012; Wei et al., 2013). Based on inversion of ground deformation measurements, this unrest is interpreted as resulting from a shallow intrusion of basaltic magma centered at 2–6 km beneath the volcano's summit. During this "active period," thousands of volcano-tectonic (VT) earthquakes were recorded. Most of them were small-magnitude events, and the largest event occurred in December 2004 had a local magnitude M_L of 4.4.

On June 28, 2002, an *Mw* 7.2 deep-focus earthquake occurred at a depth of 566 km approximately below the city of Wangqiang, which is about 290 km northeast of Changbaishan volcano (**Figure 1A**). This is the largest deep-focus earthquake occurred within 500 km (horizontal distance) of the volcano since 2000. A few previous studies have argued that the 2002 Wangqing earthquake may have triggered the volcanic unrest, which started in early July of 2002 (Lv et al., 2007; Liu et al., 2017). However, the available earthquake catalogue in this region did not show any clear increase of seismicity between the 2002 Wangqing earthquake and the onset of the volcanic unrest. Hence, the triggering relationship is still not clear.

Wu et al. (2005) deployed 15 temporary seismic stations to study volcanic seismic activities in Changbaishan volcano during the summer months from 2002 to 2007. They identified thousands of VT events with dominant frequency of 5–15 Hz, as well as 38 volcanic HS events with several harmonic frequency peaks. However, they failed to identify any clear LP events or

volcanic tremor signals during their observations (Wu et al., 2005; Ming et al., 2007).

In this study, we obtain a complete and accurate VT catalogue based on a template matching technique (Shelly et al., 2007; Peng and Zhao, 2009; Zhang and Wen, 2015). We attempt to address two important issues that are crucial for understanding the physical processes involved in the 2002–2005 Changbaishan volcanic unrest. The first issue is related to the possible triggering relationship between the 2002 Wangqing deep-focus earthquake and the unrest. The second is whether any LP signals (either LP events or volcanic tremors) occurred within thousands of VT earthquakes during the 2002–2005 volcanic unrest period, which are typically used to infer magma or fluid movement (Chouet, 1996; McNutt, 2002).

BACKGROUND

Changbaishan volcano has been widely recognized as an active volcano of global significance due to its Millennium eruption (VEI ≈ 7) in 946 CE (Xu et al., 2012; Oppenheimer et al., 2017; Hakozaki et al., 2018; Zhang et al., 2018). Seismic tomography (e.g., Zhao et al., 2009) has revealed that Changbaishan volcano is located above a big mantle wedge (BMW) defined by the subducting Pacific plate that is horizontally stagnant in the mantle transition zone (MTZ) and the overriding Eurasian plate. The BMW is thus widely considered as the first-order geodynamic feature responsible for origin of Changbaishan volcano (Kuritani et al., 2011; Zhao and Tian, 2013; Zhang et al., 2018). Recently, Tang et al. (2014) also performed seismic tomography in this region with dense temporary seismic network, and imaged a possible gap in the subducted slab that may be responsible for producing the decompression melting material that feeds Changbaishan and other active volcanoes in this region (e.g., Wudalianchi and Jingbohu volcanoes).

The magma plumbing system of Changbaishan volcano remains less understood at present. However, geophysical inversions indicate that there are at least three layers of magma reservoirs beneath Changbaishan volcano. The lowermost one is approximately located at Moho/lower crustal depths (~30–40 km; Ri et al., 2016; Kim et al., 2017). The intermediate one is within mid-crustal depths (~15–25 km; Tang et al., 2001), and the depths of the uppermost one is constrained to be within 10 km below the surface (Tang et al., 2001; Iacovino et al., 2016; Hammond et al., 2020). Geodetic inversions of inflation during the 2002–2005 unrest revealed a possible shallow magma chamber at the depth range of ~5 km (Xu et al., 2012).

Lv et al. (2007) studied the relationship between Changbaishan volcanic earthquakes and intermediate-depth (60–300 km) and deep-focus (>300 km depth) earthquakes (including the 2002 Wangqing earthquake) that occurred along the subduction zone of the western Pacific Plate. Based on a comparison between the occurrence times of deep subduction-zone earthquakes and the VT earthquake rates, they suggested that earthquake swarms around Changbaishan volcano might be triggered by intermediate-depth and deep-focus subduction earthquakes (Lv et al., 2007). Based on historic documents in China and Korea, Li et al. (2012) showed that a magnitude greater than 8 deep-focus earthquake occurred in the "Hunchun-Wangqing deep-focus seismic zone" on October 6, 1597, and likely triggered numerous lake seiches in East China and a small-medium scale explosive eruption at Mt. Wangtian'e volcano (about 30 km away from Changbaishan volcano). These studies suggest a possible triggering relationship between deep earthquakes and volcanic eruptions in our study region.

Liu et al. (2017) investigated the triggering relationship between microearthquakes around Changbaishan volcano and five nuclear explosions in North Korea, as well as large shallow earthquakes at remote distances. They did not find any clear changes in microseismicity during the nuclear explosions with the maximum equivalent magnitude of 6.3. This is consistent with a recent numerical simulation indicating that a nuclear explosion of equivalent magnitude 7 is needed to produce dynamic stresses high enough to trigger eruptions of Changbaishan volcano (Hong et al., 2016). However, Liu et al. (2017) did identify a few large distant earthquakes (e.g., the 2004 *Mw* 9.2 Sumatra, the 2008 *Mw* 7.9 Wenchuan, and the 2011 *Mw* 9.1 Tohoku-Oki earthquakes) that triggered microearthquakes during their large-amplitude surface waves. These studies suggest that Changbaishan volcano may be sensitive to external stress perturbations due to seismic waves from shallow distant earthquakes.

DATA AND METHODOLOGY

During the volcanic unrest period of Changbaishan volcano (2002–2005), there were six seismic stations operated by CHVO (**Figure 1B**). Among these, station CBS was deployed on stable bedrock in an observation tunnel 3 km from Tianchi caldera and recorded continuously, while the other five seismic stations were deployed in the volcanic area. Due to harsh weather and other environmental conditions, these five stations only work intermittently during summer (June–October) every year, and the quality of their data is not as high as that from station CBS. To ensure the consistency of results for the entire time period, we use the catalogue produced by the single station CBS as a proxy of seismic activities of Changbaishan volcano.

In this study, we use the Match and Locate (M&L) method (Zhang and Wen, 2015) for earthquake detection. Similar to the standard matched-filter technique (e.g., Peng and Zhao, 2009), the M&L method first detects small events through continuous waveforms from stacked cross-correlation traces between template waveforms and potential events in the continuous waveforms over multiple stations and components. It then identifies the best-fitting locations of newly detected events by performing a grid search with differential travel times. In this study, we use three-component waveforms from the single station CBS, instead of multiple stations. Therefore, we do not perform any grid search for the newly detected event, but take the location of best-matching template event as that of newly detected events To improve the signal-to-noise ratio (SNR) of local seismic

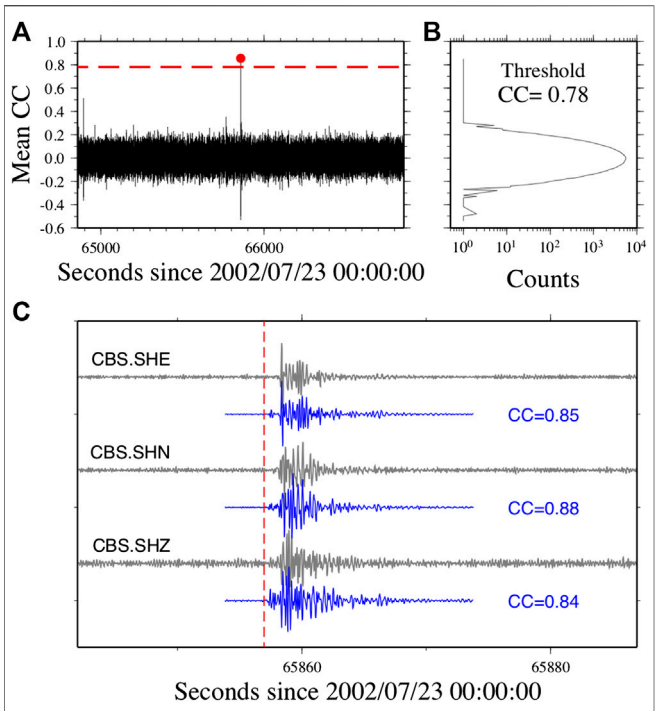

FIGURE 2 | (A) Mean correlation coefficients between the template seismograms and the continuous waveforms in **(C)**. The red dashed line indicates the mean CC threshold (0.78) for detection, the black line the mean CC value, and the red point the mean CC value of a positive detection. **(B)** Histogram of the mean CC in **(A)**. **(C)** Template seismograms (blue traces) and continuous waveforms (gray traces). The red dashed line indicates the origin time of a positive detection and the template earthquake. The channel name and CC value are given on the left- and right-hand sides of each trace, respectively.

signals, we apply a bandpass filter of 2–8 Hz to both the template and continuous waveforms. We use a 25-s-long window starting 5 s before the hand-picked S arrival as template waveform. To confirm positive detections, we use two thresholds: a mean correlation coefficient (CC) value >0.78 and an SNR of the stacked cross-correlograms >2.0, following Zhang and Wen (2015). We test a large number of combinations of CC and SNR thresholds during the search process, and determine the optimum threshold of CC >0.78 and SNR >2.0 for this work. We choose a relatively high CC value because we have only one station recording with three components, which is subject to a higher false-detection rate than it would be the case for multiple stations. Once the mean CC and SNR values of a potential event exceed the pre-defined thresholds, we consider this as a positive detection (**Figure 2**).

From July 1999 to July 2007, there are 3,427 seismic events in the CHVO manually picked catalogue (**Supplementary Table S1**). We visually examine waveforms of all events, and manually remove 1661 listed in the CHVO catalogue as possible false detections. These false detections are mainly of two types: interference signals and explosion-type signals from nearby industry activities (**Supplementary Figure S1**). To ensure the operational efficiency of the M&L program and to guarantee that all the remaining 1766 events can be recovered by the procedure, we first select 50 events with clear P and S waves and highly accurate locations as initial templates and scan through the time windows that include the remaining 1766 events. Any time an event is not detected by the M&L procedure, we manually stop the scanning and add this event to the templates, after which we restart the procedure. In this way, all of the 1766 remaining events can be detected by the new catalogue. In the end, the number of template events grows to 536 (**Supplementary Table S2**).

The locations of the 536 template events used in this study are obtained from three different catalogues. The first is the catalogue provided by the temporary seismic network (Wu et al., 2005), which only works during summer every year from 2002 to 2007. A total of 15 seismic stations close to Tianchi caldera, with a station spacing of 5 km provides reasonable station coverage. Here, we term this the Wu Catalogue. The second catalogue is that provided by the regional seismic network operated by the Jilin Earthquake Agency (the JEA catalogue), which consists of 10 regional seismic stations with an average distance of 100 km around Tianchi caldera. The third catalogue is that provided by the CHVO, which has been manually picked with continuous waveforms of the single station CBS (CHVO catalogue, **Supplementary Table S1**). The events are subsequently located if they are recorded by more than three stations in the CHVO. Among these three catalogues, the location accuracy of the Wu catalogue is the highest, and that of the CHVO catalogue is the lowest. Thus, if one event has been listed in two or three catalogues, we use the location listed in the catalogue with highest accuracy. For any new event detected by the M&L technique with the single station CBS, we simply assign the location of the template event with the highest mean CC value. As the combined template catalogue may not include all possible events with different locations or mechanisms, our final automatically detected catalogue is likely not complete, although it is more complete than any of manually picked catalogues.

To confirm the existence of potential triggering, we compare the seismicity changes before and after a specific event with the β-statistic value (Matthews and Reasenberg, 1988). A β-statistic value greater than 1.96 is generally considered as a statistically significant seismic increase with 95% confidence level (Gomberg et al., 2001; Hill and Prejean, 2007; Aron and Hardebeck, 2009; Peng and Gomberg, 2010; Liu et al., 2017). We use the following expression given by Aron and Hardebeck (2009):

$$\beta = \frac{N_a - N(T_a/T)}{\sqrt{N(T_a/T)(1-(T_a/T))}}, \quad (1)$$

where T_a is the length of triggering window, T is entire time period, and N_a and N are the numbers of earthquakes in the triggering window and the entire time period, respectively. We compute the β-statistic values with both the newly detected catalogue and the manually picked catalogue provided by the CHVO around the 2002 Wangqing and other deep-focus earthquakes. As expected, the β-statistic value depends on the length of triggering window. In this study, we use a relatively short triggering time window of 5 days to compute the β-statistic

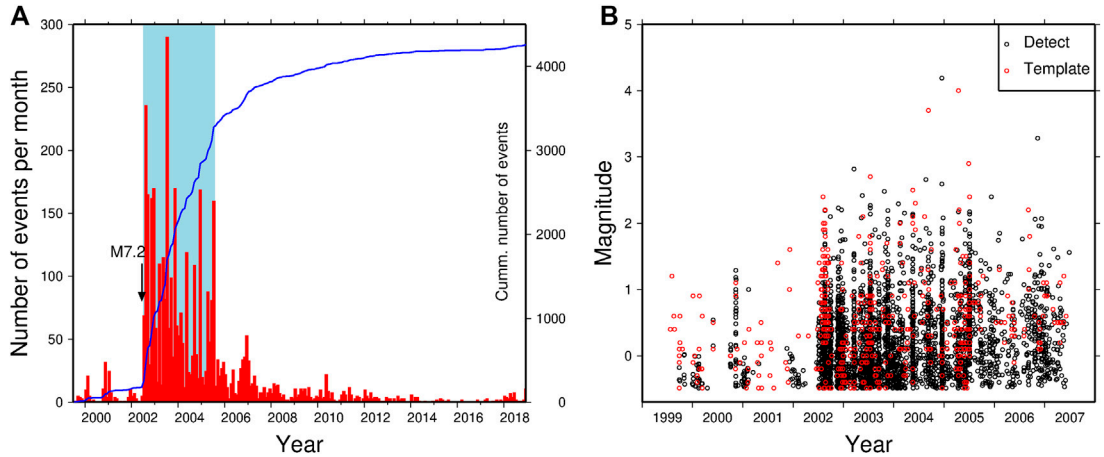

FIGURE 3 | (A) Monthly rates of seismicity listed in the joint catalogue (red bars) from 1999 to 2018 around Changbaishan volcano. The joint catalogue is produced by merging two catalogues. The first is the automatically detected catalogue from Jul. 1999 to Jul. 2007 in this study, and the second one is manually picked catalogue from Aug. 2007 to Dec. 2018. The light blue shaded area indicates the time period of volcanic unrest. The blue curve represents the cumulative number of events. **(B)** Template events (red circles) and detected events (black circles) listed in the automatically detected catalogue.

value in order to identify short-term variation of seismicity due to the occurrence of remote earthquakes. On the other hand, a longer time window (e.g., 15 or 30 days) can be used to compute the β-statistic value for long-term variation of seismicity.

RESULTS

Using 536 templates, we detect 3,763 events through waveforms of station CBS from July 1999 to July 2007 (**Figure 3B** and **Supplementary Table S3**). The automatically detected catalogue not only includes 1776 events after visual inspection of the manually picked catalogue, but also includes 1987 newly detected events. Intensive seismicity started on July 5, 2002, and lasted for about three years. After the volcanic unrest (**Figure 3A**), the seismicity of Changbaishan volcano dropped slowly, and resumed to the background level around 2008. In order to provide a comprehensive view of the seismicity of Changbaishan volcano from 1999 to 2018, we use the joint earthquake catalogue, which include events produced by automatic detection from July 1999 to July 2007 and those listed in the CHVO catalogue after August 2007.

Seismicity Changes Following the 2002 Wangqing Deep Earthquake

As mentioned before, on June 28, 2002 at 17:19:25 UTC, an *Mw* 7.2 earthquake at a depth of 566 km struck the city of Wangqing, which is about 290 km from Tianchi caldera (**Figure 1A**). The Wangqing mainshock was recorded well by five stations in the CHVO (**Supplementary Figure S2**). Before the Wangqing mainshock, the CHVO catalogue includes some false identifications, which have been removed by visual inspection (**Supplementary Figure S3**). After the mainshock, the automatically detected catalogue includes some newly detected events that were not listed in the CHVO catalogue (**Figure 4** and **Supplementary Figure S3**). On July 5, 2002, seven days after the mainshock, the number of VT events increased significantly, marking the onset of the volcanic unrest (**Figure 4**).

Using a 10-days time window before and after the Wangqing mainshock, the β-statistic values at July 5, 2002 for the newly detected and CHVO catalogues ($\beta_{\text{Automatic}}$ and $\beta_{\text{Manually picked}}$) are calculated as 5.1 and 1.0, respectively (**Figure 5**), suggesting a possible triggering relationship. We note that $\beta_{\text{Automatic}}$ is larger than $\beta_{\text{Manually picked}}$, mainly because several false detections in the manually picked catalogue were removed and additional events following the Wangqing mainshock were included during the detection process.

Seismicity Changes Following Other Deep-Focus Earthquakes

During the study time period from 2000 to 2019, 67 deep-focus earthquakes (depth >300 km, magnitude >4) occurred within 1000 km around Tianchi caldera (**Supplementary Table S4**), as listed in the International Seismological Center (ISC) catalog. We measure the peak ground velocity (PGV) of each earthquake on the vertical component of station CBS after removing the instrument response and applying a low-pass filter of 5 Hz to avoid contamination by high-frequency local noise. The PGV of the Wangqing earthquake is 1.2 cm/s (**Supplementary Table S4** and **Figure 6**), which is several times larger than that of other deep-focus earthquakes. Assuming a shear rigidity μ of 30 GPa, and a phase velocity V_{ph} of 3.0 km/s, we can convert the PGV of the Wangqing earthquake (1.2 cm/s) into the dynamic stress σ_d 120 kPa with the following equation:

$$\sigma_d = \frac{(PGV)(\mu)}{V_{ph}} \tag{2}$$

This is just an approximation since these values would likely be different at depth. But it provides a rough back-to-the-envelope

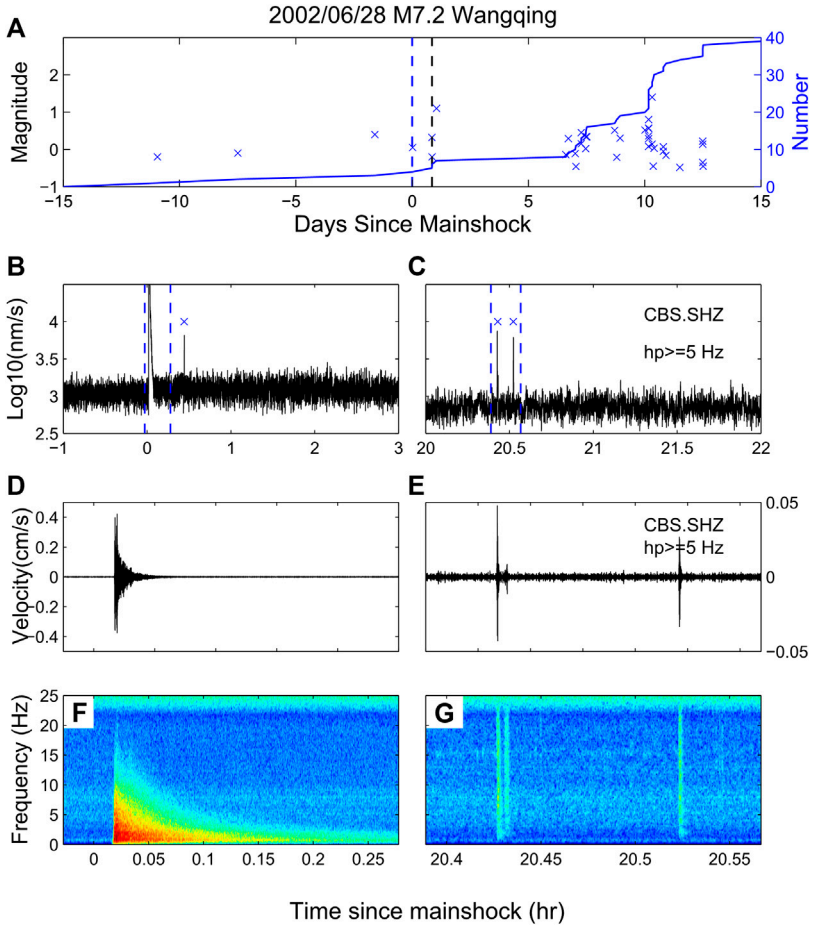

FIGURE 4 | (A) Seismicity within 15 days before and after the 2002 *M* 7.2 Wangqing earthquake. The crosses mark events listed in the newly detected catalogue, the blue curve shows the cumulative number of earthquakes, and the vertical blue lines indicate the time window plotted in **(B)** and **(C)**. **(B,C)** Envelope functions of the high-pass filtered 5 Hz waveform during and after the 2002 *M* 7.2 Wangqing earthquake. The newly detected earthquakes are marked as blue crosses. **(D,E)** Zoom-in plots of the areas between the blue dashed lines in **(B)** and **(C)**. **(F,G)** Spectrograms of **(D)** and **(E)**.

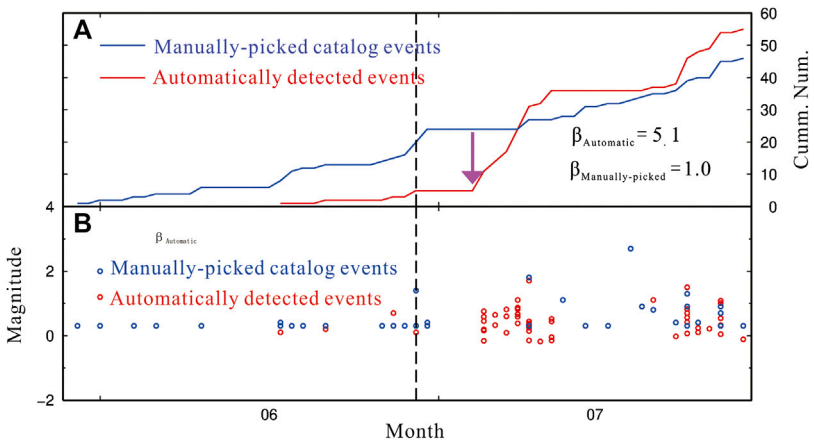

FIGURE 5 | (A) β-statistic values of automatically detected (red curve) and manually picked (blue curve) catalogues. **(B)** Changbaishan volcanic earthquake activities before and after the 2002 Wangqing deep-focus earthquake. The purple arrow marks the onset of volcanic unrest (i.e., July 5, 2002).

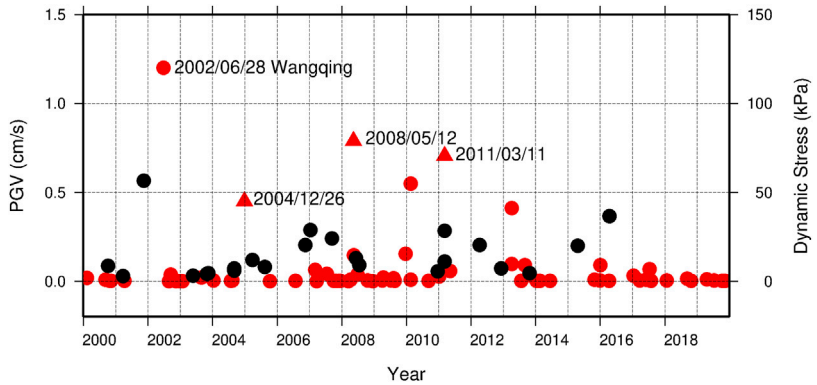

FIGURE 6 | PGV and dynamic stress of deep-focus earthquakes and large distant earthquakes. Red circles represent deep-focus earthquakes within 500 km. Black circles represent large distant earthquakes beyond 1000 km. Three large distant earthquakes (2004 *M* 9.3 Sumatra, 2008 *M* 7.9 Wenchuan, and 2011 *M* 9.1 Tohoku-Oki earthquakes) that dynamically triggered micro-seismicity in Changbaishan volcano are marked by red triangles (Liu et al., 2017).

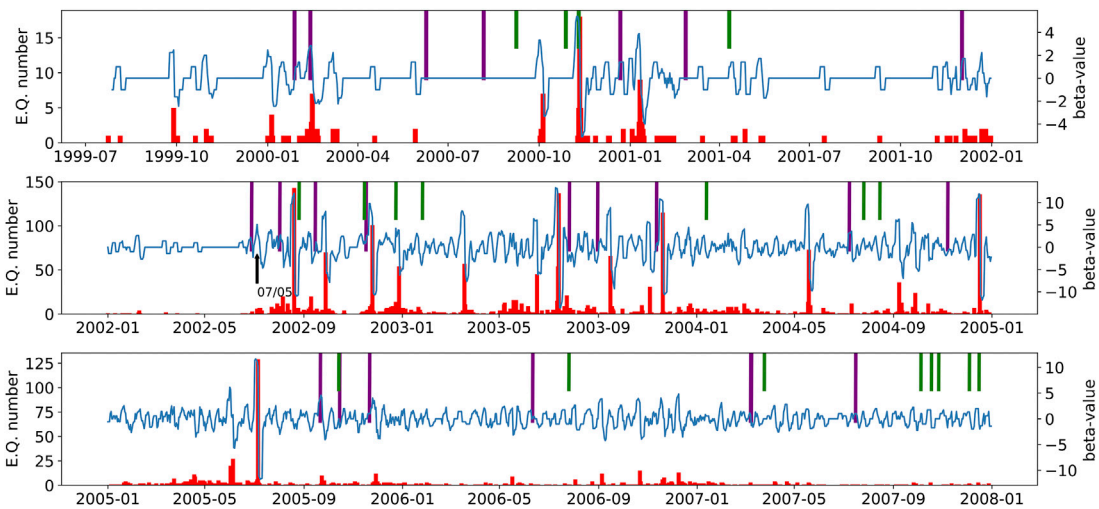

FIGURE 7 | Daily earthquake numbers, β-statistic value from the detected catalog, and occurrence time of deep-focus earthquakes. The *x*-axis represents the date, the left *y*-axis the number of earthquakes per day, and the right *y*-axis the value of the β-statistic. The red bars indicate the number of earthquakes. The purple and green bars indicate deep-focus earthquakes greater than *M* 6 within 1000 km and earthquakes greater than *M* 4 within 500 km from Changbaishan volcano, respectively. The blue curves represent time series of the β-statistic, which has been computed with T_a = 5 days and a sliding window step of 20 days.

estimation of the associated dynamic stress. **Figure 6** also includes the PGVs of large distant earthquakes analyzed by Liu et al. (2017). The PGV of the Wangqing mainshock is slightly larger than those of large distant earthquakes that triggered microseismicity during their large-amplitude surface waves (e.g., the 2004 *M* 9.3 Sumatra, 2008 *M* 7.9 Wenchuan, and 2011 *M* 9.1 Tohoku-Oki earthquakes).

As mentioned before, VT earthquakes in Changbaishan volcano might be related to deep-focus earthquakes occurring in nearby regions (Lv et al., 2007). To check the relationship between other deep-focus events and local earthquakes, we plot the daily earthquake numbers and all deep-focus earthquakes with magnitude greater than 4 within 1000 km (**Figure 7**). In addition, we compute a running-window β-statistic time series (with T = 10 days, and a sliding window step of 1 day, Ta = 5 days) to help identify the triggering relationship. As expected, the β-statistic time series reflects the seismicity rate change quite well, with each peak in the β-value corresponding to a local earthquake swarm. In particular, the β-value on July 5, 2002 seven days after the June 28, 2002 Wangqing deep-focus earthquake, is as high as 5.1, setting the highest record since 1999. We argue that such a significant increase in seismicity suggests that the Wangqing earthquake might have triggered Changbaishan volcanic activity with a delayed response of seven days.

Out of the 22 selected deep-focus earthquakes with magnitude greater than *M* 6 that occurred within nine years (1999–2007), 12 (54.5%) were followed by increased seismicity (defined as β-statistic values >2 with T = 10 days and centering around the deep-focus earthquakes) (**Figure 7**). Using the same method, we analyze the triggering relationship between deep-focus

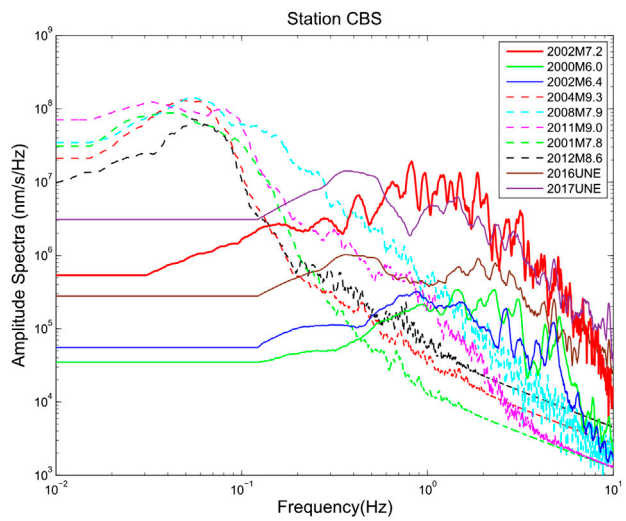

FIGURE 8 | Amplitude spectra for the Wangqing earthquake and other deep-focus earthquakes and shallow distant earthquakes. Dashed curves correspond to shallow distant earthquakes, and solid lines to deep-focus earthquakes and the largest UNEs in North Korea. The linear-like spectra at high-frequency ranges (>1 Hz) for some events are due to small gap in the continuous waveform, resulting in some high-frequency artefact.

earthquakes and Changbaishan seismic activities during 2008–2019 with the manually picked CHVO catalog (**Supplementary Figure S4**). Out of 26 selected deep-focus earthquakes during this time period, 16 (61.5%) were followed by increased seismicity. Our observations are generally consistent with previous studies, suggesting a moderate triggering relationship between deep-focus events and local seismicity at CBS (Lv et al., 2007; Liu et al., 2017).

Since July 1999, 67 (**Supplementary Table S4**) deep-focus earthquakes within 500 km (horizontal distance) occurred in this region; some are associated with increased seismicity in Changbaishan volcano, others are not. However, it is worth noting that the 2002 Wangqing mainshock is the largest deep-focus earthquakes occurred in this region in the past few decades. We also checked the local catalogue and waveforms at station CBS during other large deep-focus earthquakes at remote distances (e.g., 2013 *M* 8.3 Okhotsk Sea earthquake), and did not find any clear triggering evidence. Hence, it appears that only large deep-focus earthquakes occurring nearby (within 500 km in horizontal distance) are followed by unrest in this region.

Comparison Between Triggering by Deep-Focus Earthquakes and by Large Distant Earthquakes

In this section we compare the amplitude spectra of those distant shallow earthquakes that triggered seismicity in Changbaishan and deep-focus earthquakes with magnitude greater than 6 to identify potential differences in triggering behaviors between them (**Figure 8**). As expected, the amplitude spectra of deep earthquakes and those of large distant earthquakes show clearly different characteristics. For large distant earthquakes, the peaks appear in the low-frequency range (0.02–0.08 Hz, or 12.5–50 s), whereas for deep-focus ones, the peaks appear in the high-frequency range (0.4–2 Hz). Particularly for the 2002 Wangqing deep-focus earthquake, the high-frequency part (e.g., ~1 Hz) of the amplitude spectrum is at least one order higher than those of large distant earthquakes.

Although the Wangqing mainshock and three large distant earthquakes (2004 *M* 9.3 Sumatra, 2008 *M* 7.9 Wenchuan, and 2011 *M* 9.1 Tohoku-Oki earthquakes) triggered seismicity in Changbaishan volcano, the triggering seismic phases and the triggered seismicity are likely different. Large distant earthquakes dynamically trigger microseismicity through their large-amplitude surface wave trains, but are not followed by subsequent changes in seismic behaviors in Changbaishan volcano (Liu et al., 2017). In comparison, deep-focus earthquakes likely trigger microseismicity through their high-frequency body waves. We do not observe any instantaneous triggering during the Wangqing mainshock, but a time delay of 7 days is observed before the onset of the 2002–2005 earthquake swarm. Comparing with the spectrum of the Wangqing mainshock, the 2017 mb = 6.0 underground nuclear explosion (UNE) in North Korea has a slightly longer period of around 0.5 Hz, likely due to its surface waves (**Supplementary Figure S5**). But at higher frequency range of 1 Hz, the Wangqing earthquake spectrum is larger. The corresponding dynamic stress for the 2017 UNE is ~63 kPa, smaller than the 120 kPa for the Wangqing earthquake.

Long-Period and Harmonic-Spectra Events

We re-examine those HS events (**Figure 9**) identified and located by Ming et al. (2007) and use the clear HS events as templates to scan the continuous waveforms recorded by the single station CBS to detect more potential HSs. In contrast to previous observations (Ming et al., 2007), waveforms of HS events recorded at station CBS span the entire volcanic unrest period, resulting in a total of 125 HSs from 1999 to 2007. The most common feature of these HSs is that they all have several (>2) clear harmonic peaks in their spectral plots (**Figures 9A,B**).

By visually inspecting the waveforms originated by CHVO catalogue, we find that some waveforms show distinct low-frequency characteristics. We attribute these events with a dominant frequency of 2–3 Hz to LPs and put them into the templates. Eventually, 20 LPs have been detected in this study. Some of the representative LPs are shown in **Figures 9C,D**.

DISCUSSION

Large earthquakes are capable of producing dynamic, static, and quasi-static stress changes (Freed and Andrew, 2005). Static stress change decays rapidly with distance, and becomes negligible beyond a few fault lengths (King et al., 1994; King and Deves, 2015). Given the large depth and horizontal distance between the Wangqing mainshock epicenter and Changbaishan volcano, the static stress change from the Wangqing mainshock does not seem the primary connecting agent. There are several physical models that connect the dynamic stresses disturbances from distant

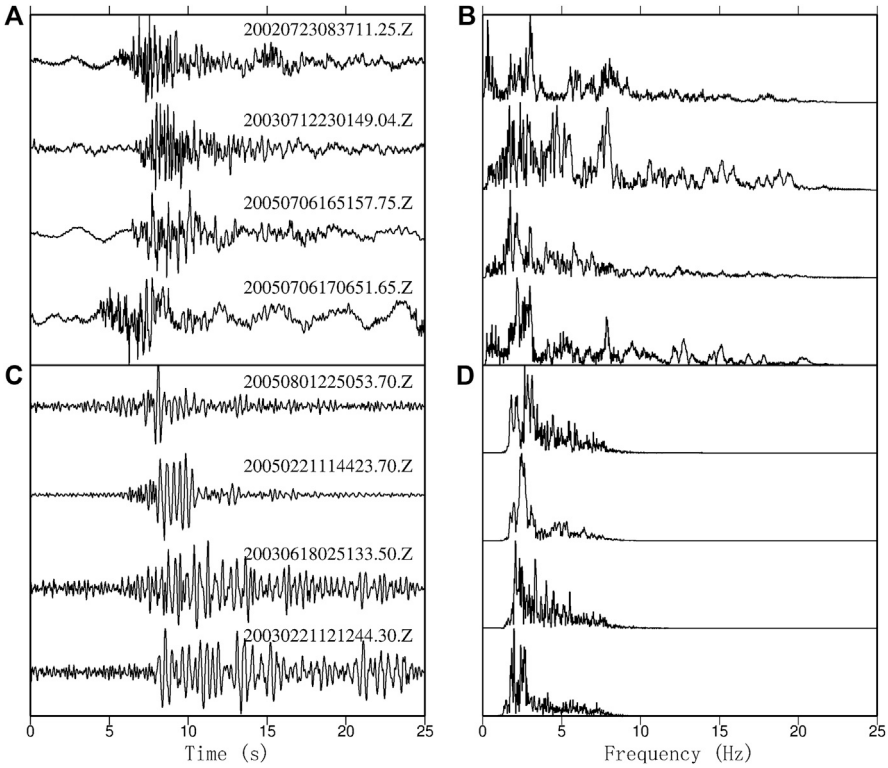

FIGURE 9 | Some representative HS and LP events recorded by station CBS. All of these waveforms have been normalized before plotting. **(A,B)** Original waveforms and normalized spectral functions of vertical components, respectively, of HS events. **(C,D)** Original waveforms and normalized spectral functions of vertical components, respectively, of LP events. The numbers above the waveforms indicate the time of origin of the events.

earthquakes with magma overpressure, thus triggering volcanic unrest/eruption and local seismicity. Most of them involve bubble excitation in idealized magmatic conditions but the physical processes are different. The rectified diffusion model involves volatiles in saturated fluids that are pumped into bubbles by dilatational phase of seismic waves from distant earthquakes (Sturtevant et al., 1996; Brodsky et al., 1998). In the advective overpressure model, bubbles are shaken from walls of the magma chamber (i.e., Pyle and Pyle, 1995; Hill and Prejean, 2015). In the sloshing model, the oscillatory motions of fluids in the magma chamber cause foam collapse and hence affect the presence and stability of bubbles (Namiki et al., 2016). Hill and Prejean (2015) also summarized a few additional models on bubble excitations by dynamic waves. In all these models, the ascending bubbles increase pressure in the shallow magma body and can cause volcanic unrest or eruption.

Brodsky and Prejean (2005) demonstrated that long-period (>30 s) waves generated by large distant earthquakes are more effective at triggering seismicity in Long Valley Caldera, California, and they proposed that fluid flow could play an important role as a low-pass filter and respond to long-period wave triggering. This is consistent with the recent observation of long-period surface waves triggering microseismicity in Changbaishan volcano (Liu et al., 2017). However, the triggering of the 2002–2005 volcanic unrest by the *M* 7.2 Wangqing deep-focus earthquake is quite different, both in terms of the triggering wave (relatively high-frequency body wave in the range of 0.4–2 Hz), and the triggered seismicity (delayed for 7 days and lasted for about 3 years). While we do not have additional evidence to distinguish between various models of bubble excitation due to dynamic shaking, our observations seem to suggest that this process is likely promoted by seismic waves in the relatively high-frequency range of 0.4 to 2 Hz, rather than at longer period. If we use the apparent lack of triggering due to the nearby UNE (Liu et al., 2017) as an additional constraint, then we could argue that the frequency range around 1 Hz is mostly relevant (see **Figure 8**).

Based on these arguments, we come up with the following scenario (**Figure 10**) to explain the apparent triggering between deep-focus earthquakes and volcanic unrest, as well as of different types of volcanic events. High-frequency body waves of the Wangqing deep-focus earthquake likely triggered some bubble growth and overpressure in the magma systems due to one of the aforementioned physical mechanisms. While it is not clear in which magma system had bubble growth, giving the apparent 7-days delay between the Wangqing mainshock and onset of volcanic unrest, we argue that it is likely that bubbles grew in the mid-crust magma system, resulting in overpressure and a small magma injection into the shallow magma chamber at a depth of ~5 km (**Figure 10B**). This process readjusted the local stress state and triggered a delayed increase in VT seismicity at the top of the magma body (**Figures 10B,C**). The persistent

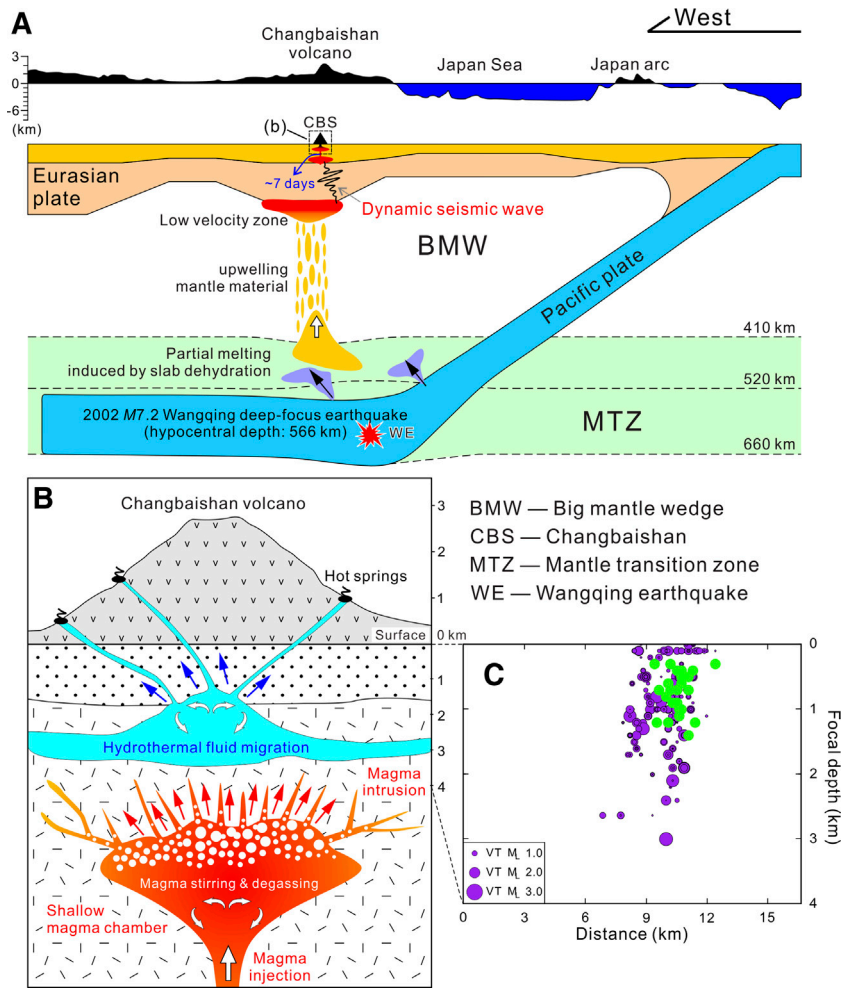

FIGURE 10 | (A) A conceptual model showing magma migration from a deep source to a shallow reservoir of Changbaishan volcano in response to dynamic stress perturbations related to the Wangqing deep-focus earthquake in the stagnant Pacific Plate beneath NE Asia. An upwelling plume derived from the mantle transition zone is shown as the magma origin of Changbaishan volcano based on studies of seismic tomography (Zhao et al., 2009) and basalt geochemistry (Zhang et al., 2018). The 410, 520, and 660 km discontinuities are from Tian et al. (2016). **(B)** Hypothetical magmatic and hydrothermal processes corresponding to the 2002–2005 unrest of Changbaishan volcano. Injection of deep-sourced magmas into the shallow magma chamber led to anomalous magma stirring and degassing, which pressurized the shallow magma chamber and facilitated intrusion of gas-enriched magmas through cracks above the magma body. Hydrothermal fluid migration was influenced by crack intrusion of magmas. **(C)** A cross-sectional view of the study region along AB in **Figure 1B**. The green circles indicate HS events, and the purple circles with different scales indicate VT events with different magnitudes.

appearance of VT events and the sporadic appearance of LP and HS events suggest transient and repetitive processes, respectively. The LP and HS events can be interpreted as resonances of the cracks filled by fluids above the magma system (**Figures 10B,C**). As mentioned before, the magmatic movement is supported by the independent observation of increasing volcanic gas emissions and ground deformations during the volcanic unrest period (Xu et al., 2012). However, because we did not have enough high-quality continuous recordings to relocate all the seismicity, we cannot provide additional evidence for magmatic or fluid movements such as spatio-temporal migration of aseismic slip and seismic swarms (e.g., Shelly et al., 2016).

Hong et al. (2016) suggested that a hypothetical UNE in North Korea (about 130 km from Changbaishan volcano) with magnitude M = 7.0 can generate ~67 kPa dynamic stress change on the volcano surface and ~120 kPa in the magma chamber at depth, which are enough to disturb magma chambers and trigger volcanic eruptions. The dynamic stress of Wangqing earthquake is in the range of the hypothetical M 7 North Korea underground nuclear explosion. In addition, while the spectra of the 2017 mb = 6.0 UNE and the 2002 Wangqing mainshock do not completely overlap (**Figure 8**), it is expected that the spectrum of a hypothetical M = 7.0 UNE would be above that of the Wangqing mainshock at almost all frequency ranges. Hence, if other characteristics of the triggering waves (e.g., incident angles, back-azimuths, etc) do not play any important roles, we could argue that a magnitude 7 event (either nuclear explosion or deep-focus earthquake) nearby is capable of triggering an unrest or eruption at Changbaishan volcano.

CONCLUSION

In this study, we performed a systematic detection of seismic events around Changbaishan volcano to better understand the triggering relationship between the 2002 *M* 7.2 Wangqing deep-focus earthquake and the 2002–2005 unrest. We found clear evidence of LP events during the volcanic unrest process, and identified additional HS events. Thus, we identified three types of volcanic earthquakes (VT, LP and HS) during the unrest of Changbaishan volcano. The limited magnitudes of the VTs and small numbers of HSs and LPs suggest a small-scale magmatic process, likely indicating no major eruptive hazard in the foreseeable future.

With the new catalogue obtained by this study, we investigated the relationship between the 2002 Wangqing deep-focus earthquake and seismicity in Changbaishan volcano. The β-statistic value which has been calculated with a 5-days window at 7 days after the mainshock is as large as 5.1, suggesting a clear increase of seismicity at Changbaishan volcano. The onset of the seismic swarm and unrest on Changbaishan might have been dynamically triggered by the Wangqing earthquake with a delayed response of seven days. This apparent time delay between the deep-focus earthquake and the onset of swarm activity in Changbaishan volcano likely reflects the slow magmatic movements, which were accompanied by the 3-years earthquake swarm and volcanic unrest.

DATA AVAILABILITY STATEMENT

The original contributions presented in the study are included in the article/**Supplementary Material**, and further inquiries can be directed to the corresponding author.

AUTHOR CONTRIBUTIONS

All authors listed have made a substantial, direct, and intellectual contribution to the work and approved it for publication.

FUNDING

This study was funded by National Natural Science Foundation of China Grant 41572319 (GL), National Science Foundation Grants EAR-1543399 and EAR-1925965 (ZP, CL) and Jilin Changbaishan Volcano National Observation and Research Station (Project No. NORSCBS20-03).

ACKNOWLEDGMENTS

Seismic data utilized in this study were recorded by the Changbaishan Volcanic Observatory and can be requested from the Data Management Center of the China National Seismic network at the Institute of Geophysics, China Earthquake Administration (http://www.seisdmc.ac.cn/, in Chinese). We thank Zhikun Liu from the China University of Geoscience for comments on an early version of this paper. This manuscript benefits from useful comments by three anonymous reviewers.

SUPPLEMENTARY MATERIAL

The Supplementary Material for this article can be found online at: https://www.frontiersin.org/articles/10.3389/feart.2020.599329/full#supplementary-material.

REFERENCES

Aron, A., and Hardebeck, J. L. (2009). Seismicity rate changes along the Central California coast due to stress changes from the 2003 M 6.5 San Simeon and 2004 M 6.0 Parkfield earthquakes. *Bull. Seismol. Soc. Am.* 99, 2280–2292. doi:10.1785/0120080239

Brodsky, E. E., and Prejean, S. G. (2005). New constrains on mechanisms of remotely triggered seismicity at Long Valley Caldera. *J. Geophys. Res.* 110, B04302. doi:10.1029/2004JB003211

Brodsky, E. E., Sturtevant, B., and Kanamori, H. (1998). Earthquakes, volcanoes, and rectified diffusion. *J. Geophys. Res.* 103 (B10), 23827–23838. doi:10.1029/98JB02130

Chouet, B. A. (1996). Long-period volcano seismicity: its source and use in eruption forecasting. *Nature* 380, 309–316.

Crews, J. B., and Cooper, C. A. (2014). Transient pore pressure response to confining stress excursions in Berea sandstone flooded with an aqueous solution of CO_2. Water Resources Research. 50 (6), 4775–4786. doi:10.1002/2014WR015305

Farías, C., and Basualto, D. (2020). Reactivating and calming volcanoes: the 2015 MW 8.3 Illapel megathrust strike. *Geophys. Res. Lett.* 47 (16). doi:10.1029/2020GL087738

Freed, and Andrew, M. (2005). Earthquake triggering by static, dynamic, and postseismic stress transfer. *Annual Review of Earth & Planetary Sciences*, 33 (1), 335–365. doi:10.1146/annurev.earth.33.092203.122505

Gomberg, J., Reasenberg, P. A., Bodin, P., and Harris, R. A. (2001). Earthquake triggering by seismic waves following the Landers and Hector mine earthquakes. *Nature* 411, 462–466. doi:10.1038/35078053

Hakozaki, M., Miyake, F., Nakamura, T., Kimura, K., Masuda, K., and Okuno, M. (2018). Verification of the annual dating of the 10th Century Baitoushan volcano eruption based on an AD 774–775 radiocarbon spike. *Radiocarbon.* 60, 1–8. doi:10.1017/RDC.2017.75

Hammond, J. O. S., Wu, J.-P., Ri, K.-S., Wei, W., Yu, J.-N., and Oppenheimer, C. (2020). Distribution of partial melt beneath Changbaishan/Paektu volcano, China/Democratic People's Republic of Korea. *G-cubed.* 21, e2019GC008461. doi:10.1029/2019GC008461

Hill, D. P., and Prejean, S. G. (2007). "Dynamic triggering in earthquake seismology," in *Treatise on Geophysics: earthquake seismology.* Editor H. Kanamori (Amsterdam, Netherlands: Elsevier), 4, 257–291.

Hill, D. P., and Prejean, S. G. (2015). "Dynamic triggering," in *Treatise on geophysics: earthquake seismology.* Editors H. Kanamori and G. Schubert. 2nd Edn (Oxford, United Kingdom: Elsevier), 4, 273–304.

Hill, D. P., Pollitz, F., and Newhall, C. (2002). Earthquake–volcano interactions. *Phys. Today* 55, 41–47. doi:10.1063/1.1535006

Hong, T., Choi, E., Park, S., and Shin, J. S. (2016). Prediction of ground motion and dynamic stress change in Baekdusan (Changbaishan) volcano caused by a North Korean nuclear explosion. *Sci. Rep.* 6, 21477. doi:10.1038/srep21477

Hough, S. E., Dollar, R. S., and Johnson, P. (2000). The 1998 earthquake sequence south of Long Valley Caldera, California: hints of magmatic involvement. *Bull. Seismol. Soc. Am.* 90, 752–763. doi:10.1785/0119990109

Iacovino, K., Ju-Song, K., Sisson, T., Lowenstern, J., Kuk-Hun, R., Jong-Nam, J., et al. (2016). Quantifying gas emissions from the "Millennium eruption" of Paektu volcano, democratic People's Republic of Korea/China. *Sci Adv.* 2, e1600913. doi:10.1126/sciadv.1600913

Kim, S., Tkalčić, H., and Rhie, J. (2017). Seismic constraints on magma evolution beneath Mount Baekdu (Changbai) volcano from transdimensional Bayesian inversion of ambient noise data. *J. Geophys. Res.: Solid Earth.* 122, 5452–5473. doi:10.1002/2017JB014105

King, G. C. P., and Deves, M. H. (2015). Fault interaction, earthquake stress changes, and the evolution of seismicity. *Treat. on Geophys.* 4 (10), 243–271. doi:10.1016/B978-044452748-6.00069-9

King, G. C. P., Stein, R. S., and Lin, J. (1994). Static stress changes and the triggering of earthquakes. *Bull. Seismol. Soc. Am.* 84 (3), 935–953.

Kuritani, T., Ohtani, E., and Kimura, J.-I. (2011). Intensive hydration of the mantle transition zone beneath China caused by ancient slab stagnation. *Nat. Geosci.* 4, 713–716. doi:10.1038/ngeo1250

Lara, L. E., Naranjo, J. A., and Moreno, H. (2004). Rhyodacitic fissure eruption in Southern Andes (Cordón Caulle, 40.5°S) after the 1960 (Mw: 9.5) Chilean earthquake: a structural interpretation. *J. Volcanol. Geoth. Res.* 138, 127–138. doi:10.1016/j.jvolgeores.2004.06.009

Li, Y., Shi, Z., and Cao, X. (2012). The seiches and volcanic eruption triggered by the 6 October 1597 earthquake with M≥8 in the "Hunchun-Wangqing, Northeastern China, deep-focus seismic zone". *Acta Seismolo. Sinica.* 34 (4), 557–570. doi:10.3969/j.issn.0253-3782.2012.04.012

Linde, A. T., and Sacks, I. S. (1998). Triggering of volcanic eruptions. *Nature* 395, 888–890. doi:10.1038/27650

Liu, R., Wei, H., and Li, J. (1998). *The recent eruptions of Changbaishan Tianchi volcano.* Beijing, China: Science Press.

Liu, G., Yang, J., Wang, L., and Sun, J. (2011a). Analysis of Tianchi volcano activity in Changbai Mountain, NE China. *Glob. Geol.* 14, 44–53. doi:10.3969/j.issn.1673-9736.2011.01.06

Liu, G., Sun, H., and Guo, F. (2011b). The newest monitoring information of Changbaishan volcano, NE China. *Acta Petrol. Sin.* 27, 2905–2911. CNKI:SUN:YSXB.0.2011-10-011

Liu, G., Li, C., Peng, Z., Li, X., and Wu, J. (2017). Detecting remotely triggered microseismicity around Changbaishan volcano following nuclear explosions in North Korea and large distant earthquakes around the world. *Geophys. Res. Lett.* 44, 4829–4838. doi:10.1002/2017gl072511

Lv, Z., Hong, H., and Wei, H. (2007). Research on the volcanic earthquake activity mechanism in Changbaishan Tianchi area. *Seismol. Res. Northeast China* 23, 40–48. doi:10.3969/j.issn.1674-8565.2007.01.007

Manga, M., and Brodsky, E. (2006). Seismic triggering of eruptions in the far field: volcanoes and geysers. *Annu. Rev. Earth Planet Sci.* 34, 263–291. doi:10.1146/annurev.earth.34.031405.125125

Manga, M., Fauria, K. E., Lin, C., Mitchell, S. J., Jones, M., Conway, C. E., Degruyter, W., Hosseini, B., Carey, R., and Cahalan, R. (2018). The pumice raft-forming 2012 havre submarine eruption was effusive. Earth & Planetary Science Letters, 489, 49–58. doi:10.1016/j.epsl.2018.02.025

Matthews, M. V., and Reasenberg, P. A. (1988). Statistical methods for investigating quiescence and other temporal seismicity patterns. *Pure Appl. Geophys.* 126, 357–372. doi:10.1007/BF00879003

McNutt, S. R. (2002). Volcano seismology and monitoring for eruptions. *Int. Geophys. Ser.* 81, 383–406.

Milluzzo, V., Cannata, A., Alparone, S., Gambino, S., Hellweb, M., Montalto, P., et al. (2010). Tornillos at Vulcano: clues to the dynamics of the hydrothermal system. *J. Volcanol. Geoth. Res.* 198, 377–393. doi:10.1016/j.jvolgeores.2010.09.022

Ming, Y., Wu, J., Su, W., Fang, L., and Wang, W. (2007). Harmonic-special event at Changbaishan Tianchi volcano. *Seismol. Geol.* 2, 492–501. [in Chinese with English abstract]. doi:10.3969/j.issn.0253-4967.2007.03.005

Namiki, A., Rivalta, E., Woith, H., and Walter, T. R. (2016). Sloshing of a bubbly magma reservoir as a mechanism of triggered eruptions. *J. Volcanol. Geoth. Res.* 320, 156–171. doi:10.1016/j.jvolgeores.2016.03.010

Oppenheimer, C., Wacker, L., Xu, J., Galván, J. D., and Büntgen, U. (2017). Multi-proxy dating the "Millennium Eruption"of changbaishan to late 946 CE. *Quat. Sci. Rev.* 158, 164–171. doi:10.1016/j.quascirev.2016.12.024

Peng, Z., and Gomberg, J. (2010). An integrative perspective of coupled seismic and aseismic slow slip phenomena. *Nat. Geosci.* 3, 599–607. doi:10.1038/ngeo940

Peng, Z., and Zhao, P. (2009). Migration of early aftershocks following the 2004 Parkfield earthquake. *Nat. Geosci.* 2, 877–881. doi:10.1038/ngeo697

Pyle, D. M., and Pyle, D. L. (1995). Bubble migration and the initiation of volcanic eruptions. *J. Volcanol. Geoth. Res.* 67 (4), 227–232. doi:10.1016/0377-0273(94)00111-S

Ri, K.-S., Hammond, J. O. S., Ko, C.-N., Kim, H., Yun, Y.-G., Pak, G.-J., et al. (2016). Evidence for partial melt in the crust beneath Mt. Paektu (Changbaishan), Democratic People's Republic of Korea and China. *Science Advances* 2, e1501513. doi:10.17863/CAM.7009

Sawi, T. M., and Manga, M. (2018). Revisiting short-term earthquake triggered volcanism. Bulletin of Volcanology. 80: 57. doi:10.1007/s00445-018-1232-2

Shelly, D. R., Beroza, G. C., and Ide, S. (2007). Non-volcanic tremor and low-frequency earthquake swarms. *Nature* 446, 305–307. doi:10.1038/nature05666

Shelly, D. R., Ellsworth, W. L., and Hill, D. P. (2016). Fluid-faulting evolution in high definition: connecting fault structure and frequency-magnitude variations during the 2014 Long Valley Caldera, California, earthquake swarm. *J. Geophys. Res.: Solid Earth.* 121, 1776–1795. doi:10.1002/2015JB012719

Sturtevant, B., Kanamori, H., and Brodsky, E. E. (1996). Seismic triggering by rectified diffusion in geothermal systems. *J. Geophys. Res.* 1012 (B11), 25269–25282. doi:10.1029/96JB02654

Tang, J., Deng, Q., Zhao, G., Li, W., Xuan, F., Jin, G., et al. (2001). Electric conductivity and magma chamber at the Tianchi volcano area in Changbaishan Mountain. *Seismol. Geol.* 23, 191–200. [in Chinese with English abstract]. doi:10.3969/j.issn.0253-4967.2001.02.008

Tang, Y., Obayashi, M., Niu, F., Grand, S. P., Chen, Y. J., Kawakatsu, H., Tanaka, S., Ning, J., and Ni, J. F. (2014). Changbaishan volcanism in northeast china linked to subduction-induced mantle upwelling. Nature Geoscience, 7 (6), 470–475. doi:10.1038/ngeo2166

Tian, Y., Zhu, H., Zhao, D., Liu, C., Feng, X., Liu, T., et al. (2016). Mantle transition zone structure beneath the Changbai volcano: insight into deep slab dehydration and hot upwelling near the 410 km discontinuity. *J. Geophys. Res.* 121, 5794–5808. doi:10.1002/2016JB012959

Walter, T. R., and Amelung, F. (2006). Volcano–earthquake interaction at Mauna Loa volcano, Hawaii. *J. Geophys. Res.* 111, B05204. doi:10.1029/2005JB003861

Walter, T. R., and Amelung, F. (2007). Volcanic eruptions following M≥9 megathrust earthquakes: implications of the Sumatra-Andaman volcanos. *Geology* 35 (6), 539–542. doi:10.1130/G23429A.1

Wei, H., Liu, G., and Gill, J. (2013). Review of eruptive activity at Tianchi volcano, Changbaishan, northeast China: implications for possible future eruptions. *Bull. Volcanol.* 75, 706. doi:10.1007/s00445-013-0706-5

Wu, J., Ming, Y., and Zhang, H. (2005). Seismic activity at the Changbaishan Tianchi volcano in the summer of 2002. *Chin. J. Geophys.* 48, 621–628. [in Chinese with English abstract]. doi:10.1002/cjg2.701

Xu, J., Liu, G., Wu, J., Ming, Y., Wang, Q., Cui, D., et al. (2012). Recent unrest of Changbaishan volcano, northeast China: a precursor of a future eruption? *Geophys. Res. Lett.* 39, L16305. doi:10.1029/2012GL052600

Zhang, M., Guo, Z., Liu, J., Liu, G., Zhang, L., Lei, M., et al. (2018). The intraplate Changbaishan volcanic field (China/North Korea): a review on eruptive history, magma genesis, geodynamic significance, recent dynamics and potential hazards. *Earth Sci. Rev.* 187, 19–52. doi:10.1016/j.earscirev.2018.07.011

Zhao, D., and Tian, Y. (2013). Changbai intraplate volcanism and deep earthquakes in East Asia: a possible link? *Geophys. J. Int.* 195, 706–724. doi:10.1093/gji/ggt289

Zhang, M., and Wen, L. (2015). An effective method for small event detection: Match and locate (M&L). *Geophys. J. Int.* 200, 1523–1537. doi:10.1093/gji/ggu466

Zhao, D., Tian, Y., Lei, J., Liu, L., and Zheng, S. (2009). Seismic image and origin of the Changbai intraplate volcano in East Asia: role of big mantle wedge above the stagnant Pacific slab. *Phys. Earth Planet. In.* 173, 197–206. doi:10.1016/j.pepi.2008.11.009

Conflict of Interest: The authors declare that the research was conducted in the absence of any commercial or financial relationships that could be construed as a potential conflict of interest.

Copyright © 2021 Liu, Li, Peng, Liu, Zhang, Liu, Zhang and Pan. This is an open-access article distributed under the terms of the Creative Commons Attribution License (CC BY). The use, distribution or reproduction in other forums is permitted, provided the original author(s) and the copyright owner(s) are credited and that the original publication in this journal is cited, in accordance with accepted academic practice. No use, distribution or reproduction is permitted which does not comply with these terms.

frontiers in Earth Science

ORIGINAL RESEARCH
published: 16 February 2021
doi: 10.3389/feart.2020.600223

Dike Inflation Process Beneath Sakurajima Volcano, Japan, During the Earthquake Swarm of August 15, 2015

Midori Koike[1,2] *and Haruhisa Nakamichi*[2]*

[1]Division of Earth and Planetary Sciences, Graduate School of Science, Kyoto University, Kyoto, Japan, [2]Sakurajima Volcano Research Center, Disaster Prevention Research Institute, Kyoto University, Kagoshima, Japan

Magma intrusion usually causes seismicity and deformation in the surrounding rock and often leads to eruptions. A swarm of volcano-tectonic (VT) earthquakes associated with rapid dike intrusion in hours occurred beneath Sakurajima volcano on August 15, 2015. We determined the hypocenters and focal mechanisms of the VT earthquake swarm. The distributions of pressure (P)- and tension (T)-axes of the azimuths of the mechanisms are also obtained. The results indicate spatiotemporal changes of the distributions of the hypocenters and P- and T-axes. The hypocenters are distributed at depths of 0.3–1 km and 7:00–10:30 JST, and are located at depths of 0.3–3 km and 10:30–12:00 during which the seismic activity is the largest. At 12:00–24:00, the hypocenters are distributed in shallow and deep clusters at depths of 0.2–1 km and 1.5–3.5 km, respectively. The dike induced rapid ground deformation and is located between the shallow and deep clusters. The strike and opening directions of the dike are parallel to the NE–SW and NW–SE directions, respectively, corresponding to the regional maximum and minimum compression stress. The T-axes of the shallow cluster are distributed parallel to the opening direction of the dike. The P-axes of the deep cluster exhibit a pattern corresponding to the NE–SW direction and the T-axes are distributed in the NW–SE direction. In contrast, a 90° rotated pattern of strike-slip faulting is also observed at the deep cluster at 12:00–24:00, where the P-axes are distributed in the NW–SE direction and the T-axes are distributed in the NE–SW direction. This reflects the change in the stress field due to the dike inflation during the earthquake generation, and indicates that the alteration of stress in the vicinity of the dike due to the dike inflation and VT earthquakes are induced by the differential stress exceeding the brittle fracture strength of the rock. Future seismic and deformation observations in volcanoes will verify whether the spatiotemporal changes of the hypocenters and focal mechanism shown by this study are unique features of rapid dike intrusion.

Keywords: hypocenter, focal mechanism, volcano-tectonic earthquake, dike inflation, earthquake swarm, Sakurajima

OPEN ACCESS

Edited by:
Luigi Passarelli,
Université de Genève, Switzerland

Reviewed by:
Federica Lanza,
ETH Zurich, Switzerland
Alessandro Bonaccorso,
National Institute of Geophysics and Volcanology, Italy

****Correspondence:***
Haruhisa Nakamichi
nakamiti@svo.dpri.kyoto-u.ac.jp

Specialty section:
This article was submitted to Volcanology, a section of the journal Frontiers in Earth Science

Received: *29 August 2020*
Accepted: *24 December 2020*
Published: *16 February 2021*

Citation:
Koike M and Nakamichi H (2021) Dike Inflation Process Beneath Sakurajima Volcano, Japan, During the Earthquake Swarm of August 15, 2015. Front. Earth Sci. 8:600223. doi: 10.3389/feart.2020.600223

INTRODUCTION

Magma rises or laterally moves and is accumulated in the crust or within a volcano edifice. This causes stress in the surrounding rock, leading to its deformation. Ground deformation occurs when the deformation extends to the surface. When the stress exceeds the fracture strength of the rock, or magma moves in cracks or conduits, fracturing or oscillation occur and generate an earthquake, that is, a volcanic earthquake. The frequency and duration of seismic ground motions of volcanic earthquakes vary widely; predominantly, volcano-tectonic (VT) earthquakes, low-frequency earthquakes, and volcanic tremors occur (e.g., McNutt, 2005; Nishimura and Iguchi, 2011; Chouet and Matoza, 2013). VT earthquakes are ordinary earthquakes that occur in brittle rock within a volcanic edifice or in the crust beneath it. They are characterized by sharp onsets of P- and S-waves, reflected by broad spectra extending up to 15 Hz (e.g., McNutt, 2005; Nishimura and Iguchi, 2011; Chouet and Matoza, 2013). They are called VT earthquakes because of their close similarity to tectonic earthquakes, although the stresses that induce them are derived from volcanic processes rather than from large-scale tectonic movements (e.g., McNutt, 2005; Nishimura and Iguchi, 2011; Chouet and Matoza, 2013). The VT earthquakes, which sometimes become seismic swarms, have been observed in many volcanic regions. Therefore, in many cases, seismic analyses have been applied to determine the hypocenters and focal mechanisms (e.g., Prejean et al., 2002). Compared with low-frequency earthquakes and volcanic tremors, VT earthquakes allow more precise hypocenter determination, and it is easier to determine their source mechanisms. Moreover, tracking the spatiotemporal changes in hypocenters and source mechanisms provides more information that could facilitate the estimation of the behavior of magma intrusion.

Magma transport in the crust is closely related to the magnitude and orientation of crustal stresses. Differential stresses in the crust are due to large-scale tectonic movements. Dikes represent the most natural means for magma transport at depth in the crust. The regional stress field around a volcano affects the position and orientation of a dike (Nakamura, 1977; Nakamura et al., 1977). Dikes preferentially intrude in the plane perpendicular to the direction of the minimum compressive stress. For dikes to propagate and inflate, magma must exert sufficient stress at the dike tip to overcome the fracture strength of the rock. It is well known that dike intrusions are frequently associated with VT earthquake swarms (e.g., Einarsson and Brandsdóttir, 1980; Savege and Cockerham, 1984). They occur ahead of the dike tip (Rubin and Pollard, 1988; Rubin, 1992; Ukawa and Tsukahara, 1996; Roman and Cashman, 2006; Ebinger et al., 2008; Woods et al., 2019; Ágústsdóttir et al., 2019), and in regions adjacent to dike walls (e.g., Bonafede and Danesi, 1997; Roman et al., 2004; Roman, 2005; Roman and Cashman, 2006; Ebinger et al., 2008; Ágústsdóttir et al., 2019). Following the development of new techniques for seismic data analysis in the recent two decades, hypocenters can be more accurately determined and the focal mechanisms of more events can be estimated, yielding more detailed discussions of dike intrusion processes and the stress field change corresponding to the spatiotemporal changes of the hypocenters and focal mechanisms of VT events (e.g., Hayashi and Morita, 2003; Ebinger et al., 2008; Grandin et al., 2011; Passarelli et al., 2015; Woods et al., 2019).

The studies described above were targeted at slow dike intrusions, lasting from several weeks to several months. For example, the 1998 earthquakes swarm off the east coast of Izu Peninsula, Japan was induced by a dike intruding for two weeks (Hayashi and Morita, 2003). Dike intrusions sporadically occurred and lasted several weeks from 2005 to 2010 in the Manda Harare-Dabbahu Rift, Afar, Ethiopia (Ebinger et al., 2010; Grandin et al., 2011). Episodes of dike intrusions lasting a few weeks occurred during the Bárðarbunga-Holuhraun rifting event from August 2014 to January 2015 (Woods et al., 2019). The dike intrusion at Miyakejima-Kozushima-Niijima, Japan began on June 26, 2000 and continued until September 2000 (Japan Meteorological Agency, 2000; Ukawa et al., 2000; Sakai et al., 2001). On the other hand, dike intrusions often occurred in short time period, hours to days, in basaltic volcanoes such as Kilauea's East Rift Zone in January 1983 (Okamura et al., 1988) and September 1999 (Cervelli et al., 2002), and the November 1986 eruption of Izu-Oshima (Linde et al., 2016).

Magma intrusion rate is a key parameter to understand unrest and its possible outcome, from non-eruptive unrest to phreatic explosions or explosive magmatic eruptions (Moran et al., 2011). For example, rapid magma intrusion often leads to explosive eruptions (Moran et al., 2011). Explosive eruptions are dominant at andesite volcanoes and crucial for risk mitigation, since many people live in the neighborhoods. Rapid dike intrusions cause pronounced earthquake swarm and deformation in short time periods. In these cases, it is important to obtain hypocenters and focal mechanisms to elucidate any induced spatiotemporal stress change.

On August 15, 2015, a VT earthquake swarm occurred beneath Sakurajima volcano, Japan; at the same time, rapid and significant ground deformation was observed (Hotta et al., 2016a). However, no distinct explosive eruption occurred within weeks after the VT earthquake swarm (Iguchi et al., 2019). Analysis of the ground deformation associated with the VT earthquake swarm revealed the presence of an inflating dike with the NE–SW strike direction and the NW–SE opening direction at a depth of 1–2 km below the sea level beneath the summit region of Sakurajima, suggesting shallow magma intrusion. The dike is obtained based on GNSS displacement data, tilts and strains (Hotta et al., 2016a), and 3-D deformation data from interferometric synthetic aperture radar (InSAR) images (Morishita et al., 2016). However, the intrusion process estimated from the ground deformation lacks a time resolution. Conversely, earthquakes reflect the stress release of rock, that is, the occurrence of earthquakes is sensitive to the temporal change in stress. The advantage of using earthquakes over deformation is that the time resolution is higher. Therefore, the analysis of the VT earthquake swarm allows tracing high-resolution

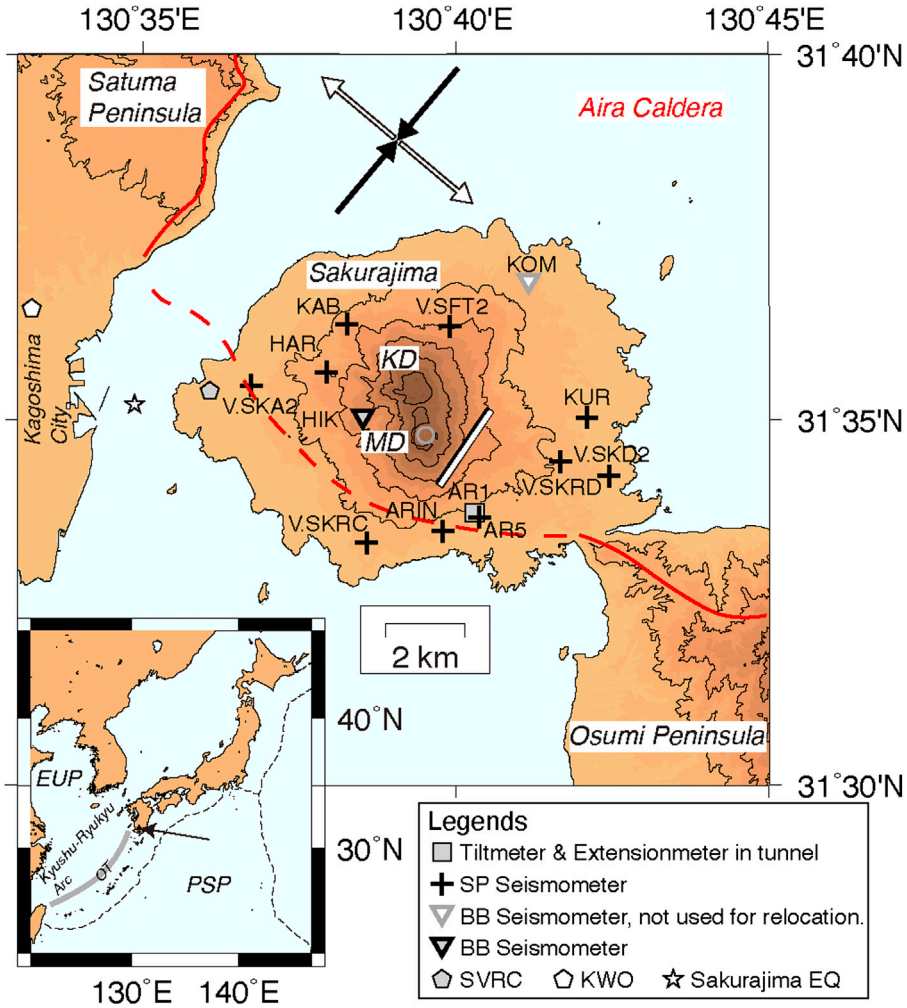

FIGURE 1 | Map showing the locations of Sakurajima volcano and seismic stations. Inset shows the location of Sakurajima relative to Japan. The abbreviation KD and MD indicate the Kita-dake (old clatter) and Minami-dake (currently the most active crater). Contours are provided every 200 m. The plus signs and inverted triangles show the locations of the short-period and broadband seismic stations, respectively, used for the analyses of the hypocenters and focal mechanisms, except for station KOM, which was used only for short-term-/long-term-average seismic detection. The gray square indicates the station AR1, which has short-period seismometer and tiltmeter and extension meters in an underground tunnel, and it was also used for the analyses. Open and solid black arrows indicate the directions of the regional maximum extension and compression, respectively, of the stress field at a depth of 10 km (Terakawa and Matsu'ura, 2010). The rectangle shows the location of the dike source obtained from the ground deformation on August 15, 2015 (Hotta et al., 2016a). The thick black line of the rectangle represents the top of the dike. The gray and open pentagons show the locations of the Sakurajima Volcano Research Center (SVRC) and the Kagoshima Weather Observatory (KWO) at the time of the Taisho 1914 eruption. The open star shows the epicenter of the Sakurajima M = 7 earthquake (Omori, 1920).

spatiotemporal changes in the stress exerted by dike emplacement on the surrounding rock.

In the present study, we determine the hypocenters and focal mechanisms of the VT earthquake swarm that occurred on August 15, 2015 beneath Sakurajima volcano. We clarify the spatiotemporal changes of the hypocenter and focal mechanisms of the VT earthquake swarm induced by rapid dike intrusion (one day). We then reveal the inflation process of the dike that penetrated the shallow depth beneath Sakurajima volcano. Finally, we discuss the generation of the VT earthquake swarm induced by dike propagation from the viewpoint of the brittle fracture strength of the crustal rock, to evaluate any difference between faster and slowing emplacing dikes.

GEOLOGICAL, GEOPHYSICAL SETTINGS, AND VOLCANIC ACTIVITY OF SAKURAJIMA

Sakurajima (Cherry Island in English) is an andesitic composite volcano located on the southern edge of the Aira caldera, southern Kyuhsu, Japan (**Figure 1**). In Kyushu, active volcanism results from the subduction of the Philippine Sea

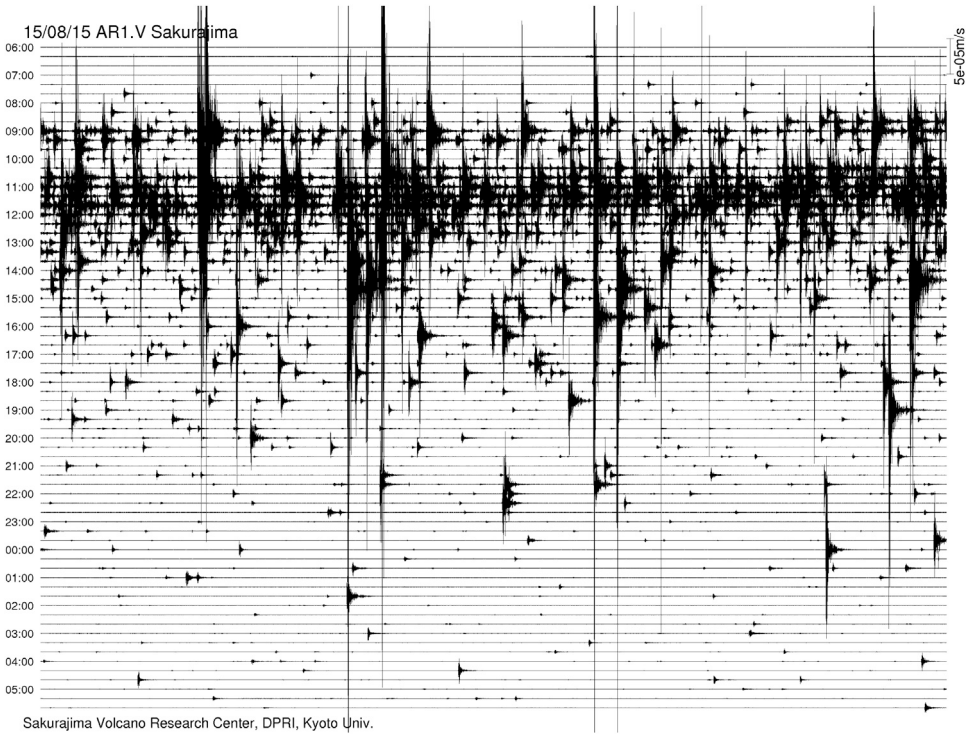

FIGURE 2 | Continuous seismogram of the vertical component of a short-period seismometer at station AR1 recorded from 6 AM on August 15 to 6 AM on August 16, 2015 (Japan Standard Time, JST).

plate (PSP) beneath the Eurasian plate (EUP) and appears to be linked to back-arc extension. The edifice of Sakurajima started to develop 26,000 years ago and is now composed of two overlapping stratovolcanoes: the older Kita-dake and younger Minami-dake (Fukuyama, 1978; Kobayashi et al., 2013; Yasui et al., 2013). Eruptive activity over the last 4500 years has mainly occurred at Minami-dake, which has produced Vulcanian explosions and continuous venting of ash clouds almost daily since 1955, making it Japan's most active volcano. Within the last six centuries, the volcano has experienced three periods of repeated Plinian eruptions of VEI 4–5 (Volcanic Explosivity Index) accompanied with voluminous lava effusion, that is, the Bunmei (1471–1476 AD), Anei (1779–1782 AD), and Taisho (1914–1915 AD) eruptions. The latter was the largest eruption in Japan in the 20th century. Initially an island, the Sakurajima volcano is now connected to the Osumi Peninsula via a narrow isthmus formed by a lava flow that was generated during the Taisho eruption. Before the beginning of the Taisho eruption, a volcanic earthquake swarm, including many felt earthquakes, was observed at the Kagoshima Weather Observatory (**Figure 1**) using a Gray–Milne seismometer (Omori, 1920). It began three days prior to the onset of the Taisho eruption on January 12, 1914 (Omori, 1920; Iguchi et al., 2019). Eight hours after the onset, a large earthquake with an M = 7.0 (Sakurajima earthquake) occurred in the southwestern part of the Sakurajima volcano (Omori, 1920). The Taisho eruption was accompanied by ~1 m subsidence of the caldera floor (Omori, 1916; Mogi, 1958; Yokoyama, 2013). Since then, the caldera has been inflating gradually. Afterward, subsidence occurred during the Showa eruption (lava flow, 1946 AD). Two main pressure sources are responsible for the recent geodetic deformation: the main source is located beneath the Aira caldera ~10 km below sea level (Hickey et al., 2016) and a supplementary source is located at a depth of 4–6 km beneath the summit (Hotta et al., 2016b). The current inflation of the Aira caldera is the result of magma accumulation at rates faster than current eruption rates, resulting in an uplift that approaches the pre-1914 level, increasing the risk of a new strong explosive event (Hickey et al., 2016). On August 15, 2015, rapid expansive ground deformation occurred in Sakurajima associated with an intense VT earthquake swarm (Hotta et al., 2016a). The latest earthquake swarm in Sakurajima occurred on May 29, 1968, including several felt earthquakes, with an M = 4 (Yoshikawa and Nishi, 1969). Nishi (1978) reported that the temporal changes in the frequency of Vulcanian explosions and focal mechanisms of VT earthquakes are correlated. Strike-slip-type mechanisms predominate during calm periods when the frequency is low, while normal fault-type mechanisms predominate in the beginning of the active eruptive period when the number of the events begin to increase toward the maximum. Subsequently, strike-slip-type mechanisms become dominant again with the decrease in frequency. The changes in the focal mechanisms prior to eruptive activity suggest that the crustal stress field varies according to magma supply.

The Kyushyu–Ryukyu Arc is a NE–SW-trending island arc that connects southwestern Japan with Taiwan (**Figure 1**). An active back-arc opening of the Okinawa Trough (OT) is located along the arc and affects the crustal stress field in

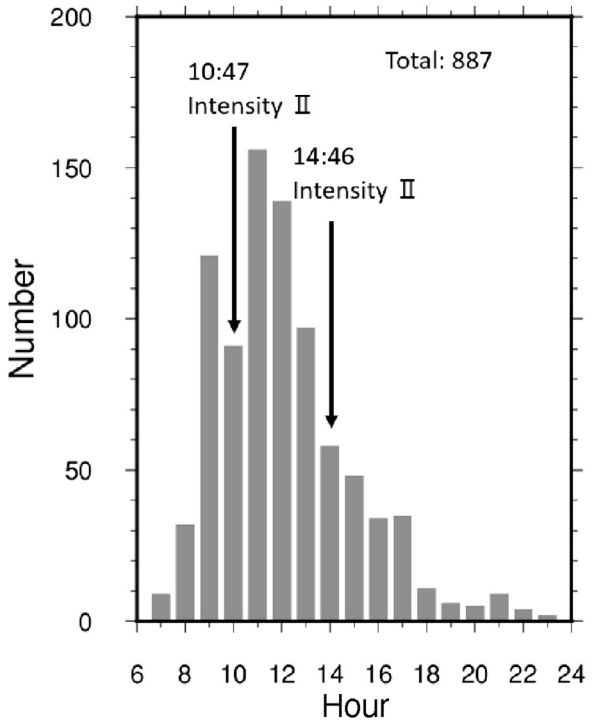

FIGURE 3 | Hourly volcano-tectonic earthquake occurrences from 6:00 to 23:59 JST on August 15, 2015.

the southern Kyushu and Ryukyu region (**Figure 1**). Based on geodetic and seismic analyses, NW–SE extension and NE–SW compression dominate in southern Kyushu (Kubo and Fukuyama, 2003; Watanabe and Tabei, 2004; Savage et al., 2016). Terakawa and Matsu'ura (2010) estimated the three-dimensional (3D) tectonic stress field in Japan from the centroid moment tensor solutions of seismic events with magnitudes in the 3.5–5.0 range. The 3D tectonic stress field shows a strike-slip-type focal mechanism with a NE–SW pressure (P)-axis and NW–SE tension (T)-axis at crustal depth (10 km) in southern Kyusyu (**Figure 1**). The VT earthquakes in the southwestern part of Sakurajima have normal fault mechanisms with NW–SE-oriented T-axes (Hidayati et al., 2007), which are strongly affected by the tectonic stress in southern Kyushu. The ground deformation on August 15, 2015, was modeled with a nearly vertical dike with a NE–SW strike and NW–SE opening (Hotta et al., 2016a; Morishita et al., 2016). The dike orientation and opening are also strongly affected by the regional tectonic stress.

DATA

Figure 1 shows the locations of Sakurajima volcano and seismic stations used in the present study. Each seismic station is equipped with a three-component short-period seismograph (sensitivity of 200 V/m/s) with a natural period of 1 s or a broadband seismograph (sensitivity of 1500 V/m/s). Two sets of water tube tiltmeters and extension meters (one directed toward Minami-dake crater and the other directed perpendicular to the crater) and a short-period seismograph are located in an underground tunnel, station AR1. The underground tunnel has a length of 283 m and is used to monitor the volcanic activity of Sakurajima. The outputs of the seismographs are digitized at 100 or 200 Hz by a 24-bit analog-to-digital converter and the data are transmitted to the Sakurajima Volcano Research Center using a wired virtual private network or wireless local area network and stored as continuous seismic waveform data.

Figure 2 shows the seismic records of a vertical component of the station AR1 during the swarm activity of August 15, 2015. The hourly occurrences of earthquakes with velocity amplitudes ≥10 μm/s at the station AR1 are shown in **Figure 3**. The VT earthquake swarm began at 7:05 Japan Standard Time (JST) and the occurrence frequency increased between 8:00 and 10:00 JST. A felt earthquake with an M = 2 occurred in Sakurajima at 10:47 JST. Subsequently, the occurrence frequency per hour decreased after the peak at 11:00–12:00 JST and another felt earthquake with an M = 2 occurred at 14:46 JST. In total, 887 VT earthquakes were observed on August 15, 2015 (Hotta et al., 2016a). We used the records of the tiltmeters at the AR1 station for the comparison of the results.

METHODS

Hypocenter Determination

We selected VT earthquakes to determine their hypocenters using the amplitude ratio of short-term average (STA) and long-term average (LTA) from continuous waveform records. The time window lengths for the calculations of the STA and LTA were 0.3 s and 60 s, respectively. The thresholds for the earthquake detections were STA/LTA ≧ 5 at the ARIN, HIK, KOM, HAR, KUR, KAB, V SKA2, V.SFT2, V.SKRC, and V.SKRD stations. The arival times of the P- and S-waves of the selected earthquakes were visually determined. The hypocenters were determined using the P- and S-wave arrival times recorded at more than eight and six stations, respectively. The seismic stations, except for station KOM, at which both the P- and S-wave arrival times were ≥200 were used for location procedures. **Figure 1** shows the locations of the selected seismic stations. The hypocenters were determined based on the method of Hirata and Matsu'ura (1987) and based on the one-dimensional P-wave velocity structure, as shown in **Supplementary Table S1**. The velocity structure was constructed by referring to the 2D P-wave velocity structure across Sakurajima volcano, which was obtained from the seismic refraction by artificial seismic sources (Miyamachi et al., 2013). The derived hypocenter locations were then treated as the initial hypocenters during further analysis, as discussed in the following section.

Hypocenter Relocation With the Double-Difference Method

We used the double-difference (DD) method (Waldhauser and Ellsworth, 2000) to obtain accurate hypocenter locations

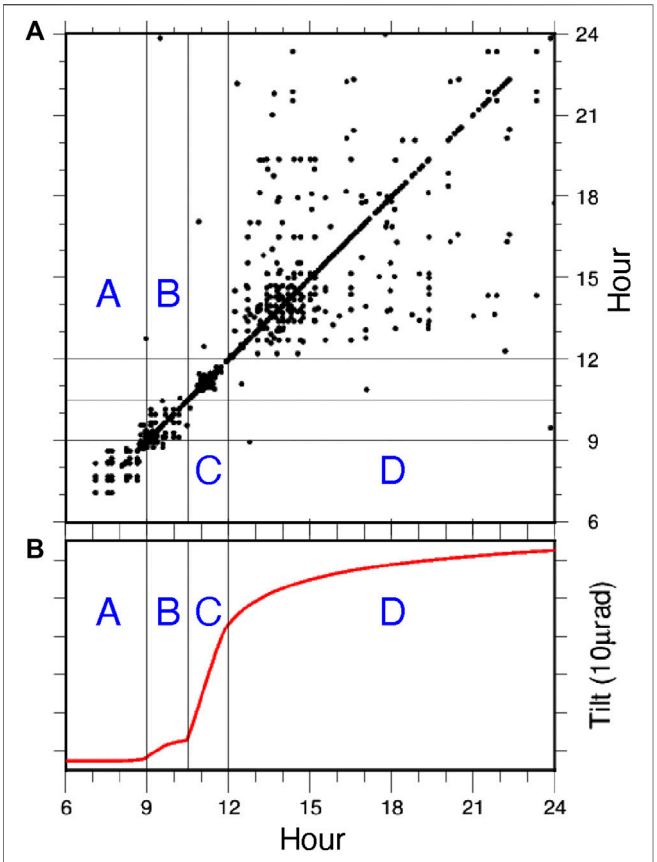

FIGURE 4 | (A) Occurrence times of the earthquakes with cross-correlation coefficients of ≥0.7 (black circle) and **(B)** tilt change at the station AR1 (red line). The tiltmeter is directed toward the Minami-dake (MD) crater. The lines indicate 9:00, 10:30, and 12:00 JST on August 15, 2015. The letters A, B, C, and D show time periods as defined in this study.

from initial hypocenters. The DD method software package, which is available to the public, consists of two programs, *ph2dt* and *hypoDD* (Waldhauser, 2001). The *ph2dt* is a preprocessing program that can be used to create DD data from the arrival times of the P-and S-waves recorded during seismic events. During *ph2dt* processing, several parameters, such as weights of readings used for hypocenter calculation and the maximum distance between paired seismic events and the stations, are set to create DD data. The *ph2dt* parameters used in the present study are shown in **Supplementary Table S2**. *hypoDD* can be used to calculate hypocenters from the DD data prepared using *ph2dt*. In *hypoDD*, the user sets the maximum distance between a cluster of hypocenters and stations. The minimum number of arrival catalog time difference data and the number of time difference data based on waveform cross-correlation in event pairs are also set in *hypoDD*. The *hypoDD* parameters used in the present study are shown in **Supplementary Tables S3,S4**. Because earthquakes with close hypocenters have similar source mechanisms and seismic wave propagation paths, the observed waveforms are likely similar. Accurate DD data can be obtained by calculating the travel time difference based on the cross-correlation of earthquake pairs with similar waveforms. We used the cross-correlation method of Deichmann and Garcia-Fernandez (1992) to obtain the travel time differences from seismic pairs using 0.64-s time windows including the recorded arrival time. A bandpass filter of 2–8 Hz was applied to the seismic waveform before the cross-correlation analysis. Only seismic pairs with cross-correlation coefficients greater than or equal to 0.8 were used as DD data.

Estimation of Focal Mechanisms

To improve the reliability of focal mechanism solutions, we estimated the focal mechanisms using the amplitude ratios of P- and S-waves as well as the P-wave polarities according to the method of Hardebeck and Shearer (2003). We visually determined the P-wave polarity and P- and S-wave amplitudes of the earthquakes relocated using the DD method, and estimated their focal mechanisms using the *HASH* program (Hardebeck and Shearer, 2002; Hardebeck and Shearer, 2003). For the earthquakes used for the estimation of focal mechanisms, the velocity waveforms were integrated into displacement waveforms, which were processed with a bandpass filter of 1–15 Hz. The time window length is half the time difference between the initial arrival times of the P- and S-waves. We measured the amplitudes of the P-waves using the peak-to-peak values of the amplitudes of the vertical component in the time window from the starting point of the time window as the P-wave initial arrival time. We measured the amplitudes of the S-waves using the maximum of the peak-to-peak values of the three components in the time window from the starting point of the time window as S-wave initial arrival time to 3 s. In the *HASH* program, we estimated the focal mechanisms of the earthquakes if the initial P-wave polarities were obtained at eight or more stations. The focal mechanisms were evaluated by sorting them into six quality categories from A to F based on the misfit of the

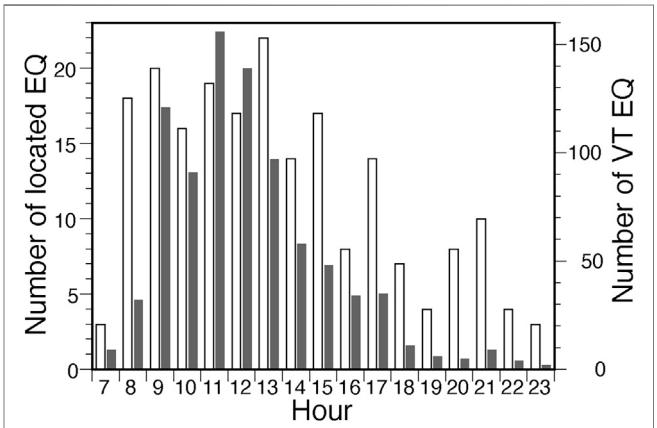

FIGURE 5 | Histogram of the number of VT earthquakes (gray bars, right axis; Hotta et al., 2016a) and number of the relocated earthquakes (open bars, left axis).

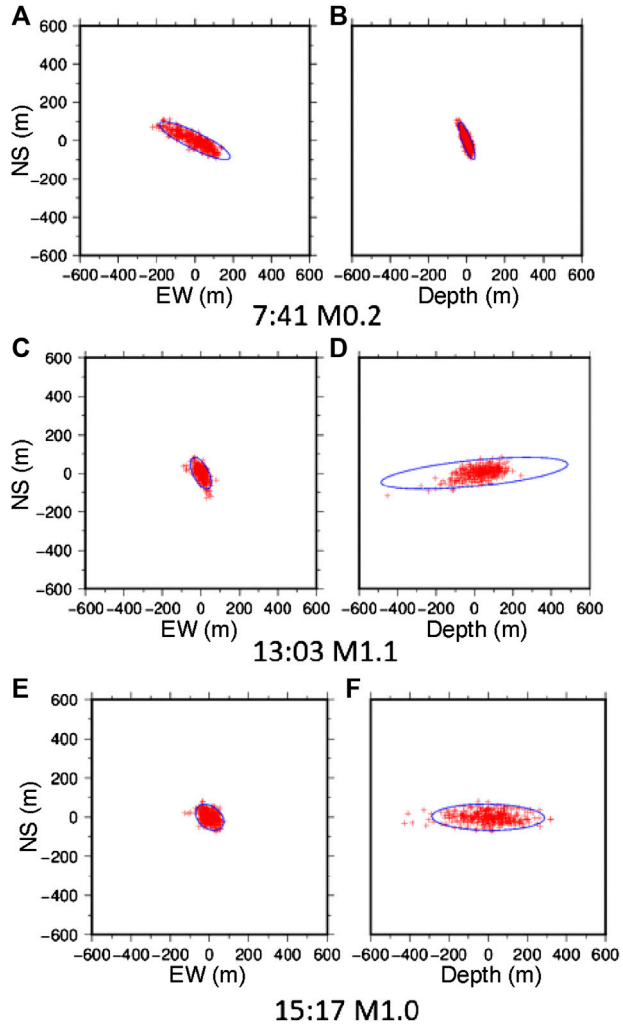

FIGURE 6 | Examples of the hypocenter distributions obtained by the bootstrap resampling method. Red cross marks and blue ellipses represent the hypocenters and the 95% confidence interval ellipses, respectively. **(A)** and **(B)** show the results for the event on 7:41 JST with M = 0.2. **(C)** and **(D)** show the results for the event on 13:03 JST with M = 1.1. **(E)** and **(F)** show the results for the event on 15:17 JST with M = 1.0. **(A) (C),** and **(E)** show the results for horizontal planes. **(B) (D),** and **(F)** show the results for NS to vertical cross sections. It is worth noting how the hypocenter distribution and confidence ellipse of the different earthquakes differ.

polarity, as shown in **Supplementary Table S5**. Only focal mechanisms with A, B, or C qualities were considered for further discussion.

RESULTS

Cross-Correlation Analysis of VT Earthquake Waveforms

We calculated the cross-correlation coefficients of the waveforms of the VT earthquakes that occurred on August 15, 2015, based on the total number of events for which P-wave arrival times were measured at station HIK. The 2–8 Hz bandpass-filtered waveforms were used to calculate the cross-correlation coefficients in a time window of 4 s including the initial P-wave motion. **Figure 4A** shows the occurrence times of the earthquakes with correlation coefficients ≥0.7. The record of the water tube tiltmeter at station AR1 directed toward Miami-dake is shown in **Figure 4B** for comparison. The tilt change began at ~8:00 JST and its rate increased before 9:00 JST. The tilt change rate decreased gradually from 9:00–10:30 JST and then began to increase rapidly. The increase in the tilt change rate continued until 12:00 JST. Subsequently, the tilt change rate decreased gradually. Event clusters with correlation coefficients ≥0.7 can be observed in the following time periods: 7:00–9:00, 9:00–10:30, 10:30–12:00, and 12:00–24:00 JST (**Figure 4A**). Event clusters are concentrated in the 10:30–12:00 JST time period. Moreover, the time boundaries corresponding to the clusters correspond with the time at which the tilt change is inflected. Therefore, the temporal change in the hypocenters of the VT swarm can be divided into four time periods: A: 7:00–9:00, B: 9:00–10:30, C: 10:30–12:00, and D: 12:00–24:00.

Evaluation of Double-Difference Relocation

By using STA/LTA, as described in **DATA** 257 events are extracted from continuous seismograms for the determination of the hypocenters. We carefully measured the arrival times of P-

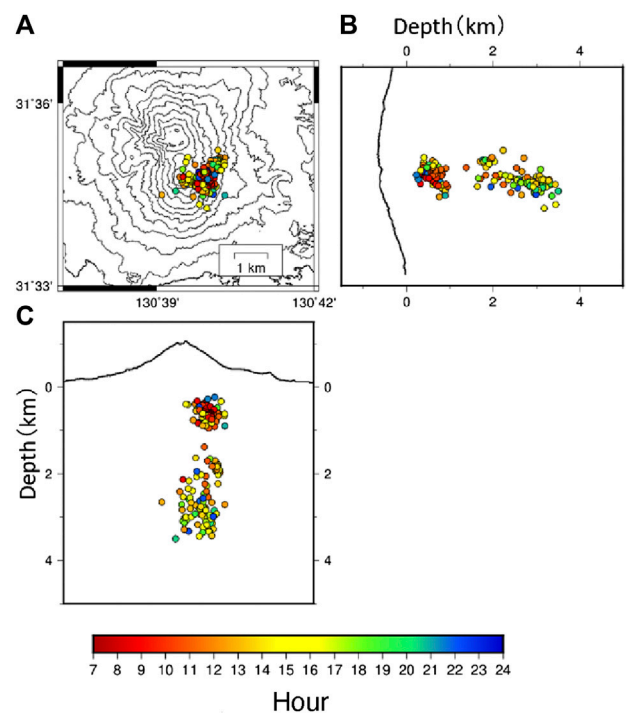

FIGURE 7 | Hypocenter distributions of the VT earthquakes on August 15, 2015, as determined by the double-difference method. The colors indicate the occurrence time. **(A)** Map view of the relocated hypocenters. Contours are provided every 100 m. **(B)** and **(C)** are the EW and NS cross sections, respectively.

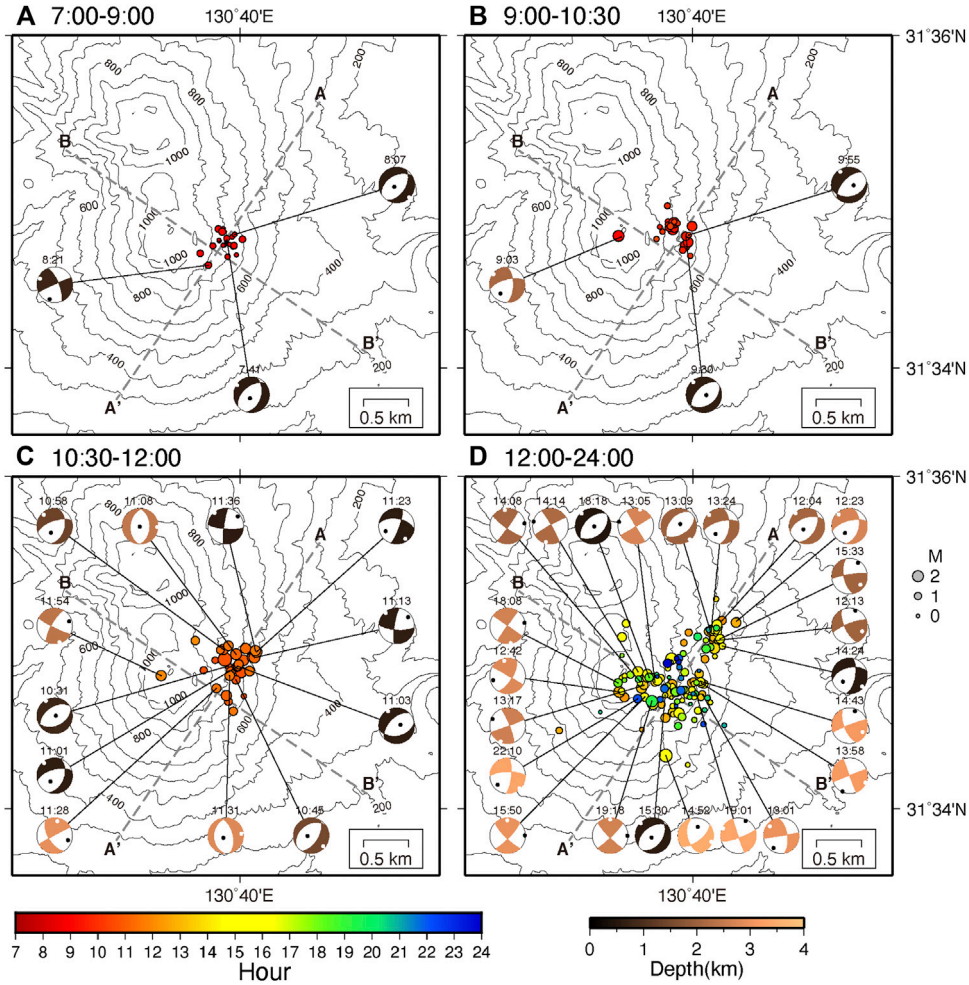

FIGURE 8 | Epicenter distributions of the VT earthquakes (circles). The colors of the circles indicate the occurrence time same as **Figure 7**. Some of focal mechanisms (beach balls) are shown along with their epicenters. The colors of the beach balls indicate focal depths. The occurrence time of the focal mechanism is also shown along with corresponding beach ball. Contours are provided every 100 m. **(A)** Period from 7:00 to 9:00 JST. **(B)** Period from 9:00 to 10:30 JST. **(C)** Period from 10:30 to 12:00 JST. **(D)** Period from 12:00 to 24:00 JST.

and S-waves. The reading accuracies of the arrival times of P- and S-waves are higher than 0.05 s (**Supplementary Figure S1**). Subsequently, the hypocenters of 242 events are determined with P arrival times of eight or more and S arrival times of six or more. Twenty-two of the events are air quakes whose hypocenters are located higher than any stations in Sakurajima. We excluded such air quakes and relocated the hypocenters using the DD method. In total, out of the numbers of DD data pairs used for the hypocenter relocation, the numbers of DD catalog data pairs derived from reading arrival times are 46,696 and 39,888 for P- and S-waves, respectively. Conversely, the numbers of DD data pairs derived from cross-correlation are 12,484 and 12,274 for P- and S-waves, respectively. The final root-mean-square residuals of the DD data after 25 iterations are 58% and 26% of the initial residuals for the recorded and cross-correlated data, respectively. In total, 204 hypocenters were relocated using the DD method. **Figure 5** shows the hourly frequencies of the relocated hypocenters. The hourly frequency of the relocated hypocenters is >10 from 9:00 to 14:00 JST, facilitating the discussion of the temporal change of the hypocenter distribution for the four time periods from A to D.

To assess the uncertainty of the relative hypocenter locations determined using the DD method, we applied the bootstrap resampling method (Shearer, 1997; Waldhauser and Ellsworth, 2000) to all relocated events. During bootstrap resampling, a sample with zero-mean normally distributed values is selected using the mean reading error for each station (**Supplementary Figure S1**) and then added to the recorded arrival times. The hypocenters are then determined by preparing DD data by randomly re-extracting the arrival times from the selected samples. This process was repeated 500 times. **Figure 6** shows the hypocenters relocated using the bootstrap resampling method and the ellipse of the 95% confidence interval (CI) for the three earthquakes. The cumulative frequency of the major axis radii of the 95% CI ellipses differs with respect to the magnitude and

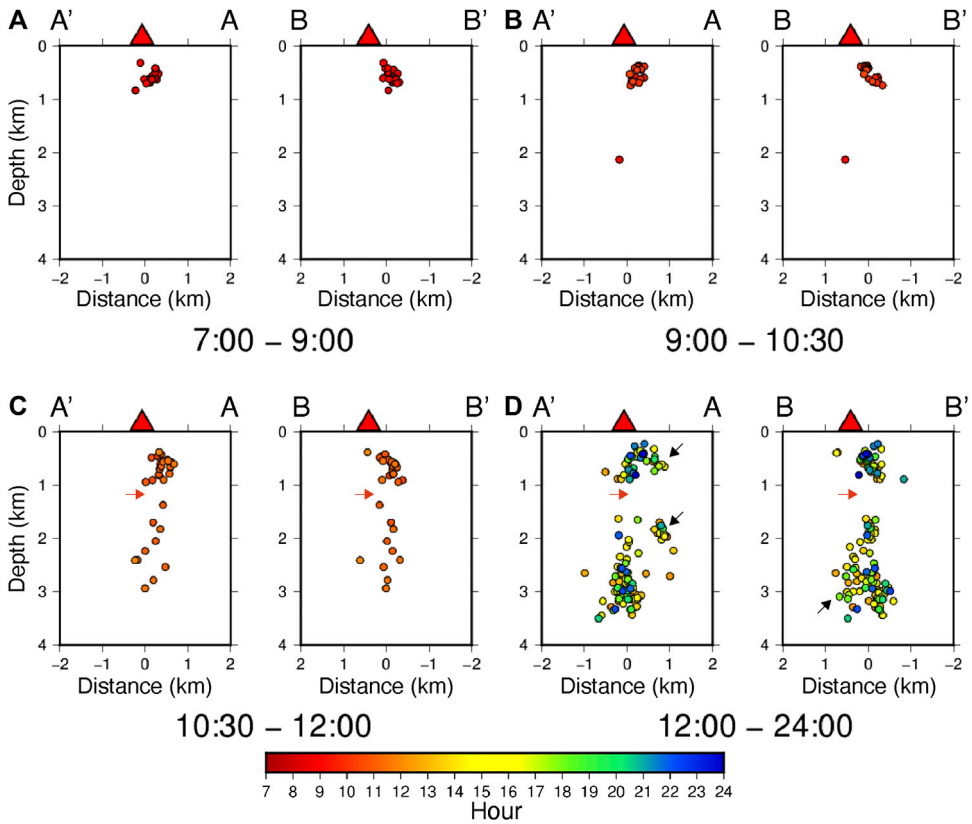

FIGURE 9 | Hypocenters of the VT earthquakes on August 15, 2015, projected on the cross sections A–A' (NE–SW) and B–B' (NW–SE), as shown in **Figure 8**. The colors indicate the occurrence time as **Figure 7**. Red arrows show the depth of the center of the aseismic zone. The black arrows show the position of the tip of the expanded area of the hypocenter distribution. **(A)** Period from 7:00 to 9:00 JST. **(B)** Period from 9:00 to 10:30 JST. **(C)** Period from 10:30 to 12:00 JST. **(D)** Period from 12:00 to 24:00 JST.

direction of the CI ellipses for each earthquake in the horizontal and vertical directions (**Supplementary Table S6**). The major axis radius, which has a cumulative frequency of 80%, is 200 m in the horizontal direction and 250 m in the vertical direction. Based on the above-mentioned error evaluation, the errors of the hypocenters relocated using the DD method are ±200 m in the horizontal direction and ±250 m in the vertical direction. A difference in the hypocenter locations exceeding the error range is considered significant.

Spatiotemporal Distribution of Relocated Hypocenters

Figure 7 shows the hypocenters of 204 VT earthquakes relocated using the DD method. The hypocenters are distributed at a depth of 0–4 km from the vicinity of Minami-dake into the northeastern direction within a distance of 1 km. In addition, a seismicity gap is detected at a depth of ~1 km; the hypocenters are concentrated above and below the seismicity gap. The hypocenter distributions for the time periods A, B, C, and D are shown using map views (**Figure 8**) and vertical cross-sections (**Figure 9**). **Figure 10** shows the temporal variation of the depths of the hypocenters and the magnitudes of the earthquakes. In time period A (7:00–9:00 JST), the hypocenters are distributed at depths of 0.3–1 km (**Figures 9A**, **10**) and 0.5–1 km east of Minami-dake (**Figure 8A**). In time period B (9:00–10:30 JST), the hypocenters are distributed within 1 km east of Minami-dake (**Figure 8B**) and at a depth of 0.3–0.9 km (**Figures 9B**, **10**), except for an event at a depth of 2 km that occurred at 9:03 JST. The magnitudes of the earthquakes in time period B (M = 1–2) are larger than those in time period A (**Figure 10**). In time period C (10:30–12:00), the epicenters shift 0.5 km northeast compared with time periods A and B (**Figure 8C**). The distribution of the hypocenters expands at depths of 0.4–3 km (**Figures 9C**, **10**). Many earthquakes with relatively large magnitude (multiple M = 2 earthquakes) occurred in time period C when compared with other time periods. In time period D (12:00–24:00 JST), the epicenters occupy a large area and are distributed from Minami-dake to 1 km east and 1 km northeast of it (**Figure 8D**). In time period D, the hypocenters are distributed in two clusters with an increase in depth; the hypocenters of the shallow and deep clusters are distributed at depths of 0.2–1 km and 1.5–3.5 km, respectively (**Figures 9D**, **10**). As described above, the VT earthquake swarm on August 15, 2015, starts at very shallow depth and, subsequently, the

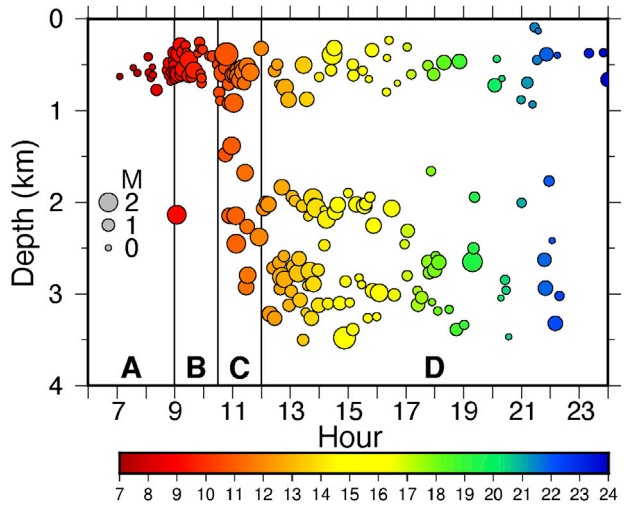

FIGURE 10 | Temporal change of the hypocenter depth of the VT earthquakes on August 15, 2015. The colors indicate the occurrence time as **Figure 7**. The size of the circle is proportional to the magnitudes of the VT earthquakes. The vertical lines indicate 9:00, 10:30, and 12:00 JST. The letters A, B, C and D represent the time periods.

seismogenic zone expands in the depth direction in a relatively short time period of ~6 hr.

It is evident that the hypocenter distribution changes based on the velocity structure model used for hypocenter determination. Therefore, we relocated the hypocenters using the same method and two additional velocity structures (**Supplementary Figure S3**). One is a homogeneous half-space structure used in Hotta et al. (2016a) and the other is a structure subdivided (fine structure) from the velocity structure used in the present study (**Supplementary Table S1**). As a result of the hypocenter relocation, no remarkable difference in epicentral distribution is observed in the three structures. However, with regard to the depth distribution, there is a difference among the three structures (**Figure 9**; **Supplementary Figures S4,S5**). For the homogeneous structure, during the time periods A and B, earthquakes cluster at 1.2–2 km depths, which are deeper than the depths obtained with the original velocity structure during the same time periods (**Figures 9A,B**). In time periods C and D, the hypocenter distribution expanded to a depth of 3 km and a small seismicity gap was observed at a depth of approximately 2 km (**Supplementary Figure S4**). For the fine structure, the hypocenters are distributed at depths of 0.3–2.5 km and a small seismicity gap is observed at approximately 1 km (**Supplementary Figure S5**). The small seismicity gap of the homogeneous and fine structures is smaller than that of the original structure (**Figures 9C,D**) and their widths are approximately equal to the error in the depth direction of the hypocenters (**Figure 6** and **Supplementary Table S6**). Therefore, it is necessary to judge carefully whether the existence of the seismic gap is significant or not. To do this, the frequency profiles of the depths of the hypocenters obtained using the three velocity structures are displayed on **Supplementary Figure S6**. The arrow in the figure corresponds to the depth of the seismicity gap shown in **Figure 9** and **Supplementary Figures S4,S5**). Considering the frequency distribution of the depths of the hypocenters of the velocity structures used in this study (**Supplementary Figure S6A**), it is evident that the frequency distribution is divided into shallow and deep clusters at depths of 0.2–1 km and 1.8–3.4 km, respectively. Conversely, the frequency distributions based on the homogeneous and fine structures (**Supplementary Figures S6B,C**) obscure the distinction between the shallow and deep clusters. However, they also show two peaks in the shallow and deep clusters as well as bimodal characteristics. Therefore, the existence of a seismicity gap between the shallow and deep clusters is confirmed regardless of the assumed velocity structure applied for the relocation of the hypocenter. However, the size of the seismicity gap varies with the velocity structure.

Focal Mechanisms

The focal mechanisms of 176 events are estimated from the P-wave polarity and amplitude ratios of the P- and S-waves. Focal mechanisms with qualities A, B, or C, as described in **Estimation of Focal Mechanisms**, are obtained for 93 events (**Supplementary Figure S2**) and are used for the discussion in this study. Some of them are also plotted on map views along with their epicenters for the time periods A, B, C, and D (**Figure 8**). The strikes of normal faulting mechanisms well

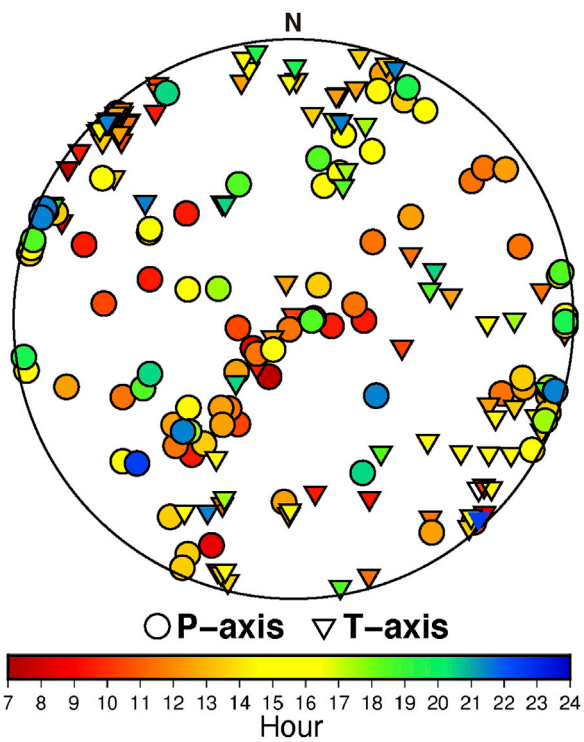

FIGURE 11 | Distribution of the tension (T)-axes (inverted colored triangles) and pressure (P)-axes (colored circles) of the focal mechanisms in an equal-area lower-hemisphere projection of the focal sphere. The colors indicate the occurrence time as in **Figure 7**.

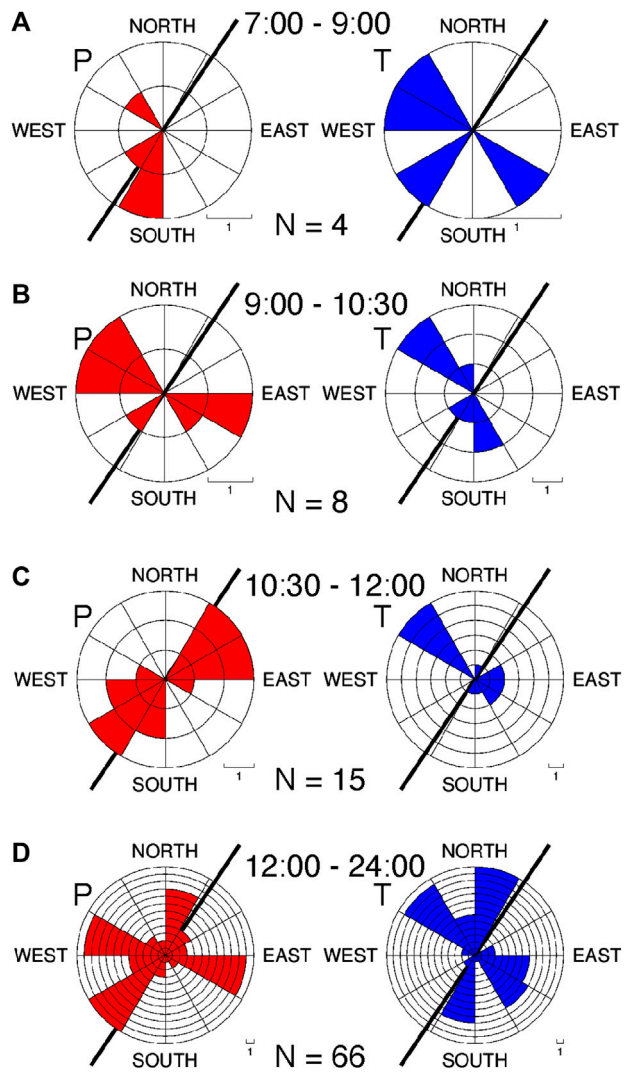

FIGURE 12 | Rose diagrams showing the frequency distribution of the azimuths of the P-axis (red) and T-axis (blue) for the time periods: **(A)** 7:00 to 9:00, **(B)** 9:00 to 10:30, **(C)** 10:30 to 12:00, and **(D)** 12:00 to 24:00 JST on August 15, 2015. The rose diagrams have a 30° interval. Each bin shows one frequency. The number of events whose P- and T-axes were determined for each time period is also shown. The thick line in each diagram shows the strike direction of the dike source of the ground deformation associated with the VT earthquake swarm (Hotta et al., 2016a).

match the A–A' (NE–SW) direction for the four time periods (**Figure 8**). The P- and T-axes of the focal mechanisms of all events with a quality of C or higher are plotted on one focal sphere in **Figure 11**. The P-axes are distributed in the NE–SW direction from the center of the focal sphere, while the T-axes are distributed in the NW–SE direction. **Figure 12** shows the azimuthal distribution of the P- and T-axes for the time periods A, B, C, and D. We classify the focal mechanisms into three types, that is, normal faulting, reverse faulting, and strike-slip faulting (**Supplementary Table S7**), using the method of Álvarez-Gómez (2019). In time period A, a regularity of the distribution of the P- and T-axes cannot be observed because the number of each azimuth angle is small and there are only four focal mechanisms (**Figure 12A**). Two normal faulting and two strike-slip faulting events occurred in time period A. Two normal faulting, four strike-slip faulting, and two reverse faulting events occurred in time period B. In time period C, eight normal faulting, five strike-strike slip faulting, and two reverse faulting events occurred. In time periods B and C, both the P- and T-axes are linearly symmetrically distributed (**Figures 12B,C**). In time zone B, the P-axes are distributed in the W–NW and E–SE directions, while the T-axes are distributed in the NW and S–SE directions (**Figure 12B**). In time period C, the P-axes are distributed in the NE–E and SW directions, while the T-axes are distributed in the NW and SE–E directions (**Figure 12C**). The dispersed distribution of the P-axis azimuths in time period C is because

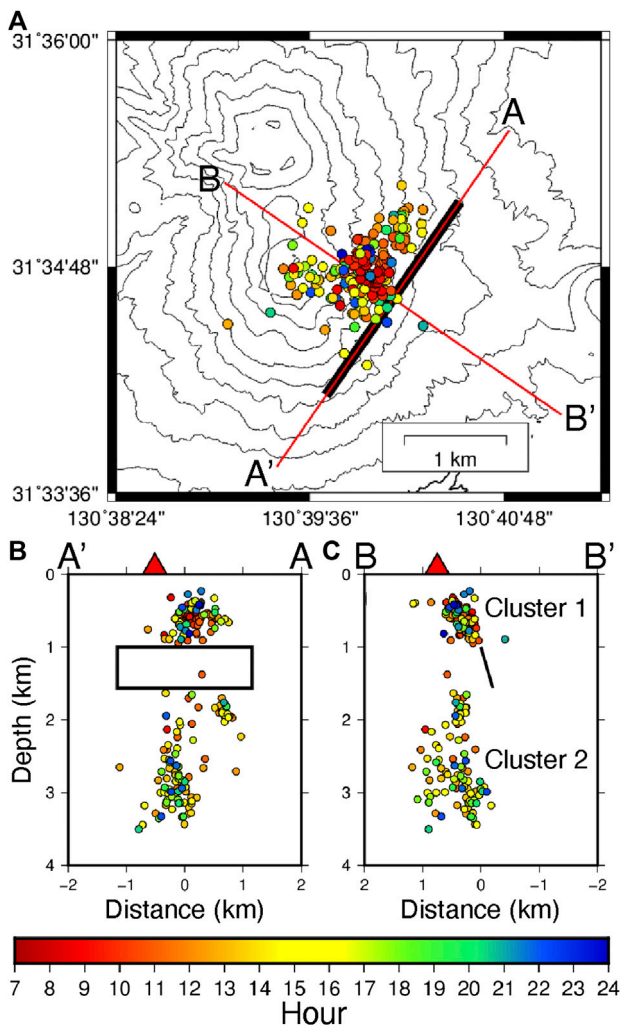

FIGURE 13 | Hypocenters of the VT earthquakes and dike source (Hotta et al., 2016a) on August 15, 2015. **(A)** Map view of the hypocenters and location of the dike source. **(B)** and **(C)** show cross sections A–A′ and B–B′ parallel and perpendicular to the strike of the dike source, respectively. The open rectangle and solid line represent the location of the dike.

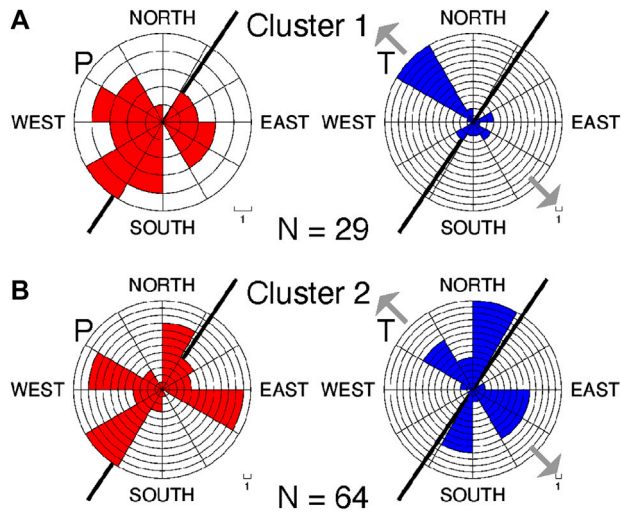

FIGURE 14 | Rose diagrams showing the frequency distribution of the azimuths of the P-axis (red) and T-axis (blue) for clusters 1 **(A)** and 2 **(B)**. The rose diagrams have a 30° interval. Each bin shows one frequency. The number of events whose P- and T-axes were determined for each time period is also shown. The thick line in each diagram shows the strike direction of the dike source of the ground deformation associated with the VT earthquake swarm (Hotta et al., 2016a). Gray arrows indicate the azimuth of the regional maximum extension of the stress field (Terakawa and Matsu'ura, 2010).

normal faulting accounts for a half of the events in the time period. In time period D, there are 18 normal faulting, 40 strike-slip faulting, and eight reverse faulting events (**Supplementary Table S7**). While normal faulting mechanism is dominant for the period A, strike-slip faulting events began to occur at higher depths in the period C, and were dominant at higher depths in the period D (**Figure 8**; **Supplementary Table S7**). In time period D, the P- and T-axes show asymmetric distributions; however, the distributions can be divided into two directions. The P-axes are distributed in two directions, that is, W–NW to E–SE and SW to NE, and the T-axes are distributed in two directions, that is, NW to E–SE and N–NE to S–SW. In time periods B, C, and D, the P- and T-axes are linearly symmetrically distributed in the strike direction of the dike (**Figures 12C,D**).

DISCUSSION

Spatial Relation Between Volcano-Tectonic Swarm Seismicity and the Dike Inflation

The VT earthquake swarm occurred in a short time period. Earthquakes with similar waveforms were concentrated in time period A when the tilt change started in the first stage of the swarm (**Figure 4**). In time periods B and C, they were concentrated when the tilt change rate increased (**Figure 4**). Further, the hypocenters clustered at very shallow depths in time periods A and B, while the hypocenter area extended to the deeper depths during time period C, with the largest tilt change rate (**Figures 4B**, **10**). Subsequently, the tilt change rate decreased gradually in time period D (**Figures 4B**, **10**). The hypocenters in the period can be divided into shallow and deep regions, corresponding to the sporadic occurrence of earthquakes with similar waveforms (**Figures 4A**, **10**). The tilt change was caused by dike inflation, as previously described (Hotta et al., 2016a). Here, we discuss the relationship between the VT swarm seismicity and dike inflation. **Figure 13** presents a comparison between the hypocenter distribution and location of the dike. As mentioned above, the VT earthquakes can be classified into shallow cluster (cluster 1) and deep cluster (cluster 2) based on depth. The results show that the dike is located in the seismic gap between clusters 1 and 2 (**Figures 13B,C**). Cluster 1 is located above the central part of the top of the dike (**Figures 13B,C**). In addition, the hypocenters of cluster 1 are distributed on the upper extension of the dip direction of the dike (**Figure 13C**). On the other hand, the hypocenters of cluster 2 are located below the bottom of the dike. However, cluster 2 is not on the lower extension line of the dip direction of the dike but offset by ~1 km toward Minami-dake. Based on the classification of the focal mechanisms into three types, i.e., normal, reverse, and strike-slip faulting, normal faulting was predominant in cluster 1, while strike-slip faulting was predominant in cluster 2 (**Supplementary Table S8**; **Figure 8**). The distributions of the P- and T-axes of clusters 1 and 2 are shown in **Figure 14**. Because normal faulting is predominant in cluster 1, the azimuth of the P-axis is uneven and the distribution of the P-axis does not converge in one direction (**Figure 14**). Most of the T-axes of cluster 1 are distributed in the NW direction. This direction is consistent with the NW–SE extension of the regional crustal stress field in the area including Sakurajima volcano, which was estimated from the moment tensor solutions of tectonic earthquakes (Terakawa and Matsu'ura, 2010). This direction also matches the direction perpendicular to the strike (NE–SW) direction of the dike or the direction parallel to the opening direction (NW–SE) of the dike (Hotta et al., 2016a). The azimuthal distributions of the P- and T-axes can be used to discuss the stress field of cluster 2 because strike-slip faulting is dominant. The P-axes are distributed both nearly parallel to the strike direction of the dike and nearly perpendicular to it (**Figure 14**). The T-axes are also distributed parallel and perpendicular to the strike direction of the dike (**Figure 14**).

Based on the above-mentioned results, we will describe the generation of earthquakes in clusters 1 and 2 caused by the dike source inflation in this section. Roman and Cashman (2006) summarized three existing models for the relationship between the magma migration and VT seismicity, including expected spatiotemporal patterns of VT hypocenters and focal mechanisms: 1) VT earthquakes occur due to slip on shear planes extending obliquely from the edges of the inflating dike (Hill, 1977); 2) VT earthquakes occur in a zone of inflation-induced tension ahead of the tip of a dike (eg, Ukawa and Tsukahara, 1996); and 3) VT earthquakes occur close to the walls (away from the tips and edges) of a dike inflating in the direction of the regional minimum compressive stress (Roman,

2005). Only a single dike was modeled for the ground deformation associated with the VT swarm seismicity (Hotta et al., 2016a; Morishita et al., 2016); multiple deformation sources have not been proposed. Therefore, we excluded the first model (Hill, 1977) and discuss the generation mechanisms of the VT earthquakes of clusters 1 and 2 using the second and third models. However, we will discuss the potential sources of the multiple deformations. Based on the second model, the P- and T-axes of the focal mechanism should be parallel to the regional maximum compression and tension, respectively (Roman and Cashman, 2006). Based on the third model, the P-and T-axes of the focal mechanism should be oriented ~90° to the regional maximum compression and tension, respectively (Roman, 2005). As described previously, VT earthquakes in cluster 1 occur in a zone ahead of the top of the inflating dike (**Figures 13B,C**). Most focal mechanisms in cluster 1 have T-axes parallel to the minimum regional compression (**Figure 14A**) and normal faulting with the NE–SW strike direction. Therefore, the generation of VT earthquakes in cluster 1 can be explained with the second model. Previous studies (Roman, 2005; Roman and Heron, 2007; Vargas-Bracamontes and Neuberg, 2012) showed that dike inflation can induce tension in the zone ahead of the dike tip; however, the source can induce compression in the obliquely extended region. The hypocenters of cluster 2 are below the dike, but are slightly skewed off a zone ahead of the bottom tip of the dike. Therefore, the hypocenters of cluster 2 could be considered located in a zone ahead of the dike tip, or in a zone of the obliquely extended region of the dike tip.

Next, we describe the stress fields around Sakurajima and close to the dike. As noted previously, the stress field around Sakurajima is characterized by extension in the NW–SE direction and compression in the NE–SW direction (**Figure 1**; Terakawa and Matsu'ura, 2010). Notably, strike-slip faulting corresponding to this stress field is predominant in cluster 2 (**Supplementary Table S8**). The P-axes of cluster 2 are distributed either in the direction nearly matching the compression direction (NE–SW) of the regional stress field or in the direction nearly matching the direction rotated by 90° with respect to the compression direction (**Figure 14B**). Similarly, the T-axes of cluster 2 are distributed either in the direction nearly coincident with the extension direction (NW–SE) of the regional stress field or in a direction nearly coincident with the direction rotated by 90° with respect to the extension direction (**Figure 14B**). Therefore, earthquakes in cluster 2 might have occurred either in a zone of inflation-induced tension ahead of the tip of the dike (Ukawa and Tsukahara, 1996) or close to the walls of the dike inflating in the direction of the regional minimum compressive stress (Roman, 2005). The earthquakes in cluster 2 occurred during time periods C and D; however, the earthquake generation in those periods differs. The second model is acceptable for time period C when the dike inflation rate is large because earthquakes in the direction of the T-axis, which corresponds to the regional stress period, are dominant. Conversely, in time period D, the P- and T-axes are distributed in the direction corresponding to the regional stress field and in the direction perpendicular to it. Therefore, the distributions of the P- and T-axes can be interpreted using a mixture of both the second and third models.

As explained in the latter part of **Spatiotemporal Distribution of Relocated Hypocenters**, the depth of the hypocenter distribution changes with a change in the assumed velocity structure (**Figure 9**; **Supplementary Figures S4,S5**). Therefore, the positional relation with the dike and the hypocenters along the depth differs depending on the assumed velocity structure. However, it is more appropriate to discuss the positional relation between the dike and the hypocenters obtained by the velocity structure in this study or the fine structure, which are both constructed from the result of the seismic refraction analysis (Miyamachi et al., 2013), rather than the hypocenters obtained based on the homogeneous structure. From the relative positional relationship between the dike and the depth distribution of the hypocenters of the structures considered in this study (**Figure 13**) as well as those of the fine structure (**Supplementary Figure S5**), the dike lies between the shallow and deep clusters. In the case of cluster 1, which is the shallow cluster, the hypocenters, based on both velocity structures, are distributed in a zone ahead the top tip of the dike. Conversely, in the case of cluster 2, which is the deep cluster, based on the velocity structure in the present study, there are numerous earthquakes in a zone ahead of the bottom tip of the dike, whereas earthquakes close to the dike wall seem to be few (**Figures 9**, **13**). However, based on the fine structure, there are numerous earthquakes close to the dike wall and not so many earthquakes in a zone ahead the bottom tip of the dike, suggesting that changes in the hypocenter distribution obtained based on the assumed velocity structure may alter the mechanism of VT seismicity interpreted based on relative positions of the dike and the seismicity.

In addition, in the focal mechanism analysis, the influence of take-off angles of seismic waves from the hypocenter on velocity structure can slightly alter the mechanism. Therefore, regarding the earthquake generation mechanism model, it is difficult to assign either the second or third model to cluster 2 as the primary earthquake generation mechanism. To address the problem, three-dimensional (3-D) seismic velocity structure should be adopted in hypocenter determination and focal mechanism estimation. For example, Alparone et al. (2020) determined with more precision the hypocenters and the focal mechanism of a preceding and accompanying seismic swarm of the Mt. Etna flank eruption in December 2018 based on a 3-D velocity structure. According to Alparone et al. (2020), the swarm began at shallower depths near the sea level, and the swam area expanded to a depth of 4 km in approximately 12 hr. Therefore, the shallow-to-deep extension of the hypocenter within a relatively short time is similar to that of the swarm of Sakurajima volcano on August 15, 2015. Based on high-sampling continuous ground deformation data associated with the seismic swarm, including GNSS, tiltmeter, and strainmeter data, Aloisi et al. (2020) estimated two dikes with different depths beneath Mt. Etna. Thereafter, they modeled the geometry, location and volume change more accurately using a finite element method based on a 3-D subsurface structure and the surface topography of the edifice. This made it possible to compare the two dikes and hypocenters more meaningfully (Aloisi et al., 2020). Practically, Bonaccorso (2020) and Giampiccolo (2020) shows a strong connection between the two dikes and the refined relocated seismicity. The single dike model (Hotta et al., 2016a) alone may be inadequate for capturing the ground deformation on August 15, 2015 at Sakurajima volcano, and the presence of multiple deformation sources may also have to be considered.

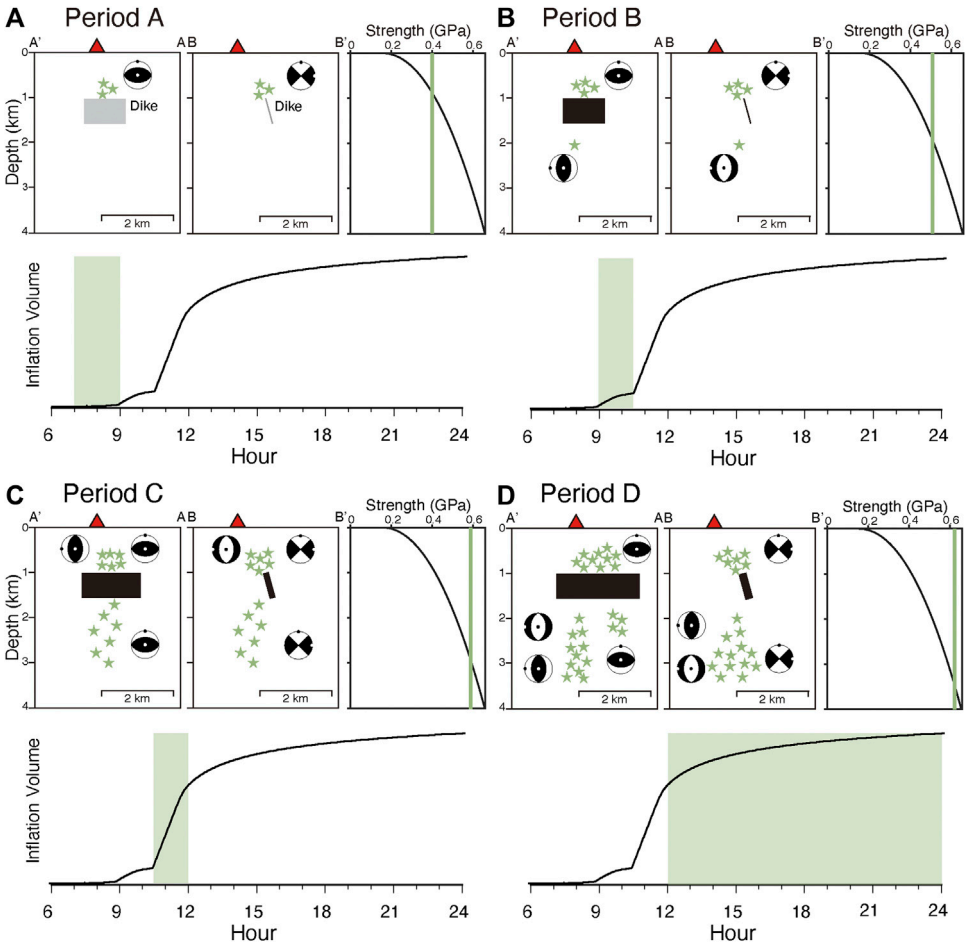

FIGURE 15 | Conceptual cross-sectional A–A′ and B–B′ views of the hypocenter distribution, location of the dike, depth profile of the brittle fracture strength of the crustal rocks, and conceptual diagram of the amount of the inflation of the dike for the time periods: **(A)** 7:00 to 9:00, **(B)** 9:00 to 10:30, **(C)** 10:30 to 12:00, and **(D)** 12:00 to 24:00 JST on August 15, 2015. Corresponding time period is shown with bright-green color. The location of the dike is shown by rectangles and lines in the cross-sections. The gray rectangle and lines indicate the initial stage of the dike inflation, while black ones indicate the evolution stage of the dike inflation. Although the size of the dike rectangle is same for period A and B, the gray dike rectangle exists only in period A, because the inflation volume of the dike in period A is smaller than the one in period **B**. Note that typical focal mechanisms (beach balls) are projected on the cross-sections for the four periods. The white and black dots show the position of T- and P-axes, respectively.

The inflation deformation associated with the swarm seismicity of Sakurajima has a relatively simple differential InSAR image, as it can be explained by a single dike (Morishita et al., 2016). Both Morishita et al. (2016) and Hotta et al. (2016a) only estimated a single dike based on the daily change in the ground deformation from the pre-earthquake swarm to the end of the swarm. They did not estimate multiple deformation sources in response to the spatiotemporal evolution of the hypocenters during the swarm. It is necessary to estimate their geometry, size, location, and volume change more accurately so as to elucidate the mechanism of generation of the swarm seismicity. It would be effective to estimate these parameters based on the finite element method using a more realistic structure that considers the topography of the mountain edifice as well as a 3-D subsurface structure.

There is a possibility of the growth of the dike or the existence of another dike corresponding to the extension of the hypocentral area toward the northeast, as observed in period D. According to a principal strain analysis of the records of extension meters installed in station AR1 during the swarm seismicity, principal strain axes rotate clockwise over time from period A to D (Higashi Uchida personal communication). In particular, the rotational speed from period C to D is greater than those in the previous periods (Higashi Uchida personal communication), which suggests the northeastward extension of the dike or the formation of a second dike. More precise modeling of the multidisciplinary high time-sampling continuous deformation data during the swarm seismicity should be explored in future.

Possible Scenario of the Swarm Seismicity Associated With the Dike Inflation on August 15, 2015

In the previous section, the relation between the dike inflation and VT earthquake swarm was discussed based on the hypocenter location and azimuthal distributions of the P- and T-axes. Here, we describe the dike inflation process and VT swarm seismicity induced by the dike inflation in the four periods A, B, C, and D. **Figure 15** shows the conceptual cross-sectional view of the hypocenter distribution and location of the inflating dike at a depth of 0–4 km for the four periods, the depth profile of the brittle fracture strength of the crustal rocks in the crust, and the conceptual diagram of the amount of inflation of the dike. Hotta et al. (2016a) stated that the inflation volume is 2.7×10^6 m^3 and the inflation rate is very large (1×10^6 m^3/hr). However, the temporal evolution of the dike inflation was not described. We assume that the temporal change of the tilt, as shown in **Figure 4B**, corresponds to the temporal change of the dike inflation volume. The brittle fracture strength is very low in the uppermost part of the crust and gradually increases with an increase in depth (Cho, 1993; Kohlstedt et al., 1995). The brittle fracture strength of the Earth's crust increases with increasing confining pressure. In this study, we used the equation for the depth change considering the confining pressure, temperature, and strain rate dependencies on the brittle fracture strength reported by Cho (1993) to produce the depth profile (see **Supplementary Description S1**). Notably, for volcanic rocks it seems to be weaker than for the granites that make up a common crust. Heap et al. (2014) investigated the effect of the porosity on the brittle fracture strength of volcanic rock and reported that the fracture strength is 0.4–0.44 GPa if the bulk porosity is 2%. This value almost corresponds to the fracture strength at the depth at which the VT earthquake swarm is initiated, as shown **Figure 15**. In time period A, the inflation volume is small in the very early stage of dike inflation. The differential stress between the maximum and minimum principal stresses induced by dike inflation is estimated to reach 0.4 GPa corresponding to the brittle fracture strength of the rocks at a depth of 1 km, where the earthquakes occur with normal faulting (**Figure 15A**). On the other hand, no earthquake has occurred below 1 km because the differential stress has not reached the fracture strength of the rock at the depth of the center of the dike and in the deeper part of the dike. In time period B, the dike inflation progressed and inflation volume increased, inducing tension and compression around the dike. Because earthquakes started to occur at a depth of 2 km below the bottom of the dike, it has been estimated that the magnitude of the induced differential stress reached ~0.5 GPa in time period B. Normal faulting occurs at a depth of around 1 km, while strike-slip faulting occurs at a depth of around 2 km. In time period C, the dike inflation proceeded and the cumulative inflation volume reached ~70% of the final cumulative inflation volume at the end of the period. At this time, the hypocenters expanded deeper to a depth of 3 km and earthquakes occurred in the upper part of the top of the dike and in the lower part of the bottom of the dike. It has been estimated that the differential stress induced by the dike inflation reached ~0.6 GPa. Finally, in time period D, the remaining 30% of dike inflation occurred and the hypocenter depth slightly increased to 3.5 km, while earthquakes occurred in the upper part of the top of the dike and in the lower part of the bottom of the dike. At this time, the differential stress induced by the dike inflation must have exceeded 0.6 GPa. The relation between the dike inflation and VT earthquake swarm described here does not include the migration of magma and dike formation due to magma intrusion. In addition, although the ground deformation caused by the dike was analyzed in previous studies (Hotta et al., 2016a; Morishita et al., 2016), the temporal change or migration of the position of the dike was not discussed. Therefore, it remains unclear where the magma moved based on the direction to which the dike inflated and the VT earthquake swarm moved. Despite these remaining challenges, it is important to estimate the seismicity associated with rapid dike intrusion that causes significant ground deformation in hours. The VT earthquake swarm initiated at shallow depth, affecting the weaker rocks due to the stress increasing in response to dike inflation; then it migrated at depth, affecting the stronger rocks. Subsequently, seismicity occurred at both shallower and deeper levels. The spatiotemporal changes of the hypocenters and focal mechanisms of the seismicity associated with this rapid dike intrusion/inflation seem different from those associated with slower dike intrusion, lasting several weeks, where dike-induced earthquakes follow to the propagation of the dike tip and dike inflation and their focal mechanisms are well aligned to the direction of the dike (e.g., Woods et al., 2019). Although there are fewer rapid dike intrusion cases compared with slow dike intrusion cases, more observations are needed to verify whether the spatiotemporal changes in hypocenters and focal mechanisms present in this study are inherent features of the rapid dike intrusion. For this purpose, it is essential to deploy highly sensitive continuous deformation sensors and a dense seismic network in volcanoes, and observe seismicity and ground deformation associated with rapid dike intrusion.

CONCLUSIONS

We relocated 204 hypocenters and derived 176 focal mechanisms of the VT earthquake swarm that occurred at Sakurajima volcano on August 15, 2015. Based on the cross-correlation of waveforms of the VT earthquakes and the change rate of the ground deformation associated with the VT swarm, we obtained the following results for four time periods:

Period A (7:00–9:00 JST) and B (9:00–10:30 JST): The hypocenters are distributed at a shallow depth of 0.3–1 km.

Period C (10:30–12:00 JST): The hypocenter distribution expands to the deeper part and is located at a depth of 0.3–3 km. The seismic activity is largest and there are multiple M2 class earthquakes and the change rate of the ground deformation is the largest.

Period D (12:00–24:00 JST): The hypocenters are distributed in two clusters at different depths. The shallow and deep clusters are located at depths of 0.2–1 km and 1.5–3.5 km, respectively.

For the four time periods, the hypocenters are divided into the shallow and deep clusters, and the P- and T-axis distributions of the focal mechanism solutions are compared with strike and opening

directions of the dike estimated from the ground deformation. The normal faulting and strike-slip faulting are dominant for the focal mechanisms during the four time periods. The T-axes of the shallow cluster were distributed parallel to the opening direction of the dike. The P-axes of the deep cluster have a pattern that is in agreement with the regional stress field in the strike direction of the dike, whereas the T-axes are parallel to the opening direction of the dike. In addition, the deep cluster also shows a 90°-rotated pattern in which the P-axes are distributed in the opening direction of the dike and the T-axes are distributed in the strike direction of the dike. Although there is only the former pattern in time period C, both patterns are mixed in time period D. This reflects the difference in how the stress field changes due to the dike inflation in earthquake generation. It is interpreted that the stress in the vicinity of the dike was modified by the dike inflation, and the VT earthquakes were induced by the differential stress exceeding the brittle fracture strength of the rock. It is suggested that dike inflation is so fast that the VT earthquake swarm initiated from shallow depths, within weaker rocks, expanded at deep within stronger rocks as dike inflation progressed, and continued for a while during the deceleration of the intrusion growth. The spatiotemporal changes of the hypocenters and focal mechanism shown here may be unique features of rapid dike intrusion. Further seismic and deformation observations are required to test this hypothesis.

DATA AVAILABILITY STATEMENT

The raw data supporting the conclusions of this article will be made available by the corresponding author, without undue reservation.

AUTHOR CONTRIBUTIONS

MK performed all the analysis in the present study and wrote his master thesis. HN and MK contributed to the planning and interpretation of the present study. HN reconstruct the thesis, refined the interpretation, drafted and revised the manuscript. All authors read and approved the final manuscript.

FUNDING

This work was supported by JSPS KAKENHI Grant Number 18K03781 to HN and the Ministry of Education, Culture, Sports, Science and Technology (MEXT) of Japan, under its Earthquake and Volcano Hazards Observation and Research Program.

ACKNOWLEDGMENTS

We thank Shiro Ohmi and Masato Iguchi for providing valuable advice and comments. We also thank Valerio Acocella and Luigi Passarelli and two other reviewers for critical inputs that improved the quality of the manuscript.

SUPPLEMENTARY MATERIAL

The Supplementary Material for this article can be found online at: https://www.frontiersin.org/articles/10.3389/feart.2020.600223/full#supplementary-material.

REFERENCES

Ágústsdóttir, T., Winder, T., Woods, J., White, R. S., Greenfield, T., and Brandsdóttir, B. (2019). Intense seismicity during the 2014–2015 Bárðarbunga-Holuhraun rifting event, Iceland, reveals the nature of dike-induced earthquakes and caldera collapse mechanisms. *J. Geophys. Res. Solid Earth* 124, 8331–8357. doi:10.1029/2018JB016010

Aloisi, M., Bonaccorso, A., Cannavò, F., Currenti, G., and Gambino, S. (2020). The 24 december 2018 eruptive intrusion at Etna volcano as revealed by multidisciplinary continuous deformation networks (CGPS, borehole strainmeters and tiltmeters). *J. Geophys. Res. Solid Earth* 125, e2019JB019117. doi:10.1029/2019JB019117

Alparone, S., Barberi, G., Giampiccolo, E., Maiolino, V., Mostaccio, A., Musumeci, C., et al. (2020). Seismological constraints on the 2018 Mt. Etna (Italy) flank eruption and implications for the flank dynamics of the volcano. *Terra. Nova.* 32, 334–344. doi:10.1111/ter.12463

Álvarez-Gómez, J. A. (2019). FMC—earthquake focal mechanism data management, cluster and classification. *SoftwareX* 9, 299–307. doi:10.1016/j.softx.2019.03.008

Bonaccorso, A., and Giampiccolo, E. (2020). Balance between deformation and seismic energy release: the dec 2018 'double-dike' intrusion at Mt. Etna. *Front. Earth Sci.* 8, 583815. doi:10.3389/feart.2020.583815

Bonafede, M., and Danesi, S. (1997). Near-field modifications of stress induced by dyke injection at shallow depth. *Geophys. J. Int.* 130 (2), 435–448. doi:10.1111/j.1365-246X.1997.tb05659.x

Cervelli, P., Segall, P., Amelung, F., Garbeil, H., Meertens, C., Owen, S., et al. (2002). The 19 September 1999 Upper East Rift Zone dike intrusion at Kilauea volcano, Hawaii. *J. Geophys. Res. Solid Earth* 107 (B7), 2150. doi:10.1029/2001JB000602

Cho, A. (1993). Fracture strength of the crust estimated from laboratory experiments: a possibility of high-pressure type fracturing in the crust. *J. Geography*. 102, 279–287. doi:10.5026/jgeography.102.3_279

Chouet, B.A., and Matoza, R.S. (2013). A multi-decadal view of seismic methods for detecting precursors of magma movement and eruption. *J. Volcanol. Geotherm. Res.* 252, 108–175. doi:10.1016/j.jvolgeores.2012.11.013

Deichmann, N., and Garcia-Fernandez, M. (1992). Rupture geometry from high-precision relative hypocentre locations of microearthquake clusters. *Geophys. J. Int.* 110 (3), 501–517. doi:10.1111/j.1365-246X.1992.tb02088.x

Ebinger, C., Ayele, A., Keir, D., Rowland, J., Yirgu, G., Wright, T., et al. (2010). Length and timescales of rift faulting and magma intrusion: the Afar rifting cycle from 2005 to present. *Annu. Rev. Earth Planet Sci.* 38, 439–466. doi:10.1146/annurev-earth-040809-152333

Ebinger, C. J., Keir, D., Ayele, A., Calais, E., Wright, T. J., Belachew, M., et al. (2008). Capturing magma intrusion and faulting processes during continental rupture: seismicity of the Dabbahu (Afar) rift. *Geophys. J. Int.* 174, 1138–1152. doi:10.1111/j.1365-246X.2008.03877.x

Einarsson, P., and Brandsdóttir, B. (1980). Seismological evidence for lateral magma intrusion during the July 1978 deflation of the Krafla volcano in NE-Iceland. *J. Geophys.* 47, 160–165. doi:10.2172/890964

Fukuyama, H. (1978). Geology of Sakurajima volcano, southern Kyushu. *J. Geol. Soc. Jpn.* 84, 309–316. doi:10.5382/GB.34

Grandin, R., Jacques, E., Nercessian, A., Ayele, A., Doubre, C., Socquet, A., et al. (2011). Seismicity during lateral dike propagation: insights from new data in the recent Manda Harare-Dabbahu rifting episode (Afar, Ethiopia). *G-cubed* 12, 4. doi:10.1029/2010GC003434

Hardebeck, J. L., and Shearer, P. M. (2002). A new method for determining first-motion focal mechanisms. *Bull. Seismol. Soc. Am.* 92 (6), 2264–2276. doi:10.1785/0120010200

Hardebeck, J. L., and Shearer, P. M. (2003). Using S/P amplitude ratios to constrain the focal mechanisms of small earthquakes. *Bull. Seismol. Soc. Am.* 93 (6), 2434–2444. doi:10.1785/0120020236

Hayashi, Y., and Morita, Y. (2003). An image of a magma intrusion process inferred from precise hypocentral migrations of the earthquake swarm east of the Izu Peninsula. *Geophys. J. Int.* 153 (1), 159–174. doi:10.1046/j.1365-246X.2003.01892.x

Heap, M. J., Xu, T., and Chen, C. (2014). The influence of porosity and vesicle size on the brittle strength of volcanic rocks and magma. *Bull. Volcanol.* 76, 856. doi:10.1007/s00445-014-0856-0

Hickey, J., Gottsmann, J., Nakamichi, H., and Iguchi, M. (2016). Thermomechanical controls on magma supply and volcanic deformation: application to Aira caldera, Japan. *Sci. Rep.* 6, 32691. doi:10.1038/srep32691

Hidayati, S., Ishihara, K., and Iguchi, M. (2007). Volcano-tectonic earthquakes during the stage of magma accumulation at the Aira caldera, southern Kyushu, Japan. *Bull. Volcanol. Soc. Jpn.* 52 (6), 289–309. doi:10.18940/kazan.52.6_289

Hill, D. P. (1977). A model for earthquake swarms. *J. Geophys. Res. Solid Earth.* 82 (8), 1347–1352. doi:10.1029/JB0821i008p01347

Hirata, N., and Matsu'ura, M. (1987). Maximum-likelihood estimation of hypocenter with origin time eliminated using nonlinear inversion technique. *Phys. Earth Planet. In.* 47, 50–61. doi:10.1016/0031-9201(87)90066-5

Hotta, K., Iguchi, M., Ohkura, T., and Yamamoto, K. (2016b). Multiple-pressure-source model for ground inflation during the period of high explosivity at Sakurajima volcano, Japan – combination analysis of continuous GNSS, tilt and strain data –. *J. Volcanol. Geoth. Res.* 310, 12–25. doi:10.1016/j.jvolgeores.2015.11.017

Hotta, K., Iguchi, M., and Tameguri, T. (2016a). Rapid dike intrusion into Sakurajima volcano on august 15, 2015, as detected by multi-parameter ground deformation observations. *Earth Planets Space* 68, 68. doi:10.1186/s40623-016-0450-0

Iguchi, M., Tamaguri, T., Hirabayashi, J., and Nakamichi, H. (2019). Forecasting volcanic eruption of Sakurajima volcano based on magma intrusion rate. *Bull. Volcanol. Soc. Jpn.* 64 (2), 33–51. doi:10.18940/kazan.64.2_33

Japan Meteorological Agency (2000). Recent seismic activity in the Miyakejima and Niijima-Kozushima region, Japan–the largest earthquake swarm ever recorded. *Earth Planets Space* 52, 8. doi:10.1186/BF03351658

Kobayashi, T., Miki, D., Sasaki, H., Iguchi, M., Yamamoto, T., and Uto, K. (2013). *Geological map of Sakurajima volcano*. 2nd edition. Geological Survey of Japan, AIST. (in Japanese with English abstract).

Kohlstedt, D. L., Evans, B., and Mackwell, S. J. (1995). Strength of the lithosphere: constraints imposed by laboratory experiments. *J. Geophys. Res. Solid Earth* 100 (B9), 17587–17602. doi:10.1029/95JB01460

Kubo, A., and Fukuyama, E. (2003). Stress field along the Ryukyu arc and the Okinawa trough inferred from moment tensors of shallow earthquakes. *Earth Planet Sci. Lett.* 210, 305–316. doi:10.1016/S0012-821X(03)00132-8

Linde, A. T., Kamigaichi, O., Churei, M., Kanjo, K., and Sacks, S. (2016). Magma chamber recharging and tectonic influence on reservoirs: the 1986 eruption of Izu-Oshima. *J. Volcanol. Geoth. Res.* 311, 72–98. doi:10.1016/j.jvolgeores.2016.01.001

McNutt, S. R. (2005). Volcanic seismology. *Annu. Rev. Earth Planet Sci.* 32, 461–491. doi:10.1146/annurev.earth.33.092203.122459

Miyamachi, H., Tomari, C., Yakiwara, H., Iguchi, M., Tameguri, T., Yamamoto, K., et al. (2013). Shallow velocity structure beneath the Aira caldera and Sakurajima volcano as inferred from refraction analysis of the seismic experiment in 2008. *Bull. Volcanol. Soc. Jpn.* 58, 227–237. doi:10.18940/kazan.58.1_227

Mogi, K. (1958). Relations between the eruptions various volcanoes and the deformations of the ground surfaces around them. *Bull. Earthq. Res. Inst. Univ. Tokyo* 36, 99–134. http://hdl.handle.net/2261/11909

Moran, S. C., Newhall, C., and Roman, D. C. (2011). Failed magmatic eruptions: late-stage cessation of magma ascent. *Bull. Volcanol.* 73, 115–122. doi:10.1007/s00445-010-0444-x

Morishita, Y., Kobayashi, T., and Yarai, H. (2016). Three-dimensional deformation mapping of a dike intrusion event Sakurajima in 2015 by exploiting the right- and left-looking ALOS-2 INAR. *Geohys. Res. Lett.* 43, 4197–4204. doi:10.1002/2016GL068293

Nakamura, K., Jacob, K. H., and Davies, J. N. (1977). Volcanoes as possible indicators of tectonic stress orientations—Aleutians and Alaska. *Pure Appl. Geophys.* 115, 87–122. doi:10.1007/BF01637099

Nakamura, K. (1977). Volcanoes as possible indicators of tectonic stress orientation—principle and proposal. *J. Volcanol. Geoth. Res.* 2 (1), 1–16. doi:10.1016/0377-0273(77)90012-9

Nishi, K. (1978). On the focal mechanism of volcanic earthquakes in Sakurajima volcano. *Annuals of Disas. Prev. Res. Inst.* 21 (B-1), 145–152. (in Japanese with English abstract). http://hdl.handle.net/2433/70195.

Nishimura, T., and Iguchi, M. (2011). *Volcanic earthquakes and tremor in Japan*. Kyoto: Kyoto University Press.

Okamura, A. T., Dvorak, J. J., Koyanagi, R. Y., and Tanigawa, W. T. (1988). "Surface deformation during dike propagation,"in *The Pu'uO'o eruption of Kilauea volcano, Hawaii: Episodes 1 through 20, January 3, 1983, through June 8, 1984*. Editor E. W. Wolfe, Washington D. C.: U. S. Geological Survey Professional Paper, 1463, 165–181.

Omori, F. (1916). The Sakura-jima eruptions and earthquakes II. *Bull. Imp. Earthq. Invest. Comm.* 8 (2), 35–179. http://hdl.handle.net/2261/16063

Omori, F. (1920). The Sakura-jima eruptions and earthquakes V. *Bull. Imp. Earthq. Invest. Comm.* 8 (5), 353–466. http://hdl.handle.net/2261/16104

Passarelli, L., Rivalta, E., Cesca, S., and Aoki, Y. (2015). Stress changes, focal mechanisms, and earthquake scaling laws for the 2000 dike at Miyakejima (Japan). *J. Geophys. Res. Solid Earth* 120, 4130–4145. doi:10.1002/2014JB011504

Prejean, S., Ellsworth, W., Zoback, M., and Waldhauser, F. (2002). Fault structure and kinematics of the Long Valley caldera region, california, revealed by high-accuracy earthquake hypocenters and focal mechanisms stress inversions. *J. Geophys. Res. Solid Earth* 107, B12. doi:10.1029/2001JB001168

Roman, D. C., and Cashman, K. V. (2006). The origin of volcano-tectonic earthquake swarms. *Geology* 34 (6), 457–460. doi:10.1130/G22269.1

Roman, D. C., and Heron, P. (2007). Effect of regional tectonic setting on local fault response to episodes of volcanic activity. *Geophys. Res. Lett.* 34, L13310. doi:10.1029/2007GL030222

Roman, D. C. (2005). Numerical models of volcanotectonic earthquake triggering on non-ideally oriented faults. *Geophys. Res. Lett.* 32, L02304. doi:10.1029/2004GL021549

Roman, D. C., Moran, S. C., Power, J. A., and Cashman, K. V. (2004). Temporal and spatial variation of local stress fields before and after the 1992 eruptions of Crater Peak vent, Mount Spurr volcano, Alaska. *Bull. Seismol. Soc. Am.* 94 (6), 2366–2379. doi:10.1785/0120030259

Rubin, A. M. (1992). Dike-induced faulting and graben subsidence in volcanic rift zones. *J. Geophys. Res.* 97, 1839–1858. doi:10.1029/91JB02170

Rubin, A. M., and Pollard, D. D. (1988). Dike-induced faulting in rift zones of Iceland and Afar. *Geology* 16 (5), 413–417. doi:10.1130/0091-7613(1988)016<0413:DIFIRZ>2.3.CO;2

Sakai, S., Yamada, T., Ide, S., Mochizuki, M., Shiobara, H., Urabe, T., et al. (2001). Magma migration from the point of view of seismic activity in the volcanism of Miyake-jima Island in 2000. *J. Geogr.* 110 (2), 145–155. doi:10.5026/jgeography.110.2_145

Savage, J. C., and Cockerham, R. S. (1984). Earthquake swarm in Long Valley caldera, california, January 1983: evidence for dike inflation. *J. Geophys. Res. Solid Earth* 89 (B10), 8315–8324. doi:10.1029/JB089iB10p08315

Savage, M. K., Aoki, Y., Unglert, K., Ohkura, T., Umakoshi, K., Shimizu, H., et al. (2016). Stress, strain rate and anisotropy in Kyushu, Japan. *Earth Planet Sci. Lett.* 439, 129–142. doi:10.1016/j.epsl.2016.01.005

Shearer, P. (1997). Improving local earthquake locations using the L1 norm and waveform cross correlation: Application to the Whittier Narrows, California, aftershock sequence. *J. Geophys. Res. Solid Earth*. 102, 8269–8283. doi:10.1029/96JB03228

Terakawa, T., and Matsu'ura, M. (2010). The 3-D tectonic stress fields in and around Japan inverted from centroid moment tensor data of seismic events. *Tectonics* 29, TC6008. doi:10.1029/2009TC002626

Ukawa, M., and Tsukahara, H. (1996). Earthquake swarms and dike intrusions off the east coast of Izu Peninsula, central Japan. *Tectonophysics* 253, 285–303. doi:10.1016/0040-1951(95)00077-1

Ukawa, M., Fujita, E., Yamamoto, E., Okada, Y., and Kikuchi, M. (2000). The 2000 Miyakejima eruption: crustal deformation and earthquakes observed by the NIED Miyakejima observation network. *Earth Planets Space* 52, 8. doi:10.1186/BF03351659

Vargas-Bracamontes, D. M., and Neuberg, J. W. (2012). Interaction between regional and magma-induced stresses and their impact on volcano-tectonic seismicity. *J. Volcanol. Geoth. Res.* 243–244, 91–96. doi:10.1016/j.jvolgeores.2012.06.025

Waldhauser, F. (2001). HypoDD: a computer program to compute double-difference earthquake locations. U. S. Geol. Surv. Open-File Report 01-113. Available at: https://pubs.usgs.gov/of/2001/0113/

Waldhauser, F., and Ellsworth, W. L. (2000). A double-difference earthquake location algorithm: method and application to the northern Hayward fault, California. *Bull. Seismol. Soc. Am.* 90 (6), 1353–1368. doi:10.1785/0120000006

Watanabe, T., and Tabei, T. (2004). GPS velocity field and seismotectonic of the Ryukyu arc, southwest Japan. *Bull. Seismol. Soc. Jpn*. 57, 1–10. doi:10.4294/zisin1948.57.1_1

Woods, J., Winder, T., White, R. S., and Brandsdóttir, B. (2019). Evolution of lateral dike intrusion revealed by relatively-relocated dike-induced earthquakes: the 2015-15 Bárðarbunga-Holuhraun rifting event, Iceland. *Earth Planet Sci. Lett.* 506, 32. doi:10.1016/j.epsl.2018.10.032

Yasui, M., Takahashi, M., Shimada, J., Miki, D., and Ishihara, K. (2013). Comparative study of proximal eruptive events in the large-scale eruption of Sakurajima: An-ei eruption vs. Taisho eruption. *Bull. Volcanol. Soc. Jpn.* 58 (1), 59–76. doi:10.18940/kazan.58.1_59

Yokoyama, I. (2013). An interpretation on secular changes in deformation caused by the 1914 eruption of Sakurajima volcano. *Bull. Volcanol. Soc. Jpn.* 58 (1), 77–90. doi:10.18940/kazan.58.1_77

Yoshikawa, K., and Nishi, K. (1969). On the earthquake activity in the deeper zone of Sakurazima. *Annuals of Disas. Prev. Res. Inst*. 12 (A), 57–65. (in Japanese with English abstract). http://hdl.handle.net/2433/69455.

Conflict of Interest: The authors declare that the research was conducted in the absence of any commercial or financial relationships that could be construed as a potential conflict of interest.

Copyright © 2021 Koike and Nakamichi. This is an open-access article distributed under the terms of the Creative Commons Attribution License (CC BY). The use, distribution or reproduction in other forums is permitted, provided the original author(s) and the copyright owner(s) are credited and that the original publication in this journal is cited, in accordance with accepted academic practice. No use, distribution or reproduction is permitted which does not comply with these terms.

frontiers in Earth Science

ORIGINAL RESEARCH
published: 23 February 2021
doi: 10.3389/feart.2020.609805

The Impact of Complex Volcanic Plumbing on the Nature of Seismicity in the Developing Magmatic Natron Rift, Tanzania

Miriam Christina Reiss[1], James D. Muirhead[2], Amani S. Laizer[3], Frederik Link[1], Emmanuel O. Kazimoto[3], Cynthia J. Ebinger[4] and Georg Rümpker[1]*

[1]Institute of Geosciences, Goethe University Frankfurt, Frankfurt, Germany, [2]School of Environment, University of Auckland, Auckland, New Zealand, [3]Department of Geology, University of Dar es Salaam, Dar es Salaam, Tanzania, [4]Department of Earth and Environmental Sciences, Tulane University, New Orleans, LA, United States

OPEN ACCESS

Edited by:
Cecile Doubre,
Université de Strasbourg, France

Reviewed by:
Joël Ruch,
Université de Genève, Switzerland
Francesco Mazzarini,
Istituto Nazionale di Geofisica e Vulcanologia (INGV), Italy

***Correspondence:**
Miriam Christina Reiss
reiss@geophysik.uni-frankfurt.de

Specialty section:
This article was submitted to Volcanology, a section of the journal Frontiers in Earth Science

Received: 24 September 2020
Accepted: 09 December 2020
Published: 23 February 2021

Citation:
Reiss MC, Muirhead JD, Laizer AS, Link F, Kazimoto EO, Ebinger CJ and Rümpker G (2021) The Impact of Complex Volcanic Plumbing on the Nature of Seismicity in the Developing Magmatic Natron Rift, Tanzania. Front. Earth Sci. 8:609805. doi: 10.3389/feart.2020.609805

Constraining the architecture of complex 3D volcanic plumbing systems within active rifts, and their impact on rift processes, is critical for examining the interplay between faulting, magmatism and magmatic fluids in developing rift segments. The Natron basin of the East African Rift System provides an ideal location to study these processes, owing to its recent magmatic-tectonic activity and ongoing active carbonatite volcanism at Oldoinyo Lengai. Here, we report seismicity and fault plane solutions from a 10 month-long temporary seismic network spanning Oldoinyo Lengai, Naibor Soito volcanic field and Gelai volcano. We locate 6,827 earthquakes with M_L −0.85 to 3.6, which are related to previous and ongoing magmatic and volcanic activity in the region, as well as regional tectonic extension. We observe seismicity down to ~17 km depth north and south of Oldoinyo Lengai and shallow seismicity (3–10 km) beneath Gelai, including two swarms. The deepest seismicity (~down to 20 km) occurs above a previously imaged magma body below Naibor Soito. These seismicity patterns reveal a detailed image of a complex volcanic plumbing system, supporting potential lateral and vertical connections between shallow- and deep-seated magmas, where fluid and melt transport to the surface is facilitated by intrusion of dikes and sills. Focal mechanisms vary spatially. T-axis trends reveal dominantly WNW-ESE extension near Gelai, while strike-slip mechanisms and a radial trend in P-axes are observed in the vicinity of Oldoinyo Lengai. These data support local variations in the state of stress, resulting from a combination of volcanic edifice loading and magma-driven stress changes imposed on a regional extensional stress field. Our results indicate that the southern Natron basin is a segmented rift system, in which fluids preferentially percolate vertically and laterally in a region where strain transfers from a border fault to a developing magmatic rift segment.

Keywords: local stress field changes, magmatic plumbing systems, volcano-rift interactions, rift seismicity, volcano seismicity

INTRODUCTION

Continental rifting is a geodynamic process in plate tectonics. However, the forces enabling the onset of rifting of comparatively strong, cold, thick continental lithosphere and the relative importance of magmatic and extensional processes remain poorly understood (e.g., Bialas et al., 2010; Brune et al., 2017). A key question is how strain accommodation is partitioned between faulting and magmatism (e.g., Ebinger and Casey, 2001; Thybo and Nielsen, 2009; Marzen et al., 2020). Tectonic thinning is commonly accompanied by decompression melting and the rise of volatiles and magma through the lithosphere (White and McKenzie, 1989; Weinlich et al., 1999; Rooney, 2010; Lee et al., 2016). Therefore, intrusion of magma and volatile release are thought to play a pivotal, yet interacting, role in the continental rifting process (Lindenfeld et al., 2012a; Wright et al., 2012; Muirhead et al., 2016; Weinstein et al., 2017).

The magma-assisted rifting model by Buck (2004) describes how, if a steady supply of magma is available, extensional strain can be largely accommodated by dike intrusion at a fraction of the force required for tectonic faulting, which reduces activity on rift-bounding border faults (also see Keir et al., 2006). Dike intrusions are enabled by the buoyancy of magma, which ascends from basaltic melt generation zones in the mantle toward a neutral buoyancy level at the base of the crust. Faulting and dike intrusion accommodate extension in the upper crust (Rubin and Pollard, 1988; Rowland et al., 2007; Baer et al., 2008; Trippanera et al., 2019), while released magmatic volatiles can weaken lithosphere through increased pore fluid pressures (Sibson, 2000; Reyners et al., 2007) and/or hydration mineral reactions (Moore and Rymer, 2007). All of these processes enhance the frequency of seismic activity and drive localization of fault-related strain (e.g., Muirhead et al., 2016; Chiodini et al., 2020).

Regions of active and evolving continental extension represent ideal locations to test the role of magma and magmatic volatiles in controlling rift processes (Wright et al., 2012; Lee et al., 2016; Hunt et al., 2017; Oliva et al., 2019a; Kämpf et al., 2019). For example, the distribution of seismicity observed in tectonically active systems can provide unprecedented constraints on the 3D distribution of deformation associated with the magmatic, tectonic, and volcanic systems that interact to achieve continental extension (Geissler et al., 2005; Lambotte et al., 2014; Hurst et al., 2016; Nakai et al., 2017). These can be compared to geologically constrained models of state-of-stress from extensional stress and surface, internal, and subsurface density contrasts that load the plate (e.g., Karlstrom et al., 2010; Oliva et al., 2019b).

Geological, geodetic, geochemical and geophysical investigations of magma-rich rift systems in East Africa have revealed arguably the most dynamic magmatic-tectonic interactions observed in any such setting (e.g., Keir et al., 2006; Ebinger et al., 2010; Rooney et al., 2014; Wauthier et al., 2015). Combined geodetic and seismic observations reveal that magma systems situated within the center of rift segments can feed up to 45 km-long lateral dike injections (Wright et al., 2006). Stress changes associated with these dike intrusions drive shallow normal faulting (Rowland et al., 2007) and can trigger eruptions from magma chambers situated tens of kilometers from the initial point of magma injection (Wright et al., 2006; Ayele et al., 2009). Seismicity and InSAR observation of active intrusions in the Erta Ale rift segment (Ethiopia) reveal that ~10 km-spaced magma chambers can synchronously feed eruptions through laterally connecting dikes (Pagli et al., 2012). Observations in the Kenya Rift reveal transient uplift and subsidence from nearby sources at some volcanoes, which is interpreted to represent magma migration through laterally connected melt bodies (Biggs et al., 2009, 2016).

This study utilizes a densely spaced seismic network in the southern Natron basin to provide unprecedented constraints on the 3D distribution of seismicity in an active magma-rich continental rift, which allows us to interpret the geometry and dynamics of the plumbing system. The early-stage Natron rift basin (~3 Ma; Foster et al., 1997) contains Earth's only active natrocarbonatite volcano Oldoinyo Lengai and represents a region of recent dike and fault activity (Calais et al., 2008; Biggs et al., 2013). This volcano and a volcanic field are located in the interaction zone between a border fault-controlled rift segment and a developing rift magmatic segment (Muirhead et al., 2015, 2016; Roecker et al., 2017; Weinstein et al., 2017), where mantle fluids drive hydraulic fracturing and associated fluid ascent along active fault systems (Lee et al., 2016; Oliva et al., 2019a). Specifically, we report on ten months of seismicity and related focal mechanisms from the temporary SEISVOL network (Seismic and Infrasound Networks to study the volcano Oldoinyo Lengai) from 2019. These data are examined to discriminate zones of active intrusion and fluid migration and to understand how these processes control spatial variations in local stress states, rift kinematics and volcanic activity.

TECTONIC SETTING

Oldoinyo Lengai is located in the North Tanzanian Divergence, which is part of the East African Rift System (EARS, **Figure 1**). This is the longest continental rift worldwide with relatively slow extension rates, which are typically between 1–7 mm yr^{-1} in the present day in the North Tanzanian Divergence (Saria et al., 2014). In the North Tanzanian Divergence, magmatism initiated at ~6 Ma (Mana et al., 2012), with evidence for faulting in the Natron basin region since 3 Ma (Foster et al., 1997), which in the present day is assisted by fluids rising through the plate as evidenced by earthquake swarms (Albaric et al., 2014; Lee et al., 2016; Weinstein et al., 2017). These interpretations are corroborated by soil CO_2 flux as well as carbon and helium isotope data from springs in the Natron basin, Tanzania, and Magadi basin, Kenya, revealing that magmatic CO_2 ascends to the surface along deeply penetrating faults in parts of the EARS (Lee et al., 2016; Lee et al., 2017; Muirhead et al., 2020).

The North Tanzanian Divergence hosts the 200 km-wide Ngorongoro-Kilimanjaro Volcanic Belt, a diachronous belt of volcanoes that formed since ~6 Ma, and shows an eastward younging trend (Le Gall et al., 2008; Mana et al., 2015; Muirhead et al., 2015, **Figure 1**). It consists of a large number of basaltic shields and composite cones that have a wide range of

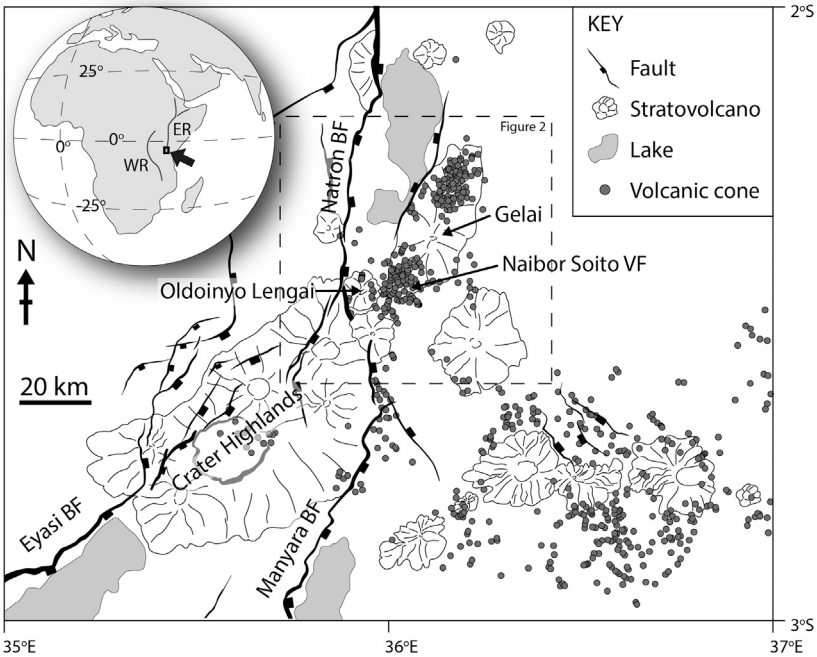

FIGURE 1 | Tectonic map of the research area with volcanoes and faults. The dashed line denotes the outline of **Figure 2**. The inset shows the two branches of the East African Rift system with the rectangle denoting the research area.

lava compositions including basanites, melilitites, basalts, nephelinites, phonolites, as well as carbonatites, implying multiple source depths and both asthenospheric and (dominantly) lithospheric mantle material (e.g., Dawson, 1992; Mana et al., 2015; Mollex et al., 2018). The unusual carbonatitic magmas are likely sourced from an enriched cratonic mantle lithosphere that experienced extensive metasomatism, with or without an asthenospheric melt component (Foley et al., 2012; Mollex et al., 2018; Muirhead et al., 2020). The magmas produced at these volcanoes exhibit high CO_2 contents, probably derived from small partial melting of a metasomatized mantle source (Fischer et al., 2009; Mana et al., 2015). Oldoinyo Lengai is situated at the southern end of the Natron basin and adjacent to its western border fault. In its immediate vicinity is Naibor Soito volcanic field, a monogenetic cone field with metasomatized mantle xenoliths, and the ~1 Ma Gelai volcano (Dawson et al., 1995; Aulbach et al., 2011; Muirhead et al., 2016; **Figure 1**).

Eruptions at Oldoinyo Lengai initiated at ~0.37 Ma (Dawson et al., 1995; Sherrod et al., 2013). Recent explosive volcanism occurred in 1917, 1940–1941, 1966–1967 and 2007–2008, and generally involved nephelinitic silicate magma (Dawson et al., 1995; Klaudius and Keller, 2006; Keller et al., 2010). The 2007–2008 explosive Oldoinyo Lengai eruption sequence was preceded and accompanied by a July-September 2007 earthquake swarm (70 earthquakes with M > 4) associated with a dike intrusion below the Naibor Soito volcanic field and the inactive Gelai volcano (Baer et al., 2008; Calais et al., 2008; Biggs et al., 2009; Kervyn et al., 2010; Biggs et al., 2013). This was the first diking event to be captured geodetically in the region (Baer et al., 2008; Calais et al., 2008). Field and InSAR observations showed extensive surface deformation, which is best explained by slip on a normal fault and successive dike-opening by stress unclamping (Calais et al., 2008; Biggs et al., 2009; Biggs et al., 2013). InSAR data also support a second diking event 3.4 km below Oldoinyo Lengai between October and December 2007 (Biggs et al., 2013). Both events were accompanied by the emptying of a shallow magmatic reservoir in close proximity as inferred from InSAR data (Calais et al., 2008; Biggs et al., 2009; Biggs et al., 2013).

The 2007 events at Oldoinyo Lengai sparked new debate on the magmatic plumbing system and the volcano's connection with Gelai, the Naibor Soito volcanic field and surrounding rift faults (Biggs et al., 2013; Weinstein et al., 2017; Jones et al., 2019). Authors suggested that an undetected dike sourced from a deep-seated magma chamber predated the initial fault slip detected during the 2007 unrest period (Baer et al., 2008; Biggs et al., 2013). From petrological observations, magma volume estimates and stress calculations, the 2007 eruptions could not have been sourced by a single shallow magmatic reservoir (Kervyn et al., 2010; Biggs et al., 2013). Instead, the volcanic-tectonic event was most likely driven by a pressurized deep magma chamber, and magma was then distributed from there in the shallow crust, and fed into the Oldoinyo Lengai chamber, according to the local background stress (Baer et al., 2008; Biggs et al., 2013). Since then, a tomographic inversion by Roecker et al. (2017) imaged a low velocity, high Vp/Vs body interpreted as a single magma chamber between both volcanoes below a depth of 15 km. The combined tomography and seismicity data sets imaged two elliptical low velocity, high seismicity zones interpreted as sills that might have fed the 2007 dike intrusion, and triggered the eruption at

Oldoinyo Lengai (Oliva et al., 2019a). Coulomb stress changes related to the volcanic-intrusive sequence may have also unclamped a section of the western Natron border fault, with the resulting slip detected on a local GPS network in early 2008 (Jones et al., 2019).

DATA AND METHODS

Data

The SEISVOL project (Seismic and Infrasound Networks to study the volcano Oldoinyo Lengai) is a temporary station deployment with 33 seismic and four infrasound stations. The deployed stations form a seismic network and array (**Figure 2**) that were operative from February/March 2019 to June 2020. The seismic network and array comprised 10 Trillium Compact 120 and 20 Mark L4-3D seismometers, three 3D 4.5-Hz geophones and 33 Digos Cube 3-channel data loggers from the Geophysical Instrument Pool Potsdam (GIPP) and Goethe University Frankfurt. The infrasound stations consisted of four MB2017 sensors (ISTerre) and four Digos Cube 3-channel data loggers from Goethe University Frankfurt. All seismic stations recorded data at 100 Hz. Due to harsh field conditions, batteries as well as GPS antennas had to be replaced on a regular basis, and resulted in occasional downtimes for many stations (**Figure 3A**). Here, we use data from March 1st to December 31st, 2019, as the remaining data were inaccessible due to the Covid-19 pandemic.

Earthquake Locations

We used the python software QuakeMigrate (Bacon et al., 2019) to detect, trigger, and locate earthquakes automatically. This software is based on the Coalescence Microseismic Mapping technique (Drew et al., 2013) and reports earthquake locations as well as P-and S-wave picks on the vertical and horizontal components, respectively. We analyzed the data using a bandpass filter of 1–25 Hz and the 1D velocity model from Albaric et al. (2010). We then filtered these results by the earthquakes' global covariance error in x, y and z directions and kept only earthquakes with less than 5 km horizontal and 7 km vertical uncertainties.

To obtain accurate hypocenter locations, we then relocated these chosen events with the probabilistic, nonlinear earthquake code NONLINLOC (Lomax et al., 2000) using the 3D-velocity model by Roecker et al. (2017) for the North Tanzanian Divergence. The final seismicity catalog consists only of earthquakes between −2.3° and −3.0° Latitude and from 35.7° to 36.4° Longitude, and with location errors less than 5 km in the horizontal and 7 km in the vertical direction as calculated from final NONLINLOC location uncertainties and at least six picks. We report 6827 earthquakes with average location errors of 1.57 km in longitude, 1.59 km in latitude and 3.8 km in depth. We have ensured the location accuracy by comparing the automatically obtained earthquake locations with a subset of manually picked and located events, as well as comparing the differences between using a 1D and 3D velocity model. We can support the assertion by Weinstein et al. (2017) that differences in earthquake locations between both models are inconsequential and mostly within the horizontal and vertical errors.

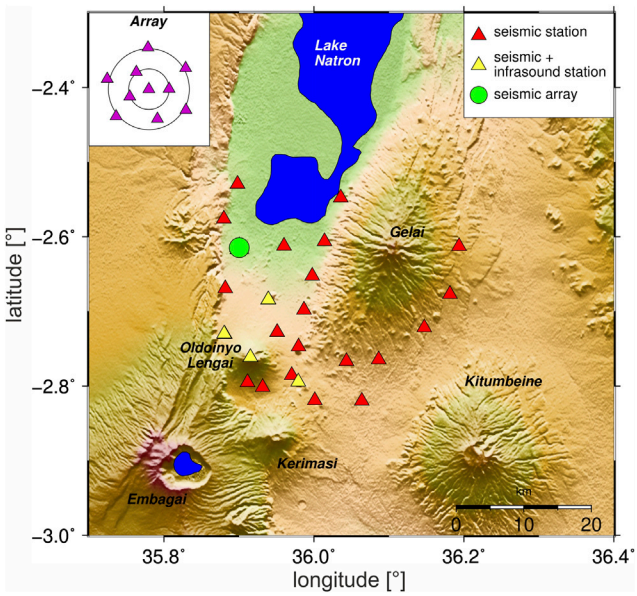

FIGURE 2 | Seismic stations are red triangles, and co-located seismic and infrasound stations are yellow triangles. The green circle denotes the seismic array which is shown in the upper left corner. Volcanoes are written in bold black letters.

Magnitudes

Magnitudes were calculated automatically in QuakeMigrate after Greenfield et al. (2018): after de-meaning and tapering the data, the instrument response is removed on each waveform. Then, waveforms are convolved with the response of a Wood-Anderson seismograph with the corrected gain of 2080 (Urhammer, 1982). For all network stations, the maximum zero-to-peak amplitude is picked on both horizontal components. Amplitudes are only picked if the maximum amplitude is greater than twice the standard deviation of a 10 s window of the data before the P-wave onset. Accordingly, only good recordings contribute to the calculated magnitude. These were then calculated on the local magnitude scale using the formula:

$$M_i = \log\left(A_{ijk}\right) + \left(n\log\left(\frac{r_{ij}}{17}\right) - K\left(r_{ij} - 17\right) + 2\right),$$

where M_i is the local magnitude of earthquake i, A_{ijk} the amplitude recorded at each station j and component k, and the second terms denotes that we normed the magnitudes by a magnitude 3 earthquake in 17 km distance, using the hypocentral distance r_{ij} and the attenuation parameters K and n (Hutton and Boore, 1987). K and n were derived for Tanzania by Langston et al. (1998) and are suitable given the small distance range for which they lead to equivalent magnitudes as compared to the parameters reported by Weinstein et al. (2017). Reported magnitudes are an average of all horizontal components per event (Greenfield et al., 2018).

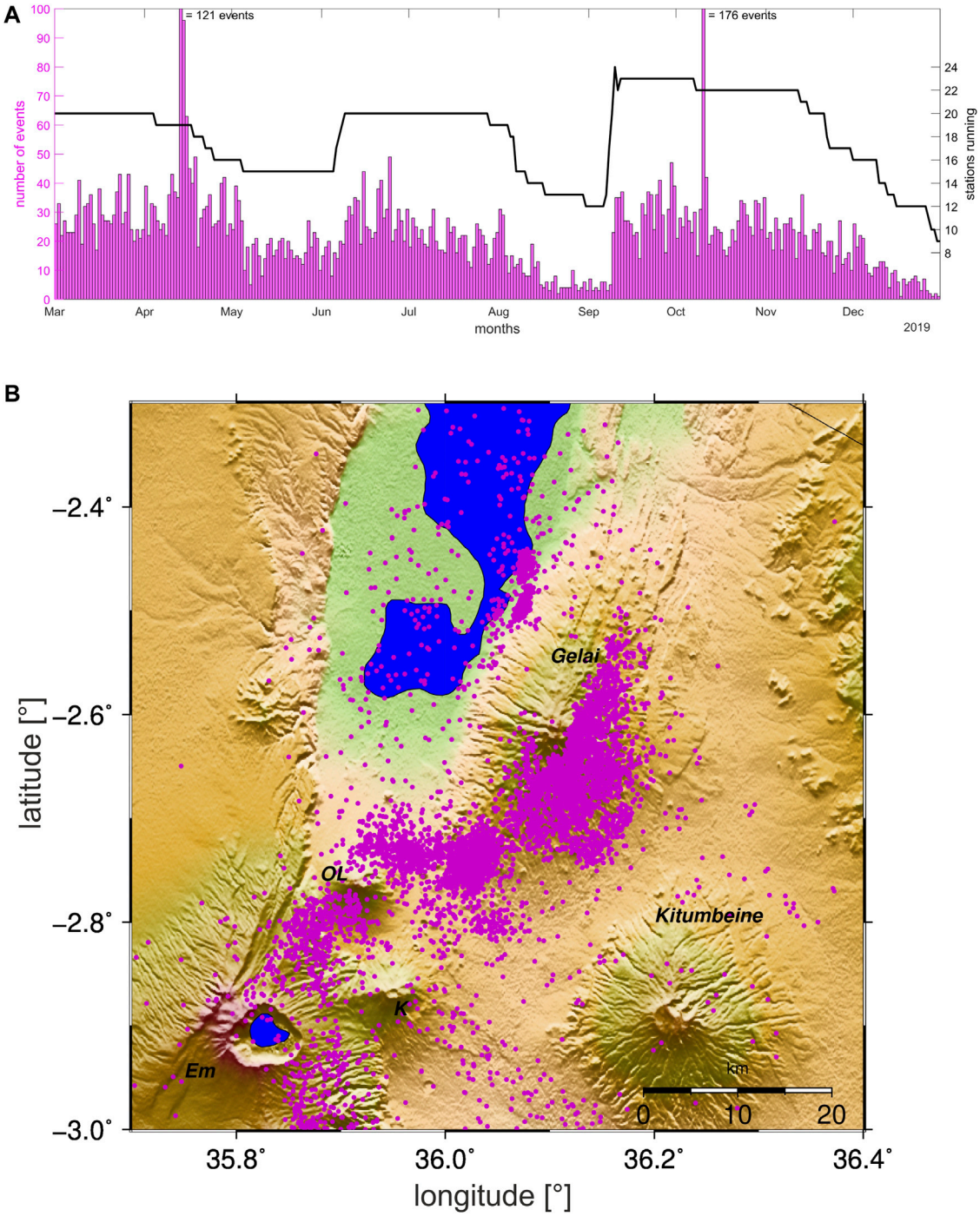

FIGURE 3 | (A) Histogram of well-located earthquakes per day **(left y-axis)** and superimposed numbers of running stations **(right y-axis)**. **(B)** Seismicity map, small circles show earthquakes.

Focal Mechanisms

We manually inspected the automatic earthquake catalog for suitable earthquakes for the calculation of focal mechanisms. We visually inspected waveforms for those earthquakes with more than 11 automatic P-and S-wave picks. We re-picked P- and S-wave arrival times on unfiltered waveforms for those events, which show little noise contamination using the SEISAN software (Havskov and Ottemöller, 1999), and relocated these earthquakes with the in SEISAN implemented HYPOCENTER algorithm by Lienert and Havskov (1995). We used the 1D velocity model by Albaric et al. (2010) as SEISAN only permits 1D velocity models. Given our previous analysis, location differences to the 3D model

are negligible. We continue to use only those earthquakes with azimuthal gaps smaller than 180° and at least eight P-wave polarity picks, which we picked on raw vertical traces.

Fault plane solutions were then derived using the FOCMEC algorithm by Snoke et al. (1984), which is also implemented in SEISAN. This is a grid search algorithm to find the orientation of nodal planes using a double-couple solution. We started our analysis with a grid of 5° and tested whether a unique solution can be obtained. If this is the case, we refine the grid down to 1° where possible. If a unique solution cannot be obtained, but solutions for a larger grid show a preferred mechanism, we manually picked SV/P amplitudes on the vertical component and included those in the inversion. We repeated our grid search for a grid of 5° and allowed for larger deviations in the amplitude ratios given large local attenuation effects. We only included those solutions that are unique for a grid of 5°, but refined the grid where possible. This procedure allowed us to constrain these fault-plane solutions accurately and enables us to report focal mechanisms for more earthquakes than using P-wave polarities alone (for categorization examples, see **Supplementary Figure S1**). In total, we report 281 fault plane solutions corresponding to three categories. 48% consist of solutions using only P-wave polarities, 48% are solutions using SV/P amplitude ratios additionally, and in 4% of cases we had to allow for one polarity error. We estimated the uncertainty of solutions by calculating a 95% confidence level for P/T plunges and trends using all solutions per event and found no systematic differences between small and large magnitude events.

RESULTS

Earthquake Locations

We located 6,827 earthquakes within and in the vicinity of our network (**Figure 3**; **Supplementary Table S1**). On average, we report 22 earthquakes per day, but the number of running stations heavily biases the number of reported events (**Figure 3A**). The locations of failed stations also impact the number of detected earthquakes. This effect is especially pronounced for stations at the network border, i.e. east of Gelai. During a period when the original setup of 20 stations was running, we detected 29 earthquakes per day on average. **Figure 3A** clearly shows two periods in time (April 13–15th, and October 10th) that greatly exceeded the average earthquake number per day. During these periods, two seismic swarms were observed, which will be discussed in (Swarms).

The observed seismicity is heavily clustered beneath volcanic centers (**Figure 3B**). More than half of the earthquakes are located beneath the eastern flank of Gelai, which is also the location for the first earthquake swarm. There is a separate cluster beneath the Naibor Soito monogenetic cone field. Earthquakes also cluster north and south of Oldoinyo Lengai, but locations below the border fault are poorly constrained given the station setup. Scattered seismicity appears beneath Lake Natron, with two distinct clusters between the lake and adjacent to the western flank of Gelai. One of these clusters corresponds to a discrete seismic swarm recorded in October 2019. Most of the seismicity occurs at a depth of 5–10 km (**Figure 4A**).

Magnitudes and B-Value

Local magnitudes M_L range between −0.85 and 3.6. The largest magnitude earthquake is part of the first seismic swarm in April 2019 beneath the eastern flank of Gelai (see (Swarms), **Figure 4**). We sort the magnitudes into 0.1 M_L bins and find that the four most populated bins lie between −0.2 and 0.2 M_L, which corresponds to 40% of the data. We derive the magnitude of completeness (M_C) using the maximum curvature method and apply the 0.2 correction factor of Woessner and Wiemer (2005) to obtain an M_C value of 0. We calculate the b-value by a robust, linear least squares fit to be ~0.99 (**Figure 4B**). We note that our b-value estimate changes slightly throughout the observational period, as the detection threshold for small magnitude events strongly depend on the number of running stations (see **Supplementary Figure S2**).

The calculated local magnitudes were used to estimate the cumulative seismic moment release throughout the 10 months observation period (**Figure 4C**). Given the sparse number of calibrated earthquakes, we adopt the crude assumption that the moment magnitude $M_W = M_L$. This assumption is supported by a comparison of local and teleseismically calculated magnitudes in the study region by Weinstein et al. (2017), who found that 2 M_L 4.7 and 4.7 earthquakes on June 3, 2013 corresponded to body wave magnitude mb 4.5 and mb 4.6 events documented in the National Earthquake Information Center (NEIC) catalog. Indeed, mb is expected to closely resemble M_w for earthquakes of mb ≤ 5 (Gasperini et al., 2013). Our results show that seismic moment release is nearly constant over time, but dominated by the 3.6 M_L event on April 13, 2019.

Spatial Distribution

Here, we focused only on well-constrained events close to and within the network by removing all earthquakes at distances larger than 2.5 km from the seismic network boundaries. A total of 5,658 earthquakes occurred within the defined boundary, with horizontal and vertical errors of 1.5 and 3.7 km, respectively. The depth distribution of seismicity varies spatially within our focus site. To illustrate these depth variations, we project the seismicity along three profiles through all clusters (**Figure 5**).

Profile X-X' transects the two clusters south and north of Oldoinyo Lengai (**Figure 5B**). Seismicity in the south, close to the border fault, typically occurs between 8 and 13 km depth and gradually deepens northward, with earthquake depths ranging ~13–17 km at the northern end of the profile. Similar earthquake depths are observed farther north of Oldoinyo Lengai below Lake Natron, with most events here ranging 12–20 km depth (**Figure 5B**). Directly beneath Oldoinyo Lengai is a notable seismic gap. Magnitudes along this profile are mostly between −0.3 and −0.2 with one larger event at M_L = 3.27.

Profile Y-Y' runs southeast from the cluster north of Oldoinyo Lengai through the Naibor Soito volcanic field (**Figure 5C**). In the center of the profile, the seismicity is located only in shallow depths of 5–10 km. Below the Naibor Soito volcanic field there are

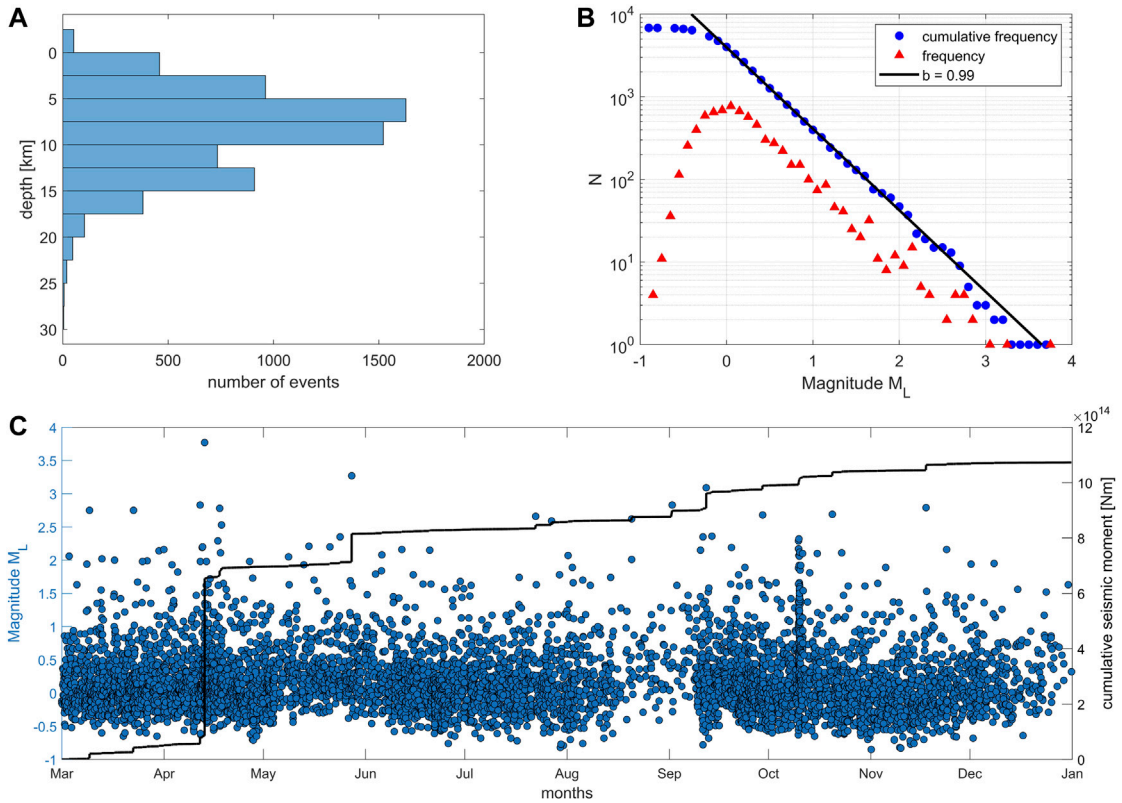

FIGURE 4 | (A) Depth distribution of earthquakes. **(B)** Cumulative magnitude-frequency and magnitude-frequency distribution. The b-value was calculated after determining M_C using the adjusted maximum curvature method of Woessner and Wiemer (2005). **(C)** Magnitude distribution per day over the reported 10 months of data overlain by the cumulative seismic moment estimate.

two clusters of seismicity, one at 5–10 km depth and another at 13–18 km depth. There is a noticeable gap between the deep cluster in the North (as seen in X-X') and the deep cluster beneath Naibor Soito. Toward the southeast end of profile Y-Y', seismicity is less abundant with scattered shallow (5–7 km) and deep (18–20 km) events. Overall, earthquake magnitudes along this profile are slightly smaller (~0.1 M_L) than in profile X-X', with the biggest event M_L = 2.83.

Profile Z-Z' runs from the southwest end of the Naibor Soito volcanic field northward along the eastern flank of Gelai (**Figure 5D**). This profile reveals an area of intense seismicity. Earthquakes at the southwestern edge of the Naibor Soito volcanic field are generally shallow, with depths ranging from 3 to 10 km. As with profile B-B', shallow and deep seismicity clusters are present at 5–10 km and 13–18 km depth, respectively, below the Naibor Soito volcanic field. This is followed by an abrupt seismic gap at 13–16 km along the profile. Beneath the gap, seismicity is first between depths of 10–13 km, and then gradually becomes shallower toward the center of Gelai. Seismicity beneath Gelai is mostly between 3–10 km, and the largest event with M_L = 3.6 is visible at ~ 28 km along the profile.

Focal Mechanisms

Following our procedure described in *Data and Methods*, we report 281 well-constrained focal mechanisms (see **Supplementary Table S2**). We use the plunge of the P- and T-axis to categorize the solutions into the three main faulting types: strike-slip (blue symbols; P- and T-axis plunge 0–45°), normal (red symbols; P- and T-axis plunge 45–90° and 0–45, respectively) and reverse mechanisms (green symbols; P- and T-axis plunge between 0–45° and 45–90°; see **Figure 6A**). Fault plane solution are dominantly strike-slip (57%), with normal mechanisms making up 39% of the data, and rare occurrences of reverse mechanisms (4%). The mean direction of T-axes is NW-SE (**Figure 6B**).

For ease of visualization, we show the best 50 solutions on a map only. We define those as being well constrained with a fine grid by using only P-wave polarizations, thus giving these focal mechanisms more importance than those constrained with amplitude ratios, and have at least 15 polarity picks (**Figure 7**, see **Supplementary Figure S1** for categories). Focal mechanisms around Oldoinyo Lengai are purely strike-slip, with T-axis trends varying between N-S to E-W. Above the Naibor Soito volcanic field and at Gelai volcano, normal faulting dominates with minor strike-slip mechanisms. The northernmost focal mechanism at Gelai is part of the first swarm. T-axis directions are ~ N-S or NW-SE. Three normal faulting events were constrained below the southern shore of Lake Natron. Owing to the network design, we cannot constrain focal mechanisms in other areas.

To study the direction of extension more closely, we plot the T-axis direction as a bar centered on the earthquake location and

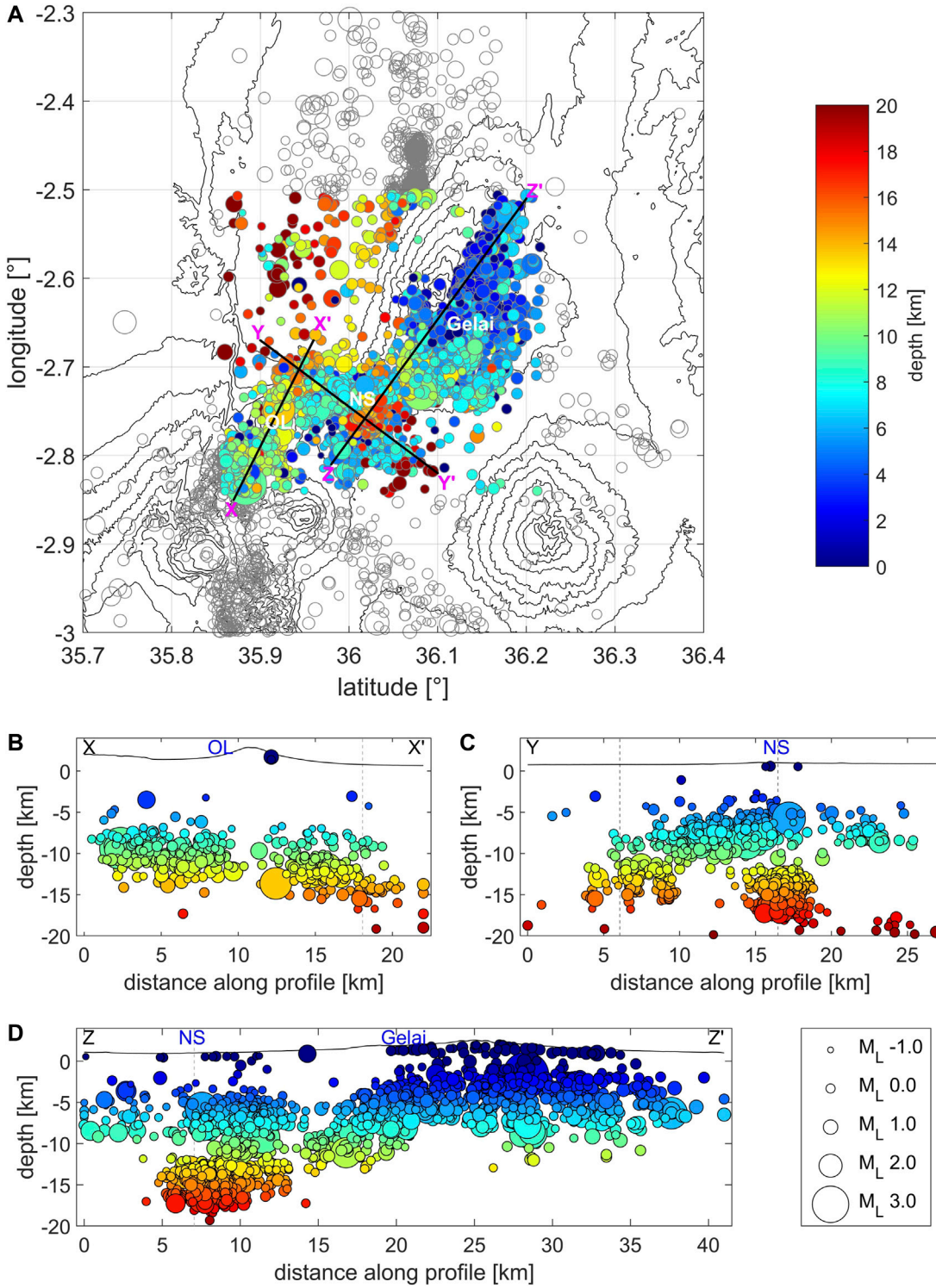

FIGURE 5 | (A) Map view of well-located earthquakes scaled by their magnitude and colored by their depth. **(B)** Enlarged vertical cross-section along the profile of X-X'. **(C)** Enlarged vertical cross-section along the profile of Y-Y'. **(D)** Enlarged vertical cross-section along the profile of Z-Z'. Intersections between profiles are marked with a gray dashed line. Color scale is saturated at 20 km for better visibility, as few events occur beneath 20 km depth.

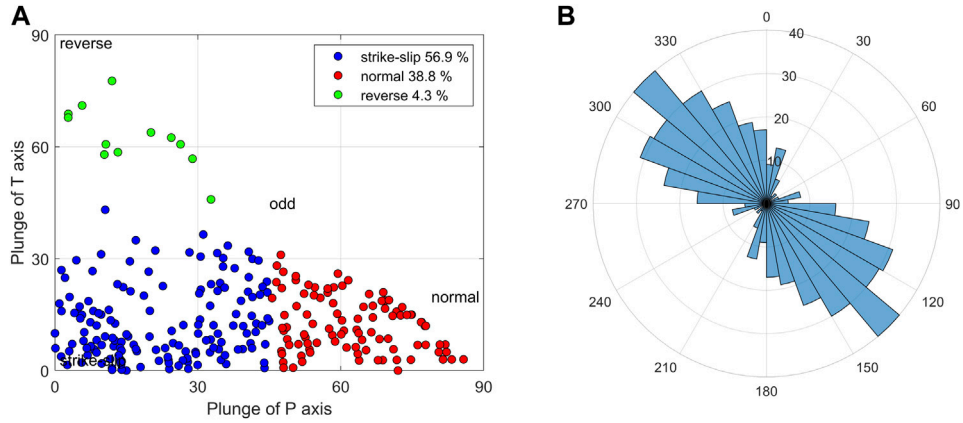

FIGURE 6 | (A) Classification and distribution of all focal mechanisms on the basis of P- and T-axis plunge. **(B)** Rose histogram of T-axis direction of all focal mechanisms.

group the data into different depth bins (**Figure 8**). Here, we omit all T-axes with confidence level widths above 40° while the remaining 82% have an uncertainty smaller than 10°. We constrain only a few mechanisms above 5 km depth of which most are located beneath Gelai in a NW-SE direction. This is more evident between 5–7 km depth and persists down to 9 km. T-axis directions below Naibor Soito volcanic field are very mixed throughout the 5–7 km, 9–11 km and below 13 km depth slices. North and East of Oldoinyo Lengai, T-axes can be divided into two groups: N-S and E-W directions. In 7–11 km depth, axes east of Oldoinyo are mostly N-S, while in 9–13 km, axes north of Oldoinyo are E-W.

Swarms

We observed two 1–3 days-long seismic swarms within the 10 months of data acquisition. During these swarms, the study region experienced a 5- to 8-fold increase in the number of earthquakes in a single day (**Figure 3A**), most of which were confined to a <10 km^2 area (**Figure 9**). The first swarm occurred April 13th–15th 2019 on the eastern flank of Gelai. We re-picked all swarm events manually, including amplitudes, in SEISAN and relocated them in NLL (see **Supplementary Table S3**). The swarm consists of 266 well-located earthquakes with a spatial distribution resembling a ~2 × 2 km-wide and ~11 km-deep pipe-like structure between 2 and 9 km depth (**Figure 9A**). Mean location errors are 0.8, 1.1 and 4 km in latitude, longitude and depth, respectively. Among the very first earthquakes was a 3.6 M_L event, which was located at the lower depth bound of the swarm pattern. The swarm has a b-value of 1.01 (see **Supplementary Figure S3** for the magnitude-frequency relation and distribution of magnitudes over time). There is no clear pattern in the distribution of seismicity in space or time, with events distributed throughout the interpreted pipe-like feature occurring the entire duration of the swarm. We are unable to constrain a fault plane solution for the largest event (M_L = 3.6), due to a small arrival before the P-wave. The second largest event with M_L = 2.2, which occurred on April 15th at 05:47, was a normal faulting event. We constrain seven mechanisms in total, with four normal, two strike-slip and one reverse mechanism (**Figure 9A** left). All mechanisms, except the reverse faulting event, have a T-axis trend of NW-SE.

The second seismic swarm comprises 151 events that occurred on October 10th, between Lake Natron and the western Gelai flank (**Figure 9B**). We did not manually re-pick this swarm as it is north of the network and the two closest stations were not running. The locations and depth are likely less well-constrained, although average location uncertainties are 1 km in longitude, 1.5 km in latitude and 4.5 km in depth. Earthquakes in this swarm were located between 6–15 km depth and their distribution resembles a 2 × 2 km-wide pipe-like structure. Given the distance to the closest seismic stations, we likely do not observe many earthquakes below M_L = 0. Our b-value estimate is 0.72 (see **Supplementary Figure S4** for the magnitude-frequency relation and distribution of magnitudes over time), and we cannot constrain any focal mechanisms for this swarm.

DISCUSSION

Here we discuss our observations in relation to previous studies. Seismicity observations from the southern Natron basin are sparse, and are only available for part of the 2007–2008 eruption (Calais et al., 2008; Albaric et al., 2010) and a 13-months deployment in 2013–2014 (Weinstein et al., 2017; Oliva et al., 2019a), which marked a time of relatively little activity at Oldoinyo Lengai as inferred from satellite data (Coppola et al., 2016; Mirova, 2020). As discussed below, our results show that some seismicity patterns observed during these previous deployments are consistent over decadal timescales, while previously unrecognized patterns reveal shorter-term variability in local magmatic-tectonic processes.

Generally, seismicity clusters below the volcanic centers, and as such we define five areas of seismic activity: 1) Oldoinyo Lengai, 2) Naibor Soito volcanic field, 3) Gelai, 4) Crater

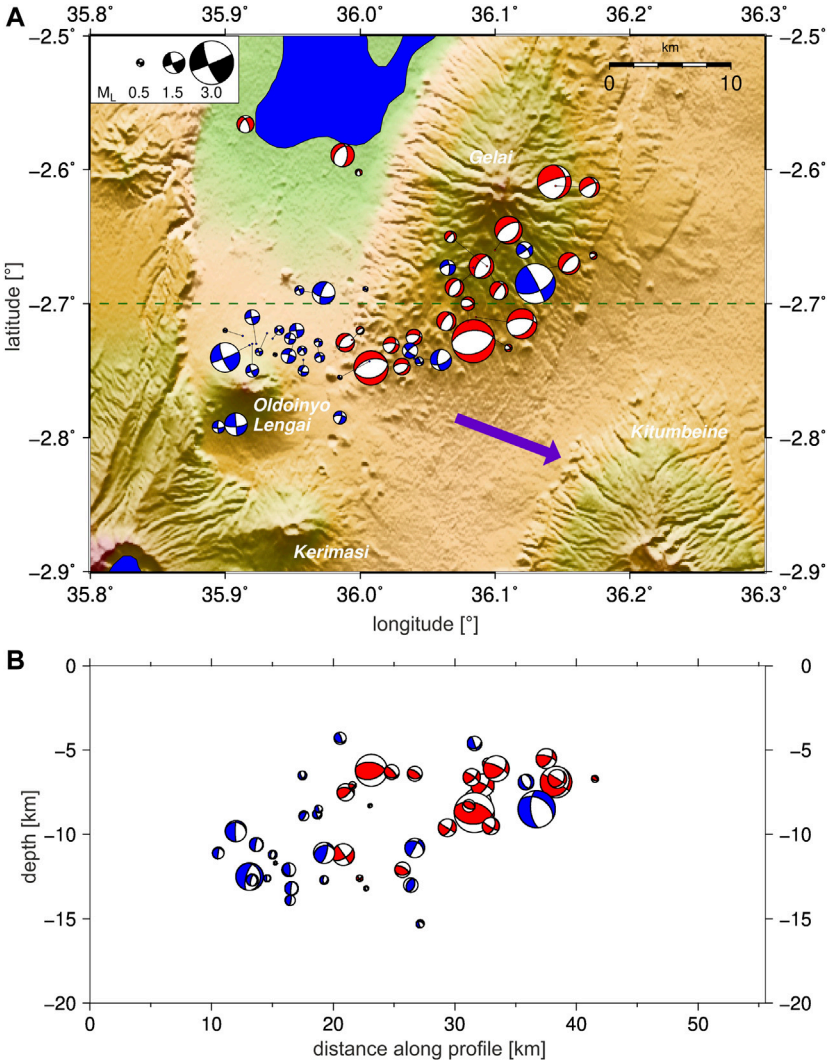

FIGURE 7 | Map and cross-section of best focal mechanisms. Blue and red beach balls show strike-slip and normal mechanisms, respectively. The size of the beach balls is given by their magnitude. **(A)** Map view. The green line denotes the cross-section shown in **(B)**. The purple vector show the GPS velocity of 1.1 mm/year from Saria et al. (2014). **(B)** Cross section.

Highlands, and 5) Lake Natron (**Figure 10A**). Given our network design, the detailed 3D seismicity patterns are best constrained and show the greatest detail below areas (1), (2) and (3), which will be the focus of the following sections. The networks lacks resolution for earthquakes below the Crater Highlands (4), which is located at the SE edge of the network, and thus we largely omit these data from further discussion. Comparatively little seismic activity is observed below Lake Natron (5) associated with the east-dipping western border fault. This is consistent with the findings of Weinstein et al. (2017), and suggests that recent extensional strain accommodation has been facilitated through magmatic activity (e.g., dike, sill intrusions) rather than slip along border faults. The only major seismic swarm observed below Lake Natron correlates with a west-dipping fault at the western edge of Gelai volcano. This fault is characterized by sets of fault-parallel springs exhibiting high $^3He/^4He$ ratios and diffuse soil CO_2 discharges, indicative of tectonic degassing of deep mantle volatiles (Lee et al., 2016; Lee et al., 2017).

Tectonic vs Fluid-Driven Seismicity in the Natron Basin

The southern Natron basin appears to have experienced persistent earthquake activity for the last 13 years, with likely more than 1,000 events of >0 M_L occurring every year (Calais et al., 2008; Albaric et al., 2010; Weinstein et al., 2017; this study). Our results indicate an increase in b-value from 2013–2014 of 0.87 (Weinstein et al., 2017) to 0.99, which is consistent with the 10–15 years eruptive cycle of Oldoinyo Lengai and increasing pressurization on the system. This persistent seismicity likely reflects the influence of a crustal magma plumbing system on the rifting process. For example, in many continental rift settings,

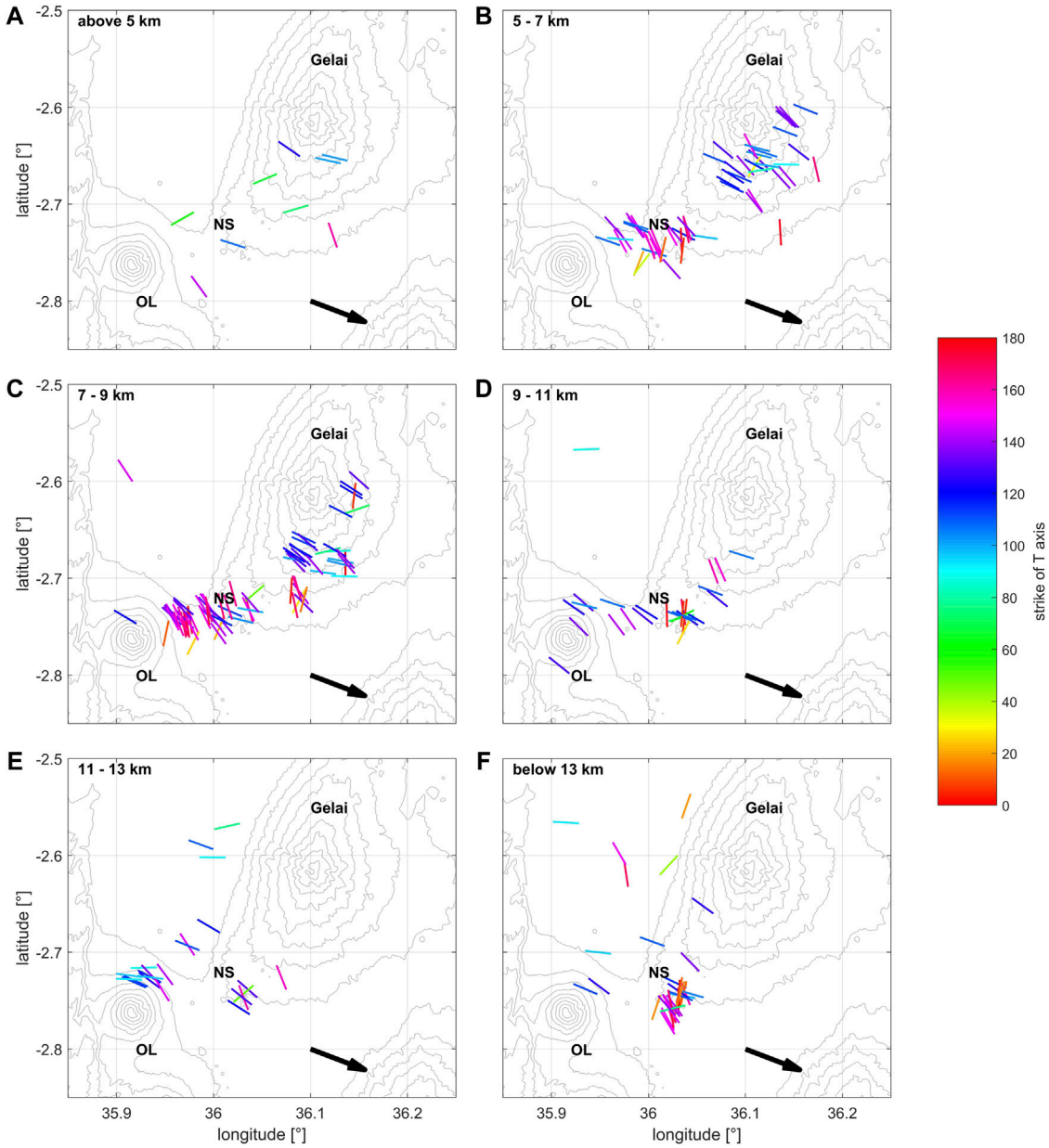

FIGURE 8 | Map view of T-axis direction of focal mechanisms. Axes are centered on earthquake location and colored by their azimuth. **(A)** 0–5 km depth. **(B)** 5–7 km depth. **(C)** 7–9 km depth. **(D)** 9–11 km depth. **(E)** 11–13 km depth. **(F)** below 13 km depth.

crustal strain is accommodated by a combination of magmatism and faulting (e.g. Buck, 2004). Melting via decompression may be generated by large lateral gradients in topography at the lithosphere-asthenosphere boundary (LAB) with or without the influence of an anomalously hot upper mantle (e.g. Ebinger and Sleep, 1998). Basaltic magma is less dense than the mantle lithosphere, and rises to the base of the crust of equivalent density (Watanabe et al., 1999). Here, these magmas will temporarily pond as melt bodies that, depending on magma flux and the efficiency of heat transfer through the lithosphere, may induce further heating and melting of surrounding rock before eventually freezing as an underplate (e.g., Thybo and Artemieva, 2013; Karakas and Dufek, 2015; Rooney et al., 2017). Heating and volatile release in these regions serve to localize magmatism, and this heating may reduce crustal strength and further localizes strain (Bialas et al., 2010). Crustal thinning and intrusion of magma cause changes in crustal density, which, in addition to rift basin topography and volcanic construction, generates loads that moderate the tectonic state-of-stress (Karlstrom et al., 2009; Maccaferri et al., 2014). Flexural isostatic compensation for the loads leads to plate bending, and depth-dependent state of stress. Intrusions

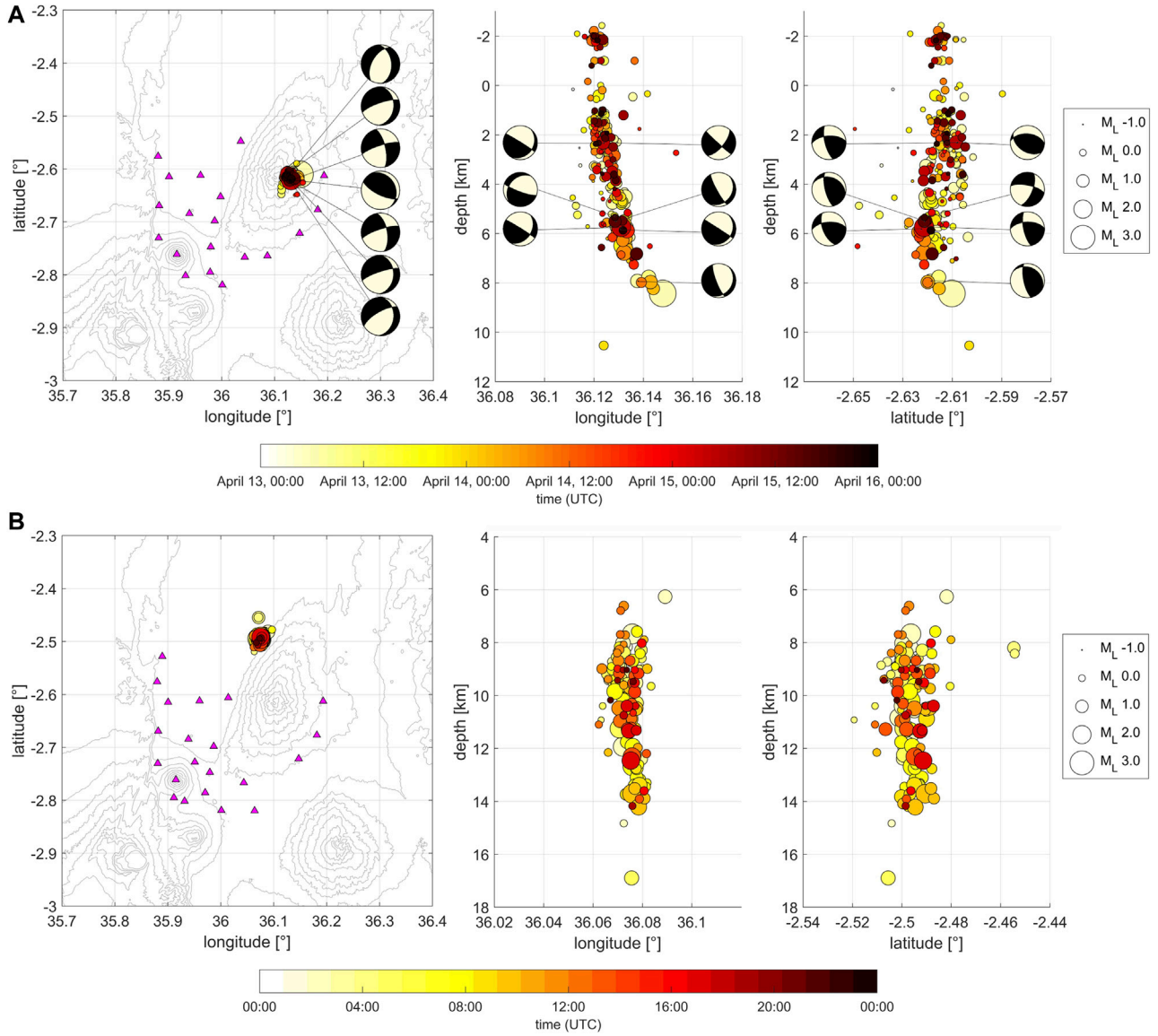

FIGURE 9 | (A) Left: Map view of first seismic swarm April 13th–15th 2019. Purple triangles are seismic stations running at the time. Circles are earthquakes colored by time and their size corresponds to their magnitude. **Center:** Enlarged vertical cross-sections of earthquakes along x-axis of **left**. **Right:** Enlarged vertical cross-section of their appearance in earthquakes along y-axis of **left)**. In every subpanel, focal mechanisms are shown in the margins and connected to the hypocenters with black lines. **(B) Left:** Map view of first seismic swarm on October 10th, 2019. Purple triangles are seismic stations running at the time. Circles are earthquakes colored by time and their size correspond to their magnitude. **Center:** Enlarged vertical cross-sections of earthquakes along x-axis of **left**. **Right:** Enlarged vertical cross-section of their appearance in earthquakes along y-axis of **left**.

moderate the stress field in the crust and in large part determine the orientation and location of subsequent intrusions (e.g., Gudmundsson, 1995; Buck et al., 2006; Karlstrom et al., 2009).

Crustal seismicity in magmatic rift zones can therefore reflect a variety of processes, from tectonic- to fluid-driven faulting, magma transport and storage, and pre-, syn- and post-eruption dynamics. Broadly, observed seismicity can roughly be differentiated into 1) fluid processes (e.g., magma ascent in conduits, gas pressurization in conduits, bubble formation) that lead to low frequency, long-period events; or 2) brittle shear failure or shear failure with dilatation, which produce high-frequency events (e.g. McNutt, 2005). Given the comparatively high frequency content of the earthquakes reported here, we assume most earthquakes are associated with brittle deformation, although fluid (over)pressures likely play an important role driving much of the observed seismicity (i.e., Lindenfeld et al., 2012b). Here, we examine seismicity patterns and focal mechanisms for 1) Oldoinyo Lengai, 2) Naibor Soito, and 3) Gelai shield volcano to characterize the extent to which both faulting and magmatic processes are active between eruptions.

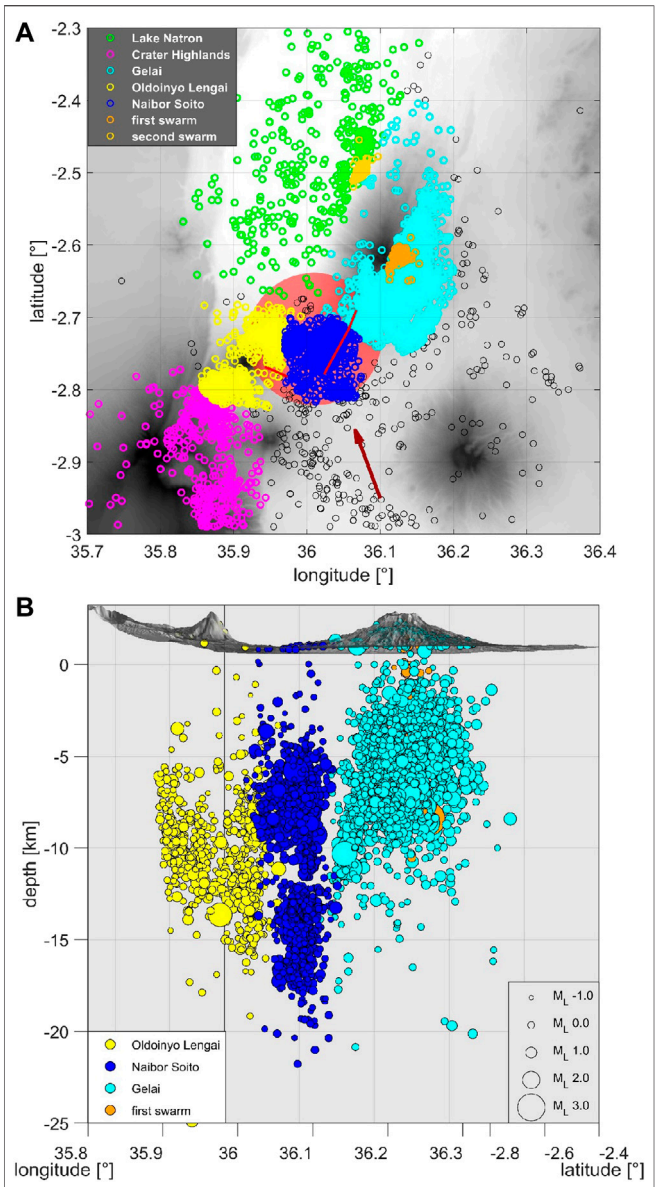

FIGURE 10 | (A) Map view of earthquakes (open circles) grouped by area: (1) yellow for Oldoinyo Lengai, (2) blue for Naibor Soito, (3), cyan for Gelai, (4) magenta for Crater Highlands, (5) green for Lake Natron. The two swarms are shown in orange and gold. Inferred dikes are shown as red lines (Calais et al., 2008; Biggs et al., 2013) and roughly dimensioned magma chamber in shaded-red inferred from Roecker et al. (2017). Purple arrow shows view angle in **(B)**. **(B)** Vertical Cross-section of **(A)** looking −20°N. Circles show earthquakes and are colored by group and scaled by their magnitude.

Oldoinyo Lengai

First, we discuss the deep crustal seismicity close to Oldoinyo Lengai, which occurs north and south of the volcano. Previously, Albaric et al. (2010) detected seismicity down to 15 km beneath the eastern flank during the early stages of the 2007 eruption, whereas Weinstein et al. (2017) detected a cluster beneath the northern flank from 2013–2014. Seismicity north of the volcano is deeper than in the south (**Figures 5**, **10**) and there is little seismicity in the vicinity of the second, late 2007 dike intrusion inferred from surface deformation patterns (Biggs et al., 2013). In Iceland, deep crustal seismicity (e.g., below the brittle-ductile transition down to 25 km) has been interpreted to represent brittle failure resulting from melt migration (e.g. Hudson et al., 2017; Greenfield et al., 2018). Weinstein et al. (2017) assume a weakly hydrated mafic granulite lower crustal composition based on crustal xenoliths from the study region, and estimate the brittle-ductile transition at ~16 km depth. Seismicity could also be caused by fluid-driven fracturing due to magmatic degassing (e.g. Lindenfeld et al., 2012b) or be related to the down-dip extension of the border fault below the volcano, along which deeply-sourced fluids such as CO_2 abundantly escape (Lee et al., 2016; Muirhead et al., 2020) and may cause fault zone weakening (Reyners et al., 2007). To conclude, seismicity at 15–20 km could thus be indicative of volatile or magmatic fluid movement.

Focal mechanisms at Oldoinyo Lengai are purely strike-slip. Similar strike-slip kinematics have been observed at other volcano-tectonics settings (e.g., Ágústsdóttir et al., 2016; Haug et al., 2018) and may be explained through a variety of mechanisms. In Afar, Pagli et al. (2019) show how linking rift segments can produce strike-slip tectonics. Dering et al. (2019) confirm the recent geophysical evidence for dike-parallel shear failure that can occur in the host rocks surrounding intruding dykes. Considering magmatic interactions, Hill (1977) suggests that observed strike-slip mechanisms result from the joining of offset opening cracks where hypocenters are located at the edges of interacting dike segments. Similarly, moment-tensor solutions from the 2014 Bárðarbunga-Holuhraun dike intrusion support strike-slip motions parallel to the advancing dike tip (Ágústsdóttir et al., 2016). Roman (2005) support a model where strike-slip earthquakes occur in the walls of inflating dikes. In this example, dike inflation causes a 90° rotation of P-axes from that predicted by the regional tectonic stress field, which allows for strike-slip motions. In all these examples, the regional extensional stress deviates locally during periods of magma influx, leading to strike-slip mechanisms as the predominant slip mode.

Support for a local magma-driven stress field around Oldoinyo Lengai comes from the spatial pattern of P-axes for strike-slip mechanisms around the volcano. These exhibit a sub-radial pattern, with the trends of the P-axes converging near the center of the volcanic edifice (**Figure 11**) in accordance with vent lineament data associated with the Naibor Soito volcanic field (Muirhead et al., 2015). This local stress pattern would also be enhanced by loading associated with both Oldoinyo Lengai and the Crater Highlands (Oliva et al., 2019b). Notably, the strike of the late 2007 dike intrusion beneath Oldoinyo Lengai also matches a predicted radial pattern, which may be best explained by a combination of the effects of magma overpressures in the volcanic feeder system and edifice loading (Biggs et al., 2013; Roman and Jaupart, 2014; Muirhead et al., 2015). Numerical studies investigating these effects (e.g. Karlstrom et al., 2009; Oliva et al., 2019b) reveal that edifice loading exerts a greater influence on the local stress state in the shallow upper crust, whereas magmatic overpressures exert the dominant stress control in vicinity of magma chambers

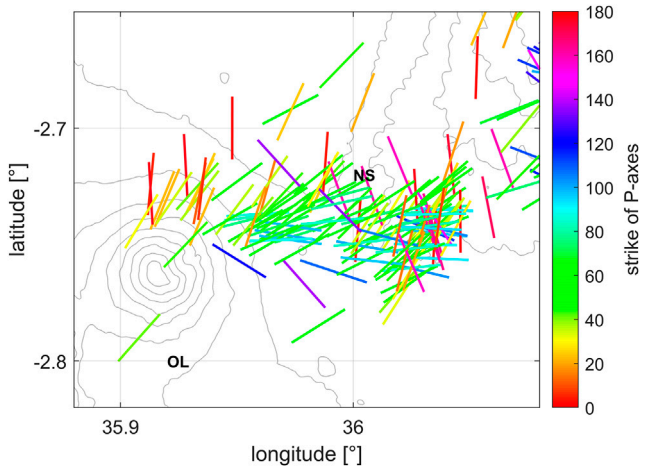

FIGURE 11 | Map view of P-axis directions of focal mechanisms below Oldoinyo Lengai and Naibor Soito. Axes are centered on their earthquake location and colored by their azimuth.

at depth. These processes play a critical role in driving local stress rotations and controlling fracture and dike orientations (e.g., Kervyn et al., 2009). In our study region, the depth of the strike-slip events (<9 km) and their proximity to magma pathways below the volcano support a role of magmatic pressures in controlling local stress deviations at depth, thereby capturing the effects of the Oldoinyo Lengai magmatic system on the surrounding stress state. Of note, our interpretation is somewhat limited by the fact we cannot utilize surface deformation patterns (e.g. InSAR data) as an additional independent dataset to support our arguments above, as the source depths of the analyzed focal mechanisms are not conducive to any detectable surface deformation.

Naibor Soito

Beneath Naibor Soito volcanic field, seismicity is divided into a shallower (5–10 km depth) and deeper cluster (12–18 km depth), with comparatively little seismicity occurring at depths of 10–12 km, except for a fine structure seemingly connecting both (**Figures 5**, **10B**). Both clusters were observed in 2012–2013 (Weinstein et al., 2017). The seismicity cluster between 12 and 18 km occurs on top of a S-wave low velocity and high Vp/Vs zone, which has been interpreted previously as a lower crustal magma body (Roecker et al., 2017). In agreement with previous authors, we assume that the seismicity detected adjacent to and above this low-velocity zone represents fluid-triggered fracturing, resulting from one or a combination of devolatization of magmas and the migration of melt from lower crustal reservoirs (Roecker et al., 2017; Weinstein et al., 2017). The shallow, disc-shaped seismicity pattern was interpreted as a complex of pressurized, hot sills likely fed by the deeper magma source (Weinstein et al., 2017). These shallow sills in-turn may have sourced the 2007 dike intrusion (Calais et al., 2008; Weinstein et al., 2017). The recurring non-double couple source mechanisms suggest that numerous intrusions from the same complex have occurred since 1995 (Oliva et al., 2019a). Thus, our and previous observations support a central, deep magmatic source which drives the volcanism locally.

Below the Naibor Soito volcanic field, our high-resolution observations allow us to distinguish a complex pattern of focal mechanisms and T/P-axis directions. Above the magma chamber (below 13 km) and in the pressurized sill complex (5–7 km; 9–11 km), there is no dominant mechanism or stress direction. Between 7 and 9 km depth, T-axes are ~ N-S (or nearly E-W P-axes, **Figure 11**), which represents a rotation of local stress away from the regional ESE-WNW extension direction (Saria et al., 2014). Both observations are best explained by magmatic processes associated with melt transported from the deeper magmatic body to the shallow sill complex. While the pressurized magmatic bodies exert a changing stress field depending on their state (i.e. inflation or deflation), earthquakes in the walls of the inflating intrusions show a local horizontal stress change according to Roman (2005). This is also supported by the findings of Oliva et al. (2019b), who predict stress rotation between Oldoinyo Lengai, Naibor Soito and Gelai driven by magmatic intrusions and magma bodies at depth. These fluid driven stress-changes as well as strong shallow and deep seismicity patterns are among the most persistent, clearly imaged features of our dataset through our observational period.

Gelai

All temporary seismic networks have recorded persistent seismic activity beneath Gelai volcano since 2007 (Calais et al., 2008; Albaric et al., 2010; Weinstein et al., 2017). However, the closer station spacing in our network allows examination of seismic activity in greater detail than previous studies (**Figures 5**, **10**). Locations reported by Calais et al. (2008) spread widely, which may largely reflect location uncertainties associated with locating events outside of the network. Albaric et al. (2010) found that seismic activity was primarily focused beneath the southern flank of Gelai, while Weinstein et al. (2017) reported activity beneath the southern and western flanks of Gelai. Overall, these previous results combined with our newly located earthquake data suggest that activity may have migrated northwards below Gelai over time, as the recent activity now reaches the northern end of Gelai (**Figure 5**). Beneath Gelai, earthquakes show predominantly normal faulting mechanisms (**Figure 7**) with T-axes sub-parallel to the regional extension direction (Saria et al., 2014; Muirhead et al., 2015; Weinstein et al., 2017), which is consistent with faulting in extensional rifts elsewhere (e.g. Keir et al., 2006; Lindenfeld et al., 2012a). These mechanisms contrast those at Oldoinyo Lengai and the Naibor Soito volcanic field. The strike of faults, dikes and previously determined focal mechanisms at Gelai typically indicate WNW-ESE extension (Calais et al., 2008; Albaric et al., 2010; Muirhead et al., 2015; Weinstein et al., 2017), which is consistent with geodetic data (Saria et al., 2014).

Gelai volcano is also associated with the April 2019 seismic swarm, which exhibits a very narrow, pipe-like shape. This swarm is in line with, and located ~10 km north of, the 2007 dike intrusion as imaged by InSAR (Calais et al., 2008), which seems to have initiated the recent recorded Gelai seismic activity (Weinstein et al., 2017). However, seismicity associated

with dike emplacement and propagation usually follows along a plane and migrates spatially through time in the direction of magma movement (e.g. Ebinger et al., 2010; Ágústsdóttir et al., 2016), and thus the 2019 swarm activity is not interpreted to relate directly to dike emplacement. Though not exhibiting a clear main shock after shock or clear temporal sequence, the 3.6 M_L event is the first and second deepest event which seems to start the sequence. Afterward, other earthquakes rupture along the pipe, which is then active along the entire segment. Focal mechanisms show normal faulting representative of the regional stress field. Similar pipe-like seismic swarms were observed by Lindenfeld et al. (2012b) in the Rwenzori region of the Albertine Rift (Uganda) of the western branch of EARS, and were interpreted to originate from fluids and gases, sourced from a magmatic body, rising through the plate. Accordingly, this swarm may be caused by degassing along a currently hidden fault and is feasible given the high amount of CO_2 degassing in the entire Natron rift (Lee et al., 2016, Lee et al., 2017; Muirhead et al., 2020). The shape and duration of the April 2019 swarm resembles the October swarm located between Gelai and Lake Natron which, given the nature of the seismicity and associated mantle volatile release at the surface (i.e., Lee et al., 2017), we attribute to ascent of deep mantle volatiles along a pre-existing fault. As crustal fluid speeds based on migrating seismic swarms are typically 10–100 m/day (Ibs-von Seht et al., 2001; Hariri et al., 2010), we assume that these earthquakes represent a mechanical response to subtle pressure changes in the fluid system due to changes in fault permeability (e.g. due mineral precipitation), in the local and/or regional stress state, and/or in the deep fluid flux (Sibson, 2000).

The 3D seismicity pattern beneath Gelai cannot be explained by slip on a single fault plane. Given our observations, the strong microseismicity in the last ~13 years and repeating earthquake swarms, indicate that fluids and volatile release must play an important role in accommodating the extensional strain, as is evident in this and other rift settings (Lindenfeld et al., 2012b; Wright et al., 2012; Muirhead et al., 2016; Weinstein et al., 2017). Diffuse, high magmatic CO_2 degassing from lower crustal intrusions throughout the entire Natron rift could cause significant earthquake activity (Lee et al., 2016; Weinstein et al., 2017). In fact, the latter suggested that the recent locus of strain accommodation has been focused in the central rift valley below Gelai, and that stress field rotation and magmatism below Oldoinyo Lengai and the Naibor Soito volcanic field have facilitated stress transfer from the western Manyara-Natron border fault to a newly developing rift segment beneath Gelai.

Plumbing System

Our detailed 3D seismicity patterns and focal mechanisms allow us to map the magmatic plumbing system associated with Oldoinyo Lengai volcano in unprecedented detail. The persistent pipe-like aseismic structures down to depths of 12 km, as well as well resolved areas of high seismicity, are particularly striking (**Figure 10B**) and may have implications about the long-debated plumbing system. We have summarized our findings in a sketch (**Figure 12**), which highlights our conceptual interpretation.

There is a distinct aseismic zone beneath the Oldoinyo Lengai edifice, which extends to a depth of 10 km and becomes successively narrower with depth (**Figures 10B**, **12**). This seismic gap may represent the region of persistent partial melt (i.e., Hudson et al., 2017) that connects the volcano to its deeper plumbing system, and/or has heated nearby country rock resulting in ductile rock behavior for extended time periods in otherwise brittle crust (Castaldo et al., 2019; Parisio et al., 2019). Indeed, renewed and persistent volcanic activity at Oldoinyo Lengai since late 2018, as inferred from satellite data (Massimetti et al., 2020), require open conduits transporting volatiles and melt to the surface. From tomography and complementary receiver function studies (Plasman et al., 2017), the volcano is underlain by a low S-wave anomaly and high Vp/Vs ratios at 5 km depth, which continue well under the rift shoulder (Roecker et al., 2017) and may represent zones of partial melt below the volcano. Alternatively, the spatially varying high and low Vp/Vs and aseismic pipes in this region may, at least in part, reflect the sustained hydrothermal system interpreted for this volcano (Mollex et al., 2018), which is closely associated with its underlying magma plumbing system.

The exact spatial extent and overall geometry of partial melt bodies and hydrothermal fluids below Oldoinyo Lengai volcano are challenging to resolve. Surface deformation observed in InSAR data in late 2007 were modeled as a deflating shallow magma chamber at 3 km depth beneath Oldoinyo Lengai (Biggs et al., 2013), and chemistry from prior eruptions has been previously considered to reflect a two-level system, with magma storage at 0.5 and 3.3 km depth (Petibon et al., 1998). In all, some models of nephelinite and natrocarbonatite magma generation at Oldoinyo Lengai require only one open magma system (de Moor et al., 2013), while others necessitate at least three distinct zones of melt accumulation and storage (Berkesi et al., 2020). Regardless of these uncertainties, our high-resolution observations of earthquake activity below the volcano are best explained by a high temperature zone of partial melt and hydrothermal circulation underlying the edifice, where this zone is too ductile to produce any earthquakes (e.g. Thurber, 1984; Bryan et al., 1999; Castaldo et al., 2019, **Figure 12**). Additionally, our seismicity data and other geophysical constraints (i.e., Roecker et al., 2017) suggest that the inferred mid-crustal magma chamber for the volcano (i.e., Mollex et al., 2018) might either be located in the aseismic zone beneath Oldoinyo Lengai, or just above the deep-seated seismicity beneath Naibor Soto, where we image a circular aseismic feature (**Figures 10**, **12**).

A second, pipe-like seismic gap separates seismicity patterns between Naibor Soito and Gelai (**Figures 10**, **12**). It is particularly interesting, as there are no detectable surface displacements accompanying volumetric expansion in the upper crust since 2007, and the ~2.4 m-wide 2007 dike (Biggs et al., 2009) would have long since cooled and solidified. This aseismic zone may instead mark a region of 1) hydrothermally altered rock following the 2007 dike intrusion, 2) a region of currently recognized weak rock or 3) part of the hydrothermal

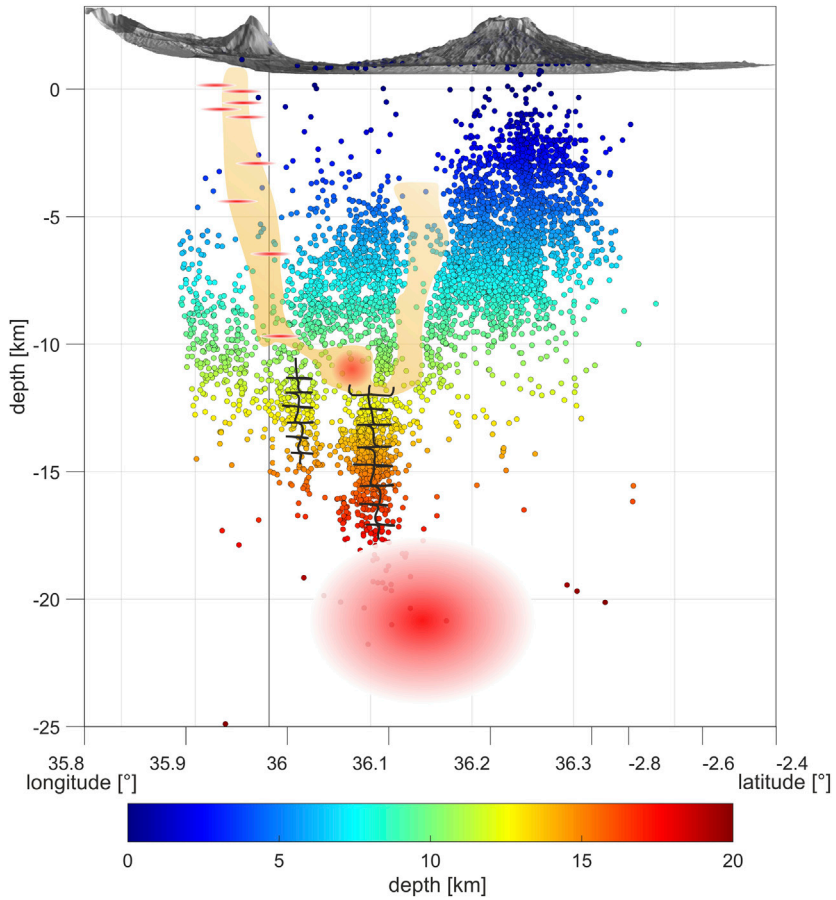

FIGURE 12 | Plumbing system of Oldoinyo Lengai with seismicity. The orange shaded areas are seismic gaps interpreted as part of the mushy plumbing system, overlain with small reddish ellipses denoting sill complexes. Black lines denote deep plumbing system, which connect the hydrothermal system to the deep magma chamber inferred from Roecker et al. (2017).

system (e.g., Mollex et al., 2018; Parisio et al., 2019). Considering the large amount of earthquakes beneath Gelai, which may be driven in large parts by fluids or degassing, this aseismic zone may also facilitate fluid transfer from the deeper parts of the plumbing system to the shallow crust beneath Gelai.

In conclusion, we cannot differentiate between different geochemical models of the natrocarbonatite genesis, but our results constrain the magmatic plumbing system of the Natron rift by interpreting areas of high and low seismicity as fluid or melt transport and locally heated, ductile zones, respectively. Focal mechanisms show the influence of magmatic intrusions and magma bodies, which together with seismicity may point to different localities for magma differentiation.

Interactions Between Rift Segments

Our observations are consistent with conceptual models of magmatic rifting revealing enhanced vertical permeability and associated fluid migration within accommodation zones between rift segments (e.g. Corti, 2004; Rowland et al., 2007; Muirhead et al., 2015; **Figure 13**). Uniquely, the North Tanzania Divergence offers the opportunity to explore strain accommodation between border fault-controlled extension in the Manyara basin, to largely magma intrusion-controlled extension within the central Natron basin, where a new, magmatically controlled segmentation is developing (e.g., Ebinger and Casey, 2001; Muirhead et al., 2015; Oliva et al., 2019a). Stress distributions in border fault-controlled segments are largely controlled by the shape of the basin and flank topography, and the Moho geometry, whereas segments with crustal magma chambers and volcanoes are controlled by crustal thinning, magma bodies, and volcanic loading (Karlstrom et al., 2009; Muirhead et al., 2015; Oliva et al., 2019b).

We image how the complex stress field in the inter-segment transfer zone drives the development of radial and rift-oblique dikes, faults and fracture systems, and how interconnected zones of magmatism feeding into these transfer zones facilitate strain transfer between the rift segments (**Figure 13**). Our seismicity and fault plane solutions reveal that the high flux of gas-rich magma into these regions produces overpressured magma reservoirs that locally perturbed stress fields. This is supported by vent alignment (Muirhead et al., 2015), InSAR data (Biggs et al., 2013; Wauthier et al., 2013) and

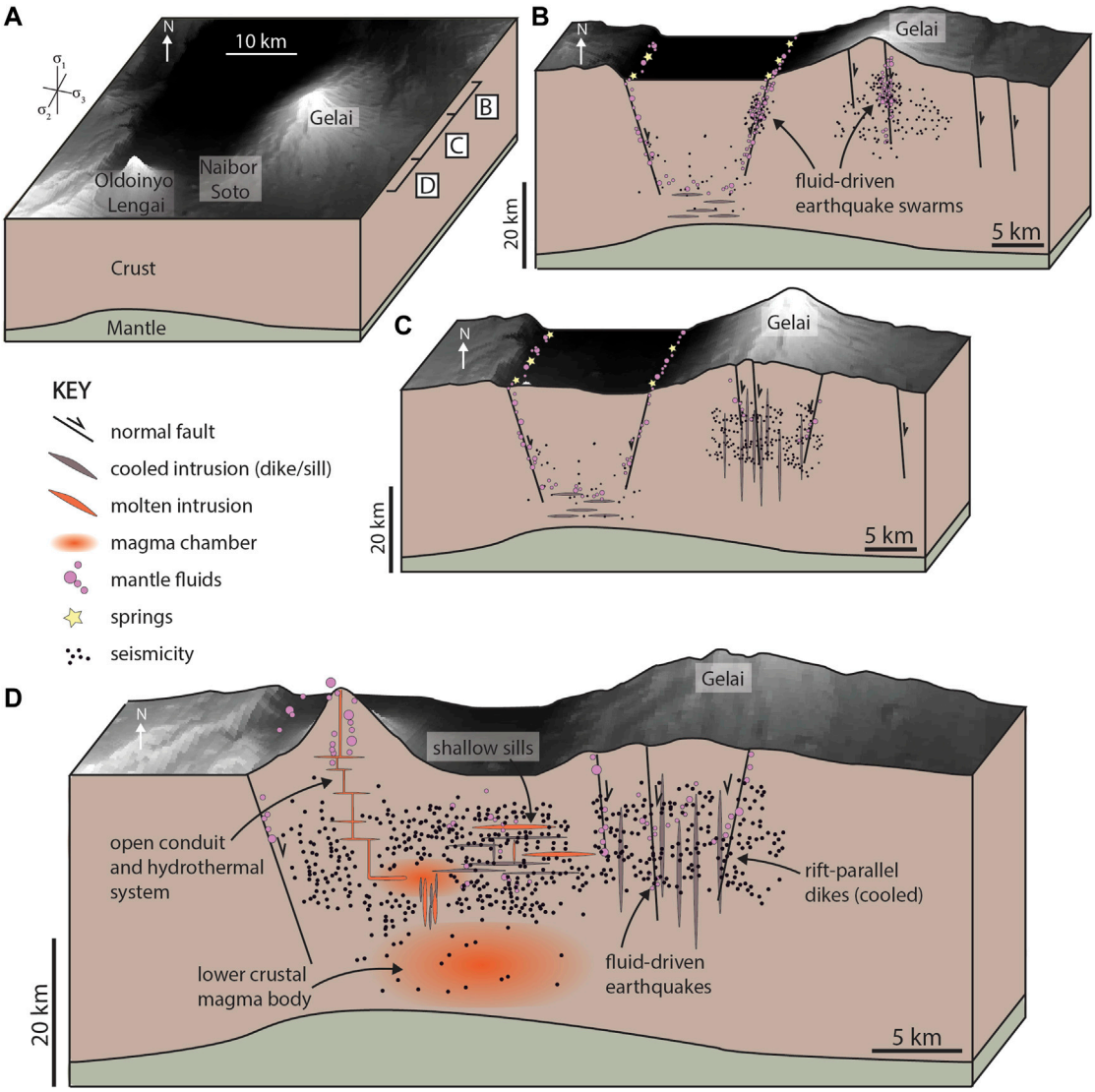

FIGURE 13 | Idealized conceptual illustration of magmatic-fluid-tectonic interactions associated with the volcanic plumbing system of the south Natron basin. The structure of the plumbing systems is based on data and interpretations presented in the current study, as well as previous seismicity and geophysical studies by Roecker et al. (2017) and Weinstein et al. (2017). Crustal thicknesses are broadly based on Plasman et al. (2017) and surface topography is from the 90 m SRTM DEM dataset. **(A)** Surface topography and general crustal structure of the south Natron basin, highlighting the position of the key volcanic features. Letters refer to the presented crustal sections in **(B–D)**. **(B)** General distribution of seismicity at the northern end of the seismic network. Deep seismicity occurs below Lake Natron, with seismic swarm behavior associated with fluid overpressures and fluid migration through the crust. Helium isotope data of dissolved spring volatiles and carbon isotopes of diffusely degassing CO_2 support mantle fluid flow through these fault systems (Lee et al., 2016, Lee et al., 2017; Muirhead et al., 2020). **(C)** General distribution of seismicity through central regions of the seismic network. Seismicity patterns generally follow those in B and support fluid-driven earthquakes, although no specific seismic swarms have been identified. Cooled dike intrusions represent regions of past magmatic rifting, although no significant melt or active diking is inferred below Gelai volcano currently. **(D)** General distribution of seismicity throughout the southern end of the seismic network, with deformation patterns strongly influenced by the presence of melt and fluids. The infrequent occurrence of seismicity in the lower crust below the Naibor Soto volcanic field support the presence of lower crustal magma bodies, consistent with the crustal velocity structure presented by Roecker et al. (2017). Distinct seismic gaps below these volcanic systems represent vertical zones of partial melt and/or thermally altered regions, and represent possible connections between partial melt bodies at different crustal depths (Weinstein et al., 2017). Melt bodies and topographic loads impose local stress perturbations (Oliva et al., 2019b) indicated by variations in fault plane solutions observed in this system. Persistent low magnitude seismicity throughout the region supports a model of earthquake activity driven by the percolation of melt and magmatic volatiles, consistent with full moment tensor analyses by Oliva et al. (2019a) who found various non-double couple earthquake source mechanisms.

temporally consistent earthquake source mechanisms (Oliva et al., 2019a). Furthermore, the shape of crustal thinning, the rift basin and flank topography guide zones of magma upwelling and storage, which promotes the transfer of strain to central volcanic systems (Oliva et al., 2019b). Extension-normal dikes inject into the rift to accommodate regional tectonic extension, while also focusing strain into newly developing rift segments (i.e., below Gelai volcano; Weinstein et al., 2017).

CONCLUSION

We report seismicity and focal mechanisms from a ten-month deployment in 2019 in the southern Natron basin, which encapsulates recent volcanic activity at the only active natrocarbonatite volcano Oldoinyo Lengai worldwide and repeated seismic swarms consistent with volatile release and dike intrusion. Seismicity patterns beneath Oldoinyo Lengai and Naibor Soito reveal a complex magmatic plumbing system in which melt is transported from a deep-seated magma chamber to the surface, and focal mechanisms reveal the influence of the edifice load, magmatic intrusions at depth and magma-driven stress changes. Seismicity at Gelai is consistent with fluid release and degassing of CO_2 and focal mechanisms point to strain accommodation within the regional extensional stress field. Our results indicate that the southern Natron basin is a segmented rift system in which strain is transferred from the western border fault to a developing rift segment. The rift basin functions as a magmatic accommodation zone where fluids preferentially percolate vertically and thus prescribe the location of magma intrusion, storage and eruptive centers. These findings provide a framework for understanding and modeling complex interactions between tectonic and magmatic processes during continental rift initiation and development.

DATA AVAILABILITY STATEMENT

The datasets generated for this study can be found at https://dx.doi.org/10.6084/m9. The dataset is archived at GEOFON Data Center, https://dx.doi.org/10.14470/4W7564850022.

AUTHOR CONTRIBUTIONS

MCR is the PI of the SEISVOL project, processed the data, composed **Figures 2–12**, and wrote the first manuscript. JDM composed **Figures 1**, **13**. MCR, ASL, FL, and GR acquired the field data, with substantial support by EOK, MCR, and GR conceived and designed the seismic and infrasound networks. All authors contributed to the interpretation of the results and writing of the paper.

FUNDING

MCR is funded by the DFG (German Research Council), grant number RE 4321/1-1. JDM received funding through an NSF EAR GeoPRISMS Program grant 1654518. Additional support for fieldwork and instrumentation was provided through funds from Goethe University to GR.

ACKNOWLEDGMENTS

We highly appreciate everyone involved in the fieldwork, especially members of Engaresero Village. We thank the Tanzania Commission for Science and Technology (COSTECH) for supporting us and providing the research permits. Instruments were kindly provided by the Geophysical Instrument Pool Potsdam (GIPP) and the Goethe University Frankfurt, and data were archived by GEOFON (GEOFON Data Center, 1993). We thank the developers of QuakeMigrate for technical support and Luca De Siena for constructive discussions. We thank both reviewers for their insightful comments.

SUPPLEMENTARY MATERIAL

The Supplementary Material for this article can be found online at: https://www.frontiersin.org/articles/10.3389/feart.2020.609805/full#supplementary-material.

REFERENCES

Ágústsdóttir, T., Woods, J., Greenfield, T., Green, R. G., White, R. S., Winder, T., et al. (2016). Strike-slip faulting during the 2014 Bárðarbunga-Holuhraun dike intrusion, central Iceland. *Geophys. Res. Lett.* 43, 1495–1503. doi:10.1002/2015GL067423

Albaric, J., Deverchere, J., Perrot, J., Jakovlev, A., and Deschamps, A. (2014). Deep crustal earthquakes in North Tanzania, East Africa: interplay between tectonic and magmatic processes in an incipient rift. *Geochem. Geophys. Geosyst.* 15, 374–394. doi:10.1002/2013GC005027

Albaric, J., Perrot, J., Deverchere, J., Deschamps, A., Le Gall, B., Ferdinand, R. W., et al. (2010). Contrasted seismogenic and rheological behaviours from shallow and deep earthquake sequences in the North Tanzanian Divergence, East Africa. *J. Afr. Earth Sci.* 58, 799–811. doi:10.1016/j.jafrearsci.2009.09.005

Aulbach, S., Rudnick, R. L., and McDonough, W. F. (2011). Evolution of the lithospheric mantle beneath the East African Rift in Tanzania and its potential signatures in rift magmas. *Geol. Soc. Am. Bull.* 478, 105–125. doi:10.1130/2011.2478(06)

Ayele, A., Keir, D., Ebinger, C., Wright, T. J., Stuart, G. W., Buck, W. R., et al. (2009). September 2005 mega-dike emplacement in the Manda-Harraro nascent oceanic rift (Afar depression). *Geophys. Res. Lett.* 36 (20), 1–5. doi:10.1029/2009GL039605

Bacon, C. A., Smith, J. D., Winder, T., Hudson, T., Greenfield, T., and White, R. S. (2019). "QuakeMigrate: a modular, open-source Python package for earthquake detection and location," AGU Fall Meeting, San Francisco, CA, October, 2019. [Abstract].

Baer, G., Hamiel, Y., Shamir, G., and Nof, R. (2008). Evolution of a magma driven earthquake swarm and triggering of the nearby Oldoinyo Lengai eruption, as resolved by InSAR'a, ground observations and elastic modeling, East African Rift. *Earth Planet Sci. Lett.* 272, 339–352. doi:10.1016/j.epsl.2008.04.052

Berkesi, M., Bali, E., Bodnar, R. J., Szabó, Á., and Guzmics, T. (2020). Carbonatite and highly peralkaline nephelinite melts from Oldoinyo Lengai Volcano, Tanzania: the role of natrite-normative fluid degassing. *Gondwana Res.* 85, 76–83. doi:10.1016/j.gr.2020.03.013

Bialas, R. W., Buck, W. R., and Qin, R. (2010). How much magma is required to rift a continent? *Earth Planet Sci. Lett.* 292 (1-2), 68–78. doi:10.1016/j.epsl.2010.01.021

Biggs, J., Anthony, E. Y., and Ebinger, C. J. (2009). Multiple inflation and deflation events at Kenyan volcanoes, East African Rift. *Geology* 37 (11), 979–982. doi:10.1130/G30133A.1

Biggs, J., Chivers, M., and Hutchinson, M. C. (2013). Surface deformation and stress interactions during the 2007–2010 sequence of earthquake, dyke intrusion and eruption in northern Tanzania. *Geophys. J. Int.* 195 (1), 16–26. doi:10.1093/gji/ggt226

Biggs, J., Robertson, E., and Cashman, K. (2016). The lateral extent of volcanic interactions during unrest and eruption. *Nat. Geosci.* 9 (4), 308–311. doi:10.1038/NGEO2658

Brune, S., Heine, C., Clift, P. D., and Pérez-Gussinyé, M. (2017). Rifted margin architecture and crustal rheology: reviewing Iberia-Newfoundland, central South Atlantic, and South China Sea. *Mar. Petrol. Geol.* 79, 257–281. doi:10.1016/j.marpetgeo.2016.10.018

Bryan, C. J., Sherburn, S., Bibby, H. M., Bannister, S. C., and Hurst, A. W. (1999). Shallow seismicity of the central Taupo Volcanic Zone, New Zealand: its distribution and nature. *N. Z. J. Geol. Geophys.* 42 (4), 533–542. doi:10.1080/00288306.1999.9514859

Buck, W. R. (2004). Consequences of asthenospheric variability on continental rifting. in *Rheology and deformation of the lithosphere at continental margins: MARGINS theoretical and experimental Earth science series.* (New York, NY: Columbia University Press), 1–30.

Buck, W. R., Einarsson, P., and Brandsdóttir, B. (2006). Tectonic stress and magma chamber size as controls on dike propagation: constraints from the 1975–1984 Krafla rifting episode. *J. Geophys. Res.: Solid Earth* 111 (B12), 1–5. doi:10.1029/2005JB003879

Calais, E., d'Oreye, N., Albaric, J., Deschamps, A., Delvaux, D., Déverchère, J., et al. (2008). Strain accommodation by slow slip and dyking in a youthful continental rift, East Africa. *Nature* 456 (7223), 783–787.

Castaldo, R., D'Auria, L., Pepe, S., Solaro, G., De Novellis, V., and Tizzani, P. (2019). The impact of crustal rheology on natural seismicity: campi Flegrei caldera case study. *Geoscience Frontiers* 10 (2), 453–466. doi:10.1016/j.gsf.2018.02.003

Chiodini, G., Cardellini, C., Di Luccio, F., Selva, J., Frondini, F., Caliro, S., et al. (2020). Correlation between tectonic CO2 Earth degassing and seismicity is revealed by a 10-year record in the Apennines, Italy. *Sci. Adv.* 6 (35), eabc2938. doi:10.1126/sciadv.abc2938

Coppola, D., Laiolo, M., Cigolini, C., Donne, D. D., and Ripepe, M. (2016). Enhanced volcanic hot-spot detection using MODIS IR data: results from the MIROVA system. *Geol. Soc. Lond. Spec. Publ.* 426, 181–205. doi:10.1144/sp426.5

Corti, G. (2004). Centrifuge modelling of the influence of crustal fabrics on the development of transfer zones: insights into the mechanics of continental rifting architecture. *Tectonophysics* 384 (1–4), 191–208. doi:10.1016/j.tecto.2004.03.014

Dawson, J. B., Keller, J., and Nyamweru, C. (1995). "Historic and recent eruptive activity of Oldoinyo Lengai," in *Carbonatite volcanism: Oldoinyo Lengai and the petrogenesis of natrocarbonatites, IAVCEI proc volcanol 4.* Editors K. Bell and J. Keller (Berlin, Germany: Springer), 4–22.

Dawson, J. B. (1992). Neogene tectonics and volcanicity in the north Tanzania sector of the gregory rift valley: contrasts with the Kenya sector. *Tectonophysics* 204, 81–83. doi:10.1016/0040-1951(92)90271-7

de Moor, M., Fischer, T. P., King, P. L., Botcharnikov, R. E., Hervig, R. L., Hilton, D. R., et al. (2013). Volatile-rich silicate melts from Oldoinyo Lengai volcano (Tanzania): implications for carbonatite genesis and eruptive behavior. *Earth Planet Sci. Lett.* 361, 379–390. doi:10.1016/j.epsl.2012.11.006

Dering, M. G., Micklethwaite, S., Cruden, A. R., Barnes, S. J., and Fiorentini, M. L. (2019). Evidence for dyke-parallel shear during syn-intrusion fracturing. *Earth Planet Sci. Lett.* 507, 119–130. doi:10.1016/j.epsl.2018.10.024

Drew, J., White, R. S., Tilmann, F., and Tarasewicz, J. (2013). Coalescence microseismic mapping. *Geophys. J. Int.* 195, 1773–1785. doi:10.1093/gji/ggt331

Ebinger, C., Ayele, A., Keir, D., Rowland, J., Yirgu, G., Wright, T.,, and Hamling, I. (2010). Length and timescales of rift faulting and magma intrusion: the Afar rifting cycle from 2005 to present. *Annu. Rev. Earth Planet Sci.* 38, 439–466. doi:10.1146/annurev-earth-040809-152333

Ebinger, C., and Casey, M. (2001). Continental brekaup in magmatic provinces: an Ethiopian example. *Geology* 29, 527–530. doi:10.1130/0091-7613(2001)029<0527:CBIMPA>2.0.CO;2

Ebinger, C. J., and Sleep, N. H. (1998). Cenozoic magmatism throughout east Africa resulting from impact of a single plume. *Nature* 395 (6704), 788–791. doi:10.1038/27417

El Hariri, M., Abercrombie, M. E., Roweland, C. A., and do Nascimento, A. F. (2010). The role of fluids in triggering earthquakes: observationsfrom reservoir induced seismicity in Brazil. *Geophys. J. Int.* 181 1566–1574.

Fischer, T. P., Burnard, P., Marty, B., Hilton, D. R., Füri, E., Palhol, F., et al. (2009). Upper-mantle volatile chemistry at Oldoinyo Lengai volcano and the origin of carbonatites. *Nature* 459, 77–80. doi:10.1038/nature07977

Foley, S. F., Link, K., Tiberindwa, J. V., and Barifaijo, E. (2012). Patterns and origin of igneous activity around the Tanzanian craton. *J. Afr. Earth Sci.* 62 (1), 1–18. doi:10.1016/j.jafrearsci.2011.10.001

Foster, A., Ebinger, C., Mbede, E., and Rex, D. (1997). Tectonic development of the northern Tanzanian sector of the east African Rift system. *J. Geol. Soc.* 154 (4), 689–700. doi:10.1144/gsjgs.154.4.0689

Gasperini, P., Lolli, B., and Vannucci, G. (2013). Body wave magnitude mb is a good proxy of moment magnitude Mw for small earthquakes (mb < 4.5–5.0). *Seismol. Res. Lett.* 84 (6), 932–937. doi:10.1785/0220130105

Geissler, W. H., Kämpf, H., Kind, R., Bräuer, K., Klinge, K., Plenefisch, T., and Nehybka, V. (2005). Seismic structure and location of a CO_2 source in the upper mantle of the western Eger (Ohře) Rift, central Europe. *Tectonics* 24 (5), 5001. doi:10.1029/2004TC001672

Greenfield, T., White, R. S., Winder, T., and Ágústsdóttir, T. (2018). Seismicity of the Askja and Bárðarbunga volcanic systems of Iceland, 2009–2015. *J. Volcanol. Geoth. Res.* 391, 106432. doi:10.1016/j.jvolgeores.2018.08.010

Gudmundsson, A. (1995). Infrastructure and mechanics of volcanic systems in Iceland. *J. Volcanol. Geoth. Res.* 64 (1-2), 1–22. doi:10.1016/0377-0273(95)92782-Q

Haug, Ø. T., Galland, O., Souloumiac, P., Souche, A., Guldstrand, F., Schmiedel, T., et al. (2018). Shear versus tensile failure mechanisms induced by sill intrusions: implications for emplacement of conical and saucer-shaped intrusions. *J. Geophys. Res.: Solid Earth* 123 (5), 3430–3449. doi:10.1002/2017JB015196

Havskov, J., and Ottemöller, L. (1999). Electronic seismologist. SeisAnEarthquake analysis software. *Seismol. Res. Lett.* 70, 532–534. doi:10.1785/gssrl.70.5.532

Hill, D. P. (1977). A model for earthquake swarms. *J. Geophys. Res.* 82, 1347–1352. doi:10.1029/JB082i008p01347

Hudson, T. S., White, R. S., Greenfield, T., Ágústsdóttir, T., Brisbourne, A., and Green, R. G. (2017). Deep crustal melt plumbing of Bárðarbunga volcano, Iceland. *Geophys. Res. Lett.* 44, 8785–8794. doi:10.1002/2017GL074749

Hunt, J. A., Zafu, A., Mather, T. A., Pyle, D. M., and Barry, P. H. (2017). Spatially variable CO_2 degassing in the main Ethiopian rift: implications for magma storage, volatile transport, and rift-related emissions. *Geochemistry, Geophysics, Geosystems* 18 (10), 3714–3737. doi:10.1002/2017GC006975

Hurst, T., Heise, W., Hreinsdottir, S., and Hamling, I. (2016). Geophysics of the taupo volcanic zone: a review of recent developments. *Geothermics* 59, 188–204. doi:10.1016/j.geothermics.2015.09.008

Hutton, L. K., and Boore, D. M. (1987). The ML scale in southern California. *Bull. Seismol. Soc. Am.* 77, 2074–2094.

Ibs-von Seht, M., Blumenstein, S., Wagner, R., Hollnack, D., and Wohlenberg, J. (2001). Seismicity, seismotectonics and crustal structure of the southern Kenya Rift–new data from the Lake Magadi area. *Geophys. J. Int.* 146(2), 439–453.

Jones, J. R., Stamps, D. S., Wauthier, C., Saria, E., and Biggs, J. (2019). Evidence for slip on a border fault triggered by magmatic processes in an immature continental rift. *Geochemistry, Geophysics, Geosystems* 20 (5), 2515–2530. doi:10.1029/2018GC008165

Kämpf, H., Broge, A. S., Marzban, P., Allahbakhshi, M., and Nickschick, T. (2019). *Nonvolcanic carbon dioxide emission at continental rifts: the bublak mofette area, western eger rift, Czech republic.* London, United Kingdom: Geofluids.

Karakas, O., and Dufek, J. (2015). Melt evolution and residence in extending crust: thermal modeling of the crust and crustal magmas. *Earth Planet Sci. Lett.* 425, 131–144. doi:10.1016/j.epsl.2015.06.001

Karlstrom, L., Dufek, J., and Manga, M. (2009). Organization of volcanic plumbing through magmatic lensing by magma chambers and volcanic loads. *J. Geophys. Res.: Solid Earth* 114 (B10). doi:10.1029/2009JB006339

Karlstrom, L., Dufek, J., and Manga, M. (2010). Magma chamber stability in arc and continental crust. *J. Volcanol. Geother. Res.* 190(2–4), 249–270.

Keir, D., Ebinger, C., Daly, E., Stuart, G., Maguire, P., and Ayele, A. (2006). Strain accommodation by magmatism and faulting as rifting proceeds to breakup: seismicity of the northern Ethiopian rift. *J. Geophys. Res.* 111, B05314. doi:10.1029/2005JB003748

Keller, J., Klaudius, J., Kervyn, M., Ernst, G. G. J., and Mattsson, H. B. (2010). Fundamental changes in the activity of the natrocarbonatite volcano Oldoinyo Lengai, Tanzania. *Bull. Volcanol.* 72, 893–912. doi:10.1007/s00445-010-0371-x

Kervyn, M., Ernst, G. G. J., Keller, J., Vaughan, G., Klaudius, J., Pradal, E., et al. (2010). Fundamental changes in the activity of the natrocarbonatite volcano

Oldoinyo Lengai, Tanzania. II. Eruptive behavior. *Bull. Volcanol.* 72, 913–931. doi:10.1007/s00445-010-0360-0

Kervyn, M., Ernst, G. G. J., van Wyk de Vries, B., Mathieu, L., and Jacobs, P. (2009). Volcano load control on dyke propagation and vent distribution: insights from analogue modeling. *J. Geophys. Res.: Solid Earth* 114 (B3), B005653. doi:10.1029/2008JB005653

Klaudius, J., and Keller, J. (2006). Peralkaline silicate lavas at Oldoinyo Lengai, Tanzania. *Lithos.* 91, 173–190. doi:10.1016/j.lithos.2006.03.017

Lambotte, S., Lyon-Caen, H., Bernard, P., Deschamps, A., Patau, G., Nercessian, A.,, and Adamova, P. (2014). Reassessment of the rifting process in the Western Corinth Rift from relocated seismicity. *Geophys. J. Int.* 197 (3), 1822–1844. doi:10.1093/gji/ggu096

Langston, C. A., Brazier, R., Nyblade, A. A., and Owens, T. J. (1998). Local magnitude scale and seismicity rate for Tanzania, East Africa. *Bull. Seismol. Soc. Am.* 88, 712–721.

Le Gall, B., Nonnotte, P., Rolet, J., Benoit, M., Guillou, H., Mousseau-Nonnotte, M., et al. (2008). Rift propagation at craton margin. Distribution of faulting and volcanism in the North Tanzanian Divergence (East Africa) during Neogene times. *Tectonophysics* 448, 1–19. doi:10.1016/j.tecto.2007.11.005

Lee, H., Fischer, T. P., Muirhead, J. D., Ebinger, C. J., Kattenhorn, S. A., Sharp, Z. D., et al. (2017). Incipient rifting accompanied by the release of subcontinental lithospheric mantle volatiles in the Magadi and Natron basin, East Africa. *J. Volcanol. Geoth. Res.* 346, 118–133. doi:10.1016/j.jvolgeores.2017.03.017

Lee, H., Muirhead, J. D., Fischer, T. P., Ebinger, C. J., Kattenhorn, S. A., Sharp, Z. D., et al. (2016). Massive and prolonged deep carbon emissions associated with continental rifting. *Nat. Geosci.* 9 (2), 145–149. doi:10.1038/NGEO2622

Lienert, B. R. E., and Havskov, J. (1995). A computer program for locating earthquakes both locally and globally. *Seismol. Res. Lett.* 66, 26–36.

Lindenfeld, M., Rümpker, G., Batte, A., and Schumann, A. (2012a). Seismicity from february 2006 to september 2007 at the Rwenzori mountains, East African rift: earthquake distribution, magnitudes and source mechanisms. *Solid Earth* 3, 251–264. doi:10.5194/se-3-251-2012

Lindenfeld, M., Rümpker, G., Link, K., Koehn, D., and Batte, A. (2012b). Fluid-triggered earthquake swarms in the Rwenzori region, East African rift—evidence for rift initiation. *Tectonophysics* 566, 95–104. doi:10.1016/j.tecto.2012.07.010

Lomax, A., Virieux, J., Volant, P., and Berge-Thierry, C. (2000). "Probabilistic earthquake location in 3D and layered models," in *Advances in seismic event location. Modern approaches in geophysics.* Editors C. Thurber and N. Rabinowitz (Dordrecht, Netherlands: Springer), 18, 101–134. doi:10.1007/978-94-015-9536-0_5

Maccaferri, F., Rivalta, E., Keir, D., and Acocella, V. (2014). O-rift volcanism in rift zones determined by crustal unloading. *Nature* 7 (4), 297300. doi:10.1038/NGEO2110

Mana, S., Furman, T., Carr, M. J., Mollel, G. F., Mortlock, R. A., Feigenson, M. D., et al. (2012). Geochronology and geochemistry of the Essimingor volcano: melting of metasomatized lithospheric mantle beneath the North Tanzanian Divergence zone (East African Rift). *Lithos.* 155, 310–325. doi:10.1016/j.lithos.2012.09.009

Mana, S., Furman, T., Turrin, B. D., Feigenson, M. D., and Swisher, C. C. (2015). Magmatic activity across the east african north Tanzanian divergence zone. *J. Geol. Soc.* 172, 368. doi:10.1144/jgs2014-072

Marzen, R. E., Shillington, D. J., Lizarralde, D., Knapp, J. H., Heffner, D. M., Davis, J. K., et al. (2020). Limited and localized magmatism in the central atlantic magmatic province. *Nat. Commun.* 11 (1), 3397–3398. doi:10.1038/s41467-020-17193-6

Massimetti, F., Coppola, D., Laiolo, M., Valade, S., Cigolini, C., and Ripepe, M. (2020). Volcanic hot-spot detection using SENTINEL-2: a comparison with MODIS–MIROVA thermal data series. *Rem. Sens.* 12, 820. doi:10.14279/depositonce-10003

McNutt, S. R. (2005). Volcanic seismology. *Annu. Rev. Earth Planet Sci.* 32, 461–491. doi:10.1146/annurev.Earth.33.092203.122459

Mirova (2020). Near real time volcanic hotspot detection system. Available at: http://www.mirovaweb.it (Accessed September 22, 2020).

Mollex, G., Füri, E., Burnard, P., Zimmermann, L., Chazot, G., Kazimoto, E. O., et al. (2018). Tracing helium isotope compositions from mantle source to fumaroles at Oldoinyo Lengai volcano, Tanzania. *Chem. Geol.* 480, 66–74. doi:10.1016/j.chemgeo.2017.08.015

Moore, D. E., and Rymer, M. J. (2007). Talc-bearing serpentinite and the creeping section of the San Andreas fault. *Nature* 448 (7155), 795–797. doi:10.1038/nature06064

Muirhead, J. D., Fischer, T. P., Oliva, S. J., Laizer, A., van Wijk, J., Currie, C. A., et al. (2020). Displaced cratonic mantle concentrates deep carbon during continental rifting. *Nature* 582 (7810), 67–72. doi:10.1038/s41586-020-2328-3

Muirhead, J. D., Kattenhorn, S. A., and Le Corvec, N. (2015). Varying styles of magmatic strain accommodation across the East African Rift. *Geochem. Geophys. Geosyst.* 16, 2. doi:10.1002/2015GC005918

Muirhead, J. D., Kattenhorn, S. A., Lee, H., Mana, S., Turrin, B. D., Fischer, T. P., et al. (2016). Evolution of upper crustal faulting assisted by magmatic volatile release during early-stage continental rift development in the East African Rift. *Geosphere* 12 (6), 1670–1700. doi:10.1130/GES01375.1

Nakai, J. S., Sheehan, A. F., and Bilek, S. L. (2017). Seismicity of the rocky mountains and Rio Grande Rift from the EarthScope Transportable Array and CREST temporary seismic networks, 2008–2010. *J. Geophys. Res.: Solid Earth* 122 (3), 2173–2192. doi:10.1002/2016JB013389

Oliva, S. J. C., Ebinger, C. J., Rivalta, E., Wauthier, C., Williams, C. A., Jr., and Currie, C. A. (2019b). "State-of-stress and stress rotations: quantifying the role of surface topography and subsurface density contrasts in magmatic rift zones (Eastern Rift, Africa)," in AGU Fall Meeting, San Francisco, CA, October, 2019. [Abstract].

Oliva, S. J., Ebinger, C. J., Wauthier, C., Muirhead, J. D., Roecker, S. W., Rivalta, E., et al. (2019a). Insights into fault-magma interactions in an early-stage continental rift from source mechanisms and correlated volcano-tectonic earthquakes. *Geophys. Res. Lett.* 46 (4), 2065–2074. doi:10.1029/2018GL080866

Pagli, C., Wright, T. J., Ebinger, C. J., Yun, S. H., Cann, J. R., Barnie, T., et al. (2012). Shallow axial magma chamber at the slow-spreading Erta Ale Ridge. *Nat. Geosci.* 5 (4), 284–288. doi:10.1038/ngeo1414

Pagli, C., Yun, S. H., Ebinger, C., Keir, D., and Wang, H. (2019). Strike-slip tectonics during rift linkage. *Geology* 47 (1), 31–34. doi:10.1130/G45345.1

Parisio, F., Vinciguerra, S., Kolditz, O., and Nagel, T. (2019). The brittle-ductile transition in active volcanoes. *Sci. Rep.* 9, 143. doi:10.1038/s41598-018-36505-x

Petibon, C. M., Kjarsgaard, B. A., Jenner, G. A., and Jackson, S. E. (1998). Phase relationships of a silicate-bearing natrocarbonatite from Oldoinyo Lengai at 20 and 100 MPa. *J. Petrol.* 39, 2137–2151. doi:10.1093/petroj/39.11-12.2137

Plasman, M., Tiberi, C., Ebinger, C., Gautier, S., Albaric, J., Peyrat, S., et al. (2017). Lithospheric low-velocity zones associated with a magmatic segment of the Tanzanian Rift, East Africa. *Geophys. J. Int.* 210(1), 465–481.

Reyners, M., Eberhart-Phillips, D., and Stuart, G. (2007). The role of fluids in lower-crustal earthquakes near continental rifts. *Nature* 446 (7139), 1075–1078. doi:10.1038/nature05743

Roecker, S., Ebinger, C., Tiberi, C., Mulibo, G., Wambura, F., Mtelela, K., et al. (2017). Subsurface images of the Eastern Rift, Africa, from the joint inversion of body waves, surface waves and gravity: investigating the role of fluids in early-stage continental rifting. *Geophys. J. Int.* 210 (2), 931–950. doi:10.1093/gji/ggx220

Roman, A., and Jaupart, C. (2014). The impact of a volcanic edifice on intrusive and eruptive activity. *Earth Planet Sci. Lett.* 408, 1–8. doi:10.1016/j.epsl.2014.09.016

Roman, D. C. (2005). Numerical models of volcanotectonic earthquake triggering on non-ideally oriented faults. *Geophys. Res. Lett.* 32, L02304. doi:10.1029/2004GL021549

Rooney, O. T., Lavigne, A., Svoboda, C., Girard, G., Yirgu, G., Ayalew, D., et al. (2017). The making of an underplate: pyroxenites from the Ethiopian lithosphere. *Chem. Geol.* 455, 264–281. doi:10.1016/j.chemgeo.2016.09.011

Rooney, T. O., Bastow, I. D., Keir, D., Mazzarini, F., Movsesian, E., Grosfils, E. B., et al. (2014). The protracted development of focused magmatic intrusion during continental rifting. *Tectonics* 33 (6), 875–897. doi:10.1002/2013TC003514

Rooney, T. O. (2010). Geochemical evidence of lithospheric thinning in the southern Main Ethiopian Rift. *Lithos.* 117 (1–4), 33–48. doi:10.1016/j.lithos.2010.02.002

Rowland, J. V., Baker, E., Ebinger, C. J., Keir, D., Kidane, T., Biggs, J., et al. (2007). Fault growth at a nascent slow-spreading ridge: 2005 Dabbahu rifting episode, Afar. *Geophys. J. Int.* 171 (3), 1226–1246. doi:10.1111/j.1365-246X.2007.03584.x

Rubin, A. M., and Pollard, D. D. (1988). Dike-induced faulting in rift zones of Iceland and Afar. *Geology* 16 (5), 413–417. doi:10.1130/0091-7613(1988)016<0413:DIFIRZ>2.3.CO;2

Saria, E., Calais, E., Stamps, D. S., Delvaux, D., and Hartnady, C. J. H. (2014). Present-day kinematics of the east African Rift. *J. Geophys. Res.: Solid Earth* 119 (4), 3584–3600. doi:10.1002/2013JB010901

Sherrod, D. R., Magigita, M. M., and Kwelwa, S. (2013). Geologic map of oldonyo Lengai (Oldoinyo Lengai) and surroundings, arusha region, United Republic of Tanzania. *U.S. Geol. Surv. Rep.* 1306, 65. doi:10.3133/OFR20131306

Sibson, R. H. (2000). Fluid involvement in normal faulting. *J. Geodyn.* 29 (3–5), 469–499. doi:10.1016/S0264-3707(99)00042-3

Snoke, J. A., Munsey, J. W., Teague, A. C., and Bollinger, G. A. (1984). A program for focal mechanism determination by combined use of polarity and SV-P amplitude ratio data. *Earthq. Notes.* 55, 51.

Thurber, C. H. (1984). Seismic detection of the summit magma complex of kilauea volcano, Hawaii. *Science* 223 (4632), 165–167. doi:10.1126/science.223.4632.165

Thybo, H., and Nielsen, C. A. (2009). Magma-compensated crustal thinning in continental rift zones. *Nature* 457 (7231), 873–876. doi:10.1038/nature07688

Thybo, H., and Artemieva, I. M. (2013). Moho and magmatic underplating in continental lithosphere. *Tectonophysics* 609, 605–619. doi:10.1016/j.tecto.2013.05.032

Trippanera, D., Ruch, J., Passone, L., and Jónsson, S. (2019). Structural mapping of dike-induced faulting in Harrat Lunayyir (Saudi Arabia) by using high resolution drone imagery. *Front. Earth Sci.* 7, 168. doi:10.3389/feart.2019.00168

Urhammer, R. A. (1982). The optimal estimation of earthquake parameters. *Phys. Earth Planet. In.* 4, 1369–1379. doi:10.1016/0031-9201(82)90095-4

Watanabe, T., Koyaguchi, T., and Seno, T. (1999). Tectonic stress controls on ascent and emplacement of magmas. *J. Volcanol. Geoth. Res.* 91 (1), 65–78. doi:10.1016/S0377-0273(99)00054-2

Wauthier, C., Cayol, V., Poland, M., Kervyn, F., d'Oreye, N., Hooper, A., and Smets, B. (2013). Nyamulagira's magma plumbing system inferred from 15 years of InSAR. *Geol. Soc. Spec. Publ.* 380 (1), 39–65. doi:10.1144/SP380.9

Wauthier, C., Smets, B., and Keir, D. (2015). Diking-induced moderate-magnitude earthquakes on a youthful rift border fault: the 2002 Nyiragongo-Kalehe sequence, DR Congo. *Geochemistry, Geophysics, Geosystems* 16 (12), 4280–4291. doi:10.1002/2015GC006110

Weinlich, F. H., Bräuer, K., Kämpf, H., Strauch, G., Tesař, J., and Weise, S. M. (1999). An active subcontinental mantle volatile system in the western Eger rift, Central Europe: gas flux, isotopic (He, C, and N) and compositional fingerprints. *Geochem. Cosmochim. Acta* 63 (21), 3653–3671.

Weinstein, A., Oliva, S. J., Ebinger, C. J., Roecker, S., and Tiberi, C. (2017). Fault-magma interactions during early continental rifting: seismicity of the Magadi-Natron-Manyara basins, Africa. *Geochem. Geophys. Geosyst.* 18 (10), 3662–3686. doi:10.1002/2017GC007027

White, R., and McKenzie, D. (1989). Magmatism at rift zones: the generation of volcanic continental margins and flood basalts. *J. Geophys. Res.: Solid Earth* 94 (B6), 7685–7729. doi:10.1029/JB094iB06p07685

Woessner, J., and Wiemer, S. (2005). Assessing the quality of earthquake catalogues: estimating the magnitude of completeness and its uncertainty. *Bull. Seismol. Soc. Am.* 95 (2), 684–698. doi:10.1785/0120040007

Wright, T. J., Ebinger, C., Biggs, J., Ayele, A., Yirgu, G., Keir, D., et al. (2006). Magma-maintained rift segmentation at continental rupture in the 2005 Afar dyking episode. *Nature* 442 (7100), 291–294. doi:10.1038/nature04978

Wright, T. J., Sigmundsson, F., Pagli, C., Belachew, M., Hamling, I. J., Brandsdóttir, B.,, and Einarsson, P. (2012). Geophysical constraints on the dynamics of spreading centres from rifting episodes on land. *Nat. Geosci.* 5 (4), 242–250. doi:10.1038/ngeo1428

Conflict of Interest: The authors declare that the research was conducted in the absence of any commercial or financial relationships that could be construed as a potential conflict of interest.

Copyright © 2021 Reiss, Muirhead, Laizer, Link, Kazimoto, Ebinger and Rümpker. This is an open-access article distributed under the terms of the Creative Commons Attribution License (CC BY). The use, distribution or reproduction in other forums is permitted, provided the original author(s) and the copyright owner(s) are credited and that the original publication in this journal is cited, in accordance with accepted academic practice. No use, distribution or reproduction is permitted which does not comply with these terms.

frontiers in Earth Science

ORIGINAL RESEARCH
published: 26 February 2021
doi: 10.3389/feart.2020.603441

Source Mechanism of Seismic Explosion Signals at Santiaguito Volcano, Guatemala: New Insights From Seismic Analysis and Numerical Modeling

Alicia Rohnacher[1], Andreas Rietbrock[1], Ellen Gottschämmer[1], William Carter[2], Yan Lavallée[2], Silvio De Angelis[2], Jackie E. Kendrick[2,3] and Gustavo Chigna[4]*

[1]Geophysical Institute, Department of Physics, Karlsruhe Institute of Technology, Karlsruhe, Germany, [2]Department of Earth, Ocean and Ecological Studies, University of Liverpool, Liverpool, United Kingdom, [3]School of Geosciences, University of Edinburgh, Edinburgh, United Kingdom, [4]Instituto Nacional de Sismología, Vulcanología, Meteorología e Hidrología (INSIVUMEH), Guatemala City, Guatemala

OPEN ACCESS

Edited by:
Derek Keir,
University of Southampton,
United Kingdom

Reviewed by:
Tim Greenfield,
University of Cambridge,
United Kingdom
Jacob Anderson,
Boise State University, United States

***Correspondence:**
Alicia Rohnacher
alicia@rohnacher.de

Specialty section:
This article was submitted to Volcanology, a section of the journal Frontiers in Earth Science

Received: 06 September 2020
Accepted: 24 December 2020
Published: 26 February 2021

Citation:
Rohnacher A, Rietbrock A, Gottschämmer E, Carter W, Lavallée Y, De Angelis S, Kendrick JE and Chigna G (2021) Source Mechanism of Seismic Explosion Signals at Santiaguito Volcano, Guatemala: New Insights From Seismic Analysis and Numerical Modeling. Front. Earth Sci. 8:603441. doi: 10.3389/feart.2020.603441

Volcanic activity at the Santiaguito dome complex (Guatemala) is characterized by lava extrusion interspersed with small, regular, gas-and-ash explosions that are believed to result from shallow magma fragmentation; yet, their triggering mechanisms remain debated. Given that the understanding of source processes at volcanoes is essential to risk assessments of future eruptions, this study seeks to shed light on those processes. We use data from a permanent seismic and infrasound network at Santiaguito volcano, Guatemala, established in 2018 and additional temporary stations, including a seismic array deployed during a 13-day field investigation in January 2019 to analyze and resolve the source characteristics of fragmentation leading to gas-and-ash explosions. Seismic data gathered within a distance of 4.5 km from the vent show a weak seismic signal 2–6 s prior to the explosions and associated main seismic signal. To resolve the source location and origin of the seismic signals, we first used ambient noise analysis to assess seismic velocities in the subsurface and then used two-dimensional spectral element modeling (SPECFEM2D) to simulate seismic waveforms. The analyzed data revealed a two-layer structure beneath the array, with a shallow, low-velocity layer (v_S = 650 m/s) above deeper, high-velocity rocks (v_S = 2,650 m/s). Using this velocity structure, possible source mechanisms and depths were constrained using array and particle motion analyses. The comparison of simulated and observed seismic data indicated that the precursory signal is associated with particle motion in the RZ-plane, pointing toward the opening of tensile cracks at a depth of ~600 m below the summit; in contrast, the main signal is accompanied by a vertical single force, originating at a shallow depth of about ~200 m. This suggests that the volcanic explosions at Santiaguito are following a bottom-up process in which tensile fractures develop at depth and enable rapid gas rise which leads to the subsequent explosion. The result indicates that explosions at Santiaguito do not occur from a single source location, but from a series of processes possibly associated with magma rupture, gas channeling and accumulation, and fragmentation. Our study

provides a good foundation for further investigations at Santiaguito and shows the value of comparing seismic observations with synthetic data calculated for complex media to investigate in detail the processes leading up to gas-ash-rich explosions found at various other volcanoes worldwide.

Keywords: volcanic explosions, volcano seismology, numerical modeling, seismic precursor, seismo-acoustic array, array analysis

INTRODUCTION

The Santiaguito dome complex is located in western Guatemala, 10 km southwest of the city of Quetzaltenango, counting approximately one million inhabitants emphasizing the importance of a good understanding of eruption processes. Protracted dome growth began in 1922, within the crater of the eruption of Santa Maria in 1902, and continues to this day (Rose, 1973; Harris et al., 2003). Volcanic activity shifted westward over the next five decades forming four domes (from east to west: El Caliente, La Mitad, El Monje and El Brujo). However, in 1977, activity resumed at El Caliente (Rose, 1987). Since then, dacitic-andesitic lava dome growth has been accompanied by lava flows (A'a and blocky flows), explosions (incl. ash clouds and fallout, ballistics and pyroclastic density currents), rock falls, sector collapse events and lahars, each of contrasting and evolving magnitudes throughout the years (Rose, 1987; Rhodes et al., 2018; Lamb et al., 2019; Carter et al., 2020). Harris et al., (2003) characterized the cyclic discharge at Santiaguito since the start of the eruption in 1922, describing periods of high and low extrusion rates lasting for 3–6 and 3–11 years, respectively. While weak to moderate gas-and-ash explosions generating 500–2000 m high plumes, have been observed in every period prior to 2015 (Bluth and Rose, 2004; Patrick et al., 2007; De Angelis et al., 2016), larger explosive events have occurred less frequently, either related to partial dome or crater rim collapse (e.g. September 2004, April 2010, November 2012; Global Volcanism Program, 2005, Global Volcanism Program, 2011; Hornby et al., 2019a) or to paroxysms due to volatile-rich magma influx (e.g., in 2015–16; Wallace et al., 2020). The larger explosions, which have subsequently excavated a deep crater in the dome, indicate deeper fragmentation (Hornby et al., 2019b; Lamb et al., 2019; Carter et al., 2020; Wallace et al., 2020). Following this last paroxysm, dome growth resumed in October 2016, as lava started to fill the crater and activity reverted back to frequent weak/moderate explosions (Carter et al., 2020).

The occurrence of gas-and-ash explosions at El Caliente has long been studied. A key observation of dome activity is the repetitive and non-destructive occurrence of explosions as well as near continuous gas emissions during inter-explosive phases, which suggest an open vent system bolstered by an active fault network (Bluth and Rose, 2004; Holland et al., 2011; Johnson et al., 2014; Scharff et al., 2014; Zorn et al., 2020). Explosions at El Caliente are often preceded by seismic precursors with signals spanning broad frequency and duration ranges. This behavior was noted in the dome activity before (Johnson et al., 2009; Sanderson et al., 2010) and after (Carter et al., 2020) the 2015–16 paroxysms. Bluth and Rose (2004) suggested that pulsatory magma ascent leads to plug flow, and stick-slip faulting induces cataclastic fragmentation, thus increasing the propensity of magma to degas and outgas. This model may explain the ring-shaped fractures sometimes observed on the crater surface (Bluth and Rose, 2004; Sahetapy-Engel et al., 2008; Lavallée et al., 2015; von Aulock et al., 2016; Hornby et al., 2019b; Zorn et al., 2020). The faulting activity has also been inferred to explain the occurrence of gas-and-ash ejection pulses every ~3 s during explosions (Scharff et al., 2014).

Combined thermic, seismic, and infrasound observations were used by Sahetapy-Engel et al., (2008) to constrain the extent of the plug. They suggested that the rupture occurred at a depth of 100–500 m. This is supported by Holland et al., (2011) who analyzed the rheology of eruptive products and advanced that critical conditions for shear fracturing are found at depths of 150–600 m. Analysis of proximal tilt data monitored in January 2012 from the flank of El Caliente indicated that the dome periodically inflates and deflates at intervals averaging 26 min (Johnson et al., 2014). The inflation phase generally lasts about 5–6 min and at the apex of tilt signals, an explosion or a gas emission event occurs. They observed that the explosions, in contrast to the emissions, generated very-long period (VLP) seismicity. Yet, noting that the inflation phases of the tilt cycles are not accompanied by seismicity, Johnson et al., (2014) suggested that they may be caused by gas pressurization in the shallow conduit at a depth estimated at 300 m below the active vent. Lavallée et al., (2015) scrutinized the dataset to reveal that tilt cycles associated with gas-and-ash explosions differ from those causing gas emission events. They base their results on the observation of more pronounced positive tilt (inflation) as well as the occurrence of VLP seismicity coincident with explosions. Following the observation that different inflation rates may lead to different styles of activity, Hornby et al., (2019b) used laboratory experiments to assess the manner in which Santiaguito lava ruptures. They constrained that low deformation rates (as observed during moderate tilt cycles) would cause slow, pervasive rupture which is argued would favor prolonged and extensive outgassing. In contrast, they found that at higher deformation rates (as observed in more pronounced tilt cycles) rupture would be sudden and localized, preventing extensive outgassing prior to complete rupture. This behavior may contribute to building excess pore pressure for fragmentation and to driving the explosions.

Looking closer at the eruptive products Lavallée et al., (2015) observed pseudotachylyte, indicating that magma was subjected to frictional melting and thermal vesiculation upon fragmentation. They argued that this would be favored during slip along localized fractures, which has been previously

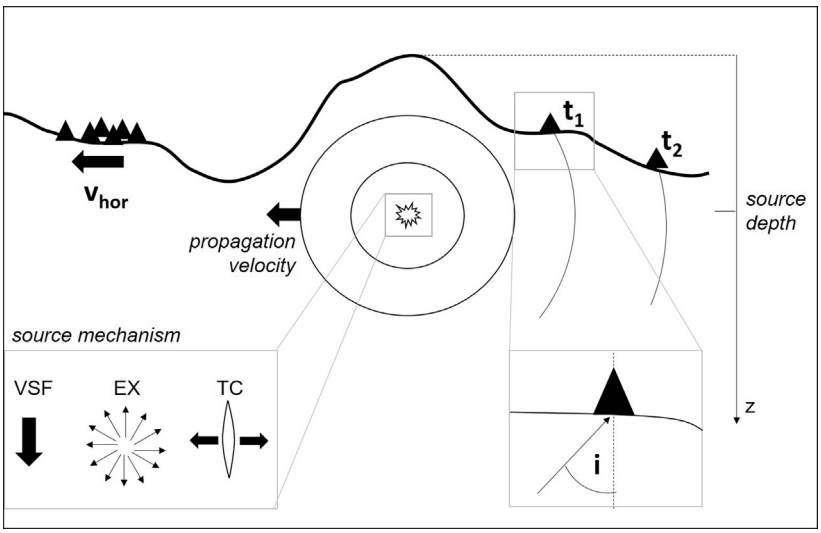

FIGURE 1 | Summary of observations (bold) used to determine source properties (italic). The observed arrival times t_j and the horizontal velocity v_{hor} (slowness) are used to estimate the propagation velocity in the subsurface. The results of numerical modeling of seismic wave propagation are then compared to the observations (including the particle motion with incident angle i) to get information about the dominant source mechanism and source depth. VSF: vertical single force; EX: explosion source; TC: tensile crack.

constrained by Johnson et al., (2008) to reach ~1 m/s. This finding is related to their observation that the dome can move up and down, like a piston, by as much as 0.5 m within 1 s. The mechanical work during such faulting activity could induce as much as 600°C of heat in the already hot magmas, causing melting and vesiculation, which may partly explain the cataclastic affinity of these dense pyroclasts (Hornby et al., 2019a). Recently, structure-from-motion analysis using photogrammetry was employed by Zorn et al., (2020) to constrain surface deformation at El Caliente, finding that deformation varies laterally and zones with increased inflation may not necessarily be related to hotter materials. Furthermore, the explosive gas bursts and the permanent weak gas rise can, at times, escape from a given set of fractures (von Aulock et al., 2016; Zorn et al., 2020). This indicates that fracture healing is likely trivial during inter-explosion phases, owing to the crystal-rich nature of the magma (cf. Kendrick et al., 2016; Lamur et al., 2019). The open nature of the fracture network to fluid flow at El Caliente is further supported by the fact that some small-to-moderate explosions can be rapidly followed (within <10 min) by a secondary event (though generally smaller in magnitude) with closely matching seismic and acoustic signatures (Carter et al., 2020). This is likely to result from identical source parameters, possible if the set of fractures employed by gas-and ash jets remains the same. The above studies propose potentially slightly contrasting explosion trigger mechanisms which leads to small discrepancies when attempting to reconcile observations and unify our interpretations, but this may simply reflect that information was collected during different periods and with different methods. Altogether, they all argue for the importance of seismogenic faulting driven by overpressure at shallow depth, associated with gas-and-ash explosions.

In order to get more information on the trigger mechanism of explosions at Santiaguito, we will analyze the precursory seismic signals that are observed before ash and gas break through the dome's surface. We first use signal arrival times at different stations and ambient noise analysis to estimate the propagation velocity in the subsurface, and then use seismic travel times, particle motion and array analysis to determine possible source mechanisms and depths for the explosions (see **Figure 1**). Due to strong topographic changes in volcanic environments as well as the short distances between stations and the source, the interpretation of seismic signals is often challenging (Neuberg and Pointer, 2000); as such we augment our investigation by comparing observations with synthetic 2D spectral element modeling.

DATASETS

Since 2014 a joint collaboration between the University of Liverpool (UK) and the Karlsruhe Institute of Technology (Germany) established a network of seismo-acoustic instruments monitoring activity at the Santiaguito dome complex. These permanent stations (**Figure 2**, STG1-X) and information about the network have previously been reported by Lamb et al., (2019), Carter et al., (2020) and Gottschämmer et al., (2020). In addition to this large dataset, we augmented our monitoring capacity during a 13-days field experiment by deploying three additional temporary short period (LE-3Dlite) stations (**Figure 2**, LIN1-3) and a seismo-acoustic array in January 2019 (**Figure 2**). The temporary deployment also included six pressure sensors (IST 2018, sensitivity: 0.02 V/Pa) and coincided with the installation of a permanent

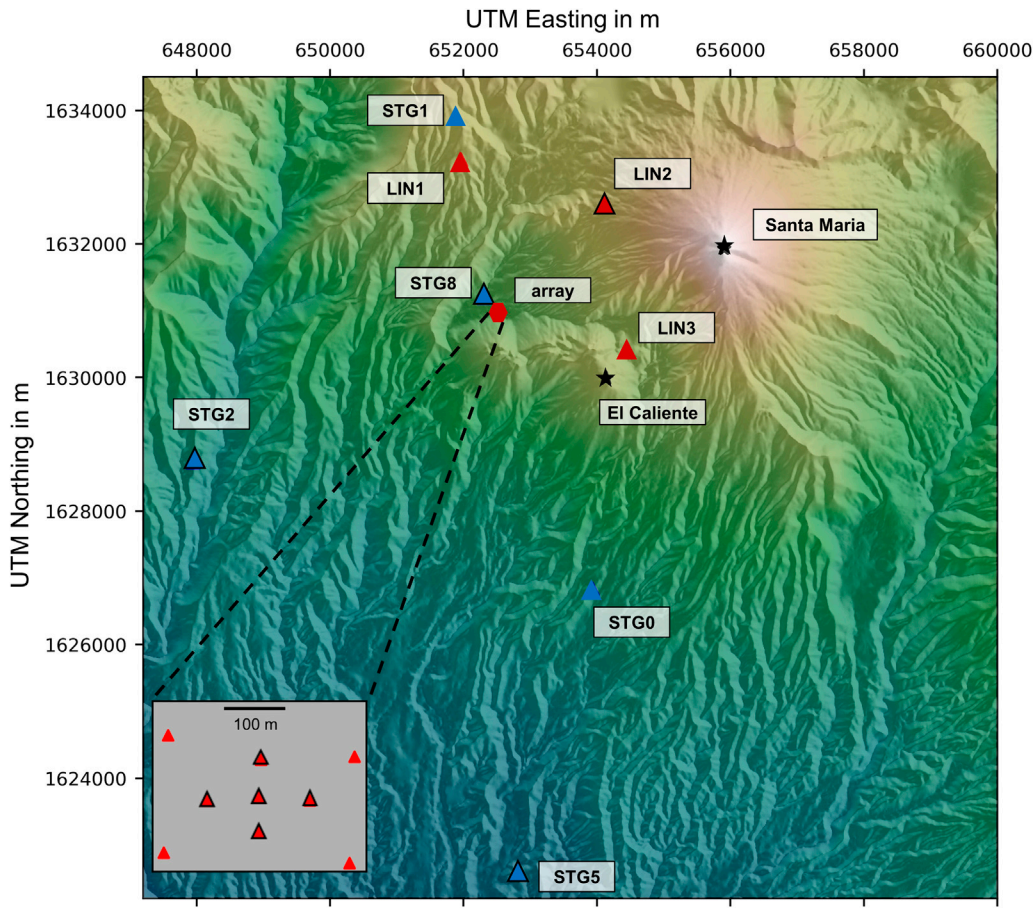

FIGURE 2 | Station distribution during the field measurements in January 2019. Blue triangles mark the stations of the permanent network of ULIV (University of Liverpool) and KIT (Karlsruhe Institute of Technology), and red triangles are stations installed temporarily. Black contour lines around the triangles indicate the additional installation of an infrasound sensor. The red hexagon marks the position of the seismo-acoustic array (also inset, lower left). The thermal camera was installed at station STG5. The peaks of Santa Maria and El Caliente are marked with black stars.

thermographic camera installed at station STG5 (7 km from El Caliente; **Figure 2**). During the field investigation, one thermographic image per second was acquired during both daytime and night time. One further seismic station was deployed 510 m north-east of the El Caliente dome to provide signals with good signal-to-noise ratio (LIN3). The other short-period stations were installed 2,600 m north (LIN2) and 3,900 m northwest (LIN1) of the dome. A list of all stations with information on location and sensors is available in the **Supplementary Table S1**. The challenging terrain east of the dome complex did not allow any installations in this area. The location of the seismo-acoustic array is in a crescent-shaped valley north of the previously active dome El Brujo at a distance of 2 km to the active crater. The valley dips slightly toward the west, but elevation differences of the stations are still less than 40 m. The subsurface is characterized by a lahar deposit veneer in the valley, underlain by dense, coherent lavas, which has been shown to favor good signal propagation in this area during previous campaigns. As illustrated in **Figure 2**, the seismo-acoustic array consists of nine short-period stations and five pressure sensors. The stations form two nested rectangles with a central station and the inner rectangle is rotated ~45° to the outer one. Pressure sensors are only deployed in the inner part of the array. inter-station distances of the seismo-acoustic array range from 50–160 m with an aperture of 360 m.

A comparison of the seismic explosion signals at a broadband (Trillium Compact 120 s) seismometer and the array seismometer (Lennartz 1 Hz) reveals that the short period instruments show reliable ground motion at frequencies below the corner frequency of the passband after restitution down to 0.1 Hz. All instruments recorded with a sampling rate of 100 Hz.

CHARACTERISTICS OF THE EXPLOSION SIGNAL

Explosive gas and ash emissions at Santiaguito occur multiple times per day and are commonly accompanied by seismic and infrasonic signals. Typical explosion signals at the closest stations are shown in **Figure 3**. The seismic signature generally consists of

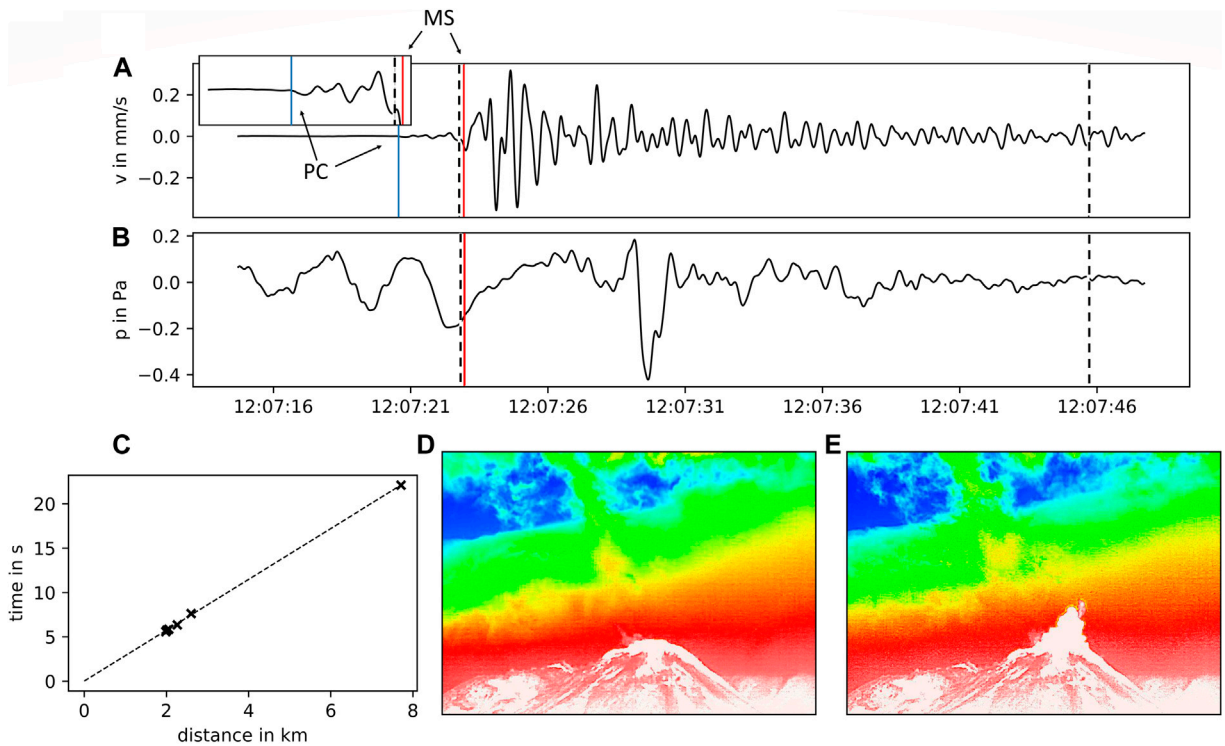

FIGURE 3 | Comparison of acoustic origin time with visual observations of an explosion on 10.01.19. **(A)** Z-component of seismic signal at LIN3 with enlarged precursor signal (PC) in the inset. The blue vertical line indicates the precursor onset, whereas the main signal (MS) starts directly at the red line. **(B)** Associated acoustic signal measured at the central array station. Acoustic and seismic data is filtered with a fourth-order Butterworth bandpass (0.125–3 Hz). In **(A)** and **(B)** the red lines indicate the origin time of the acoustic signal and the dashed lines correspond to the thermographic images in **(D)** and **(E)**, respectively. **(C)** Acoustic arrival times at different stations vs. their distance to the crater determining the acoustic origin time. The two thermographic images show the first gas emission at the dome (12:07:22, **(D)**) and the further gas rise (12:07:45, **(E)**).

two phases with a time shift of 2–6 s at a distance of 510 m to the crater (**Figure 3**). Hereinafter, the second phase, characterized by higher amplitudes will be referred to as the main signal (MS), while the first phase will be called precursor (PC). Due to the low amplitudes of the PC, its detectability in the seismogram decreases with the distance and it is often not visible at stations which are further than 4.5 km from the lava dome. The frequency of the explosion signal ranges between 0.5 Hz and 5 Hz and reaches its maximum at around 1.3–1.7 Hz (**Supplementary Figure S1**). In **Figure 3**, the comparison of seismic data to visual observations with the thermographic camera reveals that increased ground motion is only related to the onset of hot gas and ash expulsion, while the further outflow and development of the plume occurs mainly aseismically as described by Gottschämmer et al., (2020). As previous studies have reported that small explosions at Santiaguito are preceded by a ~6 min inflation of the dome (Johnson et al., 2014; Lavallée et al., 2015), we opted to calculate the mean absolute amplitude of the ground motion at the closest station LIN3 in a sliding window of 1 min. We find no significant increase in seismicity before an explosion which could be connected to the inflation process.

To enable correlation between the development of the volcanic plume and seismicity, we constrained the exact onset time using acoustic signals. Following De Angelis et al., (2016), we assume the dome surface to be the acoustic source position and calculate its origin time with a linear fit regarding hypocentral distance and arrival time at the pressure sensors, as shown in **Figure 3C**. Indeed, the origin time of the acoustic signal (red vertical line, **Figure 3**) coincides with the visual onset (first dashed line) of the explosion; therefore, the acoustic signal may be related directly to

TABLE 1 | Summary of seismic observations.

	Precursor (PC)	Main phase (MS)
Velocity in km/s	1.2–1.9	2.7–4
Slowness (onset) in s/km	0.1–0.2	0.1–0.2
Particle motion in ° to vertical	30–70	~0
Time lag between seismic and acoustic origin time (at LIN3)	−2 to −6 s	<0.5 s

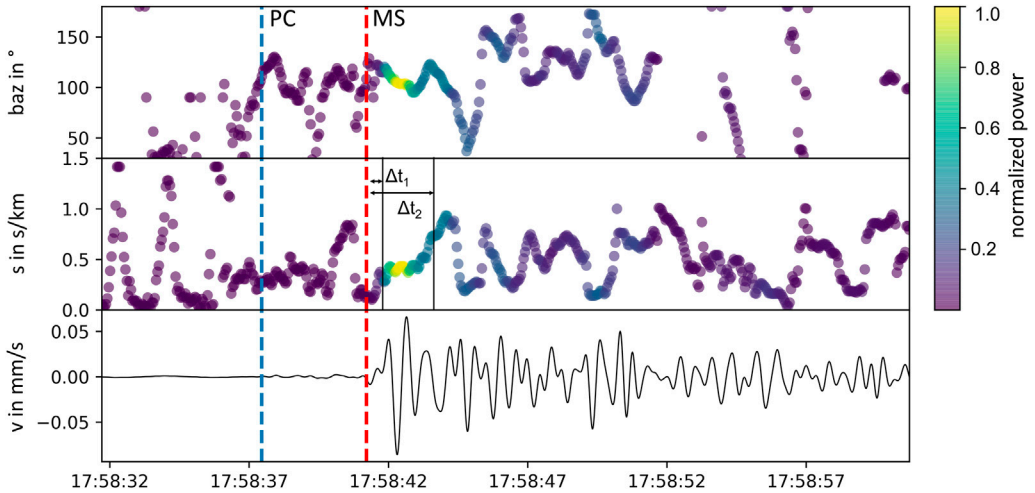

FIGURE 4 | Slowness (s) and backazimuth (baz) of a seismic explosion signal measured with the seismic array in a distance of 2 km to the dome on 7.1.19. The blue and the red dashed lines indicate the onset of PC and MS, respectively. The color code of the slowness and baz corresponds to the normalized power of the seismic signal shown below. Δt_1 = 0.5 s and Δt_2 = 2.5 s show the time difference of MS onset and slowness steps.

the sudden gas burst associated with the onset of the volcanic plume. Furthermore, we observe only a short time difference (of only <0.5 s, **Table 1**) between the acoustic origin time and arrival of the MS at the most proximal station LIN3.

We further estimate the seismic velocities of PC and MS of 14 explosions (**Supplementary Table S2**), carry out array analysis and determine the particle motion in order to collect more information about possible source depths and mechanisms. With the relative origin times of both phases we further determine whether they are the result of P- and S-wave arrivals of the same source process or caused by independent source mechanisms. In the latter case the PC could provide information about a mechanism triggering the explosion.

Slowness and Backazimuth

We use the frequency-wavenumber (FK) algorithm provided by the Python package Obspy (Capon, 1969; Beyreuther et al., 2010) to analyze the data of the seismo-acoustic array. Due to the configuration of the array (aperture of 360 m) and its distance (2 km) to the signal source location (El Caliente), we assume that the explosion signals arrive as a planar wave (Almendros, 1999). Here, a fourth order Butterworth filter (0.125–3 Hz) is applied to the data and the FK-analysis is then carried out in a sliding window (length 1 s, step: 0.05 s) using a slowness (s) grid of $-1 < s < 1$ s/km ($-3.5 < s < 3.5$ s/km for acoustic data).

The analysis of the seismic time series reveals variations of slowness and backazimuth through time (**Figure 4**). The onsets of both the precursor and main phase are characterized by low slowness values (0.1–0.2 s/km), followed by a slowness increase. For the main phase a stepwise increase (up to 0.3–0.5 s/km within 0.5–1 s, 0.6–0.8 s/km within 2.5–3.5 s after the onset) or a continuous upsweep is observed. The slowness variation of the PC is not consistent for different explosions which could be caused by the low signal-to-noise ratio after the first onset and the arrival of reflected phases.

For the acoustic signal we use a time series of 2.5 s, which starts 0.3 s before the phase onset at the center station of the array (ARR1). The resulting backazimuth of 120° matches the actual configuration of the array with respect to El Caliente. The apparent horizontal velocity, which is the inverse slowness, ranges between 0.34 and 0.40 km/s for different explosions.

Seismic Velocities

We determine seismic velocities in the subsurface in order to create a coarse velocity model for the numerical modeling with two approaches; 1) comparison of arrival times of the explosion signals at different stations and 2) dispersion analysis.

Arrival Time of Seismic Signals

As a first step we fix the horizontal position of the seismic source at the location of El Caliente. This simplification is supported by backazimuth observations of the previous section. Because the origin time as well as the depth z_s is unknown, we consider the relative arrival times $\Delta t_{i,j}$ at different stations i, j instead of the absolute arrival times. With the distance d_i and the relative elevation difference of source and station z_i we determine the length of the straight ray paths and calculate the theoretical relative arrival times:

$$\Delta t_{i,j} = t_i - t_j = \frac{1}{v}\left(\sqrt{d_i^2 + (z_s - z_i)^2} - \sqrt{d_j^2 + (z_s - z_j)^2}\right)$$

By performing a grid search we estimate the parameter pair (v, z_s) which best fits the observations. An area of reduced misfit and no clear minimum is found for both PC and MS, due to the trade-off between depth and velocity (**Supplementary Figure S2**). Furthermore, the uncertainty of the determined arrival times

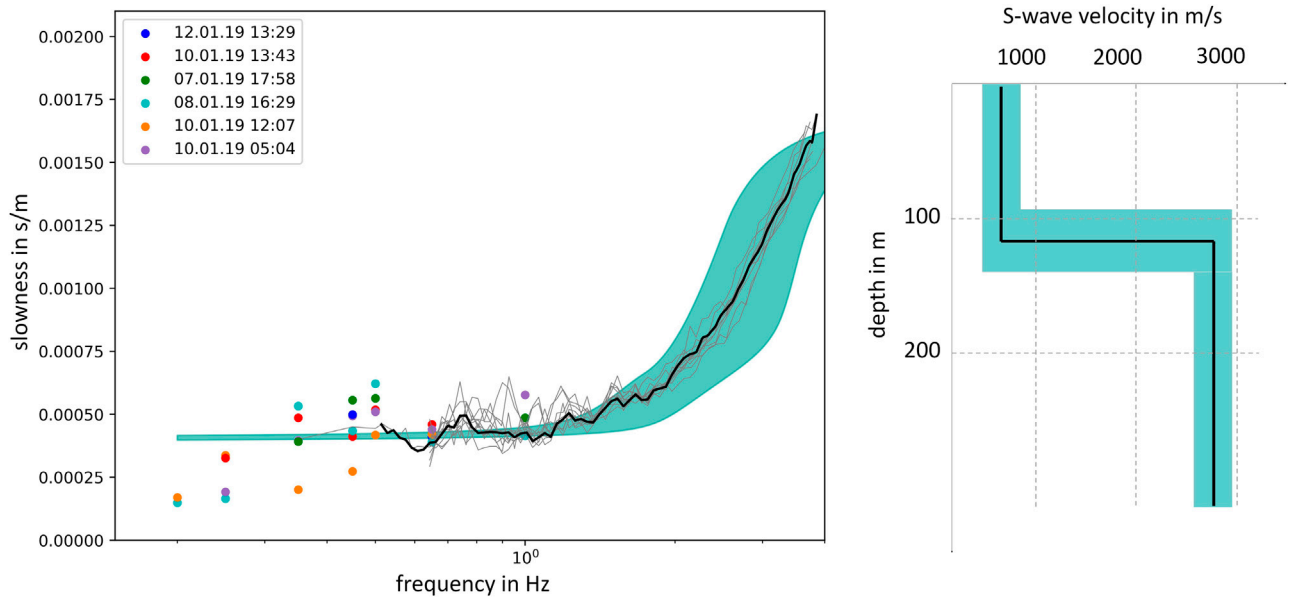

FIGURE 5 | A) Dispersion curves. The colored circles mark the propagation velocity of different explosions (color coded) depending on the frequency. The gray lines show the dispersion curves determined by the HRFK analysis of the 1 h-windows and the mean curve is shown in black. The green area marks the dispersion curves of the inverted subsurface models with the lowest misfit. **(B)** S-wave velocity determined by dispersion curve inversion.

is reflected in the results of the grid search. The inversion is mainly insensitive to depth but provides good estimates of seismic velocities. Although this simple inversion approach does not take into account lateral variations, an average velocity in the area of interest is provided, which is, to our knowledge, not well constrained at Santiaguito volcano. For the MS phase velocities vary between 2.7 and 4 km/s (indicative of P-wave propagation), while velocities for the PC are significantly lower and range between 1.2 km/s and 1.9 km/s (pointing toward S-wave velocities).

Dispersion Analysis

To further constrain seismic velocities close to the surface we analyze the dispersion characteristics of surface waves using ambient noise and the explosion signals. (Dobrin 1951; Haskell 1953; Aki and Richards, 1980). Because ambient noise vibrations largely consist of surface waves, their dispersive behavior can be used to determine S-wave velocities in the shallow subsurface (Murphy and Shah, 1988; Jongmans and Demanet, 1993). With the seismic data from the deployed array we calculate dispersion curves with the high-resolution frequency wavenumber (HRFK) approach (Wathelet et al., 2018; Capon, 1969) and following the SESAME guidelines as this approach is routinely used in engineering seismology applications (Acerra et al., 2004). We determine dispersion curves for six 1 h windows of the vertical component at all array stations and use the average of all curves for the inversion. The dispersion curves as well as the mean curve are depicted in **Figure 5** and show an increase from 0.35 s/km to 1.6 s/km up to a frequency of 4 Hz. The array geometry, with its aperture and interstation distance, controls the resolution. In order to estimate a coarse velocity structure at greater depth, larger wavelengths are needed due to their increased penetration depth. To increase the spectral information toward low frequencies we calculate the phase velocity in narrowband filtered explosion signals at all stations of the network. We use a fourth order zero-phase Butterworth bandpass filter with central frequencies of f_0 = 0.20, 0.25, 0.35, 0.45, 0.75, 1.00 Hz and a bandwidth of $f_0 * 2^{(1/2)}$. The results are depicted in **Figure 5**. The determined phase velocities are in agreement with our results of the ambient noise at the array.

The velocity inversion was carried out for a model with one layer above the halfspace using the approach of Wathelet (2008) based on a modified conditional neighborhood algorithm. Density values of the layers are implemented according to the geology of the region. The Santiaguito domes are characterized by dacite rocks, while the older material of Santa Maria underneath is composed of basaltic-andesite material (Rose, 1972). Furthermore, considering physical characterisation studies of El Caliente dome lavas (Hornby et al., 2019b) and similar stratovolcanoes (e.g., Schaefer et al., 2015) we assumed that the rocks of Santa Maria are denser than the newer material of Santiaguito. Hence, a higher density value 2,700 kg/m^3 is chosen for the deep basaltic-andesite material at depth, while a lower density of 2000 kg/m^3 is attributed to the surficial dacites (Tenzer et al., 2011). Over 2,500 models were computed with those boundary conditions and the misfit E is calculated with:

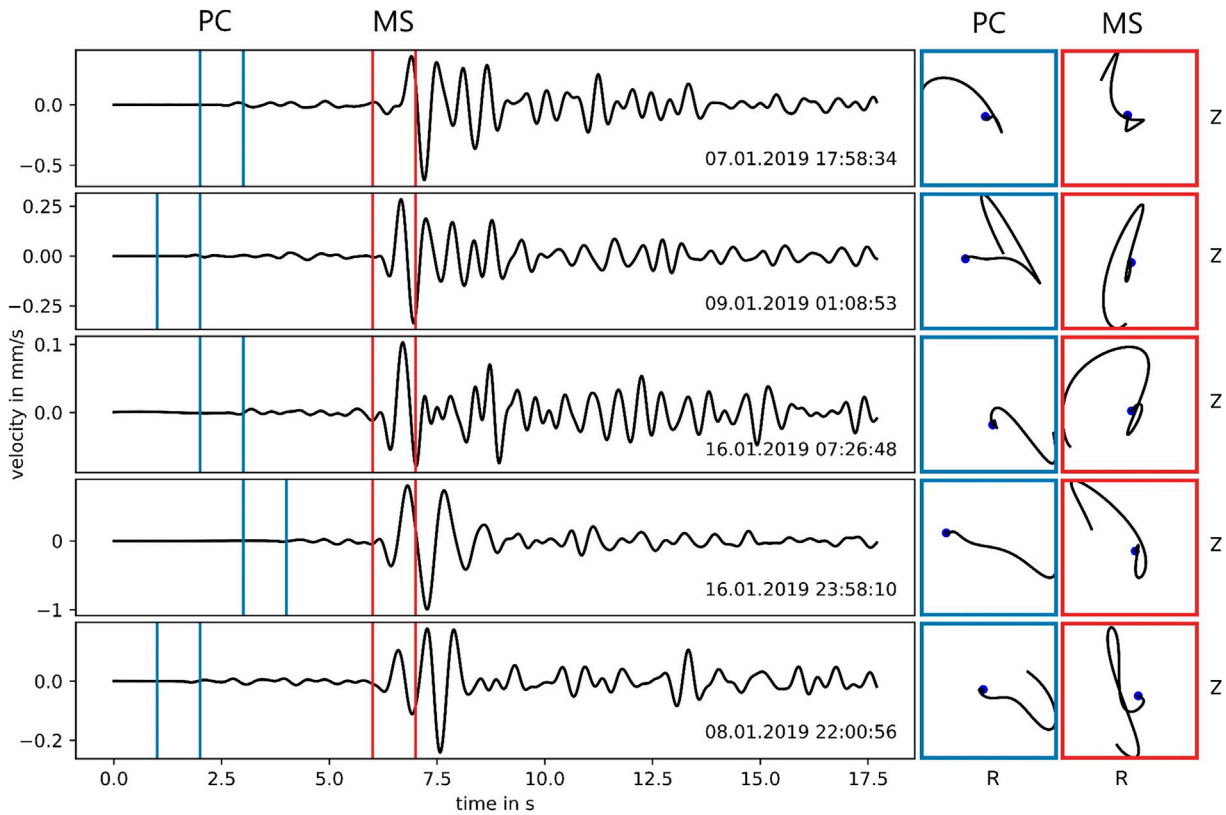

FIGURE 6 | Seismic ground motion at LIN3 (Z-component, fourth order Butterworth filter f = 0.125–3 Hz) and the particle motions in the RZ-plane. The blue and red vertical lines mark the time windows used for the particle motion analysis and correspond to the polarization diagrams on the right. The blue window includes the PC onset and the red the onset of the MS. The blue dot indicates the start of the time series.

$$E = \sqrt{\sum_{i=1}^{n} \frac{(d_i - m_i)^2}{\sigma_i^2 n}}.$$

The misfit describes the difference of the observed dispersion curve d_i and the synthetic curve m_i of the subsurface model at each of the n frequency samples (Wathelet, 2005). The uncertainty σ_i is determined by the HRFK and the differences between the dispersion curves. The model with the lowest misfit (0.05) is defined by a subsurface with v_S = 2,650 m/s starting at a depth of 120 m and is depicted in **Figure 5**. The upper layer is characterized by v_S = 650 m/s. The interface depth is not well constrained and varies within a misfit range of 0.01 (marked in light green in **Figure 5**) by 30%, while the variations of the velocities are less than 15%. As we only have ambient noise dispersion data beneath the array, the obtained velocity structure is only representative for the areas surrounding this location.

Particle Motion of Seismic Data

The particle motion of seismic phases contains information about the wave type, the source mechanism as well as the source depth. For a better understanding of the signals we rotate the components from the N, E, Z to the R, T, Z coordinate system with the theoretical backazimuth calculated from the station-volcano configuration. The radial component R is oriented in the direction from source to station, the Z-component still refers to vertical movement and together with the transverse (T) component, they form the new, station-dependent, left-handed coordinate system (Shearer, 2009, p. 89).

The particle motion observations for PC and MS are summarized in **Table 1**. **Figure 6** exhibits multiple explosion signals at station LIN3 which display the particle motion at the onset of PC and MS in the R-Z plane. The vertical lines in each seismogram depict the start and the end of the 1 s time windows, which are shown in the particle motion tiles. We observe similar particle motions of the PC onset for different explosions with a predominant polarization varying between 30° and 70° to the vertical. By correcting the angle for contributions of reflected P- and SV-waves (Müller, 1990) the possible source depth ranges between 200 and 1,300 m below the summit of El Caliente. The precursor is polarized perpendicular to the propagation direction of a wave arriving from the volcano and therefore indicating the arrival of an SV-wave. This hypothesis is supported by the low propagation velocity of the PC,

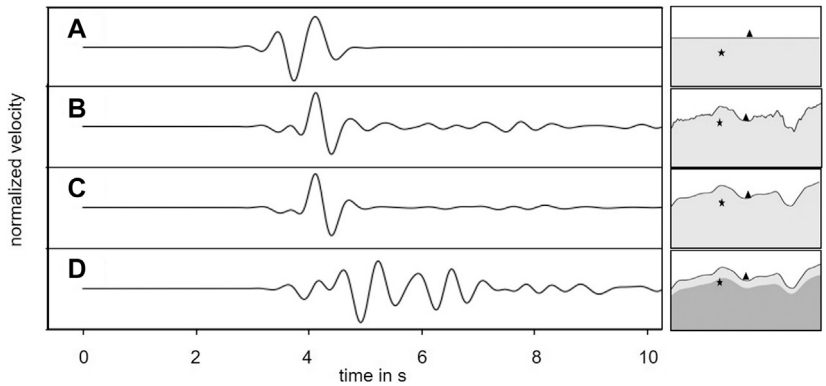

FIGURE 7 | Influence of different subsurface models on the synthetic seismogram used for the numerical modeling. Each trace shows the seismogram at the central array station and on the right a cross section of the corresponding subsurface model is shown. The star marks the source location (400 m below the domes peak) and the triangle marks the station position at 2 km distance. **(A)** Is characterized by a flat topography above a homogeneous halfspace (model 1). **(B)** real topography as a section through the position of the array and El Caliente. **(C)** Smoothed topography (model 2). **(D)** Two layer model with smoothed topography (model 3).

which was determined in the previous section. The amplitudes of the preceding P-wave are not large enough to be detected. The direction of motion is more variable for MS and a clear polarization is not observed for all explosions. Nevertheless, a common feature is a vertical particle motion of the MS onset (**Figure 6**). At more distal stations from the crater the polarization of both the PC and the MS is less consistent. Due to strong topographic variations in the area of this study, the interpretation of the measured particle motion is challenging (e.g. Neuberg and Pointer, 2000). Hence, we conduct numerical modeling to compare the influence of different source mechanisms, depths and topography on the particle motion at the stations.

2D NUMERICAL MODELING

Volcanic environments are commonly characterized by a complex topography and subsurface, thus the analysis of the seismic wave field is often challenging and simplified approaches have been used (e.g. flat surface, homogeneous half space). Numerical modeling can be employed to circumvent

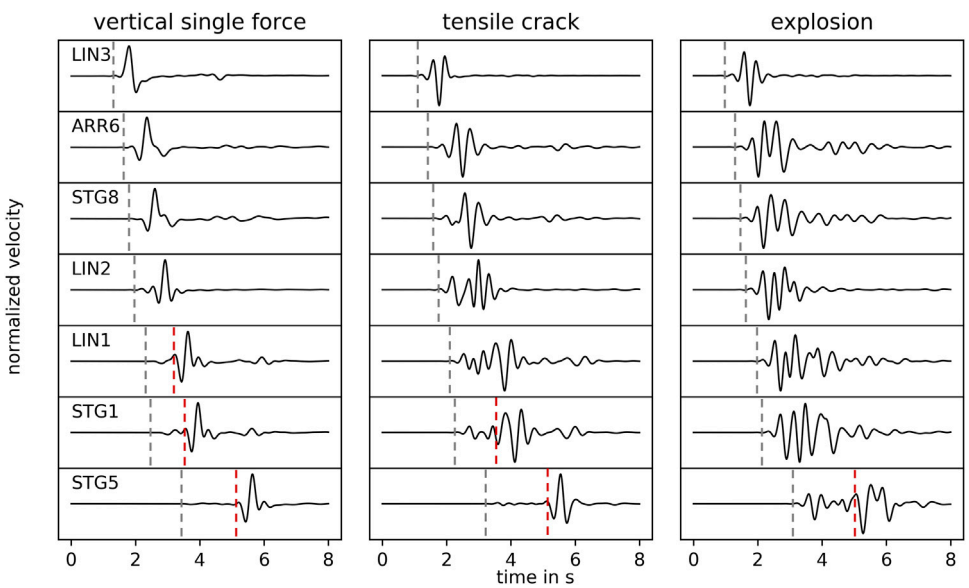

FIGURE 8 | Comparison of synthetic waveforms of the different source mechanisms using model 2. Source depth is set at 600 m below El Caliente. Seismograms are filtered between 0.125 and 3 Hz and ordered by the distance of station and source. P-wave onsets and S-wave onsets (if recognizable) are marked with gray and red dashed lines, respectively. While at the closest station (LIN3) only one phase can be seen, P- and S-wave onsets are separated at further stations (e.g. STG5). The ratio between P- and S-wave amplitudes vary for different source mechanisms. P-wave amplitudes are largest for explosions, but have much lower amplitudes in the VSF model.

difficulties in interpreting seismic signals by providing estimates of the relative influence of basic parameters such as source type, source depth and topography on seismic wave propagation. In order to simulate wave propagation in a 2D subsurface model we use a spectral element method (SPECFEM2D; Komatitsch and Vilotte, 1998). By reducing the dimensions from 3D to 2D we neglect phases which are not traveling on a straight raypath (e.g. reflections, bended ray paths) and we are aware that the relative amplitude of phases (e.g. body vs. surface waves) gets distorted. However, as we will not interpret absolute amplitudes in our analysis and mainly concentrate on phase onsets, these effects should have a low impact on our results.

Model Parameters

Wave propagation is simulated for three different models: 1) a homogeneous flat model, 2) a homogeneous subsurface with topography and 3) a two-layer model with topography (**Figure 7**). The results of the observed seismic phase velocities are used to define the physical model parameters.

For the homogeneous halfspace in model 1 and 2 we use a P-wave velocity of 3,500 m/s, which is in the range of the MS-phase velocity determined by the relative arrival times at all stations. This value is only slightly lower than the P-wave velocity (4,000 m/s) used by Anderson et al., (2012). For the S-wave velocity they implemented 2,400 m/s, which is similar to the S-wave velocity that we determined for the lower layer beneath the array. As we assume that this high velocity value is related to the dense solidified lava flows of Santa Maria and does not represent the subsurface in the surrounding of the dome complex, we use v_S = 2000 m/s, a slightly lower S-wave velocity for model 1 and 2. Since the results of the dispersion analysis indicated a low velocity layer above the halfspace at the location of the array, a further model with two layers is developed. For the halfspace we use the same velocities, which we chose for the homogenous model and we implemented a layer with lower velocities (v_P = 1800 m/s, v_S = 1,000 m/s) on top. We are aware that model 3 might not represent the subsurface in the whole model space. Nevertheless, it is a reasonable model for the subsurface within the valley of the array and it will be used to show the impact of a low velocity layer on the results of array analysis and particle motion analysis. For all models, the same density values (halfspace: 2,700 kg/m^3, top layer: 2000 kg/m^3) as for the dispersion curve inversion are used for the numerical modeling. Three different mechanisms are considered for the source: 1) explosion source, 2) downward directed vertical single force (VSF) and 3) the opening of a vertical crack. For all sources a Dirac impulse is used to calculate the Green's functions. The source is placed at depths of 200 m, 400 m, 600 m, 1,000 m and 1800 m below the top of El Caliente. The topography is extracted from a digital elevation model of the area of Santiaguito with a spatial resolution of 10 m and implemented as a free surface. Due to strong topographic contrasts, a Gaussian filter is applied to the surface which has a negligible effect on the resulting waveform (**Figure 7C**) but decreases the computational effort. 2D sections are created from the 3D topography cutting through El Caliente and each station respectively. For the array stations, as well as STG8, the same section is used due to the proximity of the stations to one another. Numerical modeling is carried out for each section and for the analysis, results of all sections are used. The interface of the 2-layer model (model 3) follows the topography at a depth of 150 m, but a stronger smoothing parameter is applied (**Figure 7**). For all simulations a minimum of 10 points per wavelength were used to decrease the effects of numerical dispersion (De Basabe and Sen, 2007). Because the main energy of the observed explosions arrives with frequencies <3.5 Hz, wavelengths of >1,000 m are expected, resulting in a maximum cell size of 100 m.

Analysis of Synthetics

Influence of Source Types

Due to contrasting radiation patterns of the implemented source mechanisms we observe differences in the synthetic seismograms (see example for the homogeneous model with topography; **Figure 8**). P- and S-wave phases of synthetics are clearly recognizable at stations farther from the source. The maximum time shift between the P- and S-wave arrival (~2 s) is observed at the farthest station (STG5). At closer stations the phases are not separated due to proximity to the source. Even a deep source (1800 m) cannot result in a time shift of >2 s between P- and S-wave arrival at proximal stations. This finding of the synthetic data thus provides important information regarding the time lag between the PC and MS phase of the observed data. It indicates independent source processes of the PC and MS phases, which are commonly separated by 2–6 s at the nearest station (**Figure 6**).

While the arrival times of the phases are independent from the source mechanisms, the P/S amplitude ratio is strongly influenced by the different sources. As shown in **Figure 8** for model 2, strong S-waves are excited by the VSF source, while P-wave amplitudes are small. In contrast, the explosion source generates strong P-wave amplitudes, while S-wave amplitudes are significantly weaker. The opening of a vertical crack shows clear P-wave arrivals as well, but amplitudes for the S-waves are still stronger. With the implementation of an additional layer the waveforms become more complex (**Figure 7D**), but the general findings regarding the influence of the source radiation pattern remain valid (**Supplementary Figures S3–S7**).

Array Analysis

We proceed in the same way for the array analysis of the synthetics, as for the real observations. As the simulations are run on a 2D subsurface, only the distances from the array stations to the source are relevant. Therefore, we perform the array analysis on a 1D array and we only consider the slowness along the line of stations. The determination of the backazimuth is superfluous, due to the missing dimension.

The absolute slowness values related to the first onsets of the seismic signals are similar for all source types, but they change with the source depth and the subsurface model. The implementation of a low velocity layer close to the surface (model 3) decreases the slowness of the signal onset at the array, especially for shallow sources (**Figures 9B,D**). The temporal variation of the slowness is controlled by the time difference between P- and S- waves and their amplitude ratio.

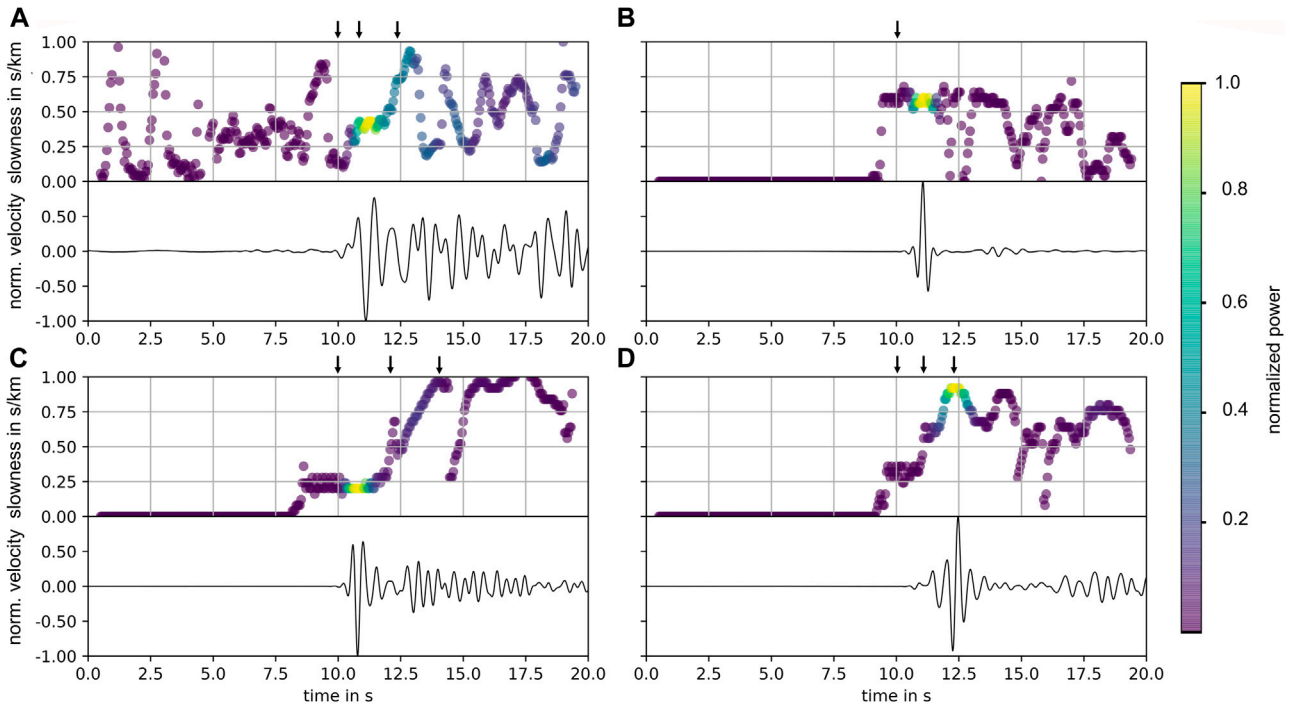

FIGURE 9 | Temporal slowness variation of the monitored data **(A)** together with the variation of the synthetics **(B, C and D)** and the corresponding seismogram of the central array station. Both synthetics and monitored data are filtered between 0.125 and 3 Hz. The black arrows mark the onset of the seismic signal and further slowness steps. **(A)** Ground motion after 07.01.19 17:58:31, black arrows correspond to MS. **(B)** VSF in a depth of 200 m (model 2). **(C)** Explosion source in a depth of 1800 m (model 3) and **(D)** VSF in a depth of 200 m (model 3).

Generally, with increasing source depth the time difference between P- and S-waves increases, and higher slowness values are observed later in time. The amplitude ratio of both phases determines the transition between these slowness steps (**Supplementary Figures S8, S9**). Therefore, the shift to higher slowness values for a deep explosion source is observed later than 1.5 s after the arrival of the seismic signal (**Figure 9C**) and the transition is better described by a continuous upsweep, than a stepwise slowness increase. High S-wave amplitudes excited by the VSF reduce this time lag and the slowness steps of a shallow VSF are similar to the ones determined for the main phase in the monitored data (**Figures 9A,B**). As seen in the synthetic seismograms for the opening of tensile cracks (**Figure 8**), the amplitude ratio of P- and S-waves is a combination of both VSF and explosion source. Similar behavior is observed with the array analysis and the slowness increase is generally observed later than for a VSF, but the stepwise slowness increase is more prominent than for an explosion source (**Supplementary Figure S10**).

Comparison of the Particle Motion

We conducted particle motion analysis of the synthetic data in the RZ-plane in the same way as it was done in *Particle Motion of Seismic Data* for the monitored dataset, using 1 s time windows around the onset of the signal at each station. In the flat homogeneous model, the particle motion is linearly polarized for distant stations. By considering the difference between the apparent and true incident angle due to reflections and P/SV conversions at the free surface (Müller, 1990), the source depth can be resolved from the incident angle of linearly polarized phases with trigonometric functions. For close stations the particle motion is a superposition of the arriving P- and S-phase and is therefore dependent on the amplitude relation. Explosion signals tend to have a linear polarization of a P-wave while the behavior of the particle motion of VSF-signals is closer to an S-wave polarization. The implementation of the topography causes the height differences of the stations and the source to become more relevant. As a result of the station and source geometry, straight ray paths from source to receiver do not exist for shallow source depths; therefore the polarization is distorted (Neuberg and Pointer, 2000). An exception is the closest station, LIN3, which is located higher or at the same elevation for all considered source depths. The particle motion is shown for the onset at this station (**Figure 10**). Both a shallow VSF as well as a deep explosion source create a vertical particle motion at LIN3 which is similar to the polarization of the monitored MS. The raypaths for both examples are illustrated in the last column of **Figure 10**. Particle motion comparable to the observations of the PC is observed for either the opening of a vertical crack or an explosion source at a depth of 600 m. The resulting angle of motion measured to the vertical axis lies within the range of the observations for both possible source mechanisms.

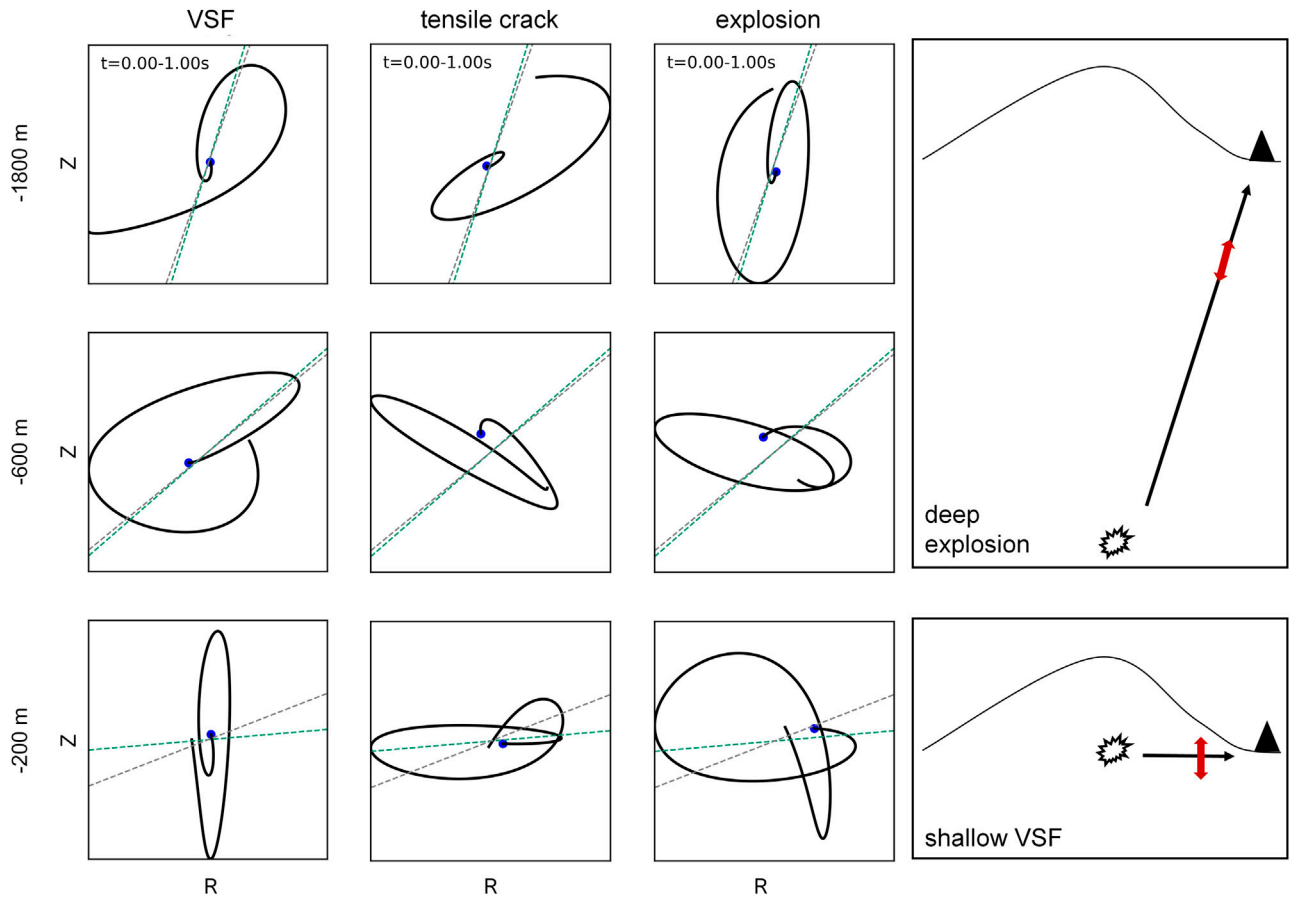

FIGURE 10 | Synthetic particle motion in the RZ-plane of the onset at LIN3 using (model 3). Each tile relates to a time window of 1 s with the radial component on the horizontal axis. The blue dot indicates the start of the time series. The first column on the left refers to the vertical single force (VSF) mechanism, the second to the opening of a tensile, vertical crack and the third depicts the particle motion of an explosion. Each row corresponds to a specific source depth. The green dashed line marks the apparent incident angle calculated for a straight raypath considering the source receiver geometry and the gray dashed line includes the correction for the influence of reflections and wave conversions at the surface (Müller, 1990). The tiles on the right show a shallow VSF and a deep explosion, which both result in a dominating vertical motion.

INTERPRETATION AND DISCUSSION

The results of the monitored signal analysis and synthetic wave modeling performed in this study provide a wealth of data which sheds light on the subsurface conditions leading to gas-and-ash explosions at Santiaguito. Below, following interpretation of the most appropriate velocity structure to explain our observations, we delve into interpreting the cause of seismic observations ascribed to explosive processes at Santiaguito.

Seismic Velocity Structure

The results of dispersion curve inversion indicate that a low velocity layer beneath the seismo-acoustic array exists which agrees with the local stratigraphy of recent lahar deposits above older volcanic units. This interpretation is supported by the low slowness values for the onset of both PC and MS. On a layer boundary the incident angle of a transmitted ray decreases due to Snell's law (Aki and Richards, 1980) and increases the horizontal velocity; synthetic results of model 3 are in agreement with this observation. The seismo-acoustic array, being located in the valley adjacent to El Brujo lava dome, sits within a veneer of debris resulting from early pyroclastic flows (though not in the last few decades to our knowledge) and recurring rockfall events, further reworked by lahar activity (common in rainy seasons) which promote a low velocity shallow layer. Older lavas from Santa Maria can be seen to extend below the lahar deposit from the edge of the valley, which would exhibit higher seismic velocities, thus leading to the dichotomy in velocity with depth. Similarly, a comparable layered velocity structure may be presented underneath LIN3, but cannot be verified due to the single station deployment.

New Insights Into Explosion Source Mechanisms at Santiaguito

Explosive eruptions have long been studied at Santiaguito, and each of these studies have offered different, yet compatible, pieces

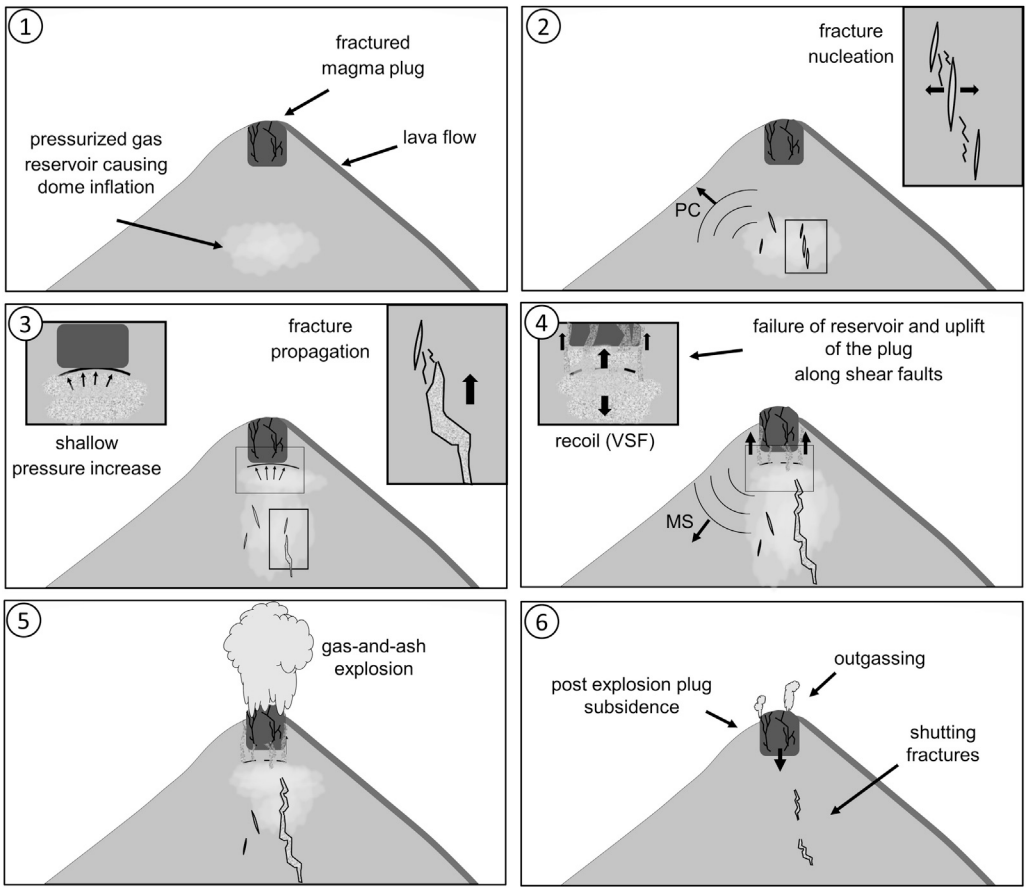

FIGURE 11 | Proposed source mechanism of weak-to-moderate explosions at Santiaguito: 1) gas accumulates at a depth of ~600 m and causes the dome to inflate (positive tilt). 2) The increased gas pressure causes fracture nucleation and the seismicity related to the opening of tensile fractures is attributed to the PC signal described in this study. 3) As fractures propagate upwards and unzip, gas rapidly rises increasing the pressure below the shallow magma plug. 4) With the propagation of tensile fractures into the shallow plug, they intersect with existing fractures and cause fault-slip controlled uplift of the plug. The recoil of the rapid upward motion of mass may cause a downward directed VSF, which is consistent with our findings for the MS. 5) Gas and ash is ejected at the crater surface. 6) In the post eruptive phase the plug subsides and the volcano edifice deflates (negative tilt). Shutting fractures in the volcano interior decreases the permeability for gas rise and the activity at the crater is characterized by weak outgassing.

of the puzzle to reconstruct the series of processes leading to, and occurring during, explosions. Here, we re-examine contributions of recent key multi-parametric studies (as described in the introduction) and supplement their observations with our findings to expand our understanding of the key underlying processes at Santiaguito.

In the last two decades, magma extrusion has been essentially continuous at Santiaguito (e.g., Johnson et al., 2014), except for the 2015–2016 period of paroxysms (which will not be considered in this discussion). Although continuous, magma extrusion has been cyclic, as revealed by inflation/deflation tilt cycles (Johnson et al., 2014; Lavallée et al., 2015; Hornby et al., 2019b) and upheaval/subsidence cycles of the dome surface (Johnson et al., 2008; Scharff et al., 2012; Zorn et al., 2020). Such pulsatory discharge is common at open-vent volcanoes and has been ascribed to contributions from non-linear evolution of magma rheology (Melnik and Sparks, 1999, 2005), a rate-dependence of shallow faulting processes (e.g., Iverson, 2008; Costa et al., 2012; Kendrick et al., 2014), changes in the plumbing system's geometry (Costa et al., 2007; Thomas and Neuberg, 2012), and non-linear gas flow and pressure development across the magmatic column (Michaut et al., 2013). At Santiaguito, the inflation/deflation cycles and the eruptive dilemma of gas-and-ash explosion vs. gas emission have been linked to gas pulses through the conduit (Johnson et al., 2014; Lavallée et al., 2015). Yet, questions remain as to whether the explosions are caused by magmatic fragmentation due to pore fluid overpressure exceeding the relaxation rate of magma (e.g. Dingwell, 1996; Spieler et al., 2004) or whether the underlying fragmentation is associated with faults via cataclasis (Bluth and Rose, 2004; Hornby et al., 2019a) or shear-heating-related thermal vesiculation (Lavallée et al., 2015).

The permeable flushing of fluids through the magmatic column would provide the impetus for both magmatic fragmentation and faulting by increasing pore pressure, buoyancy and shear stresses. The generally dense nature of the

Santiaguito lava dome means that large pore overpressure is required to trigger fragmentation (e.g., Spieler et al., 2004). In such cases, we may expect large parts of the dome to be excavated during explosions; yet, the small to moderate gas-and-ash explosions tend to develop along persistently active faults and leave the dome rather intact. Hence it has been suggested that explosions may show a better affinity to localized fault activity (Bluth and Rose, 2004; Holland et al., 2011), whereby sacrificial fragmentation along faults (i.e. cataclasis) frees space for outgassing and thus prolongs the structural stability of the dome (Lavallée et al., 2015; Hornby et al., 2019a). Rheological modeling of Santiaguito magma by Holland et al., (2011) suggests that the conditions for shear rupture are met in the shallow conduit at ca. 150–600 m depth, which agrees with the depth estimated from tilt signals (Sanderson et al., 2010; Johnson et al., 2014).

These complementary studies advanced that fracture opening would lead to gas-and-ash explosions, releasing pressure, which once concluded, would allow fracture healing and pressure build-up until the next explosion or gas emission. Here we stress that fracture healing would be difficult to achieve for such crystal-rich, high-viscosity magmas during inter-explosion timescales (cf. Yoshimura and Nakamura, 2010; Lamur et al., 2019) though it may be possible that fracture closure alone is sufficient to shut permeability (e.g., Lamur et al., 2017) and promote fluid pressure build-up until the next explosion. Faults, even in shear zones, generally develop via the nucleation, propagation and coalescence of tensile fractures (e.g., Kilburn, 2003; Lavallée et al., 2013), which may then slip if sufficient shear stress remains following rupture. As such, Hornby et al., (2019b) investigated how Santiaguito lava may rupture in tension as a function of rate, based on the observation that gas-and-ash explosions and gas emissions occur following inflation at contrasting strain rates (e.g., Lavallée et al., 2015). Hornby et al., (2019b) showed that an increased strain rate results in a reduction in strain to failure and enhanced strain localization. So, they posit whether tensile fractures are likely to develop top-down or bottom-up. Top-down may be envisaged when considering that magma viscosity and brittleness increase toward the surface, however bottom-up fracture propagation may be favored when a pressure source develops at depth.

The results of our study, and in particular the source mechanism of the precursory signal (PC), may shed light on the nucleation of fractures in magma at El Caliente. We constrained that PCs are likely triggered at a depth of ca. 600 m, which sits below or at the deeper end of the explosion depths estimated by Johnson et al., (2014) and Holland et al., (2011), respectively. The comparison of synthetics and monitored seismic signals suggest that the PCs likely result from the opening of a vertical tensile fracture or from an explosion. Thus here, we hypothesize that PCs originate from the development of a tensile fracture, vertically propagating upward from a depth of ~600 m. Varying incident angles and durations of the PCs may be attributed to small depth variations of the fracture nucleus. We hypothesize, that after the initial crack opening at 600 m depth the crack will coalesce with adjacent fractures (as commonly observed during magma rupture; Lavallée et al., 2013). Gas and ash can then rush through the developing fracture network and pore pressure builds up until the overpressure is sufficient (at shallower depth) to fragment magma via faulting and/or magmatic fragmentation where the pressurized magma locally experiences lower pressure (triggered by fault opening). This fragmentation would then lead to the generation of the main seismic signal (MS). In this scenario, the time for the tensile fracture to open, and for gas transfer between the locus of nucleation (~600 m) and the point of fragmentation (~200 m) could be determined by estimating the true time offset of PC and MS at the source from the commonly 4 s arrival time gap between PC and MS at station LIN3. According to the geometry of sources and station, the travel time difference is lower than 0.5 s. Hence, considering the variation of precursor duration, we obtain a time gap of approximately 4 s in which the fracture ruptures and the gas migrates upward to shallow depth until the gas pressure overcomes the lithospheric load.

Analysis of the main component of the seismicity (MS) associated with explosions indicated an initial vertical particle motion rapidly followed by changes in motion direction, without polarization. Wave propagation modeling suggests that the vertical particle motion could either be caused by a deep (1800 m) explosion source or a shallow (<200 m) vertical single force (VSF). The temporal slowness variation of synthetics from a shallow source shows similarities with the field measurements and thus supports a shallow source location. Shallow VSF models have been proposed in the past to explain the source mechanisms of volcanic explosions (Ohminato et al., 2006; Zobin et al., 2006; Zobin et al., 2008). Furthermore, the short (<0.5 s) time difference of MS arrival at LIN3 and the acoustic origin time (related to sudden gas and ash rise) is in agreement with this suggestion. The plethora of observations presented here (from others and this study) ascribe the source of explosive eruption at Santiaguito to the shallow magmatic column. Thus, it is highly unlikely that fragmentation depth is at 1800 m depth and thus deeper than the source of the precursory signal at ~600 m. As such, we propose that MS are likely associated with shallow VSF-driven processes, which could be associated with the recoil following rapid uplift of the dome in a plug-like flow against marginal shear faults, triggered by the burst of gas flushing through the upward propagating vertical crack at 600 m (leading to PC). This faulting activity could promote fault-related fragmentation (e.g., Lavallée et al., 2015), contributing to the generation of gas and ash. From the point at which MS is triggered, the gas-and-ash mixture would travel at extremely rapid speed, as indicated by the short time gap (<0.5 s) between MS and the acoustic signals (associated with ejection into the atmosphere). The proposed source mechanism for explosions at Santiaguito is summarized in **Figure 11**.

CONCLUSION

This study combined visual, acoustic and seismic information with numerical modeling in order to determine source characteristics of seismic explosions at Santiaguito volcano.

We showed that 2D numerical modeling in areas with a strong varying topography provides important constraints for the interpretation of observed natural seismic signals. Analysis of the seismic record associated with explosions showed that the events are associated with two contrasting signals: a weak precursory seismic signal, 2–6 s prior to the explosions, and main seismic signal associated with gas-and-ash ejection. To resolve the source location and origin of the seismic signals, we first used ambient noise analysis at the array to assess seismic velocities in the subsurface and then used two-dimensional spectral element modeling (SPECFEM2D) to constrain the source trigger mechanism.

Ambient noise measurements were first used to define the velocity structure of the subsurface. This indicated the presence of a low velocity layer with an S-wave velocity of 650 m/s in the uppermost 120 m below the array, which may be related to surficial debris from rockfalls and pyroclastic deposits. Below 120 m, our analysis suggests a halfspace containing rocks with a higher S-wave velocity of 2,650 m/s, associated with coherent lavas.

Two-dimensional spectral element modeling (SPECFEM2D) was employed to simulate seismic waveforms and assess the source mechanism for these two signals. The particle motion of the observed precursor at the closest station LIN3, shows similarities to an explosion source or to the opening of tensile cracks at a depth of around 600 m. In contrast, the vertical polarization observed at the onset of the main seismic signal may be attributed to either a shallow vertical single force or a deep explosion. As the time difference between the main signal (at the most proximal station) and the gas-and-ash ejection is short, we reject the likelihood of a deep explosion source and conclude that the main signals originate at shallow (~200 m) depth from a vertical single force associated with the explosion.

Using the constraint imposed by the modeled source mechanisms for the precursory and main signals, our preferred interpretation for the sequence of processes taking place at Santiaguito, leading to an explosion is: during magma pressurization at shallow depth, a tensile crack opens at a depth of around 600 m, which leads to the localization and intensification of gas rise and pressurization rate. The associated gas migration results in overpressure at shallow depth (~200 m), causing rupture of the dome. Uplift of the dome along shear faults, which undergo cataclasis and fragmentation, widens permeable pathways to permit the sudden expulsion of gas and ash through the fracture. Once the explosion concludes, pore pressure is lost, the fracture shuts and the plug relaxes until gas influx causes the cycle to start anew. This integrated study of eruption dynamic at Santiaguito points toward a bottom-up series of magma-gas interaction processes, including, rupture, gas flow and accumulation and fragmentation, leading to gas-and-ash explosions. More simultaneous observations at multiple arrays are needed to further constrain the preparatory and explosion phase at Santiaguito to further constrain the mechanisms and time evolution during an eruption. We speculate that similar mechanisms happen at other volcanoes exhibiting domes with ash-gas rich explosions, but high resolution near field array measurements are needed to detect and analyze weak precursory seismic signals. However, we have shown that careful analysis of weak precursory signals provides valuable constraints for the source processes at Santiaguito volcano. Similar studies should be carried out at other dome complexes exhibiting gas-and ash rich explosions, to develop a physical based model that takes into account the time evolution of the explosion process.

DATA AVAILABILITY STATEMENT

The raw data supporting the conclusions of this article will be made available by the authors, without undue reservation

AUTHOR CONTRIBUTIONS

The experiment design was conceived by ARi and ARo. ARo, EG, WC, ARi, GC were involved in preparation and realization of the field experiment in 2019. The processing and interpretation of seismic, acoustic and visual data was carried out by ARo, EG, ARi. With the expertize of YL, JK and SD a model for the eruption process was conducted. ARo wrote the manuscript to which all authors contributed.

FUNDING

YL acknowledges financial support from an ERC starting grant on Strain Localization in Magma (SLiM, no. 306488) and a Research fellowship of the Leverhulme Trust (RF-2019-526\4). JK was supported by an Early Career Fellowship of the Leverhulme Trust (ECF-2016-325). WC was financially supported by the Natural Environment Research Council (NERC) EAO Doctoral Training Partnership.

ACKNOWLEDGMENTS

We acknowledge the logistical and intellectual support of the Instituto Nacional de Sismología, Vulcanología, Meteorología e Hidrología (INSIVUMEH), Guatemala, and the staff of the Santiaguito Volcano Observatory (OVSAN). We extend our gratitude to our local guide and network manager Armando Pineda.

SUPPLEMENTARY MATERIAL

The Supplementary Material for this article can be found online at: https://www.frontiersin.org/articles/10.3389/feart.2020.603441/full#supplementary-material.

REFERENCES

Acerra, C., Havenith, H. B., and Zacharopoulos, S. (2004). Guidelines for the implementation of the H/V spectral ratio technique on ambient vibrations measurements, processing and interpretation. No. European Commission–EVG1-CT-2000-00026 SESAME. Brussels, Belgium: European Commission.

Aki, K., and Richards, P. G. (1980). Quantitative seismology–theory and methods. Vol. II. New York, NY: Freeman and Company.

Almendros, J., Ibanez, J. M., Alguacil, G., and Del Pezzo, E. (1999). Array analysis using circular-wave-front geometry:an application to locate the nearby seismo-volcanic source. *Geophys. J. Int.* 136, 159–170. doi:10.1046/j.1365-246x.1999.00699.x

Anderson, J. F., Lees, J. M., Waite, G. P., and Johnson, J. B. (2012). Source and propagation effects on near-field Co-eruptive ground motion at Santiaguito volcano, Guatemala. *Bull. Seismol. Soc. Am.* 102, 696–706. doi:10.1785/0120110106

Beyreuther, M., Barsch, R., Krischer, L., Megies, T., Behr, Y., and Wassermann, J. (2010). ObsPy: a Python toolbox for seismology. *Seismol Res. Lett.* 81, 530–533. doi:10.1785/gssrl.81.3.530

Bluth, G. J. S., and Rose, W. I. (2004). Observations of eruptive activity at Santiaguito volcano, Guatemala. *J. Volcanol. Geoth. Res.* 136, 297–302. doi:10.1016/j.jvolgeores.2004.06.0010.1016/j.jvolgeores.2004.06.001

Capon, J. (1969). High-resolution frequency-wavenumber spectrum analysis. *Proc. IEEE* 57, 1408–1418. doi:10.1109/proc.1969.7278

Carter, W., Rietbrock, A., Lavallée, Y., Gottschämmer, E., Moreno, A. D., Kendrick, J. E., et al. (2020). Statistical evidence of transitioning open-vent activity towards a paroxysmal period at Volcán Santiaguito (Guatemala) during 2014-2018. *J. Volcanol. Geoth. Res.* 398, 106891. doi:10.1016/j.jvolgeores.2020.106891

Costa, A., Melnik, O., Sparks, R. S. J., and Voight, B. (2007). Control of magma flow in dykes on cyclic lava dome extrusion. *Geophys. Res. Lett.* 34. doi:10.1029/2006gl027466

Costa, A., Wadge, G., and Melnik, O. (2012). Cyclic extrusion of a lava dome based on a stick-slip mechanism. *Earth Planet Sci. Lett.* 337–338, 39–46. doi:10.1016/j.epsl.2012.05.011

De Angelis, S., Lamb, O. D., Lamur, A., Hornby, A. J., von Aulock, F. W., and Rietbrock, A. (2016). Characterization of moderate ash-and-gas explosions at Santiaguito volcano, Guatemala, from infrasound waveform inversion and thermal infrared measurements. *Geophys. Res. Lett.* 43, 6220–6227. doi:10.1002/2016gl069098

De Basabe, J. D., and Sen, M. K. (2007). Grid dispersion and stability criteria of some common finite-element methods for acoustic and elastic wave equations. Geophysics, 72, T81–T95. doi:10.1190/1.2785046

Dingwell, D. B. (1996). Volcanic dilemma--flow or blow?. *Science* 273 (5278), 1054–1055. doi:10.1126/science.273.5278.1054

Dobrin, M. B. (1951). Dispersion in seismic surface waves. *Geophysics* 16 (1), 63–80. doi:10.1190/1.1437652

Global Volcanism Program (2005). Report on Santa Maria (Guatemala) R. Wunderman (Smithsonian Institution). *Bull. Glob. Volcanism Netw.* Vol. 40. doi:10.5479/si.GVP.BGVN200510-342030

Global Volcanism Program (2011). Report on Santa Maria (Guatemala) R. Wunderman (Smithsonian Institution). *Bull. Glob. Volcanism Netw.* Vol. 36. doi:10.5479/si.GVP.BGVN201109-342030

Gottschämmer, E., Rohnacher, A., Carter, W., Nüsse, A., Drach, K., De Angelis, S., et al. (2020). Volcanic emission and seismic tremor at Santiaguito, Guatemala: New insights from long-term seismic, infrasound and thermal measurements in 2018–2020. *Journal of Volcanology and Geothermal Research,* 107154. doi:10.1016/j.jvolgeores.2020.107154

Harris, A. J., Rose, W. I., and Flynn, L. P. (2003). Temporal trends in lava dome extrusion at Santiaguito 1922-2000. *Bull. Volcanol.* 65, 77–89. doi:10.1007/s00445-002-0243-0

Haskell, N. A. (1953). The dispersion of surface waves on multilayered media. *Bull. Seismol. Soc. Am.* 43 (1), 17–34.

Holland, A. S. P., Watson, I. M., Caricchi, L., and Dalton, M. P. (2011). Degassing processes during lava dome growth: insights from Santiaguito lava dome, Guatemala. *J. Volcanol. Geoth. Res.* 202, 153–166. doi:10.1016/j.jvolgeores.2011.02.004

Hornby, A. J., Lavallée, Y., Kendrick, J. E., De Angelis, S., Lamur, A., Lamb, O. D., et al. (2019b). Brittle-ductile deformation and tensile rupture of dome lava during inflation at Santiaguito, Guatemala. *J. Geophys. Res. Solid Earth* 124, 10107. doi:10.1029/2018jb017253

Hornby, A. J., Lavallée, Y., Kendrick, J. E., Rollinson, G., Butcher, A. R., Clesham, S., et al. (2019a). Phase partitioning during fragmentation revealed by QEMSCAN Particle Mineralogical Analysis of volcanic ash. *Sci. Rep.* 9, 1–12. doi:10.1038/s41598-018-36857-4

Iverson, R. M. (2008). "Dynamics of seismogenic volcanic extrusion resisted by a solid surface plug, Mount St. Helens, 2004-2005," in Volcano rekindled: the renewed eruption of Mount St. Helens, 2004–2006. Professional Paper 1750. Editors D. R. Sherrod, W. E. Scott, and P. H. Stauffer (U.S. Geological Survey), 425–460. doi:10.3133/pp175021

Johnson, J. B., Lees, J. M., Gerst, A., Sahagian, D., and Varley, N. (2008). Long-period earthquakes and co-eruptive dome inflation seen with particle image velocimetry. *Nature* 456, 377. doi:10.1038/nature07429

Johnson, J. B., Lyons, J. J., Andrews, B. J., and Lees, J. M. (2014). Explosive dome eruptions modulated by periodic gas-driven inflation. *Geophys. Res. Lett.* 41, 6689–6697. doi:10.1002/2014gl061310

Johnson, J. B., Sanderson, R., Lyons, J., Escobar-Wolf, R., Waite, G., and Lees, J. M. (2009). Dissection of a composite volcanic earthquake at Santiaguito, Guatemala. *Geophys. Res. Lett.* 36 (16). doi:10.1029/2009gl039370

Jongmans, D., and Demanet, D. (1993). The importance of surface waves in vibration study and the use of Rayleigh waves for estimating the dynamic characteristics of soils. *Eng. Geol.* 34 (1–2), 105–113. doi:10.1016/0013-7952(93)90046-f

Kendrick, J. E., Lavallée, Y., Hirose, T., Di Toro, G., Hornby, A. J., De Angelis, S., et al. (2014). Volcanic drumbeat seismicity caused by stick-slip motion and magmatic frictional melting. *Nat. Geosci.* 7 (6), 438–442. doi:10.1038/ngeo2146

Kendrick, J. E., Lavallée, Y., Varley, N. R., Wadsworth, F. B., Lamb, O. D., and Vasseur, J. (2016). Blowing off steam: tuffisite formation as a regulator for lava dome eruptions. *Front. Earth Sci.* 4. doi:10.3389/feart.2016.00041

Kilburn, C. R. J. (2003). Multiscale fracturing as a key to forecasting volcanic eruptions. *J. Volcanol. Geoth. Res.* 125 (3–4), 271–289. doi:10.1016/s0377-0273(03)00117-3

Komatitsch, D., Tromp, J., and Vilotte, J. P. (1998). The spectral element method for elastic wave equations: application to 2D and 3D seismic problems. *Bull. Seismol. Soc. Am.* 88, 368–392. doi:10.1190/1.1820185

Lamb, O. D., Lamur, A., Díaz-Moreno, A., De Angelis, S., Hornby, A. J., von Aulock, F. W., et al. (2019). Disruption of long-term effusive-explosive activity at Santiaguito, Guatemala. *Front. Earth Sci.* 6, 253. doi:10.3389/feart.2018.00253

Lamur, A., Kendrick, J. E., Eggertsson, G. H., Wall, R. J., Ashworth, J. D., and Lavallée, Y. (2017). The permeability of fractured rocks in pressurised volcanic and geothermal systems. *Nat. Sci. Rep.* 7 6173. doi:10.1038/s41598-017-05460-4

Lamur, A., Kendrick, J. E., Wadsworth, F. B., and Lavallée, Y. (2019). Fracture healing and strength recovery in magmatic liquids. *Geology* 47 (3), 195–198. doi:10.1130/g45512.1

Lavallée, Y., Dingwell, D. B., Johnson, J. B., Cimarelli, C., Hornby, A. J., Kendrick, J. E., et al. (2015). Thermal vesiculation during volcanic eruptions. *Nature* 528, 544–547. doi:10.1038/nature16153

Lavallée, Y., Benson, P. M., Heap, M. J., Hess, K.-U., Flaws, A., Schillinger, B., et al. (2013). Reconstructing magma failure and the degassing network of dome-building eruptions. *Geology* 41 (4), 515–518. doi:10.1130/g33948.1

Müller, G. (1990). Theorie elastischer Wellen. Institut für Meteorologie und Geophysik. Universität Frankfurt

Melnik, O., and Sparks, R. S. J. (2005). Controls on conduit magma flow dynamics during lava dome building eruptions. *J. Geophys. Res.* 110 (B2). doi:10.1029/2004jb003183

Melnik, O., and Sparks, R. S. J. (1999). Nonlinear dynamics of lava dome extrusion. *Nature* 402 (6757), 37–41. doi:10.1038/46950

Michaut, C., Ricard, Y., Bercovici, D., and Sparks, R. S. J. (2013). Eruption cyclicity at silicic volcanoes potentially caused by magmatic gas waves. *Nat. Geosci.* 6 (10), 856–860. doi:10.1038/ngeo1928

Murphy, J. R., and Shah, H. K. (1988). An analysis of the effects of site geology on the characteristics of near-field Rayleigh waves. *Bull. Seismol. Soc. Am.* 78 (1), 64–82.

Neuberg, J., and Pointer, T. (2000). Effects of volcano topography on seismic broad-band waveforms. *Geophys. J. Int.* 143, 239–248. doi:10.1046/j.1365-246x.2000.00251.x

Ohminato, T., Takeo, M., Kumagai, H., Yamashina, T., Oikawa, J., Koyama, E., et al. (2006). Vulcanian eruptions with dominant single force components observed during the Asama 2004 volcanic activity in Japan. *Earth Planets Space* 58 (5), 583–593. doi:10.1186/bf03351955

Patrick, M., Varley, N., Ramos, E., Blankenbicker, A., and Johnson, J. (2007). Ash plume dynamics at Santiaguito volcano, Guatemala, from thermal and high resolution video. AGUFM, V31E–0707. Washington, DC: American Geophysical Union.

Rhodes, E., Kennedy, B. M., Lavallée, Y., Hornby, A., Edwards, M., and Chigna, G. (2018). Textural insights into the evolving lava dome cycles at Santiaguito lava dome, Guatemala. *Front. Earth Sci.* 6. doi:10.3389/feart.2018.00030

Rose, W. I. (1972). Notes on the 1902 eruption of Santa maría volcano, Guatemala. *Bull. Volcanol.* 36, 29–45. doi:10.1007/bf02596981

Rose, W. I. (1973). Pattern and mechanism of volcanic activity at the Santiaguito volcanic dome, Guatemala. *Bull. Volcanol.* 37, 73. doi:10.1007/bf02596881

Rose, W. I. (1987). Volcanic activity at Santiaguito volcano, 1976–1984. *Geol. Soc. Am. Spec. Pap.* 212, 17–27. doi:10.1130/spe212-p17

Sahetapy-Engel, S. T., Harris, A. J. L., and Marchetti, E. (2008). Thermal, seismic and infrasound observations of persistent explosive activity and conduit dynamics at Santiaguito lava dome, Guatemala. *J. Volcanol. Geoth. Res.* 173, 1–14. doi:10.1016/j.jvolgeores.2007.11.026

Sanderson, R. W., Johnson, J. B., and Lees, J. M. (2010). Ultra-long period seismic signals and cyclic deflation coincident with eruptions at Santiaguito volcano, Guatemala. *J. Volcanol. Geoth. Res.* 198, 35–44. doi:10.1016/j.jvolgeores.2010.08.007

Schaefer, L. N., Kendrick, J. E., Oommen, T., Lavallée, Y., and Chigna, G. (2015). Geomechanical rock properties of a basaltic volcano. *Front. Earth Sci.* 3. doi:10.3389/feart.2015.00029

Scharff, L., Hort, M., and Gerst, A. (2014). The dynamics of the dome at Santiaguito volcano, Guatemala. *Geophys. J. Int.* 197, 926–942. doi:10.1029/2011jb00854210.1093/gji/ggu069

Scharff, L., Ziemen, F., Hort, M., Gerst, A., and Johnson, J. B. (2012). A detailed view into the eruption clouds of Santiaguito volcano, Guatemala, using Doppler radar. *J. Geophy. Res.*, 117 (B4), B04201. doi:10.1029/2011jb008542

Shearer, P. M. (2009). *Introduction to seismology*. 2nd edn. Cambridge, United Kingdom: Cambridge University Press. doi:10.1017/cbo9780511841552

Spieler, O., Kennedy, B., Kueppers, U., Dingwell, D. B., Scheu, B., and Taddeucci, J. (2004). The fragmentation threshold of pyroclastic rocks. *Earth Planet Sci. Lett.* 226 (1–2), 139–148. doi:10.1016/j.epsl.2004.07.016

Tenzer, R., Sirguey, P., Rattenbury, M., and Nicolson, J. (2011). A digital rock density map of New Zealand. *Comput. Geosci.* 37, 1181–1191. doi:10.1016/j.cageo.2010.07.010

Thomas, M. E., and Neuberg, J. (2012). What makes a volcano tick-A first explanation of deep multiple seismic sources in ascending magma. *Geology* 40 (4), 351–354. doi:10.1130/g32868.1

von Aulock, F. W., Lavallée, Y., Hornby, A. J., Lamb, O. D., Andrews, B. J., et al. (2016). Observing changes at Santiaguito volcano, Guatemala with an unmanned aerial vehicle (UAV). in Proceedings of the EGU General Assembly Conference Abstracts, 18, Vienna, Austria, April 17–22, 2016.

Wallace, P. A., Lamb, O. D., De Angelis, S., Kendrick, J. E., Hornby, A. J., Díaz-Moreno, A., et al. (2020). Integrated constraints on explosive eruption intensification at Santiaguito dome complex, Guatemala. *Earth Planet Sci. Lett.* 536, 116139. doi:10.1016/j.epsl.2020.116139

Wathelet, M. (2008). An improved neighborhood algorithm: parameter conditions and dynamic scaling. Geophysical Research Letters, 35, L09301, doi:10.1029/2008GL033256

Wathelet, M. (2005). Array recordings of ambient vibrations: surface-wave inversion. PhD Dissertation. Liège, Belgium: Liége University. 161.

Wathelet, M., Guillier, B., Roux, P., Cornou, C., and Ohrnberger, M. (2018). Rayleigh wave three-component beamforming: signed ellipticity assessment from high-resolution frequency-wavenumber processing of ambient vibration arrays. *Geophys. J. Int.* 215 (1), 507–523. doi:10.1093/gji/ggy286

Yoshimura, S., and Nakamura, M. (2010). Fracture healing in a magma: an experimental approach and implications for volcanic seismicity and degassing. *J. Geophys. Res.* 115 (B9), B09209. doi:10.1029/2009jb000834

Zobin, V. M., Navarro, C., Reyes-Dávila, G., Orozco, J., Bretón, M., Tellez, A., et al. (2006). The methodology of quantification of volcanic explosions from broadband seismic signals and its application to the 2004-2005 explosions at Volcán de Colima, México. *Geophys. J. Int.* 167 (1), 467–478. doi:10.1111/j.1365-246X.2006.03108.x

Zobin, V. M., Reyes, G. A., Guevara, E., and Bretón, M. (2008). Seismological constraints on the position of the fragmentation surfaces in the volcano conduit. *Earth Planet Sci. Lett.* 275 (3–4), 337–341. doi:10.1016/j.epsl.2008.08.034

Zorn, E. U., Walter, T. R., Johnson, J. B., and Mania, R. (2020). UAS-based tracking of the Santiaguito lava dome, Guatemala. *Sci. Rep.* 10, 8644–8713. doi:10.1038/s41598-020-65386-2

Conflict of Interest: The authors declare that the research was conducted in the absence of any commercial or financial relationships that could be construed as a potential conflict of interest.

Copyright © 2021 Rohnacher, Rietbrock, Gottschämmer, Carter, Lavallée, De Angelis, Kendrick and Chigna. This is an open-access article distributed under the terms of the Creative Commons Attribution License (CC BY). The use, distribution or reproduction in other forums is permitted, provided the original author(s) and the copyright owner(s) are credited and that the original publication in this journal is cited, in accordance with accepted academic practice. No use, distribution or reproduction is permitted which does not comply with these terms.

frontiers in Earth Science

ORIGINAL RESEARCH
published: 26 March 2021
doi: 10.3389/feart.2021.628967

Seismicity of the Northern Volcanic Zone of Iceland

Páll Einarsson and Bryndís Brandsdóttir*

Institute of Earth Sciences, University of Iceland, Reykjavík, Iceland

A half century of monitoring of the Northern Volcanic Zone of Iceland, a branch of the North America—Eurasia plate boundary, shows that the seismicity is very unevenly distributed, both in time and space. The four central volcanoes at the boundary, Þeistareykir, Krafla, Fremrinámar, and Askja, show persistent but very low-level seismicity, spatially coinciding with their high-temperature geothermal systems. On their rift structures, on the other hand, seismicity is almost absent, except during rifting episodes. Krafla went through a rifting episode in 1975–1984 with inflation, interrupted by 20 diking events with extensive rifting, eruptive activity, and intense seismicity along an 80 km long section of the rift. During inflation periods, the seismicity was contained within the caldera of the volcano, reflecting the inflation level of the magma chamber. Diking events were marked by seismicity propagating away from the volcano into the fissure swarms to the south or north of the volcano, accompanied by rapid deflation of the caldera magma chamber. These events lasted from 1 day to 3 months, and the dike length varied between 1 and 60 km. The area around the Askja volcano is the only section of the Northern Volcanic Zone that shows persistent moderate seismicity. The largest events are located between fissure swarms of adjacent volcanic systems. Detailed relative locations of hypocenters reveal a system of vertical strike-slip faults, forming a conjugate system consistent with minimum principal stress in the direction of spreading across the plate boundary. A diking event into the lower crust was identified in the adjacent fissure swarm at Upptyppingar in 2007–2008. Four nests of anomalously deep earthquakes (10–34 km) have been identified in the Askja region, apparently associated with the movements of magma well below the brittle-ductile transition. Several processes have been pointed out as possible causes of earthquakes in the deformation zone around the plate boundary. These include inflation and deflation of central volcanoes, intrusion of propagating dikes, both laterally and vertically, strike-slip faulting on conjugate fault systems between overlapping fissure swarms, migration of magma in the lower, ductile crust, and geothermal heat mining.

Keywords: Iceland, Northern Volcanic Zone, earthquakes, Krafla volcano, Askja volcano, dike intrusion, rifting, inflation–deflation cycle

OPEN ACCESS

Edited by:
Derek Keir,
University of Southampton,
United Kingdom

Reviewed by:
Finnigan Illsley-Kemp,
Victoria University of Wellington,
New Zealand
Luigi Passarelli,
Université de Genève, Switzerland

****Correspondence:***
Páll Einarsson
palli@hi.is

Specialty section:
This article was submitted to Volcanology, a section of the journal Frontiers in Earth Science

Received: *13 November 2020*
Accepted: *24 February 2021*
Published: *26 March 2021*

Citation:
Einarsson P and Brandsdóttir B (2021) Seismicity of the Northern Volcanic Zone of Iceland. Front. Earth Sci. 9:628967. doi: 10.3389/feart.2021.628967

INTRODUCTION

Volcanism in Iceland has its roots in two different processes. The mid-Atlantic plate boundary runs through the country, separating two of the largest lithospheric plates, the North America and the Eurasia plates and spreading at a rate of about 19 mm/year (e.g., Árnadóttir et al., 2009). At the same time the area is a hotspot fed by a mantle plume centered on the central highlands

of Iceland but affecting an area much larger than the present extent of the country (e.g., Wolfe et al., 1997). The two processes interact and lead to a high rate of eruptions from about 30 different and active volcanic systems. The rate fluctuates within the range of 20–50 eruptions per century, with 22 eruptions in the last 50 years, for example (Einarsson, 2018). Running a modern society in a highly active area requires substantial monitoring effort. In Iceland the effort is based to a large extent on a combination of two methods to track the pathways and storage of magma in the crust, seismic monitoring and surface deformation studies (Sturkell et al., 2006; Einarsson, 2018; Sigmundsson et al., 2018). The first step in the detection strategy is to identify the volcanic systems that are preparing for an eruption. This includes detecting deviation in behavior from the long-term background seismicity. This is not a trivial task in the tectonic environment of an active plate boundary, where earthquakes are common (Pedersen et al., 2007). Long time series are essential. Once the active systems are identified the next step is to install instrumentation to detect the pressure changes and magma movements within the systems. Fortunately, most of the 30 volcanic systems that have been active in the Holocene are in a passive state at present and do not require intensive attention. The last step in the monitoring and warning process requires the ability to detect and correctly identify the short-term precursors to the initiation of an eruption. This last phase of the precursory activity, when the magma breaks out of its storage volume and propagates toward the surface, is marked by intensified seismic activity and rapid crustal movements. All eruptions in the last few decades in Iceland have been preceded by such detectable short-term precursors, and in 2/3 of the cases they have led to a warning to the public before the eruption broke out (Einarsson, 2018).

In the present paper, we intend to give an overview of the long-term seismic behavior of one branch of the volcanically active zones of Iceland, the Northern Volcanic Zone (**Figure 1**), based on the experience of the last several decades, or since sensitive seismic instrumentation was installed, mostly in the early seventies. This zone includes the volcanic systems of Þeistareykir, Krafla, Fremrinámar, and Askja, all of which show different seismic characteristics. Krafla went through an episode of magmatic rifting in the period 1975–1984 with many lateral dike intrusions, nine basaltic fissure eruptions, and extensive surface rifting. The Askja area has persistent, intermediate-level seismicity that has been ascribed to several different tectonic and magmatic processes in the crust. All the systems have low-level, persistent seismicity that correlates spatially with the surface manifestation of hydrothermal systems.

VOLCANIC ZONES AND VOLCANIC SYSTEMS OF ICELAND

A good part of the volcanism in Iceland takes place at or near the mid-Atlantic plate boundary. As it crosses the Iceland platform, the plate boundary breaks up into a series of segments, rifts, transforms and oblique segments. In some places the boundary branches out and small microplates or tectonic blocks are formed that may move independently of the large plates. The spreading across the plate boundary in South Iceland is divided between two sub-parallel branches, the Western and Eastern Volcanic Zones. The two zones are connected by a transform zone, the South Iceland Seismic Zone. Together with the Central Iceland Volcanic Zone these branches demarcate a microplate, the Hreppar Microplate (Einarsson, 2008), a diamond-shaped, 100 × 100 km crustal block that appears to move independently of the major plates. The 19 mm/year total spreading rate is partitioned unevenly among the two divergent branches (Sigmundsson et al., 1995; La Femina et al., 2005), about one-fifth taken up by the western branch and the rest by the eastern branch. The plate divergence in the northern part of Iceland takes place along a single boundary, the Northern Volcanic Zone (e.g., Drouin et al., 2017a). Oblique segments also exist and contain volcanism and strike-slip tectonism in close proximity to each other. The Reykjanes Peninsula Rift (RPR) and the offshore Grímsey Oblique Rift (GOR) are examples of this type. The structure of the divergent branches of the boundary is characterized by rifting. Normal faults, fissures, and eruptive fissures are abundant and are arranged into swarms that form volcanic systems together with one or two central volcanoes, where the volcanic activity is more concentrated than elsewhere (Saemundsson, 1974, 1978).

In addition to the plate boundary volcanism there are three zones of intraplate volcanism, or flank zones. The Snaefellsnes Volcanic Zone, the South Iceland group of volcanoes, and the Öraefajökull-Snaefell zone located east of the Eastern Volcanic Zone.

Note on terminology: The term "fissure swarm" in Iceland is used for an array of fissures and normal faults. Similar structure is called "rift zone" in other areas, e.g., in Hawaii. A "rift zone" in Iceland consists of several volcanic systems, i.e., several subparallel fissure swarms.

THE NORTHERN VOLCANIC ZONE

This branch of the plate boundary separates the two major plates, the North America and the Eurasia plates. The vector of plate separation is slightly oblique to the trend of the zone, so the volcanic systems are arranged en echelon. Most of the swarms extend along a large portion of the zone, so crossing the boundary one may have to cross a 50 km wide deformation zone with four or five semi-parallel fissure swarms. This means that the total plate velocity is partitioned between several fissure swarms and is not taken up by only one. The principal volcanic systems are Þeistareykir, Krafla, Fremrinámar, and Askja, all accompanied by impressive fissure swarms (Saemundsson, 1974; Hjartardóttir et al., 2016a). Sometimes two more are added to the list, Heiðarsporður and Hrúthálsar, both with traces of evolved rocks but limited fissure swarms (Saemundsson, 1991).

The seismicity of the Icelandic rift zones is highly clustered, both in time and space (Einarsson, 1991a). Most of the seismicity occurs at the central volcanoes, whereas the fissure swarms are generally very quiet. And the seismicity of the central volcanoes is only moderate, except during major volcano-tectonic events or episodes. Thus, the background seismicity of the Northern Volcanic Zone for the last few decades has

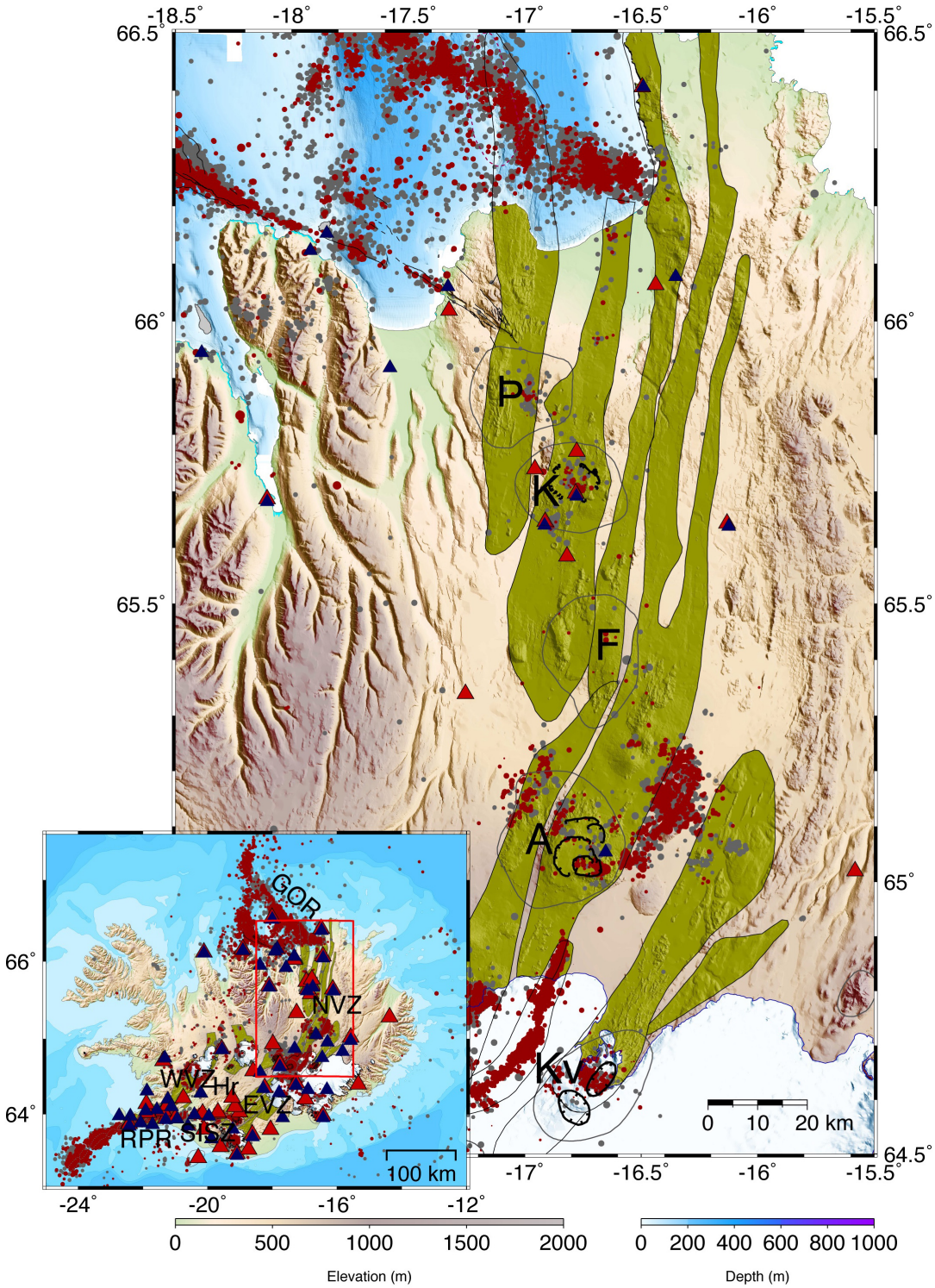

FIGURE 1 | The Northern Volcanic Zone of Iceland. Volcanic systems are shown (Hjartardóttir et al., 2012), usually named by the main central volcano: **Þ** Þeistareykir, **K** Krafla, **F** Fremrinámar, **A** Askja, and **Kv** Kverkfjöll. Their respective fissure swarms (or rift zones) are shown in yellow. Epicenters of earthquakes for the period 1995–2020, shown with black and red dots, are from the Icelandic Meteorological Office. Black dots are epicenters of the period 1995–2010 and M ≥ 2.0, and red dots are events of 2011–2020 with M ≥ 1.5. Shown are the Northern, Eastern, and Western Volcanic Zones (NVZ, EVZ, and WVZ), the Reykjanes Peninsula Rift (RPR), the South Iceland Seismic Zone (SISZ), the Grímsey Oblique Rift (GOR), and the Hreppar Microplate (Hr). Digital elevation and bathymetric models from the National Land Survey of Iceland and the Hydrographic Survey of the Icelandic Coast Guard. Seismic stations are shown with triangles, red for the Krafla period 1974–1994 and black for the digital stations 1995–2020.

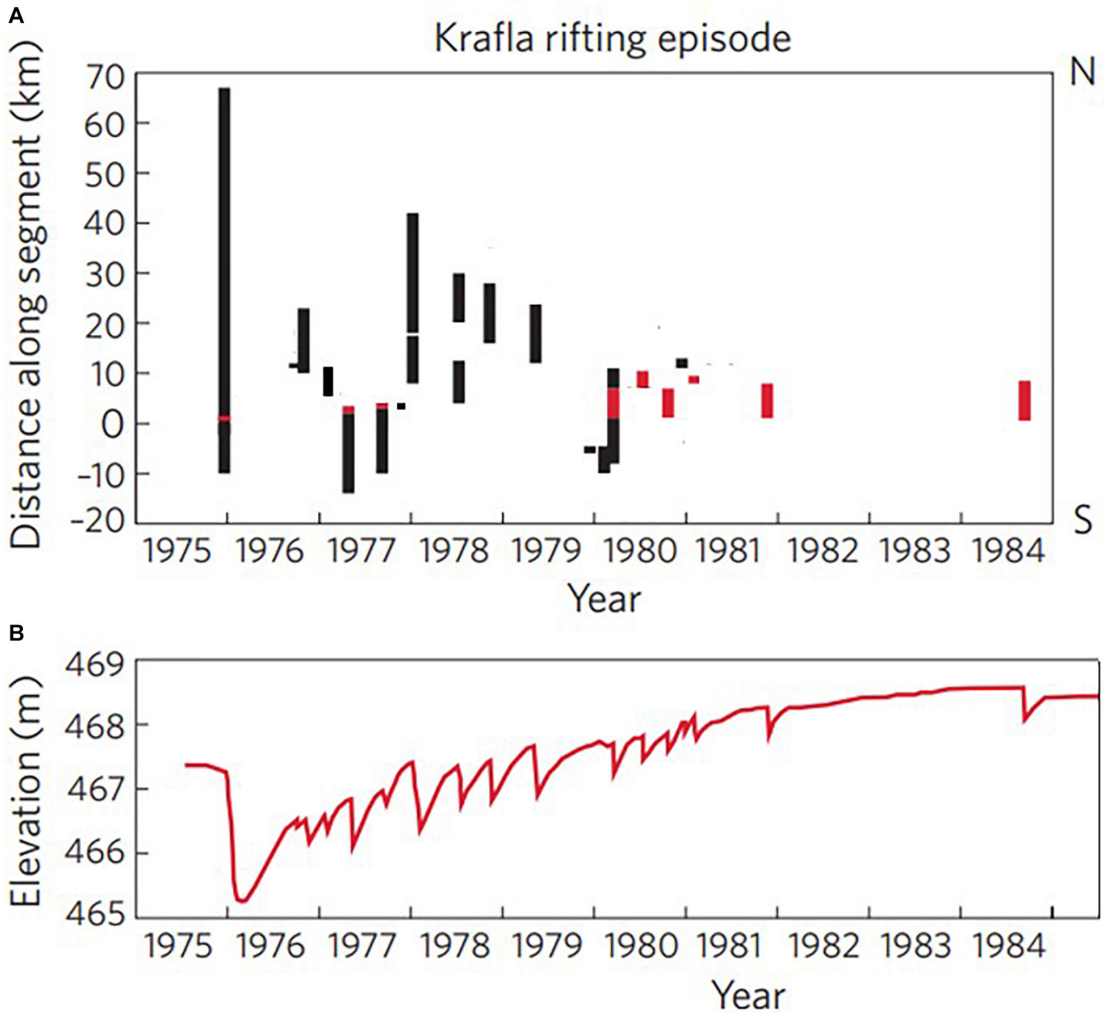

FIGURE 2 | Timeline of the Krafla rifting episode. **(A)** Distance of the rifting section of the fissure swarm during deflation of the caldera. Red bars indicate the occurrence and location of eruptions. **(B)** Elevation of the caldera center (modified from Einarsson, 1991b, and Wright et al., 2012). The graph is based on data from leveling, interpolated with the help of a water level tilt meter record. The activity ended with the Krafla volcano in an inflated state.

been characterized by weak seismicity of the main central volcanoes and moderate seismicity of an area east of the Askja volcano, 15 × 20 km in dimensions. The main fissure swarms of the rift, with their impressive normal faults and fissures, are seismically virtually inactive, however, even at the microearthquake level. The weak seismicity of the central volcanoes of **Þeistareykir**, **Fremrinámar**, and part of the Askja activity, appears to be spatially linked with the high-temperature geothermal areas of these volcanoes. Geothermal heat mining and cooling contraction, or other geothermal processes, may be responsible for this seismicity (Einarsson, 1991a). It is also noteworthy that silicic rocks are associated with these sites and may play a part in the causal process.

The most significant seismic activity of the Northern Volcanic Zone in the last decades took place in two areas: The Krafla volcanic system during the major magmato-tectonic events of 1975–1984 and in the Askja area persistently during the whole period of observations. These events will be discussed in Sections Krafla and Askja, respectively.

The monitoring capacity for earthquakes in the Northern Volcanic Zone has improved greatly during the last half century. An overview of the history of the seismograph system is given by Einarsson and Jakobsson (2020). The first network in North Iceland with the capability to distinguish between the activities of different volcanoes was installed in 1974, just in time to detect the beginning of the Krafla rifting episode (Einarsson, 2018). The network had 6–11 stations within 80 km distance from Krafla (**Figure 1**), and earthquakes down to magnitude 2 could be located with uncertainties less than 1–2 km (Einarsson, 1991a). The network was augmented by portable seismographs during critical times if conditions allowed, which was not very often. The studies of S-wave attenuation (Einarsson, 1978) and of the swarms of September 1977 and July 1980 (Brandsdóttir and Einarsson, 1979; Einarsson and Brandsdóttir, 1980) were

done with a network with a few extra stations added to the permanent network. The hypocentral locations were calculated by inversion programs like HYPOELLIPSE by Lahr and Ward (1976) and subsequent inversion programs developed at the USGS in Menlo Park, CA. Crustal velocity structure was based on the extensive work of Pálmason (1963) and calibrated with explosions in a crater lake (Einarsson, 1978). The accuracy of depth determinations was uneven within the network. Close to the seismic stations the uncertainty was of the order of 1 km, but farther away it was not so good. Therefore, the depth determination of activity close to the central volcano and the southern fissure swarm was good, but in a large part of the uninhabited northern fissure swarm the depth is not well constrained.

The first epicentral maps for the whole zone reveal the clustered seismic activity, with most of the background seismicity occurring in the central volcanoes (Einarsson, 1991a). It also showed the unexplained persistent seismic activity in the volcanic zone east of the Askja volcano.

After 1990, the seismic network in the country was gradually replaced by a digital, semi-automated network (Stefánsson et al., 1993) (**Figure 1**), and the last analog seismograph station was decommissioned in 2010. The Askja seismicity attracted attention, and in 2005 and following years, the permanent network was augmented with temporary stations around Askja, by initiative from Cambridge University. The level of detection was lowered by up to two magnitude units (Greenfield et al., 2018), with a stream of research papers on this remarkable cluster of activity within the Northern Volcanic Zone (e.g., Soosalu et al., 2009; White et al., 2011; Green et al., 2014, 2015).

Krafla

The Krafla volcanic system consists of a central volcano with a 10 × 8 km caldera of about 110 ka age, partly buried by later lavas (Saemundsson, 1991; Rooyakkers et al., 2020). The caldera is transected by fissure swarms that extend about 45 km to the south and 60 km to the north of the volcano, subparallel to the plate boundary. The only known previous historic rifting episode occurred in 1724–1746, with extensive rifting, apparently mainly in the southern fissure swarm, and several fissure eruptions in the caldera and southern fissure swarm (Saemundsson, 1991; Hjartardóttir et al., 2012). The big lessons in volcano seismicity were provided by the Krafla magmatic episode that occurred in 1974–1989 (Björnsson et al., 1977; Tryggvason, 1984; Einarsson, 1991b; Buck et al., 2006). During this time interval about twenty inflation-deflation cycles of the Krafla central volcano were detected (**Figure 2** and **Table 1**). During inflation of the central volcano the seismicity was limited to the caldera (**Figure 3**) and generally increased toward the end of the inflation phase. In several cases it can be demonstrated to follow the Kaiser effect (Heimisson et al., 2015), i.e., the seismicity was at a minimum until the inflation level exceeded the maximum level of the previous inflation. Then, it increased abruptly. An important corollary is that inflation and deflation of a caldera can occur without significant or detectable change in seismicity. This range of aseismic inflation-deflation was of the order of one meter vertical displacement at the center. A high proportion of the caldera earthquakes showed anomalously small S-waves, indicative of S-wave shadowing by a magma body (Einarsson, 1978), later confirmed by seismic profiling and seismic imaging of the caldera (Brandsdóttir and Menke, 1992; Schuler et al., 2015). Most of the caldera earthquakes originated in the uppermost 3 km of the crust, below which an aseismic layer extended to a depth of 7 km. Several earthquakes at 7 km depth delivered S-waves to regional seismic stations, indicating a bottom to the attenuating body (Einarsson, 1978).

During the deflation part of the cycle, the fissure swarm was activated (**Figure 3**) with propagating earthquakes and large-scale rifting (Brandsdóttir and Einarsson, 1979; Einarsson and Brandsdóttir, 1980).

The activity can be divided into phases, each of which was accompanied by characteristic seismicity.

The Preparatory Phase, 1974–1975

A newly installed seismograph system began picking up events originating within the caldera of Krafla in the winter of 1974–1975. This was unexpected. No significant activity had been known there before, and the increase was confirmed by local residents who had never before felt local earthquakes. This increase was limited to the caldera. The issue was politically

TABLE 1 | Dikes and deflation events of the Krafla episode.

Y	M	D	Dur	Dir	L (km)	Speed (m/s)	Defl. cm	Erupt.	Prec.t	Vol. lava Mm^3
1975	12	20	90 d	S, N	60		203	Y	15 m	Small
1976	09	29	5 d	N	12		14			
1976	10	31	2 d	N	24		57			
1977	01	20	2 d	N	10		29			
1977	04	27	2 d	S	17		77	Y	(1 h)	Small
1977	09	08	1 d	S	13	0.35	21	Y	2 1/4 h	Small
1977	11	02	1 d	N	<3		<4			
1978	01	06	20 d	N	45	0.2	105			
1978	07	10	3 d	N	25	0.5	57			
1978	11	10	5 d	N	18		64			
1979	05	13	5 d	N	24		84			
1979	12	02	6 d	S?	4?		3			
1980	02	10	10 d	S	10		10			
1980	03	16	1 d	N, S	20	0.9	38	Y	65 m	Small
1980	07	10	6 d	N	9		40	Y	5 h	30
1980	10	18	5 d	N	7		30	Y	82 m	40
1980	12	24	4 d	N	10		10			
1981	01	30	5 d	N	6		27	Y	7 h	32
1981	11	18	5 d	N	8	1.8	50	Y	76 m	40
1984	09	04	14 d	N	8.5	0.6	55	Y	264 m	80

Characteristics of the 20 deflation/diking events of Krafla 1975–1984: Date of the beginning, duration of the event from the beginning of deflation until inflation sets in again, direction of propagation into the N or S fissure swarms, length of the dike measured from the center of the caldera to the distal end of the epicenter distribution (Einarsson, 1991b), maximum speed of propagation, vertical subsidence at the center of deflation (Björnsson and Eysteinsson, 1998), eruption, and precursor time from the beginning of deflation until an eruption begins (Einarsson, 2018).

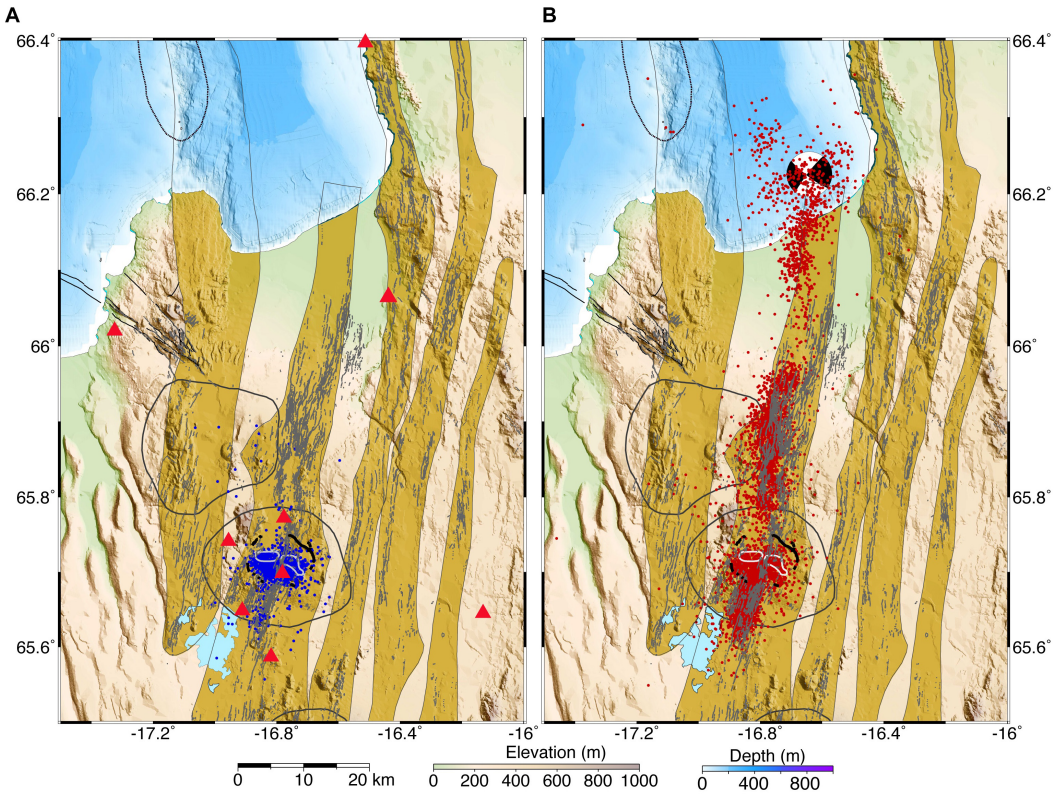

FIGURE 3 | Maps of epicenters during inflation periods of Krafla 1975–1984 in blue **(A)** and during deflation periods of the caldera in red **(B)**. Focal mechanism of the Kópasker earthquake (M_S 6.4) that occurred at the rift-transform intersection during the first rifting event is shown (Einarsson, 1986). Seismic stations are shown with red triangles in **(A)**. Digital elevation and bathymetric models from the National Land Survey of Iceland and the Hydrographic Survey of the Icelandic Coast Guard.

very sensitive because a new and controversial power station was under construction within the caldera.

The Initial Rifting Event, December 1975–March 1976

A new phase of the activity began suddenly on December 20 when a small basaltic fissure eruption broke out in the center of the caldera, preceded by only 15 min of intense earthquake activity (Einarsson, 2018) that was detected by seismic stations throughout Iceland. The earthquake activity soon propagated out of the caldera, first to the south and then to the north. The eruption then came to an end, and only lasted about 2 h. The activity south of the caldera lasted a few hours, but the earthquakes north of the caldera kept propagating for several days until they reached the intersection of the fissure swarm with the Grímsey Oblique Rift offshore. All together about 60 km section of the fissure swarms was activated in this event. The earthquakes continued, however, and so did the deflation of the caldera. Large-scale rifting was observed along the northern end of the fissure swarm.

On January 13 a magnitude 6.4 earthquake occurred offshore at the intersection with the Grímsey Oblique Rift. The focal mechanism indicated strike-slip faulting (Einarsson, 1986, 1987). The earthquake caused considerable damage in the surrounding area, particularly in the Kópasker village. The earthquake was clearly triggered by the widening of the Krafla fissure swarm that was still going on immediately to the south (e.g., Passarelli et al., 2013).

The initial rifting event ended in March, both the deflation of the caldera and the earthquake swarm and rifting at the northern end of the fissure swarm. Soon after that the caldera began inflating.

Intrusive Activity North of the Caldera, September 1976–January 1977

The re-inflation of the caldera was an indication that the activity at Krafla had not come to an end. This was confirmed when earthquake activity in the caldera began increasing in the summer of 1976 (Björnsson et al., 1977; Heimisson et al., 2015). The number of detected earthquakes in the caldera increased from a few events per day to more than a hundred. This activity suddenly stopped in September, when the caldera began to slowly subside. A flurry of earthquakes was detected in the fissure swarm north of the caldera indicating an intrusion in that area. This event only lasted five days and the caldera started inflating again. Much more dramatic intrusive activity followed, in October 1976 and January 1977, after the inflation level in the caldera had reached and exceeded the previous maxima, reached before the September deflation. This activity was accompanied by intense earthquake swarms and surface rifting in the northern fissure swarm.

Intrusive Activity in the Southern Fissure Swarm, April and September 1977

The caldera seismicity was very low after the deflation of January 1977, only a few detected events per day. It remained low despite re-inflation of the caldera. When the inflation level exceeded the previous maximum, however, the seismicity increased rather abruptly. The inflation continued for about two months until finally the magma storage was ruptured, and a dike began propagating from the caldera into the southern fissure swarm. A small eruption began at the northern caldera rim but stopped as soon as the dike began propagating. Extensive surface rifting occurred inside the caldera as well as in the southern fissure swarm (**Figure 4**).

Inflation of the caldera set in as soon as the April dike became inactive. This inflation (about 1 m, **Figure 2**) was aseismic and continued until the level of the previous inflation was almost reached. Then, a new diking event began rather abruptly with a small eruption at the northern caldera rim, in the same place as in the previous diking event. The eruption lasted about 2 h. Also this time, the dike propagated southwards, and the eruption came to an end (Brandsdóttir and Einarsson, 1979). A unique event took place when the dike had propagated through the Bjarnarflag geothermal area about 10 km south of the caldera. One of the drillholes used for power production erupted, punctured a steam pipe, and erupted a few tons of basaltic pumice for a while (Larsen et al., 1979). The dike did not propagate as far as the one in April (**Figure 4**), but extensive surface rifting was observed in the fissure swarm. The diatomite factory at Bjarnarflag was seriously damaged by the surface ruptures. The hypocentral depth of the earthquakes in the swarms of April and September was also consistent with a shallow intrusion. They occurred down to 3–4 km.

The dike intrusions of 1977 into the southern fissure swarm were accompanied by surface rifting and crustal extension within the caldera. The subsequent inflation of the caldera did therefore not lead to earthquake activity at the same inflation level as before. The correlation between the inflation and earthquake activity in the caldera became weaker (Heimisson et al., 2015).

Intrusions in the Northern Fissure Swarm, 1978–1979

The inflation following the southern intrusions of 1977 by far exceeded the previous maximum level and was interrupted only by a small deflation event in November. In the beginning of the year 1978 the rate of inflation had decreased, and the caldera seismicity was low. A debate about the possible end of the activity was quickly silenced on January 6th when a new intrusion event began with a slow deflation at the caldera. The rate quickly increased, and earthquakes propagated into the northern fissure swarm. This event turned into the second largest dike intrusion of the Krafla rifting episode, in terms of volume, distance, and duration (**Table 1**). No eruption accompanied this intrusion but rifting occurred near the distal end of the dike, where it cut the main road. A re-measurement of a leveling profile there shows that the rifting has the form of a graben of 7 km width that subsided 1.2 m. The flanks were uplifted by 0.5 m (Sigurdsson, 1980; Hjartardóttir et al., 2012).

Similar events took place in July and November 1978, and May 1979 (Einarsson and Brandsdóttir, 1980). They were all accompanied by similar amount of deflation, 60–70 cm. The length of the dike became progressively shorter, however, and the surface rifting took place in different parts of the northern fissure swarm (**Figure 4**). No eruptions occurred but one drill hole within the caldera got clogged during the May 1979 intrusion. Repair and clearing of the hole revealed fresh basaltic glass.

Intrusions Into the Southern Fissure Swarm, February and March 1980

Inflation during the next seven months was interrupted by a small episode of slow deflation in the beginning of December 1979. A few small earthquakes at the southern caldera rim indicated that magma may have migrated a short distance to the south during this deflation. Inflation resumed and continued until February 10 when a new deflation event began with a swarm of small earthquakes south of the southern caldera rim (**Figure 4**). The activity slowly migrated southwards with varying intensity. The hypocenters of these earthquakes were unusually deep, between 5 and 7 km, deeper than during the intrusions in the same area in 1977. Very little surface rifting was observed. Apparently, this dike was intruding below the dikes formed in 1977. After ten days of deflation the caldera began inflating again.

The elevation of the caldera just about reached the previous maximum when a new deflation event began rather abruptly on March 16. This time the course of events was very rapid. The rate of deflation was unusually high and vigorous spasmodic tremor was recorded on the seismograph network with increasing amplitude, accompanied by earthquakes. An eruption broke out on a fissure within the caldera 65 min after the beginning of the deflation. The erupting fissure propagated toward the north, and in 25 min, it had attained a length of 4.5 km. The opening of the fissure was not accompanied by any noticeable increase in seismic activity. The earthquakes kept propagating to the north, however, at least for 5 more kilometers. Then, the events took an unexpected course. A new dike began propagating southwards from the caldera with larger earthquakes than before, exceeding magnitude 3 (**Figure 4**). This dike followed the same path as the February dike, but at shallower level. The eruption vigor decreased when the new dike began propagating and came to an end. The volume of this eruption was small, but still considerably larger than the three previous eruptions of the episode. It marked the end of the primarily intrusive part of the Krafla magmatotectonic episode.

Eruption Phase, July and October 1980, January and November 1981, and September 1984

The remaining deflation events at Krafla were mostly eruptive, i.e., most of the mobilized magma found its way to the surface to feed eruption on long fissures within the caldera and adjacent northern fissure swarm. The only exception was a small deflation event in December 1980 when magma apparently was injected into the northern fissure swarm. The five eruptions shared several characteristics, even though the time scale and rate of change were variable. The beginning of the deflation was indistinguishable from what was observed in previous intrusive

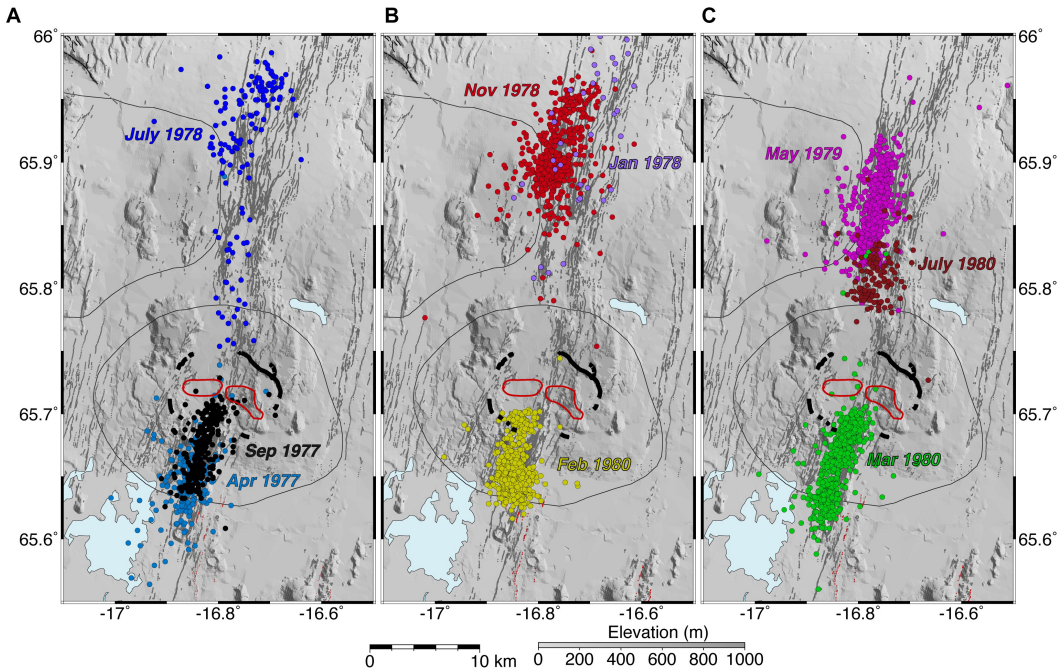

FIGURE 4 | Epicenters during intrusive activity in the fissure swarms of Krafla in April and September 1977, and July 1978 **(A)**; January and November 1978, and February 1980 **(B)**; May 1979, and March and July 1980 **(C)**. The caldera rims of Krafla and the outlines of the central volcanoes are shown for reference. Red lines within the caldera show the outlines of the S-wave shadows (Einarsson, 1978). Faults and fissures are from Hjartardóttir et al. (2016b). Red lines are eruptive fissures. Digital elevation model from the National Land Survey of Iceland.

events. It was not until the dike approached the surface that a difference in seismicity was noticeable. Often low-frequency earthquakes were the last signal that an eruption was about to break out (Einarsson, 2018). Usually, the earthquake activity decreased markedly when the eruption began and remained low during the eruption. The eruptive fissures of two of the eruptions (July 1980 and January 1981) were 4 and 2 km long, respectively, and located 5–7 km north of the caldera. The other three eruptions took place on much longer fissures, extending from the center of the caldera and 8–9 km to the north. The eruptions were most vigorous during the first day and then declined quickly. The activity concentrated on one or very few craters and faded out in 5–8 days. The last eruption (September 4–18, 1984) was an exception. The first few days it behaved like the previous eruptions, but after the activity had been limited to one crater the vigor of the eruption began to increase. This increase continued until the 14th day of the eruption when it suddenly ended.

Inflation, 1984–1989

The Krafla volcano began inflating again when the eruption of September 1984 was over. The inflation continued intermittently for several years, until 1989. The inflation was accompanied by a persistent background of small earthquakes, rarely exceeding magnitude 2, showing heterogeneous stress, with horizontal shear, extensional and compressional sources in close juxtaposition. A part of these events had sources with a large non-double couple component (Foulger et al., 1989). By 1989, the inflation had exceeded the level reached before the 1984 eruption (Sturkell et al., 2008). Since then, a slow deflation has been the main characteristic of the crustal deformation of the volcano, most likely reflecting gradual cooling of the caldera crustal volume and harnessing of the geothermal system (Drouin et al., 2017b). The seismicity of Krafla during this phase of slow deflation has been low, similar to that of other central volcanoes of the zone with a geothermal system, Þeistareykir, Fremrinámar and Askja, with a couple of events per year of magnitude 2 and larger.

General Pattern

The course of events was governed by magma chamber inflation that continued for at least 15 years (**Figure 2**), interrupted by about 20 short deflation events when magma escaped from the holding chamber in the middle of the caldera and formed a dike that propagated along the fissure swarms, either to the north, the south, or both (**Table 1**) (Buck et al., 2006; Wright et al., 2012). These events were of variable magnitude, even though the deformation pattern in the caldera was the same. The shape of the deformation indicates a depth to the pressure source of about 3 km (Johnsen et al., 1980; Tryggvason, 1980). Thus, since the shape of the deformation field was unchanged, the relative size of the deflation events may be quantified by the total vertical displacement in the center of deflation that coincided with the center of the caldera and scales linearly with the volume of the deflation. The central maximum subsidence ranged between 3 and 203 cm (**Table 1**). Similarly, the final length of the dike that was formed in the fissure swarms ranged between a few

km and 60 km (**Figure 2**). The seismicity changed dramatically during these deflation events. The caldera seismicity stopped instantaneously when the deflation began (**Figure 3**). Then, a flurry of events began near the caldera, propagating outward along the fissure swarm (Hjartardóttir et al., 2012). The speed of propagation was high in the beginning but slowed down as the distance from the caldera increased, see **Figure 5** (Einarsson and Brandsdóttir, 1980). The rate of deflation followed the same pattern, was high in the beginning and then slowing down. The magnitude of the fissure swarm earthquakes increased as the swarm progressed and formed a cluster in a particular part of the fissure swarm, where large scale surface rifting was also observed in the largest events. The maximum speed of propagation was quite variable between deflation events, ranging between 0.2 and 1.8 m/s (**Table 1**). The duration of the deflation events was also quite variable, between one day and three months.

The dikes reached the surface in nine of the cases, producing eruptions of basaltic lava from fissures of variable length, up to 9 km (Saemundsson, 1991). The first three eruptions were tiny, almost like geological accidents. The fourth eruption was slightly larger but of short duration. The volume of all these four eruptions was only a very small fraction of the volume of the dike or the deflation bowl. A new stage was reached with the eruption in July 1980. Then, most of the mobilized magma appears to have reached the surface. A good fraction of it flowed back into open fissures, however, and caused secondary rifting. The fissure that received the lava dilated and extended in both directions. Apparently, a dike was formed, fed from the surface, a phenomenon observed here for the first time. The flow into the fissures lasted at least 18 h, and for several of those hours, the whole lava production went this way. Subsequent dikes also led to eruptions. The largest one was the last event in this remarkable sequence. All the eruptions except the first one were anticipated or predicted based on the combination of deformation and seismicity, and the warnings were issued to the local population before them (Einarsson, 2018).

During injection of dikes outside the caldera the deflation of the caldera was generally accompanied by very low caldera seismicity, sometimes with almost no detectable caldera earthquakes. Only in the two largest deflation events was there a detectable increase in the caldera seismicity. Earthquakes as large as m_b 5 occurred during the first deflation event (Einarsson, 1986), and a slight increase in small earthquakes was detected toward the end of the deflation event of January 1978. Deflation at the caldera center was 2 m and 1 m, respectively, in these events (**Table 1**). Deflation of less than 1 m apparently took place within the elastic range of the caldera floor. Dikes intruded within the caldera were clearly accompanied by seismicity during their propagation. Caldera earthquakes during inflation were significantly smaller than during deflation. They only rarely reached magnitude 4.

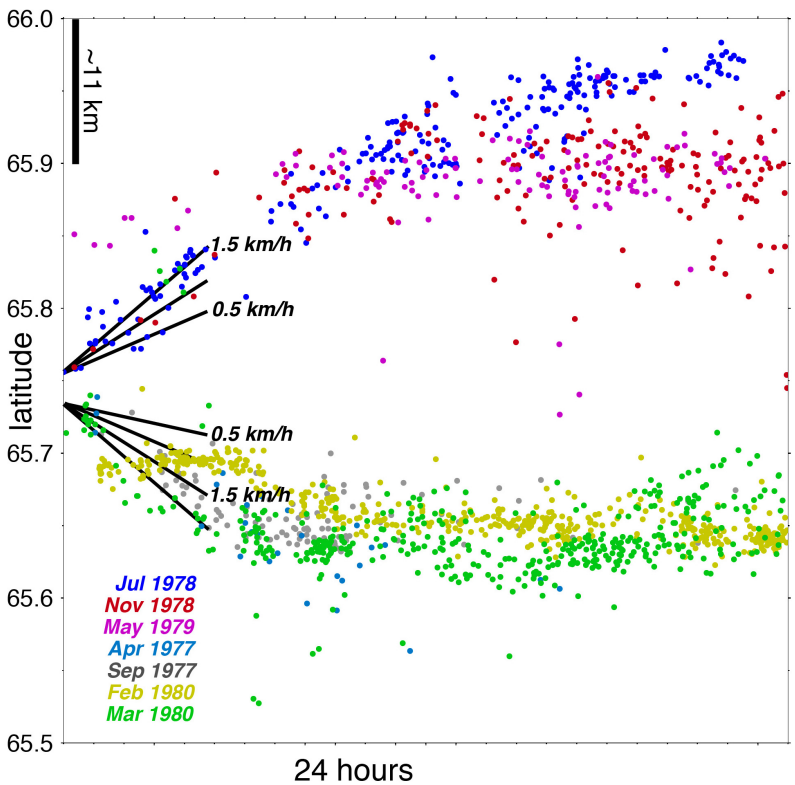

FIGURE 5 | Propagation of seismicity from the Krafla caldera during the swarms of 1977–1980, see **Figure 4**. The latitude of the epicenters is plotted as function of time during the first 24 h of each swarm.

Attempts to estimate the volume of magma transported from depth to the shallow crust give varying results. Hollingsworth et al. (2013) used digital elevation models derived from aerial and spy photographs to estimate a total volume of intruded dikes 0.9–1.7 × 10^9 m^3. They also estimate a volume of erupted lava of 0.2–0.4 × 10^9 m^3. Values in the range 0.25–0.35 × 10^9 m^3 were estimated from the surface flows (e.g., Einarsson, 1991b, 2018; Saemundsson, 1991). Using the cumulative deflation of the caldera to estimate the total volume of dikes and flows gives 0.79–0.85 × 10^9 m^3 (Harris et al., 2000).

Askja

The Askja volcanic system consists of a central volcano and fissure swarms extending to the north and south. The northern swarm extends all the way to the north coast. The extent of the southern swarm is more uncertain. It interfingers with the swarms of the Bárðarbunga volcano and disappears beneath the Vatnajökull glacier. The structure of the Askja volcano is dominated by at least four overlapping caldera structures (Saemundsson, 1982; Hjartardóttir et al., 2009). Seismic tomographic studies reveal bodies of anomalous V_P/V_S ratios underlying the calderas at discrete levels as deep as 20 km (Greenfield et al., 2016). The most recent caldera was formed in 1874 and following years, after a major rifting episode with basaltic eruptions in the fissure swarm and a large silicic explosive eruption of the central volcano (e.g., Sigurdsson and Sparks, 1978; Brandsdóttir, 1992). The activity since then has been limited to the central volcano, most recently in 1961. Since about 1973, the main caldera has been slowly deflating. The cumulative subsidence of the caldera center is approaching 0.4 m (Tryggvason, 1989; Pagli et al., 2006; Sturkell et al., 2006; de Zeeuw-van Dalfsen et al., 2013). The cause of the subsidence is generally thought to be a combination of a cooling and contracting magma chamber at a divergent plate boundary.

The Askja area in general is moderately seismically active (**Figures 1**, **6**), and only a part of the activity appears to

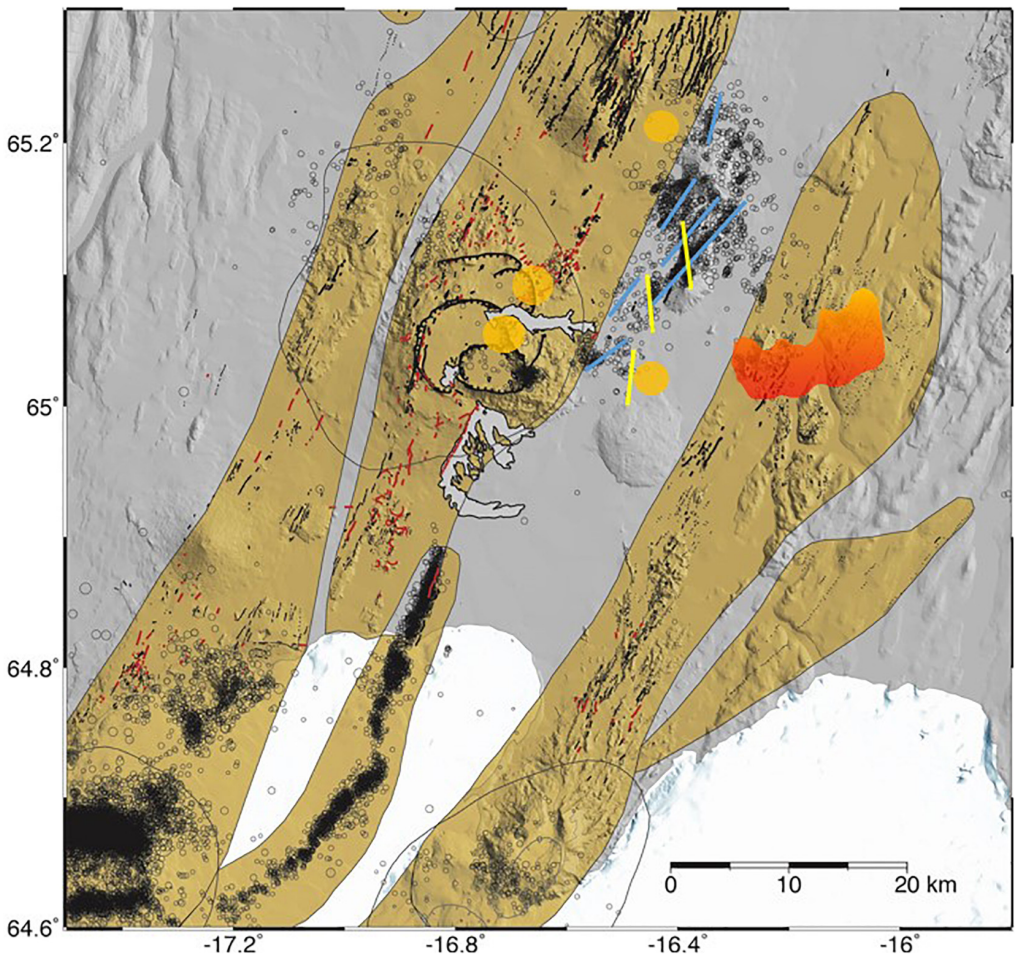

FIGURE 6 | Epicenters of the Askja area 1995–2010 (M ≥ 2.0) and 2011–2020 (M ≥ 1.5). Fissures and surface faults (black) and eruptive fissures and craters (red) are from Hjartardóttir et al. (2009), seismogenic, conjugate faults east of Askja volcano are from Greenfield et al. (2018), the blue ones are left-lateral, and the yellow ones are right-lateral. Locations of deep earthquake nests from Soosalu et al. (2009) are shown with orange patches. The Upptyppingar dipping dike is shown with the red-orange patch, from Hooper et al. (2011). The high earthquake activity in the SW-corner of the map accompanied the dike propagation and caldera collapse of the Bárðarbunga volcano in 2014–1015 (Sigmundsson et al., 2015; Gudmundsson et al., 2016). Digital elevation model from the National Land Survey of Iceland.

be related to the volcano itself (Einarsson, 1991a; Greenfield et al., 2018). Several processes have been suggested as sources of the different classes of earthquakes, including geothermal heat mining, transfer of spreading between overlapping fissure swarms, intrusion of a dike in the lower crust, and deep magma movements.

Geothermal Heat Mining

A persistent cluster of shallow level hypocenters is spatially correlated to the high-temperature geothermal field in the SE corner of the main caldera, suggesting a causal relationship between geothermal heat mining and brittle failure. This is also an area of silicic rock outcrops, and in 2014, this part of the caldera fault collapsed in a major rockslide, causing a large tsunami in the caldera lake (Gylfadóttir et al., 2017). Small swarms of shallow earthquakes occasionally occur in other parts of the caldera and to the N and NW of it. Most likely these events are related to the gentle deflation of the caldera.

Transfer of Spreading Between the Askja and Kverkfjöll Fissure Swarms

A large majority of the seismicity in the Askja area occurs east of Askja and appears to have no direct connection to the volcano. This activity was first described by Einarsson and Saemundsson (1987) and Einarsson (1991a). One NE-striking seismogenic fault was defined by the epicentral distribution, highly oblique to the fissure swarms nearby. Fault plane solutions showed strike-slip faulting (Jakobsdóttir, 2008). More detailed work using a dense temporary network by Soosalu et al. (2009) and Green et al. (2014) revealed more active faults in the area. Relative locations of numerous events show a system of conjugate faults bridging the gap between the fissure swarms of Askja and Kverkfjöll (Greenfield et al., 2018), NE-striking faults with left-lateral strike slip on them, and N-striking faults of right-lateral faulting (**Figure 6**). None of these faults are visible at the surface. The conjugate faults suggest a causative stress field with the least compressive principal stress in a WNW-ESE direction, consistent with the direction of plate spreading. The depth of the hypocenters is less than 8 km, well within the brittle part of the crust. This activity therefore appears to be caused by transfer of spreading between the two overlapping fissure swarms.

Upptyppingar Lower Crustal Intrusion

An unusual sequence of small earthquakes was detected in the Northern Volcanic Zone, near the hyaloclastite mountain Upptyppingar east of the Askja volcano, beginning in February 2007 (**Figure 6**). The events were ordinary in appearance, but originated at unusually large depth, 10–20 km. The swarm was very persistent and spread out along a planar structure (Jakobsdóttir, 2008; White et al., 2011; Horálek et al., 2015) beginning at depth and then spreading upwards and eastwards. After a year the activity faded away and stopped. The swarm was accompanied by uplift of a large area. Modeling of the surface deformation revealed a planar intrusion with a strike of 80°E and dip of 45° to 49°coinciding with the planar structure outline by the hypocentral distribution (Martens et al., 2010). The volume was (42–47) $\times$ 10^6 m^3 (Hooper et al., 2011).

The intrusion is located within the Kverkfjöll fissure swarm (**Figures 1**, **6**), about 40 km north of the Kverkfjöll central volcano. No deflation was detected of the Kverkfjöll central volcano in association with this intrusion, nor was the Askja volcano affected, the nearest neighboring central volcano. Apparently, the intrusion was fed directly from below. It is noteworthy that the orientation of the dike plane does not conform to any known structure at the surface. Fracture orientations are generally consistent with the stress field at a divergent plate boundary with the least compressive principal stress in the direction of relative plate motion (Hjartardóttir and Einarsson, 2012). Hooper et al. (2011) suggested that the stress field implied by the dike intrusion was modified by the presently ongoing retreat of the ice caps in Iceland, leading to enhanced capture of magma within the crust.

Abnormally "Deep" Swarms

A special class of abnormally deep earthquakes was first identified and described by Soosalu et al. (2009) in the area within and around the Askja volcano. These events originate in the depth range 10–34 km, i.e., well below the brittle-ductile transition. They are typically small, $M < 2$, and occur in dense and short-lived swarms of a few minutes' duration. The rapid succession of the events within a swarm may sometimes give the swarm the appearance of a tremor burst. The sources are quite persistent, on a time scale of years (Greenfield et al., 2018). Four nests of deep events have been located in the Askja area, two in the area of the central volcano, one about 10 km east of the volcano and one about 15 km NNE of the volcano (**Figure 6**). Key et al. (2011) suggested that these events represent magmatic injections along the fissure swarm of Askja, and Greenfield and White (2015) suggested that they represent magma transport through the lower crust.

DISCUSSION

Lateral Diking

The observations at Krafla of propagating earthquakes away from the central volcano and into the fissure swarms on either side of the volcano, accompanied by deflation of the caldera and extensive rifting in the fissure swarms, were interpreted as a consequence of dikes propagating laterally from a magma chamber within the caldera and into the rift zone (e.g., Björnsson et al., 1977; Einarsson and Brandsdóttir, 1980; Tryggvason, 1980). The interpretation was inspired by similar events at Kilauea volcano in Hawaii (e.g., Fiske and Jackson, 1972), despite differences in tectonic setting. The horizontal extensional stress, providing the conditions for lateral propagation, was generated by plate divergence in Iceland but by gravitational sliding of the flank of Kilauea in Hawaii. There was no general consensus about this interpretation, however. Alternative interpretations were proposed (e.g., Gudmundsson, 1995). Cases of lateral diking accompanied by deflation of a magma storage or even collapse of a caldera have been documented since the Krafla activity began. These include the Piton de la Fournaise in 2007 (Staudacher et al., 2009), Miyakejima in 2000 (Geshi et al., 2002), Asal rifting

of 1978, Dabbahu in Afar 2005–2010 (Wright et al., 2012), Bárðarbunga in Iceland in 2014–2015 (Sigmundsson et al., 2015; Gudmundsson et al., 2016), and Kilauea, Hawaii 2018 (Neal et al., 2019). Lateral draining of magma reservoirs is an important mechanism to form collapse calderas, involving processes like external tectonic stress, magma density and buoyancy in the crust, magma viscosity, and viscoelasticity in the crust (Buck et al., 2006; Sigmundsson et al., 2020).

Magmatic and Non-magmatic Rifting

One of the remarkable features of the Icelandic plate boundary rift zones is their highly variable seismicity, even on a time scale of decades. The rifting segment of the Eastern Volcanic Zone is, for example, almost totally aseismic, and so are segments of the Northern Volcanic Zone. Yet the relative plate divergence rate across these zones is 15–20 mm/year. Other parts of the divergent plate boundary, such as the segments of the Western Volcanic Zone, are moderately seismically active despite much lower spreading rate. Hjartardóttir et al. (2016a,b) suggested that this discrepancy was the result of cyclic activity. The deviatoric stress in a rift zone immediately following a rifting episode is low and the deformation due to plate spreading occurs within the elastic limit of the crust. The seismicity will be very low. With increasing stress, the deformation will gradually lead to failure and the background seismicity will increase. If magma becomes available, the failure limit of the crust is lowered and rifting may ensue even if the background seismicity is still low (Sigmundsson, 2006; Acocella and Trippanera, 2016). This was the case before the Krafla rifting episode in the early seventies. If, on the other hand, magma is not available, the stress may increase to the dry failure limit of the crust and failure takes place by normal faulting without the help of magma, as seems to be the case in a segment of the WVZ. This may be the explanation for the different level of seismicity in different segments of the Northern Volcanic Zone, evident in **Figure 1**. The recent large rifting episode of the Askja system in 1874–1875 relieved stress in the central part of the zone and the stress has not yet built up to seismogenic levels.

Faulting Between Overlapping Rifting Structures

Rifting in the rift zones of Iceland occurs within fissure swarms, apparently mostly by diking during rifting episodes. Modern examples of this type of activity include the Krafla rifting episode of 1975–1984 and the Bárðarbunga dike of 2014 (Sigmundsson et al., 2015; Gudmundsson et al., 2016). Each rift zone includes several fissure swarms that are arranged within the zone parallel to each other or en-echelon. Each dike or rifting event may only affect a limited length of one fissure swarm. This leads to accumulated horizontal shear stress between adjacent fissure swarms that is released in some kind of transfer motion on sets of conjugate strike-slip faulting. Two examples of such tectonism exist in the Icelandic rifts, the persistent seismicity east of the Askja volcano in the Northern Volcanic Zone, and the seismic activity in the Reykjanes Peninsula Oblique Rift (Hjaltadóttir, 2009; Parameswaran et al., 2020). In both areas, the orientation of the inferred least principal stress is horizontal and in the general direction of plate spreading.

"Deep" Crustal and Upper Mantle Earthquakes

Majority of earthquakes in Iceland originate in the upper, brittle part of the crust, in the depth range 0–10 km, and are apparently linked with relative plate movements across the plate boundaries. There are, however, occasional deeper earthquakes, originating in material that would, at normal strain rates, deform in a ductile way under the pressure and temperature conditions corresponding to the depth. Two classes of deep earthquakes may be identified: (1) earthquake sequences occurring immediately preceding or during eruptions and (2) small events occurring in short-lived swarms in persistently active "nests" beneath some parts of the volcanic zones.

Examples of the first class of deep events are provided by the Heimaey eruption of 1973 and the Eyjafjallajökull eruptions of 2010. Most earthquakes during the Heimaey eruption occurred at 15–25 km depth and most likely also the swarm of events immediately preceding the eruption (Björnsson and Einarsson, 1974; Einarsson, 1991a). The Eyjafjallajökull eruptions of 2010 were preceded by a series of shallow-level sill intrusions in 1994, 1999, 2009, and 2010 (Pedersen and Sigmundsson, 2004, 2006; Sigmundsson et al., 2010), and a period of anomalously deep earthquakes in 1996 (Dahm and Brandsdóttir, 1997; Hjaltadóttir et al., 2009). Some of the earthquakes during the eruptions also occurred at lower-crustal depths and were clearly related to the feeding channels of the eruptions (Tarasewicz et al., 2012a,b). The prolonged earthquake sequence during the Upptyppingar dipping dike intrusion of 2007–2008 may also be included in this class, although no eruption ensued.

The second class of deep events, first identified on the temporary Askja network by Soosalu et al. (2009) in the area around the Askja volcano, occur in short-lived swarms, of a few minutes' duration. In addition to the four nests of deep events located in the Askja area, at least three additional nests of deep swarms have been identified and are regularly recorded by the permanent network. The most active one of them is located 15–20 km ESE of Bárðarbunga volcano, slightly south of the dike that propagated laterally from the volcano in August 2014 and fed the Holuhraun eruption (Sigmundsson et al., 2015). The relationship of this nest to the dike and the plumbing of the Bárðarbunga volcanic system is still unclear (Hudson et al., 2017). Several swarms per month are detected in this nest at the present time and the activity is not decreasing. Another nest with a spatial relationship to the Bárðarbunga system is located beneath the Trölladyngja lava shield, within the NE-fissure swarm of Bárðarbunga. Only one deep nest is yet known in South Iceland. It is located beneath the eastern rim and flank of the Katla volcano (Vogfjörð et al., 2009).

The detection of the deep nests depends critically on the seismic network. A seismic station in the nearfield of the earthquakes is required for sufficient depth control on the location of the events. It is rather likely that more of these nests will be identified in the future. The known nests are all,

except one, located in the central area of the Iceland Hotspot. Some parts of the plate boundary areas seem to be devoid of deep nests. None have been found in the Reykjanes Peninsula Oblique Rift or in the Krafla volcanic system despite relatively dense networks in operation there. The deep swarms in Iceland show great similarity with recently discovered events in the Eifel volcanic field in Germany (Hensch et al., 2019; Dahm et al., 2020).

Stages Within Eruptive Cycle

A majority of the eruptions of Icelandic volcanoes within the last several decades occurred after a time of inflation of the respective volcano (Einarsson, 2018; Sigmundsson et al., 2018). The eruption is then accompanied by deflation and followed by repeated inflation. This includes the nine Krafla eruptions of 1975–1984, the three eruptions of Grímsvötn 1998–2011, and the three eruptions of Hekla 1980–2000. In the cases of Krafla and Grímsvötn, the seismicity follows the cyclic behavior; it increases during the inflation part of the cycle and is greatly reduced when the deflation sets in. If a dike propagates away from the inflated area, its propagation can often be traced by the earthquakes that are generated around the dike tip. The re-inflation is accompanied by little seismicity during its first stage. It may increase rather suddenly if the inflation level exceeds the previous maximum, a phenomenon called Kaiser effect (Heimisson et al., 2015). The deflation itself takes place almost aseismically as long as the strain remains within the elastic limits. In the case of Krafla, the elastic limit was exceeded only twice. The first deflation was about 2 m and was accompanied by considerable seismicity, with maximum magnitude 5.0. The second case was the January 1978 deflation (**Table 1**) when the subsidence in the caldera reached 1 m. There was a slight increase of the daily number of small caldera earthquakes during the last days of deflation. Based on these observations, it may be concluded that the elastic range of the Krafla caldera is about 1 m. Earthquakes associated with the inflation part of the cycle only reached magnitude 3.5.

Similar behavior is observed in Grímsvötn. The seismic activity of the volcano is generally very low but increases slowly in the latter half of the inflation period. The maximum magnitude does not exceed 3. The deflation has so far always been within the elastic limit.

The large Bárðarbunga 65 m deflation of 2014–2015 was accompanied by numerous earthquakes, more than 70 of which exceeded magnitude 5 (Gudmundsson et al., 2016). The caldera seismicity decreased greatly when the deflation stopped in February 2015. The volcano began inflating again after the eruption and deflation ended but the seismicity remained low until September 2015 (Sigmundsson et al., 2018). Then, both the earthquake frequency and the maximum magnitude increased and remained high for several years (Pálsson et al., 2019). The maximum magnitude exceeded 4 but has remained below 5, however. All three volcanoes appear to have a similar seismic behavior with respect to inflation and deflation. Inflation-related earthquakes are generally smaller than the earthquakes accompanying deflation.

Geothermal Activity and Seismicity

It has been noted in many publications that there is a general correlation between persistent microearthquake activity within the volcanic zones of Iceland and the high-temperature geothermal areas (e.g., Ward and Björnsson, 1971). It may be argued that temperature changes associated with geothermal systems and the transfer of heat from the heat source to the colder bodies of rock leads to stress changes and thus to micro-cracking in the brittle part of the crust. The non-double-couple part of the earthquake source mechanisms identified by Foulger (1988); Miller et al. (1998), and Schuler et al. (2016) in the Hengill and Krafla areas may be taken as evidence for this. This mechanism has also been suggested as one of the possible sources of the seismicity of the Katla and Askja calderas, Torfajökull volcano, and the subglacial Loki Ridge (Einarsson, 1991a; Soosalu and Einarsson, 1996, 1997; Sturkell et al., 2008; Sgattoni et al., 2019). It is rather unlikely, however, that all the background seismicity of these locations is due to the geothermal mining of heat. The case of the Kerlingarfjöll area within the Hofsjökull volcanic system serves as a counterexample. This central volcano has a very powerful geothermal system, and yet, the seismicity is very low. This case suggests that the geothermal effect is likely to act as a trigger rather than the main driving force of the seismicity. The Kerlingarfjöll volcano is located outside the main deformation zone of the plate boundary. The driving force may therefore be missing even though the trigger is there.

Elevated pressure in the pore fluid may be another mechanism to release rock stress in a geothermal system close to a volcano by lowering the effective stress on pre-stressed faults. The validity of this mechanism is demonstrated in cases where the pore pressure change is induced by man, e.g., at the Hellisheiði Geothermal Power Station in SW-Iceland, where seismicity and crustal deformation is induced by injection of wastewater into the crust (Juncu et al., 2020).

We point out that many of the high-temperature geothermal systems are spatially correlated with outcrops of silicic rocks. This raises the question whether shallow, unstable, low-density bodies of silicic rocks (cryptodomes) may be the source of both the geothermal activity and the earthquakes.

CONCLUSION

Seismicity serves as the most important element in the long-term monitoring of the 30 + active volcanic systems of Iceland. About half of them have shown evidence of magma movements in the last 46 years of coverage by sensitive seismographs.

Processes identified as causes of earthquakes within the volcanic zones include volcano inflation and deflation, caldera collapse, dike and sill intrusion, amagmatic rifting by normal faulting, geothermal heat mining, strike-slip faulting on systems of conjugate faults, and unspecified movements of magma in the deep crust. Dome and cryptodome activity may also play a role.

Seismicity within the volcanically active areas of Iceland is very unevenly distributed, both in time and space. Persistent seismic sources are mostly associated with central volcanoes. The fissure swarms of the volcanic systems are usually inactive, even at the

microearthquake level, except during rifting episodes when dikes propagate within them. The major rifting episode in the Krafla area 1975–1984 showed lateral injection of dikes, a model that was verified by the Bárðarbunga dike injection and rifting of 2014.

The long-term behavior of the different volcanic systems of the Northern Volcanic Zone is quite varied, ranging from very low-level background activity like Fremrinámar and Þeistareykir, to almost continuous, intermediate-level seismicity, like that of the area around the Askja volcano. For successful monitoring it is therefore essential to have a long time-history of the seismicity. A part of the seismic activity east of Askja is generated by strike-slip faulting on conjugate fault sets, taking up differential strain between overlapping rift zones of adjacent volcanic systems.

The rifting events at Krafla in 1975–1984 occurred during a phase of cyclic behavior, with periods of magma accumulation at depth and inflation punctuated by deflation, dike intrusions, rifting and eruptions. The cycle of inflation and deflation was reflected in seismicity that provides an additional parameter to apply in the monitoring effort. The examples of this process so far suggest that the largest earthquakes during deflation are significantly larger than the inflation-related earthquakes of the same volcano.

Persistent activity of small earthquakes in all four volcanic systems appears to be spatially correlated with high-temperature hydrothermal systems. The causal relationship is not always obvious. Cooling of hot rock bodies and consequent contraction and associated stress change may provide part of the explanation, also pore pressure fluctuations within the geothermal system. It is also pointed out that both phenomena, seismicity and geothermal activity, in some cases could have a common cause, such as a rising cryptodome.

DATA AVAILABILITY STATEMENT

The raw data supporting the conclusions of this article will be made available by the authors, without undue reservation.

AUTHOR CONTRIBUTIONS

Both authors contributed equally to the subject of the study. PE with emphasis on the text and BB with emphasis on data analysis and construction of the figures. Both authors have worked for several decades on seismic monitoring and tectonics of Iceland and were actively involved in the seismic monitoring of the Krafla rifting episode.

ACKNOWLEDGMENTS

This study is based on data and active cooperation of many people and institutions, including the Lamont-Doherty Earth Observatory and Cambridge University. The monitoring effort during the Krafla rifting episode relied to a large extent on the work of devoted local attendants of the analog seismograph system. The seismic data since 1990 are obtained from the Icelandic Meteorological Office. Seismic monitoring in the Northern Volcanic Zone has been partly supported by Landsvirkjun, the National Power Company of Iceland. The Generic Mapping Tools software (Wessel et al., 2019) was used to generate most of the Figures. Comments from the Editor and two reviewers improved the study considerably.

REFERENCES

Acocella, V., and Trippanera, D. (2016). How diking affects the tectonomagmatic evolution of slow spreading plate boundaries: overview and model. *Geosphere* 12, 867–883. doi: 10.1130/GES01271.1

Árnadóttir, T. H., Lund, B., Jiang, W., Geirsson, H., Björnsson, H., Einarsson, P., et al. (2009). Glacial rebound and plate spreading: results from the first countrywide GPS observations in Iceland. *Geophys. J. Int.* 177, 691–716. doi: 10.1111/j.1365-246X.2008.04059.x

Björnsson, A., and Eysteinsson, H. (1998). *Breytingar á landhæð við Kröflu 1974-1995. Samantekt á landhæðarmælingum (Changes in Elevation at Krafla 1974-1995. Compilation of Elevation Measurements, in ICELANDIC)*. Reykjavík: Nordic Volcanological Institute. National Energy Authority, Report OS-98002, Report 9801.

Björnsson, A., Sæmundsson, K., Einarsson, P., Tryggvason, E., and Grönvold, K. (1977). Current rifting episode in north Iceland. *Nature* 266, 318–323. doi: 10.1038/266318a0

Björnsson, S., and Einarsson, P. (1974). "Seismicity of Iceland," in *Geodynamics of Iceland and the North Atlantic Area*, ed. L. Kristjánsson (Dordrecht: Reidel Publ. Co), 225–239. doi: 10.1007/978-94-010-2271-2_16

Brandsdóttir, B. (1992). Historical accounts of earthquakes associated with eruptive activity in the Askja volcanic system. *Jökull* 42, 1–12.

Brandsdóttir, B., and Einarsson, P. (1979). Seismic activity associated with the September 1977 deflation of the Krafla central volcano in NE-Iceland. *J. Volc. Geotherm. Res.* 6, 197–212. doi: 10.1016/0377-0273(79)90001-5

Brandsdóttir, B., and Menke, W. H. (1992). Thin low-velocity zone within the Krafla caldera, NE-Iceland attributed to a small magma chamber. *Geophys. Res. Lett.* 19, 2381–2384. doi: 10.1029/92gl02541

Buck, W. R., Einarsson, P., and Brandsdóttir, B. (2006). Tectonic stress and magma chamber size as controls on dike propagation: constraints from the 1975-1984 Krafla rifting episode. *J. Geophys. Res.* 111:B124041.

Dahm, T., and Brandsdóttir, B. (1997). Moment tensors of microearthquakes from the Eyjafjallajökull volcano in South Iceland. *Geophys. J. Int.* 130, 183–192. doi: 10.1111/j.1365-246x.1997.tb00997.x

Dahm, T., Stiller, M., Mechie, J., Heimann, S., Hensch, M., Woith, H., et al. (2020). Seismological and geophysical signatures of the deep crustal magma systems of the Cenozoic volcanic fields beneath the Eifel, Germany. G^3 21:e2020GC009062. doi: 10.1029/2020GC009062

de Zeeuw-van Dalfsen, E., Rymer, H., Sturkell, E., Pedersen, R., Hooper, A., Sigmundsson, F., et al. (2013). Geodetic data shed light on ongoing caldera subsidence at Askja, Iceland. *Bull. Volcanol.* 75:709. doi: 10.1007/s00445-013-0709-2

Drouin, V., Sigmundsson, F., Ófeigsson, B. G., Hreinsdóttir, S., Sturkell, E., and Einarsson, P. (2017a). Deformation in the Northern Volcanic Zone of Iceland 2008-2014: an interplay of tectonic, magmatic, and glacial isostatic deformation. *J. Geophys. Res. Solid Earth* 122, 3158–3178. doi: 10.1002/2016JB013206

Drouin, V., Sigmundsson, F., Verhagen, S., Ófeigsson, B. G., Spaans, K., and Hreinsdóttir, S. (2017b). Deformation at Krafla and Bjarnarflag geothermal areas, Northern Volcanic Zone of Iceland, 1993-2015. *J. Volcan. Geotherm. Res.* 344, 92–105. doi: 10.1016/j.jvolgeores.2017.06.013

Einarsson, P. (1978). S-wave shadows in the Krafla caldera in NE-Iceland, evidence for a magma chamber in the crust. *Bull. Volc.* 41, 1–9.

Einarsson, P. (1986). "Seismicity along the eastern margin of the North American Plate," in *The Western North Atlantic Region: Geological Society of America*, eds P. R. Vogt and B. E. Tucholke (Boulder, CO: The Geology of North America), 99–116. doi: 10.1130/dnag-gna-m.99

Einarsson, P. (1987). "Compilation of earthquake fault plane solutions in the North Atlantic and Arctic Oceans," in *Recent Plate Movements and Deformation, Geodynamics Series*, Vol. 20, ed. K. Kasahara (Washington, DC: America Geophysical Union), 47–62. doi: 10.1029/gd020p0047

Einarsson, P. (1991a). Earthquakes and present-day tectonism in Iceland. *Tectonophysics* 189, 261–279. doi: 10.1016/0040-1951(91)90501-i

Einarsson, P. (1991b). "The Krafla rifting episode 1975-1989," in *Náttúra Mývatns*, eds A. Garðarsson and A. Einarsson (Reykjavík: Icelandic Nature Science Society), 97–139. doi: 10.1016/0377-0273(84)90036-2

Einarsson, P. (2008). Plate boundaries, rifts and transforms in Iceland. *Jökull* 58, 35–58.

Einarsson, P. (2018). Short-term seismic precursors to Icelandic eruptions 1973-2014. *Front. Earth Sci. Volcanol. Res. Topic* 6:45. doi: 10.3389/feart.2018.00045

Einarsson, P., and Brandsdóttir, B. (1980). Seismological evidence for lateral magma intrusion during the July 1978 deflation of the Krafla volcano in NE-Iceland. *J. Geophys.* 47, 160–165.

Einarsson, P., and Jakobsson, S. (2020). Scanning the analog seismogram archives of Iceland. *Jökull* 70:16. doi: 10.33799/jokull2020

Einarsson, P., and Saemundsson, K. (1987). "Earthquake epicentres 1982-1985 and volcanic systems in Iceland: A map," in *Í hlutarins eðli, Festschrift for Þorbjörn Sigurgeirsson*, ed. Þ. Sigfússon (Reykjavík: Menningarsjóður).

Fiske, R. S., and Jackson, E. D. (1972). Orientation and growth of Hawaiian volcanic rifts: the effect of regional structure and gravitational stresses. *Proc. R. Soc. Lond.* 329, 299–326. doi: 10.1098/rspa.1972.0115

Foulger, G. R. (1988). Hengill triple junction, SW Iceland; 2. Anomalous earthquake focal mechanisms and implications for process within the geothermal reservoir and at accretionary plate boundaries. *J. Geophys. Res.* 93, 507–523.

Foulger, G. R., Long, R. E., Einarsson, P., and Björnsson, A. (1989). Implosive earthquakes at the active accretionary plate boundary, Northern Iceland. *Nature* 337, 640–642. doi: 10.1038/337640a0

Geshi, N., Shimano, T., Chiba, S., and Nakada, S. (2002). Caldera collapse during the 2000 eruption of Miyakejima Volcano. *Jpn. Bull. Volcanol.* 64, 55–68. doi: 10.1007/s00445-001-0184-z

Green, R. G., Greenfield, T., and White, R. S. (2015). Triggered earthquakes suppressed by an evolving stress shadow from a propagating dyke. *Nat. Geosci.* 8, 629–632. doi: 10.1038/ngeo2491

Green, R. G., White, R. S., and Greenfield, T. (2014). Motion in the north Iceland volcanic rift zone accommodated by bookshelf faulting. *Nat. Geosci.* 7, 29–33. doi: 10.1038/ngeo2012

Greenfield, T., and White, R. S. (2015). Building icelandic ignieous crust by repeated melt injections. *J. Geophys. Res.* 120, 1–14. doi: 10.1016/j.tecto.2007.11.024

Greenfield, T., White, R. S., and Roecker, S. (2016). The magmatic plumbing system of the Askja central volcano, Iceland, as imaged by seismic tomography. *J. Geophys. Res. Solid Earth* 121, 7211–7229. doi: 10.1002/2016JB013163

Greenfield, T., White, R. S., Winder, T., and Ágústsdóttir, T. H. (2018). Seismicity of the Askja and Bárðarbunga volcanic systems of Iceland, 2009-2015. *J. Volcanol. Geotherm. Res.* 391, 106432. doi: 10.1016/j.jvolgeores.2018.08.010

Gudmundsson, A. (1995). Infrastructure and mechanics of volcanic systems in Iceland. *J. Volcanol. Geotherm. Res.* 64, 1–22. doi: 10.1016/0377-0273(95)92782-q

Gudmundsson, M. T., Jónsdóttir, K., Hooper, A., Holohan, E. P., Halldórsson, S. A., Ófeigsson, B. G., et al. (2016). Gradual caldera collapse at Bárdarbunga volcano, Iceland, regulated by lateral magma outflow. *Science* 353:aaf8988. doi: 10.1126/science.aaf8988

Gylfadóttir, S. S., Kim, J., Helgason, J. K., Brynjólfsson, S., Höskuldsson, Á, Jóhannesson, T., et al. (2017). The 2014 Lake Askja rockslide-induced tsunami: Optimization of numerical tsunami model using observed data. *J. Geophys. Res. Oceans* 122:496. doi: 10.1002/2016JC012496

Harris, A., Murray, J., Aries, S., Davies, M., Flynn, L., Wooster, M., et al. (2000). Effusion rate trends at Etna and Krafla and their implications for eruptive mechanisms. *J. Volcanol. Geotherm. Res.* 102, 237–270. doi: 10.1016/s0377-0273(00)00190-6

Heimisson, E. R., Einarsson, P., Sigmundsson, F., and Brandsdóttir, B. (2015). Kilometer- scale Kaiser effect identified in Krafla volcano, Iceland. *Geophys. Res Lett.* 42, 7958–7965. doi: 10.1002/2015GL065680

Hensch, M., Dahm, T., Ritter, J., Heimann, S., Schmidt, B., Stange, S., et al. (2019). Deep low-frequency earthquakes reveal ongoing magmatic recharge beneath Laacher See Volcano (Eifel, Germany). *Geophys. J. Int.* 216, 2025–2036. doi: 10.1093/gji/ggy532

Hjaltadóttir, S. (2009). *Use of Relatively Located Microearthquakes to Map Fault Patterns and Estimate the Thickness of the Brittle Crust in Southwest Iceland*. M. Sc. thesis, University of Iceland, Reykjavík. Available online at: https://skemman.is/bitstream/1946/3990/1/Sigurlaug-MS-fixed.pdf

Hjaltadóttir, S., Vogfjörð, K., and Slunga, R. (2009). *Seismic signs of magma pathways Through the Crust in the Eyjafjallajökull Volcano, South Iceland. Icelandic Meteorological Office, Report VÍ 2009-013, 3*. Available online at: https://www.vedur.is/media/vedurstofan/utgafa/skyrslur/2009/VI_2009_013.pdf

Hjartardóttir, ÁR., and Einarsson, P. (2012). The Kverkfjöll fissure swarm and the eastern boundary of the Northern Volcanic Rift Zone, Iceland. *Bull. Volcanol.* 74, 143–162. doi: 10.1007/s00445-011-0496-6

Hjartardóttir, ÁR., Einarsson, P., Bramham, E., and Wright, T. J. (2012). The Krafla fissure swarm, Iceland, and its formation by rifting events. *Bull. Volcanol.* 74, 2139–2153. doi: 10.1007/s00445-012-0659-0

Hjartardóttir, ÁR., Einarsson, P., Magnúsdóttir, S., Björnsdóttir, Þ, and Brandsdóttir, B. (2016a). "Fracture systems of the Northern Volcanic Rift Zone, Iceland - An onshore part of the Mid-Atlantic plate boundary," in *Magmatic Rifting and Active Volcanism*, eds T. J. Wright, A. Ayele, D. J. Ferguson, T. Kidane, and C. Vye-Brown (London: Geological Society), 420. doi: 10.1144/SP420.1

Hjartardóttir, Á. R., Einarsson, P., and Björnsdóttir, S. G. (2016b). Fissure swarms and fracture systems within the Western Volcanic Zone, Iceland – effects of spreading rates. *J. Struct. Geol.* 91, 39–53, doi: 10.1016/j.jsg.2016.08.007

Hjartardóttir, ÁR., Einarsson, P., and Sigurðsson, H. (2009). The fissure swarm of the Askja volcanic system along the divergent plate boundary of N Iceland. *Bull. Volc.* 71, 961–975. doi: 10.1007/s00445-009-0282-x

Hollingsworth, J., Leprince, S., Ayoub, F., and Avouac, J. P. (2013). New constraints on dike injection and fault slip during the 1975-1984 Krafla rift crisis, NE Iceland. *J. Geophys. Res.: Solid Earth* 118, 3707–3727. doi: 10.1002/jgrb.50223

Hooper, A., Ofeigsson, B. G., Sigmundsson, F., Lund, B., Geirsson, H., Einarsson, P., et al. (2011). Increased capture of magma in the crust promoted by ice-cap retreat in Iceland. *Nat. Geosci.* 4, 783–786. doi: 10.1038/NGEO1269

Horálek, J., Fischer, T., Einarsson, P., and Jakobsdóttir, S. S. (2015). "Earthquake swarms," in *Encyclopedia of Earthquake Engineering*, eds M. Beer, E. Patelli, I. A. Kougioumtzoglou, and S.-K. Au (Berlin: Springer), doi: 10.1007/978-3-642-36197-5_294-1

Hudson, T. S., White, R. S., Greenfield, T., Ágústsdóttir, T. H., Brisbourne, A., and Green, R. G. (2017). Deep crustal melt plumbing of Bárðarbunga volcano, Iceland. *Geophys. Res. Lett.* 44, 8785–8794. doi: 10.1002/2017GL074749

Jakobsdóttir, S. (2008). Seismicity in Iceland: 1994-2007. *Jökull* 58, 75–100.

Johnsen, G., Björnsson, A., and Sigurðsson, S. (1980). Gravity and elevation changes caused by magma movement beneath the Krafla caldera, Northeast Iceland. *J. Geophys.* 47, 132–140.

Juncu, D., Árnadóttir, T., Geirsson, H., Guðmundsson, G. B., Lund, B., Gunnarsson, G., et al. (2020). Injection-induced surface deformation and seismicity at the Hellisheidi geothermal field, Iceland. *J. Volc. Geotherm. Res.* 391:106337. doi: 10.1016/j.jvolgeores.2018.03.019

Key, J., White, R. S., Soosalu, H., and Jakobsdóttir, S. S. (2011). Multiple melt injection along a spreading segment at Askja, Iceland. *Geophys. Res. Lett.* 38:L05301. doi: 10.1029/2010GL046264

La Femina, P. C., Dixon, T. H., Malservisi, R., Árnadóttir, T. H., Sturkell, E., Sigmundsson, F., et al. (2005). Geodetic GPS measurements in south Iceland: strain accumulation and partitioning in a propagating ridge system. *J. Geophys. Res.* 110:B11405. doi: 10.1029/2005JB003675

Lahr, J. J. C., and Ward, P. L. (1976). *Hypoellipse: A Computer Program for Determining Local Hypocentral Parameters, Magnitude and First Motion Pattern*. Reston, VA: U. S. Geological Survey. U. S. Geological Survey Open File Report.

Larsen, G., Grönvold, K., and Thorarinsson, S. (1979). Volcanic eruption through a geothermal borehole at Námafjall, Iceland. *Nature* 278, 707–710. doi: 10.1038/278707a0

Martens, H. R., White, R. S., Key, J., Drew, J., Soosalu, H., and Jakobsdóttir, S. S. (2010). Dense seismic network provides new insight into the 2007 Upptyppingar dyke intrusion. *Jökull* 60, 47–66.

Miller, A. D., Julian, B. R., and Foulger, G. R. (1998). Three-dimensional seismic structure and moment tensors of non-double-couple earthquakes at the Hengill-Grensdalur volcanic complex, Iceland. *Geophys. J. Int.* 133, 309–325. doi: 10.1046/j.1365-246x.1998.00492.x

Neal, C. A., Brantley, S. R., Antolik, L., Babb, J. L., Burgess, M., Calles, K., et al. (2019). The 2018 rift eruption and summit collapse of Kilauea Volcano. *Science* 363, 367–374. doi: 10.1126/science.aav7046

Pagli, C. F., Sigmundsson, L., Árnadóttir, T., Einarsson, P., and Sturkell, E. (2006). Deflation of the Askja volcanic system: constraints on the deformation source from combined inversion of satellite radar interferograms and GPS measurements. *J. Volc. Geotherm. Res.* 152, 97–108. doi: 10.1016/j.jvolgeores.2005.09.014

Pálmason, G. (1963). Seismic refraction investigation of the basalt lavas in northern and eastern Iceland. *Jökull* 13, 40–60.

Pálsson, M., Einarsson, P., and Hrafnkelsson, B. (2019). Variation in b-value of caldera earthquakes during recent activity of the Bárðarbunga volcano in Iceland. *Jökull* 69, 71–82. doi: 10.33799/jokull2019.69.071

Parameswaran, R. M., Thorbjarnardóttir, B. S., Stefánsson, R., and Bjarnason, I. T. H. (2020). Seismicity on conjugate faults in Ölfus, South Iceland: case study of the 1998 Hjalli-Ölfus earthquake. *J. Geophys. Res. Solid Earth* 125:e2019JB019203. doi: 10.1029/2019JB019203

Passarelli, L., Maccaferri, F., Rivalta, E., Dahm, T., and Boku, E. A. (2013). A probabilistic approach for the classification of earthquakes as 'triggered'or 'not triggered'. *J. Seismol.* 17, 165–187. doi: 10.1007/s10950-012-9289-4

Pedersen, R., and Sigmundsson, F. (2004). InSAR based sill model links spatially offset areas of deformation and seismicity for the 1994 unrest episode at Eyjafjallajökull volcano, Iceland. *Geophys. Res. Lett.* 31:L14610. doi: 10.1029/2004GL020368

Pedersen, R., and Sigmundsson, F. (2006). Temporal development of the 1999 intrusive episode in the Eyjafjallajökull volcano, Iceland, derived from InSAR images. *Bull. Volcanol.* 68, 377–393. doi: 10.1007/s00445-005-0020-y

Pedersen, R., Sigmundsson, F., and Einarsson, P. (2007). Controlling factors on earthquake swarms associated with magmatic intrusions; constraints from Iceland. *J. Volcanol. Geotherm. Res.* 162, 73–80. doi: 10.1016/j.jvolgeores.2006.12.010

Rooyakkers, S. M., Stix, J., Berlo, K., and Barker, S. J. (2020). Emplacement of unusual rhyolitic to basaltic ignimbrites during collapse of a basalt-dominated caldera: The Halarauður eruption, Krafla (Iceland). *GSA Bull.* 132, 1881–1902. doi: 10.1130/B35450.1

Schuler, J., Greenfield, T., White, R. S., Roecker, S. W., Brandsdóttir, B., Stock, J. M., et al. (2015). Seismic imaging of the shallow crust beneath the Krafla central volcano, NE Iceland. *J. Geophys. Res. Solid Earth* 120, 7156–7173. doi: 10.1002/2015JB012

Schuler, J., Pugh, D. J., Hauksson, E., White, R. S., Stock, J. M., and Brandsdóttir, B. (2016). Focal mechanisms and size distribution of earthquakes beneath the Krafla central volcano, NE Iceland. *J. Geophys. Res. Solid Earth* 121, 5152–5168. doi: 10.1002/2016jb013213

Sgattoni, G., Lucchi, F., Einarsson, P., De Astis, G., and Tranne, C. A. (2019). The 2011 unrest at Katla volcano: seismicity and geological context. *Jökull* 69, 53–70. doi: 10.33799/jokull2019.69.053

Sigmundsson, F. (2006). *Iceland Geodynamics: Crustal Deformation and Divergent Plate Tectonics*. Chichester: Springer-Praxis, 209.

Sigmundsson, F., Einarsson, P., Bilham, R., and Sturkell, E. (1995). Rift-transform kinematics in south Iceland: deformation from Global Positioning system measurements, 1986 to 1992. *J. Geophys. Res.* 100, 6235–6248. doi: 10.1029/95jb00155

Sigmundsson, F., Hooper, A., Hreinsdóttir, S., Vogfjörd, K. S., Ófeigsson, B. G., Heimisson, E. R., et al. (2015). Segmented lateral dyke growth in a rifting event at Bárðarbunga volcanic system, Iceland. *Nature* 517, 191–195. doi: 10.1038/nature14111

Sigmundsson, F., Hreinsdóttir, S., Hooper, A., Árnadóttir, T. H., Pedersen, R., Roberts, M. J., et al. (2010). Intrusion triggering of the 2010 Eyjafjallajökull explosive eruption. *Nature* 468, 426–430. doi: 10.1038/nature09558

Sigmundsson, F., Parks, M., Pedersen, R., Jónsdóttir, K., Ófeigsson, B. G., Grapenthin, R., et al. (2018). "Magma movements in volcano plumbing systems and their associated ground deformation and seismic pattern. Chapter 11," in *Volcanic and Igneous Plumbing Systems*, ed. S. Burchardt (Amsterdam: Elsevier), 285–322. doi: 10.1016/B978-0-12-809749-6.00011-X

Sigmundsson, F., Pinel, V., Grapenthin, R., Hooper, A., Halldórsson, S., Einarsson, P., et al. (2020). Unexpected large eruptions from buoyant magma bodies within viscoelastic crust. *Nature Commun.* 11:2403. doi: 10.1038/s41467-020-16054-6

Sigurdsson, H., and Sparks, S. R. J. (1978). Rifting episode in North Iceland in 1874-1875 and the eruptions of Askja and Sveinagja. *Bull. Volcanol.* 41, 149–167. doi: 10.1007/bf02597219

Sigurdsson, O. (1980). Surface deformation of the Krafla fissure swarm in two rifting events. *J. Geophys.* 47, 154–159.

Soosalu, H., and Einarsson, P. (1996). "Torfajökull seismicity - Hydrothermal cooling of a magma body?," in *Seismology in Europe*, ed. B. Thorkelsson (Reykjavík: European Seismological Commission), 467–472.

Soosalu, H., and Einarsson, P. (1997). Seismicity around the Hekla and Torfajökull volcanoes, Iceland, during a volcanically quiet period, 1991-1995. *Bull. Volcanol.* 59, 36–48. doi: 10.1007/s004450050173

Soosalu, H., Key, A. J., White, R. S., Knox, C., Einarsson, P., and Jakobsdóttir, S. S. (2009). Lower-crustal earthquakes caused by magma movement beneath Askja volcano on the north Iceland rift. *Bull. Volcanol.* 72, 55–62. doi: 10.1007/s00445-009-0297-3

Staudacher, T., Ferrazzini, V., Peltier, A., Kowalski, P., Boissier, P., Catherine, P., et al. (2009). The April 2007 eruption and the Dolomieu crater collapse, two major events at Piton de la Fournaise (La Réunion Island, Indian Ocean). *J. Volcanol. Geotherm. Res.* 184, 126–137. doi: 10.1016/j.jvolgeores.2008.11.005

Stefánsson, R., Böðvarsson, R., Slunga, R., Einarsson, P., Jakobsdóttir, S., Bungum, H., et al. (1993). Earthquake prediction research in the South Iceland seismic zone and the SIL project. *Bull. Seismol. Soc. Am.* 83, 696–716.

Sturkell, E., Einarsson, P., Sigmundsson, F., Geirsson, H., Pedersen, R., Van Dalfsen, E., et al. (2006). Volcano geodesy and magma dynamics in Iceland. *J. Volc. Geotherm. Res.* 150, 14–34. doi: 10.1016/j.jvolgeores.2005.07.010

Sturkell, E., Sigmundsson, F., Geirsson, H., Ólafsson, H., and Theodórsson, T. (2008). Multiple volcano deformation sources in a post-rifting period: 1989-2005 behaviour of Krafla, Iceland constrained by levelling, tilt and GPS observations. *J. Volcanol. Geotherm. Res.* 177, 405–417. doi: 10.1016/j.jvolgeores.2008.06.013

Saemundsson, K. (1974). Evolution of the axial rifting zone in Northern Iceland and the Tjörnes fracture zone. *Geol. Soc. Am. Bull.* 85, 495–504. doi: 10.1130/0016-7606(1974)85<495:eotarz>2.0.co;2

Saemundsson, K. (1978). "Fissure swarms and central volcanoes of the neovolcanic zones in Iceland," in *Crustal Evolution in Northwestern Britain and Adjacent Regions*, Vol. 10, eds D. R. Bowes and B. E. Leake (Washington, DC: Geological Society), 415–432.

Saemundsson, K. (1982). "Calderas in the Neovolcanic zones of Iceland," in *Eldur er í norðri (Fires in the North), Festschrift for Sigurður Þórarinsson*, eds H. Þórarinsdóttir, Ó. H. Óskarsson, S. SteinÞórsson, and Þ. Einarsson (Reykjavík: Sögufélag), 221–239.

Saemundsson, K. (1991). "Geology of the Krafla area," in *Náttúra Mývatns, (The Nature of lake Mývatn)*, eds A. Gardarsson and A. Einarsson (Reykjavík: Icelandic Nature Science Society), 25–95.

Tarasewicz, J., Brandsdóttir, B., White, R. S., Hensch, M., and Thorbjarnardóttir, B. (2012a). Using microearthquakes to track repeated magma intrusions beneath the Eyjafjallajökull stratovolcano, Iceland. *J. Geophys. Res.* 117:B00C06. doi: 10.1029/2011JB008751

Tarasewicz, J., White, R. S., Woods, A. W., Brandsdóttir, B., and Gudmundsson, M. T. (2012b). Magma mobilization by downward-propagating decompression of the Eyjafjallajökull volcanic plumbing system. *Geophys. Res. Lett.* 39:L19309. doi: 10.1029/2012GL053518

Tryggvason, E. (1980). Subsidence events in the Krafla caldera, North Iceland, 1975-1979. *J. Geophys.* 47, 141–153.

Tryggvason, E. (1984). Widening of the Krafla fissure swarm during the 1975-1981 volcano-tectonic episode. *Bull. Volcanol.* 47, 47–69. doi: 10.1007/bf01960540

Tryggvason, E. (1989). Ground deformation in Askja, Iceland: Its source and possible relation to flow of the mantle plume. *J. Volcanol. Geotherm. Res.* 39, 61–71. doi: 10.1016/0377-0273(89)90021-8

Vogfjörð, K. S., Hjaltadóttir, S., Kjartansson, E., Roberts, M. J., and Slunga, R. (2009). "Interpreting seismic signals from Icelandic volcanoes," in *Proceedings of the Conference on Earthquakes and Pre-Earthquake Processes*, Reykjavík.

Ward, P. L., and Björnsson, S. (1971). Microearthquakes, swarms and the geothermal areas of Iceland. *J. Geophys. Res.* 76, 3953–3982. doi: 10.1029/jb076i017p03953

Wessel, P., Luis, J. F., Uieda, L., Scharroo, R., Wobbe, F., Smith, W. H. F., et al. (2019). The generic mapping tools version 6. *Geochem. Geophys. Geosyst.* 20, 5556–5564. doi: 10.1029/2019GC008515

White, R. S., Drew, J., Martens, H. R., Key, J., Soosalu, H., and Jakobsdóttir, S. S. (2011). Dynamics of dyke intrusion in the mid-crust of Iceland. *Earth Planet. Sci. Lett.* 304, 300–312. doi: 10.1016/j.epsl.2011.02.038

Wolfe, C. J., Bjarnason, I. T. H., VanDecar, J. C., and Solomon, S. C. (1997). Seismic structure of the Iceland mantle plume. *Nature* 385, 245–247. doi: 10.1038/385245a0

Wright, T. J., Sigmundsson, F., Ayele, A., Belachew, M., Brandsdottir, B., Calais, E., et al. (2012). Geophysical constraints on the dynamics of spreading centres from rifting episodes on land. *Nat. Geosci.* 5, 242–250. doi: 10.1038/NGEO1428

Conflict of Interest: The authors declare that the research was conducted in the absence of any commercial or financial relationships that could be construed as a potential conflict of interest.

Copyright © 2021 Einarsson and Brandsdóttir. This is an open-access article distributed under the terms of the Creative Commons Attribution License (CC BY). The use, distribution or reproduction in other forums is permitted, provided the original author(s) and the copyright owner(s) are credited and that the original publication in this journal is cited, in accordance with accepted academic practice. No use, distribution or reproduction is permitted which does not comply with these terms.

frontiers in Earth Science

ORIGINAL RESEARCH
published: 03 May 2021
doi: 10.3389/feart.2021.610165

Thermo-Rheological Properties of the Ethiopian Lithosphere and Evidence for Transient Fluid Induced Lower Crustal Seismicity Beneath the Ethiopian Rift

Ameha A. Muluneh[1]*, *Derek Keir*[2,3] *and Giacomo Corti*[4]

[1] School of Earth Sciences, Addis Ababa University, Addis Ababa, Ethiopia, [2] School of Ocean and Earth Science, University of Southampton, Southampton, United Kingdom, [3] Dipartimento di Scienze della Terra, Università degli Studi di Firenze, Florence, Italy, [4] CNR, Istituto di Geoscienze e Georisorse, UOS Firenze, Florence, Italy

OPEN ACCESS

Edited by:
Yosuke Aoki,
The University of Tokyo, Japan

Reviewed by:
Sarah Jaye Oliva,
University of British Columbia, Canada
Steven Roecker,
Rensselaer Polytechnic Institute,
United States

***Correspondence:**
Ameha A. Muluneh
ameha.atnafu@aau.edu.et;
amugeol@gmail.com

Specialty section:
This article was submitted to
Volcanology,
a section of the journal
Frontiers in Earth Science

Received: 25 September 2020
Accepted: 29 March 2021
Published: 03 May 2021

Citation:
Muluneh AA, Keir D and Corti G (2021) Thermo-Rheological Properties of the Ethiopian Lithosphere and Evidence for Transient Fluid Induced Lower Crustal Seismicity Beneath the Ethiopian Rift.
Front. Earth Sci. 9:610165.
doi: 10.3389/feart.2021.610165

Lower crustal earthquakes at plate boundaries and intraplate settings occur at depth where deformation is normally expected to occur in a ductile manner. Here we use the available earthquake catalogs and compute theoretical predictions for a range of conditions for the occurrence of lower crustal earthquakes beneath the Main Ethiopian Rift (MER) and adjacent north-western (NW) plateau. Yield strength envelops are constructed using information on geothermal gradient, strain rate, and composition constrained by geophysical observations. Our models suggest that away from the MER beneath the NW plateau the depth distribution of earthquakes in the lower crust is best explained by strong mafic lower crustal rheology and hydrostatic fluid pore pressure conditions. In the same region the effective elastic thickness is similar to seismogenic thickness showing that the lower crust has long-term strength and hence can physically support brittle deformation. On the contrary, in the central MER the seismogenic thickness is much larger than the effective elastic layer thickness implying that the lower crust has no long-term strength. Here our models show that both hydrostatic and near-lithostatic fluid pore pressures fail to explain the observed seismicity and instead a combination of near-lithostatic pore fluid pressure and transient high strain rate due to the movement of fluids provide a plausible mechanism for the occurrence of seismicity in the lower crust. Our interpretations are supported by occurrence of swarms of deep earthquakes beneath the MER, as opposed to more continuous background deep seismicity away from the rift. Using time-depth progression of earthquakes, we estimate permeability values of 5.9×10^{-15} m^2 and 1.8×10^{-14} m^2 at lower crustal depth. The range of permeability implies that seismicity can be induced by pore-pressure diffusion, likely from fluids sourced from the mantle that reactivate preexisting faults in the lower crust. Our thermo-rheological models explain the first order differences in lower crustal earthquakes both directly beneath and outboard of the rift valley.

Keywords: pore fluid pressure, rheology, main Ethiopian rift, lower crustal seismicity, strain rate, geothermal gradient

1. INTRODUCTION

Lower crustal earthquakes have been observed at both plate boundaries and intraplate settings at a depth where deformation is normally expected to occur in a ductile manner. As such, the origin of these deep crustal earthquakes is debated (e.g., Maggi et al., 2000; Jackson, 2002). In some studies from the East African Rift System (EARS), strong lower crust is invoked for lower crustal earthquakes to occur (e.g., Albaric et al., 2009). Modeling studies from the EARS show that earthquakes at lower crustal pressure-temperature (P-T) conditions can nucleate in mafic (Hellebrekers et al., 2019), and/or anhydrous materials (Craig and Jackson, 2021). Brittle faults penetrating the entire crust in regions with more normal crustal compositions are interpreted to occur beneath the Tanganyika rift (Craig et al., 2011; Lavayssiere et al., 2019a), with the brittle failure enabled by the exceptionally thick lithosphere and low geothermal gradient keeping the lower crust relatively cool (O'Donnell et al., 2016; Lavayssiere et al., 2019a). Alternatively, other studies suggest that lower crustal earthquakes are facilitated by high pore fluid pressure (Lindenfeld et al., 2012; Lee et al., 2016; LaRosa et al., 2021), which can locally induce high enough strain rates to cause earthquakes even in areas with high heat flow and weak long-term rheology. However, it is usually unclear whether the high pore fluid pressure is a transient or a long-term feature.

Lower crustal seismicity has also specifically been observed in the volcanically active Main Ethiopian Rift (MER) as well as beneath the NW plateau (**Figure 1**; Keir et al., 2009; Lapins et al., 2020), two regions which are characterized by contrasting deformation history and thermo-rheological properties. Here, we aim to investigate the role of thermo-rheological properties and fluid flow in controlling the depth of lower crustal earthquakes in and around the MER, a major volcanically and tectonically active continental rift.

2. GEOLOGICAL BACKGROUND

The MER accommodates the ongoing opening of the Nubia and Somalia plates at the northern part of the EARS. The MER is largely defined by NNE to NE striking border faults that separate the rift valley from the adjacent NW plateau and the southeastern (SE) plateau. Pre-existing lithospheric scale heterogenities are thought to significantly control the initial locus of extension to the border faults (e.g., Corti, 2009; Corti et al., 2018), which accommodated most of the opening of the rift during Miocene times starting at ∼20 Ma (e.g., Wolfenden et al., 2004). In the northern MER, faulting has generally progressively localized in rift to the point that since the Quaternary, extension has been mainly focused in narrow magmatic segments arranged en-echelon in the rift floor (e.g., Ebinger and Casey, 2001). In contrast, in the central and southern MER faulting is still mainly accommodated by the border faults with subordinate activity in the rift center (Corti et al., 2020).

The NW plateau and the MER show a marked contrast in crustal thickness. Wide-angle controlled source seismic imaging shows that the crust beneath the NW plateau is ∼45 km thick, with a 28 km thick upper crust (e.g., Mackenzie et al., 2005). The P-wave seismic velocity variations coupled with inversion of gravity data for rock density suggest that the upper crust is similar to standard continental crust, whereas the middle and lower crust include a significant proportion of mafic rock (Mackenzie et al., 2005; Cornwell et al., 2010). On the contrary, the SE plateau has been interpreted to be underlain by only felsic or intermediate compositions (Mackenzie et al., 2005). The plateaus have contrasting patterns of strain, with GPS and seismicity data showing that the NW plateau experiences distributed extension (Birhanu et al., 2016), which is accompanied by earthquakes in the upper and lower crust down to ∼32 km depth (**Figures 2A,B**; Keir et al., 2009).

In the central MER the crust has a thickness of 38 km with upper crustal thickness of ∼20 km (Keranen et al., 2009). Similar to the plateaus, the upper crust in the rift is dominated by felsic rheology (e.g., Keranen et al., 2009), which is in line with the Vp/Vs ratio of ∼1.75 recorded for upper crustal local earthquakes (Keir et al., 2006; Greenfield et al., 2019), as well as recent modeling studies suggesting that upper/middle crustal seismicity is best explained by wet quartzite rheology (Muluneh et al., 2020). In contrast, the Vp/Vs ratio based on shear wave velocity from Rayleigh wave/receiver function joint inversion (Keranen et al., 2009) and compressional wave velocity determined by wide-angle data (Maguire et al., 2006) indicates that the lower crust is dominated by mafic granulite composition (Keranen et al., 2009).

Earthquakes within the MER were until recently thought to be confined to depths of less than ∼18 km, where they are mainly localized on both the border faults and fault systems within the magmatic segments (Keir et al., 2006; Wilks et al., 2017; Greenfield et al., 2019; Lavayssiere et al., 2019b). However recently, Lapins et al. (2020) reported lower crustal earthquakes beneath the eastern side of the central MER in the vicinity of Corbetti caldera (**Figure 2C**). Subsequent studies nearby did not observe deep events, which coupled with the anomalous depths and swarm like nature of deep seismic sequence led Lapins et al. (2020) to conclude that the mechanism for lower crustal seismicity in the area might be due to transient high strain rate and pore fluid pressure conditions.

3. DATA AND MODELING

3.1. Earthquake Catalogs

In our study we used the earthquake catalogs of Keir et al. (2006) and Lapins et al. (2020) to test thermo-rheological property of the Ethiopian lithosphere. For the Keir et al. (2006) catalog local earthquakes were derived during October 2001 to February 2003 from arrival times of earthquakes at four or more seismic stations composing the EAGLE seismic network (Keir et al., 2006), and using a best-fit 1-D seismic velocity model derived from tomography (Daly et al., 2008). The seismic network was mostly composed of 30 broadband seismic stations distributed in the central and northern Ethiopian rift and both adjacent plateaus. The catalog includes 1957 earthquakes with local magnitude (ML) between 0 and 4 and a magnitude of completeness of ∼ ML 2.1. The error bars on the earthquake locations are on average ±600 m in horizontal directions and ±2000 m in depth (Keir et al., 2006; Mazzarini et al., 2013). In contrast, the Lapins

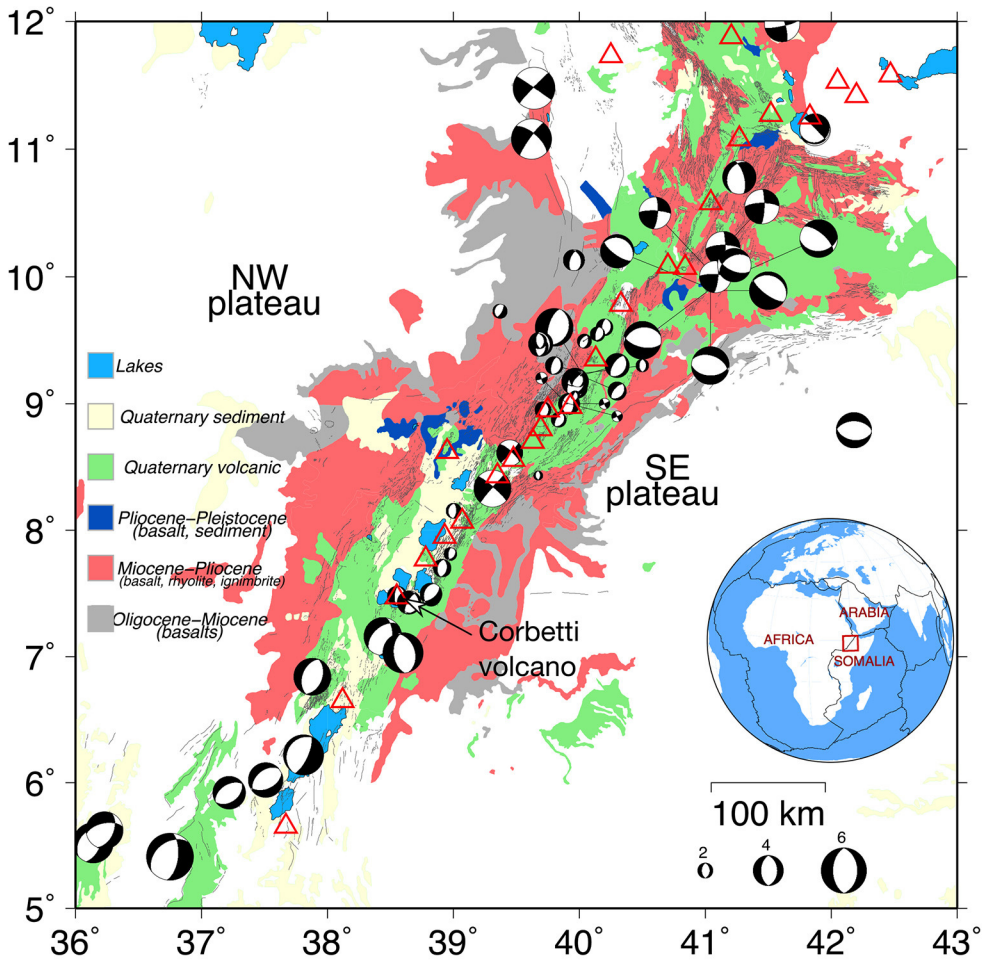

FIGURE 1 | Location of the Main Ethiopian Rift (MER) and adjacent plateau. Earthquakes focal mechanisms are taken from Hofstetter and Beyth (2003) and Keir et al. (2006). The geology and faults are taken from 1:2M scale geological map (Tefera et al., 1990). The open red box on the inset map shows the location of the main map. The red triangles show active volcanoes.

et al. (2020) catalog uses 15 seismic stations deployed on Aluto and Corbetti volcanoes during 2012 and 2013. Earthquakes were located with seven or more phase arrivals, including at least one S phase. A number of 1D velocity models, including the (Daly et al., 2008) model were tested and yielded similar locations. The catalog includes 58 earthquakes up to a maximum Mw of 3.7, with most of the earthquakes occurring in March and April 2012. Due to sub-optimal seismic stations positions relative to the earthquakes individual error bars of earthquake depth are larger, and approximated at ±5 km (Lapins et al., 2020).

3.2. Yield Strength Envelope

3.2.1. Brittle Regime

Brittle behavior of the upper crust can be modeled using Equation (1) (Sibson, 1974).

$$(\sigma_1 - \sigma_3)(z) = \beta\rho g z(1 - p_f) \quad (1)$$

where (σ_1-σ_3) is differential stress; β is a parameter that depends on the tectonic setting and friction coefficient (e.g., Ranalli, 1997) and is equal to 0.6 (Muluneh et al., 2018); ρ is density; g is acceleration due to gravity and p_f is the pore fluid factor. The linear frictional failure bounds the strength envelop.

3.2.2. Ductile Regime

The ductile regime is represented by power law dislocation creep (e.g., Turcotte and Schubert, 2002) and is given by Equation (2)

$$(\sigma_1 - \sigma_3)(z) = (\frac{\dot{\epsilon}}{A})^{1/n} \exp(\frac{E}{nRT(z)}) \quad (2)$$

where $\dot{\epsilon}$ is the strain rate in s^{-1}; $T(z)$ is temperature in degrees Kelvin; R is the universal gas constant; A, E, and n depend on the rheology considered.

Numerical simulation of lithospheric deformation using wet quartzite upper crust and seismic moment release show that upper to middle crustal earthquakes in the MER can be explained by the rheology of the crust (Muluneh et al., 2020). For the lower crust, we use mafic granulite rheology for the NW plateau

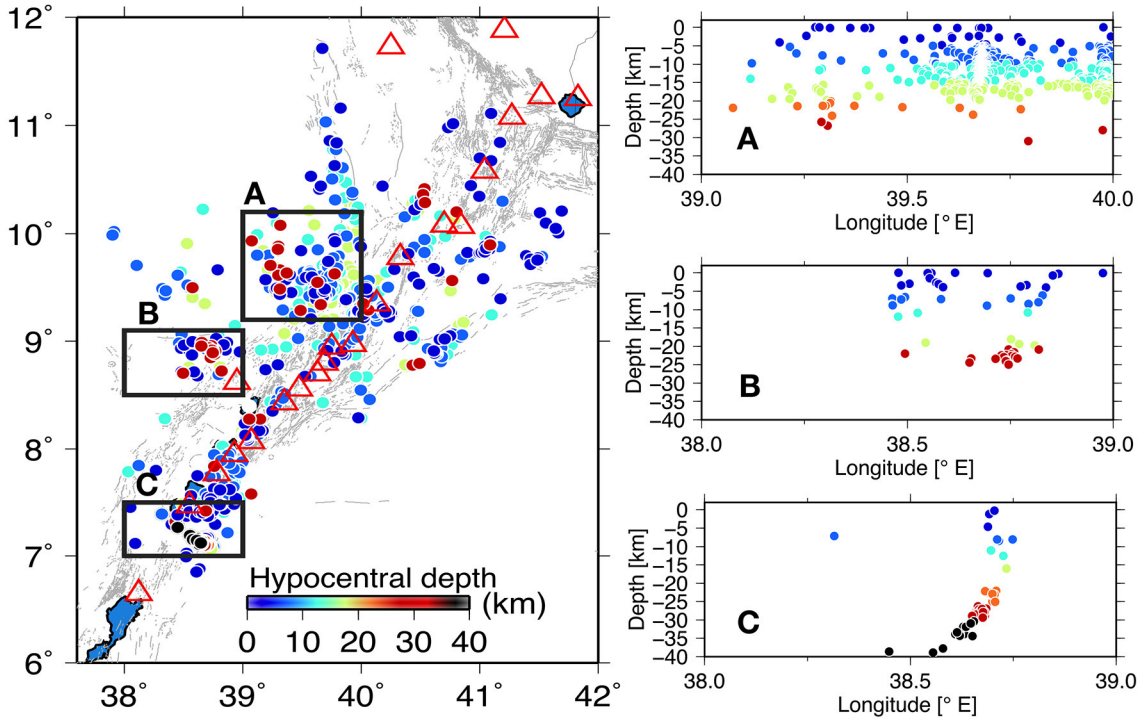

FIGURE 2 | Depth distribution of seismicity in the NW plateau **(A)**, Yerrer Tullu-Wellel volcanic lineament (YTVL) **(B)** and central MER **(C)**. The open black boxes show the location of cross-sections in **(A–C)**. Seismicity extends to ∼32 km **(A)**, whereas in the central MER earthquake occurs to a depth of ∼38 km. In cross section **(C)**, we show only earthquakes from Lapins et al. (2020). These earthquakes have maximum lateral uncertainty <10 km (Lloyd et al., 2018).

and beneath the rift. The inferred rheology agrees with the elevated Vp/Vs ratio (e.g., Keranen et al., 2009) and high densities constrained by inversion of gravity data (Mahatsente et al., 1999; Cornwell et al., 2006). The creep parameters for mafic granulite are A = 1.4 × 10^4 MPa^n s^{-1}, E = 445 KJ/mol and n = 4.2 (Ranalli, 1997). The density for wet quartzite is 2,640 kg/m^3.

Calculation of ductile rheology is sensitive to temperature variation with depth (Equation 2). The steady state, one-dimensional heat conduction equation with exponentially decreasing radioactive heat production is given as (e.g., Pasquale et al., 2014).

$$K\nabla^2 T = -A_0 e^{-z/b} \tag{3}$$

where A_0 is crustal radioactive heat production, K is thermal conductivity, b is the Characteristics thickness of the layer enriched with radioactive elements and taken here to be 10 km (Pasquale et al., 2014).

Integration of Equation (3) results in the geothermal gradient given by the following equation:

$$T(z) = T_0 + \left(\frac{Q_0 - bA_0 e^{-z/b}}{K}\right)z + \frac{A_0 b^2}{K}(1 - e^{-z/b}) \tag{4}$$

where T_0 is surface temperature and considered here to be equal to 273 K, Q_0 is surface heat flow. Crustal heat production, A_0, is assumed to be 2 μW/m^3 and thermal conductivity, K, is equal to 3 W/m K (Pasquale et al., 2014).

We use P-T independent thermal conductivity and hence the $T(z)$ (Equation 4) depends mainly on the surface heat flow value, which is estimated to be 50 and 70 mW/m^2 for NW plateau and the MER, respectively. We compute these values by using a steady state geothermal gradient by assuming the lithosphere is in a state of thermal equilibrium (e.g., Sippel et al., 2017). However, this assumption may not hold for the rift, beneath which active upwelling and small scale convections likely occur in the asthenosphere (Civiero et al., 2016; Gallacher et al., 2016) and where crustal magmatism is ongoing (Chambers et al., 2019). This is well-shown by the difficulty in constructing a typical geotherm for the rift due to a wide range of temperature estimates even for a single locality (Rooney et al., 2005).

In the calculation of ductile strength (Equation 2), strain rate ($\dot{\epsilon}$) is one of the questionable parameters. Rheological profiles can be modeled by considering spatially invariable strain rate (10^{-15} s^{-1}; Albaric et al., 2009; Sippel et al., 2017). Here we use strain rate determined using a finite element numerical modeling of deformation across the MER (Muluneh et al., 2020). The model in **Figure 3** shows the present day strain rate in the MER, which is comparable to GPS observations (Birhanu et al., 2016; Knappe et al., 2020). Both GPS observation and numerical modeling of deformation indicate that strain rate is distributed over a wide region (Knappe et al., 2020; Muluneh et al., 2020) but with a significant proportion localized to the magmatic segments with

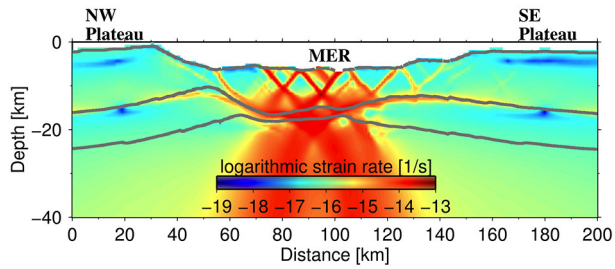

FIGURE 3 | Present day 2D strain rate in the MER and adjacent plateau (from Muluneh et al., 2020). In the MER, high strain rate is localized in ∼30 km wide zone.

strain rate of $\sim 2 \times 10^{-14}$ s^{-1} (Kogan et al., 2012; Muluneh et al., 2020). We then consider a strain rate of 10^{-16} and 10^{-15} s^{-1} for the NW plateau.

4. RESULTS AND DISCUSSION

4.1. Thermo-Mechanical Property of the Crust

The results of our yield strength envelopes (YSE) calculations presented in **Figure 4** allow us to model both the long-term strength of the crust as well as short term earthquake processes (Bürgmann and Dresen, 2008; Hauksson and Meier, 2018). Several studies have evaluated the consistency between crustal rheology and depth distribution of earthquakes (Déverchere et al., 2001; Albaric et al., 2009; Dong et al., 2018; Hauksson and Meier, 2018; Muluneh et al., 2020) by making an assumption that increased strength results in more seismicity (Hauksson and Meier, 2018). In the present study, we also make a similar assumption.

Figures 4A,B show the YSE calculated for the NW plateau and the rift, respectively. In the NW plateau brittle deformation occurs down to depth of ∼28 km under hydrostatic pore fluid pressure conditions. Increasing the pore fluid pressure to near-lithostatic fluid pressure conditions increases the brittle layer to a depth of 32 km. Comparing the yield strength envelope with depth distribution of earthquakes in the lower crust shows that hydrostatic pore fluid pressure explains the observed seismicity (**Figures 2A,B**, **4A**). Considering the hypocentral depth uncertainty (∼2 km; Keir et al., 2006), we interpret that hydrostatic pore pressure and mafic rheology are sufficient conditions for lower crustal seismicity.

Similarly, we construct the YSE for the central MER using strain rate that varies by an order of magnitude and pore fluid factor of 0.4 and 0.95 (**Figure 4C**). The higher strain rate corresponding to the strain rate value beneath the magmatic segments increases the brittle layer thickness by about ∼1 km in both upper and lower crust. Increasing the pore fluid factor to 0.95 allows brittle deformation down to ∼28 km depth, which is a similar depth to the peak in lower crustal seismicity beneath the MER (**Figure 4D**).

Here we discuss our interpretation of the depth distribution of earthquake beneath the NW plateau and MER alongside independent geodynamic constraints. Support of our interpretation of hydrostatic pore pressure and mafic rheology being sufficient to generate lower crustal earthquakes beneath the NW Plateau comes from insights into the long-term strength of the crust from comparison of between the effective elastic (T_e) and seismogenic (T_s) thickness (Maggi et al., 2000; Watts and Burov, 2003; Pérez-Gussinyé et al., 2009). The depth distribution of earthquakes constrain the seismogenic layer thickness (Watts and Burov, 2003). Ebinger and Hayward (1996) estimate the T_e for different tectonic sectors of Ethiopia including the NW plateau, by computing the transfer function between gravity and topography as a function of wavelength of coherence. The T_e is ∼40 km in the NW plateau, which agrees well with the seismogenic layer thickness (∼32 km). Therefore, the lower crust in the region has a long-term strength to allow brittle failure (Keir et al., 2009).

The deep seismicity is broadly distributed beneath the NW plateau and Yerrer-Tullu-Wellel volcanic lineament, in areas where magnetotelluric (MT) shows intermediate conductivities (Whaler and Hautot, 2006; Keir et al., 2009). A caveat to this is that denser and localized clusters of deep seismicity are also observed in localized regions of high conductivity beneath volcanoes near the rift, suggesting that in some localized regions fluid pressure higher than hydrostatic may also contribute to deep seismicity in some regions. However, in general we observe a good correlation between the depth distribution of earthquakes and modeled crustal rheology in the NW plateau (**Figures 4A,B**).

In contrast beneath the MER, estimates of plate strength are that T_e is 17 ± 2 km in the central MER (Ebinger and Hayward, 1996). However, deeper earthquakes (down to 38 km) occur in the central MER than is predicted by both our rheological model and the estimate of T_e (**Figure 2C**; Lapins et al., 2020). Therefore, in the following sections we present theoretical considerations for a range of conditions that allow lower crustal seismicity in the central MER.

4.2. Strain Rate During Fluid Migration

The lower crust exhibits variable behavior over different time scales in thermally active areas (Thatcher and Pollitz, 2008). Transient high strain rate during localized creep in the lower crust allows earthquakes to occur (Campbell and Menegon, 2019). Similarly, magma injection laboratory experiments shows that the strain rate could reach about ten orders of magnitude faster than plate tectonic rates (Tuffen et al., 2008). Such high strain rate localizes deformation in a narrow zone in otherwise underformed lower crust (Hawemann et al., 2018; Campbell and Menegon, 2019). Translating the laboratory determined strain rates to natural shear zones show that the value ranges from 10^{-9} to 10^{-13} s^{-1} (Bürgmann and Dresen, 2008). Geophysical observations from the MER show that high strain rates at lower crustal depth can be induced by movement of magma and/or fluids exsolved from magma (Chambers et al., 2019; Iddon and Edmonds, 2020; Lapins et al., 2020).

Figure 4C shows that near-lithostatic pore fluid pressure allows brittle failure only down to ∼30 km, yet deeper

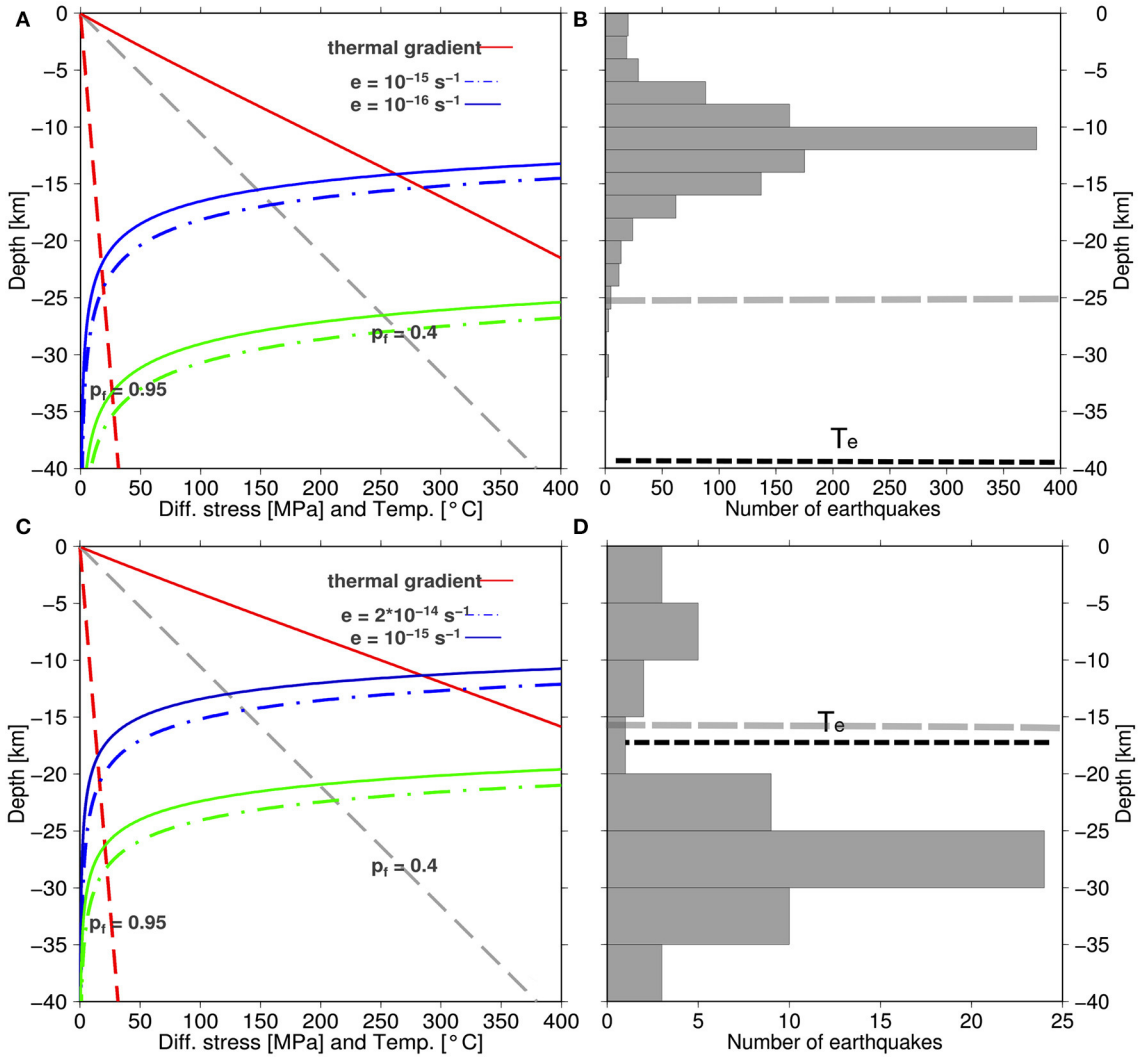

FIGURE 4 | Yield Strength Envelope (YSE) and seismicity in the NW plateau (**A,B**; respectively) and the MER (**C,D**; respectively). There is a good match between modeled BDT and depth distribution of seismicity in the NW plateau. In the rift, there is a big mismatch between the two parameters. The seismicity is in 2 and 5 km depth bins in the NW plateau and the MER, respectively. The YSE is constructed for wet quartzite upper crust (blue lines) and mafic granulite (green lines) lower crust for both NW plateau and the MER. The p_f is the pore fluid factor [0.4 for hydrostatic and 0.95 for (near-) lithostatic states shown in broken gray and red lines, respectively]. T_e refers to the effective elastic thickness (Ebinger and Hayward, 1996). The broken gray line in **(B,D)** is the boundary between upper and lower crust (Mackenzie et al., 2005).

earthquakes down to a depth of ∼38 km occur beneath the MER (Lapins et al., 2020). We therefore conduct an alternative experiment using a strain rate of 10^{-9} and 10^{-10} s^{-1} and pore-fluid pressure approaching the lithostatic condition (**Figure 5**). Strictly speaking, transient deformations should be modeled using a dynamic approach (e.g., Albert et al., 2000). However, here we make the simpler assumption that the crust reaches instantaneous equilibrium with the migrating fluid. The transient deformation modifies the strength envelope greatly.

The results of our new YSE calculation in **Figure 5** shows that the load bearing element under near-lithostatic pore fluid pressure conditions moves down to ∼35 and ∼38 km under a strain rate of 10^{-10} and 10^{-9} s^{-1}, respectively. The stress due to transient fluid flow allows failure to occur at a depth of 38 km with a differential stress with a magnitude of 32 MPa (**Figure 5**). The differential stress at 38 km depth is consistent with the minimum shear stress (i.e., ∼15 MPa; Muluneh et al., 2018) measured as $(\sigma_1 - \sigma_3)/2$ to cause seismicity in the crust. Unlike previous studies which uses seismicity cut-off of either D90 or D95 (i.e., a depth above which 90 or 95% of seismicity occurs), we consider the maximum depth of earthquake here (38 km) in order not to lose earthquakes due to hypocentral uncertainty. However, choosing 38 km or D90 or D95 does not significantly affect the analysis presented here as only three earthquakes are located below 35 km.

We interpret the results as strong evidence that the combined effect of transient high strain rate and pore fluid pressure due to the movement of magma and volatiles provide a straightforward

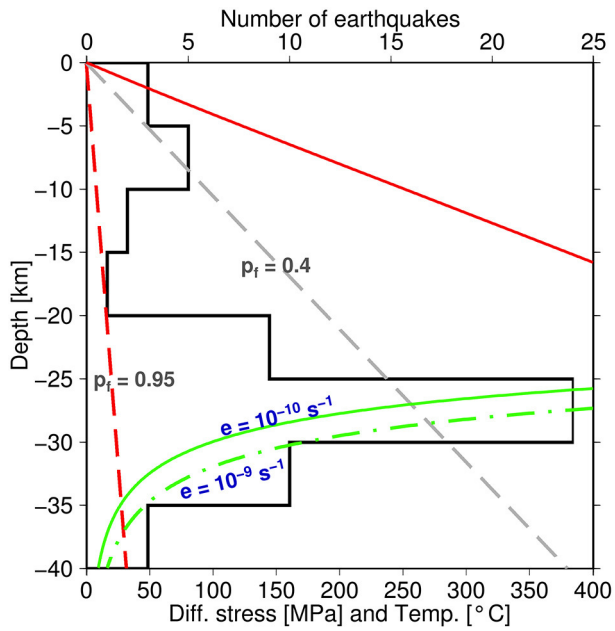

FIGURE 5 | Yield Strength Envelope (YSE) constructed using transient strain rate of 10^{-10} and 10^{-9} s^{-1} (For the sake of clarity, we only show the curves for the lower crust). The stairs-step shows the depth distribution of earthquakes in the rift, similar to **Figure 4D**. This transient high pore fluid pressure and strain rate explains the observed lower crustal seismicity in the central MER (Lapins et al., 2020). The flow law and geothermal gradient are similar to **Figure 4C**.

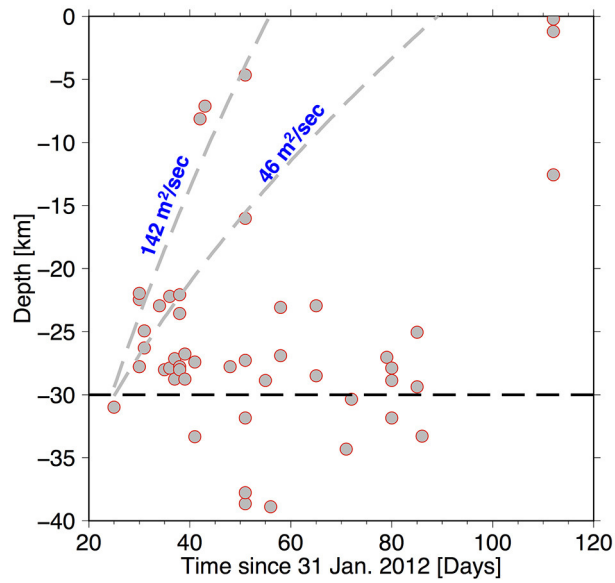

FIGURE 6 | Time-depth progression of earthquakes in the central MER (Lapins et al., 2020) for hydraulic diffusivity, D, of 142 and 46 m^2/s. The broken black line at 30 km depth shows where most of the seismicity nucleates.

mechanism to cause lower crustal seismicity. Unless these conditions are met, the maximum depth of lower crustal earthquakes in the central MER remain difficult to explain.

Here we discuss our interpretation in light of global evidence for deep fluid related seismicity. High strain rates due to the intrusion of magma in the lower crust facilitates lower crustal seismicity, as for example observed at Lake Tahoe, California (Smith et al., 2004). Introduction of fluids to initially dry lower crust is associated with earthquakes, which in turn causes fracturing and allow fluids to migrate (Jamtveit et al., 2019). The intimate link between high pore fluid pressure and lower crustal seismicity has been interpreted in a number of settings (Reyners et al., 2007; Lindenfeld et al., 2012; Martens and White, 2013; Weinstein et al., 2017). Compelling evidence from other parts of the EARS argue that the pore fluid pressure in the lower crust must be in near-lithostatic conditions mainly due to fluid migrating from the mantle and consequently induce lower crustal seismicity (Lindenfeld et al., 2012; Weinstein et al., 2017). The lower crustal earthquakes reported by Lapins et al. (2020) and modeled here, are the first observed in the MER.

4.3. Pore Fluid Pressure and Permeability in the Lower Crust

Based on the framework provided above by the modeling in the previous section we use the space-time pattern of the observed lower crustal earthquake swarm to model the flow of fluid through the crust. We assume that the pore fluid pressure in the lower crust is in near-lithostatic condition, and sourced from a reservoir of partial melt localized near the Moho (Chambers et al., 2019) and/or exsolved volatiles from solidified melt in the lowermost crust (Keir et al., 2009; Iddon and Edmonds, 2020).

We assume that the earthquakes show space-time progression as given by the square root of time, t, and hydraulic diffusivity, D, (Equation 5)

$$r = (4\pi Dt)^{\frac{1}{2}} \tag{5}$$

where r is the distance (depth). The above equation assumes isotropic media. We assume that the fluid migrates from ∼30 km depth to the upper crust and also that seismicity starts and ends on the 25th and 120th day from the beginning of seismicity on the 31 January 2012 (Lloyd et al., 2018; Lapins et al., 2020). We have started our modeled flow at 30 km depth since this is assumed to be the depth at which the migration front starts (**Figure 6**).

The results of the modeling in **Figure 6** shows the diffusivity values by fitting the envelope of migrating front of seismicity (Shapiro et al., 1999). We estimate two values of hydraulic diffusivity, i.e., D = 46 and 142 m^2/s, which are at least an order of magnitude higher than the expected crustal hydraulic diffusivity values ranging from 0.01 to 10 m^2/s (Scholz, 2002). The permeability, κ, in m^2 is estimated using Equation (6)

$$\kappa = D\eta(\phi^*\beta_f + (1-\phi^*)\beta_r) \tag{6}$$

where η is viscosity; ϕ^* is porosity; $\beta_{f,r}$ are the compressibility of the fluid and the rock, respectively.

Considering the standard values for the above parameters (i.e., $\beta_{f,r} = 10^{-9}$ and 10^{-11}Pa $^{-1}$, respectively; $\phi^* = 3\times10^{-3}$), CO_2 as fluid medium ($\eta = 10^{-5}$ Pa s) and diffusivity of 46 and 142 m^2/s result in permeability values of 5.9×10^{-15} m^2 and 1.8×10^{-14} m^2, respectively. The permeability values increase to 4.7×10^{-14}

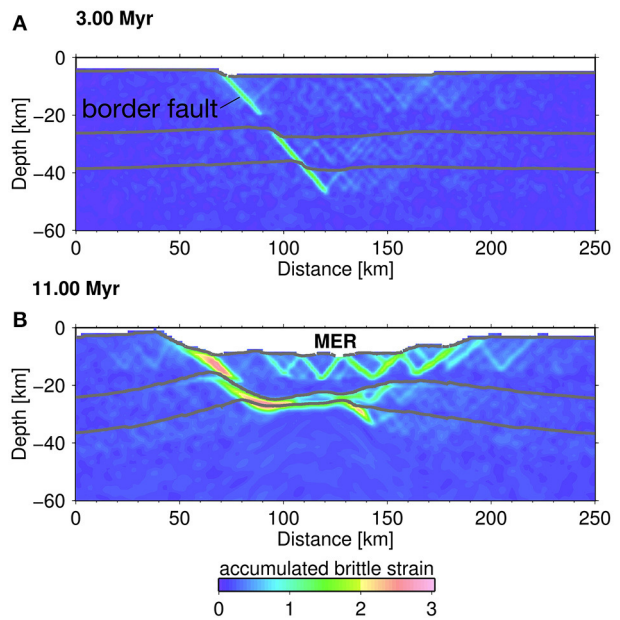

FIGURE 7 | Sequence of formation of faults in the MER (from Muluneh et al., 2020) at 3 Myr **(A)** and 11 Myr **(B)** after model initiation. The high pore fluid pressure can potentially reactivate faults in the lower crust.

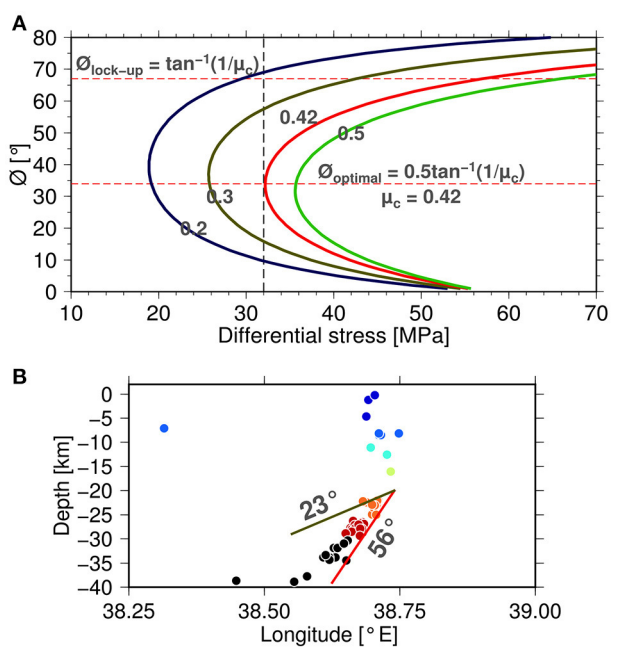

FIGURE 8 | (A) Dip (90-ϕ) of reactivated fault in the lower crust for pore fluid factor of 0.95 for different friction coefficients. **(B)** Depth distribution of earthquakes projected on E-W line, along the dip direction of rift parallel faults. The linear seismicity streak in the lower crust is bounded by an optimal (56°) and lock-up (23°) dip angles for friction coefficient of 0.42.

m^2 and 1.5×10^{-13} m^2 for hydraulic diffusivity of 46 and 142 m^2, respectively, if we consider water as a dominant fluid.

Comparison of our results to other similar studies shows that the permeability estimated here is similar to the permeability estimates at seismogenic depth [i.e., 5×10^{-16}–5×10^{-14} m^2–referred to as seismogenic permeability by Talwani et al. (2007)]. According to Talwani et al. (2007) permeability values less or greater than the seismogenic permability do not allow pore-fluid diffusion and hence no seismicity. Therefore, our estimate of permeability indicate that high pore fluid pressure can form and hence seismicity occurs in the lower crust.

Our permeability values are two to four orders of magnitude higher than the expected permeability at lower crustal depth (Ingebritsen and Manning, 2010), which implies that the diffusivity must be controlled by large scale fractures (Scholz, 2002). The high pore fluid pressure eventually reactivates preexisting faults in the lower crust and results in the enhancement of permeability and as a result the fluid pressure drops (Scholz, 2002). Rock fracture experiment shows that seismicity is continuous even after fluid pressure drops (Passelégue et al., 2018). Despite such high permeability, CO_2 degassing measurement in the region does not observe anomalously high flux (Hunt et al., 2017), which might indicate that the permeability estimate is transient.

4.4. Reactivation of Preexisting Faults in the Lower Crust

Fault reactivation in the upper crust due to magmatic fluids have been reported from the other parts of the EARS (Muirhead et al., 2016; Jones et al., 2019). These studies argue that optimally oriented faults act as passageways for fluids from deep-seated magma chambers.

Figure 7 shows accumulated plastic strain, interpreted here as faults, in numerical models at 3 and 11 Myr since model initiation (Muluneh et al., 2020). Sibson (2000) presented an expression (Equation 7) to relate the differential stress ($\sigma_1 - \sigma_3$) for frictional reactivation of cohesion-less normal faults at earthquake focal depth to dip angle (90°-ϕ; where ϕ is the angle σ_1 makes with the fault plane) of faults.

$$(\sigma_1 - \sigma_3) = [\frac{\mu(\tan\phi + \cot\phi)}{1 + \mu\cot\phi}]\rho g z(1 - p_f) \quad (7)$$

Using the near-lithostatic pore fluid factor (p_f = 0.95) and the corresponding differential stress of 32 MPa (**Figure 5**) results in reactivation of optimally oriented preexisting normal fault with a friction coefficient of less than 0.42, which corresponds to a dip angle of 56° and lockup dip angle of 23° (**Figure 8A**). The lock-up angle is less than the 30° dip angle below which faults are not expected to slip (Anderson, 1951). High pore fluid pressure may allow slip to occur on faults which dip <30°. It is also possible that faults with low cohesion slip with dip angle < 20° (Reston, 2020).

The optimal dip angle of the reactivated pre-existing fault is similar to the dip of upper crustal earthquake focal mechanisms (ranging from 33° to 75°; Keir et al., 2006; Muluneh et al., 2018), and the surface expression of active faults (~60°; Agostini et al., 2011). In addition, similar dip angles for crustal scale border faults feature at rift initiation of the MER in numerical models (Muluneh et al., 2020). The reactivated faults channeling fluids from the lower crust to the upper crust explain the fault geometry

and crustal permeability values constrained by the lower crustal seismicity swarm (**Figure 8B**).

5. CONCLUSIONS

We present thermo-rheological models for the Main Ethiopian Rift and adjacent NW plateau to understand the mechanism for lower crustal earthquakes. Lower crustal earthquakes are observed in both regions, despite difference in crustal structure and thermal regimes. Our findings showed lower crustal earthquakes in the NW plateau is mainly controlled by the strong rheology under hydrostatic pore fluid pressure conditions. Comparison between the effective elastic thickness (T_e) and seismogenic layer thickness (T_s) also supports the long-term strength of the lower crust in the region. On the contrary, the lower crust in the rift shows no long-term strength, in agreement with our modeling of yield strength envelope and comparison between T_e and T_s. Instead, earthquakes at this depth require transient stress pulses with a combination of high pore fluid pressure and transient strain rate inducing the seismicity in the lower crust. In addition, our modeling suggests that high pore fluid pressure reactivates preexisting faults in the lower crust which enhances the permeability and hence fluid migration through the crust.

DATA AVAILABILITY STATEMENT

The datasets presented in this study can be found in online repositories. The names of the repository/repositories and accession number(s) can be found below: Lapins et al. (2020): https://doi.org/10.1029/2020JB020030; Keir et al. (2006): https://doi.org/10.1029/2005JB003748.

AUTHOR CONTRIBUTIONS

AM conceived the study, carried out the calculations, created the figures and wrote the first draft. DK contributed to the interpretation of the results and writing of the paper. GC contributed to the writing of the paper. All authors gave final approval for publication.

FUNDING

DK was supported by NERC grant NE/L013932/1. DK and GC are supported by Ministero dell'Università e della Ricerca (MiUR) through PRIN grant 2017P9AT72.

ACKNOWLEDGMENTS

AM acknowledges the support from the Canon Foundation, Japan-Africa Exchange program for sponsoring his stay at Kyoto University, where a significant portion of this study was conducted. Constructive comments from the two reviewers and chief Editor, Prof. Valerio Acocella, improved the quality of the manuscript. Python (https://www.python.org/) was used to construct the yield strength envelopes. Figures were drafted using Generic Mapping Tools (Wessel and Smith, 1998).

REFERENCES

Agostini, A., Bonini, M., Corti, G., Sani, F., and Manetti, P. (2011). Distribution of Quaternary deformation in the central Main Ethiopian Rift, East Africa. *Tectonics* 30:TC4010. doi: 10.1029/2010TC002833

Albaric, J., Deverchere, J., Petit, C., and Gall, B. L. (2009). Crustal rheology and depth distribution of earthquakes: insight from the central and Southern East African Rift System. *Tectonophysics* 468, 28–41. doi: 10.1016/j.tecto.2008.05.021

Albert, R., Phillips, R., Dombard, A., and Brown, C. D. (2000). A test of the validity of yield strength envelopes with an elastoviscoplastic finite element model. *Geophys. J. Int.* 140, 399–409. doi: 10.1046/j.1365-246x.2000.00006.x

Anderson, E. (1951). *The Dynamics of Faulting*. Edinburgh: Oliver and Boyd.

Birhanu, Y., Bendick, R., Fisseha, S., Lewi, E., Floyd, M., King, R., et al. (2016). GPS constraints on broad scale extension in the Ethiopian highlands and Main Ethiopian Rift. *Geophys. Res. Lett.* 43, 6844–6851. doi: 10.1002/2016GL069890

Bürgmann, R., and Dresen, G. (2008). Rheology of the lower crust and upper mantle: evidence from rock mechanics geodesy and field observations. *Annu. Rev. Earth Planet. Sci.* 36, 531–567. doi: 10.1146/annurev.earth.36.031207.124326

Campbell, L., and Menegon, L. (2019). Transient high strain rate during localized viscous creep in the dry lower continental crust (Lofoten, Norway). *J. Geophys. Res.* 124, 10240–10260. doi: 10.1029/2019JB018052

Chambers, E., Harmon, N., Keir, D., and Rychert, C. (2019). Using Ambient noise to image the northern East African Rift. *Geochem. Geophys. Geosyst.* 20, 2091–2109. doi: 10.1029/2018GC008129

Civiero, C., Goes, S., Hammond, J., Fishwick, S., Ahmed, A., Ayele, A., et al. (2016). Small-scale thermal upwellings under the northern East African Rift from S travel time tomography. *J. Geophys. Res.* 121, 7395–7408. doi: 10.1002/2016JB013070

Cornwell, D., Mackenzie, G., England, R., Maguire, P., Asfaw, L., and Oluma, B. (2006). "Northern main Ethiopian Rift crustal structure from new high-precision gravity data," in *From Yirgu, G., Ebinger, C., and Maguire, P.K.H. (eds) The Afar Volcanic Province Within the East African Rift System. Geological Society of London, Special Publications*, Vol. 259 (London), 307–321.

Cornwell, D., Maguire, P., England, R., and Stuart, G. (2010). Imaging detailed crustal structure ad magmatic intrusion across the Ethiopian Rift using a dense linear broadband array. *Geochem. Geophys. Geosyst.* 11:Q0AB03. doi: 10.1029/2009GC002637

Corti, G. (2009). Continental rift evolution: from rift initiation to incipient break-up in the Main Ethiopian Rift, East Africa. *Earth Sci. Rev.* 96, 1–53. doi: 10.1016/j.earscirev.2009.06.005

Corti, G., Molin, P., Sembroni, A., Bastow, I., and Keir, D. (2018). Control of Pre-rift lithospheric structure on the architecture and evolution of continental rifts: insights from the Main Ethiopian Rift, East Africa. *Tectonics* 37, 477–496. doi: 10.1002/2017TC004799

Corti, G., Sani, F., Florio, A., Greenfield, T., Keir, D., Erbello, A., et al. (2020). Tectonics of the Asela-Langano marin, Main Ethiopian Rift (East Africa). *Tectonics* 39:e2020TC006075. doi: 10.1029/2020TC006075

Craig, T., Jackson, A., Priestley, K., and McKenzie, D. (2011). Earthquake distribution patterns in Africa: their relationship to variations in lithospheric and geological structure, and their rheological implications. *Geophys. J. Int.* 185, 403–434. doi: 10.1111/j.1365-246X.2011.04950.x

Craig, T., and Jackson, J. (2021). Variations in the seismogenic thickness of East Africa. *J. Geophys. Res.* 126:e2020JB020754. doi: 10.1029/2020JB020754

Daly, E., Keir, D., Ebinger, C., Stuart, G. W., Bastow, I., and Ayele, A. (2008). Crustal tomographic imaging of a transitional continental rift: the Ethiopian rift. *Geophys. J. Int.* 172, 1033–1048. doi: 10.1111/j.1365-246X.2007.03682.x

Déverchere, J., Petit, C., Gileva, N., Radziminovitch, N., Melnikova, V., and Sankov, V. (2001). Depth distribution of earthquakes in the Baikal rift system and its

implications for the rheology of the lithosphere. *Geophys. J. Int.* 146, 714–730. doi: 10.1046/j.0956-540x.2001.1484.484.x

Dong, Y., Ni, S., Yuen, D., and Li, Z. (2018). Crustal rheology from focal depths in the North China Basin. *Earth Planet. Sci. Lett.* 497, 123–138. doi: 10.1016/j.epsl.2018.06.018

Ebinger, C., and Casey, M. (2001). Continental breakup in magmatic provinces: an Ethiopian example. *Geology* 29, 527–530. doi: 10.1130/0091-7613(2001)029<0527:CBIMPA>2.0.CO;2

Ebinger, C., and Hayward, N. (1996). Soft plates and hot spots: views from Afar. *J. Geophys. Res.* 101, 21859–21876.

Gallacher, R., Keir, D., Stuart, N. H. G., Leroy, S., Hammond, J., Kendall, J.-M., et al. (2016). The initiation of segmented buoyancy-driven melting during continental breakup. *Nat. Commun.* 7:13110. doi: 10.1038/ncomms13110

Greenfield, T., Keir, D., Kendall, J.-M., and Ayele, A. (2019). Seismicity of the Bora-Tullu Moye volcanic field, 2016-2017. *Geochem. Geophys. Geosyst.* 20, 548–570. doi: 10.1029/2018GC007648

Hauksson, E., and Meier, M. (2018). Applying depth distribution of seismicity to determine thermo-mechanical properties of the seismogenic crust in southern california: comparing lithotectonic blocks. *Pure Appl. Geophys*. 176, 1061–1081. doi: 10.1007/s00024-018-1981-z

Hawemann, F., Mancktelow, N., Pennacchioni, G., Wex, S., and Camacho, A. (2018). Weak and slow, strong and fast: how shear zones evolve in a dry continental crust (Musgrave Ranges, central Australia). *J. Geophys. Res.* 124, 219–240. doi: 10.31223/OSF.IO/58WA7

Hellebrekers, N., Niemeijer, A. R., Fagereng, Å., Manda, B., and Mvula, R. L. (2019). Lower crustal earthquakes in the East African Rift System: insights from frictional properties of rock samples from the Malawi rift. *Tectonophysics* 767:228167. doi: 10.1016/j.tecto.2019.228167

Hofstetter, R., and Beyth, M. (2003). The Afar Depression: interpretation of the 1960-2000 earthquakes. *Geophys. J. Int.* 155, 715–732. doi: 10.1046/j.1365-246X.2003.02080.x

Hunt, J., Zafu, A., Mather, T., Pyle, D., and Barry, P. (2017). Spatially variable CO_2 degassing in the Main Ethiopian Rift: implications for magma storage, volatile transport and rift related emissions. *Geochem. Geophys. Geosyst.* 18, 3714–3737. doi: 10.1002/2017GC006975

Iddon, F., and Edmonds, M. (2020). Volatile-rich magmas distributed through the upper crust in the Main Ethiopian Rift. *Geochem. Geophys. Geosyst.* 21:e2019GC008904. doi: 10.1029/2019GC008904

Ingebritsen, S., and Manning, C. (2010). Permeability of the continental crust: dynamic variations inferred from seismicity and metamorphism. *Geofluids* 10, 193–205. doi: 10.1002/9781444394900.ch13

Jackson, J. (2002). Faulting, flow and the strength of the continental lithosphere. *Int. Geol. Rev.* 44, 39–61. doi: 10.2747/0020-6814.44.1.39

Jamtveit, B., Petley-Ragan, A., Incel, S., Dunkel, K., Aupart, C., Austrheim, H., et al. (2019). The effects of earthquakes and fluids on the metamorphism of the lower continental crust. *J. Geophys. Res.* 124, 7725–7755. doi: 10.1029/2018JB016461

Jones, J., Stamps, D., Wauthier, C., Saria, E., and Biggs, J. (2019). Evidence for slip on a border fault triggered by magmatic processes in an immature continental rift. *Geochem. Geophys. Geosyst.* 20, 2515–2530. doi: 10.1029/2018GC008165

Keir, D., Bastow, I., Whaler, K., Daly, E., Cornwell, D., and Hautot, S. (2009). Lower crustal earthquakes near the Ethiopian Rift induced by magmatic processes. *Geochem. Geophys. Geosyst.* 10:Q0AB02. doi: 10.1029/2009GC002382

Keir, D., Ebinger, C., Stuart, G., Daly, E., and Ayele, A. (2006). Strain accommodation by magmatism and faulting as rifting proceeds to breakup: seismicity of the northern Ethiopian rift. *J. Geophys. Res.* 111:B05314. doi: 10.1029/2005JB003748

Keranen, K., Klemprer, S., Julia, J., Lawrence, J., and Nyblade, A. (2009). Low lower crustal velocity across Ethiopia: is the Main Ethiopian Rift a narrow rift in a hot craton? *Geochem. Geophys. Geosyst.* 10. doi: 10.1029/2008GC002293

Knappe, E., Bendick, R., Ebinger, C., Birhanu, Y., Lewi, E., Floyd, M., et al. (2020). Accommodation of east African Rifting across the Turkana depression. *J. Geophys. Res.* 125:e2019JB018469. doi: 10.1029/2019JB018469

Kogan, L., Fisseha, S., Bendick, R., Reilinger, R., McClusky, S., King, R., et al. (2012). Lithospheric strength and strain localization in continental extension from observations of the East African rift. *J. Geophys. Res.* 117. doi: 10.1029/2011JB008516

Lapins, S., Kendall, J.-M., Ayele, A., Wilks, M., Nowacki, A., and Cashman, K. (2020). Lower crustal seismicity on the Eastern Border faults of the Main Ethiopian Rift. *J. Geophys. Res.* 125:e2020JB020030. doi: 10.1029/2020JB020030

LaRosa, A., Keir, D., Doubre, C., Sani, F., Corti, G., Leroy, S., et al. (2021). Lower crustal earthquakes in the March 2018 sequence along the western Margin of Afar. *Geochem. Geophys. Geosyst.* 22:e2020GC009614. doi: 10.5194/egusphere-egu2020-3084

Lavayssiere, A., Drooff, C., Ebinger, C., Gallacher, R., Illsley-Kemp, F., Oliva, S., et al. (2019a). Depth extent and kinematics of faulting in the southern Tanganyika Rift, Africa. *Tectonics* 38, 842–862. doi: 10.1029/2018TC005379

Lavayssiere, A., Greenfield, T., Keir, D., Ayele, A., and kendall, J.-M. (2019b). Local seismicity near the actively deforming Corbetti volcano in the Main Ethiopian Rift. *J. Volcanol. Geotherm. Res.* 381, 227–237. doi: 10.1016/j.jvolgeores.2019.06.008

Lee, H., Muirhead, J., Fischer, T., Ebinger, C., Kattenhorn, S., Sharp, Z., et al. (2016). Massive and prolonged deep carbon emissions associated with continental rifting. *Nat. Geosci.* 9, 145–149. doi: 10.1038/ngeo2622

Lindenfeld, M., Rumpker, G., Link, G., Koehn, D., and Batte, A. (2012). Fluid-triggered earthquake swarms in the Rwenzori region, East African Rift-Evidence for rift initiation. *Tectonophysics* 566, 95–104. doi: 10.1016/j.tecto.2012.07.010

Lloyd, R., Biggs, J., Wilks, M., Nowacki, A., Kendall, J.-M., Ayele, A., et al. (2018). Evidence for cross rift structural controls on deformation and seismicity at a continental rift caldera. *Earth Planet. Sci. Lett.* 487, 190–200. doi: 10.1016/j.epsl.2018.01.037

Mackenzie, G., Thybo, H., and Maguire, P. (2005). Crustal velocity structure across the Main Ethiopian Rift: results from two-dimensional wide-angle seismic modeling. *Geophys. J. Int.* 162, 994–1006. doi: 10.1111/j.1365-246X.2005.02710.x

Maggi, A., Jackson, J., McKenzie, D., and Priestley, K. (2000). Earthquake focal depths, effective elastic thickness, and the strength of the continental lithosphere. *Geology* 28, 495–498. doi: 10.1130/0091-7613(2000)28<495:EFDEET>2.0.CO;2

Maguire, P., Keller, G., Klemperer, S., Mackenzie, G., Keranen, K., Harder, S., et al. (2006). "Crustal structure of the northern Main Ethiopian Rift from the EAGLE controlled-source survey; a snapshot of incipient lithospheric break-up," in *From Yirgu, G., Ebinger, C., and Maguire, P.K.H. (eds) The Afar volcanic province within the East African Rift System. Geological Society of London, Special Publications*, Vol. 259 (London), 269–291.

Mahatsente, R., Jentzsch, G., and Jahr, T. (1999). Crustal structure of the Main Ethiopian Rift from gravity data: 3-dimensional modeling. *Tectonophysics* 313, 363–382.

Martens, H. and White, R. (2013). Triggering of micro earthquakes in Iceland by volatiles released from a dyke intrusion. *Geophys. J. Int.* 194, 1738–1754. doi: 10.1093/gji/ggt184

Mazzarini, F., Keir, D., and Isola, I. (2013). Spatial relationship between earthquakes and volcanic vents in the central-northern Main Ethiopian Rift. *J. Volcanol. Geotherm. Res.* 262, 123–133. doi: 10.1016/j.jvolgeores.2013.05.007

Muirhead, J., Kattenhorn, S., Lee, H., Mana, S., Turrin, B., Fischer, T., et al. (2016). Evolution of upper crustal faulting assisted by magmatic volatile release during early-stage continental rift development in the East African Rift. *Geosphere* 12, 1670–1700. doi: 10.1130/GES01375.1

Muluneh, A., Brune, S., Illsley-Kemp, F., Corti, G., Keir, D., Glerum, A., et al. (2020). Mechanism for deep crustal seismicity: insight from modeling of deformation processes at the Main Ethiopian Rift. *Geochem. Geophys. Geosyst.* 21:e2020GC008935. doi: 10.1029/2020GC008935

Muluneh, A., Kidane, T., Corti, G., and Keir, D. (2018). Constraints on fault and crustal strength of the Main Ethiopian Rift from formal inversion of earthquake focal mechanism data. *Tectonophysics* 731–732, 172–180. doi: 10.1016/j.tecto.2018.03.010

O'Donnell, J., Selway, K., Nyblade, A., Brazier, R., and Tahir, N. E. (2016). Thick lithosphere, deep crustal earthquakes and no melt: a triple challenge to understanding extension in the western branch of the East African Rift. *Geophys. J. Int.* 204, 985–998. doi: 10.1093/gji/ggv492

Pasquale, V., Verdoya, M., and Chiozzi, P. (2014). *Geothermics - Heat Flow in the Lithosphere*. Heidelberg: Springer.

Passelégue, F., Brantut, N., and Mitchell, T. (2018). Fault reactivation by fluid injection: controls from stress state and injection rate. *Geophys. Res. Lett.* 45, 12837–12846. doi: 10.1029/2018GL080470

Pérez-Gussinyé, M., Metois, M., Fernandez, M., Verges, J., Fullea, J., and Lowry, A. (2009). Effective elastic thickness of Africa and its relationship to other proxies for lithospheric structure and surface tectonics. *Earth Planet. Sci. Lett.* 287, 152–167. doi: 10.1016/j.epsl.2009.08.004

Ranalli, G. (1997). Rheology and deep tectonics. *Ann. Geophys.* 40, 671–680.

Reston, T. (2020). On the rotation and frictional lock-up of normal faults: explaining the dip distribution of normal fault earthquakes and resolving the low-angle normal fault paradox. *Tectonophysics* 790:228550. doi: 10.1016/j.tecto.2020.228550

Reyners, M., Eberhart-Philips, D., and Stuart, G. (2007). The role of fluids in lower-crustal earthquakes near continental rifts. *Nature* 446, 1075–1078. doi: 10.1038/nature05743

Rooney, T., Furman, T., Yirgu, G., and Ayalew, D. (2005). Structure of the Ethiopian lithosphere: Xenolith evidence in the Main Ethiopian Rift. *Geochim. Cosmochim. Acta* 69, 3889–3910. doi: 10.1016/j.gca.2005.03.043

Scholz, C. (2002). *The Mechanics of Earthquakes and Faulting*. Cambridge: Cambridge University Press.

Shapiro, S., Audigane, P., and Royer, J. (1999). Large-scale *in situ* permeability tensor of rocks from induced microseismicity. *Geophys. J. Int.* 137, 207–213.

Sibson, R. (1974). Frictional constraints on thrust, wrench and normal faults. *Nature* 249, 542–544.

Sibson, R. (2000). Fluid involvement in normal faulting. *J. Geodyn.* 29, 469–499. doi: 10.1016/S0264-3707(99)00042-3

Sippel, J., Meeßen, C., Cacace, M., Mechie, J., Fishwick, S., Heine, C., et al. (2017). The Kenya rift revisited: insights into lithospheric strength through data-driven 3D gravity and thermal modeling. *Solid Earth* 8, 45–81. doi: 10.5194/se-8-45-2017

Smith, K., von Seggern, D., Blewitt, G., Preston, L., Anderson, J., Wernicke, B., et al. (2004). Evidence for deep magma injection beneath Lake Tahoe, Nevada-California. *Science* 305, 1277–1280. doi: 10.1126/science.1101304

Talwani, P., Chen, L., and Gahalaut, K. (2007). Seismogenic permeability, k_s. *J. Geophys. Res.* 112:B07309. doi: 10.1029/2006JB004665

Tefera, M., Chernet, T., and Haro, W. (1990). *Geological Map of Ethiopia. Scale 1:2,000,000.* Addis Ababa: Ethiopian Institute of Geological Survey.

Thatcher, W., and Pollitz, F. (2008). Temporal evolution of continental lithospheric strength in actively deforming regions. *GSA Today* 18, 55–62. doi: 10.1130/GSAT01804-5A.1

Tuffen, H., Smith, R., and Sammonds, P. (2008). Evidence for seismogenic fracture of silicic magma. *Nature* 453, 511–514. doi: 10.1038/nature06989

Turcotte, D., and Schubert, R. (2002). *Geodynamics*. Cambridge: Cambridge University Press.

Watts, A., and Burov, E. (2003). Lithospheric strength and its relationship to the elastic and seismogenic layer thickness. *Earth Planet. Sci. Lett.* 213, 113–131. doi: 10.1016/S0012-821X(03)00289-9

Weinstein, A., Oliva, S., Ebinger, C., Roecker, S., Tiberi, C., Aman, M., et al. (2017). Fault-magma interactions during early continental rifting: seismicity of the Magadi-Natron-Manyara basins, Africa. *Geochem. Geophys. Geosyst.* 18, 3662–3686. doi: 10.1002/2017GC007027

Wessel, P., and Smith, W. (1998). New, improved version of the generic mapping tools released. *EOS* 79, 579. doi: 10.1029/98EO00426

Whaler, K., and Hautot, S. (2006). "The electrical resistivity structure of the crust beneath the northern Main Ethiopian rift," in *From Yirgu, G., Ebinger, C., and Maguire, P.K.H. (eds) The Afar volcanic province within the African Rift System. Geological Society of London, Special Publications*, Vol 259 (London), 293–305.

Wilks, M., Kendall, J.-M., Nowacki, A., Biggs, J., Wookey, J., Birhanu, Y., et al. (2017). Seismicity associated with magmatism, faulting and hydrothermal circulation at Aluto Volcano, Main Ethiopian Rift. *J. Volcanol. Geotherm. Res.* 340, 52–67. doi: 10.1016/j.jvolgeores.2017.04.003

Wolfenden, E., Ebinger, C., Yirgu, G., Deino, A., and Ayalew, D. (2004). Evolution of the northern Main Ethiopian Rift: birth of a triple junction. *Earth Planet. Sci. Lett.* 224, 213–228. doi: 10.1016/j.epsl.2004.04.022

Conflict of Interest: The authors declare that the research was conducted in the absence of any commercial or financial relationships that could be construed as a potential conflict of interest.

Copyright © 2021 Muluneh, Keir and Corti. This is an open-access article distributed under the terms of the Creative Commons Attribution License (CC BY). The use, distribution or reproduction in other forums is permitted, provided the original author(s) and the copyright owner(s) are credited and that the original publication in this journal is cited, in accordance with accepted academic practice. No use, distribution or reproduction is permitted which does not comply with these terms.

frontiers in Earth Science

ORIGINAL RESEARCH
published: 04 May 2021
doi: 10.3389/feart.2021.619587

Imaging the Subsurface Structure of Mount Agung in Bali (Indonesia) Using Volcano-Tectonic (VT) Earthquake Tomography

Ardianto Ardianto[1], Andri Dian Nugraha[2,3], Haunan Afif[4], Devy Kamil Syahbana[4], David P. Sahara[2], Zulfakriza Zulfakriza[2,3], Sri Widiyantoro[2,5], Awali Priyono[2], Shindy Rosalia[2], Asep Saepuloh[6,7], Kasbani Kasbani[4], Faiz Muttaqy[1], Puput P. Rahsetyo[1], Imam C. Priambodo[1,4] and Martanto Martanto[1,4]*

[1] Geophysical Engineering Department, Faculty of Mining and Petroleum Engineering, Institut Teknologi Bandung, Bandung, Indonesia, [2] Global Geophysics Research Group, Faculty of Mining and Petroleum Engineering, Institut Teknologi Bandung, Bandung, Indonesia, [3] Center for Earthquake Science and Technology, Research Center for Disaster Mitigation, Institut Teknologi Bandung, Bandung, Indonesia, [4] Center for Volcanology and Geological Hazards Mitigation, Geological Agency, Ministry of Energy and Mineral Resources, Bandung, Indonesia, [5] Faculty of Engineering, Maranatha Christian University, Bandung, Indonesia, [6] Center for Remote Sensing, Institut Teknologi Bandung, Bandung, Indonesia, [7] Geology Engineering Study Program, Faculty of Earth Sciences and Technology, Institut Teknologi Bandung, Bandung, Indonesia

OPEN ACCESS

Edited by:
Derek Keir,
University of Southampton,
United Kingdom

Reviewed by:
Michele Paulatto,
Imperial College London,
United Kingdom
Fabien Albino,
University of Bristol, United Kingdom

***Correspondence:**
Andri Dian Nugraha
nugraha@gf.itb.ac.id

Specialty section:
This article was submitted to Volcanology, a section of the journal Frontiers in Earth Science

Received: *20 October 2020*
Accepted: *06 April 2021*
Published: *04 May 2021*

Citation:
Ardianto A, Nugraha AD, Afif H, Syahbana DK, Sahara DP, Zulfakriza Z, Widiyantoro S, Priyono A, Rosalia S, Saepuloh A, Kasbani K, Muttaqy F, Rahsetyo PP, Priambodo IC and Martanto M (2021) Imaging the Subsurface Structure of Mount Agung in Bali (Indonesia) Using Volcano-Tectonic (VT) Earthquake Tomography. Front. Earth Sci. 9:619587. doi: 10.3389/feart.2021.619587

Local seismic tomography is a well-known and commonly used method for obtaining detailed information about the internal structure of volcanoes. The eruption of Mt. Agung in 2017 was a vital opportunity scientifically because it is the first eruption that had sufficient seismic observation networks to carry out local seismic tomography at this volcano. In this study, we investigate the subsurface structure of Mt. Agung in Bali, which is one of the highest risk volcanoes in Indonesia. We conducted travel-time tomography using P- and S-wave arrival times of volcano-tectonic (VT) events to determine the three-dimensional (3D) Vp, Vs, and Vp/Vs ratio structure beneath Mt. Agung. We used 1,926 VT events, with corresponding 9482-P and 8683-S wave arrival times recorded by eight seismic stations over an observation time spanning from October 18 to December 31, 2017. We obtain the hypocenter solution for VT events using the maximum likelihood estimation algorithm and use an optimum 1D velocity model as input for the Joint 3-D seismic tomographic inversion. Local earthquake tomography revealed five anomalous regions that are useful to describe the overall seismic activity around Mt. Agung. We interpret these anomalous regions qualitatively due to limited data resolution in this study. We have successfully localized a high Vp/Vs ratio (∼1.82), low Vs (−1.9%) and high Vp (+3.8%), within a low seismicity zone at depths between 2 and 5 km below the Mt. Agung summit, which may be related to a shallow magma reservoir. There is also an anomalous region between Mt. Agung and Batur with moderate to high Vp/Vs ratios (1.76–1.79) where most of the earthquakes recorded before the 2017 eruption originated. We interpret this anomaly to be related to the existence of sub-vertical dyke

complex at depths between 8 and 14 km. The results of our study provide new insights into the subsurface structure of the magma plumbing system beneath Mt. Agung, which can be used to improve the quality of determining the location of the hypocenter and source modeling for future eruption forecasting.

Keywords: seismic tomography, Mt. Agung, magma plumbing system, 3D seismic structure, volcano seismology

INTRODUCTION

Seismic delay time tomography is one of the most commonly used methods to provide detailed information about the internal structure of a volcano. Subsurface velocity structures can provide knowledge about geometry, location and dimensions of volcano's plumbing system, and can be used to improve the quality of hypocenter location and source modeling that are useful for eruption forecasting. Seismic tomography has been proven successful in providing images of the magmatic system beneath volcanoes in Indonesia, such as Mt. Merapi (Widiyantoro et al., 2018) and Mt. Sinabung (Nugraha et al., 2019). The 2017 Mt. Agung eruption was a vital opportunity scientifically because it was instrumentally recorded for the first time at this volcano. This event encourages more advanced studies of the subsurface magmatic system of Mt. Agung.

Mt. Agung in Bali island is one of the highest-risk volcanoes in Indonesia, given the dense population and the intense socio-economic activities around the volcano; moreover, the volcano is one of the most popular tourist destinations in Indonesia. In August 2017, Mt. Agung started to show a significant increase in volcanic activity indicated by the emergence of an earthquake swarm, thermal anomaly, and deformation that eventually followed by series of eruptions from November 21, 2017 to June 13, 2019. The overall crisis has triggered the evacuation of ∼140,000 people within an area of 9–12 km from the volcano's summit (Syahbana et al., 2019). Prior to the 2017 eruption, Mt. Agung experienced a VEI 5 eruption in 1963 that led to ∼1,700 casualties and considerable damage to buildings and infrastructures, mainly due to volcanic bombs, pyroclastic flows, and lahars (Zen and Hadikusumo, 1964). The 1963 eruption produced significant stratospheric aerosol clouds and affected global climate conditions (Rampino and Self, 1982). Consequently, this event was considered one of the most important volcanic eruptions in the twentieth century (Rampino and Self, 1984). Based on tephrostratigraphic analysis, Mt. Agung has, on average, one VEI $\geq$2–3 eruption per century with the possibility of about 25% of the eruptions having an equal or larger magnitude than the 1963 event (Fontijn et al., 2015). Therefore, studying this volcano's behavior is very important as a basis in the framework of volcanic disaster mitigation.

Mt. Agung is an active Sunda arc stratovolcano which was formed in the subduction zone where the Indo-Australian plate subducts below the Sunda block (**Figure 1A**). The edifice of Mt. Agung consists of an almost symmetrical cone, aligned along a NW-SE direction with the nearby Abang and Batur-Pawon volcanoes (PVMBG, 2014). Mt. Agung's composition range is limited to basaltic andesite, and occasionally andesite, e.g., the 1963 lava flow and the 1843 eruption, and there is no evidence for large Plinian-style fall or ignimbrite deposits (Fontijn et al., 2015). In contrast Mt. Batur has a broader compositional range from basalt to rhyolite, over time the composition of erupted rocks becomes more mafic (Sutawidjaja, 2009). Mt. Batur has several dacitic ignimbrite deposits as markers of the formation of Batur Caldera. The volcanic activities of Mt. Agung and Mt. Batur were correlated a number of times, such as in the eruptions in 1821 and 1963 (PVMBG, 2014). This temporal correlation and occurrence of an earthquake swarm between Mt. Agung and Mt. Batur before the 2017 eruption raises the possibility of a subsurface connection between these two volcanoes. However, currently there is no concrete evidence regarding the connectivity of the magma chamber between Mt. Agung and Mt. Batur. Furthermore, the lavas from the two volcanoes have different compositions (Geiger et al., 2018), and fumarolic activity prior to the 2017 eruption was limited to the Mt. Agung crater (Syahbana et al., 2019).

Several studies have been conducted to infer the structure of the volcanic features. A petrological analysis using mineral-melt thermobarometry data of the 1963 lava flows shows the existence of two major magma storage regions: the first region is located around the Moho depth at about 18–22 km, and the second one is in the shallower region at about 3–7 km depth (Geiger et al., 2018). The most recent study of the ambient seismic noise tomography around the areas also shows a low-velocity anomaly zone between Mt. Agung and Mt. Batur at a depth of about 2 km below the surface (Zulfakriza et al., 2020). The authors interpreted the low-velocity zone as volcanic deposits from past eruptions in the topographic saddle between Mt. Batur and Mt. Agung and the presence of over-pressurized hydrothermal fluids where seismicity may be induced at shallow depths. Unfortunately, these studies were limited to the shallower structures; thus, there is still little information about this volcano's magma plumbing system.

Syahbana et al. (2019) proposed two conceptual models of Mt. Agung, using multi-disciplinary approaches, including seismicity, deformation, geochemistry, and remote sensing analysis. The authors explained that the first model was initially used during the beginning of the crisis; they speculated that the magma rising beneath the Agung volcano led to over-pressurization of groundwater; the stress then activated a pre-stressed fault causing VT earthquakes between Mt. Agung and the Batur Caldera. The fault geometry was deduced based on the focal mechanism of the existing earthquake swarm. However, the authors found that this model was not consistent with the newly acquired InSAR Sentinel-1 data (i.e., Albino et al., 2019). Therefore, they preferred the second model based on the intrusion of a dyke at ∼10 km depth northwest of Mt. Agung.

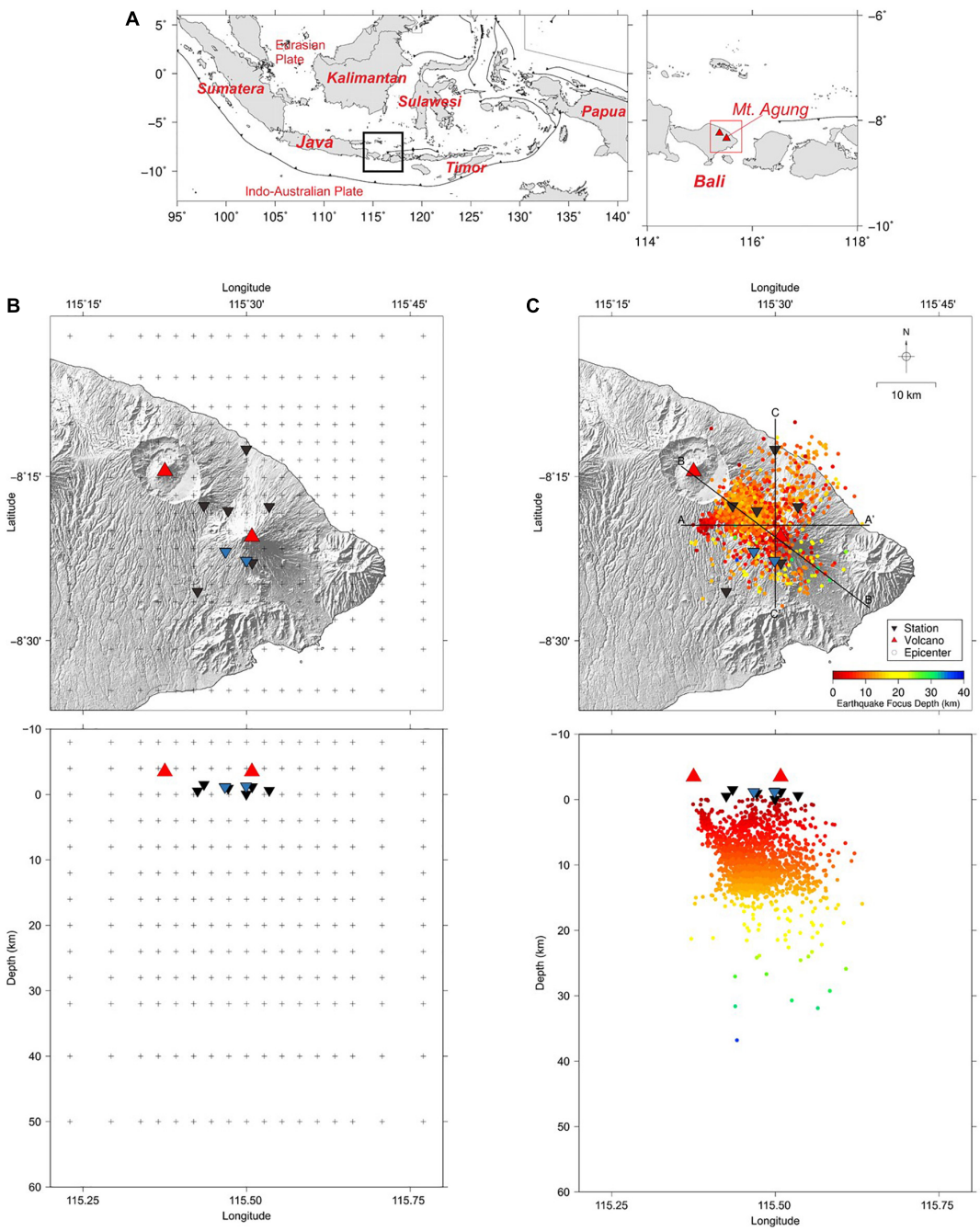

FIGURE 1 | (A) Map of Indonesia: jagged black lines denote the subduction trench; the black square denotes the local area of Bali (right); the red square in the inset map defines the study area. **(B)** Map of the study area. The red triangles represents the summits of Mt. Agung and Mt. Batur; blue and black inverted triangles show the distribution of the one and three component seismic stations used in this study; exact locations of the seismic stations are provided in **Supplementary Table 1**. The grid node location used for tomographic inversion is denoted by black plus symbols. **(C)** Epicenter and hypocenter distributions of 1, 926 VT events used in this study are shown as colored dots; color indicates the event focal depth. The hypocenters are projected along longitude (below) to show focus depth distribution. Three labeled black lines: A-A' (east to west), B-B' (southwest to northeast), and C-C' (north to south) depict the locations of the vertical cross-sections through Mt. Agung; these sections are used for plotting the synthetic resolution test results (**Figure 2**) and the seismic velocity structures (**Figures 3**, **4**).

This dyke intrusion model would further imply that pre-eruptive seismicity was due to magma intrusion. However, pressurization of groundwater or magmatic fluids in the region above the inferred dyke could have played a role in triggering earthquakes. The intrusion of the dyke was responsible for the observed inflation and the swarm of VT earthquakes. These conceptual models provide an opportunity for more detailed subsurface investigations for validation.

In developing the previous conceptual models, the authors have used the data from the Center for Volcanology and Geological Hazard Mitigation (CVGHM) of Indonesia and the regional station network of the Indonesian Meteorology, Climatology, and Geophysics Agency (BMKG). The seismicity analysis used local observation networks. In this paper, we mainly employed seismic tomography to provide more detailed information on subsurface structures and refine the aforementioned conceptual models.

DATA AND METHOD

Data

The data used throughout this paper were obtained from eight seismic stations installed around Mt. Agung by the CVGHM (**Figure 1B**). Initially, there were only 2 vertical (1-C) short-period seismometers (TMKS and PSAG) to monitor seismic activity on Mt. Agung. In response to increased seismic activity, 6 three components (3-C) broadband seismometers (ABNG, CEGI, REND, YHKR, BATU, and DUKU) were deployed and the installation was completed on 18 October 2017. All stations record seismic data continuously with sample rates of 100 and 50 samples per second. We analyzed seismic data from 18 October to 31 December 2017, where the station network was sufficiently large. This timeframe includes the period before, during, and after the Mt. Agung eruption, which occurred on November 21, 2017. Syahbana et al. (2019) show that the seismic activity increased rapidly in mid-September 2017 and then started to decrease significantly on 20 October. Our data captured the end of the seismic crisis. The spatiotemporal distributions of the earthquake hypocenter we used (**Supplementary Figure 1**) showed an earthquake swarm at a shallow depth between Mt. Agung and Batur, and then the seismicity cluster moved toward Mt. Agung. After the eruption, the number of recorded VT earthquakes decreased and the distribution of the hypocenter location became more diffuse than before the eruption.

Data processing begins with event identification; we used the Filter Picker algorithm from Lomax et al. (2012) for automatic event detection. The minimum signal to noise ratio (SNR) value for the signal categorized as an event is 1.5 in all detecting stations. Additionally, at least two other stations are required to have identified the signal as an event within 10 s of the detection time from one of the stations. This criteria effectively reduces false positives, which may occur due to random noise. We have successfully used this algorithm for identifying the aftershocks of the 2018 Lombok earthquakes (Sasmi et al., 2020).

Afterward, the waveform traces were manually picked using Seisgram2K software (Lomax and Michelini, 2009) to determine the P- and S-wave first arrival times of each identified event. Only local volcano-tectonic (VT) earthquake arrival times that were successfully determined by at least three stations were used in the next stage. In total, 4,618 VT events were identified using automatic event detection. The events' selection and arrival times picking resulted in 3,948 VT events with 18,741 P- and 17,237 S-phases, respectively. Our results show that most of the VT events occurred in October 2017 and diminished as the date of the initial eruption drew nearer; this result is in accordance with that described by Syahbana et al. (2019).

Determination of VT Events Hypocenter

We used the Non-LinLoc program (Lomax et al., 2000), a non-linear inversion method to determine the hypocenter's location and its origin time. The program uses the octree approach, namely, recursive sampling and division of cells in 3D space based on the maximum posterior density function (pdf) in the center of the cell being evaluated. The optimum solution for the hypocenter location and origin time is obtained based on the maximum likelihood or the minimum misfit. The Non-LinLoc hypocenter solution's quality is evaluated using the RMS error value and the largest principal axis value of 68% confidence ellipsoid, which was obtained by conducting singular value decomposition (SVD) of the matrix covariance.

The initial hypocenter solution and its origin time were obtained using the 1D seismic velocity model of Central Java (Koulakov et al., 2009) to generate the travel time calculated; this model was used because there is no local seismic velocity model available in this area. The 1D velocity model was then updated using the VELEST program (Kissling et al., 1994) to obtain the optimum local 1D velocity model. The seismicity catalog used for inversion tomography was obtained after inverting the data using Non-LinLoc by utilizing the optimum 1D velocity model. Further details regarding the hypocenter location's determination and the final catalog can be seen in Sahara et al. (2020), along with this publication.

Tomographic Inversion

We used the 3-D inversion program SIMULPS12 (Evans et al., 1994) to invert the 3-D velocity structure and relocate the hypocenter solution. This program applied an iterative, damped least-squares algorithm to simultaneously update the hypocenter solution and 3-D Vp and Vp/Vs structure. The Vp/Vs structure was updated using S-P times directly; this approach is considered to be more robust than computing Vp/Vs by Vp and Vs division (Eberhart-Phillips, 1986). The synthetic travel times for P- and S-waves were solved using a pseudo-bending technique through an updated 3D velocity model (Um and Thurber, 1987; **Supplementary Figure 2**).

Prior to the stated processes, we selected events from the seismic catalog based on the following criteria: hypocenter spatial uncertainty of less than 5 km, an azimuthal gap of less than 300°, and the number of recorded P and S phase pairs at more than three stations. After the quality control process, there were a total of 1,926 VT events, corresponding to 9,482 and 8,683 P- and S-wave arrival times, respectively. Although this selection process significantly reduced the number of used events, it yields well-constrained hypocenters to stabilize inversion results. The hypocenter distribution used as input can be seen in **Figure 1C**. Most of the VT events were located inside the seismic network between Mt. Agung and Mt. Batur. The VT event's focus depth is shallower than 30 km, with the highest density of VT events located at a depth range of 5–15 km on the northwest side of Mt. Agung.

Appropriate grid parameters were obtained by considering the recovery of checkerboard resolution tests (CRT) for a wide variety of grid sizes. Due to the inverse problem's mix-determined nature, damping was imposed to produce a stable solution for each tested grid parameter. Optimum values for Vp and Vp/Vs initial damping parameters were derived by comparing data variance (misfit) with model variance for a series of one-step inversions with a variation of damping values forming an L-curve or trade-off curve (Eberhart-Phillips, 1986), and we allow the SIMULPS program to automatically update the damping values for succeeding iterations. CRT was performed using these damping parameters for each tested grid parameter. In order to evaluate the synthetic resolution test results more appropriately, we add Gaussian noise with a mean of 0 and a standard deviation of 0.2 s to the synthetic data. The grid parameters that provided the best recovery for this data set were a grid node size of 3 × 3 km horizontally and 4 km for vertical parameterization (**Figure 1B**). The appropriate station, Vp, and Vp/Vs damping values for this configuration are 10, 50, and 40, respectively (**Supplementary Figure 3**).

The tomographic inversion was first performed to obtain a 3-D Vp model using the optimum 1-D velocity in determining the hypocenter solution as the initial velocity model (**Supplementary Figure 4**). We used an initial Vp/Vs value of 1.70 as constant, estimated from a Wadati diagram of the data recorded on our local network (Sahara et al., 2020). We compared the results of the two tomographic inversion workflows. The first method starts with generating a detailed Vp model and then proceeds to a simultaneous inversion for both Vp and Vp/Vs. When inverting the 3-D Vp model, the S-wave travel time was used to constrain the hypocenter location, but the Vp/Vs value was kept constant. The 3-D Vp model was used as the initial model for the Vp/Vs inversion. This second inversion process allows for updating both 3-D Vp and Vp/Vs. The second method is to directly invert Vp and Vp/Vs simultaneously from the initial 1D velocity model. Both inversion processes use the same grid and damping parameters, as obtained in the preliminary steps.

Then we evaluate the effect of the inversion grid by comparing the inversion results of the grid parameters that have been shifted from their initial position. We shift the grid 1 km upward, eastward, and northward. For the initial grid velocity model that is shifted eastward and northward, it remains the same as the initial grid, because the initial model used is 1D, but in the upward direction it is necessary to make adjustments by doing linear interpolation. If the grid spacing is close to the true resolution capability and the damping is properly chosen, then the inversion result of the shifted grid should give comparable results.

Resolution Testing

To investigate the robustness of our new 3-D seismic velocity model, the inversion result was tested using mathematical parameters and a synthetic model. The mathematical parameters used are: ray hit count (RHC), derivative weight sum (DWS) (Toomey and Foulger, 1989), and diagonal resolution elements (DRE) (Menke, 1989), while checkerboard resolution tests (CRT) were used for synthetic tests. The synthetic test was first performed by making a synthetic velocity model, an alternating positive and negative perturbation (±10%) of the optimum 1D velocity model. We added Gaussian noise with a mean of 0 and a standard deviation of 0.2 s to the synthetic data. Then the inversion was carried out using the same procedure, parameters, and grid spacing as used in the inversion of real observation data. The well-resolved regions are indicated by the excellent recovery of synthetic velocity anomaly patterns in CRT and high RHC, DWS, and DRE values. In general, this method is useful for detecting regions that lack resolution but provides limited information regarding the real model recovery (Lévěque et al., 1993; Rawlinson and Spakman, 2016).

RESULTS

First, we compare the results of the two inversion workflows. The resulting total weighted RMS, final P- and S-P data variance from the first method (first invert 3D Vp with constant Vp/Vs, then do simultaneous inversion of Vp, Vp/Vs, and hypocenter from the initial 3D Vp velocity model) is 0.09030 s, 0.00773 s^2, and 0.00860 s^2, respectively. Whereas the second method (simultaneous inversion of Vp, Vp/Vs, and hypocenter from the 1D velocity model) is 0.09057 s, 0.00788 s^2, and 0.00855 s^2. Comparison of the final travel time residuals for P- and S-waves of the two methods is plotted as histograms in **Supplementary Figure 5** and seismic velocity structure in vertical cross-sections (A-A', B-B', C-C') in **Supplementary Figures 6–10**. It can be observed that the first method can give better results in terms of misfit compared to the second method. The Vp and Vp/Vs results of the two methods appear comparable, but Vs produces a slightly different pattern. However, in the first method, it can be seen that the result of the velocity structure Vs is very similar to the Vp. This may be due to the inversion scheme. Because the Vp value is optimum and the program inverts the Vp/Vs value instead of Vs, so the Vs value will only be slightly updated. These two factors cause the anomaly pattern of Vs to have a tendency to follow the anomaly pattern of Vp, while the second method does not have such a tendency. We, therefore, decided to use the second method even though first method has a smaller misfit.

The RHC, DWS, and DRE values for horizontal and vertical cross-sections are presented in **Supplementary Figures 11–18**. The CRT results for horizontal slices and vertical cross-sections are presented in **Supplementary Figures 19–23** and **Figure 2**. Reconstruction of the synthetic test results shows reasonably good recovery for depths from 0 to 8 km but lower resolution for the deeper layer (**Supplementary Figures 19–23**); this is similar to regions with relatively high DRE, DWS, and RHC values. A fair resolution was achieved in the area between Mt. Agung and Batur (northwest of Mt. Agung). The eastern region of Mt. Agung lacks resolution because most of the events and the stations are in the western part of the volcano. The results of the inversion of the velocity model obtained have sufficient resolution, this is indicated by the similarity of the Vp, Vs, and Vp/Vs patterns between the initial grid parameters and those that have been shifted upward, eastward, and northward (**Supplementary Figures 24–26**).

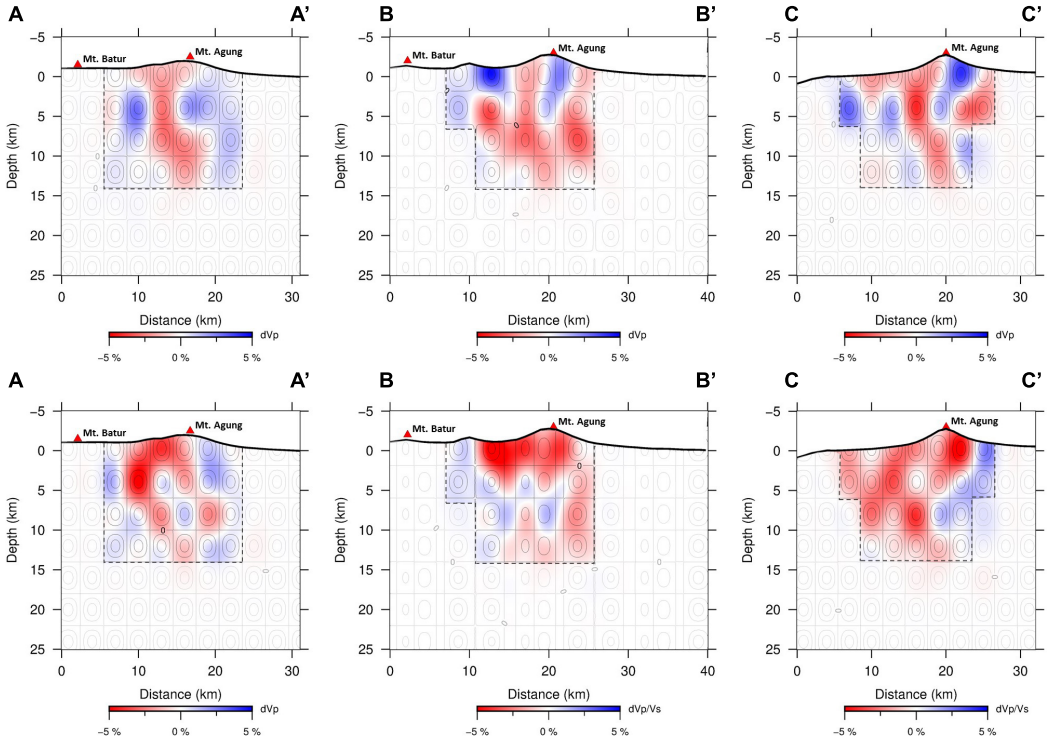

FIGURE 2 | Vertical cross-sections of recovered Vp checkerboard resolution tests (CRT) model (top row), and recovered Vp/Vs CRT model (bottom row). The thin black line is the contour of the initial CRT model for Vp and Vp/Vs with interval of 4. Dashed black lines define the area which has a good resolution. Blue and red colors respectively represent high and low seismic velocity anomaly values, according to the scale at the bottom of each row. The vertical cross-section is taken at **(A-A')** (first column), **(B-B')** (second column), **(C-C')** (third column), the spatial location of each cross-section, as seen in **Figure 1C**.

Our tomographic inversion procedure produced a 3-D velocity model and relocated the VT events, which led to a total weighted RMS reduction from 0.125 to 0.09057 s. The initial P- and S-P data variance associated with the initial model is 0.01588 and 0.01522 s^2. The P- and S-P data variances for the final model are 0.00788 and 0.00855 s^2, respectively. This inversion procedure allowed to simultaneously update the velocity model and hypocenter solution resulting in a reduction of the total RMS to 27.5%, with a 90% value of travel time between 1.65 and 4 s, so the average percentage of data misfit estimates from source to receiver ranges from 2.5 to 5.5%. We visualize the final 3-D Vp, Vs, and Vp/Vs ratio model along with the CRT results as a series of horizontal slice sections in **Supplementary Figures 19–23**. We also show three vertical cross-sections (A-A', B-B', C-C') for CRT results, 3-D velocity models, and 3-D absolute velocity in **Figures 2–4**, respectively. In these figures, the Vp and Vs are plotted as percent perturbations relative to the 1-D initial velocity model, while Vp/Vs are plotted as absolute values.

There are three relocated VT event clusters visible in vertical cross-sections (**Figures 3**, **4**). The first cluster is a swarm earthquake with a depth of 5–15 km below sea level between Mt. Agung and Mt. Batur, shown in vertical cross-sections of A-A', and B-B'. The second cluster is located below the summit of Mt. Agung at depths of about 1–5 km below sea level; this cluster appears in three vertical cross-sections. The third cluster is located west of Mt. Agung at depths of about 1–5 km below sea level, trending southwest to northeast as identified in the A-A' slice but less visible in the B-B' cross-section. The fact that the third cluster is only clearly visible in cross-section A-A' shows this only appears in a limited area. Based on these relocated hypocenters and 3-D velocity structure results, we identified five anomalous regions (marked as R1–R5 in **Figures 3**, **4**).

1. Region 1 (R1) is identified in cross-section A-A', B-B', and C-C'; this region is located right below the summit of Mt. Agung at depths between −2 and 2 km relative to sea level or ∼1 to 5 km relative to the summit of the volcano and has high Vp (+3.8%), low Vs (−1.9%), and high Vp/Vs (1.82) with low seismicity.
2. Region 2 (R2) is located around 10 km west of the Mt. Agung (section C-C') with depths of 0–4 km below sea level; this region is characterized by low Vp (−16%) and Vs (−8.5%), and low Vp/Vs (1.55) with high seismicity.
3. Region 3 (R3) is located slightly northwest of Mt. Agung (section A-A' and B-B') at depths between 6 and 10 km below sea level; this region is characterized by low Vp (−8.1%), low Vs (−4.2%), and low Vp/Vs (1.63) with high seismicity.
4. Region 4 (R4) is located beneath the summit of Mt. Agung at a depth 6–10 km below sea level; it is identified in cross-sections A-A', B-B', and C-C' as low Vp (−4.5%), low Vs (−8.1%), and moderate to high Vp/Vs (1.77) with low

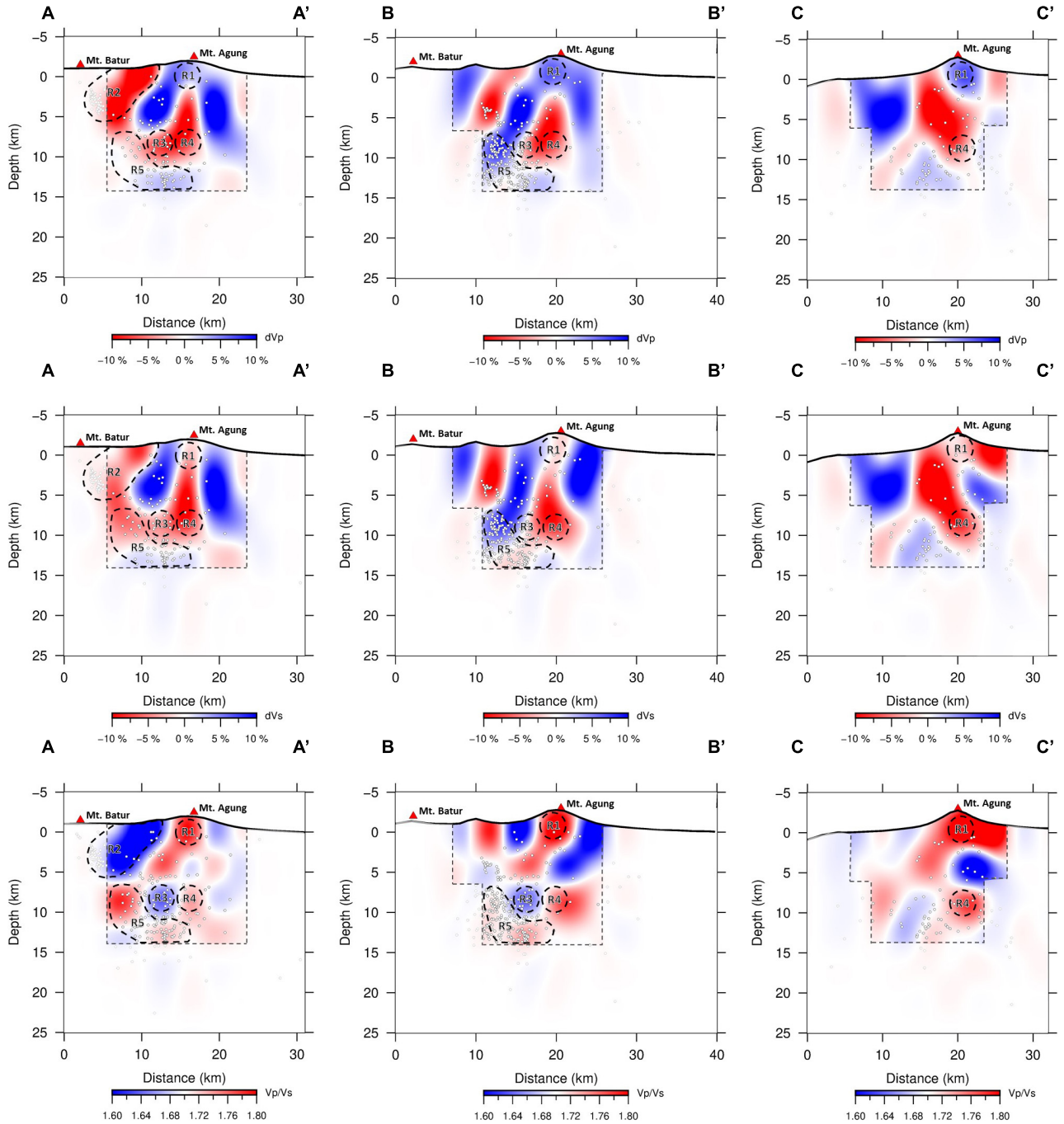

FIGURE 3 | The vertical cross-sections of the Vp, Vs, and Vp/Vs models from top to bottom, respectively; for slice **(A-A')** (first column), **(B-B')** (second column), **(C-C')** (third column), the spatial location of each cross-section can be seen in **Figure 1C**. Blue and red colors respectively represent high and low seismic velocity anomaly values and inverted for Vp/Vs, according to the scale at the bottom of each column. Vp and Vs are plotted as percent perturbations relative to the 1-D optimum initial velocity model, and Vp/Vs are plotted as absolute values. The white dot represents the hypocenter's projection to the vertical cross-section; only events with depths less than 0.5 km from the centerline are plotted here. Dashed black lines define the area which has a good resolution based on resolution test results. Labeled regions (R1–R5) depicted by these figures are discussed in the text.

seismicity. High Vp/Vs indicates that Vs' value is reduced more than the Vp anomaly value in this area.

5. Region 5 (R5) is co-located with a large cluster of VT events 6 km northwest of Mt. Agung at depths between 8 and 14 km below sea level (sections A-A' and B-B'). This region is imaged as a sub-vertical structure characterized by a transition from low to high Vp and Vs, moderate to high Vp/Vs (1.76–1.79), and very high seismicity.

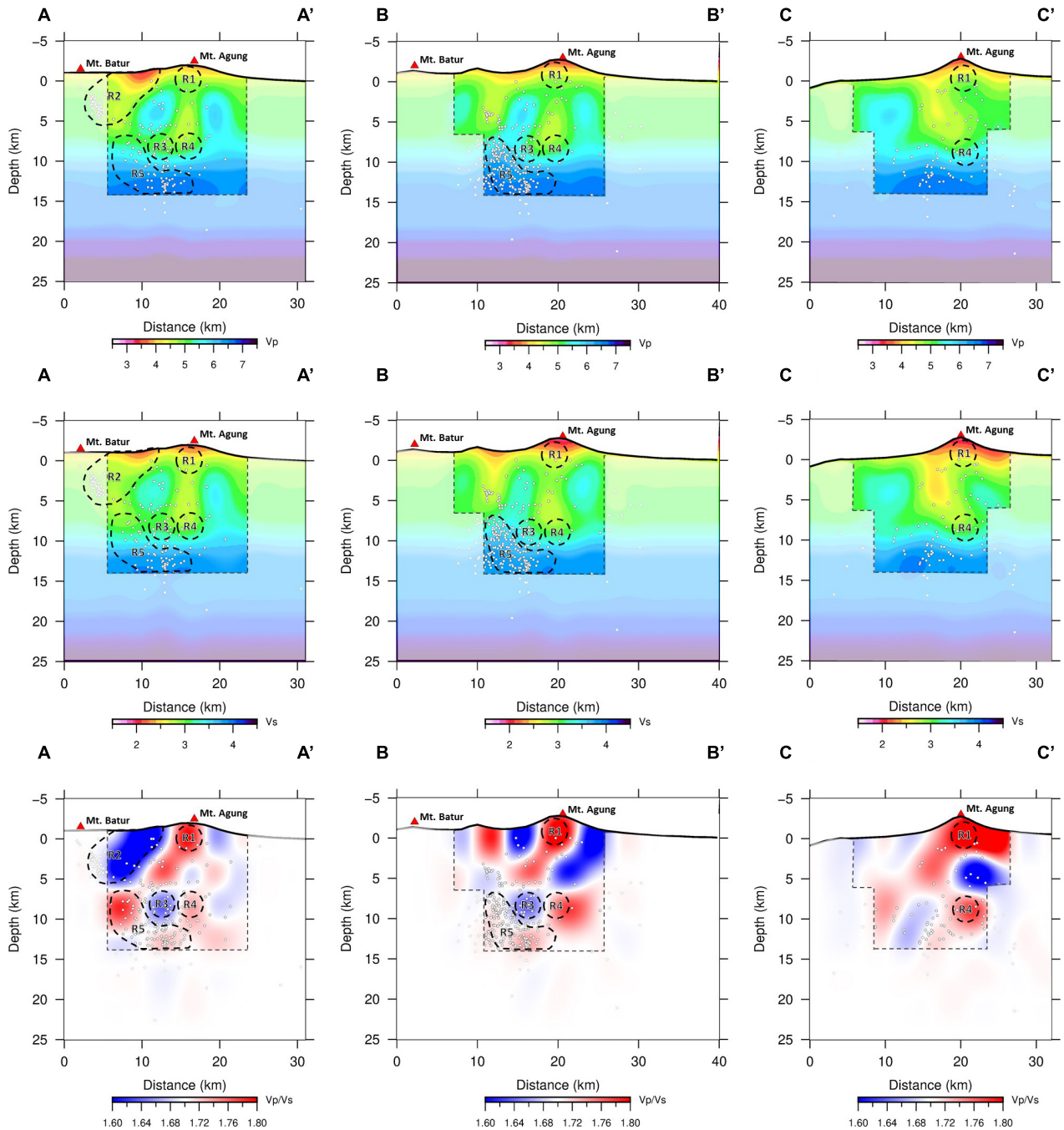

FIGURE 4 | The vertical cross-sections of the Vp, Vs, and Vp/Vs models from top to bottom, respectively; for slice **(A-A')** (first column), **(B-B')** (second column), **(C-C')** (third column), the spatial location of each cross-section can be seen in **Figure 1C**. Vp, Vs and Vp/Vs are plotted as absolute values. The white dot represents the hypocenter's projection to the vertical cross-section; only events with depths less than 0.5 km from the centerline are plotted here. Dashed black lines define the area which has a good resolution based on resolution test results. Labeled regions (R1–R5) depicted by these figures are discussed in the text.

DISCUSSION

We qualitatively interpret our results using known relationships between seismic velocity and rock physics parameters. A quantitative analysis of volcanic tomography data (such as temperature determination or fractions of partial melt) has two sources of uncertainty; namely, the inaccuracy of the amplitude determination of the anomalous seismic velocity due to limited resolution and an imperfect understanding of the relationship between physical parameters and seismic velocity (Hammond and Humphreys, 2000). Besides, there are many physical rock parameters such as pressure, temperature, rock

composition, porosity, fluid content, saturation, and crack density, which can affect the Vp, Vs values and Vp/Vs ratios (Nur and Simmons, 1969; Toksoz et al., 1976; Moos and Zoback, 1983; Hammond and Humphreys, 2000; Takei, 2002; Lees, 2007). Therefore, if we want to make a quantitative analysis of rock physic parameters using seismic tomograms, this problem will be highly underdetermined. We also acknowledge that our seismic observation network is less than ideal due to the lack of ray path coverage in the eastern part of Mt. Agung, limiting the resolution beneath the volcano. Because most of the VT events are located within the station's coverage the data set is sufficient to produce a subsurface velocity structure that can be interpreted qualitatively.

Considering the limitations mentioned earlier, we interpret the five anomalous regions labeled in **Figure 3** as follows. The first region (R1) has low seismicity, high Vp (+3.8%), low Vs (−1.9%), and is characterized by a high Vp/Vs value, reaching 1.82 at that location. We interpret this region as a shallow magma reservoir confined by consolidated, older volcanic intrusive rocks from previous large eruptions. Similar conditions are also observed at other stratovolcanoes, such as Mt. Etna (Laigle et al., 2000), Tungurahua volcano (Molina et al., 2005), and Sinabung volcano (Nugraha et al., 2019). The location of the high Vp/Vs anomaly (∼1.82) is at the sea level and the Vp/Vs value is significantly reduced to 1.7 at a depth of 4 km. Based on these significant changes in Vp/Vs value, we speculate that there may be shallow magma reservoirs at a depth of between −2 and 2 km relative to the sea level or about 1–5 km below the summit of the volcano.

There have been several studies regarding the presence of shallow magma reservoirs at Mt. Agung. Chaussard and Amelung (2012) conducted deformation analysis using ALOS InSAR time-series data from 2006 to 2009. Their results showed a clear uplift signal in a circular pattern inflating at rates of 3–8 cm/yr. Using inversion with the pressurized finite spheres approach in an elastic half-space, they estimated the existence of a pressure source at a depth of 4.4 km below the summit. But based on the results of a recent study for that data, Yip et al. (2019) show that the deformation signals previously reported at Agung are not the result of magmatic sources but correlate with atmospheric artifacts. Albino et al. (2019) after correcting the atmosphere and removing the deformation related to the dyke intrusion found a small concentric pattern of uplift remains at the summit of Agung. They interpret this inflation as pressurization of the hydrothermal system rather than magmatic source because the location of the source is very shallow and local. Despite the absence of evidence of sufficient surface deformation, the shallow magma chambers at Mt. Agung can still exist because it is probably not resolved by the data; this depends on the rate of accumulation and the depth of the source (Yip et al., 2019). The existence of shallow magma chambers is supported by the results of Geiger et al. (2018), based on mineral-melt equilibrium thermobarometry of lavas produced by the 1963 eruption, Their results show the existence of magma from an upper crustal chamber at 3–5 km depth.

Region 2 (R2) is located 10 km west of the Mt. Agung summit with high seismic activity and is just low Vp (−16%), Vs (−8.5%), and low Vp/Vs (1.55). This region is on the boundary of the area with resolution, so the interpretation of this seismic velocity anomaly should be performed carefully. However, considering this area is located in the lowlands west of Mt. Agung and that there is a continuation of low-velocity patterns at shallow depths between Mt. Agung and this area, we associate this low-velocity anomaly with the accumulation of volcanic deposits. Previous studies using ambient seismic noise tomography also describe the low Vs at depths up to 2 km at the topographic saddle between Mt. Agung and Mt. Batur (Zulfakriza et al., 2020). High seismicity in this area forms a separate cluster in a fairly limited area; it may be related to activated faults triggered by the over-pressurization of groundwater or gas exsolution from the magma intrusion beneath the volcano (Coulon et al., 2017; Syahbana et al., 2019).

Region 3 (R3) is located between 5 and 10 km below the summit characterized by low Vp (−8.1%), low Vs (−4.2%), and low Vp/Vs (1.63), and high seismic activity during the observation period. The anomaly may indicate that the rock mass has a high crack density that is dry or filled with supercritical fluid. The effect of supercritical fluid is similar to adding a small amount of gas: the reduction in Vp value will be much faster than that in the Vs, so that the Vp/Vs value will also decrease (Ponko and Sanders, 1994). Because of its location, which is close enough to a high-temperature heat source to cause evaporation of fluids and gas expansion, this can further reduce seismic velocity and become one of the factors that affect seismic activity in these fractured rocks. An increase in pore-pressure decreases the normal stress on the rock volume, which becomes more prone to slippage (Pearson, 1981). In their study, Bachmann et al. (2012) use data from the natural laboratory of the Basel-1 enhanced geothermal systems to explain the mechanism of pore-pressure changes that causes the presence of high b-value anomalies (increased probability of small earthquakes); similar mechanisms can also occur in volcanoes.

Region 4 (R4) is under the summit at a depth of 6–10 km; this area is next to Region 3. Similar to R3, this area has low Vp (−4.5%), low Vs (−8.1%), anomalies but moderate to high Vp/Vs (1.77) values, and low seismicity. Low Vp, low Vs, and high Vp/Vs anomalies are often found in active volcanic areas (Nakajima and Hasegawa, 2003; Lees, 2007; Ramdhan et al., 2019). These researchers agree that this anomaly provides evidence of melt or fluid accumulation. Therefore, we interpret that this region may be related to high crack density rock mass with high-temperature melts or increased fluid content saturation, compared to R3. Differentiation between high temperatures and fluid melts can be achieved with additional information, such as heat flow or earthquake occurrence (Sanders et al., 1995); therefore, we consider this area to be more affected by melts due to low seismicity.

Region 5 (R5) has low to high Vp and Vs, moderate to high Vp/Vs (1.77–1.79), which is similar to R1; however, this region has significantly high seismic activity. The results of earthquake relocation using a 3D velocity model, or using a 1D velocity model from the initial location, show that most of the recorded earthquakes are around the anomalous zone at a depth of 8–14 km. We interpret this as a dyke complex; the observed seismic swarm during the observation period was

related to the dyke intrusion. Albino et al. (2019) performed a non-linear inversion using InSAR deformation data to obtain the position and the volume change of the dyke and then viewed the temporal relationship with seismic activity. They conclude that the optimum location of the dyke is between Mt. Agung and Mt. Batur at a depth of ∼10 km below sea level. They also find a positive correlation between the rate of change in dyke volume and seismic activity. The compatibility of this anomaly location and the spatio-temporal relationship between seismicity and the dyke volume can further confirm that the second conceptual model proposed by Syahbana et al. (2019) is the most appropriate for describing the subsurface structures of Mt. Agung.

The high temperature melts described as high Vp values in R1 and R5 seem quite puzzling. However, this type of anomalies is frequently found in seismic tomography results carried out at active stratovolcanoes around the world and often interpreted as new magma penetrated through older intrusives rock (Lees, 2007). In our study, most stations are located in the low-velocity zone (Zulfakriza et al., 2020); therefore, the 1D optimum velocity model produced by VELEST for shallow depths is low. As a result, the anomaly below the top of the mountain is described as high velocity. This argument is acceptable to explain R1 but not R5. Perhaps using a denser seismic network and a 3D initial velocity model, or a graded inversion scheme (inversing using a finer and finer grid) could produce appropriate anomalies in these regions. De Natale et al. (2004) analyzed the Somma-Vesuvius volcano using local earthquake data and dense artificial sources as well as a 3D initial velocity model. Their results show these anomalous features (high Vp, high Vp/Vs, and high seismicity) as found by previous studies, but with detailed petrological analysis they interpreted this as a region of quenched magma.

Based on our hypocenter relocation and 3D Vp, Vs, and Vp/Vs model, and the results of previous studies, we summarize our interpretation using a schematic model, as shown in **Figure 5**. First, magma rose from deep magma storage up to a depth of about 14 km from the mean sea level below R3. This first phase occurred between mid-May and late August 2017; sufficient seismicity has been detected to confirm this, but no significant surface deformation has been observed; this may be because the source is still very deep. The magma then migrated to Region 4 with a flow rate lower than the inflow from the deep magma reservoir, accounting for the accumulation of high melt temperature under R3. An increase in temperature or magma devolatilization in this area caused an increase in pressure distributed to the surrounding area, which explains the triggered VT events in R2 and R3. Then the dyke penetrated upward toward the west-northwest of Mt. Agung (R5) and its size continued to increase, although at a decreasing rate; this may have been due to an increased flow rate from Region 4 to Region 1 or reduced inflow from the deep magma reservoir. Then, between November 8 and November 20, 2017 (1 day before the first eruption), a significant reduction in intrusion dyke volume took place, which is interpreted as magma withdrawal into a shallow reservoir.

Based on our ray coverage, getting a more accurate picture of the subsurface beneath Mt. Agung would need to add seismic stations on the east side. If we aim at defining the shallow magma reservoir geometry we would have to rearrange or add observation stations, so that the spacing between stations reaches the same order as the minimum size of the target anomalies. Then the resolved depth of the local tomography would not be larger than the maximum depths of sources, so that the seismic station

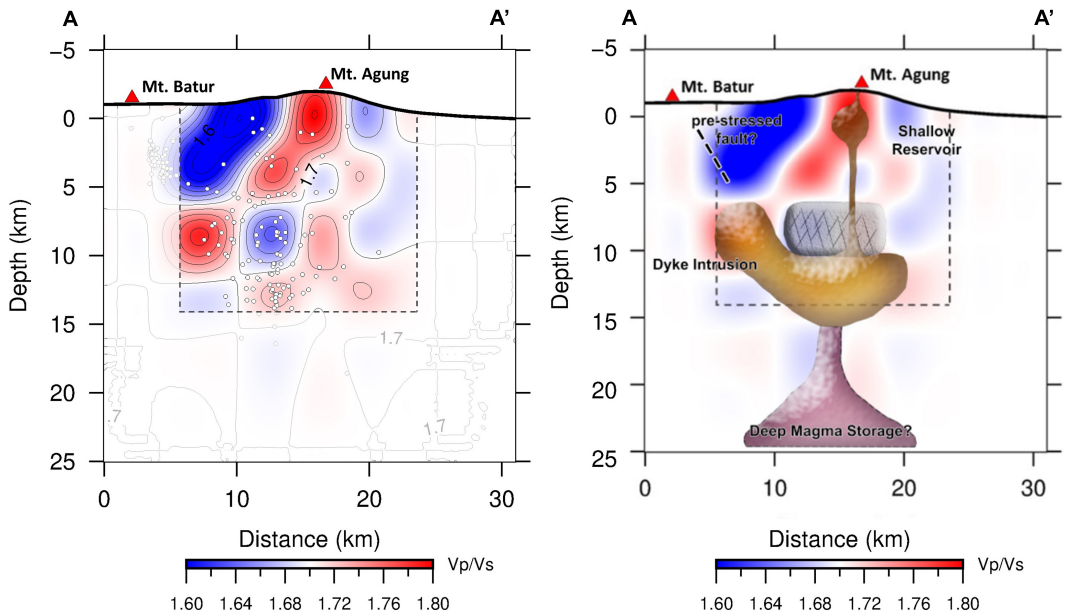

FIGURE 5 | (A) Vp/Vs vertical cross-sections along section **A-A'**, This image description is the same as in **Figure 3** with the addition of the Vp/Vs contour. **(B)** The schematic diagram for interpretation of the results along section **A-A'** is derived from the Vp/Vs ratio structure. Dyke intrusion penetrated upward toward the west-northwest of Mt. Agung. Based on the resolution test results, we define well-resolved regions inside dashed black lines.

should fully capture a seismic crisis and give information about the deeper location of the magma.

CONCLUSION

We have successfully relocated the VT earthquakes and determined the first 3D seismic velocity structure (Vp, Vs, and Vp/Vs ratio) to describe subsurface conditions beneath Mt. Agung. We used a combination of permanent [2 vertical short-period seismometers (1-C)] and temporary [6 three components (3-C) broadband seismometers] observation stations installed by the CVGHM during the period from October 18 to December 31, 2017. Based on resolution tests, the area between Mt. Agung and Mt. Batur has a reasonably satisfactory resolution down to a depth of 15 km.

The results of our VT earthquakes tomography reveal five anomalous regions, which we interpret as follows: (i) a shallow magma reservoir located just below the summit of Mt. Agung at depths between ∼1 and 5 km, which is characterized by very high Vp/Vs ratio and low seismicity; (ii) a fault zone characterized by shallow seismicity with depths up to ∼5 km below sea level, which may be triggered by over-pressurization of groundwater due to magma intrusion; (iii) high crack density dry rock mass or filled with a supercritical fluid, as indicated as low Vp, Vs, and Vp/Vs with high seismicity; (iv) the same rock mass as Region 3 but dominated by high-temperature melt. This area is probably a conduit associated with a shallow magma reservoir as characterized by moderate to high Vp/Vs and low seismicity; (v) a sub-vertical dyke complex at depths of 8–14 km below sea level, which is described as moderate to high Vp/Vs with significantly high seismicity around this anomalous body.

Our study reveals new insight into the magma plumbing system's subsurface structure beneath Mt. Agung. However, we are not able to delineate the deeper magma storage due to the limited resolution. We have succeeded in obtaining the shallow magma reservoir's location, and the estimated location and dimensions show good agreement with previous studies (Chaussard and Amelung, 2012; Geiger et al., 2018). We confirm the presence of a dyke complex intrusion with an accompanying seismic swarm prior to the 2017 eruption of Mt. Agung (Albino et al., 2019; Syahbana et al., 2019). The temporal relationship between seismicity and changes in dyke volume (Albino et al., 2019) and the spatial relationship between the hypocenter solution and the high Vp/Vs anomaly increases the level of confidence for our interpretation of the dyke complex intrusion. Further research is still needed, employing different geophysical methods such as gravity, magnetic, electromagnetic, to provide better constraints in the conceptual model, especially at greater depths, so that we can have a better comprehension of the subsurface conditions of Mt. Agung, which may contribute to better mitigation of volcanic disasters in the future.

DATA AVAILABILITY STATEMENT

The original contributions presented in the study are included in the article/**Supplementary Material**, further inquiries can be directed to the corresponding author/s.

AUTHOR CONTRIBUTIONS

ZZ, AN, SW, DSa, IP, and MM conceived the survey and seismic study on ABVC. AA, AN, AS, HA, DSy, and FM contributed to the writing of the manuscript. All authors contributed to the preparation of the manuscript, read and approved the final manuscript.

FUNDING

This study was supported by the ITB Research 2019–2020 Program and the Master's Thesis Research Program BP-PTNBH Kemristek/BRIN 2020, World Class Research Kemristek/BRIN 2021 awarded to AN. The study was also partially supported by the USAID's PEER (Partnership for Enhance Engagement in Research) program with agreement number AID-OAA-A-11-00012, and the Center for Earthquake Science and Technology, Research Center for Disaster Mitigation, Institut Teknologi Bandung (CEST, PPMB, ITB).

ACKNOWLEDGMENTS

This study was a collaboration between Institut Teknologi Bandung (ITB), the Geological Agency of Indonesia c.q. the Center for Volcanology and Geological Hazard Mitigation (CVGHM), and the Volcano Disaster Assistance Program (VDAP) of the United States Geological Survey (USGS). Generic Mapping Tools (Wessel and Smith, 1998) were used to produce the figures.

SUPPLEMENTARY MATERIAL

The Supplementary Material for this article can be found online at: https://www.frontiersin.org/articles/10.3389/feart.2021.619587/full#supplementary-material

REFERENCES

Albino, F., Biggs, J., and Syahbana, D. K. (2019). Dyke intrusion between neighbouring arc volcanoes responsible for 2017 pre-eruptive seismic swarm at Agung. *Nat. Commun.* 10:748. doi: 10.1038/s41467-019-08564-9

Bachmann, C. E., Wiemer, S., Goertz-Allmann, B. P., and Woessner, J. (2012). Influence of pore-pressure on the event-size distribution of induced earthquakes. *Geophys. Res. Lett.* 39:L09302. doi: 10.1029/2012GL051480

Chaussard, E., and Amelung, F. (2012). Precursory inflation of shallow magma reservoirs at west Sunda volcanoes detected by InSAR. *Geophys. Res. Lett.* 39:21311. doi: 10.1029/2012GL053817

Coulon, C. A., Hsieh, P. A., White, R., Lowenstern, J. B., and Ingebritsen, S. E. (2017). Causes of distal volcano-tectonic seismicity inferred from hydrothermal modeling. *J. Volcanol. Geotherm. Res.* 345, 98–108. doi: 10.1016/j.jvolgeores.2017.07.011

De Natale, G., Troise, C., Trigila, R., Dolfi, D., and Chiarabba, C. (2004). Seismicity and 3-D substructure at Somma-Vesuvius Volcano; evidence for magma quenching. *Earth Planet Sci. Lett.* 221, 181–196. doi: 10.1016/S0012-821X(04)00093-7

Eberhart-Phillips, D. (1986). Three-dimensional velocity structure in northern California coast ranges from inversion of local earthquake arrival times. *Bull. Seismol. Soc. Am.* 76, 1025–1052.

Evans, J. R., Eberhart-Phillips, D., and Thurber, C. H. (1994). User's manual for SIMULPS12 for imaging vp and vp/vs: a derivative of the 'Thurber' tomographic inversion SIMUL3 for local earthquakes and explosions. *U.S. Geol. Surv. Open File Rep.* 94–431, 101. doi: 10.3133/ofr94431

Fontijn, K., Costa, F., Sutawidjaja, I., Newhall, C. G., and Herrin, J. S. (2015). A 5000-year record of multiple highly explosive mafic eruptions from Mt. Agung (Bali, Indonesia): implications for eruption frequency and volcanic hazards. *Bull. Volcanol.* 77:59. doi: 10.1007/s00445-015-0943-x

Geiger, H., Troll, V. R., Jolis, E. M., Deegan, F. M., Harris, C., Hilton, D. R., et al. (2018). Multi-level magma plumbing at Agung and Batur volcanoes increases risk of hazardous eruptions. *Sci. Rep.* 8:10547. doi: 10.1038/s41598-018-28125-2

Hammond, W., and Humphreys, E. (2000). Upper mantle seismic wave velocity: effects of realistic partial melt geometries. *J. Geophys. Res. Solid Earth* 105, 10975–10986. doi: 10.1029/2000JB900041

Kissling, E., Ellsworth, W. L., Phillips, D. E., and Kradolfer, U. (1994). Initial reference models in local earthquake tomography. *J. Geophys. Res.* 99, 19635–19646. doi: 10.1029/93JB03138

Koulakov, I., Jakovlev, A., and Luehr, B. G. (2009). Anisotropic structure beneath central Java from local earthquake tomography. *Geochem. Geophys. Geosyst.* 10:Q02011. doi: 10.1029/2008GC002109

Laigle, M., Hirn, A., Sapin, A., and Le' pine, J. C. (2000). Mount Etna dense array local earthquake P and S tomography and implications for volcanic plumbing. *J. Geophys. Res. Solid Earth* 105, 21633–21646. doi: 10.1029/2000JB900190

Lees, J. M. (2007). Seismic tomography of magmatic systems. *J. Volcanol. Geotherm. Res.* 167, 37–56. doi: 10.1016/j.jvolgeores.2007.06.008

Lévěque, J.-J., Rivera, L., and Wittlinger, G. (1993). On the use of the checker-board test to assess the resolution of tomographic inversions. *Geophys. J. Int.* 115, 313–318. doi: 10.1111/j.1365-246X.1993.tb05605.x

Lomax, A., and Michelini, A. (2009). Mwpd: a duration-amplitude procedure for rapid determination of earthquake magnitude and tsunamigenic potential from P waveforms. *Geophys. J. Int.* 176, 200–214. doi: 10.1111/j.1365-246X.2008.03974

Lomax, A., Satriano, C., and Vassallo, M. (2012). Automatic picker developments and optimization: filterpicker – a robust, broadband picker for real-time seismic monitoring and earthquake early warning. *Seismol. Res. Lett.* 83, 531–540. doi: 10.1785/gssrl.83.3.531

Lomax, A., Virieux, J., Volant, P., and Berge-Thierry, C. (2000). "Probabilistic earthquake location in 3D and layered models BT – Advances in seismic event location," in *Advances in Seismic Event Location. Modern Approaches in Geophysics*, eds C. H. Thurber and N. Rabinowitz (Dordrecht: Springer), 101–134. doi: 10.1007/978-94-015-9536-0_5

Menke, W. (1989). *Geophysical Data Analysis: Discrete Inverse Theory*, 1st ed. San Diego, CA: Academic Press.

Molina, I., Kumagai, H., Le Pennec, J. L., and Hall, M. (2005). Threedimensional P-wave velocity structure of Tungurahua volcano, ecuador. *J. Volcanol. Geotherm. Res.* 147, 144–156. doi: 10.1016/j.jvolgeores.2005.03.011

Moos, D., and Zoback, M. D. (1983). In situ studies of velocity in fractured crystalline rocks. *J. Geophys. Res. Solid Earth* 88, 2345–2358. doi: 10.1029/JB088iB03p02345

Nakajima, J., and Hasegawa, A. (2003). Tomographic imaging of seismic velocity structure in and around the Onikobe volcanic area, northeastern Japan: implications for fluid distribution. *J. Volcanol. Geotherm. Res.* 127, 1–18. doi: 10.1016/S0377-0273(03)00155-0

Nugraha, A. D., Indrastuti, N., Kusnandar, R., Gunawan, H., Triastuty, H., and McCausland, W. (2019). Joint 3-D tomographic imaging of Vp, Vs and Vp/Vs and hypocenter relocation at Sinabung volcano, Indonesia from November to December 2013. *J. Volcanol. Geotherm. Res.* 382, 210–223. doi: 10.1016/j.jvolgeores.2017.09.018

Nur, A., and Simmons, G. (1969). The effect of saturation on velocity in low porosity rocks. *Earth Planet Sci. Lett.* 7, 183–193. doi: 10.1016/0012-821X(69)90035-1

Pearson, C. (1981). The relationship between microseismicity and high porepressures during hydraulic stimulation experiments in low permeability granitic rocks. *J. Geophys. Res. Solid Earth* 86, 7855–7864. doi: 10.1029/JB086iB09p07855

Ponko, S. C., and Sanders, C. O. (1994). Inversion for P and S wave differential attenuation structure, long valley Caldera, California. *J. Geophys. Res. Solid Earth* 99, 2619–2635. doi: 10.1029/93JB03405

PVMBG, (2014). *Gunung Agung, Kementrian Energi dan Sumber Daya Mineal, Badan Geologi*. Available online at: https://vsi.esdm.go.id/index.php/gunungapi/data-dasar-gunungapi/468-g-agung?start=2 (accessed December 13, 2020).

Ramdhan, M., Widiyantoro, S., Nugraha, A. D., Métaxian, J. P., Rawlinson, N., Saepuloh, A., et al. (2019). Detailed seismic imaging of Merapi volcano, Indonesia, from local earthquake travel-time tomography. *J. Asian Earth Sci.* 177, 134–145. doi: 10.1016/j.jseaes.2019.03.018

Rampino, M. R., and Self, S. (1982). Historic eruptions of Tambora (1815), Krakatau (1883), and Agung (1963), their stratospheric aerosols, and climatic impact. *Quat. Res.* 18, 127–143. doi: 10.1016/0033-5894(82)90065-5

Rampino, M. R., and Self, S. (1984). Sulphur-rich volcanic eruptions and stratospheric aerosols. *Nature* 310, 677–679. doi: 10.1038/310677a0

Rawlinson, N., and Spakman, W. (2016). On the use of sensitivity tests in seismic tomography. *Geophys. J. Int.* 205, 1221–1243. doi: 10.1093/gji/ggw084

Sahara, D. P., Rahsetyo, P. P., Nugraha, A. D., Syahbana, D. K., Widiyantoro, S., Zulfakriza, Z., et al. (2021). Use of local seismic network in analysis of volcano-tectonic (VT) events preceding the 2017 agung volcano eruption (Bali, Indonesia). *Front. Earth Sci.* (Accepted).

Sanders, C., Ponko, S., Nixon, L., and Schwartz, E. (1995). Seismological evidence for magmatic and hydrothermal structure in Long Valley caldera from local earthquake attenuation and velocity tomography. *J. Geophys. Res. Solid Earth* 100, 8311–8326. doi: 10.1029/95JB00152

Sasmi, A. T., Nugraha, A. D., Muzil, M., Widiyantoro, S., Zulfakriza, Z., Wei, S., et al. (2020). Hypocenter and magnitude analysis of aftershocks of the 2018 Lombok earthquakes, Indonesia, UsinglLocal seismographic networks. *Seismol. Res. Lett.* 91, 2152–2162. doi: 10.1785/0220190348

Sutawidjaja, I. (2009). Ignimbrite analyses of Batur Caldera, Bali, based on 14C dating. *J. Geol. Indones.* 4, 189–202.

Syahbana, D. K., Kasbani, K., Suantika, G., Prambada, O., Andreas, A. S., Saing, S. L., et al. (2019). The 2017–19 activity at Mount Agung in Bali (Indonesia): intense unrest, monitoring, crisis response, evacuation, and eruption. *Sci. Rep.* 9:8848. doi: 10.1038/s41598-019-45295-9

Takei, Y. (2002). Effect of pore geometry on Vp/Vs: from equilibrium geometry to crack. *J. Geophys. Res. Solid Earth* 107:2043. doi: 10.1029/2001JB000522

Toksoz, M. N., Cheng, C. H., and Aytekin, T. (1976). Velocities of seismic waves in porous rock. *Geophysics.* 41, 621–645. doi: 10.1190/1.1440639

Toomey, D. R., and Foulger, G. R. (1989). Tomographic inversion of local earthquake data from the Hengill-Grensdalur central volcano complex, Iceland. *J. Geophys. Res. Solid Earth* 94, 17497–17510. doi: 10.1029/JB094iB12p17497

Um, J., and Thurber, C. H. (1987). A fast forward algorithm for two-point seismic ray tracing. *Bull. Seismol. Soc. Am.* 77, 972–986.

Wessel, P., and Smith, W. H. F. (1998). New, improved version of generic mapping tools released. *Eos Trans. Am. Geophys. Union* 79:579. doi: 10.1029/98EO00426

Widiyantoro, S., Ramdhan, M., Métaxian, J. P., Cummins, P. R., Martel, C., Erdmann, S., et al. (2018). Seismic imaging and petrology explain highly explosive eruptions of Merapi Volcano, Indonesia. *Sci. Rep.* 8:13656. doi: 10.1038/s41598-018-31293-w

Yip, S. T. H., Biggs, J., and Albino, F. (2019). Reevaluating volcanic deformation using atmospheric corrections: implications for the magmatic system of Agung volcano, Indonesia. *Geophys. Res. Lett.* 46, 13704–13711. doi: 10.1029/2019GL085233

Zen, M. T., and Hadikusumo, D. (1964). Preliminary report on the 1963 eruption of Mt. Agung in Bali (Indonesia). *Bull. Volcanol.* 27, 269–300. doi: 10.1007/BF02597526

Zulfakriza, Z., Nugraha, A. D., Widiyantoro, S., Cummins, P. R., Sahara, D. P., Rosalia, S., et al. (2020). Tomographic imaging of the Agung-Batur volcano complex, Bali, Indonesia, from the ambient seismic noise field. *Front. Earth Sci.* 8:43. doi: 10.3389/feart.2020.00043

Conflict of Interest: The authors declare that the research was conducted in the absence of any commercial or financial relationships that could be construed as a potential conflict of interest.

Copyright © 2021 Ardianto, Nugraha, Afif, Syahbana, Sahara, Zulfakriza, Widiyantoro, Priyono, Rosalia, Saepuloh, Kasbani, Muttaqy, Rahsetyo, Priambodo and Martanto. This is an open-access article distributed under the terms of the Creative Commons Attribution License (CC BY). The use, distribution or reproduction in other forums is permitted, provided the original author(s) and the copyright owner(s) are credited and that the original publication in this journal is cited, in accordance with accepted academic practice. No use, distribution or reproduction is permitted which does not comply with these terms.

frontiers in Earth Science

ORIGINAL RESEARCH
published: 17 May 2021
doi: 10.3389/feart.2021.653164

Repeating Earthquakes During Multiple Phases of Unrest and Eruption at Mount Agung, Bali, Indonesia, 2017

John J. Wellik[1], Stephanie G. Prejean[2] and Devy K. Syahbana[3]*

[1]U.S. Geological Survey, Volcano Disaster Assistance Program, Vancouver, WA, United States, [2]U.S. Geological Survey, Volcano Disaster Assistance Program, Anchorage, AK, United States, [3]Center for Volcanology and Geological Hazards Mitigation, Geological Agency, Ministry of Energy and Mineral Resources, Bandung, Indonesia

In 2017, Mount Agung produced a small (VEI 2) eruption that was preceded by an energetic volcano-tectonic (VT) swarm (>800 earthquakes per day up to M4.9) and two months of declining activity. The period of decreased seismic activity complicated forecasting efforts for scientists monitoring the volcano. We examine the time history of earthquake families at Mount Agung in search of additional insight into the temporal changes in the shallow crust prior to eruption. Specifically, we analyze the period of declining seismic activity about five weeks prior to the eruption when forecasting uncertainty was greatest. We use REDPy (Hotovec-Ellis and Jeffries, 2016) to build a catalog of 6,508 earthquakes from 18 October 2017–15 February 2018 and group them into families of repeating earthquakes based on waveform similarity using a cross-correlation coefficient threshold of 0.8. We show that the evolution of earthquake families provides evidence that Mount Agung was progressing toward eruption even though overall earthquake rates and seismic-energy-release declined. We find that earthquake families that dominated seismicity during the beginning of the crisis ceased near the onset of tremor on 12 November 2017. Then, earthquake families took on characteristics commonly observed during effusive phases of eruptions on 15 November—a full six days before the first phreatomagmatic eruption on 21 November 2017 and a full ten days before the actual onset of lava effusion on 25 November 2017. We interpret the transitions in seismicity as the manifestation of a three-phase physical model including an Intrusion Phase, a Transition Phase, and a Eruptive Phase. During the Intrusion Phase, seismicity was dominated by VT earthquakes with a relatively high percentage of repeaters (59%) grouped into numerous (65) simultaneous families. During the Eruptive Phase, seismicity included both VT and low frequency earthquakes that grouped into relatively long-lived families despite a low overall percentage of repeaters (14%). The Transition Phase exhibited characteristics of earthquake families between the Intrusion Phase and Eruptive Phase. We conclude that the time history of earthquake families provides insight into the evolution of the stress distribution in the volcanic edifice, the development of the volcanic conduit, and seismogenesis of magma effusion. Finally, we discuss the role that repeating earthquakes could play in real-time monitoring at

OPEN ACCESS

Edited by:
Jessica Helen Johnson, University of East Anglia, United Kingdom

Reviewed by:
Patrick J Smith, Dublin Institute for Advanced Studies (DIAS), Ireland
Jacqueline Caplan-Auerbach, Western Washington University, United States

***Correspondence:**
John J. Wellik
jwellik@usgs.gov

Specialty section:
This article was submitted to Volcanology, a section of the journal Frontiers in Earth Science

Received: *13 January 2021*
Accepted: *29 April 2021*
Published: *17 May 2021*

Citation:
Wellik JJ, Prejean SG and Syahbana DK (2021) Repeating Earthquakes During Multiple Phases of Unrest and Eruption at Mount Agung, Bali, Indonesia, 2017. Front. Earth Sci. 9:653164. doi: 10.3389/feart.2021.653164

restless volcanoes. Our work suggests eruption forecasts can be improved by incorporating automatic processing codes to assist seismologists during sustained periods of high earthquake rates, even at sparsely monitored volcanoes.

Keywords: volcano seismology, repeating earthquakes, cross-correlaion, eruption forecasting, intrusion seismogenesis, seismic precursor, agung volcano

INTRODUCTION

Continuous seismic data have been the primary data stream used to forecast eruptive activity during volcanic crises since modern volcano monitoring began. Examples of forecasts from seismic data are numerous (e.g., Endo et al., 1981; Malone et al., 1983; Klein, 1984; Swanson et al., 1985; Power and Lalla, 2010; Chouet et al., 1994; Harlow et al., 1996; Soosalu et al., 2005; Power and Lala, 2010; Buurman and West, 2010; and; Ruppert et al., 2011). The most established seismic indicators of incipient eruption include increasing number and amplitude of seismic events and shifts in types of seismic events from VTs (volcano-tectonic) to LFs (low frequency) and tremor as magma nears the surface (e.g., Minakami, 1974; Voight, 1988; Chouet, 1996; McNutt, 1996; Boué et al., 2015; McCausland et al., 2019; White and McCausland, 2019). Many of these methods are most reliable for explosive eruptions, whereas small and slowly evolving eruptions can be more difficult to forecast reliably (e.g., Cameron et al., 2018) and require a detailed understanding of a volcano's structure, tectonic framework, hydrologic system, and eruptive history.

Seismicity escalated dramatically in the months prior to the 2017–2018 eruption at Mount Agung, Bali, Indonesia, providing ample warning of an impending eruption (Syahbana et al., 2019) and raising fears of a violent eruption, similar to the VEI 5 in 1963 (Kusmandinata, 1964). Although the eruption was expected in the long term, forecasting the size and onset time of the eruption in the short term was difficult. Ultimately, the eruption was only a VEI 2, characterized by relatively small explosions and the extrusion of 24 million m^3 of lava at the summit crater (Syahbana et al., 2019). Ash fall affected local farmland and small lahars traveled down drainages on the N and S flanks, and there were no fatalities.

Several challenges presented themselves throughout the crisis:

(1) Scientists with CVGHM (Indonesia's Center for Volcanology and Geologic Hazard Mitigation), who were responsible for monitoring, had very few automatic processing tools to assist them in their work. Aside from RSAM (Realtime Seismic Amplitude Measurement: Endo and Murray, 1991), staff manually counted and classified earthquakes to interpret volcanic activity and provide information to decision makers and the public.
(2) There were no records of seismicity from the 1963 eruption, and there had been no detected unrest on the local network in the decades prior to 2017 to serve as a comparison.
(3) After an initial intense swarm of earthquakes, overall rates of seismicity decreased for almost two months leading into the first phreatomagmatic and magmatic eruptions, thus creating uncertainty as to when or if activity would progress toward an eruption (Syahbana et al., 2019).
(4) Seismic signatures that commonly reflect shallowing magma (McNutt, 1996; White and McCausland, 2019)–tremor, low frequency earthquakes, and proximal brittle failure earthquakes—were subtle, low in amplitude, and difficult to detect through cultural noise.

Small eruptions can be difficult to forecast precisely because precursory signals can be subtle, but in densely populated areas small eruptions still pose a great threat. Thus, new approaches and analysis tools are needed. Studies of repeating earthquakes, or earthquake families, have been successful, though often in retrospect, of showing notable changes in eruptive activity at a variety of volcanoes (e.g., Green and Neuberg, 2006; Umakoshi et al., 2008; Arambula-Mendoza et al., 2011; Thelen et al., 2011; Buurman et al., 2013; Rodgers et al., 2013). Repeating earthquake families can include either broad-band brittle failure or low-frequency earthquakes and are observed when seismic sources are stationary, non-destructive and of the same mechanism (Geller and Mueller, 1980). Processes that cause them vary widely, including brittle failure associated with deep pressurization and conduit building under the summit (Buurman and West, 2010; Deshon et al., 2010; Budi-Santoso and Lesage, 2016), shallow fluid movement and lava dome growth at the surface (Stephens and Chouet, 2001; Rowe et al., 2004; Green and Neuberg, 2006; Umakoshi et al., 2008; Matoza and Chouet, 2010; Thelen et al., 2011), magma-water interaction in the shallow system (Rodgers et al., 2013; Rodgers et al., 2015), and degassing (Caplan-Auerbach and Petersen, 2005; Waite et al., 2008; Matoza et al., 2015).

In this retrospective study, we examine the time history of earthquake families at Mount Agung in search of additional insight into the temporal changes in the shallow crust (upper 20 km) prior to eruption. Specifically, we analyze the period of declining seismic activity ~5 weeks prior to the eruption. We show that the evolution of earthquake families illustrates that Mount Agung was progressing toward eruption even though overall earthquake rates and seismic-energy-release declined.

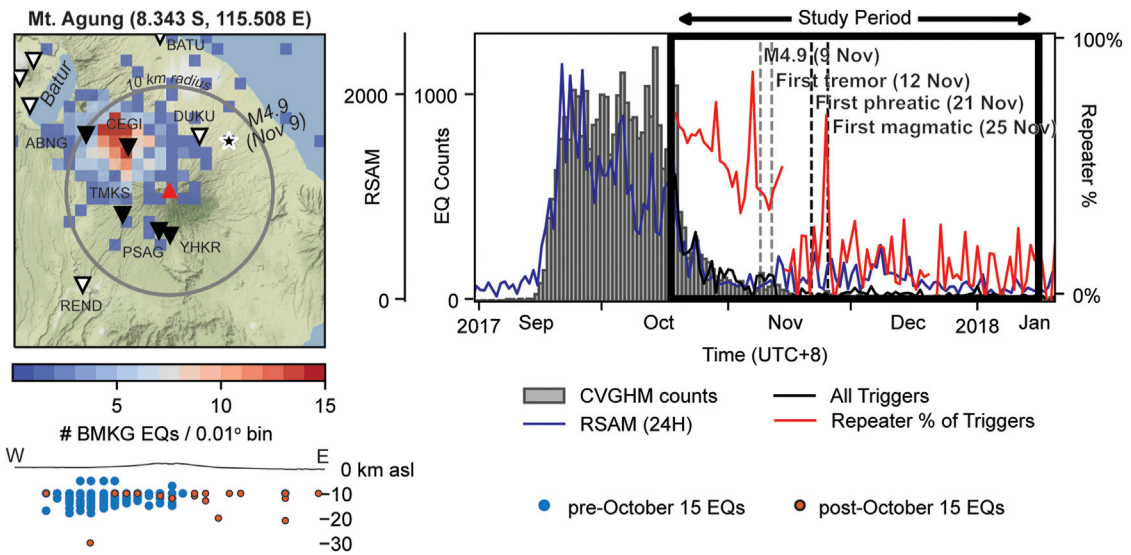

FIGURE 1 | Map **(left)** and timeseries (right) of seismicity throughout the entire crisis. The map displays information about locations for the 423 earthquakes located near Mount Agung by Indonesia's Meteorological, Climatological, and Geophysical Agency (BMKG) from September 2017 through February 2018. Specifically, the map shows the number of earthquakes in the BMKG by Indonesia's Meteorological, Climatological, and Geophysical Agency (BMKG) catalog per 0.01x0.01° bin, the resolution of the BMKG catalog (~1.1km x 1.1km at this latitude). Black triangles represent seismic stations used in this study. White triangles represent additional stations that were not included due to frequent data outages or high levels of noise. The EW cross-section below the map shows the BMKG depth for all earthquakes on the map. Earthquakes before 15 October are plotted in blue, and earthquakes after 15 October are plotted in orange. The apparent shift in hypocenters from west of the volcano to east of the volcano in mid-October was noticed during the crisis (Syahbana et al., 2019) and is discussed in the text. The timeseries shows the Center for Volcanology and Geologic Hazard Mitigation's (CVGHM) earthquake counts (gray bars), 24-Hour RSAM derived from the filtered (1–10 Hz) seismic data of station TMKS (blue line), all triggers produced by REDPy (black line), and the repeater percentage of triggers (red line). Key dates, such as the largest earthquake in the sequence (M4.9 on 9 Nov SGT), the first appearance of tremor (12 Nov SGT), the first phreatic eruption (21 Nov SGT), and the first magmatic eruption (25 Nov SGT) are also included. All dates are Agung local time (UTC+8; "SGT"). **Figure 2** shows more detail for the study period.

ERUPTION TIMELINE AND RESPONSE

After a 50 + year period of repose, unrest at Mount Agung began in mid-July with anomalous levels of seismicity, thermal anomalies, and an increase in steaming at the volcano's summit (Syahbana et al., 2019). Earthquake rates and magnitudes intensified in September, and reports of felt seismicity and locations for the largest earthquakes (>M2.3)—computed by Indonesia's Meteorological, Climatological, and Geophysical Agency (BMKG), which runs the national seismic network—suggested the earthquakes were located between the edifices of Mount Agung and Batur (NW of Mount Agung) at depths between 10 and 20 km below sea level (**Figure 1**). The growing swarm of brittle failure VTs was interpreted as the seismic response of the crust as a deep intrusion under the summit of Mount Agung (White and McCausland, 2016). Later work helped clarify the path magma took to reach the surface. A series of InSAR images from 21 September 2017 UTC to 8 November 2017 UTC show a pattern of inflation that is consistent with a dike intrusion between 7 and 13 km depth on the NW flank of Mount Agung (Albino et al., 2018). The location of the magma reservoir below the depth of the dike is not known, but Syahbana et al. (2019) favor a model where a the dike propagated laterally from a deeper magma reservoir (12 to >15 km) beneath the summit of Mount Agung before magma continued to the summit.

One day before the peak seismic earthquake rates on 23 September 2017, CVGHM raised the alert level to IV (the highest of 4 levels). Earthquake magnitudes reached a new maximum (M4.2) a day later on 23 September 2017 (Syahbana et al., 2019), but subsequently earthquake rates and RSAM values decreased significantly (**Figure 1**). After a month of reduced earthquake rates and declining RSAM values, the alert level was lowered to III on 29 October 2017 (Syahbana et al., 2019).

During this time of uncertainty, CVGHM staff were vigilant for any signs of shallowing magma, such as the emergence of tremor and low-frequency (LF) seismicity or a shift of seismicity toward the summit (Chouet, 1996; White and McCausland, 2019). On 9 November 2017, a M4.9 earthquake, the largest of the crisis, and a series of aftershocks occurred in a prominent new location NE of the mountain at ~10 km depth, according to BMKG. According to global solutions by the U.S. Geological Survey (USGS) National Earthquake Information Center[2] and the Global Centroid Moment Tensor[3] (Dziewonski et al., 1981; Ekström et al., 2012), the earthquake occurred on an approximately E-W striking, south-dipping thrust fault—consistent with seismicity in the back-arc of the Sunda

[2]https://earthquake.usgs.gov/
[3]https://www.globalcmt.org/

convergent margin (Supendi et al., 2020). On 12 November, CVGHM staff noted the first significant tremor as well as the first appearance of LF earthquakes. These tremor bursts were ~40–120 s each, were broadband (1–10 Hz), and were barely strong enough to rise above the amplitudes of daytime cultural noise on the analog stations TMKS and PSAG (Syahbana et al., 2019). Together, the M4.9 earthquake and appearance of tremor and LFs were interpreted by CVGHM as a possible shift toward a more phreatic phase of precursory unrest as heat interacted with the shallow hydrologic system and fluids and gases moving toward the surface began opening the conduit. Later work by (Sahara et al., 2021) (submitted) lend credence to this interpretation by showing a gradual shift in earthquake locations toward the summit.

The fact that tremor did not continue and that shallow LF earthquakes were few in number, however, suggested that if processes in the volcanic conduit were progressing toward eruption, they were doing so slowly. The lack of convincing evidence for shallow conduit seismicity and the increased lag time since the energetic VT swarm increased CVGHM's uncertainty that an eruption would occur in the near future (Syahbana et al., 2019), and CVGHM opted not to raise the alert level. In hindsight, another InSAR image from 20 November showed significant depletion from the inflation source under the NW flank, which Albino et al. (2018) interpret as a sign that magma had begun to migrate toward the summit. The first gas measurements, which were taken by unoccupied aircraft systems early on 21 November, also showed high levels of CO_2, which was interpreted as a significant sign of unrest (Syahbana et al., 2019).

Earthquake rates remained at low levels and fluctuations in RSAM stayed within normal bounds leading up to the first phreatomagmatic eruption on 21 November. LF earthquakes and tremor increased after the first phreatomagmatic eruption, and on 25 November, CVGHM staff documented 21 larger LF signals with a dominant frequency of ~2 Hz over a 90-min period (Syahbana et al., 2019). These earthquakes were closely associated in time with the onset of lava at the summit, and within just a few days, 24 million m^3 of lava had filled one-third of the summit crater, and regular explosions occurred until mid-January 2018 (Syahbana et al., 2019).

METHODS

We used REDPy (Hotovec-Eills and Jeffries, 2016) to build an earthquake catalog at Mount Agung prior to, during, and after the late-November 2017 eruptions, and we group those earthquakes into families based on waveform similarity to assess changes in seismicity over time. We focus on the time period of greatest forecasting uncertainty—i.e., when seismicity decreased following peak rates in late September, and then in the period after the eruption started.

REDPy is designed to comb through real-time or archived continuous data to produce a catalog of triggered signals using a short-time-average/long-time-average (STA/LTA) algorithm. It then cross-correlates all triggered signals against each other, and earthquakes with cross-correlation coefficients above a certain threshold are grouped into families of repeating earthquakes. Earthquakes from a single family are presumed to have originated from a similar location and a similar source mechanism, thus providing some information about earthquake source properties even if the network is insufficient to compute hypocenters or focal mechanisms (Geller and Mueller, 1980). Earthquakes whose cross-correlation coefficients with prior events are below a defined threshold are labeled "orphans" and remain in the catalog to be compared to future earthquakes. We also use REDPy to compute the Frequency Index (FI) of each earthquake by comparing energy in a high frequency band (5–10 Hz) to energy in a low frequency band (1–2.5 Hz) (Buurman and West, 2010). Frequency index is an arithmetical method to describe earthquake frequency content, and in our case, we empirically define the boundary between VT and LF earthquakes at 0 (**Figure 2**).

Prior to the crisis, the seismic monitoring network at Mount Agung consisted of two short-period, vertical seismometers that were transmitted via analog telemetry back to the observatory post at Pos Rendang. The stations were ~4 and 5 km away from the summit. Between mid-October and early November, CVGHM and VDAP (USGS-USAID Volcano Disaster Assistance Program) installed seven new seismometers — 6 broadband and 1 short-period—with digital telemetry back to the observatory post (**Figure 1**). Four of those stations were located <10 km from the volcano while the other three were located farther away. For this analysis, we used 5 stations (the two original short-period analog stations (TMKS, PSAG), the short-period digital station (ABNG) and two of the closest broadbands (CEGI, YHKR) (**Figure 1**). We did not include the other proximal broadband, DUKU, because it had significant data outages during our study.

We filtered all data between 1 and 10 Hz before applying the recursive STA/LTA algorithm (short-time widow: 3 s; long-time window: 8 s; trigger on threshold: 1.8; trigger off threshold: 1.3). We required a detection at 3 stations in order to produce a trigger, and we required a cross-correlation coefficient of 0.8 at 3 stations in order to be considered a matching waveform. Finally, we required families comprise five earthquakes or more for the events to be grouped as a family and counted as a repeater for the purposes of **Figures 1–3** and **Table 1**.

We reviewed all earthquake waveforms in Swarm[4] to verify that regional earthquakes and noise were not included in our analysis. We also repeated our analysis with cross-correlation coefficients of 0.6 and 0.7 to verify that the interpretation of our results is not sensitive to this value (**Supplementary Table S1**). Finally, we extended our analysis to the beginning of the crisis (early September) by using just the 2 original analog stations and a cross-correlation coefficient of 0.8 to verify that observations made in the study period are representative of the beginning of the crisis.

[4]https://volcanoes.usgs.gov/software/swarm/index.shtml

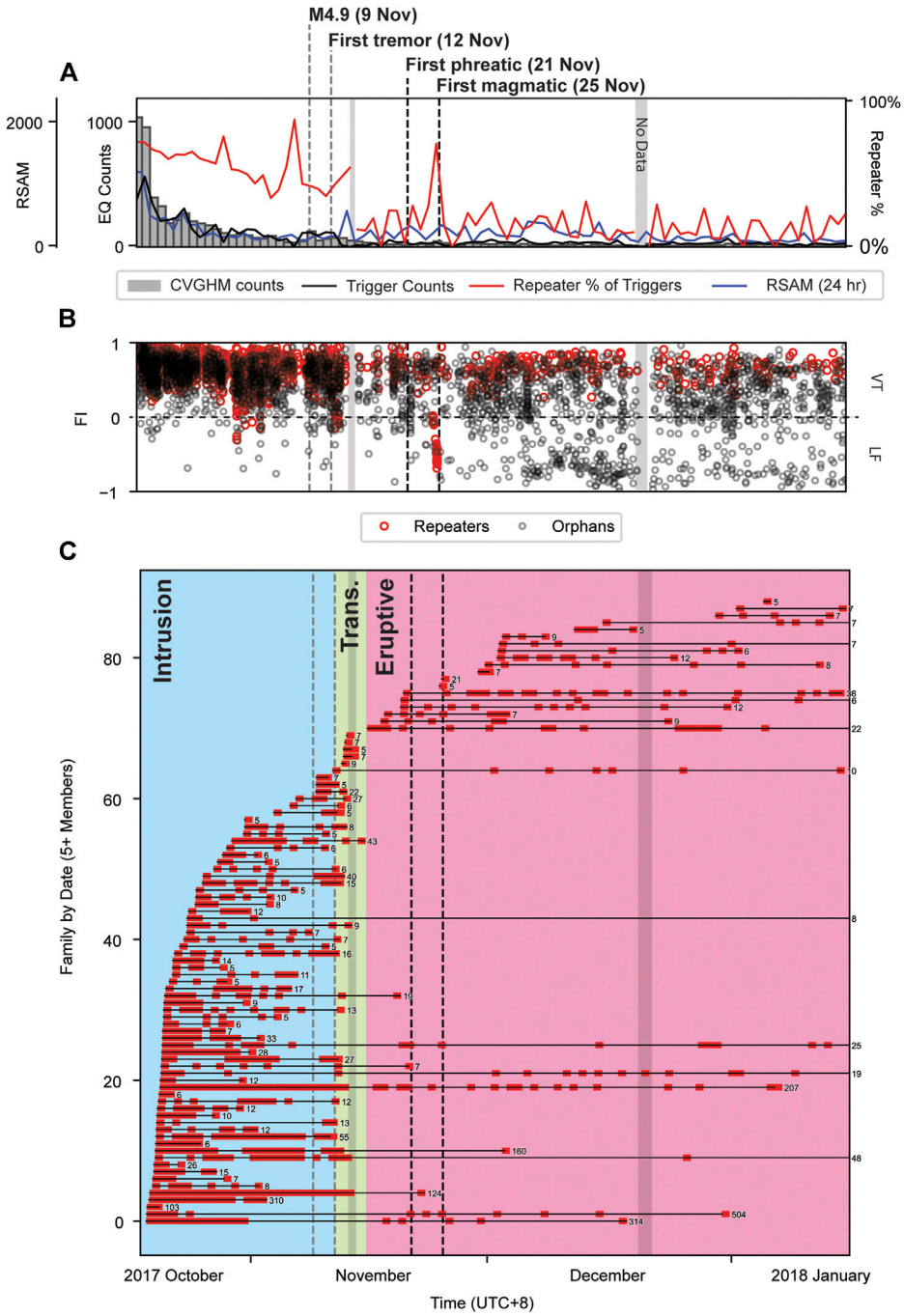

FIGURE 2 | Detailed look of the study period from **Figure 1**. **(A)** Detailed look at **Figure 1**. See **Figure 1** for explanation. The gray bars in mid-November and mid-to late-December labeled "No Data" represent times when there were not enough stations (i.e., less than 3) for REDPy to produce a trigger. These gray bars extend to subplots B and C **(B)** Frequency Index of all triggers and repeaters in the REDPy catalog. The swarm of 21 LF earthquakes on 25 November SGT is clearly distinguishable. We empirically define the boundary between VTs and LFs at 0. See text for details. **(C)**. Each horizontal line represents one earthquake family (5 + members). Red boxes represent hours when the family was active. Numbers to the right of each line represent the total number of repeaters in the family. The definitions for the start and stop of the Intrusion Phase (blue), Transition Phase (green), and Eruptive Phase (pink) are based on the patterns of earthquake families in this plot (see Discussion). Vertical dashed lines and vertical gray bar are extensions of labels from A.

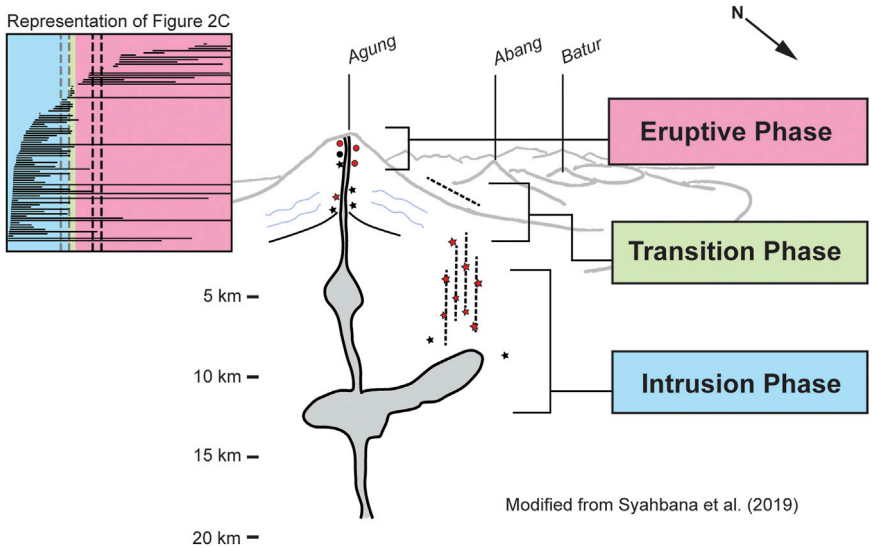

FIGURE 3 | Schematic of the preferred model from Syahbana et al. (2019). Each phase of activity from the Discussion and **Figure 2C** is tied to a general location of earthquake activity. A generalized version of **Figure 2C** is reproduced in the top left for easy reference. In the model sketch, stars represent high-frequency VT earthquakes, and circles represent low-frequency earthquakes. Red represents a preponderance of repeaters while black represents a preponderance of orphans. The representation of VTs, LFs, repeaters, and orphans in this figure is for illustrative purposes only. This figure modifies **Figure 2B** from Syahbana et al. (2019).

TABLE 1 | Percentage of earthquakes that are repeaters during each phase of activity. In general, the Intrusion Phase of seismicity is dominated by repeaters while the Transitional Phase and Eruptive Phase are overwhelmingly dominated by orphans. CCC = cross-correlation coefficient.

Timeline of Earthquake Families at Mount Agung: October 2017–February 2018					
CCC = 0.8	**Date Times (UTC+8)**	**Repeaters / Total EQs**		**# of families (EQs per fam.)**	
Intrusion Phase	2017/10/18–2017/11/12	2,395 / 4,065	(59%)	65	(36.8)
Transition Phase	2017/11/12–2017/11/15	69 / 183	(38%)	5	(13.8)
Eruptive Phase	2017/11/15–2018/02/01	311 / 2,260	(14%)	22	(14.1)
Full Sequence	2017/10/18–2018/02/15	2,775 / 6,508	(43%)	92	(30.2)

RESULTS

Our analysis resulted in a catalog of 6,508 earthquakes from 21 October 2017 to 15 February 2018 (**Table 1**). The calculated daily counts correspond well with manual counts conducted by CVGHM during the crisis (**Figure 2**). Over the course of the entire study period, 43% of earthquakes in our catalog—including 9 of the 24 BMKG earthquakes recorded on three local stations or more (**Supplementary Table S2**) — group into one of 92 families of 5 earthquakes or more (**Table 1**). Several characteristics of repeating earthquake families—including the percentage of repeating earthquakes as a portion of total seismicity and the longevity of each family—change throughout the course of the unrest and eruption.

From the beginning of the study (21 October) through the onset of tremor on 12 November 2017, the pattern of repeating earthquakes was defined by a large number of simultaneous families, each with a large number of events (**Figure 2**; **Table 1**). In total, this time period included 4,065 earthquakes, 2,395 (~59%) of which grouped into 65 different families (**Table 1**). These earthquakes ranged in magnitude from <M1 to M3, and all were brittle-failure or volcano-tectonic (VT) events.

Coinciding with the beginning of our study period, the BMKG catalog shows that earthquake locations began to occur N and NE of the volcano as well as on the W flank near Abang where a large majority of earthquakes had previously occurred (Syahbana et al., 2019). None of the BMKG-located earthquakes were part of an earthquake family until some of the 50 + located aftershocks that followed the M4.9 earthquake on 9 November 2017 05:54 SGT grouped into various earthquake families (**Supplementary Table S2**).

On 12 November, the behavior of earthquake families changed for a brief period. Most (54 of 65, or ~83%) pre-existing families ceased on or shortly after 12 November, and new families appeared. The first new family (Family 66) appeared during the onset of tremor. Over the course of the next three days, a total of five new families appeared, comprising 35 earthquakes. The new families ranged in longevity from ~1 h to ~25 h. Waveforms were emergent and low-frequency (<5 Hz). None

were large enough to be located with the BMKG network. Overall, from 12 November to 15 November, there were 183 total earthquakes, 69 (~38%) of which were in earthquake families—including those that belonged to pre-existing families (**Table 1**).

The nature of earthquake families changed again several days prior to the onset of the eruptions. Starting on 15 November, earthquake families were defined by a small number that comprised a relatively low percentage of the overall seismicity but were long-lived. A majority of earthquakes during this time period were small (<M3) and were a mix of VT events and LF events. Overall, only 14% of earthquakes (311 out of 2260) were part of earthquake families (**Table 1**). Several families remained active through the end of the study. After 15 November, the BMKG catalog includes 13 earthquakes with sufficient data for our study, and 5 of them had repeating waveforms. All belong to families that appeared after 15 November (**Supplementary Table S2**).

Seismic rates remained low in the days prior to the initial phreatomagmatic eruption on 21 November, and there were no unique patterns among the few repeating earthquakes that occurred. The swarm of larger, low frequency earthquakes that roughly coincided with the onset of lava effusion on 25 November (see Eruption Timeline and Response), however, is clearly highlighted in our results. Starting at ~0530h SGT, a new family of 21 highly repetitive (cross-correlation coefficient, CCC ~0.95) earthquakes appeared (**Supplementary Figure S1**). These earthquakes had a strong peak energy at ~2 Hz and are clearly identifiable by their frequency index in **Figure 2B**.

The remainder of the study period, which included continuous to semi-continuous ash explosions until 19 January 2018, was characterized by low rates of seismicity, low numbers of repeating earthquakes, and long-lasting families (**Figure 2**).

Extending the analysis to the beginning of the crisis using just the 2 analog, short-period stations resulted in a larger number of detected earthquakes. Many of the additional earthquakes were either lower amplitude with lower signal-to-noize ratio or were larger magnitude, clipped signals from the most intense part of the unrest. This resulted in a smaller proportion of repeating earthquakes overall (~30%), but certain key observations remained consistent between this longer term analysis with lower quality data and our primary results—a large number of simultaneous families at the beginning of the crisis, the cessation of a most families (>90%) on or shortly after 12 November, the overall decrease in repeating earthquake percentage over time, a prominent swarm of 20 + LFs on 25 November, and notably longer-lived families after the onset of lava effusion.

DISCUSSION

Earthquake families—based on cross-correlation analyses—have long-been studied at a large number of volcanoes. However, very few examples document earthquake family evolution associated with the lateral emplacement of a dike, followed by magma migration and eruption (White et al., 2011). The evolution of earthquake families at Mount Agung illustrates a changing volcanic system. We interpret the transitions in seismicity as the manifestation of a three-phase physical model. The three phases inferred by our analysis in context of other observations are: 1) the Intrusion Phase, 2) the Transitional Phase, and 3) the Eruptive Phase (**Figure 2**; **Figure 3**).

Intrusion Phase (Pre-15 October–12 November)

During the Intrusion Phase, earthquakes were occurring mostly under the NW flank of Mount Agung, proximal to an intruded dike (Syahbana et al., 2019; Albino et al., 2018; **Figure 1**). The large number of repeating earthquakes from a large number of earthquake families fits well with the conceptual model that dike intrusion can cause small, repeated failures, and rapid reloading of shear stress on a large number of small faults in the shallow crust near the dike. The large number of families as well as the significant percentage of orphaned earthquakes (~40%) may also speak to the diversity of faulting at different orientations in the shallow crust (Barton et al., 1995; Townend and Zoback, 2000). If dike intrusion increases pore pressure in the region through heating existing ground water or through exsolution of fluid and gas, in addition to gradually increasing shear stress across favorably oriented faults, faults of a wide variety of orientations may fail as the effective normal stresses across faults are decreased systematically in the area.

None of the earthquakes from the BMKG catalog group into a family until the series of aftershocks after the M4.9 earthquake on 9 November, which was located to the NE of the Mount Agung (**Figure 1**; **Supplementary Table S2**). During the crisis, CVGHM staff noted variable aftershock productivity for some of the largest earthquakes. This may reflect temporal variability in how 'primed' area faults were to fail in a typical brittle failure cascade as high seismicity rates continued. For example, the M4.9 earthquake produced a large number of aftershocks whereas a M4.0 earthquake on 16 November, located on the NW flank of the mountain, produced relatively few aftershocks. Although this observation is interesting and deserving of further study, a rigorous analysis of aftershock productivity at Mount Agung is beyond the scope of this study.

Transition Phase (12 November–15 November)

New observations of tremor and LF earthquakes on 12 November marked a significant change in the state of the system at Mount Agung and a new phase of unrest. During the crisis, this was the first indication that magma had started to move toward the summit. At the time, there was uncertainty interpreting the M4.9 that occurred 3 days prior on 9 November. In retrospect, one possibility was that this earthquake, which occurred in a prominent new location NE of the volcano, was the result of redistribution of stress in the shallow crust as magma moved to a new location closer to the summit. The delay between the large earthquake and the subtle, short-lived LF seismicity on 12 November suggests that stress transfer across the region occurred gradually. Although BMKG earthquake locations

available during the crisis did not reveal a shallowing of hypocenters between early September and mid-November, later work by Sahara et al. (submitted, this issue) did show a shallowing trend of hypocenters over this time frame, consistent with the interpretation that magma was moving toward the summit.

Changes in earthquake families, revealed by our analysis, provide additional evidence that Agung was entering a new phase of unrest close to 12 November. Almost all (54 of 65) earthquake families from the Intrusion Phase ceased on or shortly after 12 November, when the appearance of LF earthquakes marked the start of new families. This suggests that as magma started to move toward the summit around 12 November (Albino et al., 2018), the effective shear to normal stress ratio on faults surrounding the dike, located NE of the summit, decreased, unloading these faults. The short duration of the families born on 12 November suggests that the source processes and locations for these earthquakes were ephemeral and likely represent an intermediary step between magma intrusion into the dike and shallow magmatic activity closer to the summit. The relative lack of seismicity during this time period (all the way up to and through the beginning stages of the eruption; see next section) suggests that the crust under the summit was much hotter and more ductile than originally assumed due to the fact that the volcano had not erupted in 50 years.

Interpreting subtle changes in seismicity during a crisis is often difficult. Any additional line of evidence that suggests a change can help clarify the state of the system. Thus, observed changes in earthquake families may not be a diagnostic indication of magma movement toward the surface, but they can lend confidence to other observations.

Eruptive Phase (15 November–End of Study)

The first phreatomagmatic eruption did not occur until 21 November, and lava effusion did not begin until 25 November, but characteristics of earthquake families changed as early as 15 November and persisted throughout the eruptive phase of the eruption. A large majority of earthquakes after this date (86%) are orphans. The BMKG catalog includes 15 earthquakes from this time period, most of which were located on the N to NE side of the mountain, but CVGHM staff noted that many of the smaller earthquakes appeared to be located shallowly and near the summit based on their waveforms. These earthquakes included both brittle failure VT earthquakes and LF earthquakes (Syahbana et al., 2019). One possible explanation is that these earthquakes occurred at shallow levels on a network of new cracks that was created by continually destructive processes. Following this model, waveforms became much more complex and less similar to other waveforms leading to a drastically smaller percentage of seismicity represented by repeating earthquakes as magma/water interaction occurred along the evolving pathway in the few kilometers below the summit.

Families that do appear during this phase tend to be long-lived. As pathways are developed and magma is able to migrate toward the surface, the few repetitive sources that exist remain stable. At Mount Agung, these sources remain stable despite significant changes in behavior at the surface including periods of continuous ash emission, discrete explosions, Strombolian activity, and a drastic decrease in eruptions in mid-January 2018 (**Figure 2** in Syahbana et al., 2019). This is consistent with observations by Green and Neuberg (2006) and Thelen et al. (2011) where earthquake families during the eruptive phase of eruptions at Soufriere Hills, Mount St. Helens, and Bezymianny persisted through small explosions and collapses of the dome. In those systems, it is likely that the earthquakes were located deep enough to not be affected by small explosions and dome collapse at the surface.

The swarm of 21 larger LF earthquakes (peak energy ~2 Hz) that occurred on 25 November is one notable exception to the general trend of long-lived families during the eruptive phase. Lasting only 90 minutes, these earthquakes represent a temporarily stable seismic source associated with the magma's final push to the summit. Satellite observations confirm that lava effusion into the summit crater first started sometime on 25 November, but there are no direct visual observations that allow us to note the exact time of onset (Syahbana et al., 2019). Thus, we can only say that this swarm is roughly coincident with the first magmatic explosions and the appearance of lava at the surface. It is possible that these earthquakes are the manifestation of gas escape around the plug or shallow magma movement prior to or coincident with the onset of lava effusion at the surface. The pattern of repetitive co-eruptive seismicity or repetitive inter-eruption seismicity is common at frequently active, volcanic systems that are open to degassing (e.g., White and McCausland, 2019). The repeating waveforms are commonly attributed to conduit convection and bubble bursts, either at the surface or in the conduit (e.g., Caplan-Auerbach and Petersen, 2005), resonance associated with gas flow through the conduit (e.g., Chouet, 1996; Molina et al., 2008; Lyons et al., 2016), or stick-slip processes in a hot, viscous environment (e.g., Iverson et al., 2006).

After the initial emplacement of lava at the surface and the swarm of 21 LFs, extrusion rates remained high, emplacing 24 million m^3 of lava within less than a week. The surface of the lava flow was punctuated by a series of near continuous explosions, but the explosion craters were quickly filled in and covered by newly extruded lava (Syahbana et al., 2019). Earthquake rates during this period of high extrusion, however, remained low with very little repetitive seismicity. On 5 December, the rate of ash explosions decreased, and cracks began to appear on the surface of the lava dome as effusion rates slowed. At this same time, new families begin to occur, and orphans became notably more LF although earthquakes in families did not shift frequency content (**Figure 2**).

We interpret the relative lack of seismicity during the highest rates of effusion followed by the increased rate of LF earthquakes as effusion slowed as a manifestation of the rate-dependent nature of seismicity in a conduit (Dmitrieva et al., 2013). Changes in magma viscosity may have also played a role, but this information is not available at this time. As lava cooled at the surface and restricted flow through the conduit, pressure increased, which allowed more repetitive earthquakes to occur.

THE ROLE OF REPEATING EARTHQUAKES IN REAL-TIME ERUPTION FORECASTING

Although our study was completed retrospectively, we can speculate on the role of our analysis in real-time eruption forecasting. In general, the operational value of repeating earthquakes depends on the ability to recognize patterns and interpret the processes that drive those patterns. This depends, in part, on the characteristics of the crust, the conduit, and the magma itself. It also depends on the availability of seismic records from past eruptions because volcanoes can display similar precursors to multiple eruptions.

Traditionally, seismologists rely on metrics such as earthquake rates, amplitudes, and frequency-based classifications to interpret unrest at a particular volcano. Repeating earthquake analyses provide additional metrics—such as the repeater percentage of total seismicity, the number of concurrent families, and the longevity of each family—that can aid the interpretation of unrest.

We are generally successful at detecting and alarming on the precursors we expect to see, while we are far less successful if we do not know what to expect from a volcano. Automatic detection of changes in repeating earthquakes could be an exceptionally valuable tool for eruption forecasting at well-understood volcanoes. For example, some studies suggest that certain sequences may be alarmable. Explosions at Volcán de Colima in 2004–2005 (Arámbula-Mendoza et al., 2011) and at Augustine in 2006 (Buurman and West, 2010) were preceded by diagnostic occurrences of certain earthquake families. In addition, cyclic patterns of dome deflation at Soufrière Hills in 1997 were preceded by the same pattern of repeating earthquakes (Green and Neuberg, 2006).

Repeating earthquakes have been most well-studied during episodes of dome growth, thus providing several models and common observations to explain their occurrence. For example, Thelen et al. (2011) note that earthquake families tended to be longer-lived during stable phases of effusion across multiple eruptions at Mount St. Helens and Bezymianny. This is consistent with our observation of relatively long-lived families after lava extruded at Agung.

Although repeating earthquakes have been most well-studied at domes, earthquake sources repeat throughout the crust beneath volcanoes of all types. Therefore, all phases of unrest that produce seismicity are likely to produce repeating seismicity. When we lack a clear paradigm for eruption precursors at a volcano, we interpret repeating earthquakes by applying generic models that incorporate knowledge of the magma properties, the stability of the conduit and degassing pathways, and the overall geomechanics of the crust. For example, increasing numbers of VT earthquake families at a closed-system volcano, particularly in combination with increasing seismic amplitudes, may be a concerning sign of pressurization of the edifice as more faults are activated. In contrast, increasing numbers or amplitudes of LP earthquakes within stable earthquake families at a volcano open to degassing, may simply mean that the degassing rate has increased without a significant increase in the overall hazard. Or during an intrusive phase of unrest, for example, rapidly changing sets of earthquake families may indicate migrating magma, while stable earthquake family may indicate rapid reloading of shear-stress on the same faults.

At Agung, little was known about crustal and conduit conditions or about seismicity associated with prior eruptions. However, clear changes in repeating earthquakes—such as those on 12 November and 15 November—could have given observatory scientists an indication that the volcanic system was evolving when other monitoring parameters were stable. This could have increased vigilance and encouraged more cross disciplinary discussion of the volcano's current state. During a protracted unrest sequence, such as this one, scientist fatigue can be a significant problem, and any clear indication of meaningful changes in monitoring parameters is an advantage.

CONCLUSION

Seismicity is often the most readily available data stream for tracking unrest during volcanic crizes. Interpreting changes in earthquake rates, earthquake magnitudes, earthquake classifications, and RSAM has led to many successful forecasts. When unrest does not progress in a traditional pattern, however, relying on these metrics leads to uncertainty. In these scenarios, other tools add value. We analyzed the evolution of earthquake families with time during the Mount Agung volcanic crisis. We find that when considered in context of other observations, the time history of earthquake families provides insight into the evolution of the stress distribution in the volcanic edifice, the development of the volcanic conduit, and seismogenesis of magma effusion.

CVGHM staff noted the new appearance of volcanic tremor—nominally a harbinger for an evolving magmatic system—on 12 November 2017 after months of elevated seismicity at Mount Agung, but volcanic tremor and LF seismicity were subtle and earthquake rates were not high compared to prior months. Thus, the time frame over which to expect eruption remained uncertain.

Our retrospective study shows that earthquake families that dominated seismicity during the early stages of unrest ceased near the onset of tremor, highlighting that stress in the crust had been re-distributed as magma migrated toward the summit. Furthermore, earthquake families at Mount Agung took on characteristics commonly observed during effusive phases of eruptions on 15 November—a full six days before the first phreatomagmatic eruption on 21 November 2017 and a full ten days prior to the first magmatic eruption on 25 November 2017.

It is feasible to conduct advanced analyses like this in near-real time thanks to the availability of high-quality open-source codes written by the seismology community in recent years. This study demonstrates how analyzing earthquake families can be used to improve future eruption-response efforts.

DATA AVAILABILITY STATEMENT

The data analyzed in this study is subject to the following licenses/restrictions: They may not be used without the permission of

Indonesia's Center for Volcanology and Geologic Hazard Mitigation. Requests to access these datasets should be directed to pvmbg@esdm.go.id.

AUTHOR CONTRIBUTIONS

JW conducted the analysis. DK and SP helped guide the direction of the study, and SP made many contributions to the prose. All authors provided critical insights that shaped this work.

FUNDING

This work was born of the collaboration between Indonesia's Center for Volcanology and Geologic Hazard Mitigation (CVGHM) and the Volcano Disaster Assistance Program (VDAP). CVGHM receives funding from the Ministry of Energy and Mineral Resources of the Republic of Indonesia, and VDAP receives funding from the USAID Bureau of Humanitarian Assistance and the USGS Volcano Hazards Program.

ACKNOWLEDGMENTS

Jeremy Pesicek, Mike Poland, Jake Lowenstern, Alicia Hotovec-Ellis, and Aaron Wech provided feedback on the manuscript that improved the quality of this work. Thoughtful reviews from Wes Thelen and two journal reviewers also improved the final product. We'd like to thank Alicia Hotovec-Ellis for answering questions about REDPy and maintaining the code. Numerous people provided support in the field and the office during the crisis in 2017–2018 that facilitated the response to the eruption and ultimately made this work possible.

SUPPLEMENTARY MATERIAL

The Supplementary Material for this article can be found online at: https://www.frontiersin.org/articles/10.3389/feart.2021.653164/full#supplementary-material

Supplementary Figure 1 | This figure shows the waveform similarity within a given family and the dissimilarity of waveforms across families. The top of the figure shows a zoomed in look (~5 sec) of all waveforms from station TMKS (**Figure 1**) that make up Family #78. This is a family of 21 low-frequency earthquakes that occurred on 25 November roughly coincident with the onset of lava extrusion at the surface (**Figure 2**). The thick black line represents the stack from station TMKS, and the think grey lines show each individual earthquake in the family. The bottom of the figure shows the stacked waveform for the largest earthquake families in the study (20+ members). Each stack was computed from station TMKS. The family number (corresponding to the y-axis on **Figure 2**) is listed to the left of each waveform, and the frequency index for the stack at TMKS is listed to the right of each waveform. In this study, a frequency index above 0 indicates a volcano-tectonic earthquake, and a frequency index below 0 indicates a low-frequency earthquake. See text for details. All signals were band-pass filtered between 1–10 Hz on station TMKS before being stacked.

REFERENCES

Albino, F., Biggs, J., and Syahbana, D. K. (2018). Dyke Intrusion between Neighbouring Arc Volcanoes Responsible for 2017 Pre-eruptive Seismic Swarm at Agung. *Nat. Commun.* 10 (1), 748. doi:10.1038/s41467-019-08564-9

Arámbula-Mendoza, R., Lesage, P., Valdés-González, C., Varley, N. R., Reyes-Dávila, G., and Navarro, C. (2011). Seismic activity that accompanied the effusive and explosive eruptions during the 2004-2005 period at Volcán de Colima, Mexico. *J. Volcanol. Geothermal Res.* 205 (1–2), 30–46. doi:10.1016/j.jvolgeores.2011.02.009

Barton, C. A., Zoback, M. D., and Moos, D. (1995). Fluid Flow along Potentially Active Faults in Crystalline Rock. *Geol*, 23(8), 683. doi:10.1130/0091-7613(1995)023<0683:FFAPAF>2.3.CO;2

Boué, A., Lesage, P., Cortés, G., Valette, B., and Reyes-Dávila, G. (2015). Real-time Eruption Forecasting Using the Material Failure Forecast Method with a Bayesian Approach. *J. Geophys. Res. Solid Earth* 120 (4), 2143–2161. doi:10.1002/2014jb011637

Budi-Santoso, A., and Lesage, P. (2016). Velocity Variations Associated with the Large 2010 Eruption of Merapi Volcano, Java, Retrieved from Seismic Multiplets and Ambient Noise Cross-Correlation. *Geophys. J. Int.* 206 (1), 221–240. doi:10.1093/gji/ggw145

Buurman, H., West, M. E., and Roman, D. C. (2013). Using Repeating Volcano-Tectonic Earthquakes to Track Post-eruptive Activity in the Conduit System at Redoubt Volcano, Alaska. *Geology* 41 (4), 511–514. doi:10.1130/g34089.1

Buurman, H., and West, M. E. (2010). "Seismic Precursors to Volcanic Explosions during the 2006 Eruption of Augustine Volcano," in *The 2006 Eruption of Augustine Volcano, Alaska*. Editors J. A. Power, M. L. Coombs, and J. T. Freymueller (U.S. Geological Survey). Chapter 2.

Cameron, C. E., Prejean, S. G., Coombs, M. L., Wallace, K. L., Power, J. A., and Roman, D. C. (2018). Alaska Volcano Observatory Alert and Forecasting Timeliness: 1989–2017. *Front. Earth Sci.* 6, 86. doi:10.3389/feart.2018.00174

Caplan-Auerbach, J., and Petersen, T. (2005). Repeating Coupled Earthquakes at Shishaldin Volcano, Alaska. *J. Volcanology Geothermal Res.* 145 (1–2), 151–172. doi:10.1016/j.jvolgeores.2005.01.011

Chouet, B. A. (1996). "New Methods and Future Trends in Seismological Volcano Monitoring," in *Monitoring and Mitigation of Volcano Hazards*. Editors R. Scarpa and R. I. Tilling (Berlin: Springer), 23–97. doi:10.1007/978-3-642-80087-0_2

Chouet, B. A., Page, R. A., Stephens, C. D., Lahr, J. C., and Power, J. A. (1994). Precursory Swarms of Long-Period Events at Redoubt Volcano (1989-1990), Alaska: Their Origin and Use as a Forecasting Tool. *J. Volcanol. Geothermal Res.* 62 (1–4), 95–135. doi:10.1016/0377-0273(94)90030-2

Deshon, H. R., Thurber, C. H., and Power, J. A. (2010). Earthquake Waveform Similarity and Evolution at Augstine Volcano from 1993 to 2006. in *The 2006 Eruption of Augustine Volcano, Alaska*. Editors J. A. Power, M. L. Coombs, and J. T. Freymueller (U.S. Geological Survey Professional Paper 1769). Chapter 5

Dmitrieva, K., Hotovec-Ellis, A. J., Prejean, S., and Dunham, E. M. (2013). Frictional-faulting Model for Harmonic Tremor before Redoubt Volcano Eruptions. *Nat. Geosci* 6 (8), 652–656. doi:10.1038/ngeo1879

Dziewonski, A. M., Chou, T.-A., and Woodhouse, J. H. (1981). Determination of Earthquake Source Parameters from Waveform Data for Studies of Global and Regional Seismicity. *J. Geophys. Res.* 86, 2825–2852. doi:10.1029/JB086iB04p02825

Ekström, G., Nettles, M., and Dziewoński, A. M. (2012). The Global CMT Project 2004-2010: Centroid-Moment Tensors for 13,017 Earthquakes. *Phys. Earth Planet. Interiors* 200-201, 1–9. doi:10.1016/j.pepi.2012.04.002

Endo, E. T., Malone, S. D., Noson, L. L., and Weaver, C. S. (1981). "Locations, Magnitudes, and Statistics of the March 20–May 18 Earthquake Sequence," in *The 1980 Eruption of Mount St. Helens*. Editors P. W. Lipman and D. R. Mullineaux (Washington, U.S: Geological Survey Professional Paper 1250).

Endo, E. T., and Murray, T. (1991). Real-time Seismic Amplitude Measurement (RSAM): a Volcano Monitoring and Prediction Tool. *Bull. Volcanol* 53 (7), 533–545. doi:10.1007/bf00298154

Geller, R. J., and Mueller, C. S. (1980). Four Similar Earthquakes in Central California. *Geophys. Res. Lett.* 7 (10), 821–824. doi:10.1029/gl007i010p00821

Green, D. N., and Neuberg, J. (2006). Waveform Classification of Volcanic Low-Frequency Earthquake Swarms and its Implication at Soufrière Hills Volcano, Montserrat. *J. Volcanology Geothermal Res.* 153 (1–2), 51–63. doi:10.1016/j.jvolgeores.2005.08.003

Harlow, D. H., Power, J. A., Laguerta, E. P., Ambubuyog, G., White, R. A., and Hoblitt, R. P. (1996). "Precursory Seismicity and Forecasting of the June 15, 1991, Eruption of Mount Pinatubo," in *Fire and Mud: Eruptions and Lahars of Mount Pinatubo, Philippines*. Editors C. G. Newhall and R. S. Punongbayan (University of Washington Press).

Hotovec-Ellis, A. J., and Jeffries, C. (2016). Near Real-Time Detection, Clustering, and Analysis of Repeating Earthquakes: Application to Mount St. Helens and Redoubt Volcanoes. Available at: https://github.com/ahotovec/REDPy (Accessed December 31, 2019).

Iverson, R. M., Dzurisin, D., Gardner, C. A., Gerlach, T. M., LaHusen, R. G., Lisowski, M., et al. (2006). Dynamics of Seismogenic Volcanic Extrusion at Mount St Helens in 2004-05. *Nature* 444 (7118), 439–443. doi:10.1038/nature05322

Klein, F. W. (1984). Eruption Forecasting at Kilauea Volcano, Hawaii. *J. Geophys. Res.* 89, 3059-3074. doi:10.1029/JB089iB05p03059

Kusmandinata (1964). The Eruption of the Agung Volcano in Bali in 1963. *Bull. Geol.Surv. Indonesia* (1.1), 12–15.

Lyons, J. J., Haney, M. M., Werner, C., Kelly, P., Patrick, M., Kern, C., et al. (2016). Long Period Seismicity and Very Long Period Infrasound Driven by Shallow Magmatic Degassing at Mount Pagan, Mariana Islands. *J. Geophys. Res. Solid Earth* 121 (1), 188–209. doi:10.1002/2015jb012490

Malone, S. D., Boyko, C., and Weaver, C. S. (1983). Seismic Precursors to the Mount St. Helens: Eruptions in 1981 and 1982. *Science* 221 (4618), 1376–1378. doi:10.1126/science.221.4618.1376

Matoza, R. S., Chouet, B. A., Dawson, P. B., Shearer, P. M., Haney, M. M., Waite, G. P., et al. (2015). Source Mechanism of Small Long-Period Events at Mount St. Helens in July 2005 Using Template Matching, Phase-Weighted Stacking, and Full-Waveform Inversion. *J. Geophys. Res. Solid Earth* 9 (120), 6351–6364. doi:10.1002/2015JB012279

Matoza, R. S., and Chouet, B. A. (2010). Subevents of Long-Period Seismicity: Implications for Hydrothermal Dynamics during the 2004–2008 Eruption of Mount St. Helens. *J. Geophys. Res.* 115 (B12), B12206. doi:10.1029/2010jb007839

McCausland, W. A., Gunawan, H., White, R. A., Indrastuti, N., Patria, C., Suparman, Y., et al. (2019). Using a Process-Based Model of Pre-eruptive Seismic Patterns to Forecast Evolving Eruptive Styles at Sinabung Volcano, Indonesia. *J. Volcanology Geothermal Res.* 382, 253–266. doi:10.1016/j.jvolgeores.2017.04.004

McNutt, S. R. (1996). "Seismic Monitoring and Eruption Forecasting of Volcanoes: A Review of the State-Of-The-Art and Case Histories," in *Monitoring and Mitigation of Volcano Hazards*. Editors R. Scarpa and R. I. Tilling (Berlin: Springer), 99–146. doi:10.1007/978-3-642-80087-0_3

Minakami, T. (1974). "Seismology of Volcanoes in Japan," in *Physical Volcanology*. Editors L. Civetta, P. Gasparini, G. Luongo, and A. Rapolla (Berlin: Amsterdam), 6, 1–27. doi:10.1016/b978-0-444-41141-9.50007-3

Molina, I., Kumagai, H., García-Aristizábal, A., Nakano, M., and Mothes, P. (2008). Source Process of Very-Long-Period Events Accompanying Long-Period Signals at Cotopaxi Volcano, Ecuador. *J. Volcanol. Geothermal Res.* 176 (1), 119–133. doi:10.1016/j.jvolgeores.2007.07.019

Power, J. A., and Lalla, D. J. (2010). "Seismic Observations of Augustine Volcano, 1970-2007," in *The 2006 Eruption of Augustine Volcano, Alaska*. Editors J. A. Power, M. L. Coombs, and J. T. Freymueller (U.S. Geological Survey Professional Paper 1769).Chapter 1

Rodgers, M., Roman, D. C., Geirsson, H., LaFemina, P., McNutt, S. R., Muñoz, A., et al. (2015). Stable and Unstable Phases of Elevated Seismic Activity at the Persistently Restless Telica Volcano, Nicaragua. *J. Volcanol. Geothermal Res.* 290, 63–74. doi:10.1016/j.jvolgeores.2014.11.012

Rodgers, M., Roman, D. C., Geirsson, H., LaFemina, P., Muñoz, A., Guzman, C., et al. (2013). Seismicity Accompanying the 1999 Eruptive Episode at Telica Volcano, Nicaragua. *J. Volcanol. Geothermal Res.* 265, 39–51. doi:10.1016/j.jvolgeores.2013.08.010

Rowe, C., Thurber, C., and White, R. (2004). Dome Growth Behavior at Soufriere Hills Volcano, Montserrat, Revealed by Relocation of Volcanic Event Swarms, 1995–1996. *J. Volcanol. Geothermal Res.* 134 (3), 199–221. doi:10.1016/j.jvolgeores.2004.01.008

Ruppert, N. A., Prejean, S. G., and Hansen, R. A. (2011). Seismic Swarm Associated with the 2008 Eruption of Kasatochi Volcano, Alaska: Earthquake Locations and Source Parameters. *J. Geophys. Res. Solid Earth* 116 (B2), 1–8. doi:10.1029/2010JB007435@10.1002/(ISSN)2169-8996

Sahara, D. P., Rahsetyo, P. P., Nugraha, A. D., Syahbana, D. K., Widiyantoro, S., Zulfakriza, Z., et al. (2021). Use of Local Seismic Network in Analysis of Volcano-Tectonic (VT) Events Preceding the 2017 Agung Volcano Eruption. *Front. Earth Sci.*. This issue. 10.3389/feart.2021.619801.

Soosalu, H., Einarsson, P., and Porbjarnardóttir, B. S. (2005). Seismic Activity Related to the 2000 Eruption of the Hekla Volcano, Iceland. *Bull. Volcanol.* 68 (1), 21–36. doi:10.1007/s00445-005-0417-7

Stephens, C. D., and Chouet, B. A. (2001). Evolution of the December 14, 1989 Precursory Long-Period Event Swarm at Redoubt Volcano, Alaska. *J. Volcanol. Geothermal Res.* 109 (1–3), 133–148. doi:10.1016/s0377-0273(00)00308-5

Supendi, P., Nugraha, A. D., Widiyantoro, S., Pesicek, J. D., Thurber, C. H., Abdullah, C. I., et al. (2020). Relocated Aftershocks and Background Seismicity in Eastern Indonesia Shed Light on the 2018 Lombok and Palu Earthquake Sequences. *Geophys. J. Int.* 221 (3), 1845–1855. doi:10.1093/gji/ggaa118

Swanson, D. A., Casadevall, T. J., Dzurisin, D., Holcomb, R. T., Newhall, C. G., Malone, S. D., et al. (1985). Forecasts and Predictions of Eruptive Activity at Mount St. Helens, USA: 1975-1984. *J. Geodynamics* 3 (3–4), 397–423. doi:10.1016/0264-3707(85)90044-4

Syahbana, D. K., Kasbani, K., Suantika, G., Prambada, O., Andreas, A. S., Saing, U. B., et al. (2019). The 2017–19 Activity at Mount Agung in Bali (Indonesia): Intense Unrest, Monitoring, Crisis Response, Evacuation, and Eruption. *Sci. Rep.* 9 (1), 8848. doi:10.1038/s41598-019-45295-9

Thelen, W., Malone, S., and West, M. (2011). Multiplets: Their Behavior and Utility at Dacitic and Andesitic Volcanic Centers. *J. Geophys. Res.* 116 (B8), B08210. doi:10.1029/2010jb007924

Townend, J., and Zoback, M. D. (2000). How Faulting Keeps the Crust Strong. *Geology* 28 (5), 399. doi:10.1130/0091-7613(2000)28<399:HFKTCS>2.0.CO;2

Umakoshi, K., Takamura, N., Shinzato, N., Uchida, K., Matsuwo, N., and Shimizu, H. (2008). Seismicity Associated with the 1991–1995 Dome Growth at Unzen Volcano, Japan. *J. Volcanol. Geothermal Res.* 175 (1–2), 91–99. doi:10.1016/j.jvolgeores.2008.03.030

Voight, B. (1988). A Method for Prediction of Volcanic Eruptions. *Nature* 332 (6160), 125–130. doi:10.1038/332125a0

Waite, G. P., Chouet, B. A., and Dawson, P. B. (2008). Eruption Dynamics at Mount St. Helens Imaged from Broadband Seismic Waveforms: Interaction of the Shallow Magmatic and Hydrothermal Systems. *J. Geophys. Res.* 113 (B2), B02305. doi:10.1029/2007jb005259

White, R. A., and McCausland, W. A. (2019). A Process-Based Model of Pre-eruption Seismicity Patterns and its Use for Eruption Forecasting at Dormant Stratovolcanoes. *J. Volcanol. Geothermal Res.* 382, 267–297. doi:10.1016/j.jvolgeores.2019.03.004

White, R. A., and McCausland, W. A. (2016). Volcano-tectonic Earthquakes: A New Tool for Estimating Intrusive Volumes and Forecasting Eruptions. *J. Volcanol. Geothermal Res.* 309, 139–155. doi:10.1016/j.jvolgeores.2015.10.020

White, R. S., Drew, J., Martens, H. R., Key, J., Soosalu, H., and Jakobsdóttir, S. S. (2011). Dynamics of Dyke Intrusion in the Mid-crust of Iceland. *Earth Planet Sci Lett* 304, 300-312. doi:10.1016/j.epsl.2011.02.038

Conflict of Interest: The authors declare that the research was conducted in the absence of any commercial or financial relationships that could be construed as a potential conflict of interest.

Copyright © 2021 Wellik, Prejean and Syahbana. This is an open-access article distributed under the terms of the Creative Commons Attribution License (CC BY). The use, distribution or reproduction in other forums is permitted, provided the original author(s) and the copyright owner(s) are credited and that the original publication in this journal is cited, in accordance with accepted academic practice. No use, distribution or reproduction is permitted which does not comply with these terms.

frontiers in Earth Science

ORIGINAL RESEARCH
published: 20 May 2021
doi: 10.3389/feart.2021.619801

Use of Local Seismic Network in Analysis of Volcano-Tectonic (VT) Events Preceding the 2017 Agung Volcano Eruption (Bali, Indonesia)

David P. Sahara[1], Puput P. Rahsetyo[2], Andri Dian Nugraha[1,3], Devy Kamil Syahbana[4], Sri Widiyantoro[1,5], Zulfakriza Zulfakriza[1,3], Ardianto Ardianto[2], Aria W. Baskara[2], Shindy Rosalia[1], Martanto Martanto[2,4] and Haunan Afif[4]*

[1] Global Geophysics Research Group, Faculty of Mining and Petroleum Engineering, Institut Teknologi Bandung, Bandung, Indonesia, [2] Department of Geophysical Engineering, Faculty of Mining and Petroleum Engineering, Institut Teknologi Bandung, Bandung, Indonesia, [3] Center for Earthquake Science and Technology, Research Center for Disaster Mitigation, Institut Teknologi Bandung, Bandung, Indonesia, [4] Center for Volcanology and Geological Hazards Mitigation, Geological Agency, Ministry of Energy and Mineral Resources, Bandung, Indonesia, [5] Faculty of Engineering, Maranatha Christian University, Bandung, Indonesia

OPEN ACCESS

Edited by:
Jessica Helen Johnson,
University of East Anglia,
United Kingdom

Reviewed by:
Yosuke Aoki,
The University of Tokyo, Japan
Aude Lavayssière,
UMR 7154 Institut de Physique du Globe de Paris (IPGP), France

***Correspondence:**
Andri Dian Nugraha
nugraha@gf.itb.ac.id;
andridn104@gmail.com

Specialty section:
This article was submitted to Volcanology, a section of the journal Frontiers in Earth Science

Received: 21 October 2020
Accepted: 20 April 2021
Published: 20 May 2021

Citation:
Sahara DP, Rahsetyo PP, Nugraha AD, Syahbana DK, Widiyantoro S, Zulfakriza Z, Ardianto A, Baskara AW, Rosalia S, Martanto M and Afif H (2021) Use of Local Seismic Network in Analysis of Volcano-Tectonic (VT) Events Preceding the 2017 Agung Volcano Eruption (Bali, Indonesia). Front. Earth Sci. 9:619801. doi: 10.3389/feart.2021.619801

This study provides an attempt to analyze the pre-eruptive seismicity events for volcano eruption forecasting. After more than 50 years of slumber, Agung volcano on Bali Island erupted explosively, starting on November 21, 2017. The eruption was preceded by almost 2 months of significant increase of recorded seismicity, herein defined as "seismic crisis." Our study provides the first analysis of VT events using data from eight local seismic stations deployed by the Center for Volcanology and Geological Hazard Mitigation of Indonesia (CVGHM) to monitor the Agung Volcano activity. In total, 2,726 Volcano-Tectonic (VT) events, with 13,023 P waves and 11,823 S wave phases, were successfully identified between October 18 and November 30, 2017. We increased the accuracy of the hypocenter locations of these VT events using a double-difference (DD) relative relocation and a new velocity model appropriate to the subsurface geological conditions of Agung volcano. We found two types of seismicity during the recording period that represent the VT events relating to fracture network reactivation due to stress changes (during the seismic crisis) and magma intrusion (after the seismic crisis). The characteristics of each event type are discussed in terms of Vp/Vs values, phase delay times, seismic cluster shapes, and waveform similarity. We interpret that the upward migrating magma reached a barrier (probably a stiff layer) which prohibited further ascent. Consequently, magma pressurized the zone above the magma chamber and beneath the barrier, reactivated the fracture zone between Agung and Batur volcanoes, and caused the seismic crisis since September 2017. In early November 2017, the barrier was finally intruded, and magma and seismicity propagated toward the Agung summit. This reconstruction provides a better depth constraint as to the previous conceptual models and explains the long delay (∼10 weeks) between the onset of the seismic crisis and the eruption. The distinction between the fracture reactivation and

magma intrusion VT events observed in this study is significant for eruption forecasting and understanding the subsurface structure of the magmatic system. Based on the results obtained in this study, we emphasize the importance of prompt analysis (location and basic seismic characteristics) of the seismic crisis preceding the Agung eruption.

Keywords: volcano-tectonic events, volcano monitoring, magma migration, 2017 Agung eruption, volcano seismology, Mt. Agung, seismic crisis

INTRODUCTION

Volcanic earthquakes occur as magma rises to the surface from depth, a condition that involves significant stress changes in the crust as the material migrates upward (White and McCausland, 2016). Therefore, during unrest volcanologists detect seismic signature variations in the type, location, and intensity of seismic activity. The interpretation of seismic signature during unrest may be supportive in assessing the eruption probability, as exemplified at various volcanoes, e.g., Pinatubo (1991), Unzen (1989–1995), Cotopaxi (2001), Popocatepetl (2001–2003), Mauna Loa (1984), Taal (2010), and others (Zobin, 2012; Zlotnicki et al., 2018). In general, however, it remains difficult for volcanologists to forecast an eruption precisely. This study intends to analyze the Volcano-Tectonic (VT) seismicity events as a possible indicator for forecasting eruptions.

Agung is one of the most active volcanoes in Indonesia and is located on the island of Bali. After more than 50 years of slumber, Agung Volcano erupted explosively on November 21, 2017 (PVMBG, 2017; Albino et al., 2019; Syahbana et al., 2019; Gunawan et al., 2020). The last major eruption happened in 1963; with a VEI 5, it was described as one of the largest eruptions in the twentieth century (Zen and Hadikusumo, 1964). It is suggested that the 1963 eruption affected global climate (Cadle et al., 1976; Hansen et al., 1978; Self et al., 1981; Rampino and Self, 1982; Self and Rampino, 2012). The eruption caused the tragic death of more than 1,000 people, mostly as a result of the high-speed pyroclastic flows on the volcano's southern and northern slopes, which swept over nearby settlements (Kusumadinata, 1964).

The 2017 eruption followed a "seismic crisis" that culminated in September 2017 when local earthquakes numbered more than 800 events per day (Albino et al., 2019; Syahbana et al., 2019; Gunawan et al., 2020). Due to the increasing seismicity, the Center for Volcanology and Geological Hazard Mitigation of Indonesia (CVGHM) raised the volcanic alert level (VAL) to Level 2 on September 14, 2017, this then went to Level 3 on September 18, 2017, as seismicity continued to accelerate rapidly; the Real-time Seismic Amplitude Measurements (RSAM) values peaked on September 22, 2017, prompting the CVGHM to elevate the VAL to Level 4 (the highest level). This crisis triggered the evacuation of over 140,000 people within an area of 9–12 km from the volcano's summit (Syahbana et al., 2019). Due to a decrease in daily seismic event rates, the CVGHM lowered the VAL to Level 3 on October 29, 2017.

It is worth noting that, although seismic unrest peaked in September, the volcano did not erupt until November 2017 (Syahbana et al., 2019). The eruption eventually started on November 21, 2017; a series of phreatomagmatic explosions and high SO_2 emissions continued. The most intense explosive eruptions with accompanying rapid lava effusion occurred during the period of 25–29 November 2017.

The relatively long delay between the seismic swarm and the eruptions caused considerable challenges to CVGHM and the populace living near the volcano. During the crisis, the rate of VT events surrounding Agung volcano and RSAM were calculated using TMKS and PSAG seismic stations (**Figure 1**). At the beginning of the crisis, only two seismic stations were available; therefore, an estimation of the location and source mechanisms of the seismic events could not be performed. The CVHM responded rapidly by installing more seismic stations. By October 18, 2017, another six stations had been successfully installed, forming a better seismic monitoring network around the volcano. Given the peculiar characteristics of the seismic patterns before the 2017 Agung eruption, localization of VT events prior to the 2017 eruption could help researchers better understand the magma migration process.

So far, there is no published catalog of VT events preceding the Agung 2017 eruption obtained using the local seismic network. Previous publications employed the regional Indonesian Meteorological, Climatological, and Geophysical Agency (BMKG) catalog in analyzing the magma migration beneath Agung Volcano, e.g., Syahbana et al. (2019) used catalog from BMKG as one of the inputs for their conceptual model, and later Gunawan et al. (2020) relocated the BMKG catalog using the double-difference method. In this study, for the first time, we processed the recorded waveform data of the local CVGHM seismic station network and estimated the hypocenter locations of VT events preceding the 2017 eruption. The identified VT event arrival times were manually picked. Hypocenter accuracy was improved using the updated velocity model, which is suitable for the subsurface condition of Agung, and by applying the double-difference relocation technique. A waveform cross-correlation was also conducted to give a better constraint of the event locations. Our study produced a catalog of VT events preceding the 2017 Agung eruption that can be further used to improve the Agung conceptual model and reveal the magma migration processes that led to the eruption.

AGUNG VOLCANO

History of Agung Eruption

The recorded history of the Agung volcano eruption could date back to 1808, based on geological samples of eruptions in the form of ashfall and pumice (PVMBG, 2014). Eruptions occurred again in 1821 and 1843. After that, Agung was in a

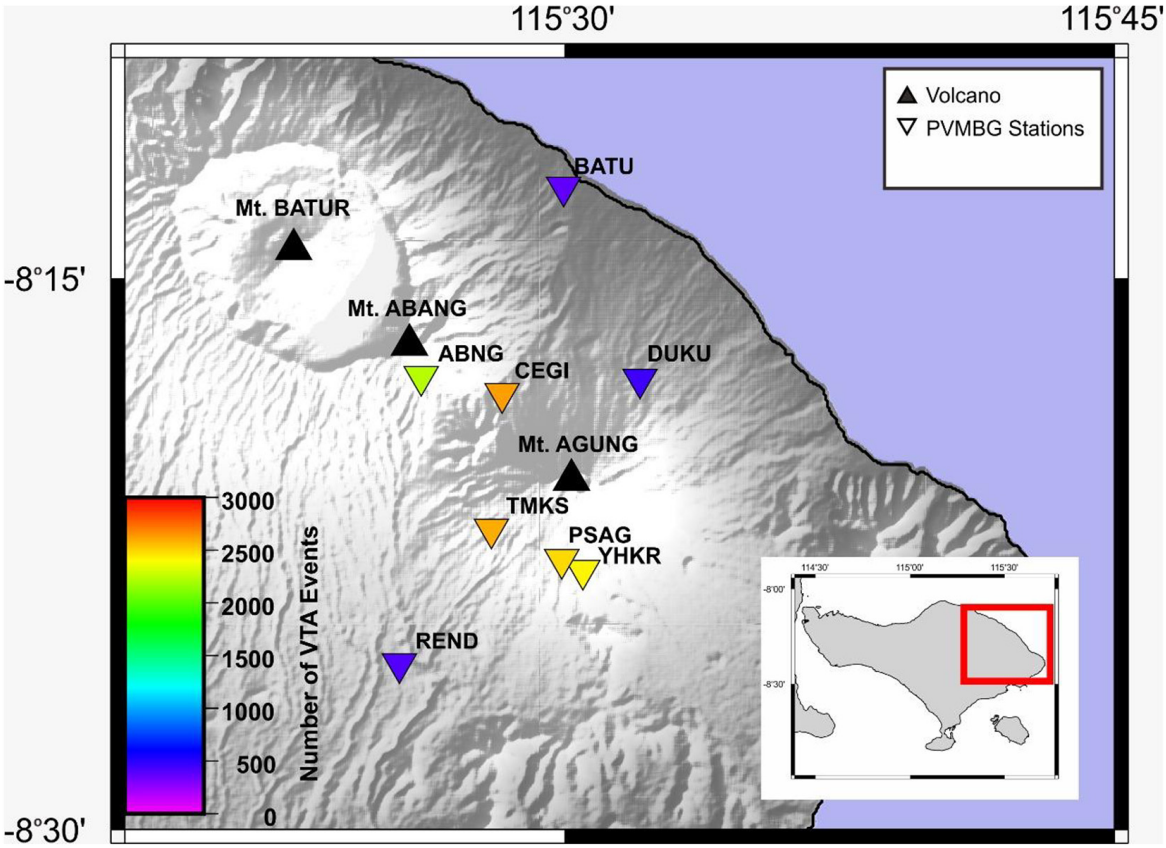

FIGURE 1 | Map of the eight local permanent stations deployed by CVGHM to monitor activity at Mt. Agung (inverted triangles). The number of detected VT events at each station during the study period is represented in a color scale. Black triangles show Agung, Abang, and Batur volcanoes. Inserted map shows Bali Island.

dormancy stage until the 1963 eruption, which was one of its most powerful eruptions.

The significant eruptions in 1963 occurred twice: on March 17 and May 16, 1963, with an explosivity level of VEI 4+ (Fontijn et al., 2015). The column of the eruption reached more than 20 km above the summit of Agung. This eruption had a considerable impact on global climate as it ejected about 6.2 Mt (million metric tons, or 1012 grams) of SO_2 into the stratosphere (Rampino and Self, 1982; Self and Rampino, 2012; Fontijn et al., 2015), causing reduced sunlight and a temperature drop (Self et al., 1981). However, in terms of global climate impact, the 1963 eruption was not comparable to the 1815 Tambora or the 1883 Krakatau eruptions (Cadle et al., 1976; Hansen et al., 1978; Self et al., 1981; Rampino and Self, 1982; Self and Rampino, 2012). After 1963, Agung Volcano began to show an increase in activity once again in September 2017 and erupted in November 2017.

Conceptual Model of Agung Volcano

Previous studies have proposed several models for estimating the subsurface processes beneath Agung volcano using various data; e.g., Geiger et al. (2018) base their proposal on thermobarometry data from an analysis of the 1963 eruption deposits, Albino et al. (2019) use InSAR data, and Syahbana et al. (2019) use a multi-disciplinary approach including seismicity, geology, geochemistry, GPS deformation, and InSAR data. These proposed models describe the magma intrusion pathway to the surface.

The models agree that there are two magma reservoirs beneath Agung volcano. The deep reservoir is located at around 12–15 km, while the shallow one is around 4 km. Syahbana et al. (2019) analyzed the seismic crisis of the 2017 Agung eruption in their model. They propose two possible models; (i) the first model speculated that upward magma migration suppressed the aquifer, which then reactivated the fault between Agung and Batur volcanoes resulting in a swarm of VT earthquakes; while (ii) the second model suggests that there is a deep intrusion of a inclined dike striking N300° underneath the area between Agung and Batur volcanoes which caused an uplift at the summit of Agung as well as a VT earthquake swarm.

The VT swarm hypocenter catalog was used in part to construct the Syahbana et al. (2019) conceptual model, which was taken from the Indonesian Meteorological, Climatological, and Geophysical Agency (BMKG) catalog. This catalog is based on BMKG regional data, which has relatively low resolution. Therefore, a well-constrained VT event catalog using the local CVGHM seismic network deployed in the vicinity of Agung volcano is needed to improve the physical understanding of magma migration toward the summit.

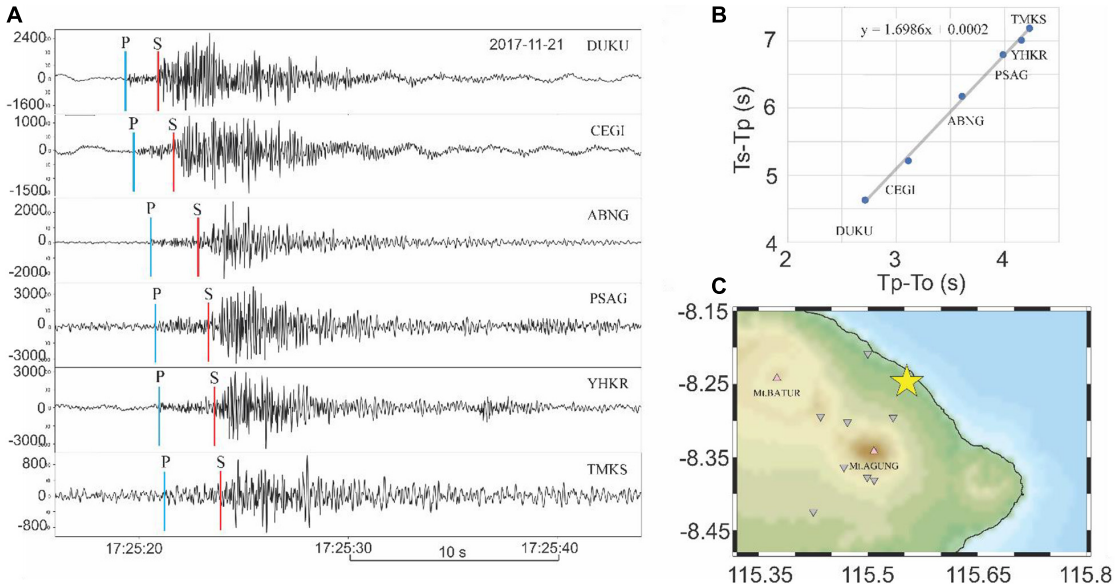

FIGURE 2 | (A) Example of picked waveforms of an event occurring on November 21, 2017 17:25:16 UTC. The event was recorded by six stations (out of eight). Only the vertical component of each recorded seismogram is shown. The P and S wave arrival times are indicated by the blue and red vertical bars, respectively. The names of the stations are written at the end of each waveform. **(B)** The Wadati diagram; i.e., the difference between S and P wave travel times vs. P wave travel times of the picked event. **(C)** Plotting of event location (indicated as yellow star) and station network (inverted triangles).

DETERMINING THE HYPOCENTER OF THE VT EARTHQUAKES

The earthquake waveform data used to construct the 2017 Agung VT events catalog in this study were taken from eight seismometers deployed by the CVGHM (**Figure 1**). TMKS and PSAG were the first two stations deployed in early 2015 and 2017, respectively. As the seismic crisis culminated at Agung volcano, those stations were used to monitor the rate of the daily VT earthquake occurrences. On October 18, 2017, the PVMBG deployed the ABNG, CEGI, REND, YHKR, BATU, and DUKU stations. Together, these form an eight-station network surrounding Agung volcano. In this study, we use the recorded waveform data from these eight seismic stations from October 18 to November 30, 2017. The locations of the eight seismometers surrounding Agung volcano are shown in **Figure 1**. In the following result subsections, we briefly describe the methods at the beginning of each subsection.

Identification of VT Events

Seismic events that occur in a volcanic area can be classified into several types, which are characterized by their waveforms and frequency contents with specific source mechanisms (Wassermann, 2011). We follow the classification of volcanic seismic types done by Minakami (1974). Minakami divided the seismic events in a volcanic area into four types according to the location of the hypocenters, their relationship to the eruptions, and the nature of the earthquake motion. They are volcano-tectonic (VT), low frequency (LF), explosion, and volcanic tremors.

Volcano Tectonic (VT) earthquakes are the most common seismic events observed at volcanoes which have a characteristic of the clear onset of P and S phase arrival and high frequency (>5 Hz). Low-frequency (LF) (1–5 Hz) events occur due to the resonance of fluid movement inside the conduit. The explosion events originate from an eruption or sonic boom in the conduit of the volcano. Volcanic tremors occur due to continuous fluid flows at shallow depths. In this study, we are primarily interested in VT as these could be used as a proxy of the migration of magma to the surface, leading to a volcanic eruption.

We manually identified the occurrences of the VT events preceding the 2017 Agung volcanic eruption. The P- and S-wave arrival times of each identified event were also manually picked. Only events recorded by at least four stations and having an apparent onset of P and S wave arrivals were used. In total, 2,726 VT events were obtained; 13,023 and 11,823 P- and S-wave arrival times, respectively. An example of P and S wave arrival times of a VT event is presented in **Figure 2A**.

The Wadati diagram and epicenter location the detected event were also plotted in **Figures 2B,C**, respectively. The purpose for this was to evaluate the picking (remove the poorly picked data) as well as infer the average Vp/Vs of the rock through which the seismic wave passed. The Wadati diagram of all detected events is plotted in **Figure 3**. The average Vp/Vs beneath Agung Volcano obtained from all detected events prior to the 2017 eruption is 1.62. Interestingly, the Vp/Vs value of VT events changed over time. VT events in October (blue dots) tend to have a lower gradient (Vp/Vs of 1.50) compared to events that occurred in November (orange dots) (Vp/Vs of 1.72).

The event rate was also time-varying. Based on previous published studies, e.g., Albino et al. (2019), Syahbana et al. (2019),

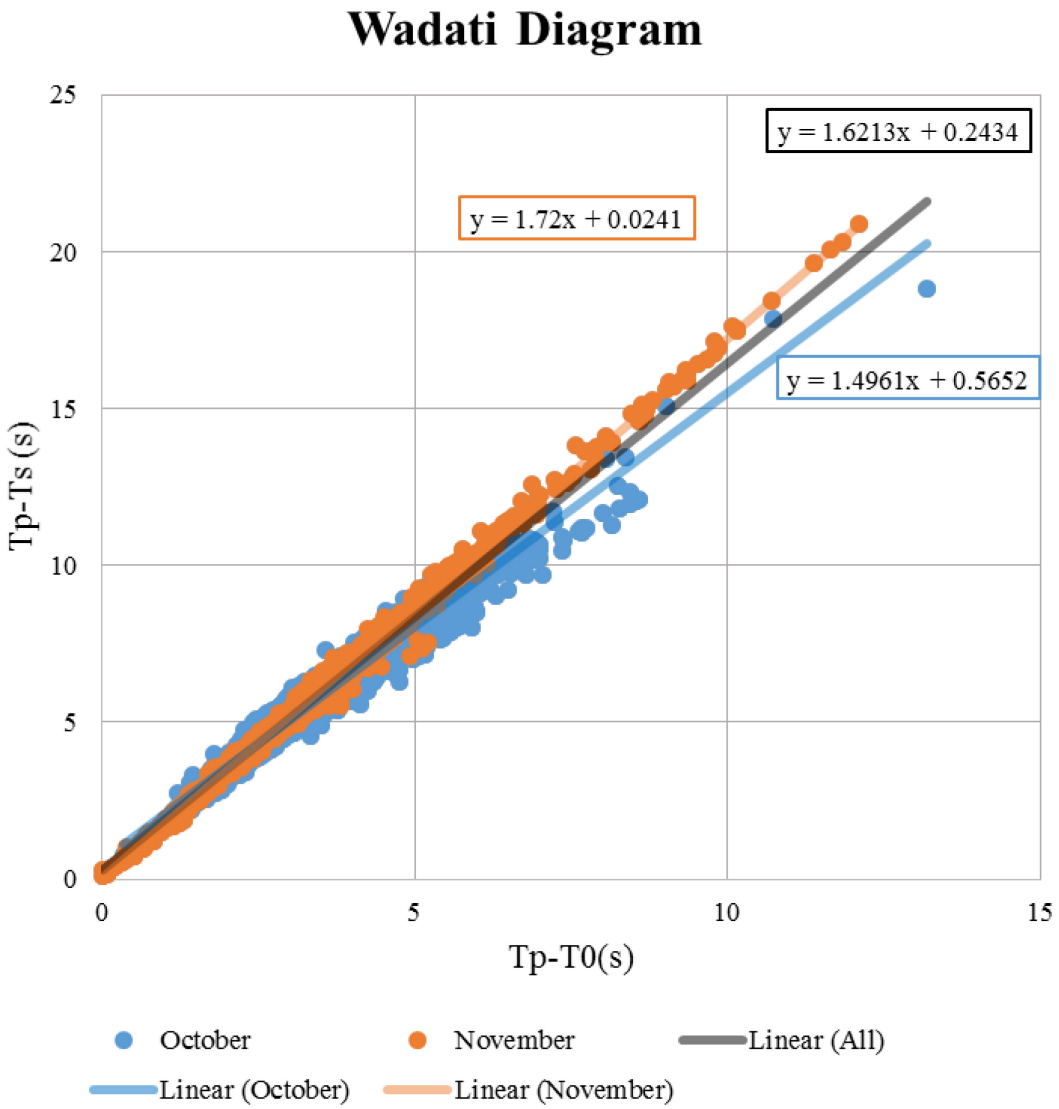

FIGURE 3 | The Wadati diagram of 2,726 VT events recorded during the study period. Based on this diagram, an average Vp/Vs of about 1.62 was found. Two patterns in this Wadati diagram are observed: VT events occurring in October 2017 (blue dots) have smaller gradients compared to the ones in November (orange dots). Consequently, lower- and higher-than-average Vp/Vs were given, respectively. VT events in October and November indicate a Vp/Vs of 1.50 and 1.72, respectively.

and Gunawan et al. (2020), seismic activity on Agung began to increase significantly in early September, with the number of detected VT events reaching more than 700 events per day for 4 weeks. The seismic crisis stopped at the end of October (insert **Figure 4**). In this study, we could observe the end of the 2017 Agung seismic crisis, in which more than 400 events/day were detected and located on October 18 and 19, 2017 (**Figure 4**). The event rate decreased rapidly in the following days. Until the eruption on November 21, 2017, around 87.5% of days had less than 80 events per day.

We also determined the time delay between S and P waves arrival of each VT event at each station. The time delay represents the distance between the event to the station, i.e., the longer time delay indicates the farther event and vice versa. The pattern of the arrival time delay between the S and P waves (Ts-Tp) was presented in **Figure 5**. Remarkably, the events during the seismic crisis tend to have a constant Ts-Tp compared to the events after the crisis. Four stations located between Agung and Batur (ABNG, CEGI, PSAG, and TMKS) indicated a constant low value of Ts-Tp before October 22, 2017, and higher but fluctuating values afterward. The constant but low phase arrival time delays observed in ABNG, CEGI, PSAG, and TMKS during the seismic crisis indicated that the events are primarily concentrated in the area between Agung and Batur Volcanoes. As ABNG (located NW from Agung Volcano) has the lowest phase arrival time delays of around 1.2 s, it could remark that this was the closest station to the VT events clusters during the seismic crisis. This is in contrast with the pattern observed in YHKR (located south

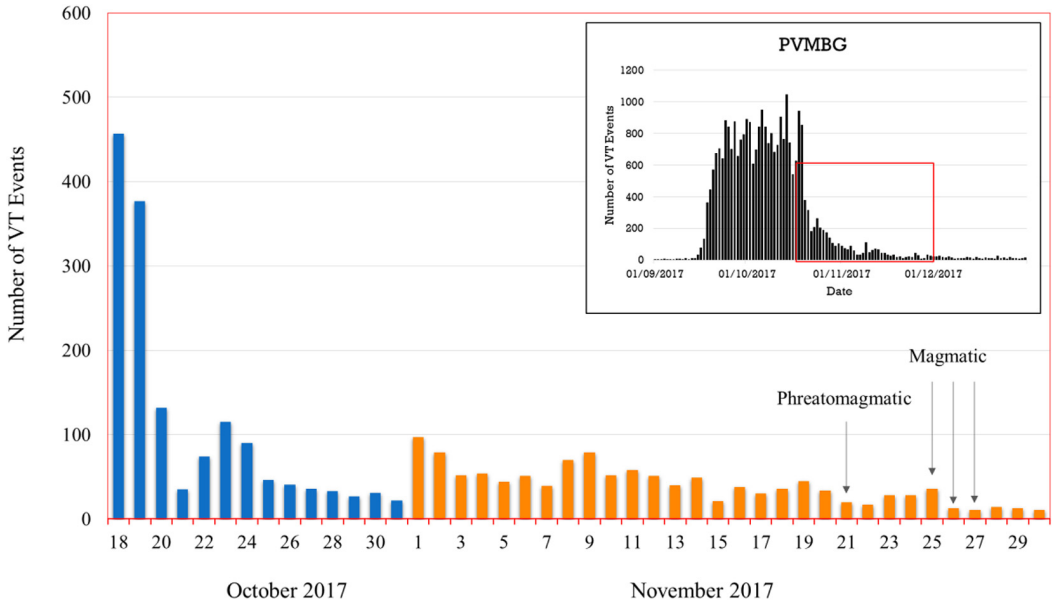

FIGURE 4 | Histogram of the number of detected and located VT events per day from October 18 to November 30, 2017. Colors indicate the date (blue and orange bars are October and November, respectively). Black arrows indicate eruption dates and eruption types. A phreatomagmatic eruption occurred on November 21, 2017; and a magmatic eruption occurred on November 25–27, 2017 (Syahbana et al., 2019).

of Agung Volcano), i.e., the phase arrival time delays fluctuated but were lower after the seismic crisis. Meanwhile, three other stations (DUKU, BATU, and REND) recorded only a few events. Therefore, no pattern was observed in those three stations.

Determining Initial Hypocenter Locations

To obtain a well-constrained hypocenter catalog, we determined the hypocenter locations of the seismic events preceding the 2017 Agung volcanic eruption in several sequential steps. First, the NonLinLoc program (Lomax et al., 2000, 2012; Lomax and Curtis, 2001; Lomax and Michelini, 2009) was used to determine the locations of the initial aftershocks. The 1D velocity model and station corrections were then updated to suit the local geological condition. Afterward, the relative relocation using the double-difference method was implemented to increase the accuracy of the obtained hypocenter.

In the first step, we used the initial 1-D seismic velocity model (Vp, Vs) from the tomography results of Central Java (Koulakov et al., 2009); hereafter known as the Kou09 model. The Kou09 model was selected because no velocity model of Agung region was available. Recently, Zulfakriza et al. (2020) performed an S-wave velocity inversion using ambient noise tomography called the Zul20 model. However, in their S-wave data inversion, the Vp/Vs ratio for each layer remained fixed, whereas the density was estimated from the P-wave velocity. This gave us a good variation of S-wave velocities in the region but might have failed to provide its absolute value. Compared to the Kou09 model, the Zul20 model showed around 50% lower S-wave velocity which would cause the located hypocenter almost twice deeper. Thus, we used the Zul20 model to constrain the distribution of correction stations determined in this study.

The map view of the located VT events is presented in **Figure 6**. The location uncertainty was estimated for each event determined in this study. The locations of all 2726 located VT events are presented in **Figure 6A**. 2298 VT events had uncertainty lower than 5 km. The majority of the events with higher uncertainty were located outside the seismic network. Therefore, in this study, we only used the best-constrained events with location uncertainty less than 5 km. The residual travel times of the selected events range from −0.2 to 0.2 s (**Figure 7A**). Given the mean velocity is around 5 km/s (see **Figure 8**), the average uncertainty of the VT events is around 1 km. This value is considerably low for volcano monitoring.

1D Velocity Model Update and Station Corrections

We updated the 1D velocity model to meet the geological conditions of Agung Volcano by minimizing the residual travel time of VT events observed in this study. The velocity model update was done using the Joint Hypocenter Determination (JHD) technique implemented in the Velest program (Kissling et al., 1994). The JHD technique is used to account for lateral velocity variations, which is not considered in the 1D velocity models used to locate the seismic events. The concept includes the simultaneous location of a cluster of events, the determination of a set of suited station corrections, and the update of the 1D velocity model. Under appropriate conditions, the station corrections minimize the impact of unmodeled velocity variations, thus improving the locations of the events (Kissling et al., 1995). The rough topography of the study area (the difference in elevation between stations is as much as 1,474 m) might indicate a significant lateral velocity variation.

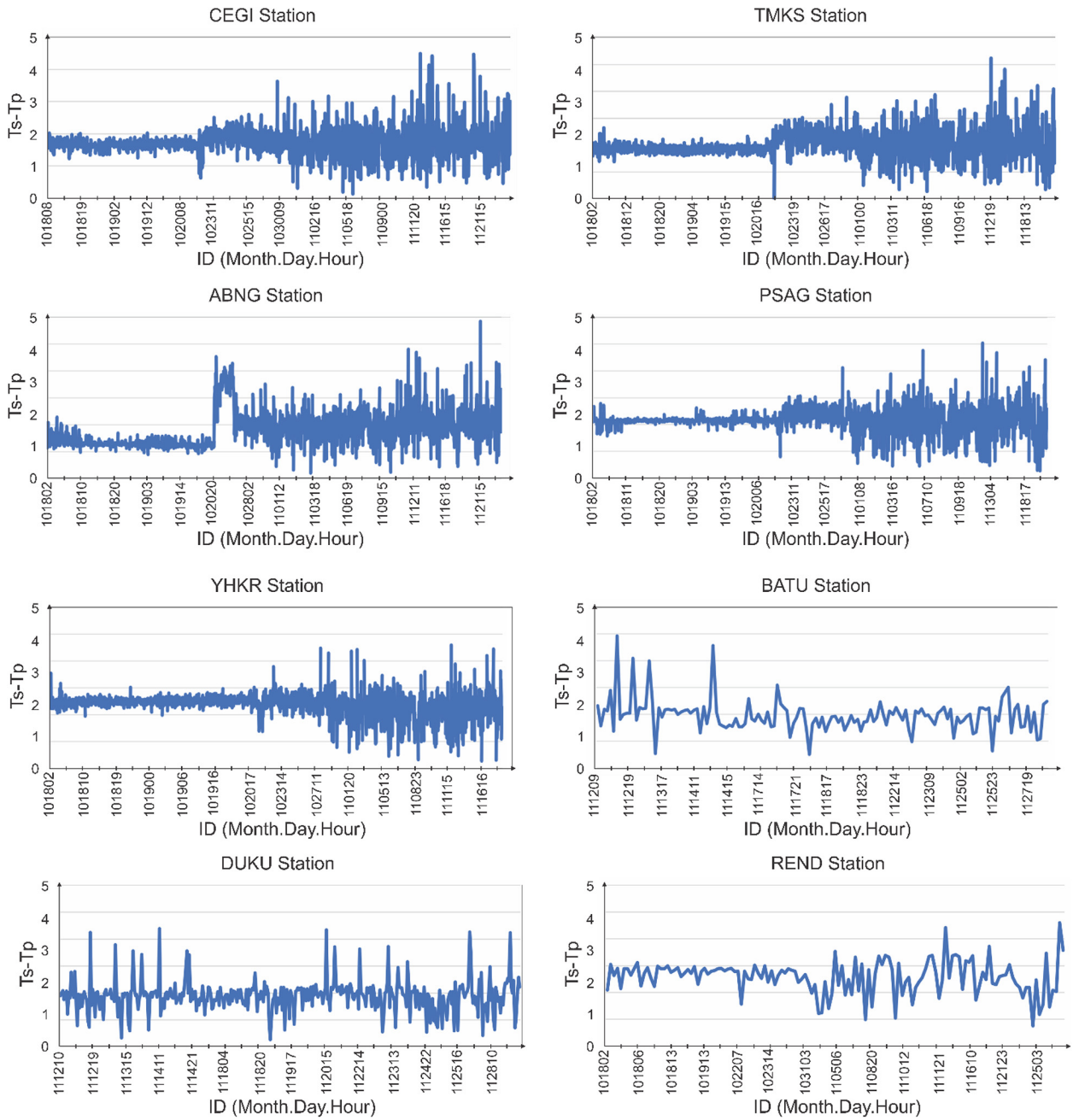

FIGURE 5 | Arrival time delay between primary (Tp) and secondary waves (Ts) at each seismographic station surrounding Agung volcano. The *x* axis is the ID of detected events at each station. The ID consists of six digits character representing month, day, and hour of each event's origin time.

The inversion was performed iteratively. Throughout the inversion, the event hypocenter locations, velocity model, and correction stations were jointly determined. Several sets of parameters were exercised to find the best combination, given a minimum arrival time misfit. We discovered that a neighboring radius of 200 m, with damping for the velocity model set twice as high as the station corrections, gave the best results. The Vp/Vs ratio was fixed according to our observed Vp/Vs ratio (**Figure 3**). To ensure a robust solution, we made a slight maximum adjustment of hypocenter location, velocity model, and correction station in each iteration. In this case, a longer iteration and, therefore, a longer running time were required. However, this approach could minimize the possibility of getting a minimal local solution, especially in noisy data. The solution was found to be convergent after 26 iterations, and the RMS residual dropped by 45% to 0.3 s.

The updated 1D seismic velocity model obtained in this study, shown in **Figure 8**, is the Agu20 model. The Agu20 model is

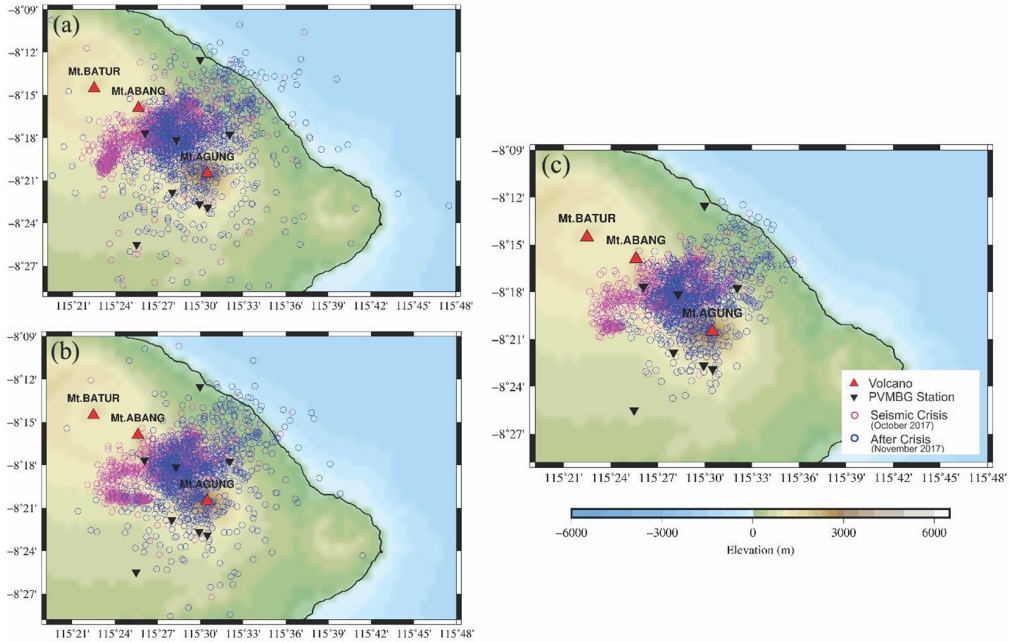

FIGURE 6 | Map of epicenters of VT earthquakes preceding the 2017 Agung volcanic eruption. **(A)** Initial locations derived using a non-linear approach. **(B)** Updated epicenter distribution after updated 1D velocity model, and **(C)** after DD relocation. In **(B)** and **(C)** only events with uncertainty less than 5 km are shown. Purple and blue circles represent events during (October 2017) and after seismic crisis (November 2017), respectively.

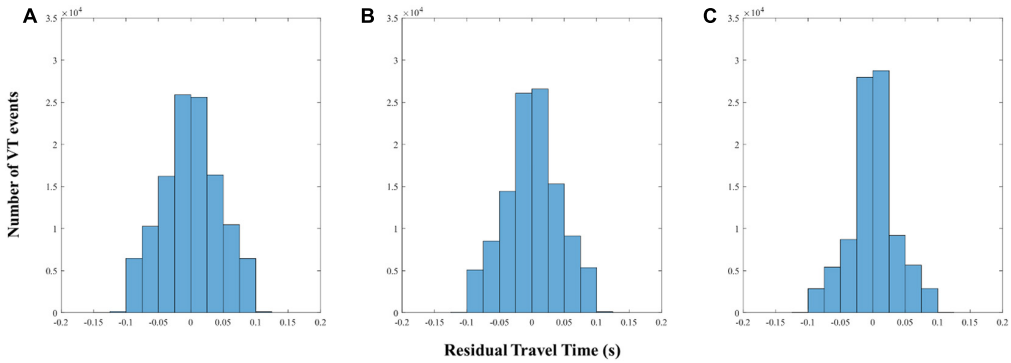

FIGURE 7 | Travel time residual of hypocenters for each step determined in this study; i.e., **(A)** initial locations for all events, **(B)** after updated 1D velocity model, and **(C)** after DD relocation.

slightly different from the Kou09 model. On average, at depths above 8 km, the Agu20 model shows about 10% higher Vp and Vs compared to the Kou09 model. While from a depth of 8 to 24 km, the Agu20 model shows slightly lower Vp and Vs compared to the Kou09 model. The velocity model remained unchanged below depths of 24 km.

The station corrections obtained in this study ranged from −0.05 to 0.22 and −0.12 to 0.39 for P and S waves, respectively (plotted in **Figure 9** and listed in **Table 1**). These values could be positive or negative, depending on the relative local velocity contrast in the region of the station, i.e., a positive value indicates the station was in a low-velocity anomaly and vice versa. Stations ABNG and CEGI have high positive station corrections (0.22 and 0.07 for P waves and 0.39 and 0.16 for S waves, respectively). In contrast, stations TMKS, PSAG, YHKR, and DUKU show correction around zero for both P and S. The two far-field stations, REND and BATU, indicate an intermediate value (−0.14, −0.08, respectively) for S waves and a very small value for P waves.

We overlaid the Zul20 S-wave velocity distribution, obtained from surface waves, at depths between 0.5 and 1 km with the station correction obtained in this study (**Figure 9**). The red and blue areas indicate low and high S-wave velocities, respectively. The same color scheme was used to plot the correction stations, with the radius of each plot indicating the magnitude of the correction. Interestingly, this is consistent with the S-wave

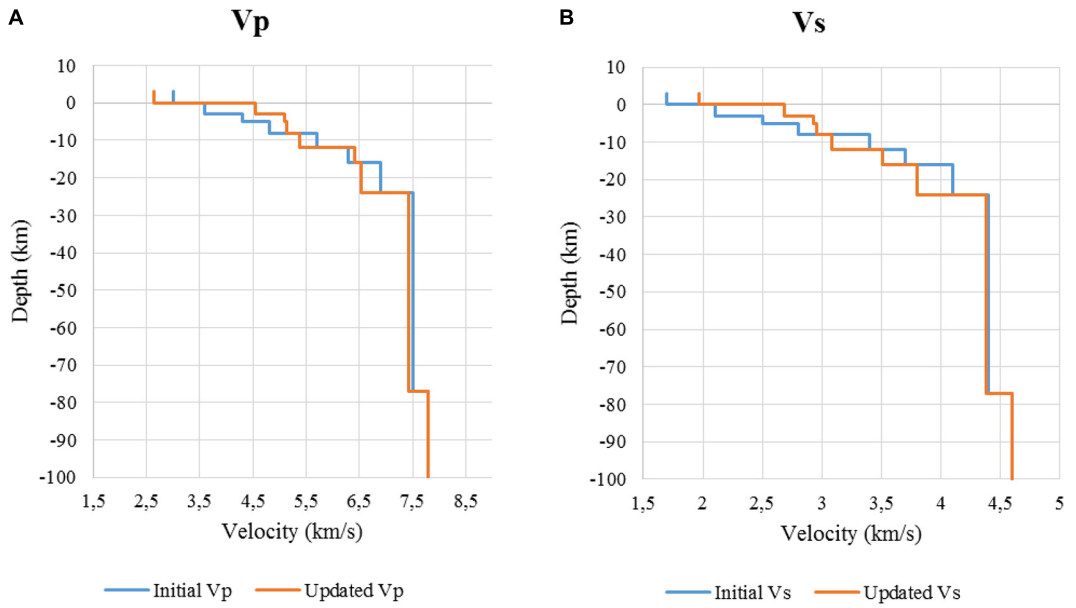

FIGURE 8 | Plot of the initial **(A)** P-wave and **(B)** S-wave 1D velocity of Kou09 model taken from Koulakov et al. (2009) (blue line) and the updated velocity model (Agu20) used in this study (orange line).

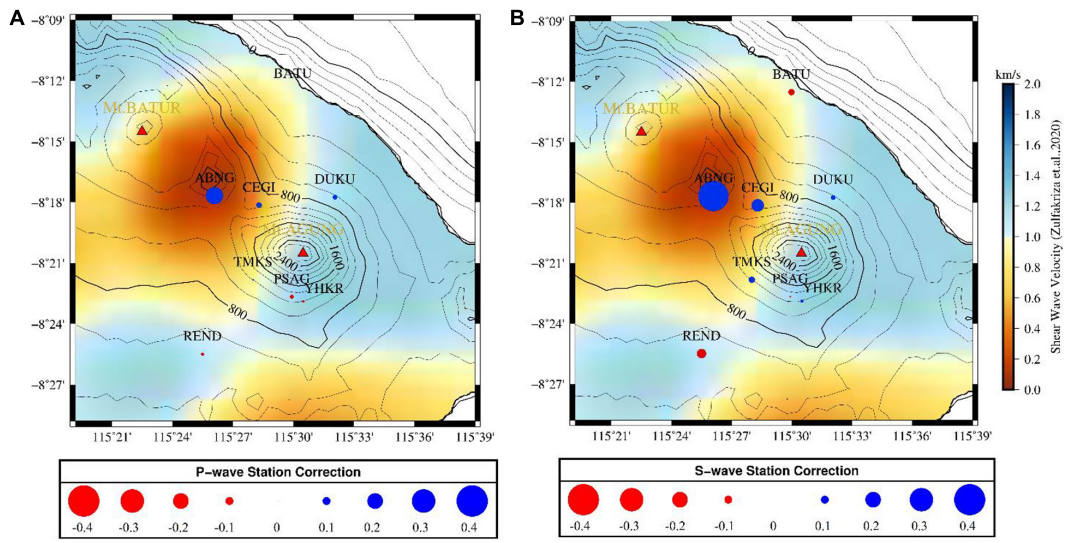

FIGURE 9 | Distributions of **(A)** P-wave and **(B)** S-wave corrections at each station calculated using joint velocity-hypocenter determination technique. The station correction at each seismographic station is plotted with filled circles. The absolute magnitude of station corrections is represented by its size; whereas, the sign is denoted by its color; i.e., red and blue indicate negative and positive values, respectively.

velocity Zul20 model at a shallower depth. A good agreement could also be observed between the topographical and station corrections. The relatively high station corrections obtained indicate that the lateral velocity variation beneath Agung volcano, especially at lower depths, is quite significant.

Following the update of the velocity model and station corrections, the event hypocenter locations were relocated accordingly. The relocation process in this stage slightly reduced the residual travel time (**Figure 7B**). On average, the updated hypocenter locations were relocated by around 4 km from their initial locations. The most notable relocations were observed 10 km west of Agung volcano; after these relocations, two seismic trends were observed during the seismic crisis (**Figure 6B**).

Double-Difference Relative Relocation

The DD technique takes advantage of the fact that if the inter-event distance between a pair of earthquakes is small compared to the distance between event-station and the scale length of

TABLE 1 | Station corrections of each local station surrounding Agung volcano obtained through joint hypocenter location, velocity model, and station correction inversion which were performed in this study.

Station	Latitude	Longitude	P Correction	S Correction
ABNG	−8.2946°	115.4348°	0.22 s	0.39 s
CEGI	−8.3024°	115.4716°	0.07 s	0.16 s
DUKU	−8.2958°	115.5344°	0.06 s	0.06 s
YHKR	−8.3816°	115.5083°	−0.03 s	0.04 s
PSAG	−8.3777°	115.4987°	−0.05 s	−0.02 s
TMKS	−8.3638°	115.4667°	0.02 s	0.08 s
REND	−8.4249°	115.4249°	−0.04 s	−0.12 s
BATU	−8.2087°	115.4996°	0 s	−0.08 s

velocity heterogeneity, then the ray paths between the events pair and the station are similar (Waldhauser and Ellsworth, 2000). In this case, the difference of travel times of events pair observed at the same station can be addressed to the spatial offset between the events with high accuracy. In this study, the travel times difference of each events pair was obtained from the manual phase arrival picking.

To comply with the DD concept, some parameters have to be well defined. In this study, the maximum hypocentral separation for categorizing a cluster is 1.5 km, i.e., significantly less than the event-station distance and heterogeneity scale. We define that these events within one cluster have to be recorded by at least four common stations to be defined as neighboring events. Furthermore, to ensure that events within the cluster could be well paired, the maximum number of neighbors per event in one cluster is set to be moderate (30). A least-square damping value of 150 was chosen since it could give a stable solution, i.e., the condition number of the inversion matrix falls within a certain range (Tarantola and Valette, 1982). The updated Agu20 model was then used as the velocity model.

The combination of parameters mentioned above could relocate 2,095 paired events (out of 2298 well-defined events) and reduce the residual travel times obtained in the previous stage. The rest, 203 (∼10%) events, remains un-relocated. These events might be located far away from the other events or recorded by a few stations only. **Figure 7C** shows that more than 90% of the events fall below 0.12 s of residual travel times. The epicenter of the DD relocated events are plotted in **Figure 6C**.

Two vertical sections of the final hypocenter catalog (after DD relocation) are presented in **Figure 10**. In both cross sections, it can be seen that VT events during the seismic crisis are dominated by events located deeper than 6 km (**Figures 10B,C**). In a NE-SW vertical section, crossing the area between Batur and Agung Volcanoes, it can be seen that two branching magma paths rise to the summit of Agung Volcano and the valley between Agung and Batur Volcanoes (**Figure 10C**). Interestingly, the pattern of events migrating toward the valley between Agung and Batur was observed during the seismic crisis.

To assess the reliability of the event locations after the DD relocation, a statistical resampling approach, i.e., the "bootstrap" method, was implemented (Efron, 1982; Billings, 1994; Shearer, 1997; Supendi et al., 2019). The arrival times of both P and S waves of the 2,095 relocated events were substituted by samples drawn in the time residual distributions. Gaussian noise with a standard deviation of 0.1 s was added to this sample data. The shift in location due to these bootstrap samples was determined and repeated 1,000 times. The error ellipsoids were obtained at a 95% confidence level for these 1,000 sample data. The analysis of event uncertainties from the final relocated events (**Figure 11**) indicates that the mean of major uncertainty ellipsoid is around 181 m.

Waveform Cross-Correlation

The similarity of VT events is analyzed using the waveform cross-correlation of recorded VT events. The idea is that if the events occurred on the same pre-existing fracture zones, some fractures with similar characteristics, e.g., geometry and orientation, had been reactivated. In this case, we might expect that the recorded waveform of some events would be identical as they come from the same source region and source mechanism. Therefore, the application of cross-correlation analysis allows the definition of groups of dependent events (multiplets) characterized by similar location, fault mechanism, and propagation pattern (Waldhauser and Ellsworth, 2000; Baisch et al., 2008).

The waveform cross-correlation was then applied to analyze the similarity of VT event's source. It was done using recorded waveforms at station CEGI and TMKS. Those stations were chosen as they recorded the most VT events during the study period, and the noise level was small. The sample of similar waveforms from different events is presented in **Figure 12**. Interestingly, we found that 165 events with waveforms similarity greater than 0.8 were recorded during the seismic crisis, while none was found after the seismic crisis.

Applying the procedure of clustering in DD relocation used in this study, those events with high similarity formed 3,925 difference arrival times of event pairs; less than 3% than the difference arrival times of event pairs obtained from the manual picking catalog. Adding the waveform cross-correlation data into the DD relocation would shift the VT events obtained by DD using a picking catalog only by less than 1 km for events that occurred during the seismic crisis, while events after a seismic crisis relatively remain relatively unchanged. The residual travel times were also very similar to the one using only a manual picking catalog. As the shifting is relatively small, the relocation also could not sharpen the seismicity trend. Therefore, we decided that the catalog of VT events obtained by the DD relocation using the manual picking catalog data is the final one.

DISCUSSION

The analysis of event uncertainties from the final relocated events (**Figure 11**) indicates that the mean of the major uncertainty ellipsoid is much smaller when compared to the seismic cluster formed in October and November 2017. In this case, we are confident in interpreting the details of the seismic clusters obtained in this study. The distinct seismic pattern difference between October and November 2017

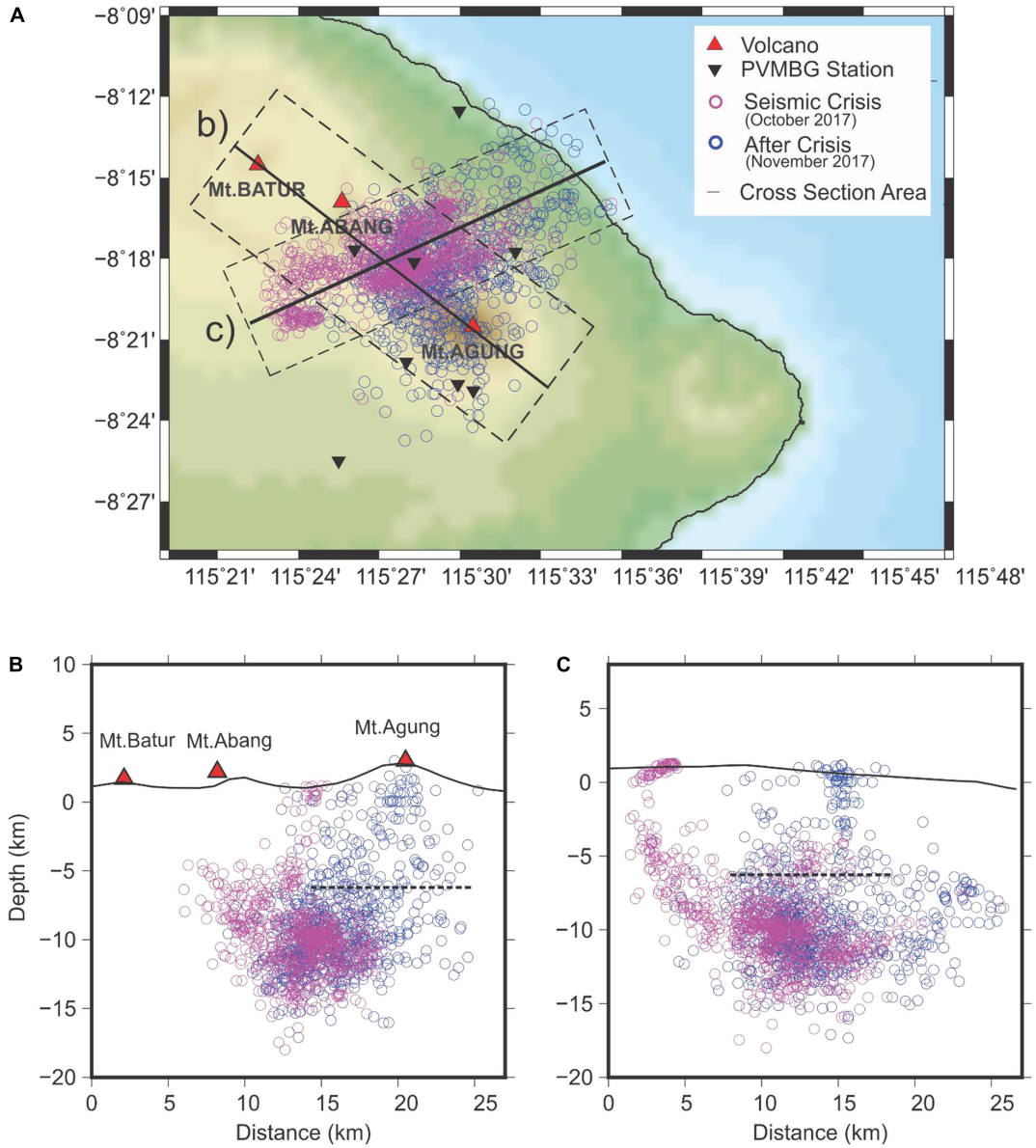

FIGURE 10 | (A) Distribution of epicenters. **(B,C)** Map of the vertical distribution of the VT events preceding the 2017 Agung volcanic eruption in two vertical cross-sections. The two cross-sections are shown in the epicenter map in **(A)**. Purple and blue circles represent events during and after seismic crisis respectively, respectively. The dashed black horizontal line at 6 km depth represent the interpreted depth boundary described in the text.

highlights the different phases of magma intrusion that occurred underneath Agung volcano.

The VT seismic events during the seismic crisis presented in **Figures 6C**, **10A** indicate that most of the seismic events were located midway between Agung and Batur, along a ∼N65°E seismic trend. Interestingly this trend is also in agreement with the S-wave velocity boundary obtained by Zulfakriza et al. (2020). This trend also acted as a boundary between the positive and negative station corrections obtained in this study. This gave us the first suggestion that this was a weak zone oriented in a NE-SW trend which was reactivated due to the magma migration toward the surface.

The hypothesis of fault reactivation during the seismic crisis was supported by the Vp/Vs anomaly and waveform cross-correlation analysis. We found that the seismic pattern in October 2017 shows an anomalously low Vp/Vs of 1.50 compared to 1.62 observed for the whole recording period. The low Vp/Vs ratio from the events aligned in a sharp NE-SW trend with a dip of ∼60° toward Agung during the seismic crisis indicated that this area might be highly fractured and filled with hydrothermal fluid in which the drop of the compressional wave is more significant than its shear wave drops (Ponko and Sanders, 1994). This case is analogous to the fractured rocks in geothermal areas, reactivated through pressure increase due

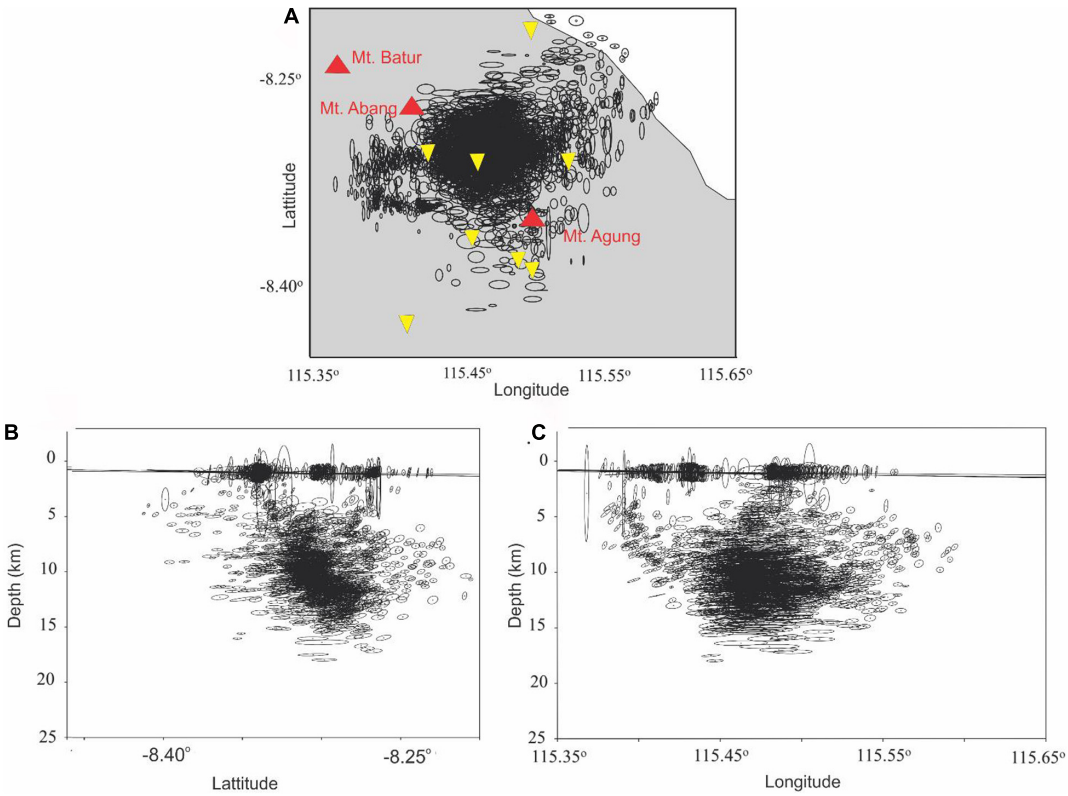

FIGURE 11 | The relative location errors for the relocated VT events of 2017 Agung volcanic eruption in **(A)** map view, **(B)** vertical cross-sections along latitude, and **(C)** vertical cross-section along longitude. Each ellipsoid represents 95% confidence obtained from a bootstrap analysis of the final double-difference vector. Red triangles show Agung, Abang, and Batur volcanoes. Yellow inverted triangles indicate the seismic network.

to injection (Bachmann et al., 2012). In our case, the magma rising beneath Agung Volcano pressurized the confining aquifers, which in turn activated the fault NW of the summit and caused the seismic crisis.

The reactivation of a fracture zone during the seismic crisis is further supported by the waveform cross-correlation of VT events, in which events with high waveforms similarity were only found during the seismic crisis. This suggests that those VT events during the seismic crisis were originated from the reactivation of this fracture zone.

Furthermore, the seismicity cloud of highly similar events was originated from 10 km depth (**Figure 12B**). This level is interpreted as the source of the stress increase due to magma migration which led to fault reactivation. This agrees with the second model of Syahbana et al. (2019) [See Figure 7 of Syahbana et al. (2019)], in which a magma intrusion below the area between Agung and Batur caused an increase in pore pressure and reactivated the pre-existing fractures in this region. Furthermore, in this study, we could give a better constraint of the depth of the magma intrusion, which caused fault reactivation as well as the geometry (orientation and dip) of the reactivated fault as to the previous conceptual models (Albino et al., 2019; Syahbana et al., 2019).

The seismic cluster then moved toward Agung Volcano in November 2017 (**Figure 6**). The pattern of migration of the seismic clusters from a NE-SW alignment located between the two volcanoes toward Agung is in accordance with the pattern of the arrival time delay between the primary and secondary waves (Ts-Tp) (**Figure 4**).

The vertical section shown in **Figure 10** depicts the distinct pattern of seismicity beneath Agung summit in October and November 2017. In October 2017, the VT events were contained at a depth of around six km beneath Agung Volcano, i.e., few VT events occurred above this depth in the direction toward Agung volcano. We suggest that there was a barrier (probably a stiffer layer) which prevented the upward migration of magma. Later, in November 2017 or after the seismic crisis, the magma and the related seismicity could penetrate the barrier and migrate upward toward the summit of Agung Volcano. As the waveform similarity analysis of VT events beneath Agung indicated complex faulting processes and its upward migration has a correlation with Agung eruption, we interpreted those events as resulting from the upward intrusion of magma.

Therefore, despite the seismicity rate decreased in November, magma migration was getting shallower, as suggested by the VT events. Furthermore, Syahbana et al. (2019) showed, starting early November 2017, an increasing value of RSAM was observed at TMKS, and LF events, as well as tremors, were observed. The VT events moved closer to the summit, increased RSAM, and the occurrence of LF events indicated that the volcano was

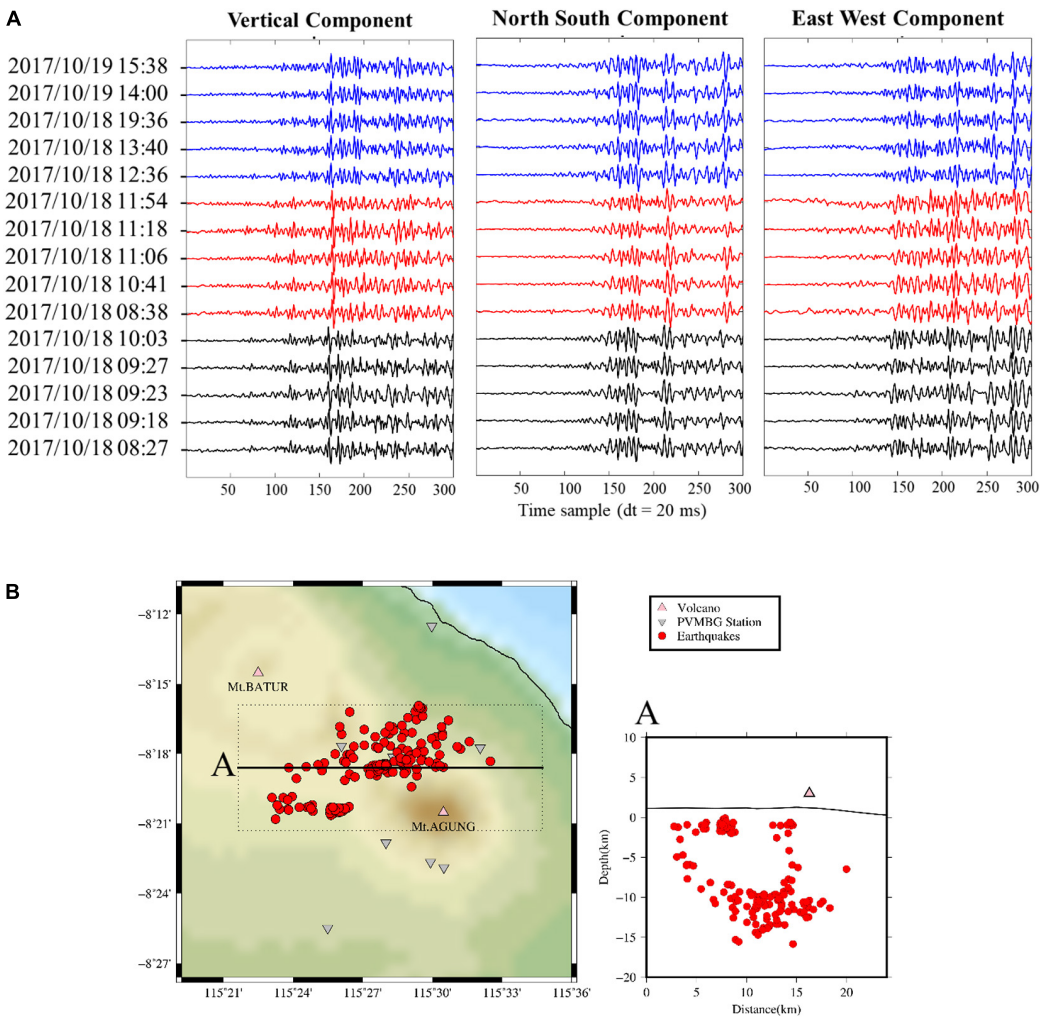

FIGURE 12 | (A) Example of waveforms of events belonging to the same cluster recorded at the same seismographic station. The three components of the seismographic stations are plotted. Clusters were determined based on waveform similarity. Events with waveform similarity of higher than 0.9 are clustered together. **(B)** Distribution of VT events which have high waveform similarity are plotted in map view and vertical section. All events with high waveform similarity occurred in October 2017.

approaching eruption. The eruption series then occurred starting on 25 November 2017. This detailed monitoring of upward migration of VT events was thus made possible thanks to the local seismic data processed in this study.

CONCLUSION

Analyzing the seismic crisis preceding a volcanic eruption is a challenging task; in particular, when the seismic network needed to monitor volcanic activity is lacking. Fortunately, the local seismic network deployed by CVGHM at the end of October 2017 allowed us to conduct an analysis of the seismic pattern preceding Agung volcano eruption. Despite the relatively late deployment of this network, we show that we were able to capture the major trend of the seismic crisis. For this purpose, 2,726 events were manually analyzed and located during the monitoring period, and 1,831 high-resolution VT events were obtained using advanced DD techniques and an updated 1D velocity model.

Based on the seismicity, we observed two patterns which represent the VT events related to the reactivation of fracture network due to stress increase (during the seismic crisis) and magma intrusion (after the seismic crisis). The characteristics of each event type are also discussed in terms of Vp/Vs values, phase delay times, waveform similarities, and seismic cluster shapes. The detailed reconstruction of upward magma migration was thus made possible thanks to the local seismic data processed in this study. We interpret that the upward magma migration reached a barrier (probably a stiff layer) at depth of around 6 km which prohibited further magma ascent. The magma pressurized the area beneath the barrier and reactivated the fault located between Agung and Batur volcanoes. Therefore, a significant increase in recorded seismicity (the "seismic crisis")

was observed for about 2 months since September 2017. Later in early November 2017, the barrier layer was finally intruded, and magma propagated toward the Agung summit. The depth of the dike, which caused fault reactivation, as well as the geometry (strike and dip) of the reactivated fault, could also be evaluated. More in general, these results provide a better depth constraint as to the previous conceptual models (Albino et al., 2019; Syahbana et al., 2019).

This study emphasizes the importance of prompt analysis (location and basic seismic characteristics) of the seismic crisis preceding Agung eruption. The distinction between VT event types observed in this study is significant for eruption forecasting and for understanding the structure of magmatic systems as these depict upward magma migration. The source mechanism of the major events needs to be further assessed for a better understanding of the role of the interpreted barrier, which acts as a boundary.

DATA AVAILABILITY STATEMENT

The original contributions presented in the study are included in the article/supplementary material, further inquiries can be directed to the corresponding author.

AUTHOR CONTRIBUTIONS

DPS, ZZ, AN, SW, AA, and MM conceived the survey and seismic study on Agung Batur Volcano Complex. DPS, PR, AN, DKS, ZZ, AB, and SR contributed to the writing of the manuscript. All authors contributed to the preparation of the manuscript and read and approved the final manuscript.

FUNDING

This study was mainly supported by USAID PEER (Partnerships for Enhanced Engagement in Research) with agreement number AID-OAA-A-11-00012. In addition, it was also partially supported by ITB Research 2019–2020 Program, and the Master's Thesis Research Program BP-PTNBH Kemristek/BRIN 2020 which were awarded to AN, and the Center for Earthquake Science and Technology, Research Center for Disaster Mitigation, Institut Teknologi Bandung (CEST, PPMB, ITB).

ACKNOWLEDGMENTS

This study was a collaboration between Institut Teknologi Bandung (ITB), the Center for Volcanology and Geological Hazard Mitigation (CVGHM), the Geological Agency of Indonesia, and the Volcano Disaster Assistance Program (VDAP) of the United States Geological Survey (USGS). Wessel et al. (2019) use of Global Mapping Tools (GMT) was used to produce the figures in this article, Anthony Lomax et al. (2000) for the Seisgram2k80 and NonLinLoc programs, Kissling et al. (1995) for the Velest program, and Waldhauser and Ellsworth (2000) for the HypoDD program.

REFERENCES

Albino, F., Biggs, J., and Syahbana, D. K. (2019). Dyke intrusion between neighbouring arc volcanoes responsible for 2017 pre-eruptive seismic swarm at Agung. *Nat. Commun.* 10:748. doi: 10.1038/s41467-019-08564-9

Bachmann, C. E., Wiemer, S., Goertz-Allmann, B. P., and Woessner, J. (2012). Influence of pore-pressure on the event-size distribution of induced earthquakes. *Geophys. Res. Lett.* 39:L09302. doi: 10.1029/2012GL051480

Baisch, S., Ceranna, L., and Harjes, H. P. (2008). Earthquake cluster: what can we learn from waveform similarity? *Bull. Seismol. Soc. Am.* 98, 2806–2814. doi: 10.1785/0120080018

Billings, S. D. (1994). Simulated annealing for earthquake location. *Geophys. J. Int.* 118, 680–692. doi: 10.1111/j.1365-246X.1994.tb03993.x

Cadle, R. D., Kiang, C. S., and Louis, J.-F. (1976). The global scale dispersion of the eruption clouds from major volcanic eruptions. *J. Geophys. Res.* 81, 3125–3132. doi: 10.1029/jc081i018p03125

Efron, B. (1982). *The Jackknife, The Bootstrap and Other Resampling Plans*. Philadelphia: Society for Industrial and Applied Mathematics.

Fontijn, K., Costa, F., Sutawidjaja, I., Newhall, C. G., and Herrin, J. S. (2015). A 5000-year record of multiple highly explosive mafic eruptions from Gunung Agung (Bali, Indonesia): implications for eruption frequency and volcanic hazards. *Bull. Volcanol.* 77:59. doi: 10.1007/s00445-015-0943-x

Geiger, H., Troll, V. R., Jolis, E. M., Deegan, F. M., Harris, C., Hilton, D. R., et al. (2018). Multi-level magma plumbing at Agung and Batur volcanoes increases risk of hazardous eruptions. *Sci. Rep.* 8:10547. doi: 10.1038/s41598-018-28125-2

Gunawan, M. T., Kusnandar, R., Supendi, P., Nugraha, A. D., Puspito, N. T., and Sahara, D. P. (2020). Analysis of swarm earthquakes around Mt. Agung Bali, Indonesia prior to November 2017 eruption using regional BMKG network. *Geosci. Lett.* 7:14. doi: 10.1186/s40562-020-00163-7

Hansen, J. E., Wang, W.-C., and Lacis, A. A. (1978). Mount agung eruption provides test of a global climatic pertubation. *Science* 199, 1065–1068. doi: 10.1126/science.199.4333.1065

Kissling, E., Ellsworth, W. L., Phillips, D. E., and Kradolfer, U. (1994). Initial reference models in local earthquake tomography. *J. Geophys. Res.* 99, 19635–19646. doi: 10.1029/93JB03138

Kissling, E., Kradolfer, U., and Maurer, H. (1995). *Velest User's Guide*. Zurich: ETH Zurich.

Koulakov, I., Jakovlev, A., and Luehr, B. G. (2009). Anisotropic structure beneath central Java from local earthquake tomography. *Geochem. Geophys. Geosyst.* 10:Q02011. doi: 10.1029/2008GC002109

Kusumadinata (1964). The eruption of the Agung volcano in Bali in 1963. *Bull.Geol.Surv. Indones.* 1, 12–15.

Lomax, A., and Curtis, A. (2001). Fast, probabilistic earthquake location in 3D models using Oct-tree importance sampling. *Geophys. Res. Abstr.* 3:955.

Lomax, A., and Michelini, A. (2009). Mwpd: a duration-amplitude procedure for rapid determination of earthquake magnitude and tsunamigenic potential from P waveforms. *Geophys. J. Int.* 176, 200–214. doi: 10.1111/j.1365-246X.2008.03974

Lomax, A., Satriano, C., and Vassallo, M. (2012). Automatic picker developments and optimization: filterpicker – a robust, broadband picker for real-time seismic monitoring and earthquake early warning. *Seismol. Res. Lett.* 83, 531–540. doi: 10.1785/gssrl.83.3.531

Lomax, A., Virieux, J., Volant, P., and Berge-Thierry, C. (2000). "Probabilistic earthquake location in 3D and layered models," in *Advances in Seismic Event Location. Modern Approaches in Geophysics*, eds C. H. Thurber and N. Rabinowitz (Dordrecht: Springer Netherlands), 101–134.

Minakami, T. (1974). "Seismology of volcanoes in japan," in *Physical Volcanology*, eds L. Civetta, P. Gasparini, G. Luongo, and A. Rapolla (Amsterdam: Elsevier Scientific Publishing Company).

Ponko, S. C., and Sanders, C. O. (1994). Inversion for P and S wave differential attenuation structure, long valley caldera, California. *J. Geophys. Res. Solid Earth* 99, 2619–2635. doi: 10.1029/93JB03405

PVMBG (2014). *Gunung Agung, Kementrian Energi dan Sumber Daya Mineal*. Bandung: Badan Geologi.

PVMBG (2017). *Letusan Gunung Agung 21 November 2017 pukul 17:05 WITA, Kementrian Energi dan Sumber Daya Mineal, Badan Geologi*. Available online at: https://magma.esdm.go.id/v1/press-release/111?signature=0213885802d252e70e6b3a7c194ddadb0ce9500b18a0eeccd09884174a3871e5 (Accessed: February 22, 2020).

Rampino, M. R., and Self, S. (1982). Historic eruptions of Tambora (1815), Krakatau (1883), and Agung (1963), their stratospheric aerosols, and climatic impact. *Quat. Res.* 127–143. doi: 10.1016/0033-5894(82)90065-5

Self, S., and Rampino, M. R. (2012). The 1963-1964 eruption of Agung volcano (Bali, Indonesia). *Bull. Volcanol.* 74, 1521–1536. doi: 10.1007/s00445-012-0615-z

Self, S., Rampino, M. R., and Barbera, J. J. (1981). The possible effects of large 19th and 20th century volcanic eruptions on zonal and hemispheric surface temperatures. *J. Volcanol. Geothermal Res.* 11, 41–60. doi: 10.1016/0377-0273(81)90074-3

Shearer, P. M. (1997). Application to the Whittier aftershock sequence Narrows California. *J. Geophys. Res.* 102, 8269–8283. doi: 10.1029/96JB03228

Supendi, P., Nugraha, A. D., Widiyantoro, S., Abdullah, C. I., Puspito, N. T., Palgunadi, K. H., et al. (2019). Hypocenter relocation of the aftershocks of the Mw 7.5 Palu earthquake (September 28, 2018) and swarm earthquakes of Mamasa, Sulawesi, Indonesia, using the BMKG network data. *Geosci. Lett.* 6:18. doi: 10.1186/s40562-019-0148-9

Syahbana, D. K., Kasbani, K., Suantika, G., Prambada, O., Andreas, A. S., Saing, S. L., et al. (2019). The 2017–19 activity at Mount Agung in Bali (Indonesia): intense unrest, monitoring, crisis response, evacuation, and eruption. *Sci. Rep.* 9:8848. doi: 10.1038/s41598-019-45295-9

Tarantola, A., and Valette, B. (1982). Inverse problems = quest for information. *J. Geophys.* 50, 159–170. doi: 10.1002/bit.260430206

Waldhauser, F., and Ellsworth, W. L. (2000). A Double-difference earthquake location algorithm: method and application to the northern hayward fault, California. *Bull. Seismol. Soc. Am.* 90, 1353–1368. doi: 10.1785/0120000006

Wassermann, J. (2011). "Chapter 13: volcano seismology," in *New Manual of Seismological Observatory Practice*, ed. P. Bormann (Potsdam: deutsches geoforschungszentrum), 1–67.

Wessel, P., Luis, J. F., Uieda, L., Scharroo, R., Wobbe, F., Smith, W. H. F., et al. (2019). The generic mapping tools version 6. *Geochem. Geophys. Geosys.* 20, 5556–5564. doi: 10.1029/2019GC008515

White, R., and McCausland, W. (2016). Volcano-tectonic earthquakes: a new tool for estimating intrusive volumes and forecasting eruptions. *J. Volcanol. Geothermal Res.* 309, 139–155. doi: 10.1016/j.jvolgeores.2015.10.020

Zen, M. T., and Hadikusumo, D. (1964). Preliminary report on the 1963 eruption of Mt. Agung in Bali (Indonesia). *Bull. Volcanol.* 27, 269–300. doi: 10.1007/BF02597526

Zlotnicki, J., Sasai, Y., Johnston, M. J. S., Fauquet, F., Villacorte, E., and Jr, J. M. C. (2018). The 2010 seismovolcanic crisis at Taal Volcano (Philippines). *Earth Planets Space* 70:159. doi: 10.1186/s40623-018-0925-2

Zobin, V. (2012). *Introduction to Volcanic Seismology*. Amsterdam: Elsevier.

Zulfakriza, Z., Nugraha, A. D., Widiyantoro, S., Cummins, P. R., Sahara, D. P., Rosalia, S., et al. (2020). Tomographic imaging of the agung-batur volcano complex, bali, Indonesia, from the ambient seismic noise field. *Front. Earth Sci.* 8:43. doi: 10.3389/feart.2020.00043

Conflict of Interest: The authors declare that the research was conducted in the absence of any commercial or financial relationships that could be construed as a potential conflict of interest.

Copyright © 2021 Sahara, Rahsetyo, Nugraha, Syahbana, Widiyantoro, Zulfakriza, Ardianto, Baskara, Rosalia, Martanto and Afif. This is an open-access article distributed under the terms of the Creative Commons Attribution License (CC BY). The use, distribution or reproduction in other forums is permitted, provided the original author(s) and the copyright owner(s) are credited and that the original publication in this journal is cited, in accordance with accepted academic practice. No use, distribution or reproduction is permitted which does not comply with these terms.

frontiers in Earth Science

ORIGINAL RESEARCH
published: 24 June 2021
doi: 10.3389/feart.2021.662113

Campi Flegrei, Vesuvius and Ischia Seismicity in the Context of the Neapolitan Volcanic Area

Flora Giudicepietro[1], Patrizia Ricciolino[1], Francesca Bianco[1], Stefano Caliro[1], Elena Cubellis[1], Luca D'Auria[2], Walter De Cesare[1], Prospero De Martino[1], Antonietta M. Esposito[1], Danilo Galluzzo[1], Giovanni Macedonio[1], Domenico Lo Bascio[1], Massimo Orazi[1], Lucia Pappalardo[1], Rosario Peluso[1], Giovanni Scarpato[1], Anna Tramelli[1] and Giovanni Chiodini[3]*

[1]Istituto Nazionale di Geofisica e Vulcanologia, Osservatorio Vesuviano, Naples, Italy, [2]Instituto Volcanológico de Canarias (INVOLCAN), San Cristobal de La Laguna, Spain, [3]Istituto Nazionale di Geofisica e Vulcanologia, Sezione di Bologna, Italy

OPEN ACCESS

Edited by:
Derek Keir,
University of Southampton,
United Kingdom

Reviewed by:
Finnigan Illsley-Kemp,
Victoria University of Wellington,
New Zealand
Andrew Bell,
University of Edinburgh,
United Kingdom

***Correspondence:**
Flora Giudicepietro
flora.giudicepietro@ingv.it

Specialty section:
This article was submitted to Volcanology, a section of the journal Frontiers in Earth Science

Received: 31 January 2021
Accepted: 14 June 2021
Published: 24 June 2021

Citation:
Giudicepietro F, Ricciolino P, Bianco F, Caliro S, Cubellis E, D'Auria L, De Cesare W, De Martino P, Esposito AM, Galluzzo D, Macedonio G, Lo Bascio D, Orazi M, Pappalardo L, Peluso R, Scarpato G, Tramelli A and Chiodini G (2021) Campi Flegrei, Vesuvius and Ischia Seismicity in the Context of the Neapolitan Volcanic Area. Front. Earth Sci. 9:662113. doi: 10.3389/feart.2021.662113

Studying seismicity in a volcanic environment provides important information on the state of activity of volcanoes. The seismicity of the Neapolitan volcanoes, Campi Flegrei, Vesuvius, and Ischia, shows distinctive characteristics for each volcano, covering a wide range of patterns and types. In this study we relocated some significant volcano-tectonic earthquake swarms that occurred in Campi Flegrei and Vesuvius. Moreover, we compared the earthquake occurrence evolution, the magnitude and the seismic energy release of the three volcanoes. Also, we considered the results of seismic analysis in the light of geochemical and ground deformation data that contribute to defining the state of activity of volcanoes. In Campi Flegrei, which is experiencing a long term unrest, we identified a seismogenic structure at shallow depth in Pisciarelli zone that has been activated repeatedly. The increasing seismicity accompanies an escalation of the hydrothermal activity and a ground uplift phase. At Vesuvius a very shallow seismicity is recorded, which in recent years has shown an increase in terms of the number of events per year. Earthquakes are usually located right beneath the crater axis. They are concentrated in a volume affected by the hydrothermal system. Finally, Ischia generally shows a low level of seismicity, however, in Casamicciola area events with a moderate magnitude can occur and these are potentially capable of causing severe damage to the town and population, due to their small hypocentral depth (typically < 2.5 km). After the seismic crisis of August 21, 2017 (mainshock magnitude M = 4), the seismicity returned to a low level in terms of occurrence rate and magnitude of earthquakes. The seismicity of these three different volcanic areas shows some common aspects that highlight a relevant role of hydrothermal processes in the seismogenesis of volcanic areas. However, while the main swarms in Campi Flegrei and most of the Vesuvian earthquakes are distributed along conduit-like structures, the seismicity of Ischia is mainly located along faults. Furthermore, the temporal evolution of seismicity in Neapolitan volcanic area suggests a concomitant increase in the occurrence of earthquakes both in Campi Flegrei and Vesuvius in recent years.

Keywords: volcano seismicity, volcanic unrest, Campi Flegrei caldera, Vesuvius volcano, Ischia volcano

INTRODUCTION

The Neapolitan volcanic area (southern Italy) includes three active volcanic complexes: Campi Flegrei, Vesuvius, and Ischia (**Figure 1**). These volcanoes show different structural characteristics and behaviors. However, they have a common geodynamic origin and together they form the Campanian Volcanic Province (e.g. Conticelli et al., 2010; Peccerillo, 2020).

The volcanism in the Neapolitan district started about 1.5 Ma with a widespread effusive activity characterized by calc-alkaline andesitic and basaltic compositions as revealed by geothermal boreholes drilled NW of the Campi Flegrei caldera (Barbieri et al., 1979). Subsequently, from about 300 ka, new volcanic activity, fed by alkaline magmas (Scarpati et al., 2013), has generated the still active Campi Flegrei, Ischia and Vesuvius volcanic complexes.

The substructure of these volcanic areas has been investigated through several geophysical surveys (e.g. De Natale et al., 2006a; De Natale et al., 2006b and reference therein). Geophysical data, constrained by deep boreholes, showed that the deep structure of this volcanic area comprises 1.5–3 km of interbedded lavas and volcanoclastic, marine, and fluvial sedimentary rocks of Pleistocene age (Rosi and Sbrana, 1987; Brocchini et al., 2001; Di Renzo et al., 2007). These sequences overlay the Mesozoic carbonate sequences extending from two to four to roughly 8–11 km depth (Cubellis et al., 1991, Cubellis et al., 1995; Cubellis et al., 2001; Berrino et al., 1998, Berrino et al., 2008; Improta and Corciulo, 2006) on the Ercinian crystalline basement. The Moho discontinuity occurs at about 30 and 25 km depth beneath Vesuvius and Campi Flegrei and Ischia Island respectively (e.g., De Natale et al., 2006b; Nunziata, 2010). A low-velocity layer, interpreted as the top of a magmatic body, was detected by seismic tomography at 7–8 km depth beneath the Campi Flegrei caldera and Vesuvius volcano (Auger et al., 2001; Zollo et al., 2008). This evidence, that is consistent with the similarity in petrological features of the products from these volcanoes, suggests that a widely distributed magma source may be active beneath the entire Neapolitan volcanic district (Pappalardo and Mastrolorenzo, 2012).

The Neapolitan volcanic area developed on the Tyrrhenian edge of the Campanian plain that is characterized by extensive tectonic activity, which, since the Quaternary, has led to the formation of the Campanian graben (Bruno et al., 2003; Acocella and Funiciello, 2006; Torrente and Milia, 2013; Fedi et al., 2018). Extensive hydrothermal circulation is associated with these systems where several overlapping geothermal reservoirs interbedded within the volcanic succession have been identified (Aiuppa et al., 2006).

The Neapolitan volcanoes are among the longest inhabited volcanic areas, and therefore have a long historical record of natural events; moreover the high population density of this area implies a tremendous social impact of the volcanic risk. For these reasons a vast scientific literature has developed on these volcanoes, focusing mainly on Campi Flegrei and Ischia, which have shown greater variations in the last few years. A complete treatment of this literature is beyond the scope of this work, which focuses on comparing some characteristics of the seismicity of the three volcanoes, highlighting the common aspects.

Basically, the Neapolitan volcanoes cover a wide range of volcanic seismicity patterns and types (Chouet and Matoza, 2013) and well represent the behavior of different types of closed conduit active volcanoes. For this reason, they are generally studied individually. However, in recent decades some clues highlighted by seismic tomography (Auger et al., 2001) and petrographic studies of Vesuvius and Campi Flegrei (Pappalardo and Mastrolorenzo, 2012; Esposito et al., 2020a;

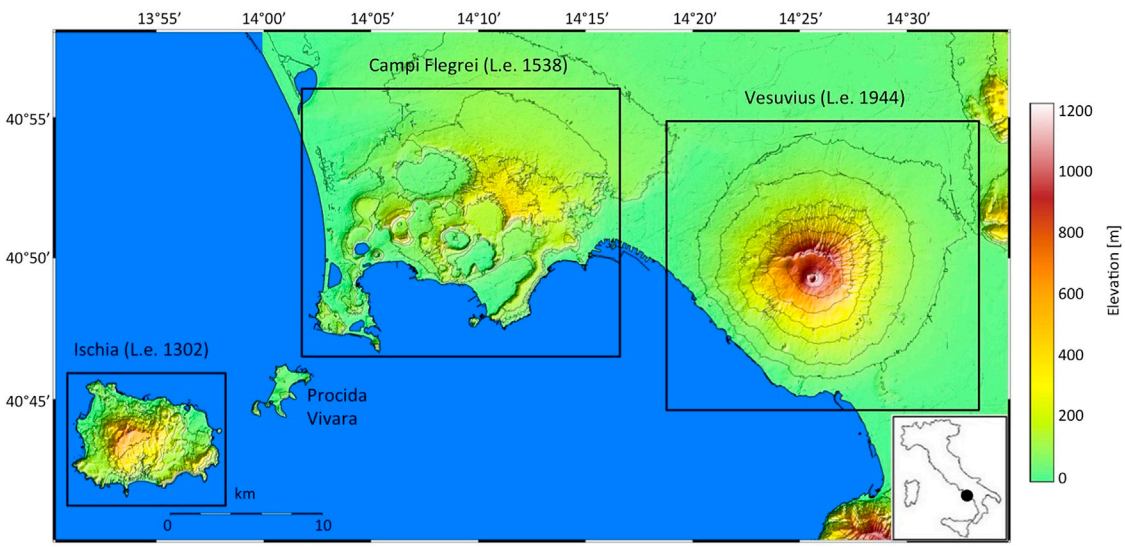

FIGURE 1 | Map of the Neapolitan volcanoes (Vesuvius, Campi Flegrei and Ischia). The figure shows the year of last eruption (L.e.) of the three volcanoes. The color scale represents elevation. The difference in height between the level lines is 150 m. See Acocella and Funiciello (2006) for structural details and Passaro et al. (2016) for bathymetry.

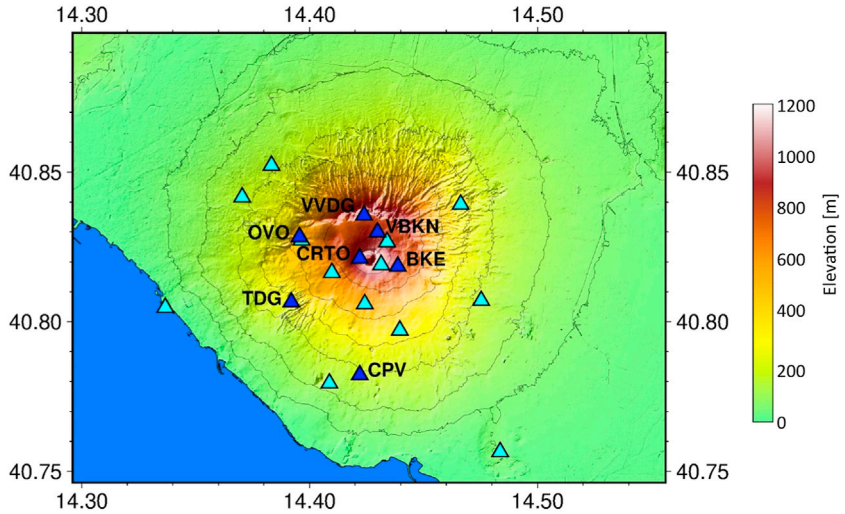

FIGURE 2 | Map of Vesuvius seismic network. The triangles are the seismic stations. The blue ones with labels are the stations used to locate a long-period transient (LP) recorded on November 16, 2020. The label is also shown for OVO station, which is installed in the historical building of the Osservatorio Vesuviano and is the reference for the seismic catalog of Vesuvius.

Esposito et al., 2020b) suggested possible links between these volcanoes. Therefore, in the following we characterize the status of the three Neapolitan volcanoes, through their seismic activity and also using geodetic (GPS) and geochemical observations, and we investigate their temporal evolution in recent years to highlight differences and similarities among them.

NEAPOLITAN VOLCANOES

Vesuvius

Somma-Vesuvio is a stratovolcano consisting of an older cone (Somma) with a polygenetic caldera where the Vesuvio (or Vesuvius) cone has been built up during the last 2000 years. The Somma activity started about 33 ka BP with prevailing emission of lava flows and scoriae. In the last 22 ka, the volcanic activity become highly explosive producing tens of 4/5 Volcanic Explosivity Index (VEI) eruptions, including the last plinian eruption of Pompeii in 79 AD (Sigurdsson et al., 1985), and, most recently, the sub-plinian 472 (Sulpizio et al., 2005) and 1,631 (Braccini, 1632) eruptions. After the 1,631 eruption, Vesuvius remained in open conduit condition and was characterized by almost continuous intra-crater activity, until the last eruption, which occurred in 1944. On March 18, 1944, the eruption began with a lava flow that partially destroyed the towns of Massa di Somma and San Sebastiano al Vesuvio and was followed by an explosive phase, a few days later (March 22). An eruptive column of approximately 6 km height developed causing abundant volcanic ash-fall that reached large distance from the vent (Pappalardo et al., 2014; Cubellis et al., 2013, Cubellis et al., 2016). After this eruption, Vesuvius changed from open to closed conduit conditions and, nowadays, it persists in a quiescent state. The activity of Vesuvius from 1,631 onwards is well documented by contemporary chronicles (Baratta, 1897; Alfano and Friedlaender, 1929; Santacroce, 1987 and reference therein; Marturano and Scaramella, 1998; Guidoboni, 2008), allowing us to establish the precursory phenomena, which generally preceded Vesuvian eruptions in the last four centuries. Among the precursors, earthquakes were the most common ones (Cubellis et al., 2007; Cubellis and Marturano, 2013 and reference therein; Marturano, 2006; Scandone and Giacomelli, 2008). Particularly, the seismicity of Vesuvius before and during the 1944 eruption was recorded by a seismic station (Giudicepietro et al., 2010) installed in the historic site of the Osservatorio Vesuviano (OVO site in **Figure 2**) and described by Imbò. (1954) and more recently re-evaluated by Pappalardo et al. (2014). Seismic data from that period include Long Period (LP) events, explosion and lava fountain signals. After 1944 the seismicity disappeared for some years. In 1964 a series of landslides occurred in the crater of Vesuvius, accompanied by a partial collapse of the bottom of the crater (Imbò, 1964; Imbò et al., 1964). After this event, the seismicity resumed in 1966.

Currently, Vesuvius shows moderate seismicity with some hundreds of earthquakes per year, with magnitudes typically between −1.0 and 2.0, mainly located in the axial zone of the crater. This zone extends to a depth of about 4 km (Cubellis and Marturano, 2002; Giudicepietro et al., 2010; Cubellis and Marturano, 2013; D'Auria et al., 2013; D'Auria et al., 2014; D'Auria and Massa, 2015; Ricco et al., 2021). The geochemical interpretation of the fumarolic compositions reveals the presence of a hydrothermal system, with temperatures as high as 400–450°C, possibly hosted between 1.5 and 4 km depth within the still hot volcanic conduits of the recent Vesuvius eruptions (Chiodini et al., 2001b).

Campi Flegrei

Campi Flegrei produced at least six large-scale explosive eruptions in the last 250 ka (e.g., Albert et al., 2019; De

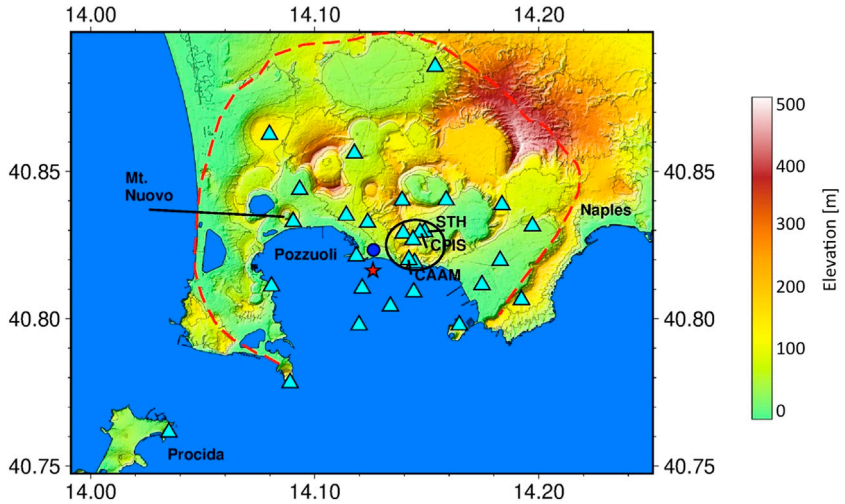

FIGURE 3 | Map of Campi Flegrei. The cyan triangles indicate the seismic network stations. STH (catalog reference station) and CPIS (used for calculating the fumarolic tremor amplitude) stations are indicated on the map. The blue circle indicates the RITE GPS station. The red star marks the area of maximum uplift (Iannaccone et al., 2018). The red dashed line indicates the edge of the caldera. The black ellipse encloses the hydrothermal area of Solfatara-Pisciarelli. Monte Nuovo is the cone formed in the last eruption (1,538).

Vivo et al., 2001). The largest of these events are the two ignimbrite eruptions of the Campanian Ignimbrite (CI, 300 km^3 DRE, 40 ka, Gebauer et al., 2014) and the Neapolitan Yellow Tuff (40 km^3, 14.9 ka, following Deino et al., 2004) that caused the collapse of the 12 km-wide Campi Flegrei caldera. In the last 15 ka this nested collapse structure was the site of a monogenetic volcanic activity producing about 70 eruptions with variable VEI, spanning from 0 to 5. The last Monte Nuovo (**Figure 3**) eruption (VEI 2) occurred in 1538 AD after a period of ca 3,000 years of quiescence and was preceded by intense and long-term precursory phenomena (Di Vito et al., 2016) such as ground deformation and seismic activity. Seismicity continued even after the eruptive event at least until the end of the 16th century (Guidoboni and Ciuccarelli, 2011). After the 16th century the area was generally under subsidence (Niccolini, 1829, Niccolini, 1839, Niccolini, 1846). The subsidence was interrupted in 1945–1953 when a first bradyseism crisis occurred, with an uplift of about 0.5 m, followed by the two main episodes of 1969–1972 (about 1.7 m uplift) and 1982–1984 (about 1.8 m uplift), which led to a total ground uplift of about 3.5 m in the central sector of the caldera (Del Gaudio et al., 2010). After 1985 subsidence reappeared and continued until 2000 leading to a ground lowering of about 85 cm. During the bradyseism crisis of 1982–84, the ground uplift was accompanied by a remarkable seismicity (more than 16,000 earthquakes, most of them with magnitude < 3, max Md = 4.0). After 1985, the seismicity in Campi Flegrei almost disappeared and resumed in July 2000 with a swarm of LP events (Saccorotti et al., 2001; D'Auria et al., 2011). From 2005 a gradual resumption of uplift occurred in Campi Flegrei with a significant increase of its rate at the end of 2012 when the Italian Department of Civil Protection raised the alert level from the base (green) to yellow (attention).

Campi Flegrei caldera is also characterized by an intense hydrothermal activity highlighted by the emission of large amounts of deeply derived gases from soil diffuse degassing and from strong fumarolic vents at Solfatara-Pisciarelli (Chiodini et al., 2001a; Cubellis et al., 2002; D'Auria et al., 2011; Chiodini et al., 2012; Amoruso et al., 2014; Cardellini et al., 2017; Tamburello et al., 2019). Seismic activity is currently increasing and it is mainly concentrated in the same hydrothermal sites of Solfatara-Pisciarelli, with hypocentral depths rarely exceeding 2 km and M < = 3.3 (Chiodini et al., 2021; Giudicepietro et al., 2021; Tramelli et al., 2021).

Ischia

Ischia is the emerged part of an active volcanic field, which rises more than 1,000 m above the seafloor (Orsi et al., 1999; Bruno et al., 2002), along the margin of an E-W trending scarp that borders to the south the Phlegraean volcanic district. At Ischia, volcanism began before 150 ka BP and has continued intermittently, with quiescent periods lasting centuries to millennia, until the last eruption in AD 1302 (Vezzoli, 1988; Orsi et al., 1996; de Vita et al., 2010). The volcanic and deformation history is dominated by the caldera-forming Monte Epomeo Green Tuff (MEGT) eruption at about 55 ka (Vezzoli, 1988), during a period of activity that generated the most voluminous and devastating eruptions of the island (Brown et al., 2008, and references therein). The MEGT caldera floor was later affected by resurgence that generated uplift of about 900 m, probably over the past 33 ka (the age of the oldest deformed rocks). Orsi et al. (1991) explain this remarkable resurgence through a simple-shearing mechanism, and tilting of differentially displaced blocks; the most uplifted one is Monte Epomeo, whereas other authors (e.g. Acocella and Funiciello, 1999), on the basis of more recent data, interpreted it as due to a trap-door like mechanism. Mount Epomeo plays an important

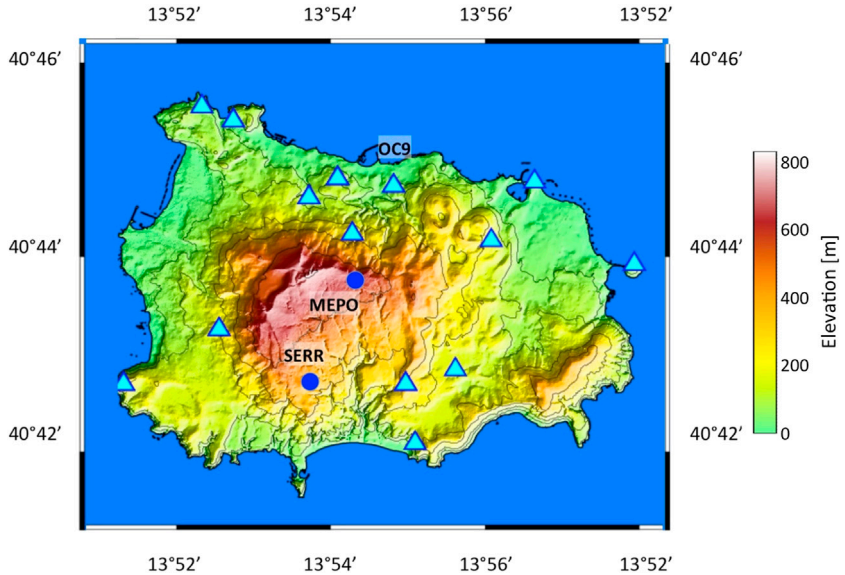

FIGURE 4 | Map of Ischia island with the seismic stations (cyan triangles) and the two GPS, stations MEPO and SERR (blue circles) that were considered in this work. OC9 is the reference station for the seismic catalog of Ischia.

role in the seismic activity of Ischia. This structure was subject to a remarkable uplift in the period between 33 ka and about 5 ka and was interpreted as a resurgent block (Vezzoli, 1988). It is not easy to date the end of the resurgence of the Mt. Epomeo block (e.g. Carlino et al., 2006; Carlino, 2012; Trasatti et al., 2019; Cubellis et al., 2020). Currently a subsidence of about 1 cm/year occurs in the northern sector of the Island, as recorded from GPS, optical leveling and DInSAR measurements (see eg: De Martino et al., 2011; Manzo et al., 2006, De Novellis et al., 2018; Trasatti et al., 2019). The post-MEGT volcanic history has been subdivided into three periods of activity based on structural and volcanological evidence, as well as geochemical and isotopic variations of the magmas erupted through time (Civetta et al., 1991). Even if, since the last eruption occurred in AD 1302, no evidence of renewal of uplift has been recorded in concurrence with more recent minor mass movements, the magmatic system of Ischia has to be considered still active. The presence of a hydrothermal system characterized by energetic circulation underneath Ischia is demonstrated by the numerous surface manifestations, including fumaroles, thermal waters, steaming grounds and mud pools. Since accurate geodetic measurements have been made (early 20th century), central-southern portion of the island has subsided. Generally, Ischia has a low level of seismicity, characterized by few events per year with a magnitude typically between -1 and 2.5 (see the catalog included in the **supplementary Datasheet S1**), which is concentrated in the Casamicciola area (D'Auria et al., 2018). However, as known, in this area, events with a relatively greater magnitude can occur (Carlino et al., 2006; Cubellis et al., 2004, 2020; De Novellis et al., 2018; D'Auria et al., 2018; Selva et al., 2021), which are potentially capable of causing severe damage to the town and population. This happened in 1883, when an earthquake with intensity XI MCS degree and magnitude of about 5 destroyed the town of Casamicciola, causing approximately 2,300 victims, and in August 2017, when an M4.0 earthquake caused severe damage to the town and two victims. The earthquake of August 2017 is the last seismic event with a significant impact on the island.

DATA

Seismic Data

The Osservatorio Vesuviano seismic network (INGV-OV) currently consists of 34 broadband digital stations and 18 short-period seismic stations (5 with only vertical component and 13 triaxial), which continuously transmit signals to the Monitoring Center. Some of them are co-located in the same site for redundancy and continuity in the catalogs. The network is designed for monitoring the active Neapolitan volcanic areas, Vesuvius (**Figure 2**), Campi Flegrei (**Figure 3**), Ischia (**Figure 4**) and provides information on seismicity at a regional scale in collaboration with the national seismic network managed by Osservatorio Nazionale Terremoti (INGV-ONT). In the period 2010–2012 the seismic network was densified on the three volcanoes. Moreover, three OBS have been installed in Campi Flegrei in recent years (Iannaccone et al., 2018). The current geometry of the network of the Neapolitan volcanoes, in low seismic noise condition, allows to reliably locate seismic events with M < 0, in Vesuvius, Campi Flegrei and Ischia.

The data are collected at Osservatorio Vesuviano in Naples through intermediate data centers (e.g. in Ercolano). The analogue station data are acquired at Posillipo data center and then transmitted to the Osservatorio Vesuviano headquarter via TCP/IP protocol using a dedicated WiFi link. Here, an Earthworm-based system (Johnson et al., 1995; Johnson 2020) is devoted to the automatic detection and location of seismic

events. This system provides a good quality location in a few tens of seconds after the detection of an earthquake.

In this article we consider the seismic catalogs of Vesuvius, Campi Flegrei and Ischia, that are routinely updated by the Osservatorio Vesuviano seismic laboratory and are available on the website www.ov.ingv.it (last accessed on March 27, 2021). The catalogs are based on single-station detections, and exploit the long historical record provided by the most ancient stations such as OVO (Vesuvius), STH (Campi Flegrei) and OC9 (Ischia). These stations are located in sites close to the main seismogenic areas of each volcano, which are the summit cone for Vesuvius, Solfatara-Pisciarelli for Campi Flegrei and the area of Casamicciola Terme for Ischia. Numerous articles analyzed in detail the catalogs of Campi Flegrei (D'Auria et al., 2011; Giudicepietro et al., 2019; Tramelli et al., 2021), Vesuvius (Giudicepietro et al., 2010; D'Auria et al., 2013) and Ischia (D'Auria et al., 2018; Selva et al., 2021). We refer to these works for an in-depth analysis of the seismological statistics of these three volcanoes. However, here we present the estimate of the completeness thresholds and the *b*-values of the entire catalogs and other basic elaborations, such as the monthly and annual distribution of all the detected earthquakes of the three areas, in order to have elements to compare the seismicity in the three volcanoes. The catalogs used in this work are also included in the **supplementary Datasheet S1**.

The traditional seismic catalog of Vesuvius is based on the earthquakes recorded at OVO station (in the historical building of Osservatorio Vesuviano in Ercolano). It begins in 1972 and includes 11,610 earthquakes, until December 2020. The catalog is based on a single station and is generated using the duration magnitude (Md), suitable for local earthquakes. The duration of the earthquakes is determined by the analysts of the seismic laboratory through visual analysis of seismograms. The same methodology is also used for the catalogs of the other volcanoes in the Neapolitan area, which are included in the **supplementary Datasheet S1**. Thanks to the BKE station (Bunker Est), which was installed on the top of Mount Vesuvius in 1999, an additional catalog of the events recorded near the crater is available. The BKE catalog (1999–2020) currently includes 18,663 events, many of which have magnitude < 1 and can only be recorded at the summit of Mount Vesuvius.

The revised catalog of Campi Flegrei covers the period from January 2007 to December 2020. It contains 4,473 earthquakes recorded at the STH reference station, installed near the Solfatara-Pisciarelli area. When the background seismic noise is particularly low, this station can detect earthquakes with magnitude < = −0.2. However, smaller earthquakes are often not locatable. Actually, only 1,437 of the 4,473 earthquakes in the catalog of the Campi Flegrei are located.

Finally, the seismic catalog of Ischia includes 147 earthquakes recorded in the 1999–2020 interval at OC9 station installed in the historical Osservatorio Geofisico della Gran Sentinella in Casamicciola Terme (Ischia), founded in 1885 by the geophysicist Giulio Grablovitz. Most of these earthquakes are located in the Casamicciola area.

We consider a period of 14 years, from January 2007 to November 2020, to compare the time evolution of the seismicity of the three volcanoes. During the selected period, the permanent seismic network of Osservatorio Vesuviano recorded a total of 16,804 events, of which 12,208 in Vesuvius, 4,473 in Campi Flegrei and 123 in Ischia.

In addition to the catalog data, we use a selection of the locations of the Campi Flegrei earthquakes, the best quality ones, e g., A and B quality with location errors typically in the range of 200–300 m (locations and related errors are reported in the **supplementary Datasheet S1**) from the INGV Osservatorio Vesuviano database. We use the hypocentral parameters of the INGV database also as initial locations to relocate the earthquakes of the April 26, 2020 swarm, the largest one that occurred in Campi Flegrei since 1984 in terms of energy released. Moreover, we calculated ex novo the locations of the Vesuvius earthquakes from 2015 to 2020 and in 1999, to compare the most relevant swarm, which occurred in October 1999, with that occurred in November-December 2018 (see. "Methods"). For Ischia we used the locations recently published in D'Auria et al. (2018) and Selva et al. (2021).

GPS Data

We use the data of few selected stations of the permanent GPS network dedicated to monitoring the Neapolitan volcanoes (De Martino et al., 2011; Tammaro et al., 2013; De Martino et al., 2014; Devoti et al., 2018; De Martino et al., 2020). In particular, to highlight the vertical ground displacements in the three Neapolitan volcanoes, we used the daily average of the vertical component from the RITE station (**Figure 3**) in Campi Flegrei (between January 2010 and November 2020); BKNO (**Figure 2**) at Vesuvius (between June 2010 and November 2020) and SERR (January 2004–November 2020) and MEPO (February 2017 - November 2020) in Ischia (**Figure 4**).

Geochemical Data

The fumaroles located in the bottom of the Vesuvius crater are sampled systematically in the frame of the surveillance of the volcano. Here we consider 68 samples (collected from 2010 to November 2020) for which we estimate the equilibrium temperatures within the gas system H_2O-H_2-CO_2-CH_4-CO using the method described in Chiodini et al. (2001a) and Caliro et al. (2011). The estimated temperatures, in the range from 379 to 441°C, are regularly reported in the Osservatorio Vesuviano surveillance reports (see, e.g., Figure. 4.3 in www.ov.ingv.it/ov/bollettini-mensili-campania/Bollettino_Mensile_Vesuvio_2020_12.pdf).

METHODS

In this study we used hypoDD (Waldhauser and Ellsworth, 2000) software to relocate the events of the seismic swarm occurred in Campi Flegrei on April 26, 2020, which was the largest swarm since the volcanic crisis of 1982–85 and included the largest Phlegraean earthquake (Md 3.3) recorded since 1984. We relocated this important swarm to compare it with two other significant swarms that occurred on October 7, 2015 and December 6, 2019, respectively, which occurred in the same

area and showed particular characteristics studied in Giudicepietro et al. (2021). As initial locations we used those determined by the Osservatorio Vesuviano seismic laboratory, with the hypo71 (Lee and Lahr, 1975) program that are available online at www.ov.ingv.it (last accessed March 27, 2021). We did not use cross-correlation derived relative picks for the relocation but we exploited the manual picking of the P and S phases carried out by the seismic laboratory analysts of the Osservatorio Vesuviano (INGV). We preprocessed the phase picking data using the ph2dt software (a utility available in the hypoDD package) to obtain travel time differences for pairs of earthquakes at common stations. Then we applied hypoDD using the conjugate gradients method (LSQR, Paige and Saunders, 1982). We reported the relocation output file in the **supplementary Datasheet S1**. This file contains the hypocentral parameters including the location errors, however the error values are not meaningful in case the relocations are computed using LSQR method (Paige and Saunders, 1982). The mean horizontal and vertical errors on the initial locations are about 300 m and 200 m respectively.

We located the earthquakes that occurred on Vesuvius between January 2015 and November 2020 using hypo71, adopting a velocity model derived from the integration of different velocity models of the Neapolitan volcanic area elaborated in D'Auria et al. (2008). To overcome the problems due to the topography of the volcano and the close spacing of the seismic network stations we considered 1,000 m altitude as the reference level on the volcanic edifice and we appropriately configured the station delays in the locator input file. In this way we were able to locate the small shallow earthquakes that occur inside the volcanic edifice above the sea level. We also located the earthquakes of a swarm that occurred in October 1999, which include the largest event recorded on Vesuvius so far (M = 3.6). The mean horizontal and vertical errors on the locations are about 350 m and 420 m respectively (see **supplementary Datasheet S1**).

Furthermore, we located a Long Period (LP) event, which occurred at Vesuvius on November 16, 2020. LP events are very rare on Vesuvius. One of them took place on July 20, 2003 and was studied by Cusano et al. (2013). This type of events is related to the presence of fluids in the seismogenic volume and can be associated with magmatic or hydrothermal fluids (Chouet and Matoza, 2013). In order to locate the LP transient recorded on November 16, 2020 we exploited the onset of the event, which is recognizable on the vertical component of 7 different stations. We estimated the time delay through cross correlation analysis of the vertical component of the signals recorded at different stations. We computed the cross correlation using the Obspy toolbox for seismology utilities (Krischer et al., 2015). So we retrieved the arrival times of the LP transient at 7 different stations and we located it with the same method illustrated above.

In order to statistically characterize the seismicity of the three areas and to be able to compare them, we estimated the magnitude of completeness (Mc) and the *b*-values for the entire catalogs of the single reference stations for the three volcanoes, STH (Campi Flegrei), BKE and OVO (Vesuvius), OC9 (Ischia). We adopted the method of Aki. (1965), which gives the *b*-value as a function of Mc. First, we varied the Mc and calculated the residual between the data with M> = Mc and the Gutenberg-Richter magnitude-frequency distribution. Then, we chose the Mc associated with the smaller residual (see **supplementary Datasheet S1**). So, we obtained the following results: OVO catalog *b*-value 1.7 Mc 1.7, BKE catalog *b*-value 1.5 Mc 1.6, STH catalog *b*-value 0.95 Mc 0.0, OC9 catalog *b*-value 0.6 Mc 0.4. We also compared our results with those reported in recent literature (D'Auria et al., 2013, D'Auria et al., 2018; Giudicepietro et al., 2019; Tramelli et al., 2021) and we found consistent values. Concerning the estimates of the *b*-value reported in Selva et al. (2021) for Ischia, where the authors found 1.11, the difference in the *b*-value is mostly due to the different adopted magnitude (Mw instead of Md) and the use of a new integrated catalog.

To highlight the changes taking place in Campi Flegrei, we updated the time series of Pisciarelli's fumarolic tremor and the "background seismicity" (Chiodini et al., 2017b), two seismological parameters that have significant correlations with geochemical variations in the Phlegraean area.

The amplitude of the fumarolic tremor is measured on the vertical component signal of the CPIS station, installed in 2010 in Pisciarelli, 8 m away from the main fumarole of Campi Flegrei caldera. The signal is filtered in the characteristic frequency band generated by the fumarole and the nearby mud pool (5–15 Hz). The amplitude is calculated as the average of the absolute value (RSAM as defined in Endo and Murray, 1991) over 30-min windows. The details are described in Chiodini et al. (2017a), Giudicepietro et al. (2019) and Giudicepietro et al. (2021). The "background seismicity" of the Campi Flegrei caldera was defined in Chiodini et al., 2017b by extracting the seismic clusters (or earthquake swarms) from the catalog and considering them as a single episode of seismicity like a single event. This parameter shows a good agreement with ground deformations and with the temporal evolution of geochemical parameters (Chiodini et al., 2017b).

For the seismic data of Ischia, where earthquakes are less frequent than at Vesuvius and Campi Flegrei, we have not carried out new analyses and have reported already available locations (D'Auria et al., 2018; Selva et al., 2021).

The results of the original analyses we performed for this article, i.e. the relocations of the April 26, 2020 swarm at Campi Flegrei, the locations of the earthquakes recorded on Vesuvius between January 2015 and November 2020 and in 1999, the location of the LP transient recorded on Vesuvius on November 16, 2020, are included in the **supplementary Datasheet S1** together with the seismic catalogs which are also available on the Osservatorio Vesuviano (INGV) website (www.ingv.it, last accessed March 30, 2021), where they are periodically updated.

RESULTS

In this section we present the results of the data analysis in the context of the knowledge on the eruptive history, historical seismicity and dynamics of the three Neapolitan volcanoes. For Campi Flegrei and Vesuvius we show results from new

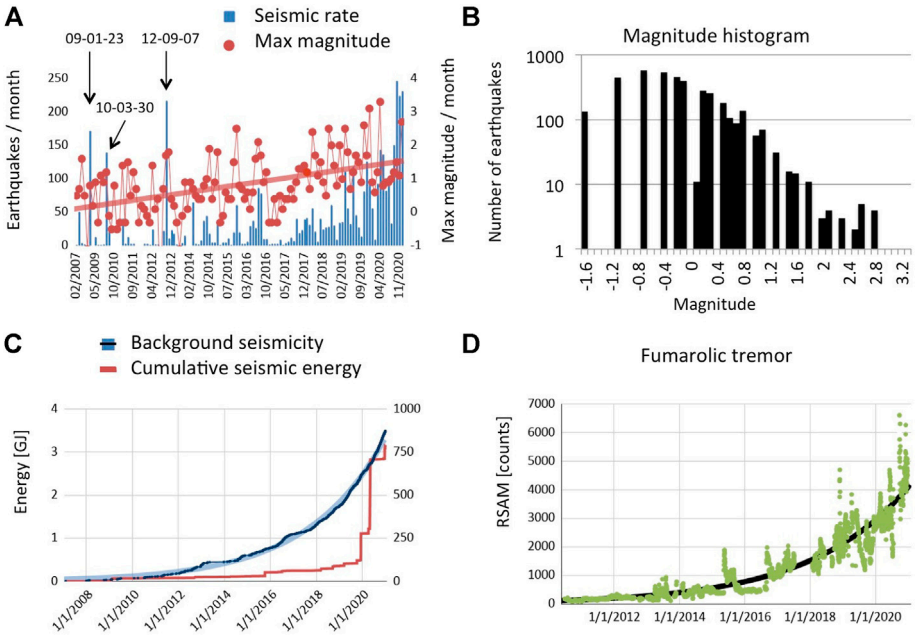

FIGURE 5 | Seismicity of Campi Flegrei. **(A)** Histogram of earthquakes per month detected by the STH seismic station since January 2007 (seismic catalog of Campi Flegrei, in **supplementary Datasheet S1**). The red curve with the circle markers shows the maximum magnitude of each month. **(B)** Histogram of earthquake magnitudes in the Campi Flegrei catalog (Log scale on vertical axis). **(C)** The red curve represents the cumulative seismic energy in GJ. The black curve is the 'background seismicity' defined in Chiodini et al. (2017b) (right axis). The light blue curve represents an exponential trend line. It can be seen that the exponential trend closely approximates the temporal evolution of the 'background seismicity'. **(D)** In green the amplitude of the fumarolic tremor since January 2010 recorded at CPIS station that was installed on January 2010. The black curve represents an exponential trend line. It can be seen that also in this case the exponential trend closely approximates the temporal evolution of the fumarolic tremor indicating an acceleration of the ongoing process.

analyses, whereas for Ischia we summarize results from previous works.

Campi Flegrei Seismicity

Over the past 2 decades a gradual increase in seismicity has occurred in Campi Flegrei (Tramelli et al., 2021). Until 2014, earthquakes were rare and occurred in swarms of numerous events with low magnitudes, such as on January 23, 2009 (173 events, $M_{max} = 0.0$), March 30, 2010 (141 events, $M_{max} = 1.2$) and September 7, 2012 (188 events, $M_{max} = 1.7$) (**Figure 5A**). After 2014, the seismicity occurrence changed: the events became more frequent over time (**Figures 5A,C**), the seismic energy release and the "background seismicity" (Chiodini et al., 2017b) increased (**Figure 5C**), the number of events in a single swarm decreased even if earthquakes with greater magnitude characterized the swarms. The histogram in **Figure 5B** shows the magnitude distribution ($M_{mean} = -0.2$). The magnitude-frequency distribution can be consistent with a Gutenberg-Richter distribution with the *b*-value = 0.95 (see Method section). The red curve in **Figure 5A** shows the monthly maximum magnitude. The fumarolic tremor that is a robust indicator of the activity of the Pisciarelli-Solfatara hydrothermal system (Chiodini et al., 2017a; Giudicepietro et al., 2019; Giudicepietro et al., 2021) showed a continuous increase and reached its maximum amplitude in September 2020 (**Figure 5D**).

A relationship between seismicity and injection of fluids into the hydrothermal system was evidenced for the two swarms of October 7, 2015 and December 6, 2019 in Giudicepietro et al. (2021). This relationship was highlighted by a sudden increase in the amplitude of the fumarolic tremor at Pisciarelli (Giudicepietro et al., 2021), recognized as a proxy of the activity of the hydrothermal system at Campi Flegrei (Chiodini et al., 2016).

In recent decades, after the 1982–1984 crisis, the most energetic earthquake swarm occurred on April 26, 2020. Here, we analyzed that swarm comparing it with the two swarms occurred on October 7, 2015 and December 6, 2019, studied in Giudicepietro et al. (2021), which are located in the same seismogenic volume. We compared the waveform of the April 26, 2020 major earthquake (Md 3.3, the largest one since 1984) with two of the largest events belonging to the swarms of October 2015 and December 2019, which form a distinct family of earthquakes (Giudicepietro et al., 2021). We calculated the cross-correlation of a 1s-sliding window of the April 26, 2020 (Md 3.3) earthquake onset (CAAM station vertical component) with the two selected events of the swarms of October 7, 2015 and December 6, 2019. We found a correlation of 0.9 with the onset of both events. This suggests that the April 26, 2020 (Md 3.3) earthquake belongs to the same family as the largest events of the swarms that occur in Pisciarelli area. **Figure 6** shows the spectrogram and waveform of this earthquake and the comparison of its onset with the two events of the October 7, 2015 and December 6, 2019 swarms. The spectrogram (**Figure 6A**) is typical of VT earthquakes with an impulsive onset characterized by a wide frequency range up to

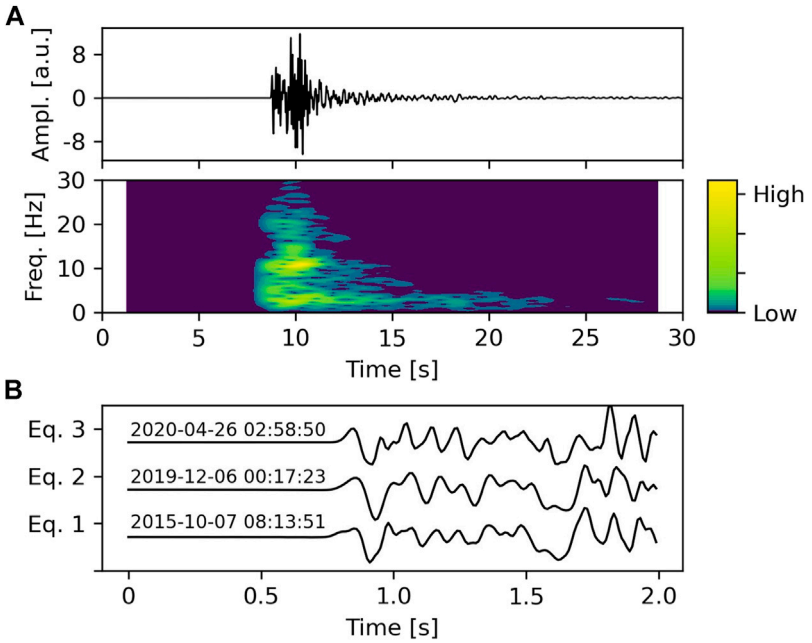

FIGURE 6 | (A) Seismogram and spectrogram of the Md 3.3 earthquake recorded during the April 26, 2020 swarm. **(B)** The onset of the earthquake (Eq. 3) is compared with one of the major events of the swarm occurred on October 7, 2015 (Eq. 1 Md = 2.3) and the strongest event of the December 6, 2019 swarm (Eq. 2 Md = 3.1). CAAM station (see **Figure 3**) vertical components are shown.

30 Hz. The comparison of the onsets (**Figure 6B**) confirms that the main event of the April 26, 2020 swarm shares with the major earthquakes occurred in recent years similar waveform characteristics. Furthermore, we calculated the focal mechanism of the April 26, 2020 Md 3.3 earthquake using FPFIT software (Reasenberg and Oppenheimer, 1985). It shows a solution that can be associated with normal-type mechanisms with an oblique component (**Figure 7D**) and it is similar to those found in Giudicepietro et al. (2021) for the major earthquakes of the October 2015 and December 2019 swarms. This further similarity with the major earthquakes of the swarms located in the Solfatara–Pisciarelli area shows that the same seismogenic structure has been reactivated several times in recent years.

We also performed relative locations of the April 26, 2020 swarm (blue circles in **Figure 7**) using the hypoDD software (Waldhauser and Ellsworth, 2000). The relocation confirmed that the April 26, 2020 swarm occurred along the same conduit-like path already identified in Giudicepietro et al. (2021) for the October 7, 2015 and December 6, 2019 swarms (**Figure 7**).

Typically the relatively high magnitude events (Md max = 3.3) of the swarms occurred in Solfatara–Pisciarelli area, and in particular for the three main swarms considered in this work (Oct 2015, Dec 2019 and Apr 2020), are deeper than those of the ordinary Campi Flegrei seismicity (Chiodini et al., 2021). In the December 6, 2019 swarm a clear migration of the hypocenters toward the surface was also observed (Giudicepietro et al., 2021).

The double-difference locations of the swarms of October 7, 2015 and December 6, 2019 are published as **supplementary Datasheet S1** in Giudicepietro et al. (2021). The double-difference locations of the events of the swarm that occurred on April 26, 2020 are included in the **supplementary Datasheet S1** of this article. The locations of the earthquakes from 2000 to 2020 are available online on the Osservatorio Vesuviano (INGV) website (www.ov.ingv.it), as well as the seismic catalogs.

More recently, four earthquakes with magnitude Md > 2 were recorded in December 2020 (see **supplementary Datasheet S1**, **Table 1**). Two of these earthquakes belong to a swarm of 51 events, which occurred on December 19, 2020. In this case a sudden increase in the amplitude of the fumarolic tremor was observed during and after the swarm, confirming a mechanism linked to fluid injection in the hydrothermal system, similar to that observed for the swarms of the October 7, 2015 and December 6, 2019 (Giudicepietro et al., 2021). This shows that at least since 2015 a seismicity directly linked to injections of fluids in conduit-type paths has occurred in the Campi Flegrei, even if this is not the only source of earthquakes acting in the Phlegraean caldera.

Mt. Vesuvius Seismicity

Vesuvius is a very active volcano, with a predominantly explosive eruptive style (Arnò et al., 1987; Scandone and Giacomelli, 2008), that is located in a densely populated area (**Figure 2**). These factors make Vesuvius one of the highest risk volcanoes in the world.

After the 1944 eruption the seismicity of Vesuvius was very low, with few earthquakes per year, until 1966, when a local seismicity appeared, consisting of Volcano Tectonic events (VT), located in axis with the crater. The complete catalog from 1944 was reconstructed in Giudicepietro et al. (2010). Since 1972 the

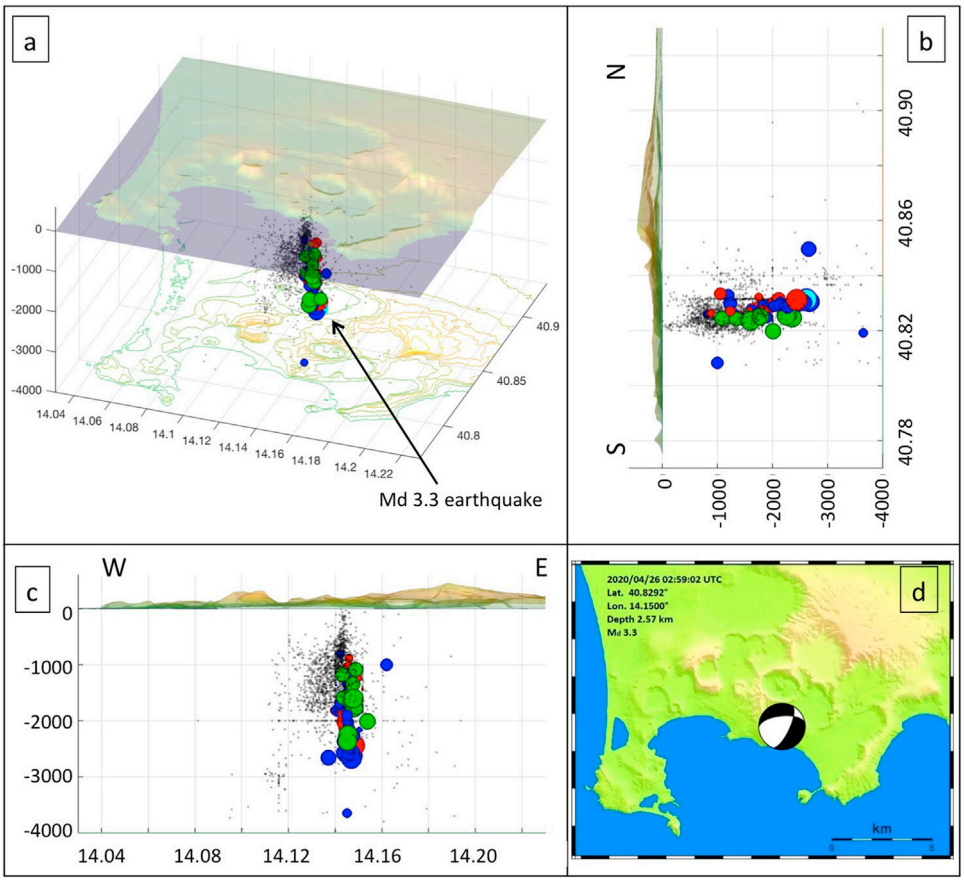

FIGURE 7 | Locations (A and B quality) of the earthquakes recorded in Campi Flegrei between January 2000 and November 2020. The hypocenters are indicated with a black dot (70% transparency). The green circles mark the earthquakes of the October 7, 2015 swarm. The red circles highlight the earthquakes of the December 6, 2019 swarm. The blue circles indicate the earthquake locations of the April 26, 2020 swarm (included in **supplementary Datasheet S1**). Only for events that belong to these three swarms the diameter of the circle is proportional to the magnitude. The location of the April 26, 2020 Md 3.3 earthquake is shown in cyan (lat: 40.831319N; lon: 14.147029E; depth: 2,618 m b.s.l.).

TABLE 1 | Parameters of the frequency-magnitude distribution (*b*-value and Mc) of the three Neapolitan volcanic areas on the basis of single station catalogs.

Area	Last eruption	Station	Start time	Mc	*b*-value
Vesuvius	1944	OVO	1972	1.7	1.7
Vesuvius	"	BKE	1999	1.6	1.5
Campi flegrei	1538 AD	STH	2007	0.0	0.95
Ischia	1302 AD	OC9	1999	0.4	0.6

estimation of Vesuvian earthquake magnitude became systematic and allowed to create the seismic catalog (**Figure 8A**) based on the OVO station, installed at the Osservatorio Vesuviano historical site (**Figure 2**).

The study of Vesuvius seismicity that occurred in the last 50 years and the densification of the seismic network in the summit area (**Figure 2**) made it possible to recognize two seismogenic volumes (Giudicepietro et al., 2010; D'Auria et al., 2013), one at a depth of about 4 km below the top of the edifice and the other one much shallower, where very small magnitude earthquakes are concentrated. The OVO station is mainly sensitive to earthquakes originated in the deep seismogenic zone whereas the BKE station can record even the shallow small earthquakes. Therefore, the comparison of OVO and BKE catalogs gives a picture of the two seismogenic volume temporal evolutions. Since 2008, earthquakes located in the deepest seismogenic zone decreased whereas shallow earthquakes were increasingly recorded (**Figure 8B**).

The implementation of a dense network in the summit area of Vesuvius between 2009 and 2011 made it possible to locate the very small magnitude (typically <0.5) earthquakes recorded at the top of Vesuvius, and so to discover the shallow seismogenic volume within the volcanic edifice (**Figure 9A**).

The most significant seismic crisis recorded at Vesuvius after the last eruption was on October 9, 1999 when a swarm of earthquakes with a relatively large magnitude occurred (M_{max} = 3.6, the highest magnitude recorded so far at Vesuvius) (**Figure 9C**). In more recent times, a significant swarm occurred between November 29 and December 1, 2018 (**Figure 9B**). We compared the earthquake locations of the

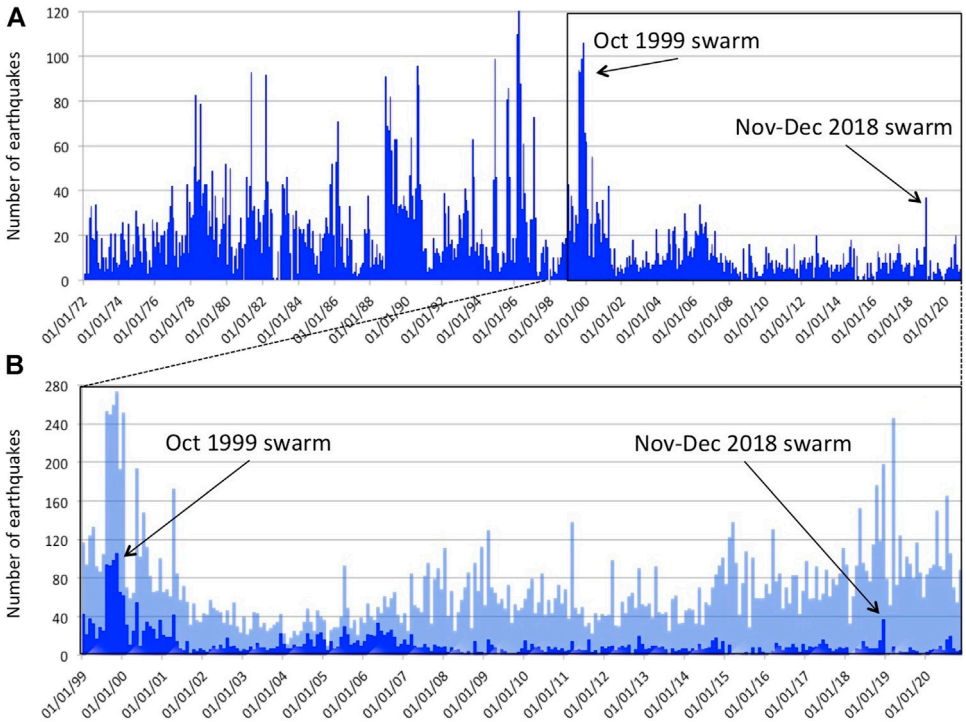

FIGURE 8 | (A) Number of earthquakes per month detected by the OVO station from 1972 to December 31, 2020. **(B)** Comparison between the number of earthquakes per month detected by the OVO station (blue) and the BKE station (light blue) from 1999 to 2020 (November 30). The catalogs are included in the **supplementary Datasheet S1**.

two swarms and we found that the events of both swarms are predominantly located in the deep seismogenic volume (**Figure 9D**). In addition, some events of the 2018 swarm were located in the shallower seismogenic zone. The lack of earthquakes in the shallow zone during the 1999 swarm (**Figure 9C**) is due to the seismic network configuration, which did not allow their location at that time. Actually, they were recorded by the BKE station, but it was not possible to locate them because the other stations did not register them.

Vesuvius seismic events are generally VT earthquakes (**Figure 10A**) with a magnitude that rarely exceeds 2 (**Figure 10B**). The magnitude-frequency distribution in **Figure 10B** is reasonably consistent with a Gutenberg-Richter distribution with the *b*-value = 1.5 (see Method section). Recently, the Vesuvius network recorded three seismic transients characterized by frequencies between 1 and 5 Hz that occurred between 5:58 and 6:00 (UTC) on November 16, 2020. These events, which can be classified as LP events based on their frequency content (**Figure 10C**), have emergent onset and duration of about 30 s each. However, the second has a clearer onset than the others so we located it by calculating the time delay of its onset at different stations using cross-correlation (**Figure 10D**). The location falls at the base of the deep seismogenic zone (cyan circle in **Figure 9**).

Ischia Seismicity

The seismicity of Ischia island has been instrumentally monitored since 1993. Before then we can still count on a historical catalog that goes up to the 8th century BC (**Figure 11**). This richness of historical information is to be attributed to the tourist attraction that the Ischia island has always exercised on people who have left written traces of what they have seen and heard during their holidays. Besides, since 1885 a seismic tank was working in the Geophysical Observatory of Casamicciola. This innovative instrument capable of measuring and recording the oscillations of the water contained in a tank was installed by the scientist Giulio Grablovitz (1846–1928) and maintained until 1923 (Luongo et al., 2012; Cubellis and Luongo, 2018; D'Auria et al., 2018). After a gap of 70 years, the first seismic station was installed in the same place of the seismic tank, Casamicciola Observatory (OC9 in **Figure 4**).

The network was gradually improved until the four seismic sites equipped in 2011. After the 2017 M4.0 earthquake the network was improved reaching a total of 9 permanent and 5 mobile seismic stations. The complete (hystorical and instrumental) catalog has been recently revised by Selva et al. (2021). Their analysis evidenced that the Ischia seismicity is not stationary: the annual rate for earthquakes with a magnitude higher than 3.6 in the past (1750–1884) was six times larger than the current one (1885–2019) (Selva et al., 2021). These authors estimated a *b*-value higher than 1, as usual for volcanic areas, but the non-stationarity of the distribution of the seismic events makes the Gutenberg-Richter not the most appropriate relationship to describe the process. For the instrumental catalog the magnitude is estimated from the duration of the seismogram recorded at a seismic station located in the Casamicciola

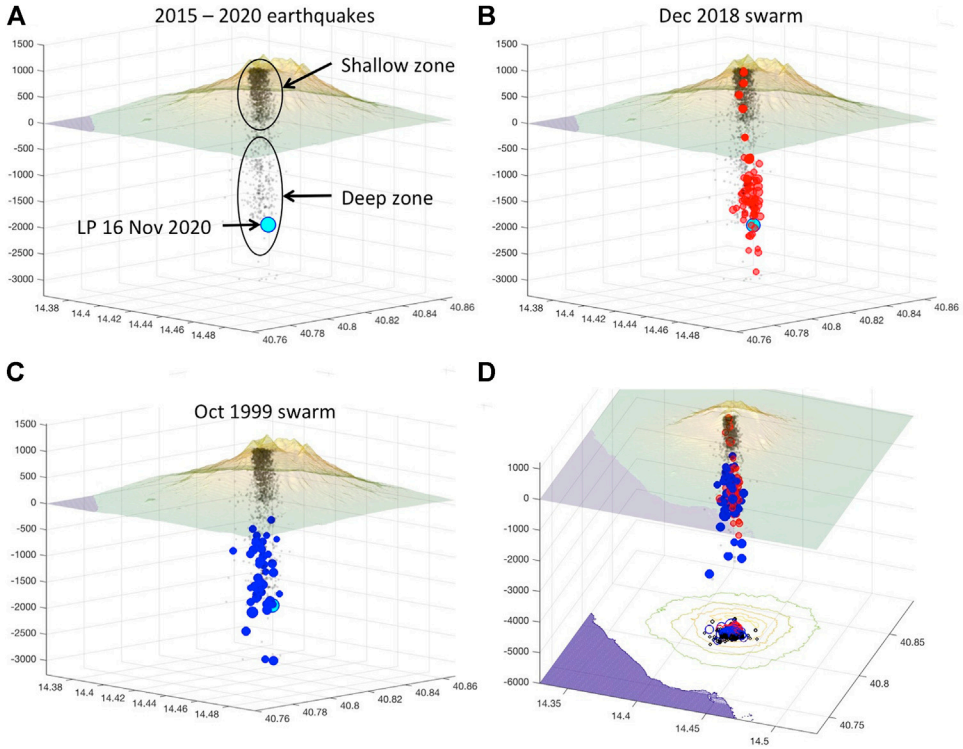

FIGURE 9 | Earthquake locations at Vesuvius. **(A)** Location of earthquakes recorded on Vesuvius between January 2015 and November 2020. The events are indicated with a black dot (70% transparency). The cyan circle indicates the location of the LP transient recorded on November 16, 2020 at 5:58:55 (UTC). The two ellipses surround the "shallow" and "deep" seismogenic zones. **(B)** The red circles highlight the earthquakes of the swarm that occurred on November 30 December 1, 2018. **(C)** The blue circles indicate the earthquakes of the October 1999 swarm. The plot in panel **(D)** shows the comparison between the locations of the two swarms. In all plots the location of the LP transient is reported as a cyan circle. The sizes of the red and blue circles are proportional to the magnitudes of earthquakes of 2018 and 1999 swarms, respectively. The locations of the swarms and the LP transient are included in the **supplementary Datasheet S1**.

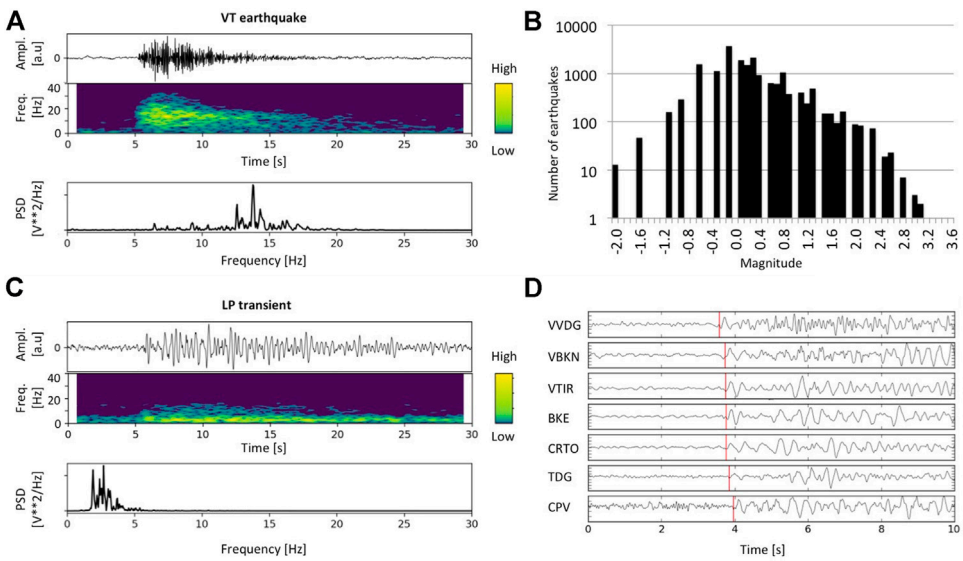

FIGURE 10 | (A) Seismogram, spectrogram and spectrum of a typical Vesuvian VT earthquake recorded on November 29, 2020 at 5:16 am. **(B)** Distribution of the magnitude of the earthquakes recorded by the BKE station from 1999 to 2020 (BKE catalog; Log scale on vertical axis). **(C)** Seismogram, spectrogram and spectrum of the LP transient recorded on November 16, 2020 at 5:16 am. **(D)** Picking of the onset of the LP transient recorded on November 16, 2020 at 5:59 am. For the position of the seismic stations see **Figure 1**.

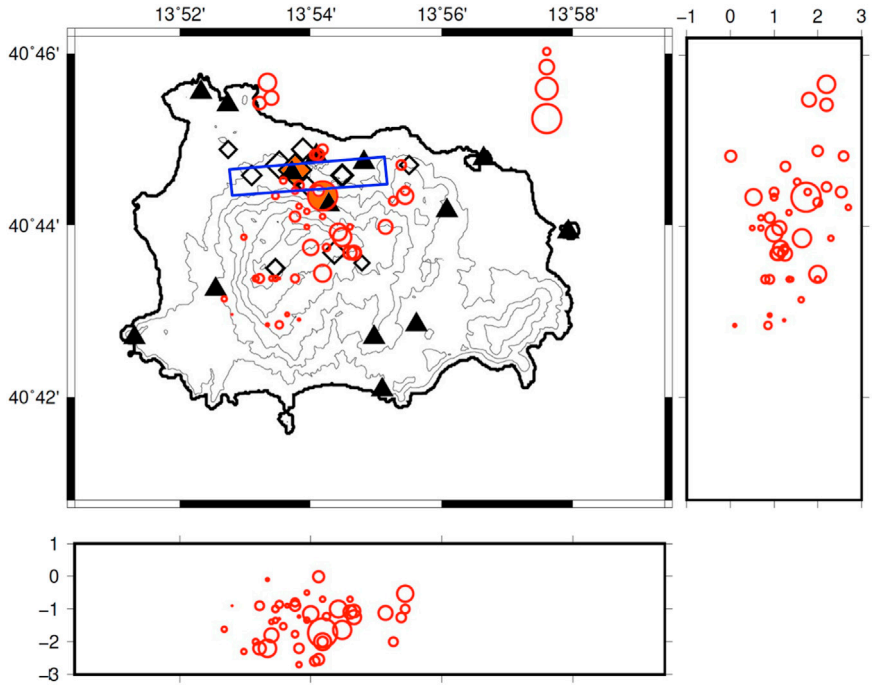

FIGURE 11 | Map of Ischia island with the seismic stations (black triangles), the locations of earthquakes (red circles) recorded by the seismic network and the locations of historical earthquakes (black diamonds). Instrumental and hystorical catalogs are from Selva et al. (2021) and integrated with the earthquakes occurred in 2020. Diamond and circle filled in with orange indicate the July 28, 1883 and the August 21, 2017 earthquakes, respectively. For instrumental earthquakes, the size of the circle indicates the magnitude according to the scale shown at the top right of the figure. East-West and North-South sections are shown. The blue rectangle shows the fault trace of the August 21, 2017 earthquake retrieved in De Novellis et al. (2018). In the lower and lateral panels, the depths of the hypocenters are expressed in km.

Observatory (D'Auria et al., 2018). The magnitude of the historical earthquakes has been converted from the intensity (Selva et al., 2021 and reference therein). As expected, the completeness magnitude highly decreases with time thanks to the improvement of the seismic network in the last decades.

The seismicity of Ischia is mainly associated with the faults of the northern boundary of the Mt. Epomeo block. Ischia indeed experienced one of the highest uplift measured at any volcano (more than 900 m in 35–55 ka) (Trasatti et al., 2019 and references therein), which produced a fault-bounded block (the Mt. Epomeo block) with topmost uplift to the NW and an overall tilt downward SE (Acocella and Funiciello, 1999). Currently the Epomeo block is subject to subsidence.

Several destructive earthquakes have been located in the northern part of the island with shallow hypocentre and estimated magnitude between 3.6 and 5.2: in 1,228 (700 casualties), 1796 (7 casualties), 1828 (30 casualties), 1881 (126 casualties), 1883 (2,333 casualties), and 2017 (2 casualties) (Cubellis and Luongo, 1998, 2018; D'Auria et al., 2018; De Novellis et al., 2018; Cubellis et al., 2020; Selva et al., 2021; Carlino et al., 2021).

DISCUSSION

Using the catalogs based on single stations, edited and periodically updated by the seismic laboratory of the Osservatorio Vesuviano INGV, we obtained the *b*-values for the three areas shown in **Table 1** (see Methods section).

As is known (Wiemer and Benoit, 1996), a positive anomaly of the *b*-value may indicate a higher pore pressure and a higher temperature of the earthquake source region. This is found in the analysis of the Vesuvius catalogs (OVO and BKE stations), whereas for Campi Flegrei the *b*-value does not show significant anomalies. On the contrary, the area of Casamicciola Terme in Ischia, where the OC9 station is located, shows a negative anomaly that could be consistent with the tectonic nature of the island's seismicity. By applying the frequency-magnitude distribution analysis to a sliding window of a given number of earthquakes, Tramelli et al. (2021) showed that the *b*-value in Campi Flegrei increased over time and exceeded 1 in 2020. An increase over time of the *b*-value in Campi Flegrei was also highlighted by Giudicepietro et al. (2019). Similarly, Selva et al. (2021) found a *b*-value greater than 1 for Ischia using a new integrated seismic catalog. An in-depth discussion of this aspect is beyond the scope of this article. Taking into account the results of Tramelli et al. (2021), which were obtained by analyzing the same catalog used for this article, here we can highlight that the *b*-values calculated on the entire catalogs based on single stations suggest differences in the seismogenic conditions of Ischia with respect to Campi Flegrei and Vesuvius. Furthermore, the positive anomaly of the *b*-value at Vesuvius suggests a plumbing system characterized by high temperature and pore pressure. These physical conditions of

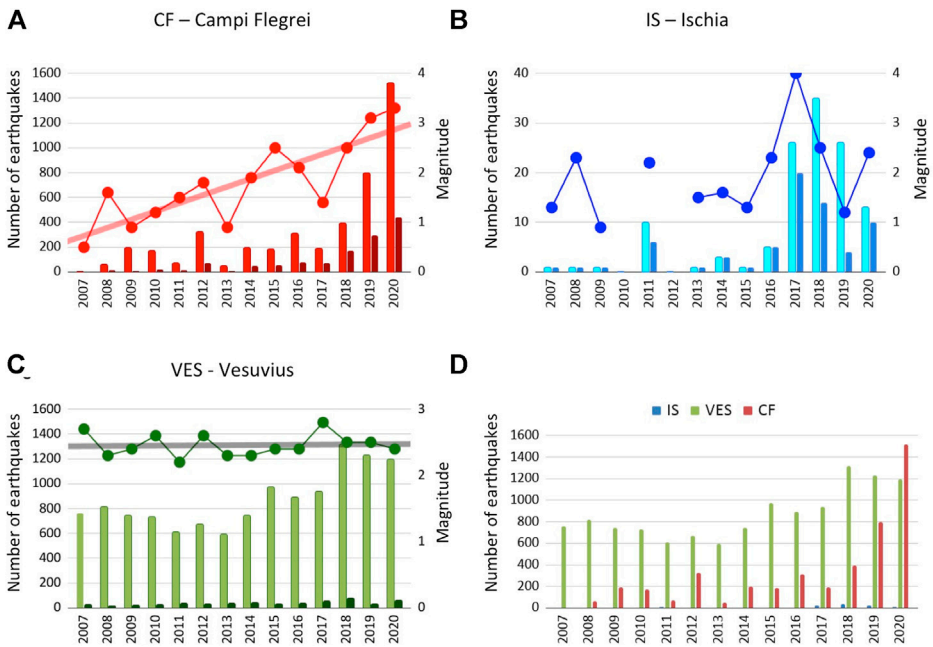

FIGURE 12 | Comparison of the seismicity of the three Neapolitan volcanoes in the period 2007–2020. **(A)** Histogram of occurrence of earthquakes in Campi Flegrei (all detected events in red and earthquakes of M> = Mc in dark red) and maximum magnitude (red curve). **(B)** Histogram of occurrence of earthquakes in Ischia (all detected events in cyan and earthquakes of M> = Mc in blue) and maximum magnitude (blue curve). **(C)** Histogram of occurrence of earthquakes in Vesuvius (all detected events in green and earthquakes with M> = Mc in dark green. For the latter the values on the *y* axis are multiplied by 2) and maximum magnitude (green curve). Linear trend lines are reported for the maximum magnitude curve in the three volcanoes. **(D)** Histogram summarizing the occurrence of earthquakes in the three volcanoes. IS = Ischia; Ves = Vesuvius; CF = Campi Flegrei.

TABLE 2 | Earthquakes per year in Vesuvius, Campi Flegrei and Ischia volcanoes in 2007–2020.

Area	2007	2008	2009	2010	2011	2012	2013	2014	2015	2016	2017	2018	2019	2020
VES	760	817	744	731	608	673	593	743	974	891	938	1,315	1,227	1,195
CF	1	62	193	174	72	323	48	198	183	315	189	396	799	1,520
IS	1	1	1	0	10	0	1	3	1	5	26	35	26	13

the seismogenic volumes are consistent with the fact that Vesuvius erupted more recently than the other volcanoes (**Table 1**).

For describing the temporal evolution of the seismicity of the Neapolitan volcanoes in recent years, we consider the period January 2007–December 2020 (**Figure 12** and **Table 2**), which is covered by the catalogs of all three volcanoes. In the selected period some changes in seismicity were observed in the area. Particularly Campi Flegrei, as already mentioned, have been subject to a gradual intensification of the seismicity which became remarkable in the last year (**Figure 12A**), when the number of earthquakes has, for the first time, exceeded those of Vesuvius (**Figure 12D**). The seismicity of Ischia was dominated by the Md 4.0 earthquake of August 21, 2017 and by the aftershocks that followed it. For this reason the seismic activity of Ischia showed variations in recent years (**Figure 12B**). Finally, Vesuvius was characterized by a rate of several hundred events per year. From 2018 to 2020 this rate exceeded 1,000 events/year (**Figure 12C**). This variation, visible in the annual rate of all detected Vesuvius earthquakes, is also recognizable in the annual rate of earthquakes of M> = Mc (**Figure 12C**). Therefore, Vesuvius also showed a modest increase in seismicity in the last years, starting from 2018, when a significant swarm occurred (**Figure 9B**).

In terms of the number of earthquakes, Ischia is the least active volcano in the Neapolitan area (**Figure 13A**). However, in terms of seismic energy released in January 2007–December 2020, Ischia seismicity is more relevant than that of the other two volcanoes (**Figure 13B**).

The seismicity of Ischia is interpreted as the effect of a stress field dominated by the gravitational and thermal loading of the block of Mount Epomeo that undergoes rotation northwards and translation southwards by gravitational spreading action (Cubellis et al., 2020). Cubellis et al. (2020) propose for the seismic energy release a stick-slip mechanism as it provides a seismicity of the island characterized by single transients and precludes the generation of significant aftershocks, as it was observed with the earthquake of August 21, 2017.

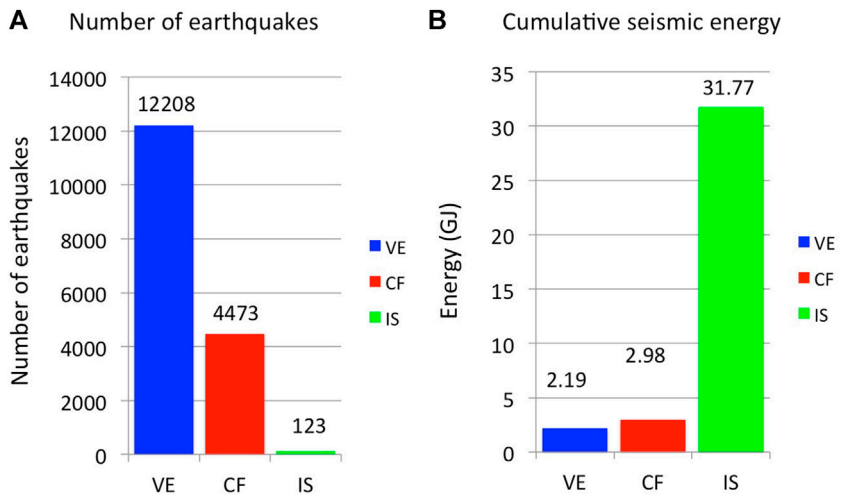

FIGURE 13 | (A) Bar charts showing the number of earthquakes recorded on Vesuvius (blue), Campi Flegrei (red) and Ischia (green) from January 2007 to December 2020. **(B)** Cumulative energy of the earthquakes from January 2007 to December 2020 of Vesuvius (blue), Campi Flegrei (red) and Ischia (green).

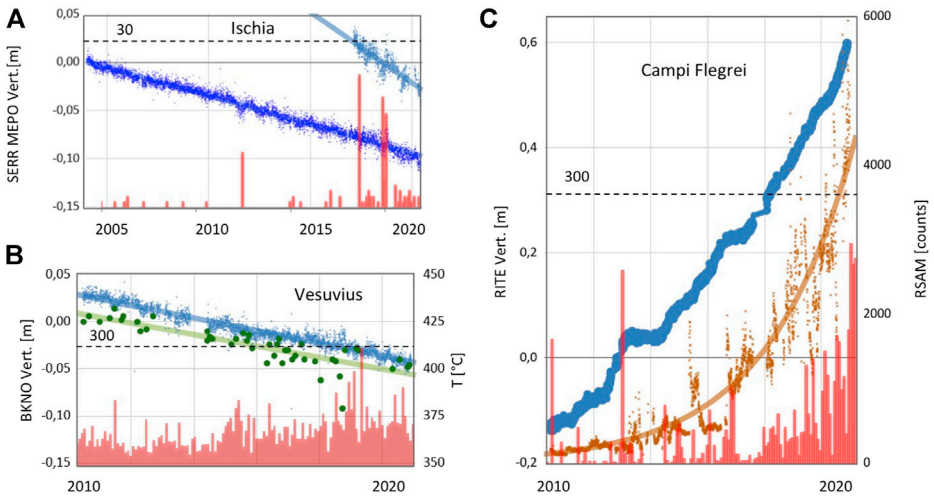

FIGURE 14 | (A) Time series of seismic and geodetic parameters recorded in Ischia from 2004 to 2020. In light blue the daily time series (2017–2020) of the vertical component of MEPO GPS station and in blue the daily time series (2004–2020) of the vertical component of SERR GPS station (see **Figure 4** for station locations) in meters (a linear trend line is drawn). In red, the histogram of the monthly occurrence of earthquakes from the catalog of the OC9 station (**Figure 4**). The dotted horizontal line marks the limit for the histogram scale (30 events/month). **(B)** Time series of the seismic, geodetic and geochemical parameters recorded at Vesuvius from 2010 to 2020. In blue the daily time series of the vertical component of BKNO GPS station (site VBKN in **Figure 2**), in meters (a linear trend line is drawn). In green the temperature in Celsius degrees estimated based on the composition of the FC2 and FC5 (since 2018) fumaroles (a linear trend line is drawn). The histogram of the monthly occurrence of earthquakes from the BKE station catalog (**Figures 2**, **8B**) is in red. The dotted horizontal line marks the limit for the histogram scale (300 events/month). **(C)** Time series of seismic, geodetic and geochemical parameters recorded at Campi Flegrei from 2010 to 2020. In blue the daily time series of the vertical component of the RITE GPS station (**Figure 3**), in meters. In ocher the amplitude of the fumarolic tremor of the CPIS station, proxy of hydrothermal activity (an exponential trend line is drawn). The histogram of the monthly occurrence of earthquakes from the STH station catalog (**Figure 3**) is in red. The dotted horizontal line marks the limit for the histogram scale (300 events/month).

To compare the recent activity of Neapolitan volcanoes and investigate their differences and similarities we must consider the seismicity in the context of multidisciplinary (geodetic and/or geochemical) observations.

The modern geodetic measurements, made it possible quantifying the subsidence of Ischia (Luongo et al., 1987; Carlino, 2012; Cubellis and Luongo, 2018; Cubellis et al., 2020). In particular the leveling measurements along the coast line established by the Istituto Geografico Militare Italiano (IGMI) in 1913, showed the maximum subsidence in the Serrara Fontana area (Luongo et al., 1987; Manzo et al., 2006; Del Gaudio et al., 2011). For this reason, one of the first

permanent GPS stations installed on the island was located in Serrara Fontana (SERR in **Figure 4**). In 2017 a permanent GPS station was installed on Mount Epomeo (MEPO in **Figure 4**), which showed a subsidence rate of about 12 mm/year in the summit area of the island, higher than that typically measured at Serrara Fontana. This station allowed measuring a differential subsidence of the island central sector, which corresponds to an associated tilt of the Mount Epomeo block. The northern edge of this block shows a higher subsidence rate (**Figure 14A**). Seismicity in Ischia is concentrated mainly along the faults bordering the northern edge of the Mount Epomeo block where an important hydrothermal system is active (Casamicciola Terme).

Thus, due to the strict relationship between faults and hydrothermal activity, in addition to the peculiar structural factors described above, an important role in the genesis of the Ischia earthquakes is recognized in the dynamics of the hydrothermal system of the Island (Chiodini et al., 2004; D'Auria et al., 2018; Trasatti et al., 2019). Overall, the geochemical investigations have led to general consensus for the existence at Ischia of two distinct geothermal reservoirs, at temperatures of 150–180°C (Panichi et al., 1992; Di Napoli et al., 2009) and 220–280°C, respectively (Panichi et al., 1992; Inguaggiato et al., 2000; Di Napoli et al., 2009). The former, shallower (150–300 m of depth) and colder, is thought to be recharged by either meteoric (to the south; hydrothermal end-member B) or marine (to the west; hydrothermal end-member C) fluids. The hotter (220–280°C) and deeper (~1,000 m) reservoir would instead reflect a mainly recharge by meteoric water (hydrothermal end-member A; Di Napoli et al., 2009).

At Vesuvius two seismogenic volumes can be recognized: one deeper and one shallower already mentioned in the previous paragraphs (**Figure 9A**). In recent years the seismicity of the shallow source zone has increased. This seismicity is interpreted as linked to a spreading process (Borgia et al., 2005) that causes the subsidence of the summit area of the volcano (**Figure 14B**). The crater area of Vesuvius is also affected by hydrothermal manifestations and numerous fumaroles. For this reason, a zone with fluids above sea level is recognized in the edifice, where the shallow seismicity is concentrated. To investigate the effect of the stress field on seismicity, based on the analyzes of the earthquake focal mechanisms and applying different approaches D'Auria et al. (2014) determined spatial variations in the stress field beneath Vesuvius. They find that the stress pattern in the volcanic edifice is consistent with the hypothesis of a seismicity driven by the spreading process. This also agrees with the persistent character of the seismicity located within this volume. Conversely, they find that the stress field in the deep seismogenic volume is consistent with a regional field locally perturbed by the effects of the topography and heterogeneities in the volcanic structure. This seismogenic volume also coincides with the deep hydrothermal system of Vesuvius (Caliro et al., 2011). In any case, the locations of the main swarms, such as those of October 1999 and December 2018 analyzed in this article, show that the two seismogenic volumes, which are elongated in the direction of the crater axis, are interconnected and represent two portions of a conduit-like structure in the central zone of Vesuvius (**Figure 9**), where the transport of fluids takes place.

Other evidences suggest the important role of the fluids circulating in the volcano apparatus in the genesis of the Vesuvius seismicity. It is worth to note that, after the last eruption of 1944, the seismicity began in 1966 concurrently with important variations of the temperature of the fumaroles that progressively decreased from the high values measured from 1944 to 1966 (up to 800°C) to temperatures close to the boiling point of water after the 1990s (Chiodini et al., 2001b). This behavior was interpreted as the arrival into the hot volcanic conduits of groundwaters of meteoric origin that increased fluid pressure and in turn started to trigger seismicity (Del Pezzo et al., 2013; D'Auria et al., 2013). In the case of the most energetic event of the post 1944 period (M 3.6 in 1999) there are evidences of the involvement of deep magmatic fluids. The event was in fact followed by a clear increase of the CO_2 flux in the crater, as well as by peaks of the CO_2/CH_4 fumarolic ratio (a good indicator of the input of magmatic fluids; Chiodini, 2009) and of the PCO_2 estimated by gas equilibria applied to the Vesuvius fumaroles (Caliro et al., 2011; Del Pezzo et al., 2013). Similarly, the LP transient recorded on November 16, 2020, which we located in the lower part of the deep seismogenic volume (**Figure 9**) at the base of the hydrothermal system, probably represents an event caused by the injection of deeper magmatic fluids into the shallower parts of the hydrothermal system.

The recent seismicity of Campi Flegrei accompanies the current uplift phase, which began in 2005, and the remarkable geochemical changes taking place in the area (**Figure 14C**). Most earthquakes are concentrated at shallow depth (generally <2 km) in the subsoil of the Solfatara-Pisciarelli hydrothermal site (**Figure 7**) a piece of evidence that alone indicates the strict link between seismicity and hydrothermal activity. This aspect has been studied for a long time at the Campi Flegrei where the first hypotheses on the possible link between the dynamics of caldera and the fluids in the subsoil were born thanks to Babbage. (1847). In recent times, a link between unrest and fluids had been proposed by Bonafede. (1991) to explain several geochemical and geophysical observations made during the bradyseismic crisis of 1982–1984. Subsequently, an extensive literature has developed on this topic (eg: Macedonio et al., 2014; Giudicepietro et al., 2016; Giudicepietro et al., 2017), the detailed analysis of which is beyond the scope of this article. The relationships between seismicity and fluids were, for example, investigated by D'Auria et al. (2011) finding that fluid-transfer episodes are a primary factor causing the Campi Flegrei seismicity in the 1989–2010 period. Successively it was shown how, in 2000–2016, the cumulative background seismicity (**Figure 5C**) follows the same evolution of the fumarolic indicator of the hydrothermal temperature-pressure (see **Figure 4** in Chiodini et al., 2017b). A link between seismicity and activity of the hydrothermal system was recently stressed in Giudicepietro et al. (2021), which recognize a valve-like mechanism highlighted by the sudden step in the fumarolic tremor amplitude in coincidence with two seismic swarms (October 7, 2015 and December 6, 2019). This mechanism suggests an abrupt increase in the transport of fluids to the surface, through a

conduit-like path, where the swarms are located. The analysis of the swarm of April 26, 2020 (the most remarkable in terms of energy in the last 37 years) carried out in this paper highlights a further reactivation of the conduit-like seismogenic structure, on which are located the largest earthquakes occurred after the 1982–84 crisis in the Campi Flegrei. This structure develops from the depth in line with the hydrothermal area of Pisciarelli, the most significant fumarolic manifestation of the Phlegraean caldera, which is among the most important volcanic emissions in the world (Chiodini et al., 2021).

The aspects discussed so far show how the three Neapolitan volcanoes have different structural characteristics, different local stress fields and different states of activity. It is worth noting that the different geometries in the distribution of the earthquake hypocenters, in Ischia along faults and in Campi Flegrei and Vesuvius mainly along conduit-like paths, are consistent with the strong emissions of non-condensable gas (CO_2) in the Solfatara and Vesuvius and the absence of important emissions of this type in Ischia. Actually, the hydrothermal fluids emitted in Ischia are dominated by water (water vapor) of meteoric and/or marine shallow origin (Chiodini et al., 2004; Di Napoli et al., 2009). On the contrary, in the Campi Flegrei and Vesuvius, where seismicity delineates conduit-like structures, a greater contribution of magma degassing can be recognized in the geochemical data (Caliro et al., 2007; Caliro et al., 2011). In the light of these geochemical clues we interpret the seismicity along conduits of Campi Flegrei and Vesuvius as the outline of magmatic fluids propagation paths from the depths toward the emission zones.

CONCLUSION

We analyzed the seismic data of Vesuvius, Campi Flegrei and Ischia. We studied occurrence, magnitude and energy temporal evolutions of the earthquakes in the three Neapolitan volcanoes. Furthermore, we analyzed the magnitude-frequency distributions to derive the Mc and the *b*-values for the three volcanoes and we relocated some significant seismic swarms that occurred in Campi Flegrei and Vesuvius. We also located a LP transient recorded at Vesuvius on November 16, 2020.

We found that the seismicity of the three volcanoes had different characteristics and different temporal evolutions in recent years. Actually, in Ischia the seismicity is distributed along fault zones, predominantly in the northern sector of the Island (Casamicciola Terme), whereas in Vesuvius most of the seismicity is concentrated below the crater, outlining a continuous axial structure that coincides with the fluid path from the deep hydrothermal system, where we also located the November 16, 2020 LP event, toward the emission zones (Frondini et al., 2004). A similar pattern can be recognized also at Campi Flegrei, where earthquakes are mainly concentrated below the high hydrothermal fluid emission area of the Solfatara in Pozzuoli (Chiodini et al., 2001b; Cardellini et al., 2017; Chiodini et al., 2021). In particular the relocations of the April 26, 2020 earthquakes, compared with those of two swarms that occurred in 2015 and 2019 (**Figure 7**) (Giudicepietro et al., 2021), confirm that the main seismic swarms in Campi Flegrei delineate a conduit-like path through which hydrothermal fluids transfer from depth to Solfatara-Pisciarelli area. Furthermore, a common distinctive feature of Campi Flegrei and Vesuvius is the imprinting of magmatic degassing, in contrast with the hydrothermal systems typical of Ischia, that are dominated by meteoric or sea waters.

Nevertheless all of these volcanoes also show similarities. In all three volcanoes we can recognize an essential contribution of hydrothermal systems in the generation of earthquakes (Chiodini et al., 2004; D'Auria et al., 2011; D'Auria et al., 2018; Chiodini et al., 2021). This condition has also been recognized in other volcanoes, e.g. in Iceland (White et al., 2011; Greenfield and White, 2015) and in Mammoth Mountain (Hotovec-Ellis et al., 2018), and may be a common seismogenic factor in closed-conduit volcanoes.

Concerning the state of activity of the Neapolitan volcanoes, the seismicity of Ischia showed a decreasing trend after the M4.0 earthquake (August 21, 2017) sequence. On the contrary, the increase of seismicity in the Campi Flegrei characterized a long-term unrest that has shown acceleration in the last 2 years. Since 2018, also Vesuvius has shown an increase in the number of earthquakes per year, which suggests a possible increase in activity of this volcano.

DATA AVAILABILITY STATEMENT

The original contributions presented in the study are included in the article/**Supplementary Material**, further inquiries can be directed to the corresponding author.

AUTHOR CONTRIBUTIONS

FG, GC, LP, AT and GM conceptualization, article writing. FG, PR, FB, SC, EC, LD, WC, PM, AE, DG, GM, DB, AT and GC data analysis, interpretation of results, article revising; FG, PR, SC, WC,PM, GM, DB, MO, RP, GS, AT and GC dataset preparation and article revising. All authors contributed in article revising.

FUNDING

This work benefited from funds of the EU (DG ECHO) Project EVE n. 826292 and was partially supported by the project Progetto Strategico Dipartimentale INGV 2019. "Linking surface Observables to sub–Volcanic plumbing-system: A multidisciplinary approach for Eruption forecasting at Campi Flegrei caldera (Italy)". GM, FG and AT benefited from funding from the INGV Project "Ricerca Libera 2019–Study of the physical properties of the shallow structure of Vesuvius based on the analysis of seismic data."

ACKNOWLEDGMENTS

The authors wish to thank all the many colleagues who have contributed to the monitoring effort on CF, Vesuvius and Ischia. The authors are particularly indebted to the Istituto Nazionale di Geofisica e Vulcanologia (INGV) technical staff ensuring the regular working of the multidisciplinary monitoring networks. The data used in this study were provided by the Istituto

Nazionale di Geofisica e Vulcanologia (Osservatorio Vesuviano). The authors are also grateful to the Italian Presidenza del Consiglio dei Ministri-Dipartimento della Protezione Civile (DPC) for supporting the monitoring activities at CF. This article does not necessarily represent DPC official opinion and policies.

SUPPLEMENTARY MATERIAL

The Supplementary Material for this article can be found online at: https://www.frontiersin.org/articles/10.3389/feart.2021.662113/full#supplementary-material

REFERENCES

Acocella, V., and Funiciello, R. (1999). The Interaction between Regional and Local Tectonics during Resurgent Doming: the Case of the Island of Ischia, Italy. *J. Volcanology Geothermal Res.* 88, 109–123. doi:10.1016/S0377-0273(98)00109-7

Acocella, V., and Funiciello, R. (2006). Transverse Systems along the Extensional Tyrrhenian Margin of central Italy and Their Influence on Volcanism. *Tectonics* 25 (2). doi:10.1029/2005tc001845

Aiuppa, A., Avino, R., Brusca, L., Caliro, S., Chiodini, G., D'Alessandro, W., et al. (2006). Mineral Control of Arsenic Content in thermal Waters from Volcano-Hosted Hydrothermal Systems: Insights from Island of Ischia and Phlegrean Fields (Campanian Volcanic Province, Italy). *Chem. Geology* 229, 313–330. doi:10.1016/J.CHEMGEO.2005.11.004

Aki, K. (1965). Maximum Likelihood Estimate of B in the Formula Log N=a-b M and its Confidence Limits. *Bull. Earthquake Res. Inst.* 43, 237–239.

Albert, P. G., Giaccio, B., Isaia, R., Costa, A., Niespolo, E. M., Nomade, S., et al. (2019). Evidence for a Large-Magnitude Eruption from Campi Flegrei Caldera (Italy) at 29 Ka. *Geology* 47, 595–599. doi:10.1130/G45805.1

Alfano, G. B., and Friedlaender, I. (1929). *La storia del Vesuvio illustrata dai documenti coevi*. Ulm a.d. Donau, Germany: Karl Hohn, 69.

Amoruso, A., Crescentini, L., and Sabbetta, I. (2014). Paired Deformation Sources of the Campi Flegrei Caldera (Italy) Required by Recent (1980-2010) Deformation History. *J. Geophys. Res. Solid Earth* 119, 858–879. doi:10.1002/2013JB010392

Arnò, V., Principe, C., Rosi, M., Santacroce, R., Sbrana, A., and Sheridan, M. F. (1987). "Eruptive History," in *Somma- Vesuvius, Quaderni de La Ricerca Scientifica*. Editor R. Santacroce (Roma: CNR), 53–103.

Auger, E., Gasparini, P., Virieux, J., and Zollo, A. (2001). Seismic Evidence of an Extended Magmatic Sill under Mt. Vesuvius. *Science* 294, 1510–1512. doi:10.1126/science.1064893

Babbage, C. (1847). Observations on the temple of Serapis, at Pozzuoli, Near Naples, with Remarks on Certain Causes Which May Produce Geological Cycles of Great Extent. *Q. J. Geol. Soc.* 3, 186–217. doi:10.1144/GSL.JGS.1847.003.01-02.22

Baratta, M. (1897). *Il Vesuvio e le sue eruzioni*. Roma: Società Editrice Dante Alighieri, 203.

Barbieri, M., Di Girolamo, P., Locardi, E., Lombardi, G., and Stanzione, D. (1979). Petrology of the Calc-Alkaline Volcanics of the Parete 2 Well (Campania, Italy). *Period. Mineral.* 48, 53–74.

Berrino, G., Corrado, G., and Riccardi, U. (1998). Sea Gravity Data in the Gulf of Naples: a Contribution to Delineating the Structural Pattern of the Vesuvian Area. *J. Volcanology Geothermal Res.* 82, 139–150. doi:10.1016/S0377-0273(97)00061-9

Berrino, G., Corrado, G., and Riccardi, U. (2008). Sea Gravity Data in the Gulf of Naples. A Contribution to Delineating the Structural Pattern of the Phlegraean Volcanic District. *J. Volcanology Geothermal Res.* 175, 241–252. doi:10.1016/j.jvolgeores.2008.03.007

Bonafede, M. (1991). Hot Fluid Migration: an Efficient Source of Ground Deformation: Application to the 1982-1985 Crisis at Campi Flegrei-Italy. *J. Volcanology Geothermal Res.* 48, 187–198. doi:10.1016/0377-0273(91)90042-x

Borgia, A., Tizzani, P., Solaro, G., Manzo, M., Casu, F., Luongo, G., et al. (2005). Volcanic Spreading of Vesuvius, a New Paradigm for Interpreting its Volcanic Activity. *Geophys. Res. Lett.* 32, L03303. doi:10.1029/2004GL022155

Braccini, G. C. (1632). *Dell'incendio fattosi al Vesuvio XVI Dicembre 1631, e delle sue cause ed effetti* (Napoli: S. Roncagliolo).

Brocchini, D., Principe, C., Castradori, D., Laurenzi, M. A., and Gorla, L. (2001). Quaternary Evolution of the Southern Sector of the Campanian Plain and Early Somma-Vesuvius Activity: Insights from the Trecase 1 Well. *Mineralogy Pet.* 73, 67–91. doi:10.1007/s007100170011

Brown, R. J., Orsi, G., and de Vita, S. (2008). New Insights into Late Pleistocene Explosive Volcanic Activity and Caldera Formation on Ischia (Southern Italy). *Bull. Volcanol.* 70, 583–603. doi:10.1007/s00445-007-0155-0

Bruno, P. P. G., de Alteriis, G., and Florio, G. (2002). The Western Undersea Section of the Ischia Volcanic Complex (Italy, Tyrrhenian Sea) Inferred by marine Geophysical Data. *Geophys. Res. Lett.* 29, 57-1–57-4. doi:10.1029/2001GL013904

Bruno, P. P. G., Rapolla, A., and Di Fiore, V. (2003). Structural Setting of the Bay of Naples (Italy) Seismic Reflection Data: Implications for Campanian Volcanism. *Tectonophysics* 372 (3-4), 193–213. doi:10.1016/s0040-1951(03)00327-5

Caliro, S., Chiodini, G., Avino, R., Minopoli, C., and Bocchino, B. (2011). Long Time-Series of Chemical and Isotopic Compositions of Vesuvius Fumaroles: Evidence for Deep and Shallow Processes. *Ann. Geophys-italy* 54, 137–149. doi:10.4401/ag-5034

Caliro, S., Chiodini, G., Moretti, R., Avino, R., Granieri, D., Russo, M., et al. (2007). The Origin of the Fumaroles of La Solfatara (Campi Flegrei, South Italy). *Geochimica et Cosmochimica Acta* 71 (12), 3040–3055. doi:10.1016/j.gca.2007.04.007

Cardellini, C., Chiodini, G., Frondini, F., Avino, R., Bagnato, E., Caliro, S., et al. (2017). Monitoring Diffuse Volcanic Degassing during Volcanic Unrests: the Case of Campi Flegrei (Italy). *Sci. Rep.* 7, 6757. doi:10.1038/s41598-017-06941-2

Carlino, S., Cubellis, E., Luongo, G., and Obrizzo, F. (2006). "On the Mechanics of Caldera Resurgence of Ischia Island (Southern Italy)," in *Mechanisms of Activity and Unrest at Large Calderas*. Editors C. Troise, G. De Natale, and C. R. J. Kilburn (London: Geological Society), 269, 181–193. doi:10.1144/GSL.SP.2006.269.01.12

Carlino, S., Pino, N. A., Tramelli, A., De Novellis, V., and Convertito, V. (2021). A Common Source for the Destructive Earthquakes in the Volcanic Island of Ischia (Southern Italy): Insights from Historical and Recent Seismicity. *Nat. Hazards* 2021, 1–25. doi:10.1007/s11069-021-04675-z

Carlino, S. (2012). The Process of Resurgence for Ischia Island (Southern Italy) since 55 Ka: the Laccolith Model and Implications for Eruption Forecasting. *Bull. Volcanol.* 74, 947–961. doi:10.1007/s00445-012-0578-0

Chiodini, G., Avino, R., Brombach, T., Caliro, S., Cardellini, C., de Vita, S., et al. (2004). Fumarolic and Diffuse Soil Degassing West of Mount Epomeo, Ischia, Italy. *J. Volcanology Geothermal Res.* 133, 291–309. doi:10.1016/S0377-0273(03)00403-7

Chiodini, G., Caliro, S., Avino, R., Bini, G., Giudicepietro, F., De Cesare, W., et al. (2021). Hydrothermal Pressure-Temperature Control on CO_2 Emissions and Seismicity at Campi Flegrei (Italy). *J. Volcano. Geotherm. Res.* 414, 107245. doi:10.1016/j.jvolgeores.2021.107245

Chiodini, G., Caliro, S., De Martino, P., Avino, R., and Gherardi, F. (2012). Early Signals of New Volcanic Unrest at Campi Flegrei Caldera? Insights from Geochemical Data and Physical Simulations. *Geology* 40, 943–946. doi:10.1130/G33251.1

Chiodini, G. (2009). CO2/CH4 Ratio in Fumaroles a Powerful Tool to Detect Magma Degassing Episodes at Quiescent Volcanoes. *Geophys. Res. Lett.* 36, L02302. doi:10.1029/2008GL036347-X

Chiodini, G., Frondini, F., Cardellini, C., Granieri, D., Marini, L., and Ventura, G. (2001a). CO_2 degassing and Energy Release at Solfatara Volcano, Campi Flegrei, Italy. *J. Geophys. Res.* 106, 16213–16221. doi:10.1029/2001JB000246-X

Chiodini, G., Giudicepietro, F., Vandemeulebrouck, J., Aiuppa, A., Caliro, S., De Cesare, W., et al. (2017a). Fumarolic Tremor and Geochemical Signals during a Volcanic Unrest. *Geology* 45, 1131–1134. doi:10.1130/G39447.1

Chiodini, G., Marini, L., and Russo, M. (2001b). Geochemical Evidence for the Existence of High-Temperature Hydrothermal Brines at Vesuvio Volcano,

Italy. *Geochimica et Cosmochimica Acta* 65, 2129–2147. doi:10.1016/S0016-7037(01)00583-X

Chiodini, G., Paonita, A., Aiuppa, A., Costa, A., Caliro, S., De Martino, P., et al. (2016). Magmas Near the Critical Degassing Pressure Drive Volcanic Unrest towards a Critical State. *Nat. Commun.* 7, 13712. doi:10.1038/ncomms13712

Chiodini, G., Selva, J., Del Pezzo, E., Marsan, D., De Siena, L., D'Auria, L., et al. (2017b). Clues on the Origin of post-2000 Earthquakes at Campi Flegrei Caldera (Italy). *Sci. Rep.* 7, 4472. doi:10.1038/s41598-017-04845-9

Chouet, B. A., and Matoza, R. S. (2013). A Multi-Decadal View of Seismic Methods for Detecting Precursors of Magma Movement and Eruption. *J. Volcanology Geothermal Res.* 252, 108–175. doi:10.1016/j.jvolgeores.2012.11.013

Civetta, L., Gallo, G., and Orsi, G. (1991). Sr- and Nd-Isotope and Trace-Element Constraints on the Chemical Evolution of the Magmatic System of Ischia (Italy) in the Last 55 Ka. *J. Volcanology Geothermal Res.* 46, 213–230. doi:10.1016/0377-0273(91)90084-D

Conticelli, S., Laurenzi, M. A., Giordano, G., Mattei, M., Avanzinelli, R., Melluso, L., et al. (2010). "Leucite-bearing (Kamafugitic/leucititic) and -free (Lamproitic) Ultrapotassic Rocks and Associated Shoshonites from Italy: Constraints on Petrogenesis and Geodynamics," in *The Geology of Italy: Tectonics and Life along Plate Margins*. Editors M. Beltrando, A. Peccerillo, M. Mattei, S. Conticelli, and C. Doglioni (Clear Range, NSW, Australia: Journal of the Virtual Explorer), 1–95. doi:10.3809/jvirtex.2010.00251

Cubellis, E., Carlino, S., Iannuzzi, R., Luongo, G., and Obrizzo, F. (2004). Management of Historical Seismic Data Using GIS: The Island of Ischia (Southern Italy). *Nat. Hazards* 33, 379–393. doi:10.1023/B:NHAZ.0000048465.40413.17

Cubellis, E., Del Gaudio, C., Ferri, M., Grimaldi, M., Obrizzo, F., Ricco, C., et al. (1991). Gravity Anomalies in the Campanian Plain (Southern Italy) and Their Volcano-Tectonic Implications. *Acta Vulcanol* 1, 57–62.

Cubellis, E., Di Donna, G., Luongo, G., and Mazzarella, A. (2002). Simulating the Mechanism of Magmatic Processes in the Campi Flegrei Area (Southern Italy) by the Lorenz Equations. *J. Volcanology Geothermal Res.* 115, 339–349. doi:10.1016/S0377-0273(01)00330-4

Cubellis, E., Ferri, M., and Luongo, G. (1995). Internal Structures of the Campi Flegrei Caldera by Gravimetric Data. *J. Volcanology Geothermal Res.* 65, 147–156. doi:10.1016/0377-0273(94)00047-K

Cubellis, E., and Luongo, G. (2018). *History of Ischian Earthquakes*. Napoli, Italy: Bibliopolis, 140.

Cubellis, E., and Luongo, G. (1998). "Il Contesto Fisico," in *AAVV.,* Il terremoto del 28 luglio 1883 a Casamicciola nell'isola d'Ischia*, Presidenza del Consiglio dei Ministri - Servizio Sismico Nazionale* (Roma: Istituto Poligrafico e Zecca dello Stato), 49–123.

Cubellis, E., Luongo, G., and Marturano, A. (2007). Seismic hazard Assessment at Mt. Vesuvius: Maximum Expected Magnitude. *J. Volcanology Geothermal Res.* 162, 139–148. doi:10.1016/j.jvolgeores.2007.03.003

Cubellis, E., Luongo, G., Obrizzo, F., Sepe, V., and Tammaro, U. (2020). Contribution to Knowledge Regarding the Sources of Earthquakes on the Island of Ischia (Southern Italy). *Nat. Hazards* 100, 955–994. doi:10.1007/s11069-019-03833-8

Cubellis, E., and Marturano, A. (2013). Felt index, Source Parameters and Ground Motion Evaluation for Earthquakes at Mt. Vesuvius. Volume Speciale "Mt. Vesuvius Monitoring: the State of the Art and Perspectives. *Ann. Geophys.* 56 (4), S0439. doi:10.4401/ag-6445

Cubellis, E., and Marturano, A. (2002). Mt. Vesuvius: a Macroseismic Study of the Earthquake of 9 October 1999. *J. Volcanology Geothermal Res.* 118, 339–351. doi:10.1016/S0377-0273(02)00301-3

Cubellis, E., Marturano, A., and Pappalardo, L. (2013). Le ceneri distali dell'eruzione del Vesuvio del marzo 1944 raccolte a Devoli (Albania). *Quad. Geofis.* 113, 1–35.

Cubellis, E., Marturano, A., and Pappalardo, L. (2016). The Last Vesuvius Eruption in March 1944: Reconstruction of the Eruptive Dynamic and its Impact on the Environment and People through Witness Reports and Volcanological Evidence. *Nat. Hazards* 82 (1), 95–121. doi:10.1007/s11069-016-2182-7

Cusano, P., Petrosino, S., Bianco, F., and Del Pezzo, E. (2013). *The First Long Period Earthquake Detected in the Background Seismicity at Mt. Vesuvius*. Ann. Geophys. 55 (4), S0440. doi:10.4401/ag-6447

D'Auria, L., Giudicepietro, F., Aquino, I., Borriello, G., Del Gaudio, C., Lo Bascio, D., et al. (2011). Repeated Fluid-Transfer Episodes as a Mechanism for the Recent Dynamics of Campi Flegrei Caldera (1989-2010). *J. Geophys. Res.* 116, B04313. doi:10.1029/2010JB007837

D'Auria, L., Giudicepietro, F., Tramelli, A., Ricciolino, P., Bascio, D. L., Orazi, M., et al. (2018). The Seismicity of Ischia Island. *Seismol. Res. Lett.* 89, 1750–1760. doi:10.1785/0220180084

D'Auria, L., Massa, B., and Matteo, A. D. (2014). The Stress Field beneath a Quiescent Stratovolcano: The Case of Mount Vesuvius. *J. Geophys. Res. Solid Earth* 119, 1181–1199. doi:10.1002/2013JB010792

D'Auria, L., and Massa, B. (2015). Stress Inversion of Focal Mechanism Data Using a Bayesian Approach: A Novel Formulation of the Right Trihedra Method. *Seismological Res. Lett.* 86, 968–977. doi:10.1785/0220140153

D'Auria, L., Esposito, A. M., Lo Bascio, D., Ricciolino, P., Giudicepietro, F., Martini, M., et al. (2013). The Recent Seismicity of Mt. Vesuvius: Inference on Seismogenic Processes. *Ann. Geophys-italy* 56, S0442. doi:10.4401/ag-6448

De Martino, P., Guardato, S., Donnarumma, G. P., Dolce, M., Trombetti, T., Chierici, F., et al. (2020). Four Years of Continuous Seafloor Displacement Measurements in the Campi Flegrei Caldera. *Front. Earth Sci.* 8. doi:10.3389/feart.2020.615178

De Martino, P., Tammaro, U., and Obrizzo, F. (2014). GPS Time Series at Campi Flegrei Caldera (2000-2013). *Ann. Geophys-italy* 57, S0213. doi:10.4401/ag-6431

De Martino, P., Tammaro, U., Obrizzo, F., Sepe, V., Brandi, G., D'Alessandro, A., et al. (2011). La rete GPS dell'isola d'Ischia: deformazioni del suolo in un'area vulcanica attiva (1998-2010). *Quad. Geofis.* 95, 61..

De Natale, G., Troise, C., Pingue, F., Mastrolorenzo, G., Pappalardo, L., Battaglia, M., et al. (2006b). "The Campi Flegrei Caldera: Unrest Mechanisms and Hazards," in *Mechanisms of Activity and Unrest at Large Calderas*. Editors C. Troise, G. De Natale, and C. R. J. Kilburn (London: Geological Society), 269, 25–45. doi:10.1144/gsl.sp.2006.269.01.03*Geol. Soc. Lond. Spec. Publications*

De Novellis, V., Carlino, S., Castaldo, R., Tramelli, A., De Luca, C., Pino, N. A., et al. (2018). The 21 August 2017 Ischia (Italy) Earthquake Source Model Inferred from Seismological, GPS, and DInSAR Measurements. *Geophys. Res. Lett.* 45, 2193–2202. doi:10.1002/2017GL076336

de Vita, S., Sansivero, F., Orsi, G., Marotta, E., and Piochi, M. (2010). Volcanological and Structural Evolution of the Ischia Resurgent Caldera (Italy) over the Past 10 k.Y. *Geol. Soc. Am. Spec. Paper* 464, 193–241. doi:10.1130/2010.2464(10

De Vivo, B., Rolandi, G., Gans, P. B., Calvert, A., Bohrson, W. A., Spera, F. J., et al. (2001). New Constraints on the Pyroclastic Eruptive History of the Campanian Volcanic Plain (Italy). *Mineralogy Pet.* 73, 47–65. doi:10.1007/s007100170010

Deino, A. L., Orsi, G., de Vita, S., and Piochi, M. (2004). The Age of the Neapolitan Yellow Tuff Caldera-Forming Eruption (Campi Flegrei Caldera - Italy) Assessed by 40Ar/39Ar Dating Method. *J. Volcanology Geothermal Res.* 133, 157–170. doi:10.1016/S0377-0273(03)00396-2

Del Gaudio, C., Aquino, I., Ricciardi, G. P., Ricco, C., and Scandone, R. (2010). Unrest Episodes at Campi Flegrei: A Reconstruction of Vertical Ground Movements during 1905-2009. *J. Volcanology Geothermal Res.* 195, 48–56. doi:10.1016/j.jvolgeores.2010.05.014

Del Gaudio, C., Aquino, I., Ricco, C., Sepe, V., and Serio, C. (2011). Monitoraggio geodetico dell'isola d'Ischia: risultati della livellazione geometrica di precisione eseguita a giugno 2010. *Quad. Geofis.* 87, 1–20.

Del Pezzo, E., Chiodini, G., Caliro, S., Bianco, F., and Avino, R. (2013). New Insights into Mt. Vesuvius Hydrothermal System and its Dynamic Based on a Critical Review of Seismic Tomography and Geochemical Features. *Ann. Geophys-italy* 56, S0444. doi:10.4401/ag-6450

Denatale, G., Troise, C., Pingue, F., Mastrolorenzo, G., and Pappalardo, L. (2006a). The Somma-Vesuvius Volcano (Southern Italy): Structure, Dynamics and hazard Evaluation. *Earth-Science Rev.* 74, 73–111. doi:10.1016/j.earscirev.2005.08.001

Devoti, R., De Martino, P., Pietrantonio, G., and Dolce, M. (2018). Coseismic Displacements on Ischia Island, Real-Time GPS Positioning Constraints on Earthquake Source Location. *Ann. Geophys-italy* 61, SE337. doi:10.4401/ag-7656

Di Napoli, R., Aiuppa, A., Bellomo, S., Brusca, L., D'Alessandro, W., Candela, E. G., et al. (2009). A Model for Ischia Hydrothermal System: Evidences from the Chemistry of thermal Groundwaters. *J. Volcanology Geothermal Res.* 186, 133–159. doi:10.1016/j.jvolgeores.2009.06.005

Di Renzo, V., Di Vito, M. A., Arienzo, I., Carandente, A., Civetta, L., D'antonio, M., et al. (2007). Magmatic History of Somma-Vesuvius on the Basis of New

Geochemical and Isotopic Data from a Deep Borehole (Camaldoli Della Torre). *J. Pet.* 48, 753–784. doi:10.1093/petrology/egl081

Di Vito, M. A., Acocella, V., Aiello, G., Barra, D., Battaglia, M., Carandente, A., et al. (2016). Magma Transfer at Campi Flegrei Caldera (Italy) before the 1538 AD Eruption. *Sci. Rep.* 6, 32245. doi:10.1038/srep32245

Endo, E. T., and Murray, T. (1991). Real-time Seismic Amplitude Measurement (RSAM): A Volcano Monitoring and Prediction Tool. *Bull. Volcanol* 53, 533–545. doi:10.1007/BF00298154

Esposito, A. M., Alaia, G., Giudicepietro, F., Pappalardo, L., and D'Antonio, M. (2020a). "Unsupervised Geochemical Analysis of the Eruptive Products of Ischia, Vesuvius and Campi Flegrei," in *Progresses in Artificial Intelligence and Neural Systems. 189*. Editors A. Esposito, M. Faundez-Zanuy, F. Morabito, and E. Pasero (Singapore: Springer), 175–184. doi:10.1007/978-981-15-5093-5_17

Esposito, A. M., De Bernardo, A., Ferrara, S., Giudicepietro, F., and Pappalardo, L. (2020b). "SOM-based Analysis of Volcanic Rocks: An Application to Somma-Vesuvius and Campi Flegrei Volcanoes (Italy)," in *Neural Approaches to Dynamics of Signal Exchanges. 151*. Editors A. Esposito, M. Faundez-Zanuy, F. Morabito, and E. Pasero (Singapore: Springer), 55–60. doi:10.1007/978-981-13-8950-4_6

Frondini, F., Chiodini, G., Caliro, S., Cardellini, C., Granieri, D., and Ventura, G. (2004). Diffuse CO2 Degassing at Vesuvio, Italy. *Bull. Volcanol* 66 (7), 642–651. doi:10.1007/s00445-004-0346-x

Gebauer, S. K., Schmitt, A. K., Pappalardo, L., Stockli, D. F., and Lovera, O. M. (2014). Crystallization and Eruption Ages of Breccia Museo (Campi Flegrei Caldera, Italy) Plutonic Clasts and Their Relation to the Campanian Ignimbrite. *Contrib. Mineral. Petrol.* 167, 953. doi:10.1007/s00410-013-0953-7

Giudicepietro, F., Chiodini, G., Avino, R., Brandi, G., Caliro, S., De Cesare, W., et al. (2021). Tracking Episodes of Seismicity and Gas Transport in Campi Flegrei Caldera through Seismic, Geophysical, and Geochemical Measurements. *Seismol. Res. Lett.* 92, 965–975. (in press). doi:10.1785/0220200223

Giudicepietro, F., Chiodini, G., Caliro, S., De Cesare, W., Esposito, A. M., Galluzzo, D., et al. (2019). Insight into Campi Flegrei Caldera Unrest through Seismic Tremor Measurements at Pisciarelli Fumarolic Field. *Geochem. Geophys. Geosyst.* 20, 5544–5555. doi:10.1029/2019GC008610

Giudicepietro, F., Macedonio, G., D'Auria, L., and Martini, M. (2016). Insight into Vent Opening Probability in Volcanic Calderas in the Light of a Sill Intrusion Model. *Pure Appl. Geophys.* 173, 1703–1720. doi:10.1007/s00024-015-1190-y

Giudicepietro, F., Macedonio, G., and Martini, M. (2017). A Physical Model of Sill Expansion to Explain the Dynamics of Unrest at Calderas with Application to Campi Flegrei. *Front. Earth Sci.* 5, 1–11. doi:10.3389/feart.2017.00054

Giudicepietro, F., Orazi, M., Scarpato, G., Peluso, R., D'Auria, L., Ricciolino, P., et al. (2010). Seismological Monitoring of Mount Vesuvius (Italy): More Than a century of Observations. *Seismological Res. Lett.* 81, 625–634. doi:10.1785/gssrl/81.4.62510.1785/gssrl.81.4.625

Greenfield, T., and White, R. S. (2015). Building Icelandic Igneous Crust by Repeated Melt Injections. *J. Geophys. Res. Solid Earth* 120 (11), 7771–7788. doi:10.1002/2015jb012009

Guidoboni, E., and Ciuccarelli, C. (2011). The Campi Flegrei Caldera: Historical Revision and New Data on Seismic Crises, Bradyseisms, the Monte Nuovo Eruption and Ensuing Earthquakes (Twelfth century 1582 AD). *Bull. Volcanol.* 73, 655–677. doi:10.1007/s00445-010-0430-3

Guidoboni, E. (2008). Vesuvius: A Historical Approach to the 1631 Eruption "Cold Data" from the Analysis of Three Contemporary Treatises. *J. Volcanology Geothermal Res.* 178, 347–358. doi:10.1016/j.jvolgeores.2008.09.020

Hotovec-Ellis, A. J., Shelly, D. R., Hill, D. P., Pitt, A. M., Dawson, P. B., and Chouet, B. A. (2018). Deep Fluid Pathways beneath Mammoth Mountain, California, Illuminated by Migrating Earthquake Swarms. *Sci. Adv.* 4 (8), eaat5258. doi:10.1126/sciadv.aat5258

Iannaccone, G., Guardato, S., Donnarumma, G. P., De Martino, P., Dolce, M., Macedonio, G., et al. (2018). Measurement of Seafloor Deformation in the marine Sector of the Campi Flegrei Caldera (Italy). *J. Geophys. Res. Solid Earth* 123, 66–83. doi:10.1002/2017JB014852

Imbò, G., Casertano, L., and Bonasia, V. (1964). Considerazioni sismogravimetriche sulle manifestazioni vesuviane del Maggio 1964. *Annali Osservatorio Vesuviano* 6, 177–188.

Imbò, G. (1964). Recenti Manifestazioni Dell'attività Vesuviana. *Atti Accademia Pontiniana* 13, 3–6.

Imbò, G. (1954). Sismicità del parossismo Vesuviano del marzo 1944. *Annali Osservatorio Vesuviano, Napoli, Italy* 1, 1–211.

Improta, L., and Corciulo, M. (2006). Controlled Source Nonlinear Tomography: A Powerful Tool to Constrain Tectonic Models of the Southern Apennines Orogenic Wedge, Italy. *Geol* 34, 941–944. doi:10.1130/G22676A.1

Inguaggiato, S., Pecoraino, G., and D'Amore, F. (2000). Chemical and Isotopical Characterisation of Fluid Manifestations of Ischia Island (Italy). *J. Volcanology Geothermal Res.* 99, 151–178. doi:10.1016/S0377-0273(00)00158-X

Johnson, C. E. (2020). Beyond Earthworm: Keeping the Promise. *Seismol. Res. Lett.* 91, 581–584. doi:10.1785/0220190198

Johnson, C. E., Bittenbinder, A., Bogaert, B., Dietz, L., and Kohler, W. (1995). Newsletter April, 1995. *Anesth. Hist. Assoc. Newsl.* 13, 1–16. doi:10.1016/s1089-9634(95)50110-0

Krischer, L., Megies, T., Barsch, R., Beyreuther, M., Lecocq, T., Caudron, C., et al. (2015). ObsPy: A Bridge for Seismology into the Scientific Python Ecosystem. *Comput. Sci. Disc.* 8 (1), 014003. doi:10.1088/1749-4699/8/1/014003

Lee, W. H. K., and Lahr, J. C. (1975). HYPO71 (Revised): A Computer Program for Determining Hypocenter, Magnitude and First Motion Pattern of Local Earthquakes. *U.S. Geol. Surv. Open-File Rep.* 75-311, 116. doi:10.3133/ofr75311

Luongo, G., Carlino, S., Cubellis, E., Delizia, I., and Obrizzo, F. (2012). *Casamicciola 1883 - Il sisma tra interpretazione scientifica e scelte politiche*. Naples, Italy: Bibliopolis, 282.

Luongo, G., Cubellis, E., and Obrizzo, F. (1987). *Ischia storia di un'isola vulcanica*. Napoli: Liguori Editore, 164.

Macedonio, G., Giudicepietro, F., D'Auria, L., and Martini, M. (2014). Sill Intrusion as a Source Mechanism of Unrest at Volcanic Calderas. *J. Geophys. Res. Solid Earth* 119, 3986–4000. doi:10.1002/2013JB010868

Manzo, M., Ricciardi, G. P., Casu, F., Ventura, G., Zeni, G., Borgström, S., et al. (2006). Surface Deformation Analysis in the Ischia Island (Italy) Based on Spaceborne Radar Interferometry. *J. Volcanology Geothermal Res.* 151, 399–416. doi:10.1016/j.jvolgeores.2005.09.010

Marturano, A. (2006). "Chapter 4 Geophysical Precursors at Vesuvius from Historical and Archeological Sources," in *Vesuvius, Education, Security and prosperity*. Editor F. Dobran (Elsevier), 249–263. doi:10.1016/s1871-644x(06)80008-2

Marturano, A., and Scaramella, P. (1998). "The Role of Primary Sources in Reconstructing the History of Volcanoes: the Eruption of Vesuvius in 1631," in *Volcanoes and History*. Editor N. Morello (Genova, Italy: Brigati), 281–299.

Niccolini, A. (1846). *Descrizione della gran Terma Puteolana volgarmente detta Tempio di Serapide*. Napoli: Forgotten Books.

Niccolini, A. (1829). *Rapporto sulle acque che invadono il pavimento dell'antico edifizio detto Tempio di Serapide*. Napoli: Stamperia Reale.

Niccolini, A. (1839). *Tavola metrica cronologica delle varie altezze tracciate dalla superficie del mare tra la costa di Amalfi ed il promontorio di Gaeta nel corso di diciannove secoli*. Napoli: dalla tipografia Flautina.

Nunziata, C. (2010). Low Shear-Velocity Zone in the Neapolitan-Area Crust between the Campi Flegrei and Vesuvio Volcanic Areas. *Terra Nova* 22, 208–217. doi:10.1111/j.1365-3121.2010.00936.x

Orsi, G., Civetta, L., Del Gaudio, C., de Vita, S., Di Vito, M. A., Isaia, R., et al. (1999). Short-term Ground Deformations and Seismicity in the Resurgent Campi Flegrei Caldera (Italy): an Example of Active Block-Resurgence in a Densely Populated Area. *J. Volcanology Geothermal Res.* 91, 415–451. doi:10.1016/S0377-0273(99)00050-5

Orsi, G., Gallo, G., and Zanchi, A. (1991). Simple-shearing Block Resurgence in Caldera Depressions. A Model from Pantelleria and Ischia. *J. Volcanology Geothermal Res.* 47, 1–11. doi:10.1016/0377-0273(91)90097-J

Orsi, G., Piochi, M., Campajola, L., D'Onofrio, A., Gialanella, L., and Terrasi, F. (1996). ^{14}C Geochronological Constraints for the Volcanic History of the Island of Ischia (Italy) over the Last 5000 Years. *J. Volcanol. Geotherm. Res.* 71, 249–257. doi:10.1016/0377-0273(95)00067-4-X

Paige, C. C., and Saunders, M. A. (1982). LSQR: Sparse Linear Equations and Least Squares Problems. *ACM Trans. Math. Softw.* 8/2, 195–209. doi:10.1145/355993.356000

Panichi, C., Bolognesi, L., Ghiara, M. R., Noto, P., and Stanzione, D. (1992). Geothermal Assessment of the Island of Ischia (Southern Italy) from Isotopic and Chemical Composition of the Delivered Fluids. *J. Volcanol. Geotherm. Res.* 49, 329–348. doi:10.1016/0377-0273(92)90021-5

Pappalardo, L., D'Auria, L., Cavallo, A., and Fiore, S. (2014). Petrological and Seismic Precursors of the Paroxysmal Phase of the Last Vesuvius Eruption on March 1944. *Sci. Rep.* 4, 6297. doi:10.1038/srep06297

Pappalardo, L., and Mastrolorenzo, G. (2012). Rapid Differentiation in a Sill-like Magma Reservoir: A Case Study from the Campi Flegrei Caldera. *Sci. Rep.* 2, 712. doi:10.1038/srep00712

Passaro, S., Tamburrino, S., Vallefuoco, M., Gherardi, S., Sacchi, M., and Ventura, G. (2016). High-resolution Morpho-Bathymetry of the Gulf of Naples, Eastern Tyrrhenian Sea. *J. Maps* 12 (Suppl. 1), 203–210. doi:10.1080/17445647.2016.1191385

Peccerillo, A. (2020). "Campania Volcanoes: Petrology, Geochemistry, and Geodynamic Significance," in *Vesuvius, Campi Flegrei, and Campanian Volcanism*. Editors B. De Vivo, H. E. Belkin, and G. Rolandi (Elsevier), 79–120. doi:10.1016/B978-0-12-816454-9.00005-5

Reasenberg, P. A., and Oppenheimer, D. (1985). FPFIT, FPPLOT, and FPPAGE: Fortran Computer Programs for Calculating and Displaying Earthquake Fault-Plane Solutions. *U.S. Geol. Surv. Open-file Rept.* 109, 85–739.

Ricco, C., Petrosino, S., Aquino, I., Cusano, P., and Madonia, P. (2021). Tracking the Recent Dynamics of Mt. Vesuvius from Joint Investigations of Ground Deformation, Seismicity and Geofluid Circulation. *Sci. Rep.* 11, 965. doi:10.1038/s41598-020-79636-w

Rosi, M., and Sbrana, R. (1987). *Phlegraean Fields of Quaderni de La Ricerca Scientifica*. Roma: CNR 114, 175.

Saccorotti, G., Bianco, F., Castellano, M., and Del Pezzo, E. (2001). The July-August 2000 Seismic Swarms at Campi Flegrei Volcanic Complex, Italy. *Geophys. Res. Lett.* 28, 2525–2528. doi:10.1029/2001GL013053

Scandone, R., and Giacomelli, L. (2008). Precursors of Eruptions at Vesuvius (Italy). *J. Volcanol. Geotherm. Res.* 171, 191–200. doi:10.1016/j.jvolgeores.2007.11.018

Scandone, R. (1987). *Somma-Vesuvius, vol. 114 of Quaderni de La Ricerca Scientifica*. Roma: Consiglio Nazionale delle Ricerche, 230.

Scarpati, C., Perrotta, A., Lepore, S., and Calvert, A. (2013). Eruptive History of Neapolitan Volcanoes: Constraints from 40Ar–39Ar Dating. *Geol. Mag.* 150 (3), 412–425. doi:10.1017/s0016756812000854

Selva, J., Azzaro, R., Taroni, M., Tramelli, A., Alessio, G., Castellano, M., et al. (2021). The Seismicity of Ischia Island, Italy: an Integrated Earthquake Catalogue from 8th century BC to 2019 and its Statistical Properties. *Front. Earth Sci.* 9, 203. doi:10.3389/feart.2021.629736

Sigurdsson, H., Carey, S., Cornell, W., and Pescatore, T. (1985). The Eruption of Vesuvius in A.D. 79. *Natl. Geogr. Res.* 1, 332–387.

Sulpizio, R., Mele, D., Dellino, P., and La Volpe, L. (2005). A Complex, Subplinian-type Eruption from Low-Viscosity Tephritic to Tephritic-Phonolitic Magma: the AD 472 (Pollena) Eruption of Somma-Vesuvius, Italy. *Bull. Volcanol.* 67, 673–767. doi:10.1007/s00445-005-0414-x

Tamburello, G., Caliro, S., Chiodini, G., De Martino, P., Avino, R., Minopoli, C., et al. (2019). Escalating CO2 Degassing at the Pisciarelli Fumarolic System, and Implications for the Ongoing Campi Flegrei Unrest. *J. Volcanol. Geotherm. Res.* 384, 151–157. doi:10.1016/j.jvolgeores.2019.07.005-X

Tammaro, U., De Martino, P., Obrizzo, F., Brandi, G., D'Alessandro, A., Dolce, M., et al. (2013). Somma Vesuvius Volcano: Ground Deformations from CGPS Observations. *Ann. Geophys-italy* 56, S0456. doi:10.4401/ag-6462

Torrente, M. M., and Milia, A. (2013). Volcanism and Faulting of the Campania Margin (Eastern Tyrrhenian Sea, Italy): a Three-Dimensional Visualization of a New Volcanic Field off Campi Flegrei. *Bull. Volcanology* 75 (6), 1–13. doi:10.1007/s00445-013-0719-0

Tramelli, A., Godano, C., Ricciolino, P., Giudicepietro, F., Caliro, S., Orazi, M., et al. (2021). Statistics of Seismicity to Investigate the Campi Flegrei Caldera Unrest. *Sci. Rep.* 11, 1. doi:10.1038/s41598-021-86506-6

Trasatti, E., Acocella, V., Di Vito, A., Del Gaudio, C., Weber, G., Aquino, I., et al. (2019). Magma Degassing as a Source of Long-Term Seismicity at Volcanoes: The Ischia Island (Italy) Case. *Geophys. Res. Lett.* 46, 14421–14429. doi:10.1029/2019GL085371

Vezzoli, L. (1988). *Island of Ischia, vol. 114 of Quaderni de "La Ricerca Scientifica"*. Roma: Consiglio Nazionale delle Ricerche.

Waldhauser, F., and Ellsworth, W. L. (2000). A Double-Difference Earthquake Location Algorithm: Method and Application to the Northern Hayward Fault, California. *BSSA* 90, 1353–1368. doi:10.1785/0120000006

White, R. S., Drew, J., Martens, H. R., Key, J., Soosalu, H., and Jakobsdóttir, S. S. (2011). Dynamics of Dyke Intrusion in the Mid-crust of Iceland. *Earth Planet. Sci. Lett.* 304 (3-4), 300–312. doi:10.1016/j.epsl.2011.02.038

Wiemer, S., and Benoit, J. P. (1996). Mapping the B-value Anomaly at 100 Km Depth in the Alaska and New Zealand Subduction Zones. *Geophys. Res. Lett.* 23 (13), 1557–1560. doi:10.1029/96gl01233

Zollo, A., Maercklin, N., Vassallo, M., Dello Iacono, D., Virieux, J., and Gasparini, P. (2008). Seismic Reflections Reveal a Massive Melt Layer Feeding Campi Flegrei Caldera. *Geophys. Res. Lett.* 35, L12306. doi:10.1029/2008GL034242

Conflict of Interest: The authors declare that the research was conducted in the absence of any commercial or financial relationships that could be construed as a potential conflict of interest.

Copyright © 2021 Giudicepietro, Ricciolino, Bianco, Caliro, Cubellis, D'Auria, De Cesare, De Martino, Esposito, Galluzzo, Macedonio, Lo Bascio, Orazi, Pappalardo, Peluso, Scarpato, Tramelli and Chiodini. This is an open-access article distributed under the terms of the Creative Commons Attribution License (CC BY). The use, distribution or reproduction in other forums is permitted, provided the original author(s) and the copyright owner(s) are credited and that the original publication in this journal is cited, in accordance with accepted academic practice. No use, distribution or reproduction is permitted which does not comply with these terms.

frontiers in Earth Science

ORIGINAL RESEARCH
published: 16 August 2021
doi: 10.3389/feart.2021.664673

Revealing 60 years of Earthquake Swarms in the Southern Red Sea, Afar and the Gulf of Aden

Joël Ruch[1,2], Derek Keir[3], Luigi Passarelli[1,2], Domenico Di Giacomo[4], Ghebrebrhan Ogubazghi[5] and Sigurjón Jónsson[1]*

[1]Physical Science and Engineering Division, King Abdullah University of Science and Technology (KAUST), Thuwal, Saudi Arabia, [2]Department of Earth Sciences, University of Geneva, Geneva, Switzerland, [3]School of Ocean and Earth Science, University of Southampton, Southampton, United Kingdom, [4]International Seismological Centre, Thatcham, United Kingdom, [5]Department of Earth Sciences, Eritrea Institute of Technology, Asmara, Eritrea

Earthquake swarms occur sporadically at divergent plate boundaries but their recurrence over multiple decades and relation to magmatic spreading activity remain poorly understood. Here we study more than 100 earthquake swarms over a 60-year period in the southern Red Sea, Afar, and Gulf of Aden region. We first compiled an earthquake-swarm catalogue by integrating reexamined global and local earthquake catalogues from 1960 to 2017. This yielded 134 earthquake swarms that mainly cluster in 19 different areas in the study region, showing that in most cases swarms recur every few decades in the same area. The swarms exhibit a range of earthquake magnitudes and often include multiple M3 to M5 events with some swarms having occasional larger earthquakes over M6, primarily in southern Afar. Many of the earthquake swarms were clearly associated with rifting events, consisting of magmatic intrusions, surface faulting, and in some cases volcanic eruptions. Together, the swarms suggest that extension at these divergent plate boundaries occurs episodically along <100 km long segments, some of which were previously unrecognized. Within the study region, the Gulf of Aden shows the most frequent swarm activity, followed by Afar and then the southern Red Sea. The results show that the three areas were subject to an increase of earthquake-swarm activity from 2003 to 2013 in the form of three rifting episodes and at least seven volcanic eruptions. We interpret that the most likely controls on temporal variations in earthquake swarm activity are either temporal variations in magma supply, or rifting-induced stress change that trigger clusters of swarms.

Keywords: earthquake swarm, Afar depression, seismicity analysis, Red Sea—Gulf of Aden, rifting and breakup, volcanism, tectonics

OPEN ACCESS

Edited by:
Luis E. Lara,
Servicio Nacional de Geología y Minería de Chile (SERNAGEOMIN), Chile

Reviewed by:
Sarah Jaye Oliva,
University of British Columbia, Vancouver, Canada
Sigrún Hreinsdóttir,
GNS Science, New Zealand

****Correspondence:***
Joël Ruch
joel.ruch@unige.ch

Specialty section:
This article was submitted to Volcanology, a section of the journal Frontiers in Earth Science

Received: *05 February 2021*
Accepted: *29 July 2021*
Published: *16 August 2021*

Citation:
Ruch J, Keir D, Passarelli L, Di Giacomo D, Ogubazghi G and Jónsson S (2021) Revealing 60 years of Earthquake Swarms in the Southern Red Sea, Afar and the Gulf of Aden. Front. Earth Sci. 9:664673. doi: 10.3389/feart.2021.664673

INTRODUCTION

Earthquake swarms are observed worldwide at divergent plate boundaries. Most of these swarms occur along oceanic ridges and along transform zones (Bird et al., 2002; Boettcher and Jordan, 2004; Roland and McGuire, 2009; Passarelli et al., 2018b). Earthquake swarms are seismic sequences that cluster in space and time with the majority of moment release occurring after the start of the sequence (Roland and McGuire, 2009; Chen and Shearer, 2011). Seismicity rate during swarm-like sequences fluctuates in time with acceleration and deceleration phases that cannot be described with

the simple Omori law (e.g., Sykes, 1970; Dziak et al., 2006). They often lack a distinctive mainshock and most of the seismic moment is released through multiple earthquakes of comparable magnitude. They have characteristic durations of days to months that do not scale with the total moment released during the sequence (Passarelli et al., 2018b), which indicates that their temporal evolution is likely modulated by transient processes (e.g., fluid migration, magmatic intrusions, or aseismic slip) acting on top of the long-term tectonic load (Vidale and Shearer, 2006; Passarelli et al., 2015, 2018b). Therefore, no governing law has yet been discovered for swarm seismicity which makes it difficult to use their physical and statistical characteristics for their detection and to understand their spatial and temporal evolution. However, a thorough investigation of the patterns and evolution of the earthquake activity can give insight into both the driving mechanism and seismo-tectonic conditions leading to earthquake swarms in both tectonic and volcanic regions. Here we focus on earthquake swarms at divergent plate boundaries, which often occur contiguously with tectonic and magmatic activity.

Earthquake swarms at divergent plate boundaries have been identified in global catalogues, e.g., in the Atlantic Ocean, in some cases related to magmatic intrusions along spreading ridges (Sykes, 1970; Bergman and Solomon, 1990), at the Gakkel ridge (Arctic Ocean) with the emplacement of a new lava field (Edwards et al., 2001) and at the Indian Ocean ridge (Läderach et al., 2012; Schlindwein, 2012). Local seismic data (derived from hydrophone instruments) in the northeast Pacific ocean (Juan De Fuca, Axial Seamount, Gorda Ridge and East Pacific Rise) show earthquake swarms associated with magmatic intrusions, with detailed studies of magma propagation direction and speed (Dziak et al., 2006; Dziak et al., 2007; Dziak et al. 2011). Such sequences have been repeatedly observed inland along rift zones in Iceland (e.g., Ágústsdóttir et al., 2016; Einarsson and Brandsdottir, 2021) and also at the Kilauea volcano in Hawaii during lateral magma propagation along rift zones (e.g., Neal et al., 2019). Tectonic earthquake swarms have also been described north of Iceland, within a transform fault zone (Passarelli et al., 2018b). As of yet, global catalogues have not been extensively exploited to identify earthquake swarms, despite the significant increase of seismic instrument deployments and of available seismic data during the last 30 years, e.g., in the International Seismological Centre, 2010 (ISC, www.isc.ac.uk) catalogue that integrates local seismic data from contributing agencies all over the world.

The southern Red Sea, Afar, and Gulf of Aden (SAGA) region has been continuously affected by earthquake swarms at least since early earthquake location studies began in the 1950s (Fairhead and Girdler, 1970; Gouin, 1979 and references therein) and is thus an ideal region to study earthquake swarm activity over several decades. In the Afar region (Ethiopia; **Figure 1A**), several major earthquake sequences have occurred, such as at Serdo (1969; Abdallah et al., 1979; Kebede et al., 1969), Asal Ghoubbet (1979; Abbate et al., 1995), Dobi (Jacques et al., 1989; Jacques et al., 1996, 2011), Dabbahu (2005–2010; Wright et al., 2006; Ayele et al., 2005; Ebinger et al., 2008; Grandin et al., 2005; Hamling et al., 2010; Barnie et al., 2016), Dallol (2004; Nobile et al., 2012) and during the Nabro eruption in 2010 (Hamlyn et al., 2014; Goitom et al., 2015). In addition to these earthquake swarms in Afar, notable swarms have occurred in the southern Red Sea in the Zubair Archipelago (Jónsson and Xu, 2015; Xu et al., 2015; Eyles et al., 2018) and in the Gulf of Aden (2010–2011; Leroy et al., 2012; Shuler and Nettles, 2012; Ahmed et al., 2016; **Figure 1A**).

Relating seismicity and earthquake swarms to magma intrusions can be difficult (Peterson et al., 2020), especially for swarms occurring offshore (e.g., Passarelli et al., 2018a) and for older inland swarms from the time before regular geodetic observations (i.e., prior to the 1990s, which corresponds to the beginning of InSAR and GPS). However, most inland swarms that have occurred in the SAGA region in the past 30 years have shown unambiguous relationship with magmatic intrusions. Moreover, the presence of numerous seafloor volcanic vents, in areas where offshore swarms have occurred, shows that multiple magmatic intrusions must have taken place in the past. In this paper, we compile the first regional appraisal of the earthquake swarms and related volcanic activity for the time period from 1960 to 2020. Integrating our results with historical records back to the early 19th century (1838), based on the book of Gouin (1979), provides an overview of earthquake swarms and volcanic activity in the region for the last 180 years. We also discuss temporal variations in magma supply to the SAGA region, which is one of the most volcanically and seismically active divergent plate boundaries on Earth (Hofstetter and Beyth, 2003). This study also aims to better understand long-term, multi-decadal behavior of divergent plate boundaries and to identify areas prone to recurrent strain accommodation during rifting cycles, which is of significant importance for seismic and volcanic hazard assessments in the region.

Earthquake Swarm Detection

We used the ISC (International Seismological Center) Bulletin (2020) to extract a catalogue of earthquakes for the SAGA region and to identify and analyze earthquake swarms. The ISC bulletin is assembled from reported hypocenters and associated parametric data (station arrival times, amplitude, magnitudes, moment tensors, etc.) from over 150 contributors around the world [for details, see e.g., Section 3 of International Seismological Centre (2020)]. Within about 24–30 months, ISC analysts review monthly batches of reports and the data are revised (in a broad sense, e.g., phases, hypocenters, magnitudes). During this stage, some earthquakes may be banished, merged, or split into more events. The largest earthquakes (usually of magnitude above 3.5, and some smaller ones that are reported by multiple agencies) are relocated by the ISC using the algorithm by Bondár and Storchak (2011). All phases with a valid travel-time prediction in the 1D ak135 model (Kennett et al., 1995) are used in the location determination, along with elevation, ellipticity (Kennett and Gudmundsson, 1996; Engdah et al., 1998), and depth-phase bounce point corrections (Engdah et al., 1998). Body- and surface-wave magnitudes are also re-computed. As such, the ISC Bulletin contains both locations and magnitudes from contributing agencies (at local and global scales) beside the ISC's own re-computations (if an earthquake is relocated). While not manually reviewed by the ISC, small earthquakes,

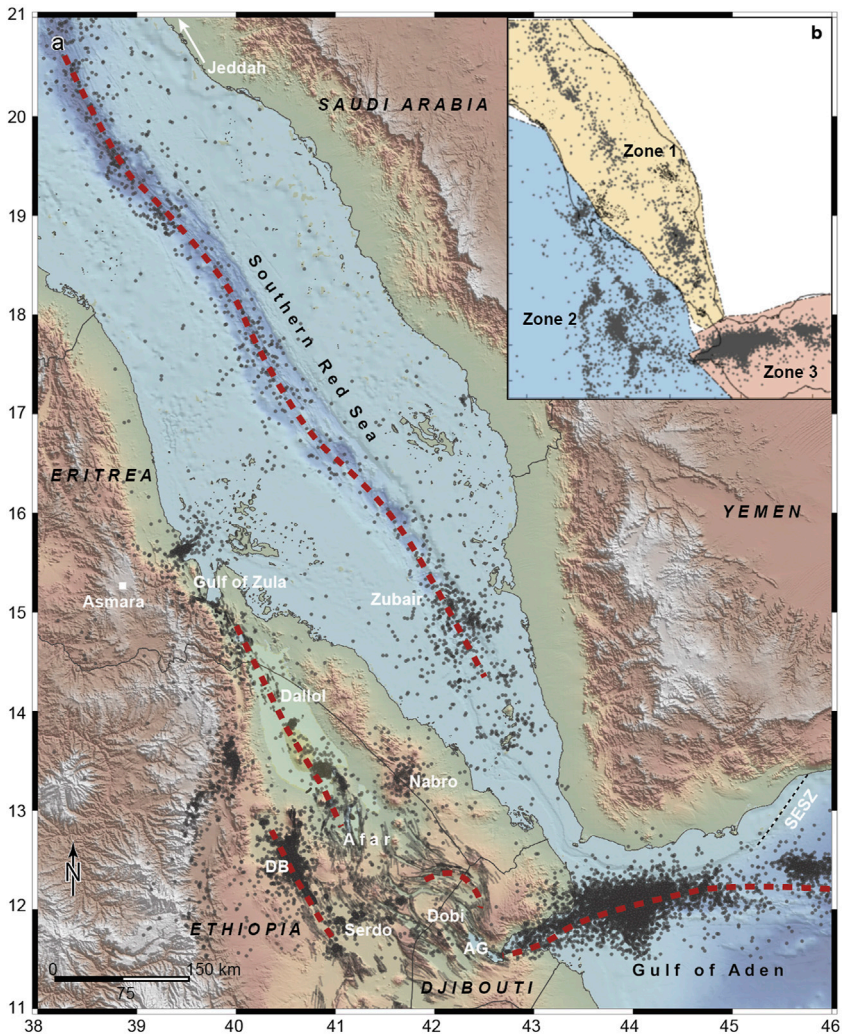

FIGURE 1 | Map of the southern Red Sea, Afar, and Gulf of Aden (SAGA) region. **(A)** Earthquake locations from the ISC catalogue are shown as black dots, country borders as thin black lines and plate boundaries in red dashed lines. **(B)** The earthquake swarm analysis was carried out separately for three different zones (zone 1: southern Red Sea, zone 2: Afar, and zone 3: Gulf of Aden).

which are normally reported by only one contributor, still undergo automatic checks to prevent (given the information available) faulty or inconsistent solutions to be released in the ISC Bulletin.

The earthquake catalogue we extracted for the SAGA region consists of over 15,200 earthquakes from 1960 to 2017. The earthquake locations are a mixture of solutions from contributing agencies and the ISC. The largest provider is UREES (http://www.isc.ac.uk/cgi-bin/agency-get?agency=UREES), with earthquake bulletins from Ebinger et al. (2008), Keir et al. (2009), and Belachew et al. (2011), followed by DHMR (http://www.isc.ac.uk/cgi-bin/agency-get?agency=DHMR), the ISC, and other agencies (**Supplementary Figure S1**). The earthquake magnitude (if any) is listed following the criteria by Di Giacomo and Storchak (2016). The catalogue is limited to earthquakes of magnitude 4 and above from 1960 until the 1990s, as only earthquakes recorded teleseismically were reported. However, in recent decades, the detection of smaller earthquakes (down to magnitude 2) improved thanks to better national seismic networks as well as temporary network deployments in the SAGA region (**Supplementary Figures S2, S3**). Reported earthquake locations extracted from the ISC Bulletin are usually constrained by data from more than five seismic stations (**Supplementary Figures S4A,B**) and the location uncertainty is within 30 km for about 86% of the events in the extracted catalogue (**Supplementary Figures S3C,D**). While the extracted catalogue is inhomogeneous in both space and time and almost half of the earthquakes (~7,400) are without a determined magnitude, making statistical analysis of the catalogue challenging, this catalogue compilation still resulted in the most extensive and updated information on the seismicity in the SAGA region to date.

In order to efficiently detect swarms, we developed a two-step methodology based on the earthquake occurrence rate and spatial

location. In the first step we identified every short time window during which the earthquake rate was higher than the background rate over a broader region. In the second step, for each selected time window, we then marked the location where the seismicity clustered in space through a density-based clustering algorithm (see details below). We divided the ~1,000 km × 1,200 km large SAGA region into three zones (**Figures 1A,B**), based on key tectonic features, and applied this swarm detection methodology separately to the seismicity of the three zones, i.e., the southern Red Sea, Afar and Gulf of Aden. Zone 1 corresponds to the southern Red Sea, from 21°N in the northwest to Bab-el-Mandeb (11°N) in the southeast, zone 2 broadly corresponds to the Afar region (from Massawa 15.6°N in the northwest to 11.5°N in the southeast), and zone 3 is the Gulf of Aden, from the Gulf of Tadjoura (40°W; Djibouti) to ~100 km east of the Shukra El Sheik fracture Zone at (46°W; Yemen; **Figure 1A**).

We want to stress that this two-step time-space approach is suitable when working with large seismically active regions. An increase in seismicity rate, with respect to high baseline activity in a large region, can either be due to clustered seismicity in space (i.e., single mainshock-aftershock sequences or earthquake swarms) or derive from a simultaneous increase in earthquake rate in more than one area. Our swarm detection algorithm is suitable for both scenarios.

In the first step, we used the classical β-statistics approach to identify time windows during which the observed seismicity rate was higher than the determined long-term background rate (Matthews and Reasenberg, 1988). The β-statistics is the standardized distribution of the number of events with respect to the long-term expected number of earthquakes and defined as $\beta=(n(t,\Delta t)-n_e(t,\Delta t))/\sigma(t,\Delta t)$, where $n(t,\Delta t)$ is the number of observed events in a time window $(t,\ t+\Delta t)$ and $n_e(t,\Delta t)$ and $\sigma(t,\Delta t)$ are the average and standard deviation of the expected number of window events given the observed background seismicity rate r (Reasenberg and Simpson, 1992). Anomalously high seismicity rate in a time window $(t,\ t+\Delta t)$ is identified when the β-statistics values is greater than a threshold value indicating how many standard deviations the window rate is higher than the expected long-term rate. Negative β-statistics values result when the number of window events is below the number expected from the background rate. The background seismicity rate r is usually calculated on declustered catalogues. However, while space-time-magnitude methods for declustering based on aftershock rate (e.g., Reasenberg, 1985) have proven effective in detecting swarm-like seismicity (Passarelli et al., 2018b), here such methods cannot be applied due to the lack of magnitude determination for nearly half of the events. We coped with this issue by instead calculating the background rate r with a time-dependent approach, i.e., by determining the background rate for each year from 1960 to 2017 (see gray horizontal bars in **Figure 2A** for Gulf of Aden catalogue), which roughly can account for both the improved catalogue completeness over time (cumulative earthquake number plot in **Figure 2A**) and for jumps in reported earthquake rate due to local and temporary seismic deployments. For the β-statistics calculation on non-overlapping windows of Δt = 30 days, we calculated the observed number of events $n(t,\Delta t)$, the expected one $n_e(t,\Delta t)$, and the standard deviation $\sigma(t,\Delta t)= n_e(t,\Delta t)^{-1/2}$ from the yearly background rate r as defined above on non-overlapping windows of Δt = 30 days (Matthews and Reasenberg, 1988). The results of the β-statistics are reported in **Figure 2B**, as well as the time periods during which we detected an increase in seismicity rate (β-statistics>3). If more than one consecutive 30-days-long time windows met the criteria of detectability, we grouped these windows into a longer one.

Once time windows of elevated seismicity rate had been identified in the first step, we used a density-based clustering algorithm in the second step to mark the spatial extent of the seismicity increase. For this we applied the widely-used DBscan algorithm (Ester et al., 1996), using the built-in function *dbscan* in Matlab, to search for neighboring points in a Euclidean space. We set the neighborhood parameter to ε = 25 km and the minimum number of events in a cluster to N_{min} = 5 after a trial-and-error procedure (Cesca, 2020).

To assess the variability of the number of swarm detections in the β-statistics calculation, we tested an alternative detection scheme in which we accounted for a time-dependent earthquake background rate, rather than keeping it constant for each calendar year (**Figure 2**). The time-dependent background rate was calculated on overlapping time windows ΔT_i = 360 days sliding every 30 days, so that ΔT_i is centered on the shorter time window Δt_i = 30 days used for the β-statistics calculation. The alternative algorithm produced minor changes in the number of swarms in the three study regions. In the Southern Red Sea, two additional swarms were identified, but for the Gulf of Aden the swarm number stayed the same, while in the Afar region nine additional swarms were detected (**Supplementary Table S1**). All these additional swarms occurred in swarm areas (i.e., clusters) that were already identified with the previous approach. In the Afar region, a few small seismic swarms occurred at the periphery of dike intrusions during the Dabbahu rifting episode (2005–2010) and went undetected by the previous approach. Although including a time-dependent earthquake background rate increases slightly the temporal resolution of our scanning algorithm, the few additional swarms do not change the overall picture of spatially distributed clusters.

We applied this swarm detection algorithm separately to all of the detected time windows in the three regions of the southern Red Sea, Afar and Gulf of Aden. We fully rely on this automatic detection procedure for earthquake swarms in the Afar and Gulf of Aden regions, as there were dozens of spatially and temporally overlapping swarms (**Supplementary Figure S5**). For the southern Red Sea, however, we also visually inspected the dataset as this region has had fewer earthquake swarms that are spatially more distributed. We looked for series of earthquakes that occur repeatedly over time (several events per day and/or hours) in the dataset. These series are typically preceded and followed by periods of no earthquake activity. Then, we looked at the earthquake mean coordinates and magnitudes, and retained them if they were all located in the vicinity (<50 km) of the ridge axis and/or in areas where other swarms have been detected automatically. We found that 25

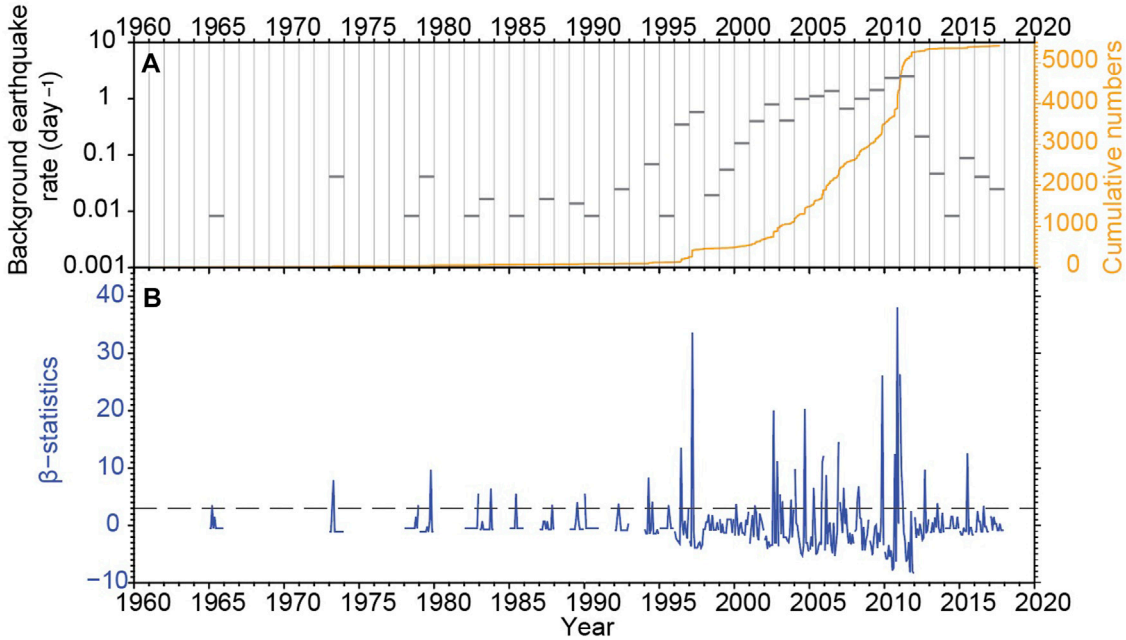

FIGURE 2 | Background seismicity rate and earthquake swarm detection for Gulf of Aden. **(A)** Horizontal bars indicate the estimated background seismicity rate for each year, with gaps representing years with no earthquakes in the catalogue. The cumulative number of earthquakes is shown by the orange curve. **(B)** The beta statistics calculated for non-overlapping windows of 30 days is shown in dark blue, with gaps reflecting lack of earthquakes in the catalogue. The horizontal dashed line represents the swarm-detection threshold value of 3 standard deviations. Note that the improved monitoring is likely accounting for some of the seismicity increase (see **Supplementary Figure S2** for more information).

TABLE 1 | List of swarms complementing the ISC catalogue.

Swarm event	Date	# Events	Longitude	Latitude	References
Bada	May 1967	5	40.1	14.60	Gouin (1979)
Dobi relocated	August 1989	25	41.77	11.84	Jacques et al. (1999)
Bada	May 1993	651	40.12	14.56	This study
Gab'ho	October 1996	10	40.51	12.64	Keir et al. (2009)
Dabbahu	June 2006	103	40.6	12.35	Keir et al. (2009)
Dabbahu	May 2010	104	40.6	12.36	Barnie et al. (2016)

earthquake swarms that we visually identified in the southern Red Sea were rejected by the automatic detection procedure, despite having all the characteristics of earthquake swarms, mainly due to poor earthquake locations in this region. To account for this problem, we complemented the set of automatically detected earthquake swarms with several manually picked swarms. To the earthquake swarm catalogue described above, we added five earthquake swarms in the Afar area that are not in the ISC catalogue and we also replaced one ISC swarm by a relocated one (**Table 1**). Furthermore, we pay special attention to the 1993 Bada swarm sequence (modified from Ogubazghi et al., 2004), as it fills a spatial seismicity gap between the Erta Ale Range in Afar and Alid volcano (South of the Gulf of Zula). Finally, we completed the earthquake swarm dataset with 11 historical events (i.e., six strong earthquake swarms and five volcanic eruptions) going back to 1838 in the Afar and Eritrea regions.

The identified earthquake swarms do not show a typical mainshock-aftershock decay, but rather contain multiple earthquakes of comparable magnitudes throughout the duration of each swarm (**Figures 3A–D**). In total for the 1960–2017 time period, we found that over half (~8,700 earthquakes) of the earthquakes extracted from the ISC catalogue for the SAGA region fall within 134 earthquake swarm sequences (145 when considering the historical events) located in 19 separate swarm areas (or clusters, i.e., distinct areas where earthquake swarms tend to reoccur).

RESULTS

In the following, we describe the earthquake swarm activity separately for the three different zones and then discuss the results in a regional context. We start with an overview of the activity from 1960 to 2020 from north to south for the southern Red Sea and the Afar regions, and from west to east for the Gulf of Aden. We first describe the different swarm cluster areas that

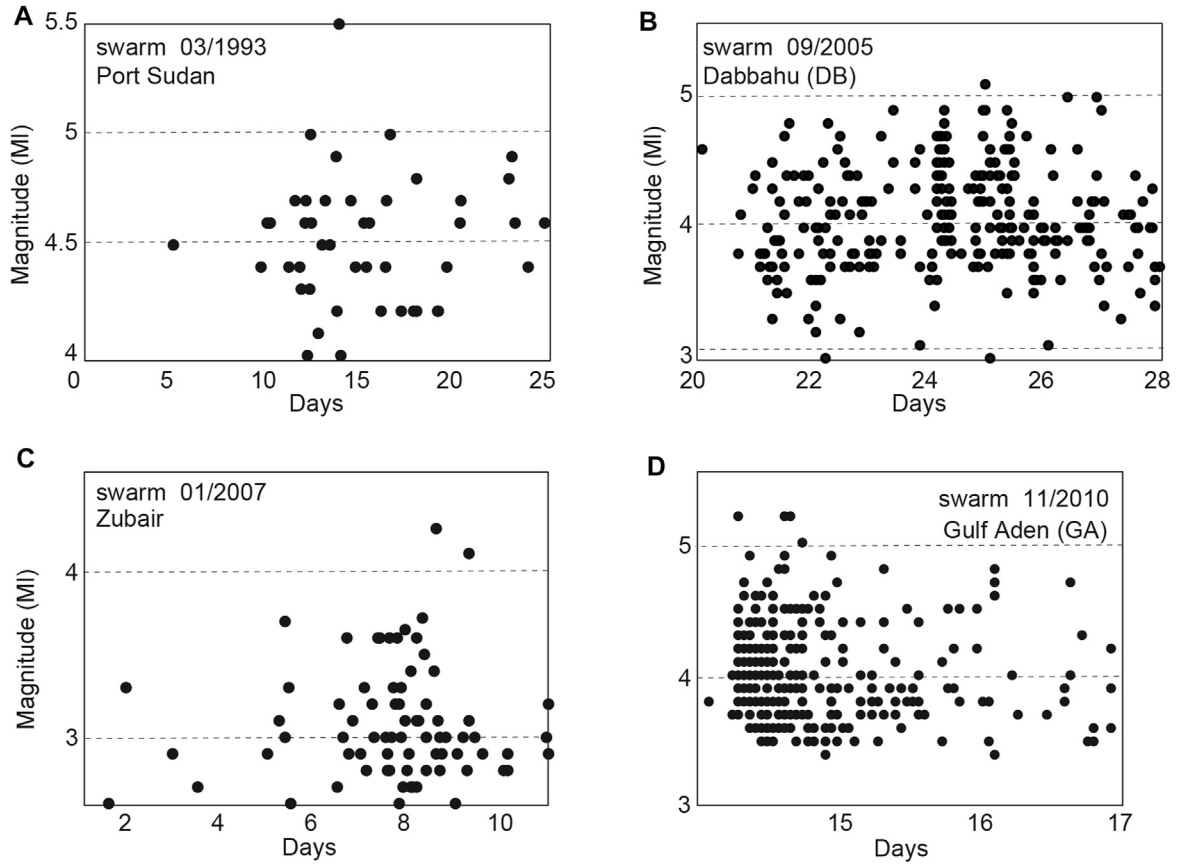

FIGURE 3 | Examples of typical earthquake swarm sequences in the SAGA region from **(A)** Port Sudan (March 1993), **(B)** Dabbahu (September 2005), **(C)** Zubair Archipelago (January 2007), and **(D)** Gulf of Aden (November 2010).

were detected, we then detail the different earthquake swarms that were identified in each cluster area, and finally we present the spatio-temporal distribution of the earthquake swarms. We complement the results with historical information going back to 1838, corresponding to the first large earthquake swarm described in Massawa, yielding a period of ~180 years of earthquake swarms for the Afar region.

Southern Red Sea Earthquake Swarms From 1960 to 2017

In the southern Red Sea, we identified seven clusters, along the southern Red Sea rift axis that together hosted a total of 45 earthquake swarms (of which 25 were detected manually). The seven distinct clusters are separated by areas that are relatively aseismic (**Figures 4A,B**). All the seven cluster areas have been prone to recurrent swarms during the study period (**Figure 4C**).

The northernmost cluster, east of Mukkawar Island and southwest of Jeddah (cluster 1, 21°N) had an earthquake swarm in 2006 and four swarms from February to December 2008, with magnitudes ranging from 2.2 to 3.9. In cluster 2 (150 km East of Port Sudan, 19.7°N; **Figure 4A**, a strong swarm of 29 detected earthquakes occurred in March 1967, with five earthquakes > M5. Another swarm took place in this cluster in March 1993 with 46 earthquakes of magnitudes ranging from 4 to 5.6, with six earthquakes larger than magnitude 5. This is the strongest earthquake swarm recorded in the southern Red Sea during the study period. A small swarm occurred in this cluster in 2014. Offshore of Kebir Island in Sudan (cluster 3, 19°N; **Figure 4A**), we identified four swarms from 2002 to 2013 with earthquake magnitude ranging from 2.3 to 5.1. In cluster 4 (17.5°N), located about 120 km further southeast along the rift axis and offshore of the town of Al Birk (Saudi Arabia), we extracted 10 earthquake swarms from 1975 to 2017. Although these are swarms with limited number of events, their magnitudes range from 3 to 5 and are closely related in time (i.e., several earthquakes per day). In 1988 and 2013, two swarms occurred at a similar latitude northeast of the Farasan Islands (cluster 5, 16.8°S). The November 1988 swarm was among the strongest in the southern Red Sea during the study period with 12 earthquakes ranging from M4.1 to M5.6. The Zubair Archipelago area (cluster 6, ~15°N; **Figures 4A,B**) was subject to four swarms from 1994 to 1997 with magnitudes ranging from 3 to 5.1, followed by intense activity from 2007 to 2013, consisting of eight discrete earthquake swarms and three volcanic eruptions. The first of the three eruptions occurred in 2007 on Jebel at Tair island (north of

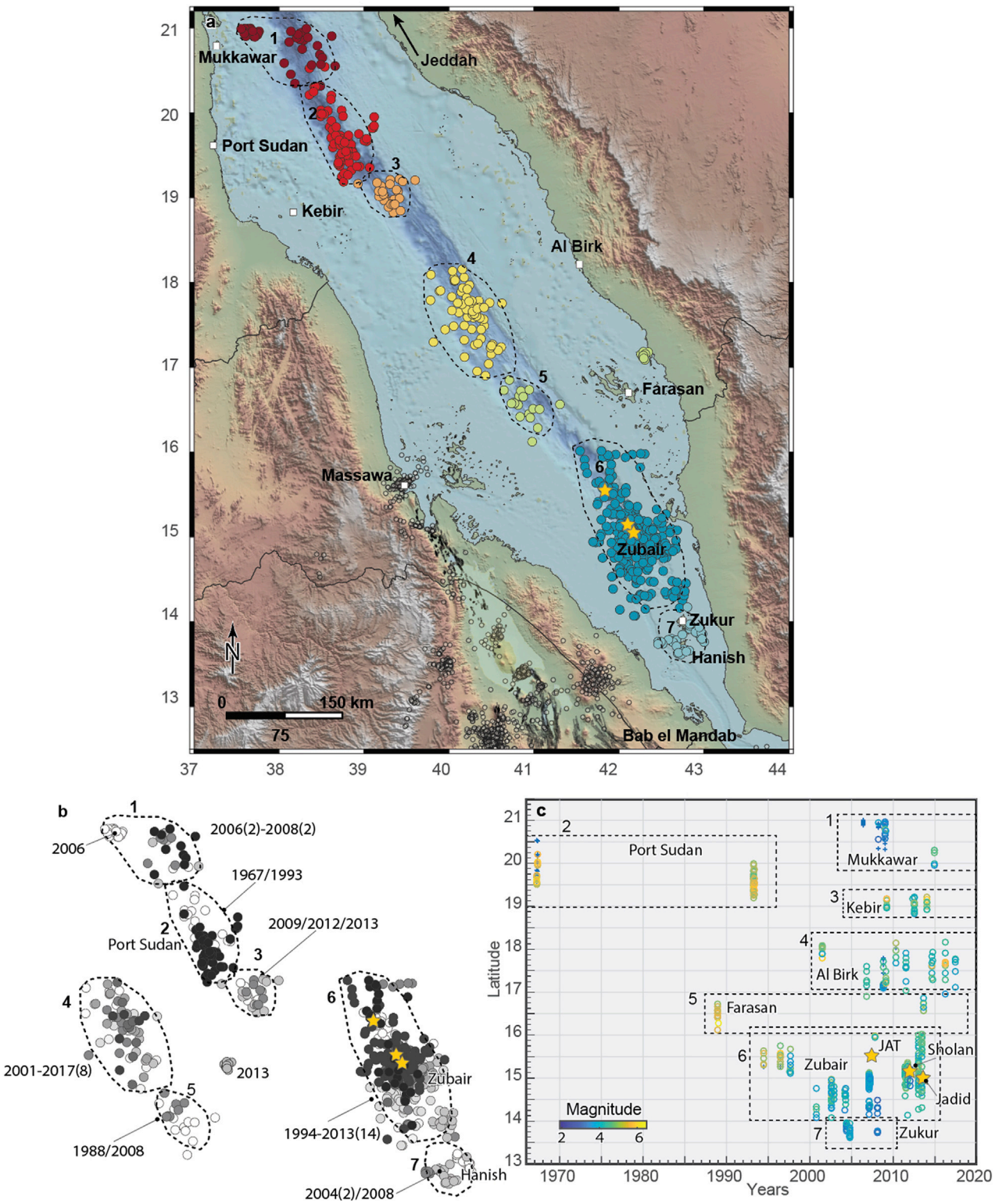

FIGURE 4 | Earthquake swarms in the southern Red Sea from 1960 to 2017. **(A)** Seven different clusters were identified along the southern Red Sea rift axis. **(B)** Each cluster contains several earthquake swarms whose timing is indicated by the grey gradient from white (older events) to black (younger events). The larger swarms are marked by the year of occurrence with the number of swarms for the noted period in brackets. **(C)** Swarm latitude as a function of time for the different clusters, with colors showing event magnitudes, blue stars earthquakes with no magnitudes, and yellow stars volcanic eruptions.

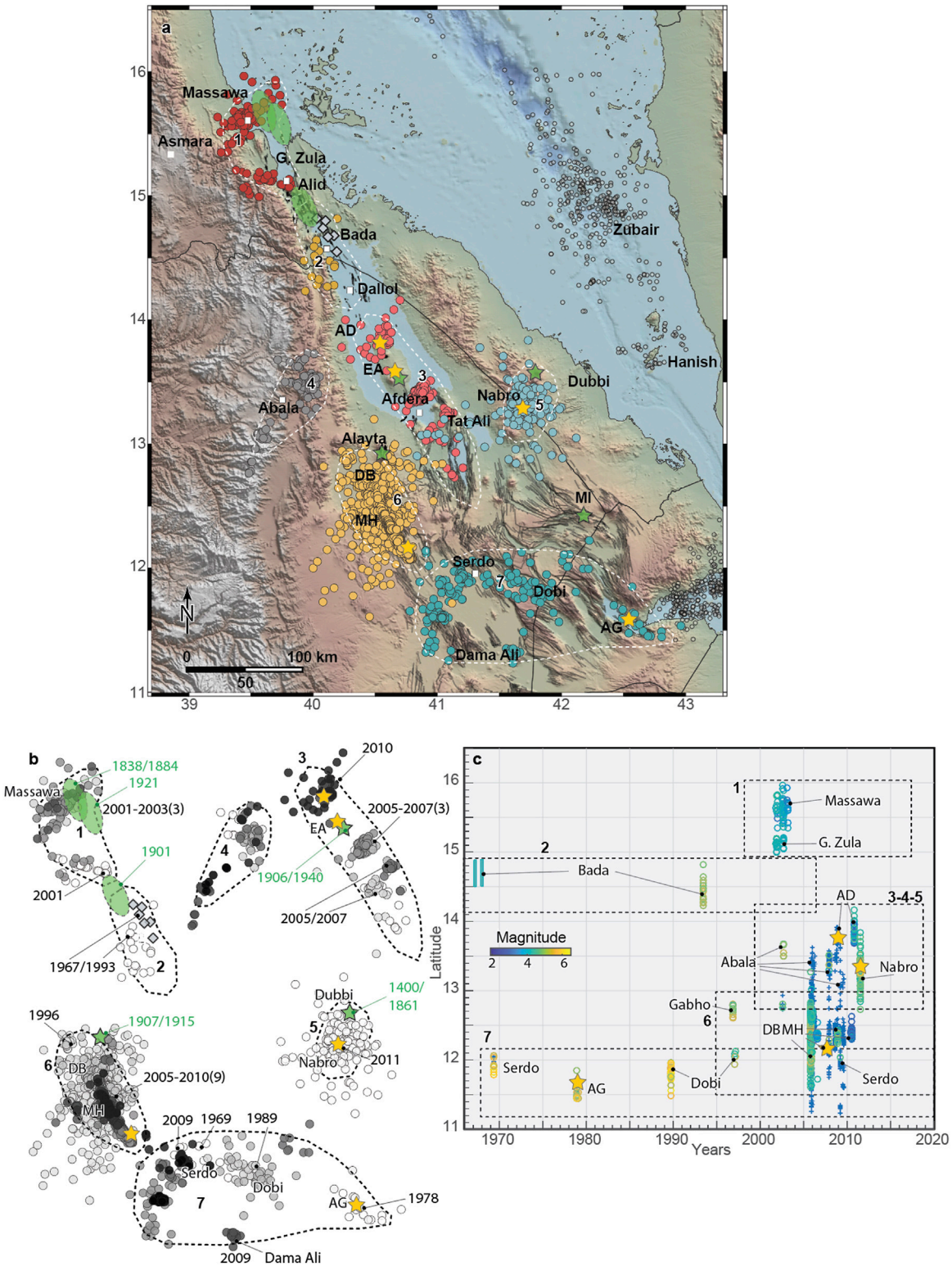

FIGURE 5 | Earthquake swarms in the Afar region from 1960 to 2017. **(A)** Seven different clusters were identified in the Afar region from Massawa (Eritrea) to Asal Ghoubbet (Djibouti). AD is for Alu Dalafilla, EA Erta Ale, MH Manda Hararo, MI Manda Inakir, AG Asal Ghoubbet. **(B)** Each cluster consists of several earthquake swarms whose timing is indicated by the grey gradient from white (older events) to black (younger events). The larger swarms are marked by the year of occurrence with the number of swarms (in brackets) for the noted period. Green polygons and green stars represent historical swarms and eruptions, respectively. **(C)** Swarm latitude as a function of time for the different clusters, with colors showing event magnitudes and blue stars representing earthquakes with no magnitudes. Yellow stars show volcanic eruptions.

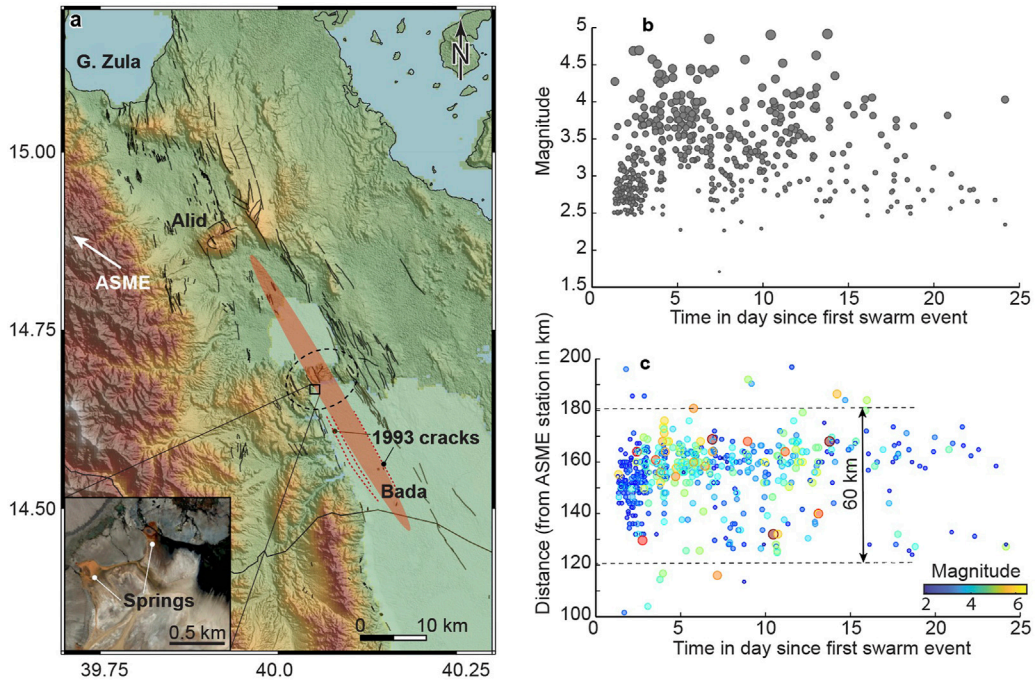

FIGURE 6 | The May 1993 Bada earthquake swarm in Eritrea. **(A)** Map of the Bada region, northern Afar, with the transparent elongated red ellipse showing the approximate extension of the 1993 Bada swarm along a 60-km-long rift segment that was activated during this swarm. Inset shows the location of ferruginous springs at the periphery of a doming area (the dashed circle). **(B)** Earthquake magnitudes with time show a typical swarm pattern with multiple max-magnitude events during the swarm and absence of a mainshock at the beginning of the sequence. **(C)** Distance of the swarm earthquakes from the ASME seismic station (see white arrow for the ASME direction located in Asmara; see **Figure 1** for location) versus time for the 25 days the swarm lasted.

Zubair; **Figure 4A**), killing four people (Jónsson and Xu, 2015). The later two eruptions gave birth to two volcanic islands, Sholan in 2011–2012, and Jadid in 2015 (Xu et al., 2015). Seven earthquake swarms occurred between 2002 and 2007, 70 km to the south of the Zubair Archipelago. For simplicity we included these swarms in the Zubair cluster (cluster 6) as they partly spatially overlap with the swarms of that cluster. Finally, the southernmost earthquake swarm cluster of the southern Red Sea (cluster 7, 13.8°N), located ~100 km to the southeast of Zubair islands, had two earthquake swarms in April and September 2004 in the Hanish-Zukur volcanic islands.

Afar and Eritrea Earthquake Swarms From 1960 to 2017

We found seven different clusters in Afar with a total of 46 swarms, located from the town of Massawa in Eritrea in the northwest to the Asal Ghoubbet rift in Djibouti about 550 km to the southeast (**Figure 5A**). The earthquake swarms took place along the entire length of Afar and, for the most part, were associated with the different active magmatic segments. A few earthquake swarms have also occurred at the rift escarpment (Abala region, **Figure 5A**) and at the complex structures of the central to eastern Afar, from Serdo to Asal Ghoubbet (**Figure 5A**).

In November 2001, a small earthquake swarm (35 earthquakes with an mean magnitude of 3.2) occurred in the vicinity of Massawa (cluster 1, 15.6°N). This was followed in 2002, by a year-long swarm with low to moderate magnitude earthquakes (1 < M < 4) (**Figures 5A,B**). The data was collected by the Eritrean seismic survey (259 earthquakes) and the determined event locations show a clear WSW-ENE oriented pattern (**Figures 5A,B**). This orientation differs by almost 70° from the roughly NNW-SSE oriented northern Afar rift axis in the Gulf of Zula region, ~100 km to the south of Massawa. In October-November 2001, another swarm occurred to the west of the Gulf of Zula (**Figures 5A–C**).

In May 1967 and in May 1968, two earthquake sequences occurred in northern Afar, between the Alid and Bada areas (cluster 2, 14.5°N), south of the Gulf of Zula (Gouin, 1979). In the May 1967 swarm, 79 earthquakes were reported, with magnitudes between 3.1 and 5.1 (Dakin, 1975). Then, following some activity in mid-November 1967, another earthquake swarm occurred in May 1968 with ~80 earthquakes. These two sequences are not in the ISC catalogue and we show here a few of the related earthquakes reported by Gouin (1979). The Bada region (Eritrea, north of the Ethiopian border; **Figure 5A**) was subject to another swarm in May 1993 that lasted 25 days and included 17 earthquakes of magnitudes ranging from 4 to 5.2 (see further analysis in **Figure 6**).

Cluster 3 extends from Alu-Dalafilla (14°N) down to 12.5°N, along the Erta Ale range, containing the Tat Ali and the Afdera volcanoes (**Figure 5A**). In 2004, an earthquake swarm occurred in the Dallol area, accompanied by a magnitude 5 earthquake, and

marked by a dike intrusion (Nobile et al., 2012). The seismic swarm induced by the intruding dike was recorded at just one station (FURI near Addis Ababa) and hence no locations are reported here. In November 2008, an eruption occurred at Alu-Dalafilla volcanic center, likely fed by a shallow sill reservoir (Pagli et al., 2012). There is again no record of swarm activity in the ISC catalogue accompanying this eruption. Three swarms occurred north of the town of Afdera in 2005, 2006 and 2007 (no magnitudes reported). This seismic activity has been interpreted as related to a tectonic rift linkage connecting the Tat Ali and the Erta Ale volcanic range systems (Illsley-Kemp et al., 2018; La Rosa et al., 2019; Pagli et al., 2019). In October 2005, yet another swarm occurred at the Afdera volcano (no magnitudes have been reported, apart from a single M3 earthquake).

The cluster 4 is offset from the main rift axis and is located near the rift border (13.5°N), partly in the marginal grabens of the western Afar margin in the Abala region (**Figure 5A**; see Zwaan et al., 2020). A total of 164 swarm earthquakes were detected in this cluster (150 earthquakes have no magnitudes reported), within 9 separate swarms. The strongest swarm occurred in November 2007, 30 km northeast of the town of Abala.

Cluster 5 is the location of the Nabro volcano (13.38°N). The period was marked by the Nabro eruption in June 2011 (east of the Afar rift zone, **Figure 5A**), the largest eruptions in the region for the last 150 years (since the Dubi eruption in 1861; **Figures 5A,B**). A total of 142 swarm earthquakes with magnitudes ranging from 3.2 to 5.6 (five larger than magnitude 5) occurred associated with the Nabro eruption.

The first recorded swarm in cluster 6 (from 12 to 13°N) occurred at Gab'ho volcano in 1996 with 10 earthquakes of magnitude from 3.2 to 5. Then, about a decade later, this area was hit by the start of the Dabbahu rifting episode that lasted for 5 years, from May 2005 to June 2010 in the Dabbahu and Manda Hararo magmatic segments (Ebinger et al., 2010). This episode consisted of 14 discrete dike intrusions. Our catalogue contains eight swarms from September 2005 to May 2010 that we describe below. Most of the swarm events have no reported magnitudes (~3,500 events). The first swarm in the ISC catalogue started in September 2005 and lasted until December 2005. We extracted 1709 earthquakes, out of which 362 have magnitudes between 2.8 and 5.5, with 18 earthquakes larger than magnitude 5. From January to March 2006, a swarm composed of 340 earthquakes (no magnitudes recorded) occurred in the central part of the Dabbahu magmatic segment. From October to November 2007, 440 earthquakes (without magnitudes) were reported. The earthquakes took place over 50 km from Dabbahu volcano south to the Manda Hararo magmatic segment. Another earthquake swarm with a similar pattern occurred from 29 June to September 28, 2008 with 272 earthquakes (no magnitudes reported). Three swarms occurred in roughly the same area in August 2008 (889 earthquakes), February 2009 (215 earthquakes) and May 2009 (48 earthquakes). No magnitudes have been reported for the earthquakes of these three swarms. The last swarm of the Dabbahu rifting episode took place in May 2010 with 104 earthquakes of magnitudes from 0.5 to 4.3.

Cluster 7 extends from Semera to Asal Ghoubbet (from 41 to 42.7°E; **Figure 5A**). In 1969, the strongest swarm of this area occurred near the town of Serdo in central Afar (**Figure 5A**). Of the 420 inhabitants, around 40 people died and 160 were wounded by the collapse of the constructions (Gouin, 1979). Ground cracks and subsidence were observed and measured, with faults showing vertical offsets of up to 95 cm and lateral offset of up to 65 cm (Gouin, 1979). Over 250 earthquakes of magnitude above 3 were recorded, with 11 of them in the magnitude range of 4.9–6.2. This area experienced a destructive earthquake swarm (6 months duration) in 1631 in the Aussa region (southeastern Afar), killing 50 people in the town of Waraba (Gouin, 1979). The 1969 activity took place within a broad depression bordered by normal faults (NE of the Tendaho graben), but the earthquake locations are widespread due to poor location determination, although they appear oriented NW-SE over distance of ~45 km, parallel to the basin direction.

In November 1978, a strong swarm occurred in the Asal Ghoubbet area (**Figure 5A**), which led to the Ardukôba eruption in December 1978. The swarm, with 16 earthquakes of magnitude ranging from 4.2 to 5.3 occurred in a rift zone that is oriented NW-SE (~40 km long), extending from offshore to inland. The Asal Ghoubbet rifting event was the first to be surveyed by geodesy in the region (Le Dain et al., 1979; Lépine and Hirn, 1992; Jacques et al., 1996; Doubre et al., 2007a, 2007b).

In August 1989, the NW-SE oriented and ~40-km-long Dobi graben (cluster 7; **Figures 5A,B**) experienced a powerful seismic swarm that generated widespread subsidence and normal faulting. For this earthquake swarm, we used relocated events by Jacques et al. (2011). The swarm included 25 recorded earthquakes with 11 earthquakes larger than magnitude 5 and five earthquakes exceeding 6. In 1997, another swarm occurred in the Dobi area with magnitudes from 3.5 to 4.9. From September to December 2005 (contemporary to the first 2005 Dabbahu intrusion event) a swarm composed of 35 recorded earthquakes (no magnitude reported) occurred in the Semera region (cluster 7; **Figure 5A**). In October 2005, eight earthquakes with magnitudes ranging from 3.4 to 4.7 were detected NW of the Asal region. In November 2007, a small earthquake swarm occurred in the Semera region, somewhat spatially overlapping with the October 2005 swarm, consisting of nine recorded earthquakes (no magnitudes reported). This swarm occurred at the same time as the November 2007 swarm of the Dabbahu rifting episode. In February 2009, an earthquake sequence occurred at the Dama Ali volcano, southeast of Semera (cluster 7; **Figures 5A,B**). During the same month, another earthquake sequence was detected 10 km west of Serdo (56 earthquakes, no magnitudes). In June 2009, a sequence (35 earthquakes, no magnitudes) occurred 15 km southwest of Semera.

In addition to the data from the ISC catalogue (**Figures 5A,B**) and to complement the swarm analysis in the poorly studied northern Afar region, we analyzed data from the Eritrean Seismic Survey to infer earthquake magnitudes and locations in the Bada area (651 earthquakes) in May—June 1993. The data are from the ASMA seismic station, located in Asmara city (Eritrea; see **Figure 1** for location), whose azimuth from Bada is roughly co-linear with the most likely orientation of the earthquake swarm locations, based on observed fresh ground cracks and

graben subsidence. We therefore use the time difference between P and S-wave arrival times at the station to estimate the distance of each earthquake from the station and relative along-rift position within the swarm (**Figure 6A**). The swarm shows earthquakes with similar magnitudes throughout the 25-days duration of the activity (**Figure 6B**). Locally, the likely earthquake swarm area corresponds to a topographic high hosting hydrothermal activity (**Figure 6A**).

Afar and Eritrea Historical Earthquake Swarms From 1838 to 1960

Historical documents contain several earthquake sequences [often referred as tremors by Gouin (1979)] that were witnessed in the SAGA region prior to 1960. For example, repeated earthquake swarms were reported in northern Afar, Gulf of Zula and Massawa (Red Sea coastal area of Eritrea, N15.5) with six major earthquake swarms from the early 19th century (Gouin, 1979) to 1921. From 25 February to the end of March 1838, strong swarms were felt in Massawa (15.6°N), followed by several other smaller sequences in 1844 and 1848 (**Figures 5A,B**). From July to October 1884, the coastal region close to Massawa was devastated by a sequence of earthquakes and a small tidal wave. The sequences likely occurred in between the Dahlak archipelago and the town of Massawa. From November 11, 1901 to March 1902, tremors were felt near Alid volcano (**Figure 5A**), south of the Gulf of Zula and in the city of Massawa. Then, during the whole year of 1921, a strong earthquake sequence almost entirely destroyed the city of Massawa. It was so intense that Eritrean folklore remembers it as "Zemene delekeleke", the era of earthquakes (Gouin, 1979). In addition to these sequences, the Dubbi volcano (13.5°N, 41.8°E) on the Red Sea coast of Eritrea erupted in May 1861 and was associated with strong earthquakes that were felt during 4 months and destroyed two villages, killing 106 people and livestock. This eruption was preceded by another eruption in 1,400. In central Afar, five older volcano-tectonic events have been reported in the Erta Ale (1906, 1940) and Alayta volcanic range (1907, 1915; https://volcano.si.edu/) and in 1928, when an eruption occurred in the Manda Inakir rift in Djibouti (Audin et al., 1990).

Gulf of Aden Earthquake Swarms From 1960 to 2017

The Gulf of Aden shows by far the strongest swarm activity of the three regions, back to the 1970s. We identified five clusters in the area and 43 swarms distributed from the Gulf of Tadjoura in the west (**Figure 7A**) and then along the Aden ridge for over 250 km to the east (**Figures 7A–C**). The Aden ridge has been divided in three structural domains, with western, central and eastern domains based on three distinct lithosphere types (Hébert et al., 2001; Leroy et al., 2012). The eastern and central domains have oceanic crust with thickness that changes from 8 to 12 km (Hébert et al., 2001), with the western domain likely being transitional crust between oceanic and continental (Dauteuil et al., 2001). In the following description, clusters 2, 3 and 4 correspond broadly to the western, central and eastern domains, respectively (see Ahmed et al., 2016). As we defined the cluster areas based on swarm event locations, we decided to merge clusters 1, 2, 3 and 4, as they appear to spatially overlap and contain relatively poor event locations, and we then describe them chronologically. From west (42.7°E) to east (45°E) the centers of the four overlapping clusters are located in the Gulf of Tadjoura area (cluster 1, 43°E), offshore of Obock town (cluster 2, 43.5°E; **Figure 7A**), south of Khor Umera (cluster 3, 44°E; south coast of Yemen; **Figure 7A**), the cluster containing most of the swarms, and southwest of the city of Aden (cluster 4, 44.7°E; **Figure 7**). These four cluster areas form an almost structural continuum made of a series of oblique rifts that are well visible in bathymetric data (Ahmed et al., 2016).

Clusters 1 and 2 contain 24 earthquake swarms from 1973 to 2011. In 1973, a year after the Asal Ghoubbet rifting event, a powerful swarm occurred offshore of Obock (**Figures 7A,B**), comprising seven earthquakes of magnitudes between 5.0 and 5.7. Six swarms occurred from 1993 to 1997 and they are relatively well located on the rift axis. From 2001 to 2003, 5 swarms occurred; two strong swarms in August and November 2002 with 188 earthquakes and magnitudes ranging from 3 to 5.1, of which 15 earthquakes were larger than magnitude 4. In January 2004, another strong swarm made of 83 earthquakes occurred along the entire Aden ridge (i.e., clusters 1, 2, 3 and 4), contrasting earlier swarms that mostly occurred within only single portions of the ridge. In this large swarm, the earthquakes were well distributed from Tadjoura (43°E) to 44.7°E, with magnitudes ranging from 2.8 to 5.3. Then, from 31 August to September 26, 2010, a strong swarm occurred in the area, hosting the largest rifting episode during the period of observation in the Gulf of Aden. From October 2010 to November 25, 2010, 379 earthquakes were recorded (ISC catalogue) with magnitudes ranging from 2.7 to 5.5, with 24 earthquakes larger than five (see Schuler and Nettles, 2012 and Ahmed et al., 2016). This was followed by another powerful swarm from January to March 2011, which included 581 earthquakes of magnitudes ranging from 2.3 to 5.2, with two earthquakes larger than 5. Although our automatic swarm detection methodology selected these earthquakes as being within a single swarm, this swarm has been split in two by Ahmed et al. (2016).

Another cluster area was found further to the east (cluster 5, 46°E; **Figures 7A–C**). We identified a total of 10 earthquake swarms within this cluster from February 2000 to November 2015 that contained some 316 earthquakes of magnitudes ranging from 2.2 to 5.6, with eight earthquakes above magnitude 5. This cluster is offset from the main ridge axis; however, volcanic vents have been observed at this location (Dauteuil et al., 2001).

DISCUSSION

Recurrent Swarm Activity Highlights Spreading Centers in the SAGA Region

Our results show that many areas in the SAGA region have been subject to recurrent earthquake swarm activity since 1960. Good examples include the swarm areas (or clusters) offshore of Port Sudan (with two strong swarms occurring in 1967 and 1993),

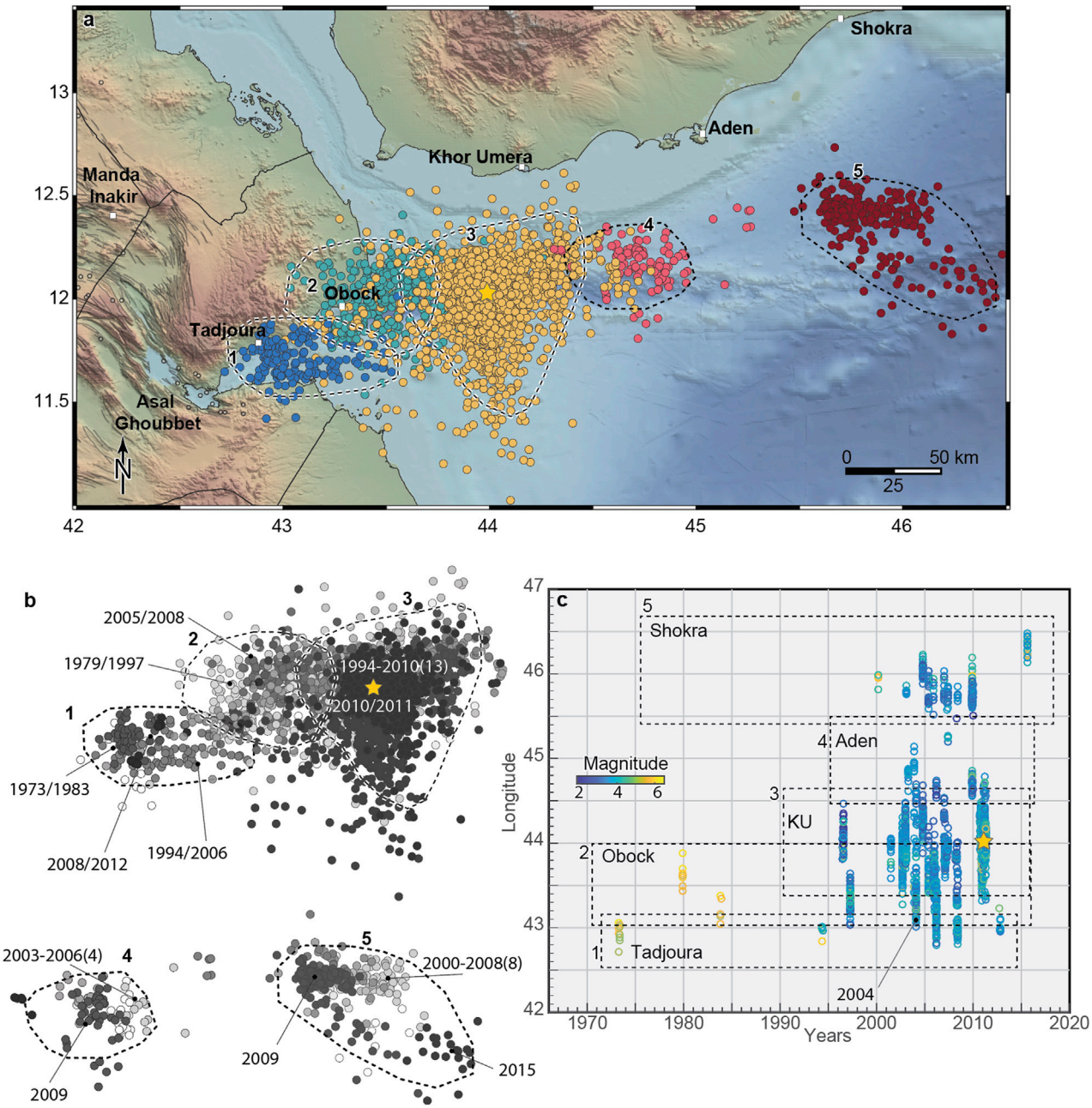

FIGURE 7 | Earthquake swarms in the Gulf of Aden from 1960 to 2017. **(A)** Five different swarm areas (clusters) were identified in the Gulf of Aden, from the Gulf of Tadjoura to the west of the town of Shokra (Yemen). **(B)** Each cluster consists of several earthquake swarms whose timing is indicated by the grey gradient from white (older events) to black (younger events). The larger earthquake swarms are marked by the year of occurrence with the number of swarms (in brackets) for the noted period. The yellow star shows the location of the 2010 submarine eruption. **(C)** Longitude location of the swarms as a function of time with colors indicating event magnitudes.

Kebir, and Al Birk, and in the Zubair archipelago (see **Figure 4A**). These clusters in the southern Red Sea likely relate to active spreading centers on the Red Sea rift axis.

The Bada region of northern Afar (**Figure 6A**) was hit by three strong swarms in 1967, 1968 and 1993, and the area north of Bada was affected recurrently by earthquake swarms in 1838, 1884, and 1920–21, destroying parts of Massawa city. This area at the northern end of the northern Afar axis has been seismically active with repeating swarms over the past two centuries, leading to questions on how the rift axis extends northward through the Gulf of Zula (Viltres et al., 2020) and connects to a transform zone from Massawa region to the central rift trough in the southern

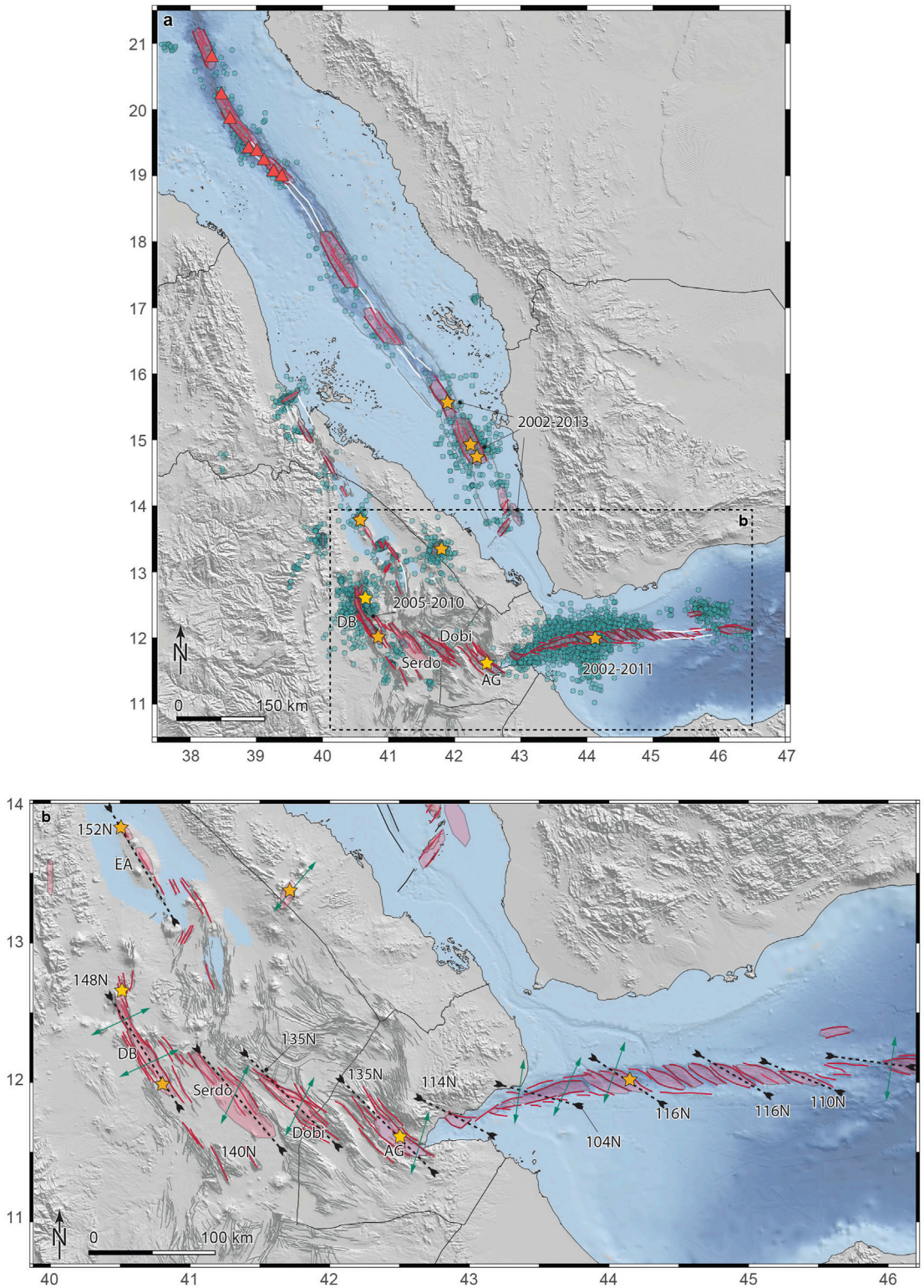

FIGURE 8 | Earthquake swarms and tectonic activity for the last 60 years in the SAGA region. **(A)** Swarm location from 1960 to 2017 (green dots). Red lines and semi-transparent pink polygons show structures and portion of the active rift zones where swarms have been observed from 1960 to 2017. White lines show areas where no swarms have been detected from 1960, along known plate boundaries. Yellow stars are volcanic eruption locations. Red triangles show volcanic vents and volcanic domes at sea bottom (after Augustin et al., 2016). **(B)** Close up view on the structural continuum from Gulf of Aden (after Ahmed et al., 2016), Asal Ghoubbet (AG), Dobi, Serdo and the Dabbahu magmatic segment (DB) characterized by oblique spreading and en-echelon extensional basins. Dashed lines with opposite arrows show the corresponding basin's mean orientation. Green double arrows show the mean extension direction, extracted from focal mechanisms analysis. Erta Ale (EA) has a similar orientation that Dabbahu magmatic segment. Grey lines are first order lineaments of the area; thin black lines show the coast line and the borders of the countries.

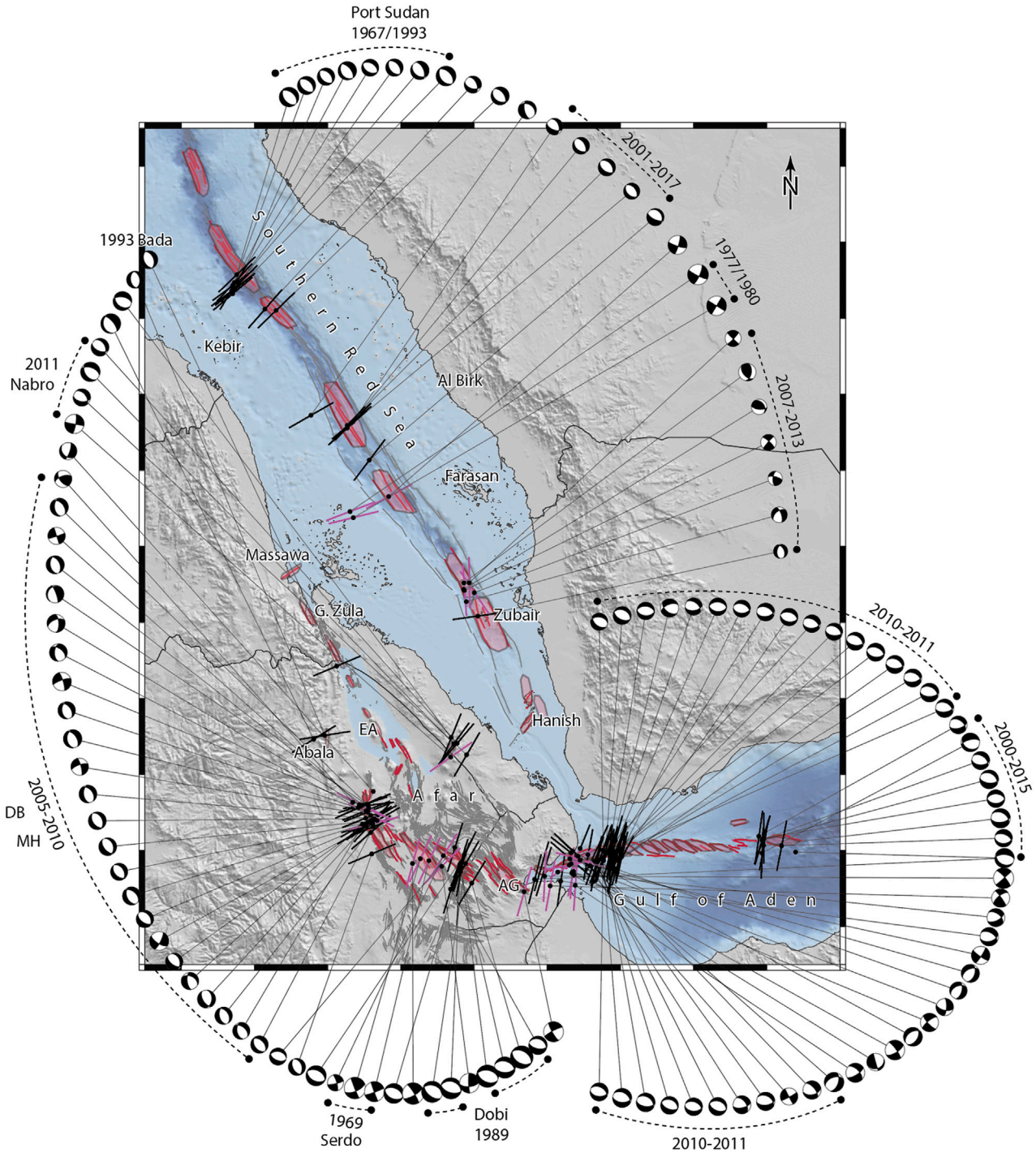

FIGURE 9 | Focal mechanisms (from Hofstetter and Beyth, 2003, and Global Centroid Moment Tensor project, GCMT, www.globalcmt.org, Dziewonski et al., 1981; Ekström et al., 2012) related to swarms in the SAGA region from 1960 to 2017 as sourced from the ISC Bulletin. Extension axes are shown by black segments (normal faulting) and pink segments (strike-slip faulting). Selected strong swarms are indicated by dates and area names (see main text for details). DB and MH for Dabbahu and Manda Hararo magmatic segments, respectively. Pink polygons and red lines represent the areas that have been affected by swarm activity (see **Figure 8** for details).

Red Sea. The 2002 Massawa earthquake swarm shows a clear WSW-ENE orientation of the activity that differs from the NNE-SSW rift orientation south of the Gulf of Zula. Two large-magnitude earthquakes (M6.6 and M6.1) occurred just west of the Red Sea trough, respectively in 1977 and 1980, suggesting a possible transform fault, an interpretation

supported by the strike-slip focal mechanisms of these earthquakes (**Figure 9**). About 340 km to southwest, on the rift escarpment, the cluster 4 shows also recurrent swarms in the Abala region with a strong event in November 2007. Then, the Dabbahu-Manda Hararo magmatic segments have been subjected to intrusions of 14 discrete dikes from 2005 to 2010 during the Dabbahu rifting episode.

The Gulf of Aden has probably produced the region's best example of recurrent swarm sequences along a spreading ridge that then hosted a rifting episode in 2010–2011 (cluster 1 to 3, **Figure 7A**). The same area had 23 other earthquake swarms along this 250 km spreading area from 1973 to 2011. Clusters 4 and 5 in the Gulf of Aden have also shown recurrent swarm activity that likely relates to other spreading centers (**Figure 7**).

More broadly, the spreading centers concentrate the strain release during magmatic and tectonic events and therefore, their locations are important for a better understanding of the overall evolution of plate motions in the SAGA region. Earthquake swarm activity in the triple junction reveals overlapping rift segments. The Southern Red Sea and the Afar ridges are located on both sides of the Danakil Alps and both spreading ridges overlap for ~150 km (**Figure 8**). In central Afar, en-echelon, partly overlapping rifts segments (Asal Ghoubbet-Dobi- Serdo- Manda Hararo) are also highlighted with both swarm activity and rift structures (**Figure 8**). These multiscale overlapping segments suggest a complex interaction between tectonics and magmatism in the SAGA region influenced by the regional geodynamics. While the earthquake swarms since 1960 highlight most of divergent plate boundaries in the SAGA region, a few zones did not show any swarm activity during the study period. For example, a 100-km-long segment between clusters 3 and 4 in the southern Red Sea (**Figure 8A**) remained quiescent. This does not necessarily mean that such quiet ridge segments are completely inactive, as the study period includes only the past 60 years. In Iceland, time intervals of ~200 years between rifting episodes appear not atypical, e.g., between periods of activity at Krafla (1724–1729 and 1975–1984) and at Holuhraun during Bárðarbunga rifting events (1797 and 2014–2015), with the inter-rifting duration characterized by relative seismic quiescence (Ruch et al., 2016).

On the Origin of Earthquake Swarms

Our results show that apart from a few quiescent segments, most of the length of the plate boundaries separating the Nubian, Arabian and Somalian plates have been activated by seismic swarms and volcanic activity since 1960 (**Figure 8A**). Focal mechanisms also show that most of the swarms are characterized by normal faulting, indicative of the extensional tectonics that dominates in the region (**Figure 9**).

The central question on the origin of these earthquake swarms is whether they are of magmatic or tectonic origin. Some of the swarms were clearly magmatic, as they were accompanied by observed volcanic activity. However, for the majority of the swarms detected in the SAGA region, the link to magma is less clear. Resolving this has important implications, as swarms are responsible for key morphological processes observed in active rift zones and often precede volcanic eruptions. The central axis of the Southern Red Sea trough hosts numerous volcanic vents and thus the earthquake swarms in this region are likely associated with magma activity. Bathymetric data of cluster areas 2 and 3 (e.g., offshore of Port Sudan, see **Figure 4A** for location) exhibit several volcanic vents and fresh lava flows (**Figure 8A**; Augustin et al., 2016), showing the contribution of magma in shaping the rift zone and pointing to a likely origin of the observed swarms. Further south, cluster 6 (Zubair Archipelago) had intense activity in 14 earthquake swarms between 1994 and 2013. Three volcanic eruptions occurred during this time period, which demonstrates a magmatic origin of the earthquake swarms, at least in these three cases. Then, most of the earthquake swarms observed inland in the SAGA region and after regular InSAR observations started (after 1990s) show unambiguous contribution of magma through dike injections (e.g., Gab'ho 1996, Dabbahu, 2005–2010, Dallol, 2004). A few other swarms relate to rift linkage and are likely of a tectonic origin (Afdera swarm, 2005–2007, Illsley-Kemp et al., 2018; La Rosa et al., 2019).

Earthquake swarms that preceded the era of InSAR ground deformation analysis (i.e. from before the early 1990s) and did not trigger volcanic eruptions have typically been associated to tectonic events, rather than to magmatic intrusions, e.g., the swarms at Serdo (1969), Dobi (1989) (e.g. Ebinger and Wijk, 2013; Keir et al., 2013; Pagli et al., 2019) and in Bada (1993). However, for these events there is no unambiguous way to attribute the swarm activity to either magmatic or tectonic processes. In Bada, rift parallel ground cracks, vertical offsets and rockfalls resulted in a formation of a graben (Ghebreab and Solomon, 1994; Ogubazghi et al., 2004). Note that 17 earthquakes larger than M4 happened after the field campaign of Ghebreab and Solomon (1994) so that final ground measurements were never completed. These surface effects, as well as the space-time evolution of the swarm with event migration away from a segment centered volcanic system and the largest earthquakes at the migration fronts, are typical of dike-induced seismicity (**Figure 6C**), e.g., as observed during the Dabbahu rifting episode (e.g., Barnie et al., 2016). The repeated swarm activity in the Bada area points to the presence of an immature spreading center, such as the one in Dallol, located about 50 km to the southeast.

Although the large-magnitude earthquakes observed during the Serdo and the Dobi earthquake sequences relate to meter-scale fault slip at the surface, the swarm patterns of the two sequences are characterized by an absence of main shock-aftershock sequences. The observed ground ruptures (graben formation, normal faulting and open fractures) are also typically observed during rifting events so that magma contribution cannot be excluded for these two sequences. Moreover, recent dike intrusions have been associated with earthquakes of similarly large magnitudes, such as the Miyakejima dike intrusion (Passarelli et al., 2015) where large dike-induced stresses both produced large earthquakes on likely newly formed normal faults and on pre-existing tectonic strike-slip structures that were favorably oriented. The Serdo area includes a few volcanic edifices (e.g., Dama Ali volcano; erupted in 1631 CE, **Figure 5A**), suggesting that magma reached the surface in

the region. Reed et al. (2014) documented high Vp/Vs ratios within the lower crust beneath the Dobi graben, which implies the presence of melt (Demissie et al., 2018). Finally, the structural framework of the region is composed of a set of left-stepping en-echelon basin structures from the Aden ridge oriented ~110°N, Asal Ghoubbet (135°N), Dobi (135°N), Serdo (140°N) and the Manda Hararo magmatic segment (148°N) forming a structural continuum (**Figure 8B**). The tensional axes derived from the focal mechanisms of swarms are all oblique with respect to the mean orientation of the basins (**Figures 8B**, **9**). These en-echelon basins are affected at both edges by magmatic intrusions (i.e., Gulf of Aden ridge and the Manda Hararo-Dabbahu magmatic segments) and the central portion (Dobi and Serdo) might originate from a mixed source of deformation where magmatic and tectonic processes may interact. Therefore, while the origin of the older swarms in this region cannot be unambiguously related to either tectonic or magmatic activity, for some of these swarms both tectonic and magmatic processes were likely at work.

Swarm and Volcanic Activity Increase During the mid 2000s to mid 2010s

Supplementary Figure S2 broadly shows a progressive increase in annual number of earthquakes reported by the ISC since the early 1990s compared to the preceding period. Much of this increase is consistent with improvements in regional seismic station density. To address this, we also plotted annual numbers of events of M4.5 and larger in order to reveal temporal changes in earthquake activity above the magnitude of completeness through the entire time period (**Figure S2**). This shows noticeable lobes of increased number of M4.5 and larger earthquakes in roughly decadal timeframes such as in the late 1970s, and the late 1980s to mid 1990s. We test this hypothesis of increase of earthquake rate for the class of M4.5 and larger earthquakes over decadal timeframes against a stationary earthquake occurrence described by a Poisson model with constant rate (Zhuang et al., 2012). In a Poissonian stationary model, the times between two consecutive earthquakes (i.e., inter-event times IETs) follow an exponential distribution with first moment equal to the long-term seismicity rate λ. The fit of seismicity rate to the observed earthquakes restitutes $\lambda = 0.026$ with 95% confidence interval $\lambda_{CI} = 0.024–0.029$. We simulate 100 synthetic catalogs of IETs from the exponential distribution with randomly varying λ_{CI}. We then compared the observed and each of the simulated distributions of IETs through a Kolmogorov-Smirnov (KS) two-sided goodness-of-fit test (Massey, 1951) under the null hypothesis that both are independent sample from the same underlying distribution. We rejected the null hypothesis 100% of times at significance level of $\alpha = 0.01$ for the 100 simulations. We applied the same test to only events with M5 and larger and obtained the same results. We conclude that at first order the observed catalog does not follow a Poissonian stationary process and the earthquake lobes over decadal timeframe are a feature in the SAGA catalog not likely caused by the aftershock activity and thus relates to temporal increase of the swarm activity.

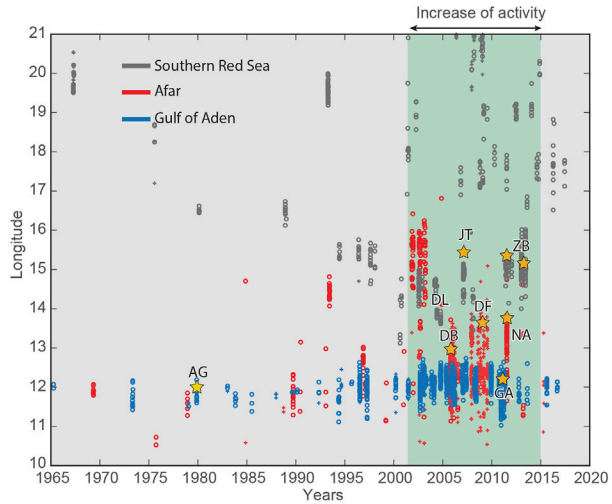

FIGURE 10 | Increase of swarm and volcanic activity observed from 2003 to 2013 in the SAGA region, preceded and followed by lower rates of swarm activity and the absence of volcanic eruptions. Yellow stars are eruptions; AG: Asal Ghoubbet; DL: Dallol; DB: Dabbahu; JT: Jebel at Tair; DF: Alu Dalafilla; GA: Gulf of Aden; NA: Nabro; ZB: Zubair Archipelago.

The most recent increase occurs during 2003–2013 in which there is an increase of the swarm activity in all the three rift branches of the southern Red Sea, Afar and the Gulf of Aden (SAGA region; **Figure 2B** and **Figure 10**). During the same time period, a total of seven volcanic eruptions occurred in all the three areas (**Figure 8A**). The three different rift branches were subject to three roughly synchronous rifting episodes, with Dabbahu (2005–2010; Wright et al., 2006), Gulf of Aden (2003–2011; Ahmed et al., 2016) and the southern Red Sea (2003–2013; Xu et al., 2015). The swarms in the Zubair Archipelago were temporally related to magmatic intrusions and eruptions (Jebel at Tair, Sholan and Jadid islands), while no volcanic activity was reported in association with two swarms further south near the Zukur and Hanish islands in 2004. Our dataset shows that the Gulf of Aden had been subject to strong swarms already from 2002 to 2004, indicating an increase of swarm activity 8 years before the main rifting activity in late 2010. This overall active 2003–2013 time period was followed by a seismically quiet period from 2013 to 2020 without any noticeable swarm activity.

These synchronous rifting episodes are focused in Afar and in the immediately adjacent parts of the southernmost Red Sea and westernmost Gulf of Aden. They suggest that this sector of the SAGA region experiences a regional rifting cycle, where the plate extension may have generated enough strain deficit at the plate boundaries to be released during a five to 10 years co-rifting period after an inter-rifting period of tectonic loading. This could suggest a common source of deformation for all three rift branches. Since rifting episodes are modulated by the interplay between magma supply and tectonic stress (e.g. Buck, 2006), we also propose that the regional increase in activity could have

been triggered by an overall increase of the magma supply rate from the underlying mantle in the SAGA region. Alternatively, the synchronous increase in activity across multiple segments of the rift might also be explained by regional stress triggering in which positive Coulomb stress changes induced by magma intrusion at one rift branch and associated earthquake swarms trigger magmatic and tectonic activity at the other rift branches that were near failure. However, there is little evidence for static stress triggering between distant (~350 km) rifting events and episodes in the region (Viltres et al., 2018). Such stress triggering has been observed at smaller scales within Afar, i.e., where several small swarms have been detected at the periphery of large dike intrusions in Afar in 2005, 2007 and 2009, synchronously with the Dabbahu rifting episode. These swarms could thus relate to static stress changes triggered by the dike intrusions inducing an increase of the seismicity at the dike periphery.

CONCLUSION

Observations of earthquake swarm activity over multiple decades can provide new information about areas prone to swarm activity (clusters), on swarm reoccurrence, and on regional magmatic and tectonic activity in general. In this study, we have generated a new earthquake swarm catalogue for the southern Red Sea, Afar and Gulf of Aden (the SAGA region) by integrating the ISC catalogue with additional local datasets, producing the first multi-decadal overview of the earthquake swarm activity of the SAGA region. The new swarm catalogue is composed of 19 clusters and 134 swarms from 1960 to 2017. Adding 11 volcano-tectonic events (six earthquake swarms and five volcanic eruptions) that occurred from 1838 to 1960, the catalogue includes a total of 145 events in the last 180 years. Most of the clusters show recurrent swarm activity over decades, supporting the presence of unnoticed active spreading centers in the SAGA region. Most of these swarms have likely a magmatic origin, as supported by eruption or ground deformation study, although we cannot rule out an unambiguous magmatic origin for all these swarms. The three rift branches show an increase of the swarm and volcanic activity between 2003 and 2013 suggesting the presence of a rifting cycle affecting part of the SAGA region.

DATA AVAILABILITY STATEMENT

The original contributions presented in the study are publicly available and the ISC catalogue for the period of observation in the SAGA region, the swarm results and the focal mechanisms are all available in a repository and can be found here: https://doi.org/10.31905/TKSACJMM. Further questions can be directed to the authors.

AUTHOR CONTRIBUTIONS

JR design the research, analyze the data, designed the Figures and wrote the paper; DK participated to the design of the research, analyzed the data and wrote the paper; LP analyzed the earthquake swarm data and wrote dedicated section of the paper; DG provided the revisited ISC catalogue and wrote dedicated section of the paper; GO provided and analyzed the data for the Bada sequence; SJ participated to the design of the research and wrote the paper.

FUNDING

This research was supported by King Abdullah University of Science and Technology (KAUST), under award number OSR-2015-CRG4-2643, and by the Swiss National Science Foundation, grant PP00P2_176869 JR. In addition, DK was supported by NERC grant NE/L013932 and by MiUR through PRIN grant 2017P9AT72 and LP was supported by NEWTON-g project, Grant Agreement No 801221.

ACKNOWLEDGMENTS

We thank SO and SH for their in-depth and very constructive comments that contribute to ameliorate the quality of the paper. We also thank the Editor LL and the Field Chief Editor Valerio Acocella for the careful handling of the paper.

SUPPLEMENTARY MATERIAL

The Supplementary Material for this article can be found online at: https://www.frontiersin.org/articles/10.3389/feart.2021.664673/full#supplementary-material

REFERENCES

Abbate, E., Passerini, P., and Zan, L. (1995). Strike-slip Faults in a Rift Area: a Transect in the Afar Triangle, East Africa. *Tectonophysics* 241, 67–97. doi:10.1016/0040-1951(94)00136-w

Abdallah, A., Courtillot, V., Kasser, M., Le Dain, A.-Y., Lépine, J.-C., Robineau, B., et al. (1979). Relevance of Afar Seismicity and Volcanism to the Mechanics of Accreting Plate Boundaries. *Nature* 282, 17–23. doi:10.1038/282017a0

Ágústsdóttir, T., Woods, J., Greenfield, T., Green, R. G., White, R. S., Winder, T., et al. (2016). Strike-slip Faulting during the 2014 Bárðarbunga-Holuhraun dike Intrusion, central Iceland, Geophys. *Res. Lett.* 6, 1–402. doi:10.1002/2015GL067423

Ahmed, A., Doubre, C., Leroy, S., Kassim, M., Keir, D., Abayazid, A., et al. (2016). Seafloor Spreading Event in Western Gulf of Aden during the November 2010-March 2011 Period Captured by Regional Seismic Networks: Evidence for Diking Events and Interactions with a Nascent Transform Zone. *Geophysical Journal International.* 205, 1244–1266. doi:10.1093/gji/ggw068

Audin, J., Vellutini, P. J., Coulon, C., Piguet, P., and Vincent, J. (1990). The 1928?1929 Eruption of Kammourta Volcano ? Evidence of Tectono-Magmatic Activity in the Manda-Inakir Rift and Comparison with the Asal Rift, Afar Depression, Republic of Djibuti. *Bull. Volcanol.* 52, 551–561. doi:10.1007/BF00301536

Augustin, N., van der Zwan, F. M., Devey, C. W., Ligi, M., Kwasnitschka, T., Feldens, P., et al. (2016). Geomorphology of the central Red Sea Rift: Determining Spreading Processes. *Geomorphology* 274, 162–179. doi:10.1016/j.geomorph.2016.08.028

Ayele, A., Jacques, E., Kassim, M., Kidane, T., Omar, A., Tait, S., et al. (2007). The Volcano-Seismic Crisis in Afar, Ethiopia, Starting September 2005. *Earth and Planetary Science Letters* 255, 177–187. doi:10.1016/j.epsl.2006.12.014

Barnie, T. D., Keir, D., Hamling, I., Hofmann, B., Belachew, M., Carn, S., et al. (2016). A Multidisciplinary Study of the Final Episode of the Manda Hararo Dyke Sequence, Ethiopia, and Implications for Trends in Volcanism during the Rifting cycleGeological Society London Special Publications. *Geol. Soc. Lond. Spec. Publications* 420, 149–163. doi:10.1144/sp420.6

Belachew, M., Ebinger, C., Cote, D., Keir, D., Rowland, J. V., Hammond, J. O. S., et al. (2011). Comparison of dike Intrusions in an Incipient Seafloor-Spreading Segment in Afar, Ethiopia: Seismicity Perspectives: Journal of Geophysical Research. *Solid Earth*. 116, 1–23. doi:10.1029/2010jb007908

Bergman, E. A., and Solomon, S. C. (1990). Earthquake Swarms on the Mid-Atlantic Ridge: Products of Magmatism or Extensional Tectonics? *J. Geophys. Res.* 95, 4943–4965. doi:10.1029/jb095ib04p04943

Bird, P., Kagan, Y. Y., and Jackson, D. D. (2002). Plate Tectonics and Earthquake Potential of Spreading Ridges and Oceanic Transform Faults: *Geodynamics Ser.* 30, 203–218. doi:10.1029/gd030p0203

Boettcher, M. S., and Jordan, T. H. (2004). Earthquake Scaling Relations for Mid-ocean ridge Transform Faults: Journal of Geophysical Research. *Solid Earth*. 109, 1–21. doi:10.1029/2004jb003110

Bondár, I., and Storchak, D. (2011). Improved Location Procedures at the International Seismological Centre. *Geophysical Journal International* 186, 1220–1244. doi:10.1111/j.1365-246x.2011.05107.x

Buck, W. R. (2006). The Role of Magma in the Development of the Afro-Arabian Rift System. *Geol. Soc. Lond. Spec. Publications* 259, 43–54. doi:10.1144/gsl.sp.2006.259.01.05

Cesca, S. (2020). Seiscloud, a Tool for Density-Based Seismicity Clustering and Visualization. *J. Seismol* 24, 443–457. doi:10.1007/s10950-020-09921-8

Chen, X., and Shearer, P. M. (2011). Comprehensive Analysis of Earthquake Source Spectra and Swarms in the Salton Trough, California: Journal of Geophysical Research. *Solid Earth*. 116, 1–17. doi:10.1029/2011jb008263

Dakin, F. M. (1975). A Preliminary Survey of the Distribution and Characteristics of Earthquake Sequences in Ethiopia and T.F.A.I. Bull. Geophys. Obs. *Ethiopia* 15, 51–70.

Dauteuil, O., Huchon, P., Quemeneur, F., and Souriot, T. (2001). Propagation of an Oblique Spreading centre: the Western Gulf of Aden. *Tectonophysics* 332, 423–442. doi:10.1016/s0040-1951(00)00295-x

Demissie, Z., Mickus, K., Bridges, D., Abdelsalam, M. G., and Atekwana, E. (2018). Upper Lithospheric Structure of the Dobi Graben, Afar Depression from Magnetics and Gravity Data. *J. Afr. Earth Sci.* 147, 136–151. doi:10.1016/j.jafrearsci.2018.06.012

Di Giacomo, D., and Storchak, D. A. (2016). A Scheme to Set Preferred Magnitudes in the ISC Bulletin. *J. Seismol* 20, 555–567. doi:10.1007/s10950-015-9543-7

Doubre, C., Manighetti, I., Dorbath, C., Dorbath, L., Jacques, E., and Delmond, J. C. (2007a). Crustal Structure and Magmato-Tectonic Processes in an Active Rift (Asal-Ghoubbet, Afar, East Africa): 1. Insights from a 5-month Seismological experiment: Journal of Geophysical Research. *Solid Earth* 112, 1–22. doi:10.1029/2005jb003940

Doubre, C., Manighetti, I., Dorbath, C., Dorbath, L., Jacques, E., and Delmond, J. C. (2007b). Crustal Structure and Magmato-Tectonic Processes in an Active Rift (Asal-Ghoubbet, Afar, East Africa): 1. Insights from a 5-month Seismological experiment: Journal of Geophysical Research. *Solid Earth* 112, 1–32. doi:10.1029/2005jb003940

Dziak, R. P., Bohnenstiehl, D. R., Cowen, J. P., Baker, E. T., Rubin, K. H., Haxel, J. H., et al. (2007). Rapid dike Emplacement Leads to Eruptions and Hydrothermal Plume Release during Seafloor Spreading Events. *Geol.* 35, 579–582. doi:10.1130/g23476a.1

Dziak, R. P., Bohnenstiehl, D. R., Matsumoto, H., Fowler, M. J., Haxel, J. H., Tolstoy, M., et al. (2006). Seafloor-spreading Event at 9°50′N, East Pacific Rise: Ridge dike Intrusion and Transform Fault Interactions from Regional Hydroacoustic Data, January 2009 Seafloor-Spreading Event at 9°50N, East Pacific Rise: Ridge dike Intrusion and Transform Fault Interactions from Regional Hydroacoustic Data: Geochemistry, Geophysics. *Geochem. Geophys. Geosyst.* 10, a–n. January. doi:10.1029/2009GC002388

Dziak, R. P., Haxel, J. H., Bohnenstiehl, D. R., Chadwick, W. W., Nooner, S. L., Fowler, M. J., et al. (2011). 2012, Seismic Precursors and Magma Ascent before Theeruption at Axial Seamount. *Nature Geoscience*. 5, 478–482. doi:10.1038/ngeo1490

Dziewonski, A. M., Chou, T.-A., and Woodhouse, J. H. (1981). Determination of Earthquake Source Parameters from Waveform Data for Studies of Global and Regional Seismicity. *J. Geophys. Res.* 86, 2825–2852. doi:10.1029/JB086iB04p02825

Ebinger, C., Ayele, A., Keir, D., Rowland, J., Yirgu, G., Wright, T., et al. (2010). Length and Timescales of Rift Faulting and Magma Intrusion: The Afar Rifting Cycle from 2005 to Present. *Annu. Rev. Earth Planet. Sci.* 38, 439–466. doi:10.1146/annurev-earth-040809-152333

Ebinger, C. J., Keir, D., Ayele, A., Calais, E., Wright, T. J., Belachew, M., et al. (2008). Capturing Magma Intrusion and Faulting Processes during continental Rupture. *Seismicity of the Dabbahu (Afar) Rift*. 174, 1138–1152. doi:10.1111/j.1365-246x.2008.03877.x

Ebinger, C., Wijk, J. V, and Keir, D. (2013). The Time Scales of continental Rifting: Implications for Global Processes. *Geol. Soc. Americav*. 2500, 1–26. doi:10.1130/2013.2500(11)

Edwards, M. H., Kurras, G. J., Tolstoy, M., Bohnenstiehl, D. R., Coakley, B. J., and Cochran, J. R. (2001). Evidence of Recent Volcanic Activity on the Ultraslow-Spreading Gakkel ridge. *Nature* 409, 808–812. doi:10.1038/35057258

Einarsson, P., and Brandsdóttir, B. (2021). Seismicity of the Northern Volcanic Zone of Iceland. *Front. Earth Sci.* 9. doi:10.3389/feart.2021.628967

Ekström, G., Nettles, M., and Dziewoński, A. M. (2012). The Global CMT Project 2004-2010: Centroid-Moment Tensors for 13,017 Earthquakes. *Phys. Earth Planet. Interiors* 200-201, 1–9. doi:10.1016/j.pepi.2012.04.002

Engdah, R., Hilst, E., Van., Der, R., and Buland, R. (1998). Global Teleseismic Earthquake Relocation with Improved Travel Times and Procedures for Depth Determination. *Bulletin of the Seismological Society of America*. 88, 722–743.

Ester, M., Kriegel, H. P., Sander, J., and Xu, X. (1996). A Density-Based Algorithm for Discovering Clusters in Large Spatial Database with Noise:. *KDD Proc.*, 226–231. doi:10.1016/B978-044452701-1.00067-3

Eyles, J. H. W., Illsley-Kemp, F., Keir, D., Ruch, J., and Jónsson, S. (2018). Seismicity Associated with the Formation of a New Island in the Southern Red Sea. *Frontiers in Earth Science*. 6, 1–10. doi:10.3389/feart.2018.00141

Fairhead, J. D., and Girdler, R. W. (1970). The Seismicity of the Red Sea, Gulf of Aden and Afar Triangle: Philosophical Transactions of the Royal Society A. *Mathematical, Physical and Engineering Sciences*. 267, 49–74. doi:10.1098/rsta.1970.0023

Ghebreab, W., and Solomon, S. (1994). Formation of a Recent Asymmetric Graben-In-Graben Structure at Bada, the Danakil Depression of Eritrea. *Geoscience and Development*. 1, 16–18.

Goitom, B., Oppenheimer, C., Hammond, J. O. S., Grandin, R., Barnie, T., Donovan, A., et al. (2015). First Recorded Eruption of Nabro Volcano, Eritrea, 2011. *Bull. Volcanol* 77. doi:10.1007/s00445-015-0966-3

Gouin, P. (1979). *Earthquake History of Ethiopia and the Horn of Africa (International Development Research Centre*. Ottawa: Canada.258

Grandin, R., Socquet, A., Binet, R., Klinger, Y., Jacques, E., de Chabalier, J.-B., et al. (2005). September 2005 Manda Hararo-Dabbahu Rifting Event, Afar (Ethiopia): Constraints provided by Geodetic Data. *J. Geophys. Res.* 114. doi:10.1029/2008JB005843

Hamling, I. J., Wright, T. J., Calais, E., Bennati, L., and Lewi, E. (2010). Erratum: Stress Transfer between Thirteen Successive Dyke Intrusions in Ethiopia. *Nat. Geosci* 3, 806. doi:10.1038/ngeo993

Hamlyn, J. E., Keir, D., Wright, T. J., Neuberg, J. W., Goitom, B., Hammond, J. O. S., et al. (2014). Seismicity and Subsidence Following the 2011 Nabro Eruption, Eritrea: Insights into the Plumbing System of an Off-Rift Volcano. *J. Geophys. Res. Solid Earth* 119, 8267–8282. doi:10.1002/2014jb011395

Hébert, H., Deplus, C., Huchon, P., Khanbari, K., and Audin, L. (2001). Lithospheric Structure of a Nascent Spreading ridge Inferred from Gravity Data: The Western Gulf of Aden. *J. Geophys. Res.* 106, 26345–26363. doi:10.1029/2000jb900391

Hofstetter, R., and Beyth, M. (2003). The Afar Depression: Interpretation of the 1960-2000. *Earthquakes*. 155, 715–732. doi:10.1046/j.1365-246x.2003.02080.x

Illsley-Kemp, F., Bull, J. M., Keir, D., Gerya, T., Pagli, C., Gernon, T., et al. (2018). Initiation of a Proto-Transform Fault Prior to Seafloor Spreading, *Geochemistry, Geophysics, Geosystems*. 19, 4744–4756. doi:10.1029/2018GC007947

International Seismological Centre (2020). *On-line Bulletin*.

International Seismological Centre (2010). *Summary of the Bulletin of the International Seismological Centre*, 2013. January -June.

Jacques, E., Kidane, T., Tapponnier, P., Manighetti, I., Gaudemer, Y., Meyer, B., et al. (1989). 2011, Normal Faulting during Theearthquakes in central Afar. Sequential Triggering and Propagation of Rupture along the Dobi Graben. *Bulletin of the Seismological Society of America*. 101, 994–1023. doi:10.1785/0120080317

Jacques, E., King, G. C. P., Tapponnier, P., Ruegg, J. C., and Manighetti, I. (1996). Seismic Activity Triggered by Stress Changes after the 1978 Events in the Asal Rift, Djibouti. *Geophys. Res. Lett.*, 23. , 1996 Djibouti, 2481–2484. Geophysical Research Letters. doi:10.1029/96gl02261

Jacques, E., Ruegg, J. C., Lépine, J. C., Tapponnier, P., King, G. C. P., and Omar, A. (1999). Relocation ofM ≥ 2 Events of the 1989 Dôbi Seismic Sequence in Afar: Evidence for Earthquake Migration. *Geophys. J. Int.* 138, 447–469. doi:10.1046/j.1365-246x.1999.00881.x

Jónsson, S., and Xu, W., 2015, Volcanic Eruptions in the Southern Red Sea during 2007-2013, *The Red Sea, Springer Earth System Sciences*, 175–186. doi:10.1007/978-3-662-45201-1_10

Kebede, F., Kim, W.-Y., and Kuhlanek, O. (1969). Serdo Earthquake Sequence in Central Afar, Ethiopia, Deduced from Teleseismic Body Waves: V. *1989, Dynamic Source Parameters of the* 94, 5603–5614.

Keir, D., Bastow, I. D., Pagli, C., and Chambers, E. L. (2013). The Development of Extension and Magmatism in the Red Sea Rift of Afar. *Tectonophysics* 607, 98–114. doi:10.1016/j.tecto.2012.10.015

Keir, D., Hamling, I. J., Ayele, A., Calais, E., Ebinger, C., Wright, T. J., et al. (2009). Evidence for Focused Magmatic Accretion at Segment Centers from Lateral dike Injections Captured beneath the Red Sea Rift in Afar. *Geology*. 37, 59–62. doi:10.1130/g25147a.1

Kennett, B. L. N., Engdahl, E. R., and Buland, R. (1995). Constraints on Seismic Velocities in the Earth from Traveltimes. *Geophysical Journal International* 122, 108–124. doi:10.1111/j.1365-246x.1995.tb03540.x

Kennett, B. L. N., and Gudmundsson, O. (1996). Ellipticity Corrections for Seismic Phases. *Geophysical Journal International* 127, 40–48. doi:10.1111/j.1365-246x.1996.tb01533.x

La Rosa, A., Pagli, C., Keir, D., Sani, F., Corti, G., Wang, H., et al. (2019). Observing Oblique Slip during Rift Linkage in Northern Afar. *Geophys. Res. Lett.* 46, 10782–10790. doi:10.1029/2019gl084801

Läderach, C., Korger, E. I. M., Schlindwein, V., Müller, C., and Eckstaller, A. (2012). Characteristics of Tectonomagmatic Earthquake Swarms at the Southwest Indian Ridge between 16°E and 25°E. *Geophysical Journal International* 190, 429–441. doi:10.1111/j.1365-246x.2012.05480.x

Le Dain, A. Y., Robineau, B., and Tapponnier, P. (1979). Les effects tectoniques de l'evenement sismique et volcanique de novembre 1978 dans le rift d'Asal-Ghoubbet. *Bull. Soc. Geol. France*. 7, 817–822. doi:10.2113/gssgfbull.s7-xxii.6.817

Lépine, J.-C., and Hirn, A. (1992). Seismotectonics in the Republic of Djibouti, Linking the Afar Depression and the Gulf of Aden. *Tectonophysics* 209, 65–86. doi:10.1016/0040-1951(92)90011-t

Leroy, S., Razin, P., Autin, J., Bache, F., d'Acremont, E., Watremez, L., et al. (2012). From Rifting to Oceanic Spreading in the Gulf of Aden: a Synthesis. *Arab J. Geosci.* 5, 859–901. doi:10.1007/s12517-011-0475-4

Massey, F. J. (1951). The Kolmogorov-Smirnov Test for Goodness of Fit.,. *J. Am. Stat. Assoc.* 46 (No. 253), 68–78. doi:10.1080/01621459.1951.10500769

Matthews, M. V., and Reasenberg, P. A. (1988). Statistical Methods for Investigating Quiescence and Other Temporal Seismicity Patterns. *Pageoph* 126, 357–372. doi:10.1007/bf00879003

Neal, C. A., Brantley, S. R., Antolik, L., Babb, J. L., Burgess, M., Calles, K., et al. (2019). The 2018 Rift Eruption and summit Collapse of Kīlauea Volcano. *Science* 363, 367–374. doi:10.1126/science.aav7046

Nobile, A., Pagli, C., Keir, D., Wright, T. J., Ayele, A., Ruch, J., et al. (2012). Dike-fault interaction during 2004 Dallol intrusion North. edge Erta Ale Ridge (Afar, Ethiopia). *Geophys. Res. Lett.* 39. doi:10.1029/2012gl053152

Ogubazghi, G., Ghebreab, W., and Havskov, J. (2004). Some Features of the 1993 Bada Earthquake Swarm of southeastern Eritrea. *J. Afr. Earth Sci.* 38, 135–143. doi:10.1016/j.jafrearsci.2003.12.002

Pagli, C., Wright, T. J., Ebinger, C. J., Yun, S.-H., Cann, J. R., Barnie, T., et al. (2012). Shallow Axial Magma Chamber at the Slow-Spreading Erta Ale Ridge. *Nat. Geosci* 5, 284–288. doi:10.1038/ngeo1414

Pagli, C., Yun, S.-H., Ebinger, C., Keir, D., and Wang, H. (2019). Strike-slip Tectonics during Rift Linkage. *v* 47, 31–34. doi:10.1130/g45345.1

Passarelli, L., Heryandoko, N., Cesca, S., Rivalta, E., Rasmid, S., Dahm, T., et al. (2018a). Magmatic or Not Magmatic? the 2015–2016 Seismic Swarm at the Long-Dormant Jailolo Volcano, West Halmahera, Indonesia. *Frontiers in Earth Science*. 6, 1–17. doi:10.3389/feart.2018.00079

Passarelli, L., Rivalta, E., Cesca, S., and Aoki, Y. (2015). Stress Changes, Focal Mechanisms, and Earthquake Scaling Laws for the 2000 dike at Miyakejima (Japan). *J. Geophys. Res. Solid Earth* 120, 4130–4145. doi:10.1002/2014jb011504

Passarelli, L., Rivalta, E., Jónsson, S., Hensch, M., Metzger, S., Jakobsdóttir, S. S., et al. (2018b). Scaling and Spatial Complementarity of Tectonic Earthquake Swarms. *Earth Planet. Sci. Lett.* 482, 62–70. doi:10.1016/j.epsl.2017.10.052

Peterson, D. E., Garibaldi, N., Keranen, K., Tikoff, B., Miller, C., Lara, L. E., et al. (2020). Active Normal Faulting, Diking, and Doming Above the Rapidly Inflating Laguna del Maule Volcanic Field, Chile, Imaged With CHIRP, Magnetic, and Focal Mechanism Data. *J. Geophys. Res. Solid Earth* 125 (8), e2019JB019329. doi:10.1029/2019jb019329

Reasenberg, P. A., and Simpson, R. W. (1992). Response of Regional Seismicity to the Static Stress Change Produced by the Loma Prieta EarthquakeAdvancement of Science. *Science* 255, 1687–1690. doi:10.1126/science.255.5052.1687 http://www.jstor.org/stable/2876633.

Reasenberg, P. (1985). Second-order Moment of central California Seismicity, 1969-1982. *J. Geophys. Res.* 90 (B7), 5479–5495. doi:10.1029/JB090iB07p05479

Reed, C. A., Almadani, S., Gao, S., Elsheikh, A., Cherie, S., Abdelsalam, M., et al.., 2014, Receiver Function Constraints on Crustal Seismic Velocities and Partial Melting beneath the Red Sea Rift and Adjacent Regions, Afar Depression. Journal of Geophysical Research: Solid Earth119(3), doi:10.1002/2013JB010719

Roland, E., and McGuire, J. J. (2009). Earthquake Swarms on Transform Faults. *Geophysical Journal International* 178, 1677–1690. doi:10.1111/j.1365-246x.2009.04214.x

Ruch, J., Wang, T., Xu, W., Hensch, M., and Jónsson, S. (2016). Oblique Rift Opening Revealed by Reoccurring Magma Injection in central Iceland. *Nat. Commun.* 7. doi:10.1038/ncomms12352

Schlindwein, V. (2012). Teleseismic Earthquake Swarms at Ultraslow Spreading Ridges. *Indicator for Dyke Intrusions?* 190, 442–456. doi:10.1111/j.1365-246x.2012.05502.x

Shuler, A., and Nettles, M. (2012). Earthquake Source Parameters for the 2010 Western Gulf of Aden Rifting Episode. *Geophysical Journal International* 190, 1111–1122. doi:10.1111/j.1365-246x.2012.05529.x

Sykes, L. R. (1970). Earthquake Swarms and Sea-Floor Spreading. *J. Geophys. Res.* 75, 6598–6611. doi:10.1029/jb075i032p06598

Vidale, J. E., and Shearer, P. M. (2006). A Survey of 71 Earthquake Bursts across Southern California: Exploring the Role of Pore Fluid Pressure Fluctuations and Aseismic Slip as Drivers: Journal of Geophysical Research. *Solid Earth,*. 111, 1–12. doi:10.1029/2005jb004034

Viltres, R., Jónsson, S., Ruch, J., Doubre, C., Reilinger, R., Floyd, M., et al. (2018). Spatio-temporal Stress Changes Caused by Rifting Episodes in the southernRed Sea Region. *Geophys. Res. Abstract* 20, EGU2018–17821. 2018EGU General Assembly 2018. doi:10.1093/gji/ggaa109

Viltres, R., Jónsson, S., Ruch, J., Doubre, C., Reilinger, R., Floyd, M., et al. (2020). Kinematics and Deformation of the Southern Red Sea Region from GPS Observations. *Geophysical Journal International* 221, 2143–2154. doi:10.1093/gji/ggaa109

Wright, T. J., Ebinger, C., Biggs, J., Ayele, A., Yirgu, G., Keir, D., et al. (2006). Magma-maintained Rift Segmentation at continental Rupture in the 2005 Afar Dyking Episode. *Nature* 442, 291–294. doi:10.1038/nature04978

Xu, W., Ruch, J., and Jónsson, S. (2015). Birth of Two Volcanic Islands in the Southern Red Sea. *Nature Communications*. 6, 7104,. doi:10.1038/ncomms8104

Zhuang, J., Harte, D., Werner, M. J., Hainzl, S., and Zhou, S., 2012, Basic Models of Seismicity: Temporal Models, Community Online Resource for Statistical Seismicity Analysis, doi:10.5078/corssa-79905851 Available at http://www.corssa.org.

Zwaan, F., Corti, G., Sani, F., Keir, D., Muluneh, A. A., Illsley-Kemp, F., et al. (2020). Structural Analysis of the Western Afar Margin, East Africa. *Evidence*

for Multiphase Rotational Rifting: Tectonics. 39, 1–25. doi:10.1029/2019tc006043

Conflict of Interest: The authors declare that the research was conducted in the absence of any commercial or financial relationships that could be construed as a potential conflict of interest.

Publisher's Note: All claims expressed in this article are solely those of the authors and do not necessarily represent those of their affiliated organizations, or those of the publisher, the editors and the reviewers. Any product that may be evaluated in this article, or claim that may be made by its manufacturer, is not guaranteed or endorsed by the publisher.

Copyright © 2021 Ruch, Keir, Passarelli, Di Giacomo, Ogubazghi and Jónsson. This is an open-access article distributed under the terms of the Creative Commons Attribution License (CC BY). The use, distribution or reproduction in other forums is permitted, provided the original author(s) and the copyright owner(s) are credited and that the original publication in this journal is cited, in accordance with accepted academic practice. No use, distribution or reproduction is permitted which does not comply with these terms.

Advantages of publishing in Frontiers

OPEN ACCESS
Articles are free to read for greatest visibility and readership

FAST PUBLICATION
Around 90 days from submission to decision

HIGH QUALITY PEER-REVIEW
Rigorous, collaborative, and constructive peer-review

TRANSPARENT PEER-REVIEW
Editors and reviewers acknowledged by name on published articles

Frontiers
Avenue du Tribunal-Fédéral 34
1005 Lausanne | Switzerland

Visit us: www.frontiersin.org
Contact us: frontiersin.org/about/contact

REPRODUCIBILITY OF RESEARCH
Support open data and methods to enhance research reproducibility

DIGITAL PUBLISHING
Articles designed for optimal readership across devices

FOLLOW US
@frontiersin

IMPACT METRICS
Advanced article metrics track visibility across digital media

EXTENSIVE PROMOTION
Marketing and promotion of impactful research

LOOP RESEARCH NETWORK
Our network increases your article's readership